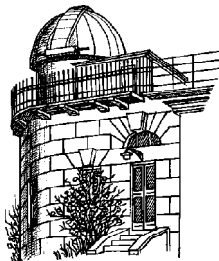


ODESSA ASTRONOMICAL PUBLICATIONS

Volume 26 Issue 2
(2013)



Odessa
«AstroPrint»

FOREWORD

This issue of the “Odessa Astronomical Publications” (vol. 26 issue 2) gathered articles that were presented at the XIII Odessa International Astronomical Gamow’s Conference-School “ASTRONOMY AND BEYOND: ASTROPHYSICS, COSMOLOGY AND GRAVITATION, COSMOMICROPHYSICS, RADIO-ASTRONOMY AND ASTROBIOLOGY”.

The Conference was organized by I.I.Mechnikov Odessa National University on August 19-25, 2013. Together with University, the following organizations took part in the Conference organization: Radio-astronomical Institute of the National Academy of Science of Ukraine and its Odessa Observatory branch “URAN-4”, the Department of Astronomy and Astronomical Observatory of I.I.Mechnikov Odessa National University, the Ukrainian Astronomical Association (Kiev), the Euro-Asian Astronomical Society (Moscow), the Odessa Astronomical Society, the Southern Scientific Center of the National Academy of Science of Ukraine. Co-chairs of the SOC were G.S.Bisnovatyi-Kogan (Russia) and V.M.Shulga (Ukraine), vice-chairs – A.I.Zhuk (Ukraine) and M.I.Ryabov (Ukraine).

The scientific program included the following sections: “Cosmology, Cosmomicrophysics and Gravitation; Astrophysics” (subsection “Virtual observatories”); “Chemical and dynamical evolution stars and galaxies”; “Radio-astronomy”; “Sun and Solar System” (subsection “Astrobiology”); Poster sessions and subsection “System and methods of data processing”; “Ukraine Planetariums”.

About 110 scientists from Ukraine, Russia, Belarus, Moldova, Kazakhstan, Czech Republic, Estonia and Armenia participated in the Conference-School. During the Plenary sessions, 20 talks were presented, 68 reports and 15 posters were presented during the regular sections. In addition, the several discussions were organized. Among them: About a current state and perspective of development of astronomy in Ukraine, Russia and the Eastern Europe (chair Ya.S.Yatskiv); Models and observations of active galaxies and quasars (chairs G.S.Bisnovatyi-Kogan, N.G.Bochkarev); Sun in a maximum 24 cycles and perspectives of solar-terrestrial connections for low cycles of activity” (chairs V.N.Obridko, L.I.Miroshnichenko).

Editor-in-Chief
S.M. Andrievsky

Vice-Chair SOC
M.I.Ryabov



CONTENTS

Foreword.....	138
Contents	139

PLENARY SESSION

DARK MATTER AND DARK ENERGY IN THE COMA CLUSTER OF GALAXIES Bisnovatyi-Kogan G.S., Chernin A.D.	142
MAGNETOROTATIONAL SUPERNOVAE AND MAGNETO-DIFFERENTIAL-ROTATIONAL INSTABILITY Moiseenko S.G., Bisnovatyi-Kogan G.S.	150
SEARCH FOR AND IDENTIFICATION OF GRAVITON EXCHANGE EFFECTS IN DRELL-YAN PROCESS AT LARGE HADRON COLLIDER Pankov A.A., Serenkova I.A., Tsytrinov A.V.	155
DATA PROCESSING PIPELINE FOR DECAMETER PULSAR/TRANSIENT SURVEY Vasylieva I.Y., Zakharenko V.V., Zarka P., Ulyanov O.M., Shevtsova A.I., Serechkina A.A.	159
ASTROCHEMISTRY OF STAR FORMATION Wiebe D.S., Kochina O.V.	162

COSMOLOGY, COSMOMICROPHYSICS AND GRAVITATION

PROPERTIES OF THE GRAVITATIONAL LENS MAPPING IN THE VICINITY OF A CUSP CAUSTIC Alexandrov A.N., Zhdanov V.I., Koval S.M.	169
THE KINEMATICS OF REGULAR STRUCTURES Anisimova G.B.	172
COMPARISON OF OPTICAL AND X-RAY MASS ESTIMATES OF THE CHANDRA GALAXY CLUSTERS AT $Z < 0.1$ Babyk Iu.V., Vavilova I.B.	175
SCHWARZSCHILD-DE SITTER AND MECHANICAL APPROACHES COMPARISON WITH RESPECT TO DARK MATTER HALOS Brilenkov R., Eingorn M., Zhuk A.	179
DARK SIDE OF QUARK BAG MODEL Brilenkov M., Eingorn M., Jenkovszky L., Zhuk A.	180
TWO-BODY PROBLEM IN KALUZA-KLEIN MODELS WITH RICCI-FLAT INTERNAL SPACES Chopovsky A.	183
THE NEW GALAXY SAMPLE FROM SDSS DR9 AT $0.003 \leq Z \leq 0.1$ Dobrycheva D.V.	187
SCALAR PERTURBATIONS IN $f(R)$ -COSMOLOGIES Eingorn M., Novak J.	190
MOTION TYPES OF NEUTRAL TEST PARTICLES IN THE FIELD OF CHARGED OBJECT IN GENERAL RELATIVITY AND THEIR CLASSIFICATION Gladush V.D., Kulikov D.A.	191
QUANTUM SPECTRUM ON THE NAKED REISSNER-NORDSTRÖM BACKGROUND Gladush V.D., Kulikov D.A.	194
DYNAMICAL FRICTION IN THE LOCAL GROUP Kudinova A.V.	197
ONE-DIMENSIONAL SIMULATIONS OF INHOMOGENEITY GROWTH IN PRESSURELESS GRAVITATING MATTER Zhdanov V.I., Sliusar V.M.	201

ASTROPHYSICS

COMPARATIVE ANALYSIS OF NUMERICAL METHODS OF DETERMINATION OF PARAMETERS OF BINARY STARS. CASE OF SPHERICAL COMPONENTS Andronov I.L., Tkachenko M.G.	204
BVRI – OBSERVATION OF AGN NGC 4151 IN 2009-2011 Artamonov B., Oknyanskij V., Ezhkova O., Metlova N.	207
NUMERICAL MODELLING OF GAS DYNAMIC STRUCTURES IN SPIRAL GALAXIES Lugovskiy A., Filistov E.	209

VARIABILITY OF NGC4151 DURING 2008-2013 Oknyanskij V.L., Metlova N.V., Artamonov B.P., Lyuty A.V., Lyuty V.M.	212
PHOTOMETRICAL STUDY OF CLOSE BINARY SYSTEM V841 Cyg Sergienko O.G., Bodryagin D.V., Panko E.A.	214
THE IONIZED GAS AROUND STARFORMING GALAXIES Vasiliev E.O., Ryabova M.V., Shchekinov Yu.A.	219
Subsection Virtual observatories are practice of application	
FLATBED SCANNERS IN GOLOSIIV PLATE ARCHIVE DIGITIZATION Andruk V., Pakuliak L.	222
INTERACTIVE POSSIBILITY OF WORKING WITH A DIGITAL VERSION OF THE JOURNAL "IZVESTIA OF THE CRAO" Bondar' N., Gorbunov M., Shlyapnikov A.	223
DIGITAL ARCHIVE OF UKRVO: THE POSITIONAL ACCURACY OF MINOR PLANETS DETERMINATIONS Golovnya V., Andruk V.	226
EXAMPLES OF DIGITAL VERSIONS OF THE CRAO SPECTRAL PHOTOGRAPHIC ARCHIVES Gorbunov M., Shlyapnikov A.	229
DEVELOPMENT OF MYKOLAIV VIRTUAL OBSERVATORY Mazhaev A., Protsyuk Yu.	233
UKRVO JOINT DIGITAL ARCHIVE: CURRENT STATUS AND PERSPECTIVES Pakuliak L., Golovnya V., Virun N., Kazantseva L., Kashuba S.	236
THE KYIV MERIDIAN AXIAL CIRCLE' OBSERVATIONAL ARCHIVE AS THE UKRVO SCIENTIFIC RESOURCE Zolotukhina A.	239
RADIO-ASTRONOMY	
ANALYSIS OF THE VARIABILITY AND THE SPECTRUM OF PERIODS OF EXTRAGALACTIC SOURCE OJ 287 IN THE RADIO WAVES Donskykh A., Ryabov M., Suharev A., Aller M.	240
OBSERVATION ON THE RADIO TELESCOPE URAN-4 OF RADIO SOURCES, CONNECTED WITH THE CORONAL MASS EJECTION ON THE SUN Galanin V.V., Derevjagin V.G., Kravetz R.O.	243
PECULIARITIES OF SPORADIC E _s LAYER IN THE PERIOD OF SOLAR CYCLE ACTIVITY MAXIMUM Kravetz R.O., Galanin V.V.	245
THE TIMING SCALE OF THE STEEP-SPECTRUM SOURCES Miroshnichenko A.P.	248
STUDY OF SATURN ELECTROSTATIC DISCHARGES IN A WIDE RANGE OF TIME SCALES Mylostna K., Zakharenko V., Konovalenko A., Kolyadin V., Zarka P., Griebmeier J.-M., Litvinenko G., Sidorchuk M., Rucker H., Fischer G., Cecconi B., Coffre A., Denis L., Nikolaenko V., Shevchenko V.	251
DATA PROCESSING CENTER FOR RADIOASTRON PROJECT HARDWARE OPTIMIZATION Shatskaya M., Abramov A., Guirin I., Isaev E., Kostenko V., Likhachev S., Pimakov A., Seliverstov S., Fedorov N.	254
STUDY ON THE VARIABILITY OF BLAZAR 3C345 IN RADIO FREQUENCY RANGE Sukharev A.L.	256
THE EVOLUTION OF THE ACCELERATION MECHANISMS OF COSMIC RAYS AND RELATIVISTIC ELECTRONS IN RADIO GALAXIES Tsvyk N.	260
SUN AND SOLAR SYSTEM	
DAILY AND SHORT-PERIOD CHANGES DYNAMICS OF THE EARTH'S MAGNETIC FIELD IN THE 24-th CYCLE OF SOLAR ACTIVITY ACCORDING TO MAGNETIC OBSERVATORY "ODESSA" Guglya L.I., Orlyuk M.I., Ryabov M.I., Suharev A.L., Orliuk I.M.	263
STATISTICAL ANALYSIS OF THE MAGNETIC FIELD MEASUREMENTS Kozak L., Lui A., Savin S.	268

DIFFERENT MODES OF TURBULENCE IN THE ACTIVE REGIONS OF THE SOLAR PHOTOSPHERE	
Kozak L.V., Kostik R.I., Cheremnykh O.K.	271
ABOUT EXPANSION OF TERRESTRIAL RADIO PHYSICAL METHODS FOR DETECTION OF ULTRA-HIGH-ENERGY COSMIC RAY	
Kozhukhar V.B., Lytvynenko I.O., Lytvynenko O.A.	274
DEVELOPMENT OF 23 CYCLES ACTIVITY IN NORTHERN AND SOUTHERN HEMISPHERES OF THE SUN	
Ryabov M.I., Sukharev A.L., Lukashuk S.A.	276
WHETHER THERE IS AN ASTROPHYSICAL SOURCE IN THE OSCILLATIONS OF GEOPHYSICAL PARAMETERS WITH A PERIOD OF 160 MINUTES?	
Samsonov S., Miroshnichenko L., Kotov V., Skryabin N., Timofeev V., Baishev D.	279
MONITORING OF THE INOPERATIVE ENVISAT SATELLITE'S BEHAVIOUR	
Shakun L., Koshkin N., Korobeynikova E., Melikyants S., Strakhova S., Terpan S.	282
GEOPHYSICAL EFFECTS OF THE EARTH'S MONTHLY MOTION	
Sidorenkov N.S., Zhigailo T.S.	285
ON THE PROPAGATION OF RADIO EMISSION IN THE CROWN OF THE QUIET SUN WITH MAGNETIC FIELD	
Tsvyk N.	288
SEA LEVEL AND GLOBAL EARTH TEMPERATURE CHANGES HAVE COMMON OSCILLATIONS	
Zotov L.V.	289
Subsection Astrobiology	
FEATURES OF VASCULAR ENDOTHELIAL FUNCTIONING IN HEALTHY PERSONS IN DIFFERENT PERIODS OF SOLAR ACTIVITY	
Parshina S.S., Tokaeva L.K., Dolgova E.M., Afanas'yeva T.N., Strelnikova O.A.	292
ENDOTHELIAL DYSFUNCTION AND BLOOD VISCOSITY IN PATIENTS WITH UNSTABLE ANGINA IN DIFFERENT PERIODS OF A SOLAR ACTIVITY	
Parshina S.S., Tokayeva L.K., Dolgova E.M., Afanasyeva T.N., Strelnikova O.A.	294
SPACE WEATHER AND A STATE OF CARDIOVASCULAR SYSTEM OF HUMAN BEING WITH A WEAKENED ADAPTATION SYSTEM	
Samsonov S.N.	297
SPACE WEATHER AND THE STATE OF CARDIOVASCULAR SYSTEM OF A HEALTHY HUMAN BEING	
Samsonov S.N., Manykina V.I., Krymsky G.F., Petrova P.G., Palshina A.M., Vishnevsky V.V.	300
STUDYING OF INFLUENCE OF THE LOW-FREQUENCY ELECTROMAGNETIC FIELD ON DNA MOLECULES IN WATER SOLUTIONS	
Tekutskaya E.E., Baryshev M.G.	303
Subsection Systems and methods of data processing	
INFORMATION TELECOMMUNICATIONS OF PUSHCHINO RADIO ASTRONOMY OBSERVATORY, ASTRO SPACE CENTER OF LEBEDEV PHYSICAL INSTITUTE	
Dumsky D.V., Isaev E.A., Samodurov V.A., Likhachev S.F., Shatskaya M.V., Kitaeva M.A., Zaytcev A.Yu., Ovchinnikov I.L., Kornilov V.V.	305
PROSPECTS OF CLOUDY TECHNOLOGIES IN THE SOLUTION OF THE TASK OF THE ANALYSIS OF LARGE VOLUMES OF THE DATA OBTAINED IN ASTRONOMICAL SUPERVISION	
Isaev E.A., Kornilov V.V., Samodurov V.A., Tarasova A.A.	306
TRANSMISSION OF LARGE VOLUME OF ASTRONOMICAL DATA	
Isaev E.A., Kornilov V.V., Samodurov V.A., Tarasov P.A., Tarasova J.A.	308
MODULAR DATA CENTER FOR SCIENTIFIC DATA PROCESSING	
Isaev E.A., Lusakov S.V., Amzarakov M.B., Suhov R.R., Isaev K.A.	309
NEW SKILLS OF RADIO ASTRONOMY DATA CENTER (RADC) AT PRAO ASC LPI	
Samodurov V.A., Kitaeva M.A., Isaev E.A., Dumsky D.V., Pugachev V.D., Logvinenko S.V., Zaitsev A.U.	311
EFFECT OF ROTATION ON CHANGES OF INTERFERENCE FRINGES IN THE MICHELSON INTERFEROMETER	
Shahrukhanov O.S.	315

PLENARY SESSION

DARK MATTER AND DARK ENERGY IN THE COMA CLUSTER OF GALAXIES

G.S. Bisnovatyi-Kogan^{1,2}, A.D. Chernin³

¹Space Research Institute RAS., Moscow, Russia, *gkogan@rssi.ru*

²National Research Nuclear University MEPhI, Moscow, Russia,

³Sternberg Astronomical Institute, MSU, Moscow, Russia, *artur.chernin@gmail.com*

ABSTRACT. The Coma cluster of galaxies is studied as a giant aggregation of dark matter and baryons embedded in the dark energy background. Key theory relations for the local dark-energy effects are given. On the basis of the theory and current observational data, three characteristic masses of the Coma cluster are introduced and evaluated. A new dark matter mass profile is suggested and used to find the upper bounds on the total mass and total size of the cluster. A solution is obtained for the hydrodynamic outflow of the polytropic gas from the gravitating center, in presence of the uniform Dark Energy (DE). The main property of the wind in presence of DE is its unlimited acceleration after passing the critical point. In application of this solution to the winds from galaxy clusters we suggest that collision of the strongly accelerated wind with another galaxy cluster, or with another galactic cluster wind could lead to the formation of a highest energy cosmic rays.

Key words: galaxies: the Coma Cluster, dark matter, dark energy, gas outflow

1. Introduction

We study the famous Coma cluster of galaxies where dark matter was originally found by Zwicky (1933,1937). Zwicky used the virial theorem to show that non-luminous dark matter dominated the cluster on megaparsec scales. He estimated the cluster total mass as $3 \times 10^{14} M_{\odot}$, if to normalize his figure to the presently adopted value of the Hubble constant $h = 0.71$ which is used hereafter. A half-century later, The & White (1986) found an order of magnitude larger value, $2 \times 10^{15} M_{\odot}$, with a modified version of the virial theorem. Hughes (1989, 1998) obtained a similar value $(1 - 2) \times 10^{15} M_{\odot}$ with X-ray data under the assumption that the cluster hot intergalactic gas is in hydrostatic equilibrium. With a similar assumption, Colles (2006) reports the mass $4.4 \times 10^{14} M_{\odot}$ inside the radius of 1.4 Mpc. A weak-lensing analysis gave the mass of $2.6 \times 10^{15} M_{\odot}$ (Kubo et al. 2007) within 4.8

Mpc radius. Geller et al. (1999, 2011) extended mass estimates to the outskirts of the cluster using the caustic technique (Diaferio & Geller 1997, Diaferio 1999) and found the mass $2.4 \times 10^{15} M_{\odot}$ within the 14 Mpc radius. Taken the figures at face value, one may see that the mass within 14 Mpc appears to be smaller than the mass within 4.8 Mpc. Most probably, this is due to uncertainties in mass determination. Indeed, the 2σ error is $1.2 \times 10^{15} M_{\odot}$ in Geller's et al. (1999,2011) data, and within this uncertainty, the result does not contradict the small-radius data.

In this paper, we consider the Coma cluster as a giant gravitationally bound aggregation of dark matter and baryons embedded in the uniform background of dark energy. Is antigravity produced by dark energy significant in the volume of the cluster? Does it alternate the structure of the cluster? Can antigravity put limits on the major gross parameters of the system? Addressing these questions, we continue our efforts to clarify and quantify the local gravity-antigravity interplay on the spatial scales of $\sim 1 - 10$ Mpc (Chernin 2001,2008,2013, Bisnovatyi-Kogan and Chernin 2012).

A solution is presented of hydrodynamic equations for the winds from galactic clusters in presence of DE. It is a generalized solution for the outflows from the gravitating body, obtained for solar and stellar winds by Stanyukovich (1955) and Parker (1963), to the presence of DE. It implies significant changes in the structure of solutions describing galactic winds, what had been investigated in the paper of Bisnovatyi-Kogan and Merafina (2013).

2. Local antigravity produced by dark energy

The local dynamical effects of dark energy can adequately be described in terms of Newtonian mechanics, if the force field it produces is weak in the standard sense. Such an approach borrows from General Relativity the major result: the effective gravitating density of a uniform medium is given by the sum

$$\rho_{\text{eff}} = \rho + 3P, \quad (1)$$

where ρ and P is the density and pressure of a uniform fluid (the speed of light is 1 hereafter). The dark energy equation of state is $P_{DE} = -\rho_{DE}$, and its effective gravitating density is negative:

$$\rho_{DEeff} = \rho_{DE} + 3P_{DE} = -2\rho_{DE} < 0, \quad (2)$$

which means that dark energy produces antigravity.

Einstein's "law of universal antigravity" says that two bodies imbedded in the dark energy background are repulsed from each other with a force that is proportional to the distance r between them:

$$F_E(r) = -\frac{4\pi G}{3}\rho_{DEeff}r^3/r^2 = +\frac{8\pi G}{3}\rho_{DE}r. \quad (3)$$

Eq.(3) may be use to describe the force field produced by a spherical matter mass M_M and the uniform dark energy background in which the mass is embedded:

$$F(R) = F_N(R) + F_E(R) = -G\frac{M_M}{R^2} + \frac{8\pi G}{3}\rho_{DE}R. \quad (4)$$

Eq.4 shows that the net force $F(R)$ is zero at the distance

$$R = R_{ZG} = \left[\frac{M_M}{\frac{8\pi}{3}\rho_{DE}}\right]^{1/3} = 11\frac{M_M}{10^{15}M_\odot} \text{ Mpc}. \quad (5)$$

Here the observed value of the dark energy density $\rho_{DE} = 0.7 \times 10^{-29} \text{ g/cm}^3$ is used. The critical physical parameter R_{ZG} is the zero-gravity radius (Chernin 2001). Gravity dominates at distances $R < R_{ZG}$, while antigravity is stronger than gravity at $R > R_{ZG}$.

3. Three masses of the cluster

The presence of dark energy in the volume of a cluster like the Coma cluster may be quantified by the effective gravitating mass of dark energy within a given clustrocentric radius R :

$$M_{DE}(R) = \frac{4\pi}{3}\rho_{DEeff}R^3 = -\frac{8\pi}{3}\rho_{DE}R^3 \quad (6)$$

$$-0.85 \times 10^{12} \left[\frac{R}{1 \text{ Mpc}}\right]^3 M_\odot.$$

The matter (dark matter and baryons) content of the cluster is characterized (in the spherical approximation) by the mass $M_M(R)$ inside the radius R :

$$M_M(R) = 4\pi \int \rho(R)R^2 dR. \quad (7)$$

Here $\rho(R)$ is the matter density within the sphere of the radius R inside the cluster. The sum

$$M_G(R) = M_M(R) + M_{DE}(R), \quad (8)$$

is the total gravitating mass within the radius R . Since dark matter and dark energy reveal themselves in observations via their gravitation only, it is the mass $M_G(R)$ that is only available for astronomical measurements. Identifying $M_G(R)$ with the value $2.4 \times 10^{15} M_\odot$ found in the Coma observations (Geller et al.1999) for the radius $R = 14 \text{ Mpc}$, we find for this radius:

$$M_{DE} = -2.3 \times 10^{15} M_\odot, \quad M_M = 4.7 \times 10^{15} M_\odot \simeq 2M_G. \quad (9)$$

As we see, the absolute value of the dark energy mass M_{DE} is (almost exactly) equal to the gravitating mass M_G at $R = 14 \text{ Mpc}$; as a result, the matter mass $M_M \simeq 2M_G \simeq 2|M_{DE}|$, within this radius. This implies that the antigravity effects are strong indeed at large radii of the Coma cluster.

4. Matter mass profile

Our estimate of the Coma matter mass within $R = 14 \text{ Mpc}$ (Eq.11) may be compared with estimates following from traditional matter density profiles for dark halos. The widely used NFW profile (Navarro et al. 1999) is

$$\rho = \frac{4\rho_s}{\frac{R}{R_s}(1 + \frac{R}{R_s})^2}, \quad (10)$$

where R is again the distance from the cluster center, $\rho_s = \rho(R_s)$, and R_s are constant parameters. At small radii, $R \ll R_s$, the matter density goes to infinity, $\rho \propto 1/R$ as R goes to zero. At long distances, $R \gg R_s$, the density slope is $\rho \propto 1/R^3$. With this profile, the matter mass profile is

$$M_M(R) = 16\pi\rho_s R_s^3 \left[\ln(1 + R/R_s) - \frac{R/R_s}{1 + R/R_s}\right]. \quad (11)$$

To find the parameters ρ_s and R_s , we may use the small-radii data from Sec.1: $M_1 = 4.4 \times 10^{14} M_\odot$ at $R_1 = 1.4 \text{ Mpc}$, $M_2 = 2.6 \times 10^{15} M_\odot$ at $R_2 = 4.8 \text{ Mpc}$. At these radii, the gravitating masses are nearly equal to the matter masses there. The values of M_1, R_1 and M_2, R_2 , together with Eq.11 lead to two logarithmic equations for the two parameters of the profile, which can easily be solved: $R_s = 4.7 \text{ Mpc}$, $\rho_s = 1.8 \times 10^{-28} \text{ g/cm}^3$. Then we find the matter mass within $R = 14 \text{ Mpc}$,

$$M_M \simeq 8.7 \times 10^{15} M_\odot, \quad (12)$$

to be considerably larger (over 70%) than given by Eq.11.

Another popular ρ density profile (Hernquist 1990) is

$$\rho(R) \propto \frac{1}{R(R + \alpha)^3}. \quad (13)$$

Its small-radius behavior is the same as in the NFW profile: $\rho \rightarrow \infty$, as R goes to zero. The slope at large

radii is different: $\rho \propto 1/R^4$. The corresponding mass profile is

$$M_M(R) = M_0 \left[\frac{R}{R + \alpha} \right]^2. \quad (14)$$

The parameters M_0 and α can be found from the same data as above on M_1, R_1 and M_2, R_2 : $M_0 = 1.4 \times 10^{16} M_\odot$, $\alpha = 6.4$ Mpc, giving another value for the mass within 14 Mpc:

$$M_M = 6.6 \times 10^{15} M_\odot, \quad R = 14 \text{ Mpc}. \quad (15)$$

Now the difference from the figure of Eq.9 is about 40%.

In a search for a more suitable mass profile for the Coma cluster, we may try the following simple new relation:

$$M_M(R) = M_* \left[\frac{R}{R + R_*} \right]^3. \quad (16)$$

This mass profile comes from the density profile:

$$\rho(R) = \frac{3}{4\pi} M_* R_* (R + R_*)^{-4}. \quad (17)$$

The density goes to a constant as R goes to zero; at large radii, $\rho \propto 1/R^4$, as in Hernquist's profile.

The parameters M_* and R_* are found again from the data for the radii of 1.4 and 4.8 Mpc: $M_* = 8.7 \times 10^{15} M_\odot$, $R_* = 2.4$ Mpc. The new profile leads to a lower matter mass at 14 Mpc:

$$M_M = 5.4 \times 10^{15} M_\odot, \quad (18)$$

which is equal to the Eq.9 value within 15% accuracy.

5. Upper limits and beyond

The strong effect of dark energy at large radii puts an absolute upper limit on the total size of the cluster. The system can be gravitationally bound only if gravity dominates in its volume (as we mentioned above). In terms of the three different masses, this criterion may be given in the form

$$M_G \geq 0, \quad M_M \geq |M_{DE}|. \quad (19)$$

Both inequalities are met, if the system is not larger than its zero-gravity radius (Eq.5): $R \leq R_{\max} = R_{ZG}$.

If the radius of a system with matter mass M_M is equal to the maximal radius $R = R_{\max}$, its mean matter density (see Bisnovatyi-Kogan & Chernin 2012) is

$$\langle \rho_M \rangle = \frac{M_M}{\frac{4\pi}{3} R_{ZG}^3} = 2\rho_{DE}. \quad (20)$$

This relation and the new profile (Eq.16) now lead to R_{\max} and the corresponding matter mass, $M_{\max} = M_M(R_{\max})$:

$$\begin{aligned} R_{\max} &= R_{ZG} = 20 \text{ Mpc}, \\ M_{\max} &= M_M(R_{ZG}) = 6.2 \times 10^{15} M_\odot. \end{aligned} \quad (21)$$

The upper mass limit evaluated by Eq.(21) is consistent with the theory of large-scale structure formation that claims the range $2 \times 10^{15} < M < 10^{16} M_\odot$ for the most massive bound objects in the Universe (Holz & Perlmutter 2012, Busha et al. 2005)

For comparison, the two profiles mentioned above lead to somewhat larger values of the sizes and mass:

$$\begin{aligned} R_{\max} &= 25 \text{ Mpc}, \quad M_{\max} = 1.5 \times 10^{16} M_\odot \text{ (NFW)}, \\ R_{\max} &= 22 \text{ Mpc}, \quad M_{\max} = 9.1 \times 10^{15} M_\odot \text{ (Hernquist)}. \end{aligned} \quad (22)$$

Our studies of nearby systems like the Local Group and the Virgo and Fornax clusters (Karachentsev et al. 2003, Chernin 2008, Chernin et al. 2006, 2007, 2010, 2012a,b, Chernin 2013) show that their sizes are near the zero-gravity radii. The systems are located in the gravity-dominated regions ($R < R_{ZG}$), and the outflows of galaxies are observed at $R > R_{ZG}$. Basing on these examples, we may suggest that the Coma cluster has the maximal possible size and mass given by Eq.(21). If this is the case, the mean matter density of the system = twice the dark energy density. This prediction (Merafina et al. 2012; Bisnovatyi-Kogan & Chernin 2012) does not depend on the density profile assumed for the cluster. Basing on this result and using the cosmological matter density parameter $\Omega_m = 0.27$, we may calculate the mean matter density contrast in the cluster:

$$\delta = \frac{\langle \rho \rangle - \rho_m}{\rho_m} = \frac{2\Omega_{DE}}{\Omega_m} - 1 = 4.2. \quad (24)$$

An observational confirmation of this figure would directly indicate the key role of dark energy in the formation of the structure of the system.

Another general prediction based on the same analogy with the earlier studied groups and clusters concerns the galaxies in the environment of the Coma cluster. We may assume that beyond the Coma size limit, at $R > R_{\max} = R_{ZG}$, there are galaxies that are not gravitationally bound with the cluster and move away from it. They may form a quasi-regular outflow in the area of the dark energy domination. The radial motions of the outflow galaxies are controlled by the equation of motion that takes into account both gravity and antigravity forces given by Eqs.(4):

$$\ddot{R} = -G \frac{M_M}{R^2} + \frac{8\pi G}{3} \rho_{DE} R, \quad (25)$$

where M_M is the total matter mass of the cluster and $R \geq R_{ZG}$.

The first integral of the equation of motion is the mechanical energy of a galaxy (per unit mass):

$$E = \frac{1}{2} V^2 - \frac{GM_M}{R} - \frac{4\pi G}{3} \rho_{DE} R^2. \quad (26)$$

It is seen from Eq.(25) that at large distances, at $R \gg R_{\max} = R_{ZG}$, the flow tends to the regular

kinematical structure with the Hubble linear velocity-distance relation:

$$V(R) \rightarrow H_{\Lambda} R, \quad (27)$$

where $H_{\Lambda} = [\frac{8\pi G}{3}\rho_{\text{DE}}]^{1/2} = 61 \text{ km/s/Mpc}$ depends on the dark energy density only.

It is also seen from Eq.(26) that at all distances $R \geq R_{\text{max}} = R_{\text{ZG}}$ the outflow velocities are higher than a critical value:

$$V \geq V_{\text{esc}} = H_{\Lambda} R [1 + 2(R_{\text{ZG}}/R)^3 - 3(R_{\text{ZG}}/R)^2]^{1/2}. \quad (28)$$

The value V_{esc} corresponds to the minimal mechanical energy

$$E_{\text{esc}} = -\frac{3}{2} H_{\Lambda}^2 R_{\text{ZG}}^2, \quad (29)$$

needed for a particle to leave the potential well of the cluster and join the outflow. The lower limit for the outflow velocities is the theory prediction which may be tested in current and future observations of the Coma environment.

6. Newtonian approximation in description of galactic winds in presence of DE

In the Newtonian approximation, in presence of DE, we have the following hydrodynamic Euler equation for the spherically symmetric outflow in the gravitational field of matter and DE

$$\begin{aligned} \rho v \frac{dv}{dr} + \frac{dP}{dr} &= -\rho \left(\frac{Gm_m}{r^2} - \frac{\Lambda c^2 r}{3} \right) \quad (30) \\ &= -\rho \left(\frac{Gm_m}{r^2} - \frac{8\pi G \rho_{\Lambda} r}{3} \right). \end{aligned}$$

Here ρ and P are a matter density and pressure, respectively, m_m is the mass of the matter inside the radius r . We use here DE in the form of the Einstein cosmological constant Λ . Newtonian gravitational potentials produced by matter Φ_g , and Φ_{Λ} by DE, satisfy the Poisson equations

$$\Delta \Phi_{\Lambda} = -8\pi G \rho_{\Lambda}, \quad \Delta \Phi_g = 4\pi G \rho, \quad \rho_{\Lambda} = \frac{\Lambda c^2}{8\pi G}. \quad (31)$$

We consider, for simplicity, the outflow in the field of a constant mass (like in stellar wind) $m_m = M$. The Eq. (30) in this case is written as

$$\begin{aligned} \rho v \frac{dv}{dr} + \frac{dP}{dr} &= -\rho \left(\frac{GM}{r^2} - \frac{\Lambda c^2 r}{3} \right) \quad (32) \\ &= -\rho \left(\frac{GM}{r^2} - \frac{8\pi G \rho_{\Lambda} r}{3} \right). \end{aligned}$$

The Eq. (30) should be solved together with the continuity equation in the form

$$4\pi \rho v r^2 = \dot{M}, \quad (33)$$

where \dot{M} is the constant mass flux from the cluster. We consider polytropic equation of state, where pressure P , and sound speed c_s are defined as

$$\begin{aligned} P &= K \rho^{\gamma}, \quad c_s^2 = \gamma \frac{P}{\rho}, \quad \rho = \left(\frac{c_s^2}{\gamma K} \right)^{\frac{1}{\gamma-1}}, \quad (34) \\ P &= \left(\frac{c_s^2}{\gamma} \right)^{\frac{\gamma}{\gamma-1}} K^{-\frac{1}{\gamma-1}}. \end{aligned}$$

Introduce nondimensional variables as

$$\begin{aligned} \tilde{v} &= \frac{v}{v_*}, \quad \tilde{c}_s = \frac{c_s}{c_*}, \quad \tilde{r} = \frac{r}{r_*}, \quad r_* = \frac{GM}{c_*^2}, \quad v_* = c_*, \\ \tilde{\rho} &= \frac{\rho}{\rho_*}, \quad \tilde{P} = \frac{P}{P_*}, \quad \rho_* = \left(\frac{c_*^2}{\gamma K} \right)^{\frac{1}{\gamma-1}}, \quad (35) \\ P_* &= \left(\frac{c_*^2}{\gamma} \right)^{\frac{\gamma}{\gamma-1}} K^{-\frac{1}{\gamma-1}}. \end{aligned}$$

In non-dimensional variables the equation (32) is written as

$$\tilde{v} \frac{d\tilde{v}}{d\tilde{r}} + \frac{2}{\gamma-1} \tilde{c}_s \frac{d\tilde{c}_s}{d\tilde{r}} + \frac{1}{\tilde{r}^2} - \lambda \tilde{r} = 0, \quad \lambda = \frac{\Lambda c^2 r_*^2}{3c_*^2}. \quad (36)$$

The continuity equation (33) in non-dimensional form is written as

$$\tilde{\rho} \tilde{v} \tilde{r}^2 = \dot{m}, \quad \tilde{c}_s^{\frac{2}{\gamma-1}} \tilde{v} \tilde{r}^2 = \dot{m}, \quad \dot{m} = \frac{\dot{M}}{M_*}, \quad (37)$$

$$\dot{M}_* = 4\pi \rho_* v_* r_*^2.$$

It follows from (34),(35),(37), that

$$\frac{d\tilde{\rho}}{\tilde{\rho}} = \frac{2}{\gamma-1} \frac{d\tilde{c}_s}{\tilde{c}_s}, \quad \frac{d\tilde{\rho}}{\tilde{\rho}} + \frac{d\tilde{v}}{\tilde{v}} + 2 \frac{d\tilde{r}}{\tilde{r}} = 0. \quad (38)$$

Using (38) we may write the equation of motion (36) in the form

$$\frac{d\tilde{v}}{d\tilde{r}} = \frac{\tilde{v}}{\tilde{r}} \frac{2\tilde{c}_s^2 - \frac{1}{\tilde{r}} + \lambda \tilde{r}^2}{\tilde{v}^2 - \tilde{c}_s^2}. \quad (39)$$

The only physically relevant solutions are those which pass smoothly the sonic point $v = c_s$, being a singular point of the Eq. (10), with

$$\tilde{v} = \tilde{c}_s, \quad 2\tilde{c}_s^2 - \frac{1}{\tilde{r}} + \lambda \tilde{r}^2 = 0 \quad (40)$$

where $\tilde{r} = \tilde{r}_c$, $\tilde{v} = \tilde{v}_c$, $\tilde{c}_s = \tilde{c}_{sc}$. Choosing $c_* = c_{sc}$, we obtain in the critical point

$$\tilde{v}_c = \tilde{c}_{sc} = 1, \quad 2 - \frac{1}{\tilde{r}_c} + \lambda \tilde{r}_c^2 = 0. \quad (41)$$

With this choice of the scaling parameters, we have from (37)

$$\dot{m} = \tilde{r}_c^2. \quad (42)$$

The physical meaning of the parameter λ becomes clear after rewriting it, using (31),(35), in the form

$$\lambda = \frac{\Lambda c^2 r_*^2}{3c_s^2} = \rho_\Lambda \frac{8\pi}{3M} r_*^3 = \rho_\Lambda \frac{8\pi}{3M} \frac{r_c^3}{\tilde{r}_c^3} = \frac{2\rho_\Lambda}{\rho_M} \frac{1}{\tilde{r}_c^3}, \quad (43)$$

where $\rho_M = \frac{3M}{4\pi r_c^3}$ is a density of the matter after smearing the central mass uniformly inside the critical radius r_c . The value of λ is proportional to the ratio of the dark energy mass inside the critical radius $M_\Lambda = \frac{4\pi}{3} r_c^3 \rho_\Lambda$ to the mass M of the central body.

The relation (41) determines the dependence $\tilde{r}_c(\lambda)$ in the solution for the galactic wind and accretion, in presence of DE. In presence of DE the critical radius of the flow is situated closer to the gravitating center (in non-dimensional units) with increasing λ . The Eq.(36) for the polytropic flow has a Bernoulli integral as

$$\frac{\tilde{v}^2}{2} + \frac{\tilde{c}_s^2}{\gamma - 1} - \frac{1}{\tilde{r}} - \frac{\lambda \tilde{r}^2}{2} = h, \quad (44)$$

$$\tilde{c}_s^2 = \left(\frac{\dot{m}}{\tilde{v} \tilde{r}^2} \right)^{\gamma-1} = \left(\frac{\tilde{r}_c^2}{\tilde{v} \tilde{r}^2} \right)^{\gamma-1}.$$

The dimensional Bernoulli integral $H = hc_{sc}^2$. The Bernoulli integral is determined through the parameters of the critical point, with account of (41), as

$$h = \frac{\gamma + 1}{2(\gamma - 1)} - \frac{1}{\tilde{r}_c} - \frac{\lambda \tilde{r}_c^2}{2} = \frac{5 - 3\gamma}{2(\gamma - 1)} - \frac{3}{2} \left(\frac{1}{\tilde{r}_c} - 2 \right). \quad (45)$$

The dependence $h(\lambda)$ for different polytropic powers γ is given in Fig.1. Note that in presence of DE the outflow is possible also for negative values of the Bernoulli integral h , defined equally.

The stationary solution for the wind is determined by two integrals: constant mass flux \dot{M} , and energy (Bernoulli) integral H . In absence of DE we obtain the known relations

$$\tilde{r}_c = \frac{1}{2}, \quad h = \frac{5 - 3\gamma}{2(\gamma - 1)}. \quad (46)$$

At small λ we have from (41),(45)

$$\tilde{r}_c = 0.5 - \frac{\lambda}{16}, \quad h = \frac{5 - 3\gamma}{2(\gamma - 1)} - \frac{3}{8}\lambda \quad (47)$$

At large $\lambda \rightarrow \infty$ it follows from (41) $\tilde{r}_c \rightarrow \tilde{r}_{c\infty} = \lambda^{-1/3}$. Making expansion in (41) around $\tilde{r}_{c\infty}$ in the form

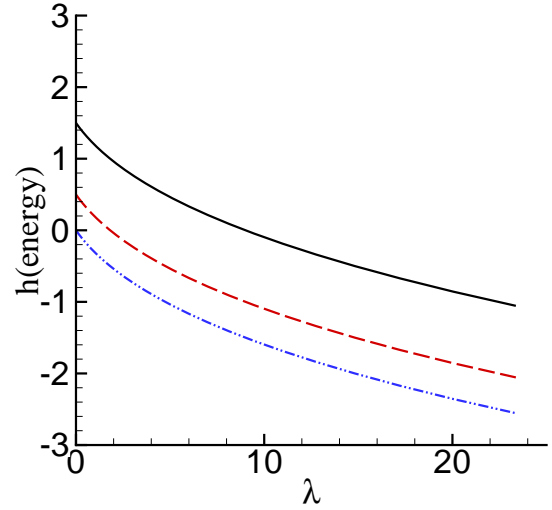


Figure 1: The function $h(\lambda)$ for $\gamma = \frac{4}{3}$ (full curve); $\gamma = \frac{3}{2}$ (dashed curve); $\gamma = \frac{5}{3}$ (dash-dot-dot curve), according to relations (41),(45)

$$\frac{1}{\tilde{r}_c} = \lambda^{1/3} + \varepsilon,$$

we obtain from (41), (45)

$$\begin{aligned} \varepsilon &= \frac{2}{3}, \quad \tilde{r}_c = \frac{1}{\lambda^{1/3} + \frac{2}{3}}, \quad h = \frac{5 - 3\gamma}{2(\gamma - 1)} - \frac{3}{2}\lambda^{1/3} + 2 \\ &= \frac{\gamma + 1}{2(\gamma - 1)} - \frac{3}{2}\lambda^{1/3} \quad \text{at } \lambda \rightarrow \infty. \end{aligned} \quad (48)$$

In the outflow from the physically relevant quasi-stationary object the antigravity from DE should be less than the gravitational force on the outer boundary, which we define at $r = r_*$. Therefore the value of Λ is restricted by the relation (see e.g. Bisnovatyi-Kogan and Chernin, 2012)

$$2\rho_\Lambda = \frac{\Lambda c^2}{4\pi G} < \bar{\rho} = \frac{4\pi M}{3r_*^3} \quad (49)$$

In non-dimensional variables this restriction, with account of (35),(36) is written as

$$\lambda < \frac{16\pi^2}{9} = 17.55 = \lambda_{lim}. \quad (50)$$

It is reasonable to consider only the values of λ smaller than λ_{lim} . It follows from (41), that \tilde{r}_c is monotonically decreasing with increasing λ . For $\lambda = \lambda_{lim} = 17.55$ we obtain $\tilde{r}_c = \tilde{r}_{c,lim} \approx 0.29$. The effective gravitational potential $\tilde{\Phi}$ is formed by the gravity of the central body, and antigravity of DE

$$\tilde{\Phi} = -\frac{1}{\tilde{r}} - \frac{\lambda \tilde{r}^2}{2}. \quad (51)$$

To overcome the gravity of the central body, the value of h should exceed the maximum value of the gravitational potential, defined by the extremum of $\tilde{\Phi}$

$$h \geq \tilde{\Phi}_{max}(\tilde{r}_{max}) = -\frac{3}{2}\lambda^{1/3}, \quad \tilde{r}_{max} = \lambda^{-1/3}. \quad (52)$$

It follows from(41), (52), that always $\tilde{r}_{max} > \tilde{r}_c$. So, in presence of DE the outflow of the gas from the cluster to the infinity is possible even at the negative values of h . In absence of DE the non-negative value of h , and the outflow are possible only at $\gamma \leq \frac{5}{3}$.

7. Solutions of the galactic wind equation in presence of DE

The equation (39) has a sound critical point of the saddle type, and two physical (critical) solutions going through this critical point. One of this solutions describes a wind outflow, and has a positive \tilde{v} . Another solution corresponds to an accretion (inflow), and has a negative \tilde{v} (Stanyukovich, 1955; Parker, 1963). To obtain a physically relevant critical solution of (39), with \tilde{c}_s^2 from (44), we obtain expansion in the critical point with $\tilde{v}^2 = \tilde{c}_s^2 = 1$, in the form

$$\begin{aligned} \tilde{v} &= 1 + \alpha(\tilde{r} - \tilde{r}_c), \quad \alpha_1 = -\frac{2}{\tilde{r}_c} \frac{\gamma - 1}{\gamma + 1}, \\ &+ \frac{1}{\tilde{r}_c} \frac{2}{\gamma + 1} \sqrt{2 + \frac{1}{4\tilde{r}_c} + \frac{\lambda\tilde{r}_c^2}{2} - \gamma \left(2 - \frac{1}{4\tilde{r}_c} - \frac{\lambda\tilde{r}_c^2}{2}\right)}, \\ \alpha_2 &= -\frac{2}{\tilde{r}_c} \frac{\gamma - 1}{\gamma + 1} \quad (53) \\ &- \frac{1}{\tilde{r}_c} \frac{2}{\gamma + 1} \sqrt{2 + \frac{1}{4\tilde{r}_c} + \frac{\lambda\tilde{r}_c^2}{2} - \gamma \left(2 - \frac{1}{4\tilde{r}_c} - \frac{\lambda\tilde{r}_c^2}{2}\right)}. \end{aligned}$$

Here α_1 corresponds to the wind solution, and α_2 is related to the case of accretion where \tilde{v} define the absolute value. At $\lambda = 0$ we have a well known expansion with

$$\begin{aligned} \alpha_1 &= \frac{4}{\gamma + 1} \left[\sqrt{\frac{5 - 3\gamma}{2}} - (\gamma - 1) \right], \\ \alpha_2 &= -\frac{4}{\gamma + 1} \left[\sqrt{\frac{5 - 3\gamma}{2}} + (\gamma - 1) \right]. \end{aligned}$$

It follows from the expansion (53), that physically relevant solutions exist only with positive value under the square root. It give the restriction for the value of γ as a function of λ in the form

$$\gamma \leq \gamma_{max} = \frac{2 + \frac{1}{4\tilde{r}_c} + \frac{\lambda\tilde{r}_c^2}{2}}{2 - \frac{1}{4\tilde{r}_c} - \frac{\lambda\tilde{r}_c^2}{2}}.$$

At $\lambda = 32$, $\tilde{r}_c = 0.25$ the limiting value γ_{max} goes to ∞ , so that at $\lambda \geq 32$ the wind solutions exist formally for all polytropic powers γ .

The numerical solution of (39) was obtained using predictor-corrector Runge-Kutta method of 4-th order, with a fixed relative precision, written in Fortran 77, see Press et al. (1992) The integration started from the critical point with $\tilde{v} = \tilde{c}_s = 1$, using the expansion (53), both inside and outside the critical point, for two types of the flow: the wind flow, corresponding to the coefficient α_1 in (53), and accretion flow, corresponding to α_2 in (53). The critical solutions of the equation (39), with account of (44), are presented in Figs.2,3 for different values of γ and λ . Both wind and accretion solutions are presented.

The wind and accretion solutions are plotted in the same figures 2,3, but the positive velocities correspond only to the wind solutions. The outflow solutions have increasing velocities in presence of DE with $\lambda > 1$, but at $\lambda = 0$ the behaviour at large radius \tilde{r} depends on the adiabatic power γ . The velocity is increasing in the wind solution at $\gamma = \frac{4}{3}$ (Fig.2). At $\gamma = \frac{5}{3}$ the wind solution has a decreasing outflow velocity with a constant Mach number, see Fig.3.

The accretion solutions in Figs.2,3 are represented by the absolute values of the inflow velocity $|\tilde{v}|$, and the inflow velocity during accretion has a negative sign. The inflow velocity inside the critical point at $\gamma = \frac{4}{3}$ at all λ converges to the same free fall velocity $\tilde{v} \rightarrow -\sqrt{\frac{2}{\tilde{r}}}$, according to the Bernoulli integral (44), with $\tilde{r} \ll 1$, in the supersonic flow with $\tilde{v} \gg \tilde{c}_s$. At $\gamma = \frac{5}{3}$ the inflow solution at $\tilde{r} \ll 1$ is approaching to the constant Mach number solution. The inflow solutions given in Fig.3 correspond to $Ma = 1$. The equation (39) is invariant to the transformation $\tilde{v} \rightarrow -\tilde{v}$, therefore the accretion solution was possible to obtain numerically for the absolute values of the velocity.

The inflow solutions for the accretion starts at large radiuses by a slow motion to the gravitating center. The velocity increases in a subsonic regime, and after crossing the critical point the supersonic infall to the gravitating center starts. Note, that the accretion solutions have a physical sense only for small λ , when the region with a attractive gravitational force is sufficiently large. In the regions with repulsing force due to DE antigravity, the critical accretion solutions of the equation (39) formally exist, but they correspond to anomalous density distribution increasing with radius, what cannot be expected in reality.

8. Discussion

It is clear that the presence of DE tends to help the outflow of the hot gas from the gravitating ob-

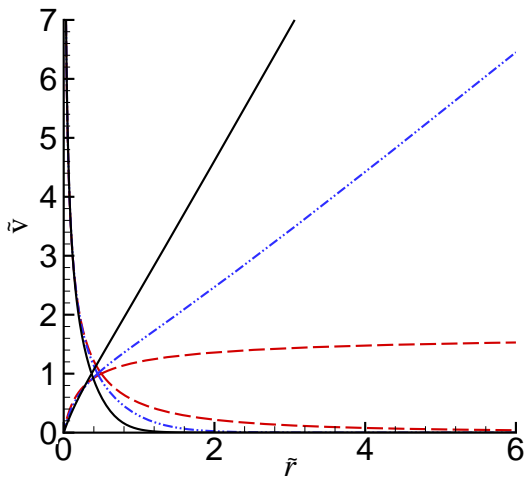


Figure 2: The integral curves of the equations (39), (44), for $\gamma = 4/3$ and $\lambda = 0$, $r_c=0.5$ (dashed curves); $\lambda = 1.10$, $r_c = 0.45$ (dash-dot-dot curves); and $\lambda = 5.13$, $r_c = 0.37$ (full curves). Wind solutions correspond to curves with increasing velocity at large radius. The curves with decreasing velocities correspond to the accretion solution with negative v , so that its absolute value is presented.

ject, as well as to the escape of rapidly moving galaxies (Chernin et al, 2013). Here we have obtained the solution for outflow in presence of DE, which generalize the well-known solution for the polytropic solar (stellar) wind. Presently the DE density exceed the density of the dark matter, and, even more, the density of the barionic matter. The clusters which outer radius is approaching the zero gravity radius, may not only loose galaxies, which join the process of Hubble expansion, but also may loose the hot gas from the outer parts of the cluster. Let us consider outer parts of the Coma cluster at radius $R_C = 15$ Mpc, with the mass inside $M_C = 5 \cdot 10^{15} M_\odot$, from Chernin et al. (2013). For the present value of $\rho_\Lambda = 0.71 \cdot 10^{-29}$ g/cm³, supposing that $R_C = r_*$ is the critical radius of the wind, we obtain from (2),(7), the nondimensional constant λ as

$$\lambda = \frac{\Lambda c^2 r_*^2}{3c_*^2} = \frac{8\pi \rho_\Lambda r_*^3}{3M} \approx 0.59, \quad (54)$$

$$c_* = \sqrt{\frac{GM_C}{R_C}} \approx 1200 \text{ km/c.}$$

It corresponds to the temperature about $T \approx 6 \cdot 10^7$ K, $kT \approx 5$ keV. Observations of the hot gas distribution in the Coma cluster (Watanabe et al., 1999) on ASCA satellite have shown a presence of hot region with $kT = 11 - 14$ keV, and more extended cool region with $kT = 5 \pm 1$ keV, what is in good accordance with our choice of parameters.

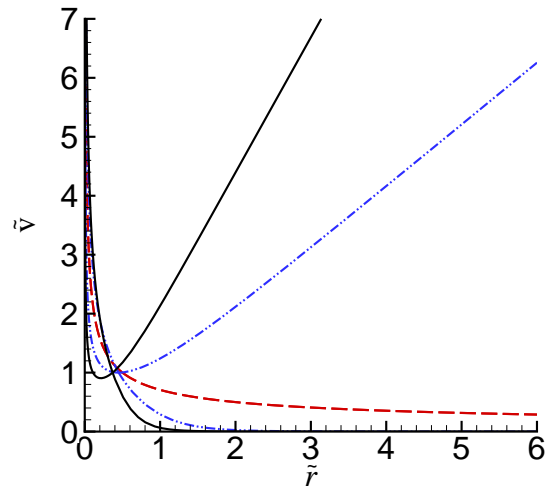


Figure 3: The integral curves of the equations (39), (44), for $\gamma = 5/3$ and $\lambda = 0$, $r_c=0.5$ (dashed curve); $\lambda = 1.10$, $r_c = 0.45$ (dash-dot-dot curves); and $\lambda = 5.13$, $r_c = 0.37$ (full curves). For nonzero λ wind solutions correspond to curves with increasing velocity at large radius. The curves with decreasing velocities correspond to the accretion solution with negative v , so that its absolute values are presented. At $\lambda = 0$ both wind and accretion solutions are presented by the same curve, which corresponds to the wind for positive v , and to the accretion for negative v .

Wind solutions for $\lambda=0$; 0.58; 1.1 are presented in Fig.4. The solution with $\lambda=0.58$ is the closest to the description of the outflow from Coma cluster. The density of the gas in the vicinity of $r = r_c$ is very small, so the flow may be considered as adiabatic (polytropic) with the power $\gamma=5/3$. Without DE such gas flow is inefficient, its velocity is decreasing $\sim 1/\sqrt{r}$, see Eq. (25). In presence of DE the wind velocity is increasing 2 times at the distance of $\sim 5r_c \sim 75$ Mpc from Coma.

After quitting the cluster the gas is moving with acceleration, acting as a snowplough for the intergalactic gas. The shell of matter, forming in such a way, may reach a high velocity, exceeding considerably the speed of galaxies in cluster. If the shell meets another cluster, or another shell moving towards, the collision of such flows may induce a particle acceleration. Due to high speed, large sizes, and low density such collisions may create cosmic rays of the highest possible energy (EHECR). We may expect the largest effect when two clusters move to each other. The influence of DE is decreasing with with a red shift, therefore the acceleration of EHECR in this model should take place in the periphery, or between, the closest rich galaxy clusters.

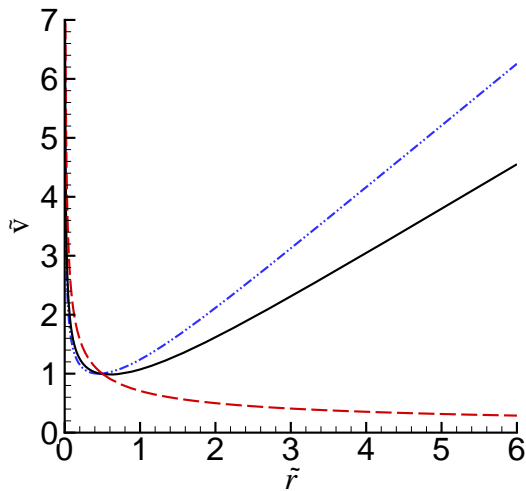


Figure 4: The integral curves of the equations (39), (44) for the wind solution, at $\gamma = 5/3$ and $\lambda = 0$, $r_c=0.5$ (dashed curve); $\lambda = 1.10$, $r_c = 0.45$ (dash-dot dot curve); and $\lambda = 0.58$, $r_c = 0.47$ (full curve).

Acknowledgements. We thank G.G. Byrd, M. Merafina, P. Teerikorpi and M.J. Valtonen for cooperation. Useful discussions with Yu.N. Efremov, I.D. Karachentsev, D.I. Makarov, and A.V. Zasov are appreciated. The work of G.B.-K. was partly supported by RFBR grant 11-02-00602, the RAN Program Formation and evolution of stars and galaxies, and Russian Federation President Grant for Support of Leading Scientific Schools NSH-3458.2010.2.

References

- Bisnovaty-Kogan G.S., Chernin A.D.: 2012, *Ap&SS*, **338**, 337
- Bisnovaty-Kogan G.S., Merafina M.: 2013, *MNRAS*, **434**, 3628
- Busha M.T., Evrard A.E., Adams F.C., Wechsler R.H.: 2005, *MNRAS*, **363**, L11
- Byrd G.G., Chernin A.D., Valtonen M.J.: 2007, *Cosmology: Foundations and Frontiers*, Moscow, URSS
- Byrd G.G., Chernin A.D., Teerikorpi P., Valtonen M.J.: 2012, *Paths to Dark Energy: Theory and Observation*, N.Y., de Gruyter
- Chernin A.D.: 2001, *Physics-Uspekhi*, **44**, 1099
- Chernin A.D.: 2008, *Physics-Uspekhi*, **51**, 267
- Chernin A.D.: 2013, *Physics-Uspekhi*, **56**, 704
- Chernin A.D., Teerikorpi P., Baryshev Yu.V.: 2000, [*astro-ph/0012021*], *Adv. Space Res.*, **31**, 459 (2003)
- Chernin A.D., Teerikorpi P., Baryshev Yu.V.: 2006, *A&A*, **456**, 13
- Chernin A.D., Karachentsev I.D., Kashibadze O.G. et al.: 2007, *Astrophysics*, **50**, 405
- Chernin A.D., Karachentsev I.D., Nasonova O.G. et al.: 2010, *A&A*, **520**, 104
- Chernin A.D., Teerikorpi P., Valtonen M.J. et al.: 2012a, *Astr. Rep.*, **56**, 653
- Chernin A.D., Teerikorpi P., Valtonen M.J. et al.: 2012b, *A&A*, **539**, A4
- Chernin A.D., Bisnovaty-Kogan G.S., Teerikorpi P. et al.: 2013, *A&A*, **553**, 101
- Colles M.: 2006, in *Encyclopedia of Astronomy and Astrophysics*, P.Murdin, ed., IOP Pubs.Ltd, UK, p.245
- Diaferio A.: 1999, *MNRAS*, **309**, 610
- Diaferio A., Geller M.J.: 1997, *ApJ*, **481**, 633
- Geller M.J., Diaferio A., Kurtz M.J.: 1999, *ApJ*, **517**, L23
- Geller M.J., Diaferio A., Kurtz M.J.: 2011, *AJ*, **142**, 143
- Hartwick F.D.A.: 2011, *AJ*, **141**, 198
- Hernquist L.: 1990, *ApJ*, **356**, 359
- Holz D.E., Perlmutter S.: 2012, *ApJL*, **755**, L36
- Hughes J.P.: 1989, *ApJ*, **337**, 21
- Hughes J.P.: 1998, "Untangling Coma Berenices: A New Vision of an Old Cluster", Proceedings of the meeting held in Marseilles, June 17-20, 1997, Eds.: Mazure, A., Casoli F., Durret F., Gerbal D., Word Scientific, p 175.
- Karachentsev I.D., Chernin A.D., Teerikorpi P.: 2003, *Astrophysics*, **46**, 491
- Kubo J.M., Stebbins A., Annis, J. et al.: 2007, *ApJ*, **671**, 1466
- Merafina M., Bisnovaty-Kogan G.S., Tarasov S.O.: 2012, *A&A*, **541**, 84
- Navarro J., Frenk C.S., White S.D.M.: 2005, *ApJ*, **463**, 563
- The L. S., White S.D.M.: 1986, *AJ*, **92**, 1248
- Zwicky F.: 1933, *Helvetica Phys. Acta*, **6**, 110
- Zwicky F.: 1937, *ApJ*, **86**, 217

MAGNETOROTATIONAL SUPERNOVAE AND MAGNETO-DIFFERENTIAL-ROTATIONAL INSTABILITY

S.G. Moiseenko¹, G.S. Bisnovatyi-Kogan^{1,2}

¹ Space Research Institute, Russian Academy of Sciences,
Moscow, Russia, *moiseenko@iki.rssi.ru*, *gkogan@iki.rssi.ru*

² National Research Nuclear University MEPhI, Moscow, Russia

ABSTRACT. Results of simulations of magnetorotational(MR) core-collapse supernova explosion mechanism are presented. For the simulations we have used specially developed Lagrangian completely conservative operator-difference scheme on triangular grid of variable structure. 2D numerical simulations show that the Magneto-Differential-Rotational Instability (MDRI) (Tayler-type instability) develops which leads to the exponential growth of all components of magnetic field. The instability reduces time evolution of the MR explosion. The explosion energy found in MR explosion corresponds to observations. We made simulations of the MR mechanism supernova explosion with different equations of state and different procedures of neutrino transport. We found that the results of the MR explosion does not significantly change.

Key words: Stars: Supernovae; Magnetohydrodynamics; Numerical simulations.

1. Introduction

Supernova explosions are ones of the brightest and most energetic events in the Universe. The explanation of the physical mechanism of core-collapsed supernova explosions is one of important problems of modern astrophysics. The mechanism of core-collapse supernova explosion connected with magnetic field and rotation is called magnetorotational(MR). The idea of MR mechanism was suggested by G.S.Bisnovatyi-Kogan in 1970 (Bisnovatyi-Kogan, 1970). Due to the collapse of the iron core significant part of the gravitational energy of the core is emitted in the form of neutrino. If the iron core has initial rotation before collapse then due to the nonuniform contraction the rotation in the core will be differential. If the core had initial poloidal magnetic field the differential rotation leads to the appearing and amplification of the toroidal component of the magnetic field. When the magnetic pressure becomes comparable with gas pressure the compression wave start to move outwards the core. Running over steeply

decreasing density profile it transforms into the fast MHD shock wave. The magnetic field plays role of the MHD piston which supports the shock.

The first simulations of the MR processes in stars have been done by LeBlanc & Wilson, 1970, after which MR processes in the stars in relation to the core collapse supernova explosion had been simulated by Bisnovatyi-Kogan et al., 1976, Ardelyan et al., 1979, Müller & Hillebrandt, 1979, Ohnishi,1983, Symbalysty, 1984.

In last several decades a number of papers were devoted to the numerical simulations of MR mechanism (Yamada and Sawai,2004, Takiwaki et al., 2004, Kotake et al., 2004, Kotake et al., 2006, Ardeljan, et al. 2005, Sawai et al., 2005, Moiseenko et al., 2006, Obergaulinger et al., 2006, Burrows et al., 2007, Dessart et al., 2007, Scheidegger et al., 2008, Bisnovatyi-Kogan et al., 2008, Mikami et al. 2008, Takiwaki et al., 2009, Takiwaki and Kotake, 2011, Endeve et al., 2012, Sawai et al, 2013).

2. Formulation of the problem

2.1. Basic equations

Consider a set of magnetohydrodynamical equations with selfgravitation and infinite conductivity:

$$\begin{aligned} \frac{d\mathbf{x}}{dt} &= \mathbf{v}, \\ \frac{d\rho}{dt} + \rho\nabla \cdot \mathbf{v} &= 0, \\ \rho \frac{d\mathbf{v}}{dt} &= -\text{grad} \left(P + \frac{\mathbf{H} \cdot \mathbf{H}}{8\pi} \right) + \frac{\nabla \cdot (\mathbf{H} \otimes \mathbf{H})}{4\pi} - \rho\nabla\Phi, \\ \rho \frac{d}{dt} \left(\frac{\mathbf{H}}{\rho} \right) &= \mathbf{H} \cdot \nabla \mathbf{v}, \quad \Delta\Phi = 4\pi G\rho, \\ \rho \frac{d\varepsilon}{dt} + P\nabla \cdot \mathbf{v} + \rho F(\rho, T) &= 0, \\ P &= P(\rho, T), \quad \varepsilon = \varepsilon(\rho, T), \end{aligned} \quad (1)$$

where $\frac{d}{dt} = \frac{\partial}{\partial t} + \mathbf{v} \cdot \nabla$ is the total time derivative, $\mathbf{x} = (r, \varphi, z)$, $\mathbf{v} = (v_r, v_\varphi, v_z)$ is the velocity vector, ρ is

the density, P is the pressure, $\mathbf{H} = (H_r, H_\varphi, H_z)$ is the magnetic field vector, Φ is the gravitational potential, ε is the internal energy, G is gravitational constant, $\mathbf{H} \otimes \mathbf{H}$ is the tensor of rank 2, and $F(\rho, T)$ is the rate of neutrino losses.

r , φ , and z are spatial Lagrangian coordinates, i.e. $r = r(r_0, \varphi_0, z_0, t)$, $\varphi = \varphi(r_0, \varphi_0, z_0, t)$, and $z = z(r_0, \varphi_0, z_0, t)$, where r_0, φ_0, z_0 are the initial coordinates of material points of the matter.

Taking into account symmetry assumptions ($\frac{\partial}{\partial \varphi} = 0$), the divergency of the tensor $\mathbf{H} \otimes \mathbf{H}$ can be presented in the following form:

$$\nabla \cdot (\mathbf{H} \otimes \mathbf{H}) = \begin{pmatrix} \frac{1}{r} \frac{\partial (r H_r H_r)}{\partial r} + \frac{\partial (H_z H_r)}{\partial z} - \frac{1}{r} H_\varphi H_\varphi \\ \frac{1}{r} \frac{\partial (r H_r H_\varphi)}{\partial r} + \frac{\partial (H_z H_\varphi)}{\partial z} + \frac{1}{r} H_\varphi H_r \\ \frac{1}{r} \frac{\partial (r H_r H_z)}{\partial r} + \frac{\partial (H_z H_z)}{\partial z} \end{pmatrix}.$$

Axial symmetry ($\frac{\partial}{\partial \varphi} = 0$) and symmetry to the equatorial plane are assumed. The problem is solved in the restricted domain. At $t = 0$ the domain is restricted by the rotational axis $r \geq 0$, equatorial plane $z \geq 0$, and outer boundary of the star where the density of the matter is zero, while poloidal components of the magnetic field H_r , and H_z can be non-zero.

At the rotational axis ($r = 0$) the following boundary conditions are defined: $(\nabla \Phi)_r = 0$, $v_r = 0$. At the equatorial plane ($z = 0$) the boundary conditions are: $(\nabla \Phi)_z = 0$, $v_z = 0$. At the outer boundary (boundary with vacuum) the following condition is defined: $P_{\text{outer boundary}} = 0$.

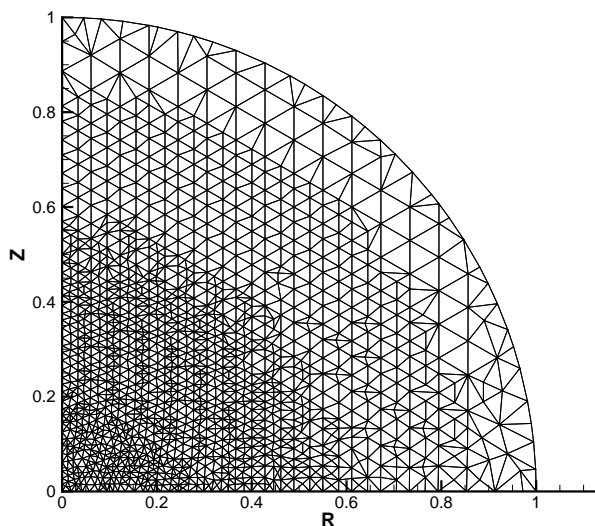


Figure 1: Example of the triangular Lagrangian grid.

2.2. Numerical method

The numerical method used in present simulations is based on the implicit operator-difference completely conservative scheme on the Lagrangian triangular grid

(Fig.1) of variable structure. The implicitness of the applied numerical scheme allows to make large time steps. It is important to use implicit scheme in such kind of problems due to the presence of two strongly different timescales. The small timescale is defined by the huge sound velocity in the central parts of the star. The big time scale is defined by the characteristic timescale of the evolution of the magnetic field. Conservation properties of the numerical scheme are important for the exact fulfillment of the energy balance and divergence-free property of the magnetic field.

During the simulation of the MRE the time step for the implicit scheme was $\sim 10 \div 300$ times larger than time step for the explicit scheme (CFL stability condition). It means that the total number of time steps is $10 \div 300$ times less than it would have been done for explicit scheme, what allows us to decrease time approximation error. We did not make direct comparison of CPU time per time step for our implicit scheme and an explicit scheme. Our estimations show that the total number of arithmetic operations for the implicit scheme is ≈ 20 times larger than it is required for explicit scheme. Considerable decrease of the required number of time steps leads to corresponding reduce of the time approximation error.

Grid reconstruction procedure applied here for the reconstruction of the triangular lagrangian grid is used both for the correction of the "quality" of the grid and for the dynamical adaptation of the grid.

The method applied here was developed, and its stability was investigated in the papers by Ardeljan, Kosmachevskii, 1995, Ardeljan N.V, Kosmachevskii K.V., Chernigovskii S.V., 1987 and references therein. It was tested thoroughly with different tests (Ardeljan N.V., Bisnovatyi-Kogan G.S., Moiseenko S.G., 2000).

3. Results

3.1. Core collapse simulation

As the initial step for the simulation of MR supernova explosion we made simulation of the collapse of non magnetized rotating iron core (Ardeljan et al 2004). The ratios between the initial rotational and gravitational energies and between the internal and gravitational energies of the star are the following:

$$\frac{E_{rot}}{E_{grav}} = 0.0057, \quad \frac{E_{int}}{E_{grav}} = 0.727.$$

At $t = 0.1424$ s the density in the center of the star reaches its maximum value $\rho_{c,max} = 5.655 \cdot 10^{14} \text{g/cm}^3$. At the final stage of the core collapse ($t = 0.261$ s.) we obtain a differentially rotating configuration. The central proto-neutron star with a radius ~ 12.8 km rotates almost rigidly with the rotational period 0.00152s. The angular velocity rapidly decreases with the increase in

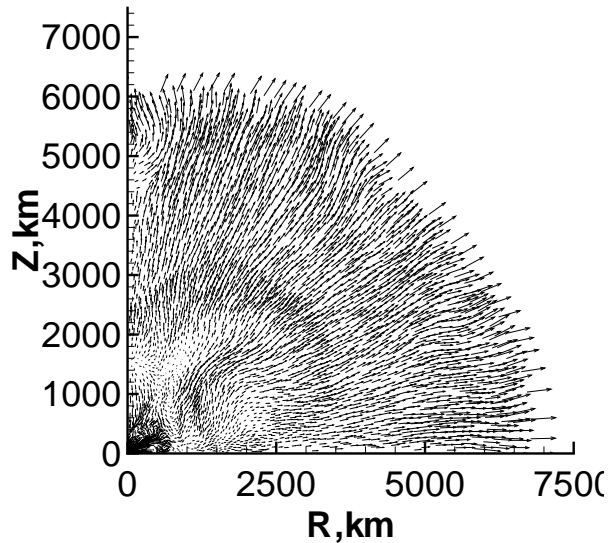


Figure 2: The MR explosion for *quadrupole-like* initial magnetic field. The velocity field at $t = 0.30s$ after 'switching on' the magnetic field.

the distance from the star center. The particles of the matter situated at the outer boundary in the equatorial plain rotate with the period $\sim 35s$ due to strong expansion of the envelope after the collapse of the core.

3.2. Magnetorotational explosion

After core collapse and formation of the proto-neutron star initial poloidal quadrupole-like magnetic field was 'switched on' (Ardeljan, Bisnovatyi-Kogan, Moiseenko, 2005). Due to the differential rotation the toroidal component of the magnetic field H_φ appears and amplifies with the time. At the beginning of the simulations the toroidal component of the magnetic field grows linearly with the time at the periphery of the proto-neutron star. At the developed stage of the H_φ evolution the toroidal magnetic energy begins to grow much faster due to developing magnetorotational instability leading also to a rapid growth of the poloidal components.

Due to the quadrupole-like type of the symmetry of the initial magnetic field the MHD shock is stronger, and it moves faster near the equatorial plane $z = 0$. The matter of the envelope of the star is ejected preferably near the equatorial plane (Figs.2,3).

The shape of the MR supernova explosion qualitatively depends on the initial configuration of the magnetic field. In the paper by Moiseenko, Bisnovatyi-Kogan, Ardeljan, 2005, we made simulations of the MR supernova explosion with the initial dipole-like poloidal magnetic field.

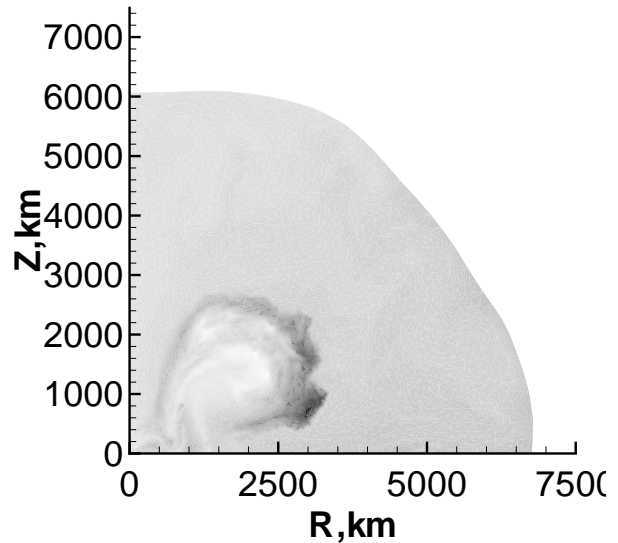


Figure 3: The MR explosion for *quadrupole-like* initial magnetic field. The specific angular momentum spatial distribution at $t = 0.30s$ after 'switching on' the magnetic field.

In the case of the dipole-like magnetic significant part of the ejected matter obtains a velocity along the rotational axis (Figs.4,5).

The explosion energy of the MR supernova was in the 'quadrupole' and the 'dipole' cases approximately the same $0.5 \sim 0.6 \times 10^{51} \text{erg}$.

At the initial stage of the evolution of the toroidal component of the magnetic field it grows linearly with the time, after about 100 rotational periods of the central core, its linear growth changes to the exponential one, and the poloidal components also start to grow exponentially. The reason for that exponential growth is an onset of the variant of MRI, which was investigated by Tayler, 1973. It is directly connected with the differential rotation, and is induced by it. We may call it Magneto-Differential-Rotational-Instability(MDRI).

We simulated an MR supernova explosion for various initial core masses and rotational energies (Bisnovatyi-Kogan, Moiseenko, Ardelyan, 2008). The initial core mass was varied from $1.2M_\odot$ to $1.7M_\odot$. The specific rotational energy at the time when the magnetic field was switched on, E_{rot}/M_{core} , was varied from $0.19 \cdot 10^{19} \text{ erg/g}$ to $0.4 \cdot 10^{19} \text{ erg/g}$. The explosive energy of an MR supernova increases substantially with the mass of the iron core and the initial rotational energy (angular velocity). The energy released in MR supernova is sufficient to explain core collapse supernova: $0.5 - 2.6 \cdot 10^{51} \text{erg}$ (Type II and Ib supernovae) (Fig.7). The energies of Type Ic supernovae can be higher, probably due to the collapse of more massive cores, of the order of several tens of M_\odot .

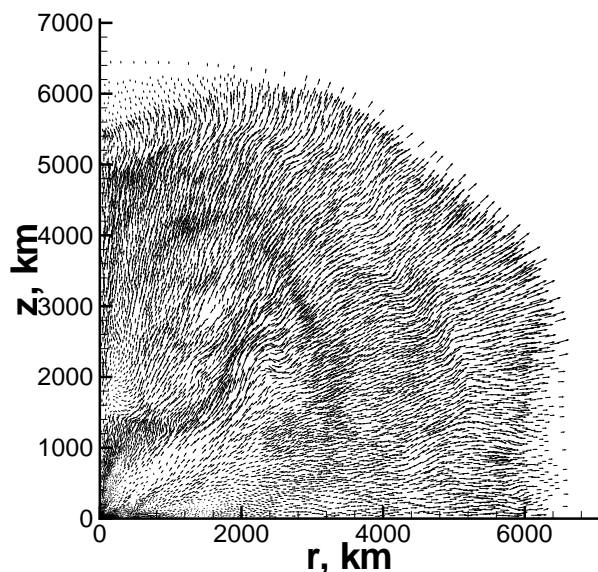


Figure 4: The MR explosion for *dipole-like* initial magnetic field. The velocity field at $t = 0.25s$ after 'switching on' the magnetic field.

3.3 Shen Equation of State(EoS).

We made 2D MR core-collapse supernova simulations by using the tabulated EoS based on the relativistic mean-field theory by Shen et al., 1998. The neutrino cooling was taken into account by a neutrino leakage scheme (Takiwaki et al., 2004).

The simulations of MR supernova explosion for Shen EoS were made using Lagrangian numerical scheme on triangular grid of variable structure. The formulation of the problem of MR supernova explosion, namely the set of equations, initial and boundary conditions, are the same as in the paper by Takiwaki et al., 2004.

We have found a qualitative agreement with the results of analogous simulations achieved by application of ZEUS-2D code in Takiwaki et al., 2004, for the case of extremely strong initial magnetic field ($H_0 = 10^{12}$ G). Namely, in the case of strong initial magnetic field ($H_0 = 10^{12}$ G) we got a prompt MR SN explosion, and formation of a collimated jet. In the case of weaker initial magnetic field ($H_0 = 10^9$ G) (this value of the initial magnetic field is still very strong for presupernova) we obtain a development of Magneto-Differential-Rotational-Instability, delayed explosion in analogy to Takiwaki et al., 2004. The difference in the results of simulations made by Eulerian and Lagrangian numerical methods is in absence of the jet-like ejection in Lagrangian case.

The details of the simulations of MR supernova explosion with the Shen EoS will be published elsewhere.

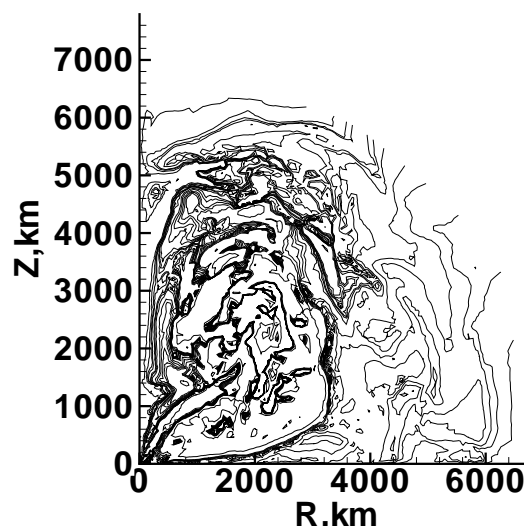


Figure 5: The MR explosion for *dipole-like* initial magnetic field. The specific angular momentum spatial distribution at $t = 0.25s$ after 'switching on' the magnetic field.

Acknowledgements. This work was partially supported by the RFBR grant 11-02-00602, leading scientific schools support program by Russian President council in the frame of the grant NSH-5440.2012.2 for support of the leading scientific schools.

References

- Ardeljan N.V., Bisnovaty-Kogan G.S., Kosmachevskii K.V., Moiseenko S.G.: 2004, *Astrophys.*, **47**, 1.
 Ardeljan N.V., Bisnovaty-Kogan G.S., Moiseenko S.G.: 2000, *A&A*, **355**, 1181.
 Ardeljan N.V., Bisnovaty-Kogan G.S., Moiseenko S.G.: 2005, *MNRAS*, **359**, 333.
 Ardelyan N.V., Bisnovaty-Kogan G.S., Popov Yu.P.: 1979, *Astron. Zh.* **56**, 1244.
 Ardeljan N.V., Kosmachevskii K.V.: 1995, *Computational mathematics and modeling*, **6**, 209.
 Ardeljan N.V., Kosmachevskii K.V., Chernigovskii S.V.: 1987, *Problems of construction and research of conservative difference schemes for magneto-gas-dynamics*, MSU, Moscow (in Russian).
 Bisnovaty-Kogan G.S.: 1970, *Astron. Zh.*, **47**, 813 (*Soviet Astronomy*: 1971, **14**, 652).
 Bisnovaty-Kogan G.S., Moiseenko S.G., Ardelyan N.V.: 2008, *Astronomy Reports*, **52**, 997.
 Bisnovaty-Kogan G.S., Popov Yu.P., Samokhin A.A.: 1976, *ApSS*, **41**, 321.
 Burrows A., Dessart L., Livne E., Ott C.D., Murphy J.: 2007, *ApJ*, **664**, 416.
 Dessart L., Burrows A., Livne E., Ott C.D.: 2007, *ApJ*,

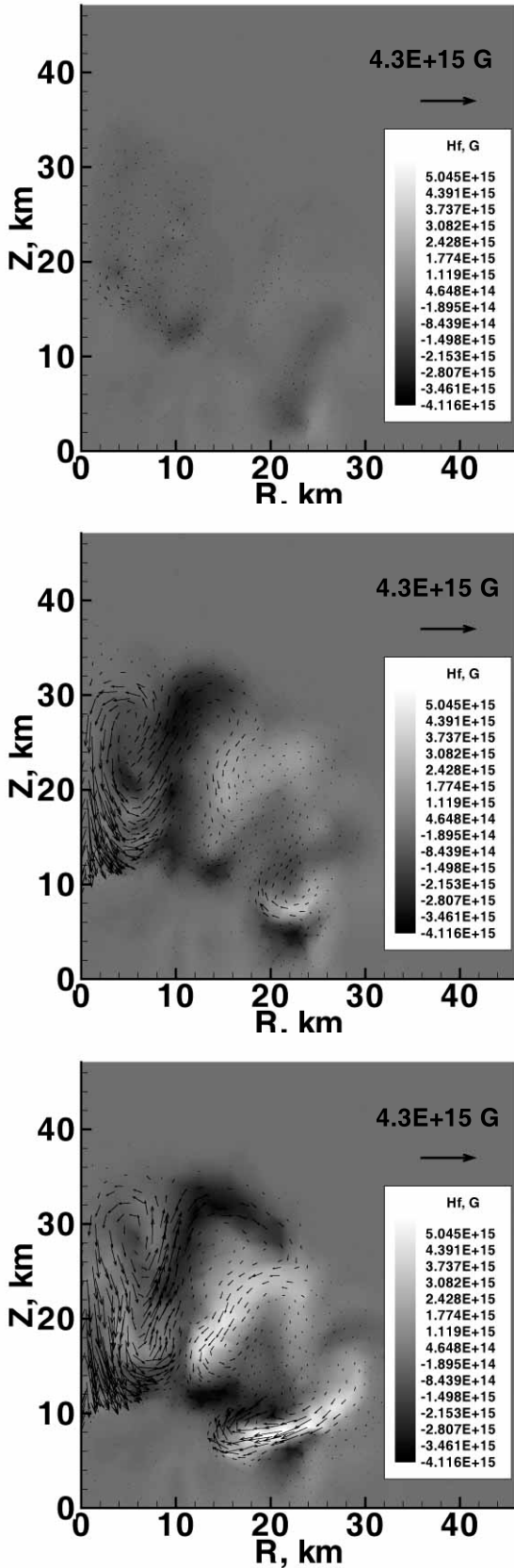


Figure 6: The MDRI development for time moments $t = 0.0045s, 0.018s, 0.042s$. Gray scale is the toroidal field H_ϕ levels. Arrows show a direction and strength of the poloidal magnetic field H_r, H_z .

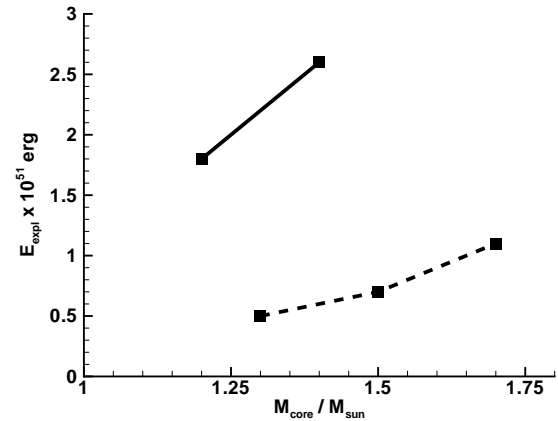


Figure 7: The dependence of the MR supernova explosion energy on the initial core mass for the different values of the specific rotational energy just before the start of the magnetic field evolution $E_{rot}/M_{core} \approx 0.39 - 0.40 \cdot 10^{19}$ erg/g (solid line) $E_{rot}/M_{core} \approx 0.19 - 0.23 \cdot 10^{19}$ erg/g (dashed line) (before collapse).

669, 585.

Endeve E., Cardall C.Y., Budiardja R.D. et al.: 2012, *ApJ*, **751**, 26.

Kotake K., Sato K., Takahashi K.: 2006, *Rep. of Progr. in Phys.*, **69**, 971.

Kotake K., Yamada S., Sato K., Sumiyoshi K., Ono H., Suzuki H.: 2004, *Phys. Rev. D*, **69**, 124004.

LeBlanc J.M., Wilson J.R.: 1970, *ApJ*, **161**, 541.

Mikami H., Sato Y., Matsumoto T., Hanawa T.: 2008, *ApJ*, **683**, 357.

Moiseenko S.G., Bisnovatyi-Kogan G.S. Ardeljan N.V.: 2006, *MNRAS*, **370**, 501.

Müller E., Hillebrandt W.: 1979, *A&A*, **80**, 147.

Obergaulinger M., Aloy M.A., Müller E.: 2006, *A&A*, **450**, 1107.

Ohnishi N.: 1983, *Tech. Rep. Inst. At. En. Kyoto Univ.*, No.198.

Shen H., Toki H., Oyamatsu K., Sumiyoshi K.: 1998, *Nucl. Phys. A*, **637**, 435.

Symbalisty E.M.D.: 1984, *ApJ*, **285**, 729.

Takiwaki T., Kotake K.: 2011, *ApJ*, **743**, 30T.

Takiwaki T., Kotake K., Nagataki S., Sato K.: 2004, *ApJ*, **616**, 1086.

Takiwaki T., Kotake K., Sato K.: 2009, *ApJ*, **691**, 1360.

Taylor R.J.: 1973, *MNRAS*, **161**, 365.

Sawai H., Kotake K., Yamada S.: 2005, *ApJ*, **631**, 446.

Sawai H., Yamada S., Kotake K., Suzuki H.: 2013, *ApJ*, **764**, 10.

Scheidegger S., Fisher T., Liebendoerfer M.: 2008, *A&A*, **490**, 231.

Yamada S., Sawai H.: 2004, *ApJ*, **608**, 907.

SEARCH FOR AND IDENTIFICATION OF GRAVITON EXCHANGE EFFECTS IN DRELL-YAN PROCESS AT LARGE HADRON COLLIDER

A.A. Pankov¹, I.A. Serenkova², A.V. Tsytrinov³

Abdus Salam ICTP Affiliated Centre at Gomel State Technical University, Gomel, Belarus

¹ pankov@ictp.it, ² inna.serenkova@cern.ch, ³ tsytrin@rambler.ru

ABSTRACT. New physics signatures arising from different sources may be confused when first observed at future colliders. Thus it is important to examine how various scenarios may be differentiated given the availability of only limited information. Here, we explore the capability of the Large Hadron Collider (LHC) to distinguish spin-2 Kaluza-Klein towers of gravitons exchange from other new physics effects which might be conveniently parametrized by the four-fermion contact interactions. We find that the LHC with planned energies and luminosities will be capable of discovering (and identifying) graviton exchange effects in the large extra dimensions with the cutoff parameter of order 4.6 - 9.4 TeV (3.6 - 6.0 TeV) depending on energy, luminosity and number of extra dimensions.

Key words: Kaluza-Klein models, extra dimensions, four-fermion contact interactions; Large Hadron Collider, ADD model

1. Introduction

Theories of low-scale quantum gravity featuring large extra spatial dimensions (LED) have attracted considerable interest because of their possible observable consequences at existing and future colliders. In one such scenario, proposed by Arkani-Hamed, Dimopoulos, and Dvali (ADD) [Arkani-Hamed, 1998], the fermions and gauge bosons of the Standard Model (SM) are confined to the three ordinary spatial dimensions, which form the boundary (“the brane”) of a space with n compact spatial dimensions (“the bulk”) in which gravitons alone can propagate. In this model, the Planck scale is lowered to the electroweak scale of $\mathcal{O}(1 \text{ TeV})$, which is postulated to be the only fundamental scale in nature. The fundamental Planck scale in the extra dimensions (M_S), the characteristic size of the n extra dimensions (R) and the Planck scale on the brane (M_{Pl}) are related via

$$M_{Pl}^2 \propto M_S^{n+2} R^n, \quad (1)$$

a purely classical relationship calculated by applying the $4 + n$ dimensional Gauss’s law. In this scenario, then, the weakness of gravity compared to the other SM interactions is explained by the suppression of the gravitational field flux by a factor proportional to the volume of the extra dimensions.

One important consequence for physics in the brane is that the discrete momentum modes of excitation of the graviton transverse to the brane propagate in our three ordinary dimensions as different mass states. Analogously to the momentum states, the spacing between these mass states is proportional to $1/R$. This collection of mass states forms what is known as a Kaluza-Klein (KK) tower of gravitons. The tower can in principle extend up to infinity, but there is a cutoff imposed by the fact the effective theory breaks down at scales above M_S and this effective theory is valid up to a scale of about M_S . Specifically, the sum over the (almost continuous) spectrum of KK states (of mass $m_{\vec{n}}$) can be expressed as [Hewett, 1999]:

$$\sum_{\vec{n}=1}^{\infty} \frac{G_N}{M^2 - m_{\vec{n}}^2} \rightarrow \frac{-\lambda}{\pi M_S^4}, \quad (2)$$

where λ is a sign factor, G_N is Newton’s constant, and M_S is the cutoff scale, expected to be of the order of the TeV scale. Equation (2) can be considered as an effective interaction at the scale M_S . λ is a dimensionless parameter of $\mathcal{O}(1)$. The different signs of λ allow for different signs of the interference between SM and LED graphs.

There are several conventions for the parameter λ/M_S^4 . In Hewett convention [Hewett, 1999], $\lambda = 1$ for constructive interference and $\lambda = -1$ for destructive interference. Other popular conventions are those of Giudice, Rattazzi, Wells (GRW) [Giudice, 1999], and Han, Lykken, Zhang (HLZ) [Han, 1999]. To translate results from Hewett to GRW convention one simply multiplies $M_S(\text{Hewett})$ by $\sqrt[4]{\pi/2}$ (constructive interference only). In HLZ convention the dependence on the number of extra dimensions n is calculated and it

is incorporated into λ . For $n > 2$:

$$M_S(\text{HLZ}) = \sqrt[4]{\frac{\pi}{2} \left(\frac{2}{n-2} \right)} M_S(\text{Hewett}). \quad (3)$$

Note, that at $n = 5$, $M_S(\text{HLZ}) \approx M_S(\text{Hewett})$. In both the GRW and HLZ formalisms gravity effects interfere constructively with the SM diagrams. Throughout the paper we will follow the HLZ parametrization.

The existence of KK gravitons can be tested at colliders by searching for two different processes: real graviton emission and virtual graviton exchange. At leading order, virtual graviton exchange includes processes in which a virtual graviton is produced by the annihilation of two SM particles in the initial state, the graviton then propagates in the extra dimension and finally decays into SM particles that appear in the brane. Real graviton production occurs when a graviton is produced together with something else by the interaction of SM particles and escapes into the extra dimensions, leaving behind missing energy. Existing collider experimental data analysis gave no observation of LED effects, but only constraints. Indirect graviton effects at LHC were searched for in processes of lepton and boson pair production. The corresponding constraints on M_S (HLZ) obtained from LHC data was found to be around 4.18 TeV for $n = 3$ [Aad, 2013].

A general feature of the different theories extending the SM of elementary particles is that new interactions involving heavy elementary objects and mass scales should exist, and manifest themselves *via* deviations of measured observables from the SM predictions. While for the supersymmetric extensions of the SM, there is confidence that the new particles could be directly produced and their properties studied, in numerous other cases, such as the composite models of fermions and the exchange of leptoquarks, existing limits indicate that the heavy states could not be produced even at the highest energy supercolliders and, correspondingly, only “virtual” effects can be expected. A description of the relevant new interaction in terms of “effective” contact-interaction (CI) is most appropriate in these cases. Of course, since different interactions can give rise to similar deviations from the SM predictions, the problem is to identify, from a hypothetically measured deviation, the kind of new dynamics underlying it. We shall here discuss the possibility of distinguishing such effects of extra dimensions from other new physics (NP) scenarios in lepton pair production at the LHC:

$$p + p \rightarrow l^+ l^- + X, \quad (4)$$

where $l = e, \mu$. The dominant Feynman diagrams that contribute to this process in ADD model is shown in Fig. 1. When KK gravitons are included, new diagrams with respect to the SM ones appear as shown in Fig. 1.

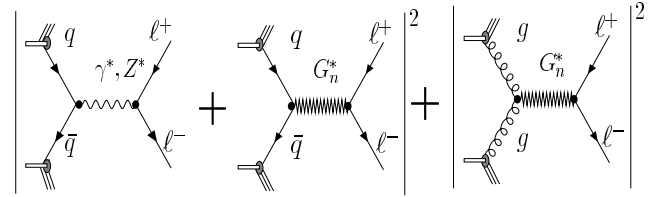


Figure 1: Feynman diagrams for dilepton production at leading order in ADD model.

Since the LED contribution to SM pair production proceeds through a KK tower of graviton states with a closely spaced mass spectrum, the extra-dimensional signal does not appear as a single resonance, but rather as an enhancement of the production cross section at high invariant mass where the SM contribution is rapidly falling and a large number of gravitons can be produced or, equivalently, more modes of the momentum in the bulk can be excited.

2. Discovery reach

In the SM, lepton pairs can at hadron colliders be produced at tree-level via the following parton-level process

$$q\bar{q} \rightarrow \gamma, Z \rightarrow l^+ l^-. \quad (5)$$

Now, if gravity can propagate in extra dimensions, the possibility of KK graviton exchange opens up two tree-level channels in addition to the SM channels, namely

$$q\bar{q} \rightarrow G_n^* \rightarrow l^+ l^- \quad \text{and} \quad gg \rightarrow G_n^* \rightarrow l^+ l^-, \quad (6)$$

where G_n^* represents the gravitons of the KK tower.

To estimate the discovery reach of graviton towers in ADD model one can use the invariant mass distributions of lepton pairs that have significantly different behavior in the SM and the ADD model. As an illustration, Fig. 2 shows the dilepton invariant mass spectrum for the case of $M_S = 4$ TeV and $n = 3, 4, 5$ and 6 with constructive interference between the SM and LED diagrams. The LED signal clearly stands out above the background at higher values of the invariant mass. Events predicted by the SM are generated by the PYTHIA 6.325 Monte Carlo (with default PDF CTEQ6L) while ADD expectations were generated by STAGEN 1.05 code.

Discovery reach of graviton towers in the ADD model was determined with χ^2 function defined as

$$\chi^2 = \sum_{bin} \left(\frac{\Delta N_{bin}}{\delta N_{bin}} \right)^2, \quad (7)$$

where $N_{bin} = \varepsilon_{l^+ l^-} \mathcal{L}_{int} \sigma_{bin}$, $\varepsilon_{l^+ l^-} = 90\%$, $\Delta N_{bin} = N_{bin}^{ADD} - N_{bin}^{SM}$, $\delta N_{bin} = \sqrt{N_{bin}^{SM}}$. Here, \mathcal{L}_{int} is time integrated luminosity, $\varepsilon_{l^+ l^-}$ reconstruction efficiency of

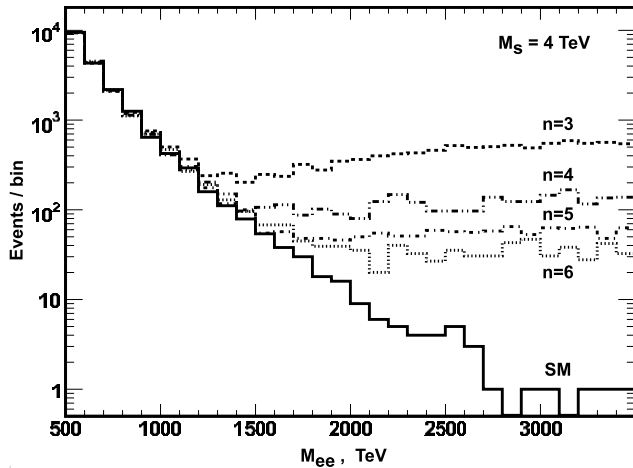


Figure 2: Effects of extra dimensions on the dilepton mass spectrum at LHC. Histograms show the spectrum in the SM as well as in ADD scenario with cutoff $M_S = 4$ TeV and different number of extra dimensions ($n = 3 - 6$) and at integrated luminosity 100 fb^{-1} .

the dilepton, σ_{bin} is integrated cross-section within the bin. Summation in Eq. (7) runs over 17 bins with the width of 100 GeV in the range of 500 GeV and 2200 GeV.

The results of the χ^2 analysis are demonstrated in Fig. 3. In particular, Fig. 3 shows discovery reach on cutoff scale M_S at 95% C.L. for $n = 3$ and $n = 6$ as a function of integrated luminosity.

3. Center-Edge Asymmetry A_{CE}

The center-edge and total cross sections can at the parton level be defined as [Osland, 2003], [Osland, 2008]:

$$\begin{aligned} \hat{\sigma}_{CE} &\equiv \left[\int_{-z^*}^{z^*} - \left(\int_{-1}^{-z^*} + \int_{z^*}^1 \right) \right] \frac{d\hat{\sigma}}{dz} dz, \\ \hat{\sigma} &\equiv \int_{-1}^1 \frac{d\hat{\sigma}}{dz} dz, \end{aligned} \quad (8)$$

where $z = \cos\theta_{cm}$, with θ_{cm} the angle, in the c.m. frame of the two leptons, between the lepton and the proton. Here, $0 < z^* < 1$ is a parameter which defines the border between the “center” and the “edge” regions.

The center-edge asymmetry at hadron level can then for a given dilepton invariant mass M be defined as

$$A_{CE}(M) = \frac{d\sigma_{CE}/dM}{d\sigma/dM}, \quad (9)$$

where a convolution over parton momenta is performed, and we obtain $d\sigma_{CE}/dM$ and $d\sigma/dM$ from

the inclusive differential cross sections $d\sigma_{CE}/dM dy dz$ and $d\sigma/dM dy dz$, respectively, by integrating over z according to Eq. (8) and over rapidity y between $-Y$ and Y , with $Y = \log(\sqrt{s}/M)$.

For the SM contribution to the center-edge asymmetry, the convolution integrals, depending on the parton distribution functions, cancel, and one finds

$$A_{CE}^{SM} = \frac{1}{2}z^*(z^{*2} + 3) - 1. \quad (10)$$

This result is thus independent of the dilepton mass M , and identical to the result for e^+e^- colliders. Hence, in the case of no cuts on the angular integration, there is a unique value, $z^* = z_0^* \simeq 0.596$, for which A_{CE}^{SM} vanishes, corresponding to $\theta_{cm} = 53.4^\circ$.

The SM center-edge asymmetry of Eq. (10) is equally valid for a wide variety of NP models: composite-like contact interactions, Z' models, TeV-scale gauge bosons, *etc.* However, if graviton exchange is possible, the graviton tensor couplings would yield a different angular distribution, leading to a different dependence of A_{CE} on z^* . In this case, the center-edge asymmetry would not vanish for the above choice of $z^* = z_0^*$. Furthermore, it would show a non-trivial dependence on M . Thus, a value for A_{CE} different from A_{CE}^{SM} would indicate non-vector-exchange of NP.

Another important difference from the SM case is that the graviton also couples to gluons, and therefore it has the additional gg initial state of Eq. (6) available. In summary then, including graviton exchange and also experimental cuts relevant to the LHC detectors, the center-edge asymmetry is no longer the simple function of z^* given by Eq. (10).

4. Numerical analysis and concluding remarks

We assume now that a deviation from the SM is discovered in the cross section in the form of “effective” CI. We will here investigate in which regions of the ADD parameter spaces such a deviation can be *identified* as being caused by spin-2 exchange. More precisely, we will see how the center-edge asymmetry (9) can be used to exclude spin-1 exchange interactions beyond that of the SM. At the LHC, with luminosity $\mathcal{L}_{int} = 10, 100$ and 1000 fb^{-1} , we require the invariant lepton mass $M > 500 \text{ GeV}$ and divide the data into 100 GeV bins as long as the number of events in each bin, $\epsilon_l \mathcal{L}_{int} \sigma(i)$, is larger than 10. Here, ϵ_l ($l = e, \mu$) is the experimental reconstruction efficiency and $\sigma(i)$ the cross section in bin i .

In order to get more statistics, one may integrate over bins i in M . We therefore define the bin-integrated center-edge asymmetry by introducing such an integra-

tion,

$$A_{\text{CE}}(i) = \frac{\int_i \frac{d\sigma_{\text{CE}}}{dM} dM}{\int_i \frac{d\sigma}{dM} dM}. \quad (11)$$

To determine the underlying new physics (spin-1 vs. spin-2 couplings) one can introduce the deviation of the measured center-edge asymmetry from that expected from pure spin-1 exchange, $A_{\text{CE}}^{\text{spin-1}}(i)$ (which in our approach is zero), in each bin,

$$\Delta A_{\text{CE}}(i) = A_{\text{CE}}^{\text{spin-2}}(i) - A_{\text{CE}}^{\text{spin-1}}(i). \quad (12)$$

The bin-integrated statistical uncertainty is then given as

$$\delta A_{\text{CE}}(i) = \sqrt{\frac{1 - A_{\text{CE}}^2(i)}{\epsilon_l \mathcal{L}_{\text{int}} \sigma(i)}}, \quad (13)$$

based on the number of events that are effectively detected and the A_{CE} that is actually measured. In the ADD scenario, the identification reach in M_S can be estimated from a χ^2 analysis:

$$\chi^2 = \sum_i \left[\frac{|\Delta A_{\text{CE}}(i)|}{\delta A_{\text{CE}}(i)} \right]^2, \quad (14)$$

where i runs over the different bins in M . The 95% CL is then obtained by requiring $\chi^2 = 3.84$, as pertinent to a one-parameter fit.

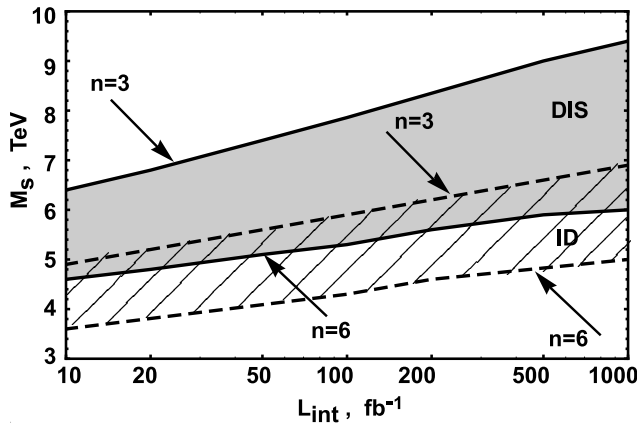


Figure 3: Discovery (gray band) and identification (hatched band) reaches on M_S (in TeV) at 95% CL for different number of extra dimensions ($n = 3 - 6$) at the LHC with 14 TeV.

From a conventional χ^2 analysis we find the ADD-scenario *identification* reach on M_S at the LHC. The results are summarized in Fig. 3 which shows the identification reaches for different number of extra dimensions ($n = 3, 6$) as a function of integrated luminosity \mathcal{L}_{int} .

In conclusion, a method proposed here and based on A_{CE} is suitable for actually *pinning down* the spin-2 nature of the KK gravitons up to very high M_S close to discovery reach. Therefore, the analysis sketched here can potentially represent a valuable method complementary to the direct fit to the angular distribution of the lepton pairs. We find that the LHC detectors will be capable of discovering and identifying graviton spin-2 exchange effects in the ADD scenario with M_S ranging in 4.6 - 9.4 TeV (3.6 - 6.0 TeV) depending on luminosity and number of extra dimensions.

Acknowledgements. This research has been partially supported by the Abdus Salam ICTP.

References

- Aad G. et al. (behalf of ATLAS Collaboration): 2013, *Phys. Rev.*, **D 87**, 015010.
- Arkani-Hamed N., Dimopoulos S., Dvali G. R.: 1998, *Phys. Lett.*, **B429**, 263.
- Giudice G. F., Rattazzi R., Wells J. D.: 1999, *Nucl. Phys.*, **B544**, 3.
- Han T., Lykken J., Zhang R.: 1999, *Phys. Rev.*, **D59**, 105006.
- Hewett J. L.: 1999 *Phys. Rev. Lett.*, **82**, 4765.
- Osland P., Pankov A. A., Paver N.: 2003, *Phys. Rev.*, **D68**, 015007.
- Osland P., Pankov A. A., Paver N., Tsytrinov A.V.: 2008, *Phys. Rev.*, **D78**, 035008.

DATA PROCESSING PIPELINE FOR DECAMETER PULSAR/TRANSIENT SURVEY

Vasylieva I.Y.^{1,2}, Zakharenko V.V.¹, Zarka P.², Ulyanov O.M.¹, Shevtsova A.I.¹, Seredkina A.A.¹

¹ Institute of radio astronomy of NAS of Ukraine
Kharkiv, Ukraine

² LESIA, Observatory of Paris of CNRS of France
Meudon, France

iaroslavna.vasylieva@gmail.com

ABSTRACT. The study of the low-frequency radio sky at short time scales provides the insights into the nature of transient radio sources as well as gives a sensitive tool for interstellar medium sensing. The decameter survey of the northern sky is aimed to discover new sources of transient and repetitive emission within more than 100 Tb of the high time resolution data. The efficient pipeline of data cleaning and processing is developed and successfully tested.

Key words: transient emission, pulsars, cleaning procedure

1. Introduction

The sources of rapidly varying pulsed radio emission (pulsars) have been investigated in the decameter range for more than 40 years. It was revealed that this range is very promising in terms of detecting new phenomena in their behavior. For example, the phenomenon of the anomalously intense pulses was discovered in the decameter range [1]. The sporadic behavior of certain pulsars is more noticeable at low frequencies [2]. The precision of interstellar medium sensing is highest in decameter range, as the dispersion measure and rotation measure increase as a square of frequency. Transient radio emission which can also be generated by neutron stars may also exhibit many interesting peculiarities at low frequencies.

The study of transient sources of radio emission is one of the key projects for the new generation of radio telescopes such as LOFAR and SKA [3,4]. The SKA mainly explores the higher band of radio spectrum, whereas LOFAR has the operating frequency range 10-240 MHz but is still optimized to work above 30MHz. Therefore the lowest part of radio spectrum, observable from the ground (10-30 MHz), will not be covered enough by investigation of transient radio sources.

The most sensitive radio telescope in this frequency range is still the UTR-2 (Ukrainian T-shaped Radio telescope, 2nd modification). It has shown the significant success in the detection of pulsed and transient radio emission [5,6]. Until recent time the sensitivity of the telescope was restricted by the receiving system, and the limited capacity of data storage prevented the massive study of all pulsar sample. Now, with the introduction of digital backend it became possible to measure the pulsar characteristics precisely and to draw statistical conclusions from the large sample of observed pulsars [5].

The low-frequency range provides special benefits for the study of neutron stars which are known to be sources

of pulsed and transient emission. These benefits are connected with expansion of their beaming fraction at lowest frequencies [5], and they allow discovering new sources which are not reachable for higher-frequency observations. This fact and the statistics of the pulsar behavior at decameter wavelengths have revealed the possibility to detect up to 100 new pulsars and/or transients in the decameter range. This was the motivation to commence a new survey of northern sky with relatively high time resolution (8 ms). In this survey we expect to discover nearby slow pulsars which haven't been detected so far due to the orientation of their narrow radiation cones, which get broader at low frequencies as well as the bursts from RRAT-like sources and other transients.

2. The data cleaning and processing pipeline

The survey strategy is related to the peculiarities of UTR-2 and is a compromise between the integration time for each source (which must be large) and the total observation time (must be the least possible). This contradiction was resolved in the technique using the Earth's rotation and the wide beam pattern of antenna. Thus, the entire northern sky can be surveyed in 40 days, implying the storage and processing of ~100 terabytes of the data. To confirm the detections, the re-observations of candidate-sources will be needed, and to detect more transients, the multiple records of the sky are essential. It will lead even to larger data amounts to be processed. The fast and efficient data processing pipeline is therefore needed to deal with all the observational data in the automatic mode.

The processing of survey data includes the following stages: (i) the interference excision, (ii) procedure of dispersive delay compensation with different trial values of dispersion measure (DM) constant (hereafter, dedispersion), (iii) search for individual dispersed pulses and (iv) search for periodicity in the processed data.

2.1. The interference excision

The most tricky and important task, the data cleaning procedure, is needed for both pulsar and transient pipelines. Due to the large area, occupied by the beam on the sky, there are much terrestrial interference and signals from other cosmic sources captured by the beam. All these artificial or natural signals may show up as the false-positive detection of the spurious sources, giving certain

periodicities in the Fourier domain or bright spots on the individual bursts search diagrams.

The level of the interference varies from time to time, depending on the time of the day, season etc. Therefore the different depth of cleaning should be used during the processing. In our case the most reasonable way is to perform an adaptive procedure, consisting of several stages, which adds or removes the additional stages depending on the percentage of data samples, contaminated by the interference. The thresholds used in the cleaning should be more severe when searching for periodic weak pulsar signals, which are normally under the noise level, and less severe when identifying the transient signals, which are supposed to be rather strong.

The implementation, best fitting to the criteria above, is made up of several stages of cleaning in the time and frequency direction.

Initially we calculate iteratively the mean and standard deviation (σ) in each frequency channel, clipping the values above 3σ at each iteration. Then we normalize the data, to eliminate the amplitude-frequency characteristic unevenness of the telescope and to make data zero-mean. The normalized data are shown in Fig. 1, a). The intense (black) features are all from terrestrial origin, and are the interference.

After that we make two stages of cleaning the ‘bad’ (interference) samples. Fig 1 shows the cleaning stages in the same order as in the pipeline. The underlying principle of first stage is described in [7], in section ‘The SumThreshold method’, and adapted to UTR-2 data. The main point is that the different thresholds are applied to the data, and the connected shapes of samples exceeding each threshold are found. A combination of N samples (either in time or in frequency direction) is flagged as interference if its average exceeds the threshold T_N (given in the absolute value or relative to the standard deviation σ). The sliding window size N is increased from iteration to iteration, and the larger is N , the lower is the threshold, applied to the average of the samples. The values that have been flagged in the previous iteration are not taken into account in the subsequent one. For UTR-2 data after normalization (zero-mean), the sizes of N and the corresponding thresholds differ for the time and frequency direction. They are listed in the table 1.

Table 1

Time direction:					
N	2	8	16	128	256
T_N	$6.67 \cdot \sigma$	$2.96 \cdot \sigma$	$1.97 \cdot \sigma$	$0.58 \cdot \sigma$	$0.4 \cdot \sigma$
Frequency direction:					
N	1	2	4	8	64
T_N	$10 \cdot \sigma$	$6.67 \cdot \sigma$	$4.44 \cdot \sigma$	$2.96 \cdot \sigma$	$0.88 \cdot \sigma$

The result of the performance of the described can be seen in Fig. 1, b).

The last stage is the modified version of cleaning procedure, described in [5], without examining of single samples (it is moved to the 1st stage). To eliminate the low-level wideband and narrowband interference, we accumulate the data by frequency or time, correspondingly. After that the σ of integrated time series

(or of average spectrum) is re-calculated and the spikes exceeding the 4σ -level are flagged (Fig. 1, c)).

All the flagged samples are stored in binary ‘bad samples map’ (Fig. 1, d)), where 1 is a good sample, 0 is a bad one. They are replaced by the median, calculated over all ‘good’ samples of the dynamic spectrum.

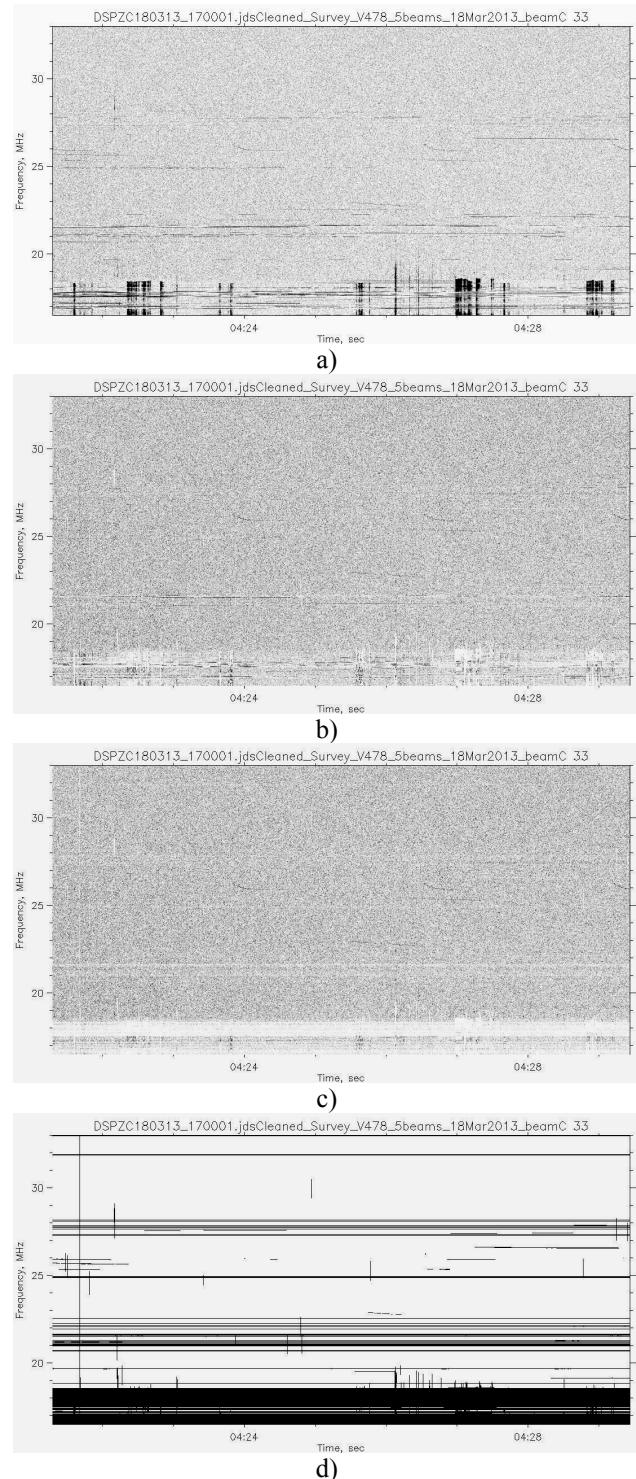


Figure 1: The successive stages of data cleaning procedure

When the data are rather clean, only with short features along the time or frequency direction, the first stage of the cleaning algorithm is applied. If the data contains numerous

wideband interference or continuously broadcasting radio stations' signals, we add the remaining two stages of the cleaning to the pipeline. At this step, the whole frequency channels or time intervals are removed from the data.

This sophisticated algorithm shows sufficient performance visible by naked eye and is well adapted to UTR-2 data. The average value of data, lost due to interference during one observational night, is about 4%. Mostly it is the data of the first and the last hours of observations, whereas the middle of the night tends to be almost interference-free.

2.2. Dispersive delay compensation

The clean data are then dedispersed with different dispersion measure (DM) trials. Initially we restrict the upper value of DM as $30 \text{ pc}\cdot\text{cm}^{-3}$, but later this value will be raised to $60 \text{ pc}\cdot\text{cm}^{-3}$ for pulsars, and $100 \text{ pc}\cdot\text{cm}^{-3}$ for transients. We have chosen the step of trial DMs to be $0.01 \text{ pc}\cdot\text{cm}^{-3}$. The precision could be higher, but we have selected this value as an optimum between the precision and the processing time. The precision reached in the higher-frequency surveys is less, because the propagation effects are not so influential there. Due to this, the decameter range is the unique probe of the interstellar medium via its dispersion, scattering and the Faraday effect.

2.3. Search for individual dispersed pulses

The further step of the pipeline is a search for individual transient events, which implies examining the data for dispersed pulses, exceeding certain threshold. At this stage we potentially can detect the giant pulses or anomalously intense pulses of pulsars, RRAT-like signals etc. The nearby pulsar will show up as a series of the intense pulses at the same dispersion measure trial value. To reduce the fluctuations of the background noise and to distinguish the useful signal, we normally apply the filtering of the low-frequency components of the data with a cut-off frequency of high-pass filter about 0.2 Hz. To increase the sensitivity, we also use the integration of 4 time samples into 1 (32 ms).

The detection algorithm denotes the suspected transient events by the circles, with the diameter proportional to the signal-to-noise ratio of the event. To reject the spurious events, we return to previous stages of processing and check the event visually. We check whether the cleaning has removed only obstructive signals, whether after dedispersion with the corresponding trial DM the signal is aligned into a straight vertical line on the dynamic spectrum and whether there are several events at the same dispersion measure (then we assume the detection of a pulsar). Fig. 2 shows the result of algorithm performance at the strong pulsar B0809+74 with the dispersion measure $5.755 \text{ pc}\cdot\text{cm}^{-3}$. We see the repetitive events of different intensity, with intervals multiple of pulsar period.

2.4. Search for periodicity

The search for weak pulsar signals is possible due to their periodicity. We make the Fourier analysis and fold the integrated time series with the trial periods of pulsar. As we restrict the lower value of pulsar periods in the survey down

to 0.1 s, we should consider the harmonics less than 10 Hz in the Fourier domain. The higher harmonics are filtered out. The Fourier transform is applied to each integrated time series, obtained by summing the shifted frequency channels with respect to one another according to the DM trial value. To increase the signal-to noise, we sum several FFT outputs of neighboring DM trials. To increase the power of the first harmonic, we add the 2, 4, 8 and 16 harmonics to it. The result is the peaks of certain shape, outstanding above the noise. Each of these peaks corresponds to $1/\text{trial period}$, which we will depict on the period-dispersion measure plane, looking for characteristic shape of average dispersed pulses.

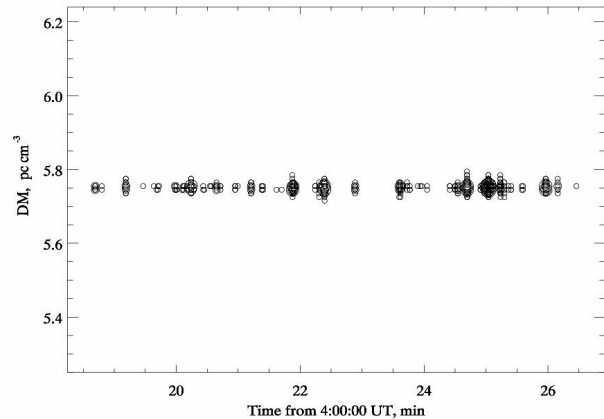


Figure 2: The result of individual pulses search algorithm with pulsar B0809+74

3. Results and perspectives

Up to now, by means of the described pipeline we have processed about 25% of survey data. A large number of transient-candidates are obtained, and we are excluding the spurious events from them.

The upper value of $\text{DM}=100 \text{ pc}\cdot\text{cm}^{-3}$ will lead into 10 000 different shifts to be made between the frequency channels in the data. For 100 Tb of data, this will take a lot of processing time. To accelerate the data processing, we are introducing the techniques of parallel and distributed computing to the pipeline. The GPU-based dedispersion and processing of the different data fragments at the available nodes of Ukrainian Academic Grid will speed-up the processing up to 200 times. Another alternative is the usage of volunteer distributed computing system BOINC [8]. The Einstein@Home project, powered by BOINC, was used to discover 24 new pulsars in Parkes Multibeam Pulsar Survey data [9].

References

1. Ulyanov O. et al.: 2006, *Radiofizika and Radioastronomia*, **11**, 113.
2. Ulyanov O., Zakharenko V.: 2012, *Astron. Rep.*, **56**, 417.
3. Stappers B.W. et al.: 2011, *A&A*, **530**, id.A80.
4. Colegate T.M., Clarke N.: *PASA*, **28**, 4, 299.
5. Zakharenko V. et al.: *MNRAS*, **431**, 4, 3624.
6. Popov M. V. et al.: 2006, *Astron. Rep.*, **50**, 562.
7. Offringa A.R.: 2012, University of Groningen, *diss*.
8. <http://boinc.berkeley.edu/>
9. Knispel B. et al.: 2013, *ApJ*, **774**, 93.

ASTROCHEMISTRY OF STAR FORMATION

D.S. Wiebe, O.V. Kochina

Institute of Astronomy of the Russian Academy of Sciences
48 Pyatnitskaya St. 119017, Moscow, Russia, *admin@inasan.rssi.ru*

ABSTRACT. Star formation is one of the key processes governing the evolution of the Universe. It is accompanied by significant transformations in the chemical composition and the physical state of the interstellar medium. Combining observations in infrared and radio bands, we obtain a wealth of observational data on the star formation both in continuum and spectral lines. These lines mostly belong to molecules, from simple diatomic species to complex organic compounds. However, interstellar molecules are not well-mixed with the bulk interstellar gas (molecular and atomic hydrogen) and possess a complex evolution of their own. Thus, a straightforward interpretation of observational data is seldom possible. One needs sophisticated chemical and physical models to decipher processes occurring in star-forming regions.

Key words: star formation, ISM, astrochemistry, numerical modeling, databases for astrochemistry

1. Introduction

For more than a century astronomers know that the space between stars is not empty. Since first guesses on calcium clouds [1] our knowledge on the interstellar medium (ISM) has expanded significantly. Thanks to powerful new observatories, both ground-based and space-based, and a great amount of spectroscopic data, we have got new insights on the chemical composition of the interstellar matter. One of the key discoveries of the second half of XX century was a detection of numerous molecular species, extending from simple diatomic molecules, like CO or OH, to complex organic compounds, with tentative detection of a simplest amino acid, glycine, in the ISM.

The molecular composition of the interstellar medium (ISM) has become a subject for the new branch of astronomy which is called astrochemistry. The field of astrochemistry goes well beyond the ISM and molecular clouds. Molecules are observed in comets, planets, their satellites, planetary nebulae, and even in stars. However, we can assume with certainty that it is the star formation theory that benefits most from the development of astrochemical models. The

lifecycle of species observed in star-forming regions is of great interest, as molecules are not just passive witnesses of the star formation. Often, they play a significant role in the formation of stars and planetary systems and eventually in the origin of life itself, by affecting the thermal balance in the ISM, defining its interaction with magnetic fields, and providing raw materials for organic synthesis in young planetary systems.

The Universe started as an almost pure mixture of hydrogen (70%) and helium (30%), with small amount of lithium and beryllium. All the other elements were synthesized later in stars and then ejected in the ISM. It was long believed that beyond planets these elements may only exist as atoms or ions as molecules cannot form in harsh interstellar conditions. However, since late 1930's it has become apparent that at least simple species like CH, CN, CH⁺ are abundant in the general ISM (by the way, the problem of their formation and survival is still far from being solved). Development of radioastronomy after the Second World War opened a new chapter in studies of the ISM. Vast cold clouds of interstellar gas have been discovered that are dense and opaque to UV photons. So, they present much more favorable conditions for formation and survival of molecules.

Molecular clouds are dense ($> 10^2 \text{ cm}^{-3}$) and cold ($\sim 10\text{K}$) components of the ISM that are known to be sites of the ongoing star formation. The chemical composition of nearby molecular clouds is typical for the general interstellar medium in the Solar vicinity. The most abundant elements are hydrogen and helium. All the other elements are significantly less abundant, with oxygen abundance being less than 10^{-3} (by number relative to H atoms). Also, many elements (like sulfur, magnesium, iron, silicon, and others) are depleted into dust grains so that their gas-phase abundances have values of the order of $10^{-9} - 10^{-8}$. The distinctive feature of molecular clouds is that hydrogen is almost totally in molecular form.

First interstellar molecules have been detected in absorption, producing very thin lines in spectra of background stars. But the real start of astrochemistry and star formation studies is also related to the advent of radioastronomy. As molecules possess additional de-

degrees of freedom related to their internal motions, they are able to emit and absorb photons not only in electronic transitions, but also in vibrational transitions, rotational transitions, etc. Low-energy rotational transitions are most important in cold molecular clouds, having their wavelengths in millimeter and centimeter ranges.

Radioastronomical studies of the ISM have started with the seminal paper by Ewen & Purcell [2], describing the detection of the 21 cm atomic hydrogen line. The first interstellar molecule, hydroxyl, has been found in 1963 [3], ammonia, water, and formaldehyde followed in late sixties. Since then, a few molecules are discovered each year. One of the most important of them, CO, has been detected by Wilson et al. [4]. This molecule is very abundant and easy to observe. It is now believed to be a proxy for molecular gas in general, as molecular hydrogen has no transitions that would be observable in molecular clouds.

It must be kept in mind that molecular clouds are not uniform, and no single molecule may serve as a true tracer of the bulk molecular gas. The star formation process starts with a formation of dense clumps ($n \sim 10^4 \text{ cm}^{-3}$) in molecular clouds. These clumps are most often traced by CO and NH_3 lines. Later, some isolated cores ($n \sim 10^6 \text{ cm}^{-3}$) form inside the clumps. These are observed in lines of HCN, CS, HCO^+ and some other. The birth of a star is accompanied by powerful outflows that can be seen in emission lines of CO, water, SO, SO_2 . Finally, a planetary system forms around a star, and it definitely borrows some molecules from a parent molecular cloud.

Molecular lines are a valuable source of information on various stages of the star formation process. Of course, some data can also be extracted from dust observations, but the utility of these data is limited. Basically, one can infer grain surface density, the radiation field (heating the grains), and grain temperature.

Molecular lines are much more diverse. Their analysis allows estimating both surface and volume gas density, velocity field, gas temperature, magnetic field (using the Zeeman effect). Only with molecular lines one can detect that a given molecular core is indeed collapsing, that is, is truly going to become a star in the future.

There is a complication, though. None of more than 150 molecules found up to date is well mixed with molecular hydrogen, that is, with gas in general. Also, molecular abundances are extremely low, typically being much less than 10^{-5} relative to molecular hydrogen. In fact, we try to infer conditions in molecular clouds using tiny admixtures that are non-evenly distributed in the parent cloud. Obviously, one cannot interpret observations of molecular lines without knowing chemical reactions that operate in a studied object.

2. Chemical reactions

To build an astrochemical model one specifies the list of compounds and reactions between them, along with the physical parameters in the medium and element abundances. In the overwhelming majority of astronomical situations only two-body processes should be taken into account. Reactions are divided into gas-phase reactions and surface reactions, occurring on dust grains. Accretion and desorption are responsible for the exchange of species between gas and dust. The contribution of each reaction type depends on the conditions in the cloud. In general, gas-phase reactions mostly produce simple molecules, while complex compounds are synthesized on grains and then returned to gas-phase by some desorption mechanism. Exceptions are possible. Some simple molecules, like CO_2 , NH_3 , water, are effectively produced on dust surfaces, while gas-phase formation routes have been proposed for a number of organic species.

2.1. Gas-phase reactions

Gas-phase reactions are usually divided into reactions of chemical bond formation, reactions of chemical bond destruction, and reactions of chemical bond rearrangement. Depending on reactants, reactions are classified as neutral-neutral, ion-molecular, recombination reactions (with electrons), photoreactions (with photons), and reactions with cosmic rays.

Rates of most neutral-neutral reactions depend on the temperature and may have potential barriers. Thus, their rates at low temperatures of molecular clouds are mostly very low. Apart from some specific cases, neutral-neutral reactions do not influence the chemical evolution of a molecular cloud significantly. On the other hand, ion-molecular reactions are free from barriers and less temperature dependent. They were recognized almost forty years ago as a main contributor to the chemical evolution of the ISM ([5]; [6]), especially, at early stages. For ion-molecular reactions to start operating, there must be some ions in the medium. The initial ionization is provided by cosmic ray particles.

Quite recently, ion-ion reactions started to be considered in astrochemical networks, as negatively charged ions have been discovered that can interact with positive ions. As soon as negatively charged ions are taken into account, reactions of associative detachment also should be included in the network. Interaction of a molecular ion with an electron results in recombination or dissociative recombination. Photoreactions lead to ionization or dissociation (or both) of a species.

2.2. Surface reactions

Gas-phase reaction networks allow explaining abundances of many molecules, but they fail in the most important case of H_2 formation. Molecular hydrogen cannot form in the gas phase, or, more accurately, gas-phase reactions of H_2 formation are extremely slow. It is widely assumed now that two H atoms unite into a molecule on a surface of a grain.

Other molecules may stick to dust grains or form on grain surfaces as well. Colliding with a grain at low temperature, a molecule freezes to its surface. It may be held by van der Waals forces (physical adsorption) or chemical bonds (chemisorption). If a molecule is chemisorbed, it cannot move over the grain surface. So, the only way for it to interact with another molecule is the direct accretion of this other molecule to the very same site on the grain. Probability of such an event is quite low.

Physical adsorption gives a molecule more freedom. It may move over the grain surface via thermal hopping. Still, at low temperatures only the lightest species can migrate this way. When migrating species encounter other (may be, heavier) species, they may combine to form some new molecule. A heavy molecule remains at the same site for a long time, so it may grow bigger than in the gas phase. Surface chemistry is invoked to explain the formation of complex molecules [7], along with the formation of molecular hydrogen.

Surface species are returned to gas via desorption processes. Desorption can be thermal, with the evaporation rate depending on the grain temperature, or non-thermal, via collision with a cosmic ray particle, UV photon absorption, or due to energy generated by exothermic surface reactions [8].

2.3. Mathematical representation

The mathematical representation of the chemical evolution is given by

$$\frac{dn_i^g}{dt} = \sum_j \sum_l K_{lj}^g n_l^g n_j^g - n_i^g \sum_j K_{ij}^g n_j^g - k_i^{\text{acc}} n_i^g + k_i^{\text{des}} n_i^g \quad (1)$$

for gas phase reactions and

$$\frac{dn_i^d}{dt} = \sum_j \sum_l K_{lj}^d n_l^d n_j^d - n_i^d \sum_j K_{ij}^d n_j^d + k_i^{\text{acc}} n_i^d - k_i^{\text{des}} n_i^d \quad (2)$$

for surface reactions. In that approach dust is considered to be continuous medium, which is not correct, generally speaking. But a more rigorous approach would require rather difficult methodology (e.g. [9]). Factors k^{acc} k^{des} are rates of accretion and desorption, respectively. Coefficients K_{ij}^g and K_{ij}^d are used to com-

pute binary reaction rates. They have different meanings for different reactions, depending on reactants.

According the Arrhenius law, for a two-body reaction

$$K_{ij} = \alpha_{ij} \left(\frac{T}{300}\right)^{\beta_{ij}} \exp(-\gamma_{ij}/T) \quad (3)$$

for reactions where both reactants are chemical species. Parameters α , β and γ should be found either by theoretical computations or by experiments. Next, for photoreactions

$$k = G_0 \alpha \exp(-\gamma A_V), \quad (4)$$

where α is a rate coefficient for the unshielded UV field, γ accounts for an extinction of the UV field, A_V is the extinction in visual band. The intensity of the radiation field is described by the dimensionless factor G_0 expressed in units of the mean interstellar field in the solar vicinity [10]. Finally,

$$k = \alpha \zeta \quad (5)$$

for direct ionization by cosmic rays. Here ζ is the cosmic ray ionization rate per H_2 molecule, typically assumed to be of the order of 10^{-17} s^{-1} [11].

This formulation allows describing rates for all the reaction types with only three parameters, α , β , and γ . In this approach the set of reactions is a set of ordinary differential equations (ODE) and can be solved by some publicly available solvers, like DVODE or VODE.

3. Databases for astrochemistry

Modeling chemical evolution requires a physical model of an object, an ODE solver to track the changes in component abundances and a database that contains information on relevant chemical reactions together with α , β and γ parameters. Modern databases mostly include only binary reactions. The reactants are molecules, ions, radicals, atoms, electrons, photons, cosmic ray particles and, sometimes, grains (in reactions of dissociative recombination). Also some additional information can be included, like the temperature range for adopted α , β , and γ or information on heat of formation. There are several databases created for special purposes, like databases for deuterium chemistry, a subset of reactions for sulfur chemistry ([12], [13]), a database for shock models [14], a database for photon-dominated regions [15]. But in modeling of the chemical evolution of the ISM, more general purpose databases are common. The two most widely used databases are the UMIST Database for Astrochemistry (UDFA) and KIDA (Kinetic Database for Astrochemistry). Another useful resource is the NIST compilation of reaction parameters that summarizes information from literature.

3.1. UDFA

The UMIST database for astrochemistry started with the work of Millar et al. [16]. The initial reaction set, called the UMIST ratefile included rate coefficients of 2880 gas-phase reactions among 313 species. The next version of the database (UMIST95; [17]) contained rate coefficients for 3864 gas-phase reactions relevant to interstellar and circumstellar chemistry that involved 395 species and 12 elements. Also heats of formation were added. The version of 1999 was updated, and its format was revised. The database contained rate coefficients, temperature ranges, and the temperature dependence of 4113 gas-phase reactions among 396 species. Also there was a new table listing the photoprocess cross sections (ionization, dissociation, fragmentation) for a few species for which these quantities are available. The version of 2006 [18] contains 4572 binary gas-phase reactions among 420 species. Major updates have been made to ion-molecular reactions, neutral-neutral reactions, particularly at low temperature, and dissociative recombination reactions. Also it includes reactions with fluorine.

The most recent update is published in early 2013 [19] as the Rate12 ratefile. It contains purely gas-phase network of reactions between 467 components. The new release includes 22 new negative ions participating in 1280 reactions. Data on dissociative recombination for 18 components are updated. Newer or better data are given for 74 neutral-neutral reactions. The network includes 174 new ion-molecular reactions. A major upgrade is also performed for a set of photoreactions. The latest version can be downloaded from the web-site <http://www.udfa.net/>.

The UMIST database is very popular and was used for modeling different objects, like protoplanetary disks ([20]; [21]; [22]), protostellar disks [23], dense cores ([24]; [25];[26]), comets ([27]; [28]).

3.2. The OSU database

The OSU (Ohio State University) database has a long history that started in the 1980's. It was partially based on the paper by Prasad & Huntress [29] that included the basic chemical model and a library of chemical reaction that contained more than 1400 gas-phase reactions among 137 species. Leung & Herbst [30] updated the reaction network, and since that time E. Herbst's group went on updating the database. The latest version of OSU appeared under that name in 2009. It contains 6046 gas-phase reactions between 468 species and is supplied by the network of surface reactions. The ratefiles can be downloaded from <http://www.physics.ohio-state.edu/~eric/research.html>.

The OSU network is also widely used. Hot cores

([31]; [32]), cold cores ([33]; [32]), protoplanetary disks [32] were modeled using this database.

3.3. KIDA

KInetic Database for Astrochemistry [34] is a new network of gas-phase reactions which is being developed in the University of Bordeaux since 2009 [35] and is derived from the OSU database. It is declared to be designed for the chemical modeling of the ISM and planetary atmospheres. One of the most remarkable features of the network is its constant development. The version of 2010 contained 6215 gas-phase reactions among 666 species. An up-to-date version can be downloaded from <http://kida.obs.u-bordeaux1.fr/>. Also KIDA contains recommendations concerning rate coefficients and uncertainties for them.

3.4. Problems and perspectives

Though the discussed networks are all relevant, sometimes they lead to different results. This is demonstrated in Wakelam et al.[34] where *kida.uva.2011*, *osu-01-2009*, and *udfa06* networks are compared. Even KIDA, initially based on OSU, shows results slightly different from the parent network. The difference stems from sources used for compiling the network, namely, literature, laboratory measurements, theoretical calculations, and other estimations. Selection of sources and their reliability are up to authors of the databases. KIDA was established as an attempt to create a uniform database, so it may become the network of choice in the future. Problems related to numerical implementation of astrochemical models are discussed in detail in Röllig [36].

Yet another problem is related to the incompleteness of databases. In particular, most researchers admit that surface reactions are very important, but the databases mentioned above still do not include them in a general way. The chemical difference of ortho- and para-hydrogen is also not yet incorporated systematically. That hampers the proper account of the deuterium chemistry. Some sets of reactions with deuterated species exist ([37],[38]; [39]) independently. Deuterium is most obvious, but not the only isotope that should be taken into account. Chemistry of isotopologues may become one of the main perspectives in the further development of databases [40].

4. Chemical models

As soon as both the reaction database and a solver for ODE are chosen, they can be used to create the

chemical model itself. The overall design of the model depends on the scientific problem and an object to be modeled. Models can be pseudo-time-dependent ([41]; [42]; [43]) that ignore changes in an object physical structure or in its physical conditions during the chemical evolution, or truly time-dependent (e.g. [44]). While most often researchers tend to create models themselves, there are some publicly available codes.

4.1. *Nahoon*

Nahoon is a pseudo-time-dependent 0D and 1D gas-phase chemical code created by the authors of KIDA [45] and written in Fortran90. The solver DLSODES from the ODEPACK package is used. The code is available online since 2007. The latest version (October 2001) can be downloaded from <http://kida.obs.u-bordeaux1.fr/models/>.

The code [34] is designed for work with KIDA and uses all its advantages. In particular, it checks the temperature range for rate coefficients and checks for duplication of chemical reactions, defined over complementary temperature ranges. Some important processes (formation of molecular hydrogen) are not included, so that the user has to do it additionally. Grains are defined as chemical species and participate in reactions of charge transfer.

4.2. *Astrochem*

Astrochem is “a code to compute the abundance of interstellar species”, written in C and distributed under the terms of the GNU General Public License (GPL). The official web-page for the code is <http://smaret.github.com/astrochem/>. The solver chosen by the author is CVODE [46] from the SUNDIALS library [47]. The code is very fast, as a Jacobian matrix of the system is computed explicitly to speed-up computations. *Astrochem* works with a number of gas-phase chemical processes as well as gas-grain interactions that are described in the manual. *Astrochem* comes with a program *Plabun* that makes plots of abundances computed by *Astrochem* and presents results of computations in a graphic form.

5. Astrochemistry and star formation studies

Suppose we constructed an astrochemical model that predicts molecular abundances as a function of location within a modeled object. There are currently two major strategies to utilize this information in star formation studies. First, one can invoke some simple considerations to relate line intensities to column densities and then compare these observed column densities with

theoretical ones. The simple line analysis also allows deriving some approximate values for gas temperature and density, that are, as a rule, represent values averaged over the line of sight. Considering Doppler shifts of various lines, one can make general conclusions on the kinematics in the studied objects.

The major advantage of this approach is its relative simplicity. It is also less demanding to the quality and amount of observational data. This opens the possibility to use it in surveys and other studies of wide areas with complex and diverse morphology.

The other approach is to use results of astrochemical (and hydrodynamical) modeling as an input for a radiation transfer model that allows computing line profiles for different molecules and transitions at various directions toward the object and then making *direct* comparison with observed profiles. This approach is definitely more adequate but this comes at a price. A good radiation transfer model even in 1D (to say nothing about 3D) is in itself a very complicated and resource-consuming numerical problem. Also, it requires some additional data on molecules, like collisional transition rates, which are not always available.

In very general terms, the mere presence of certain molecular lines is often considered as a marker of a certain evolutionary stage. We have already mentioned in Introduction that CO lines are used as a general “Universe-wide” tracer of moderately dense molecular gas. In denser clumps its utility is lessened due to significant self-absorption. While less abundant CO isotopologues (^{13}CO , C^{18}O) can still be useful, starless (prestellar) cores are more often observed in ammonia and CS lines. These lines in a core that does not show a presence of a compact infrared source indicate the earliest phase of the star-formation process. Additionally, line spectroscopy can be used to select so called infall candidates among such cores. A specific asymmetric line profile shape in these cores is a marker of inward gas motion (presumably, the beginning of a protostellar collapse).

When a protostar appears in the center of the core, it starts to warm up dust grains and evaporates icy mantles, so that complex molecules, having been synthesized on grains, are released into the gas phase where their lines can be observed. The presence of formaldehyde, methanol, methylformate lines is an evidence of a more advanced star formation phase that is called a hot core or a hot corino, depending on a protostar mass.

Yet another signposts of advanced star formation phases (as a rule, in massive star forming regions) are masers in various molecular tracers, most often methanol, water, and hydroxyl masers.

Molecular line observations may help to make a choice among the two most widely accepted paradigms of star formation. According to the “standard” star formation theory, birth of a star is a slow process which

is mainly governed by the magnetic field. Specifically, a single star history starts in an individual dense clump that is initially supported against gravitational collapse by the magnetic field. Due to a gradual loss of magnetic support, the core slowly contracts for a few million year until its density becomes high enough so that gravity wins over magnetic field. Afterwards, the core collapses rapidly and becomes a protostar.

In the gravoturbulent model, both clumps in molecular clouds and the clouds themselves are transient objects born due to collisions of turbulent flows. A density fluctuation arising in a turbulent medium may become gravitationally unstable if its density is high enough. Thus, it appears and collapses in a dynamical timescale that is generally shorter than 1 Myr.

Different timescales involved into these star formation paradigms should leave different imprints into the core molecular content as various molecules also evolve with different timescales. This gives rise to a concept of a chemical clock according to which abundance ratios of rapidly evolving molecules and slowly evolving molecules (for example, CS vs NH₃) can be used to estimate the core age.

While this concept sounds simple and logical, its practical implementation encounters many complications, mostly related to a vast number of unknown parameters. To name a few, our knowledge of CR ionization rate in molecular clouds can be incomplete; description of molecule accretion onto dust grains with a single value of a sticking probability is definitely an oversimplification, and so on. This results in degeneracy of protostellar object parameters determined from observations of only a few molecules [48]. To make model-based inferences more sound, one needs to use observations of as many molecules as possible, which implies a great demand for observing time.

On the other hand, while this information is available it can be used to validate a model and to infer object parameters with a significant certainty. For example, Kochina et al. [49] have shown that a UMIST-based model with surface chemistry allows reproducing column densities in a TMC-1 core for 46 out of 55 species for which this information is available. Among these 46 species are both diatomic molecules and complex organics, like methanol and methyl formate. However, such a detailed analysis is only possible for a limited number of individual objects.

An astrochemical modeling of molecular clouds as 3D evolving objects is still in its infancy as available resources only allow considering very limited reaction networks that are mainly focused on the formation of H₂ and main molecular tracers, mostly, CO.

On the other end of spatial scales we find protoplanetary disks that become more and more attractive from the astrochemical point of view. While only a dozen of molecules is detected in protoplanetary disks so far (compare to more than 150 molecules in interstellar

and circumstellar medium), great expectations are related to the ALMA array that currently operates in Chile. Two most advanced modern astrochemical and physical models of protostellar disks are PRODIMO [50] and ANDES [51].

6. Conclusions

Observations of molecular lines provide a powerful diagnostics of the interstellar medium and protostellar objects at various stages of the star formation process. However, due to the complex nature of interstellar chemistry and molecular emission, these observation cannot be adequately interpreted without equally detailed models. Moved by this necessity, astrochemistry has grown into the powerful and self-sustained branch of astronomy. We can now say that we understand formation and destruction pathways of all the primary molecules in various phases of the ISM, including star-forming regions.

Among the next necessary steps, incorporation of chemical networks into 3D hydrodynamical models can be listed supplied with proper radiation transfer model. This would allow making a complete transition to synthetic observations, that is, to the most rigorous way of comparing theoretical and observational data.

Other vital problems include uncertainties in various molecular parameters, including reaction rates, that can be solved with theoretical modeling and in astrochemical laboratories. Also, chemical models should include reactions with isotopologues. This is needed not only to interpret observations, but also to relate the interstellar chemistry to the chemical composition of the Solar System.

Acknowledgements. The work has been supported by the Federal Targeted Program “Scientific and Educational Human Resources of Innovation-Driven Russia” (contract with the Ministry of Science and Education 14.V37.21.0251).

References

1. Hartmann J.: 1904, *ApJ*, **19**, 268
2. Ewen H.I., Purcell E.M.: 1951, *Nature*, **168**, 356
3. Weinreb S., Barrett A.H., Meeks M.L., Henry J.C.: 1963, *Nature*, **200**, 829
4. Wilson R.W., Jefferts K.B., Penzias A.A.: 1970, *ApJ*, **161**, L43
5. Herbst E., Klemperer W.: 1973, *ApJ*, **185**, 505
6. Watson W.D.: 1973, *ApJ*, **183**, p.L17
7. Garrod R.T., Herbst E.: 2006, *A&A*, **457**, 927
8. Garrod R.T., Wakelam V., Herbst E.: 2007, *A&A*, **467**, 1103
9. Vasyunin A.I., Herbst E.: 2013, *ApJ*, **762**, id.86
10. Draine B.T.: 1978, *A&A Supplement*, **36**, 595
11. Spitzer L., Tomasko Jr., Martin G.: 1968, *ApJ*, **152**, 971

12. Wakelam V. et al.: 2004, *A&A*, **422**, 159
13. Wakelam V., Hersant F., Herpin F.: 2011, *A&A*, **529**, A112
14. Pineau Des Forets G., Roueff E., Schilke P., Flower D.R.: 1993, *MNRAS*, **262**, 915
15. Le Petit F., Nehmé C., Le Bourlot J., Roueff E.: 2006, *ApJS*, **164**, 506
16. Millar T. J. et al.: 1991, *A&A*, **87**, 585
17. Millar T.J., Farquhar P.R.A., Willacy K.: 1997, *A&A*, **121**, 139
18. Woodall J., Agúndez M., Markwick-Kemper A.J., Millar T.J.: 2007, *A&A*, **466**, 1197
19. McElroy D. et al.: 2013, *A&A*, **550**, id.A363
20. Walsh C., Millar T.J., Nomura H.: 2010, *AphJ*, **722**, 1607
21. Heinzeller D., Nomura H., Walsh C., Millar T.J.: 2011, *ApJ*, **731**, 115
22. Ilgner M., Nelson R.P.: 2006, *A&A*, **445**, 205
23. Bai X.-N., Goodman J.: 2009, *AphJ*, **701**, 737
24. Wiebe D., Semenov D., Henning Th.: 2003, *A&A*, **399**, 197
25. Aikawa Yu., Ohashi N., Herbst E.: 2003, *ApJ*, **593**, 906
26. Doty S.D., Neufeld D.A.: 1995, *Bull. of the American Astron. Soc.*, **27**, 1322
27. Canaves M.V., de Almeida A.A., Boice D.C., Sanzovo G.C.: 2007, *Advances in Space Research*, **39**, 451
28. Delanoye S.N., De Keyser J.: 2007, *Space Sci. Rev.*, **130**, 73
29. Prasad S.S., Huntress W.T., Jr.: 1980, *ApJ*, **43**, 1
30. Leung C.M., Herbst E., Huebner W.F.: 1984, *ApJ*, **56**, 231
31. Vasyunin A.I., Herbst E.: 2011, Proc. of the 280th Symp. of the International Astron. Union held in Toledo, Spain, May 30-June 3, 29
32. Semenov D. et al.: 2010, *A&A*, **522**, id.A42
33. Wakelam V. et al.: 2010, *A&A*, **517**, id.A21
34. Wakelam V. et al.: 2012 *ApJS*, **199**, 21
35. Wakelam V.: 2009, *Bull. of the American Astron. Soc.*, **41**, 665
36. Röllig M.: 2011, *A&A*, **530**, id.A9
37. Roberts H., Herbst E., Millar T.J.: SFCChem 2002, Chemistry as a Diagnostic of Star Formation, proc. of a conf., 397
38. Roberts H., Herbst E., Millar T.J.: 2004, *A&A*, **424**, 905
39. Albertsson T., Semenov D.A., Henning Th.: 2011, eprint arXiv:1110.2644
40. Röllig M.; Ossenkopf V.: 2013, *A&A*, **550**, id.A56
41. Millar T.J., Bennett A., Herbst E.: 1986, *ApJ*, **340**, 906
42. Walsh C., Harada N., Herbst E., Millar T.J.: 2009, *ApJ*, **700**, 752
43. Lee H.-H., Bettens R.P.A., Herbst E.: 1996, *A&A Suppl.*, **119**, 111
44. Shematovich V.I., Wiebe D.S., Shustov B.M., Li Zhi-Yun: 2003, *ApJ*, **588**, 894.
45. Wakelam V., Herbst E.: 2008, *ApJ*, **680**, 371
46. Cohen S. D., Hindmarsh A.C.: 1996, *Computers in Physics*, **10**, 138
47. Hindmarsh A.C. et al: 2005, *ACM Transactions on Mathematical Software*, **31**, 363
48. Pavlyuchenkov Ya., Wiebe D., Launhardt R., Henning Th.: 2006, *ApJ*, **645**, 1212
49. Kochina O.V., Wiebe D.S., Kalenskii S.V., Vasyunin A.I. – in prep.
50. Woitke, P.; Kamp, I.; Thi, W.-F.: 2009 *ApJ*, **501**, 383
51. Akimkin V. et al.: 2013, *ApJ*, **766**, id.8

COSMOLOGY, COSMOMICROPHYSICS AND GRAVITATION

PROPERTIES OF THE GRAVITATIONAL LENS MAPPING IN THE VICINITY OF A CUSP CAUSTIC

A.N.Alexandrov¹, V.I.Zhdanov², S.M.Koval³

Astronomical Observatory, Taras Shevchenko National University of Kyiv
Kiev, Ukraine

¹*alex@observ.univ.kiev.ua*, ²*valeryzhdanov@gmail.com*, ³*seregacl@gmail.com*

ABSTRACT. We derive approximate formulas for the coordinates and magnification of critical images of a point source in a vicinity of a cusp caustic arising in the gravitational lens mapping. In the lowest (zero-order) approximation, these formulas were obtained in the classical work by Schneider&Weiss (1992) and then studied by a number of authors; first-order corrections in powers of the proximity parameter were treated by Congdon, Keeton and Nordgren. We have shown that the first-order corrections are solely due to the asymmetry of the cusp. We found expressions for the second-order corrections in the case of general lens potential and for an arbitrary position of the source near a symmetric cusp. Applications to a lensing galaxy model represented by a singular isothermal sphere with an external shear γ are studied and the role of the second-order corrections is demonstrated.

Key words: gravitational lensing, analytic theory

1. Introduction

The most interesting effects of gravitational lensing involve caustics of the lens mapping. It is well known that there are only two stable catastrophes of a two-dimensional mapping: cusps and folds (see, e.g., [7]). In a neighborhood of a "regular" caustic point any caustic is a smooth curve formed by the fold points and the smoothness is violated in the cusp points. Approximate relations for image amplifications and positions near the caustic have been derived in classical works [7,8]. These relations represent main contributions of the lensing effects (zero approximation) for a vanishing distance from a point source to the caustic. In order to increase the accuracy of the relations, higher order corrections are needed. The corrections to the solutions of the lens equations and their amplifications near the folds have been found in [1,6] up to the first order and in [3,4] up to the second order (see also [9]). In the neighborhood of the cusp the first order corrections were treated in [5], and in more detail in [2]. Here we study the second order corrections.

2. Approximate solutions near the cusp

The normalized gravitational lens equation maps every point \mathbf{x} of the lens plane (image plane) onto point \mathbf{y} of the source plane [7]:

$$\mathbf{y} = \mathbf{x} - \nabla\Phi(\mathbf{x}), \quad (1)$$

where $\Phi(\mathbf{x})$ is a lens mapping potential. In a general case there are several images $\mathbf{X}^{(l)}(\mathbf{y})$ of the point source at \mathbf{y} , which are represented by a solutions of (1); here (l) stands for the number of a separate image. Potential $\Phi(\mathbf{x})$ satisfies equation $\Delta\Phi = 2k$, $k(\mathbf{x})$ being the normalized surface mass density on the line of sight. The amplification coefficient of the point source is $K^{(l)}(\mathbf{y}) = 1/|J(\mathbf{X}^{(l)}(\mathbf{y}))|$, where $J(\mathbf{x}) \equiv |D(\mathbf{y})/D(\mathbf{x})|$ is Jacobian of the lens mapping.

We remind that the critical curves of mapping (1) are determined by equation $J(\mathbf{x}) = 0$. The caustic is the image of the critical curve obtained with this mapping.

The standard approach to study the caustic neighborhoods involves approximations to the potential near point p_{cr} of the critical curve by means of a Taylor polynomial. We use a coordinate system on the source plane such that the abscissa axis is a tangent to the caustic. We assume that point p_{cr} of the critical curve is at the origin of the lens plane; it is mapped onto the origin of the source plane; $|y_2|$ is the distance from the tangent to the caustic, y_1 being a shift along the tangent. In case when point p_{cr} maps onto the cusp point, the axis y_1 is a joint limit of tangents to the two branches of the caustic; this will be referred to as axis of the cusp. We denote $k_0 \equiv k(0)$, $\sigma \equiv 1 - k_0$. Equation (1) near the critical point can be written as follows:

$$\begin{aligned} y_1 &= 2\alpha x_1 + a_1 x_1^2 - a_2 x_2^2 + 2b_2 x_1 x_2 + c_3 x_1^3 - \\ &- 3c_1 x_1 x_2^2 - d_1 x_2^3 + 3d_2 x_1^2 x_2 + g_1 x_2^4 - \\ &- 6g_2 x_1^2 x_2^2 - 4f_1 x_1 x_2^3 + 4f_2 x_1^3 x_2 + g_3 x_1^4 + \dots \\ y_2 &= b_2 x_1^2 - b_1 x_2^2 - 2a_2 x_1 x_2 + d_2 x_1^3 - \\ &- 3d_1 x_1 x_2^2 + c_3 x_2^3 - 3c_1 x_2 x_1^2 + f_3 x_2^4 + f_2 x_1^4 - \\ &- 6f_1 x_1^2 x_2^2 + 4g_1 x_1 x_2^3 - 4g_2 x_1^3 x_2 + h x_2^5 + \dots \end{aligned} \quad (2)$$

The coefficients of this expansion can be expressed by means of derivatives of $\Phi(\mathbf{x})$. In case of constant surface mass density $k(\mathbf{x}) \equiv k_0$ we have $a_1 = a_2$, $b_1 = b_2$, $c_1 = c_2$, $d_1 = d_2$, $g_1 = g_2 = g_3$, $f_1 = f_2 = f_3$.

The condition that $\mathbf{x} = 0$ represents a cusp point is $b_1 = 0$. The parameter t that defines a vicinity of the source to the caustic can be introduced as follows: $y_1 = t^2 \tilde{y}_1$, $y_2 = t^3 \tilde{y}_2$, $x_1 = t^2 \tilde{x}_1$, $x_2 = t \tilde{x}_2$. After the substitution into equation (2) we find:

$$\begin{aligned} \tilde{y}_1 &= 2\alpha\tilde{x}_1 - a_2\tilde{x}_2^2 + (2b_2\tilde{x}_1\tilde{x}_2 - d_1\tilde{x}_2^3) \cdot t + \\ &+ (a_1\tilde{x}_1^2 - 3c_1\tilde{x}_1\tilde{x}_2^2 + g_1\tilde{x}_2^4) \cdot t^2 + \dots \\ \tilde{y}_2 &= -2a_2\tilde{x}_1\tilde{x}_2 + c_2\tilde{x}_2^3 + (b_2\tilde{x}_1^2 - 3d_1\tilde{x}_1\tilde{x}_2^2 + \\ &+ f_3\tilde{x}_2^4) \cdot t + (-3c_1\tilde{x}_1^2\tilde{x}_2 + 4g_1\tilde{x}_1\tilde{x}_2^3 + h\tilde{x}_2^5) \cdot t^2 + \dots \end{aligned} \quad (3)$$

This yields the second approximation (in powers of t) in the neighborhood of the cusp. The lens model parameters are $a_1, a_2, b_2, c_1, c_2, d_1, f_3, g_1, h$; furthermore we shall omit most of the indexes assuming: $a = a_2$, $b = b_2$, $c = c_2$, $d = d_1$, $f = f_3$, $g = g_1$.

We look for the solutions of Eq. (3) in the form:

$\tilde{x}_1 = x_{10} + tx_{11} + t^2x_{12}$, $\tilde{x}_2 = x_{20} + tx_{21} + t^2x_{22}$. We write

$$J(\mathbf{x}(\mathbf{y})) = t^2 [J_0(\tilde{\mathbf{y}}) + tJ_1(\tilde{\mathbf{y}}) + t^2J_2(\tilde{\mathbf{y}})]. \quad (4)$$

The problem is reduced to the third order algebraic equation for x_{20} :

$$Cx_{20}^3 - a\tilde{y}_1x_{20} - \tilde{\sigma}y_2 = 0, \quad (5)$$

where $C = c\sigma - a^2$. Equation (5) has one or three real roots depending on the sign of $Q = \frac{\tilde{y}_2^2\sigma^2}{4C^2} - \frac{a^3\tilde{y}_1^3}{27C^3}$. We have one real root if $Q > 0$ and three real roots if $Q \leq 0$ (two of the roots are matched for $Q = 0$). On the axis $y_2 = 0$ we have a trivial root $x_{20}^{(1)} = 0$ and two additional real roots $x_{20}^{(2,3)} = \pm\sqrt{a\tilde{y}_1/C}$ for $a(\sigma - a^2)y_1 > 0$. The (real) expressions for the solutions of (5), that is a zero-order approximation for x_{20} , are obtained by means of Cardano's formula.

For the first coordinate we get:

$$x_{10} = \frac{1}{2\sigma}(\tilde{y}_1 + ax_{20}^2). \quad (6)$$

The first order corrections x_{11} and x_{21} , as well as J_1 are found in [2, 5].

3. The second order corrections in case of a locally symmetric cusp

It is an important to note that the first order correction studied in [2, 5] are related solely to an asymmetry of the lens mapping with respect to transformation $y_2 \rightarrow -y_2$. We shall say that the lens is locally symmetric near the cusp if the following conditions are satisfied (with a sufficient accuracy):

$$y_1(x_1, -x_2) = y_1(x_1, x_2), \quad y_2(x_1, -x_2) = -y_2(x_1, x_2). \quad (7)$$

It is easy to see in virtue of (3) that

$$b = d = f = 0 \quad (8)$$

and all terms of the first order in t are absent.

Equation (3) in this case takes on the form:

$$\begin{aligned} \tilde{y}_1 &= 2\alpha\tilde{x}_1 - a\tilde{x}_2^2 + (a_1\tilde{x}_1^2 - 3c_1\tilde{x}_1\tilde{x}_2^2 + g\tilde{x}_2^4) \cdot t^2 + \dots \\ \tilde{y}_2 &= -2a\tilde{x}_1\tilde{x}_2 + c\tilde{x}_2^3 + (-3c_1\tilde{x}_1^2\tilde{x}_2 + 4g\tilde{x}_1\tilde{x}_2^3 + h\tilde{x}_2^5) \cdot t^2 + \dots \end{aligned} \quad (9)$$

We seek for the solutions in the form: $\tilde{x}_1 = x_{10} + t^2x_{12}$, $\tilde{x}_2 = x_{20} + t^2x_{22}$. We obtain:

$$x_{12} = \frac{1}{8\sigma^3 C^2 E} (A_3 x_{20}^2 \tilde{y}_1^2 + A_4 x_{20} \tilde{y}_1 \tilde{y}_2 + A_5 \tilde{y}_2^2 - C^2 a a_1 \tilde{y}_1^3), \quad (10)$$

$$A_3 = -a^6 a_1 + 3\sigma a^4 a_1 c - 3\sigma^2 a^2 a_1 c^2 + \sigma^3 (24a^2 c g + 8a^3 h - 18a c^2 c_1 + 3a_1 c^3), \quad (11)$$

$$A_4 = \sigma a^5 a_1 - 3\sigma^2 a^3 a_1 c + 6\sigma^3 (2a^3 g - 3a^2 c c_1 + a a_1 c^2) + 2\sigma^4 (18a c g + 8a^2 h - 9c^2 c_1), \quad (12)$$

$$A_5 = -\sigma^2 a^4 a_1 + 3\sigma^3 a^2 a_1 c + 6\sigma^4 (2a^2 g - 3a c c_1) + 4\sigma^5 (3c g + 2a h). \quad (13)$$

For the second coordinate we find:

$$x_{22} = \frac{1}{4\sigma C^2 E} (CB_3 x_{20}^2 \tilde{y}_2 + B_4 x_{20} \tilde{y}_1^2 + B_5 \tilde{y}_1 \tilde{y}_2), \quad (14)$$

$$B_3 = a^3 a_1 - 9\sigma a^2 c_1 + 12\sigma^2 a g_1 + 4\sigma^3 h, \quad (15)$$

$$B_4 = \sigma (-6a^2 c c_1 + a a_1 c^2 + 4a^3 g) + \sigma^2 (8a c g + 4a^2 h - 3c^2 c_1), \quad (16)$$

$$B_5 = -a^4 a_1 + \sigma (3a^3 c_1 + 2a^2 a_1 c) + 4\sigma^2 (-3a c c_1 + a^2 g) + 4\sigma^3 (a h + 2c g), \quad (17)$$

For the Jacobian we find:

$$J_2 = \frac{1}{2\sigma^2 C E} (I_3 x_{20}^2 y_1^2 + I_4 x_{20} y_1 y_2 + I_5 y_1^3 + I_6 y_2^2), \quad (18)$$

$$I_3 = a^5 a_1 + \sigma (3a^4 c_1 - 2a^3 a_1 c) + 3\sigma^2 (14a^2 c c_1 - a a_1 c^2 - 16a^3 g) - \sigma^3 (16a^2 h + 9c^2 c_1), \quad (19)$$

$$I_4 = -\sigma a^4 a_1 + 3\sigma^2 (3a^3 c_1 + 2a^2 a_1 c) + 6\sigma^3 \times (18a c c_1 - 3a_1 c^2 - 22a^2 g) - 4\sigma^4 (13a h + 6c g), \quad (20)$$

$$I_5 = -C (a^2 a_1 + 3\sigma a c_1), \quad (21)$$

$$I_6 = 9\sigma^2 [a^3 a_1 + \sigma (3a^2 c_1 - 2a a_1 c) - 6\sigma^2 (2a g - c c_1) - 4\sigma^3 h] \quad (22)$$

Using (4) we get the second approximation formula for the amplification coefficient of a separate image:

$$K = \frac{1}{|J|} \approx \frac{1}{t^2} \frac{1}{|J_0 + t^2 J_2|} \approx \frac{1}{t^2 |J_0|} \left(1 - t^2 \frac{J_2}{J_0} \right). \quad (23)$$

In this derivation we have taken into account that for a sufficiently small t we have $|t^2 J_2 / J_0| < 1$. We denote the first and the second terms of expansion in powers of t in the right hand side of (23) as $K_0 \sim t^{-2}$ and $K_2 \sim O(1)$. We note that K_2 does not depend on t .

4. Role of the second order corrections

We shall illustrate this role using an example of a simple lens model, namely the singular isothermal sphere with an external shear. The normalized surface mass density of this model is

$$k = \frac{1}{2\sqrt{(X_1^2 + X_2^2)}}. \quad (24)$$

The large-scale external gravitational field causes a tidal shear γ [7]. Here (X_1, X_2) stand for coordinates with an origin in a galactic center; the corresponding coordinates in the source plane will be denoted as (Y_1, Y_2) .

The lens potential is

$$\Phi(X_1, X_2) = \sqrt{(X_1^2 + X_2^2)} - \frac{\gamma}{2}(X_1^2 - X_2^2), \quad (25)$$

and the equation (1) takes on the form:

$$Y_1 = X_1 \left[1 + \gamma - (X_1^2 + X_2^2)^{-1/2} \right], \quad (26)$$

$$Y_2 = X_2 \left[1 - \gamma - (X_1^2 + X_2^2)^{-1/2} \right]. \quad (27)$$

It is convenient to represent Jacobian $J(\mathbf{X}) \equiv |D(\mathbf{Y})/D(\mathbf{X})|$ using the polar coordinates

$$J = 1 - \gamma^2 - \frac{1}{R}(1 + \gamma \cos(2\varphi)). \quad (28)$$

The equation of a critical curve $J = 0$ yields:

$$R_{cr}(\varphi, \gamma) = \frac{1 + \gamma \cos(2\varphi)}{1 - \gamma^2}, \quad (29)$$

and substitution of (29) to (26, 27) yields the caustic equation in a parametric form. The critical curves (above) and corresponding caustics are shown on Fig.1 for three values of parameter γ (we assume that $0 < \gamma < 1$).

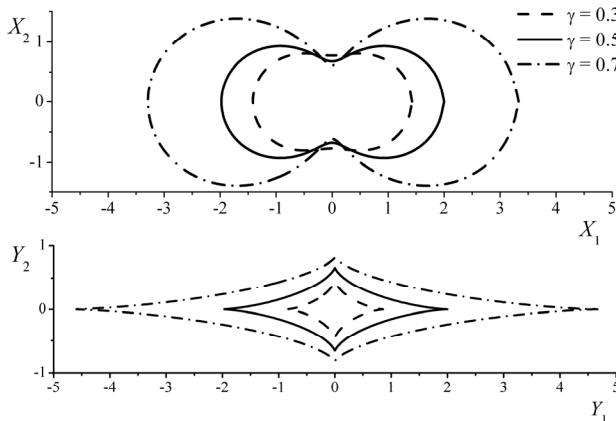


Figure 1: Critical curves and caustics of singular isothermal sphere with an external shear (for three values of γ)

For the cusps we have either $Y_1 = 0$ or $Y_2 = 0$. Consider, for example, a neighborhood of the cusp with coordinates $\mathbf{Y} = \left(\frac{2\gamma}{1-\gamma}, 0 \right)$. We shall compare exact solutions

with the approximate ones. Let $y_2 = 0$ for the point source. In this case there is a solution of (26, 27) $x_2 = 0$, $x_1 = y_1/(1-\gamma)$, which is defined for $y_1 > -(1+\gamma)/(1-\gamma)$. The corresponding Jacobian is $J = \frac{(1+\gamma)(1-\gamma)^2 y_1}{1+\gamma+(1-\gamma)y_1}$. In this case the image coordinates

are equal to their values obtained in zero approximation. However, this is not so for the Jacobian because $J_0 = (1-\gamma)^2 y_1$; $K_2 = \frac{\text{sign}(y_1)}{1-\gamma^2}$. The exact value of the

amplification in case of $\gamma = 0.5$ is compared on Fig.2 with zero and second approximations (the latter is the

same as the exact value, but this coincidence must be considered as an occasional one). In this case $K_2 \approx 1.33 \cdot \text{sign}(y_1)$ and this correction is noticeable even for rather a small distance from the cusp.

For $y_1 < 0$, when the source is inside the caustic, there are two additional solutions of (26, 27), which are symmetric with respect to x_1 -axis. Their coordinates are:

$$x_1 = \frac{y_1}{2\gamma}, \quad x_2 = \pm \sqrt{\frac{y_1}{\gamma(\gamma-1)} - \frac{y_1^2}{4\gamma^2}}.$$

The corresponding Jacobian is:

$$J = -2(1-\gamma)^2 y_1 - \frac{(1-\gamma)^3}{2\gamma} y_1^2.$$

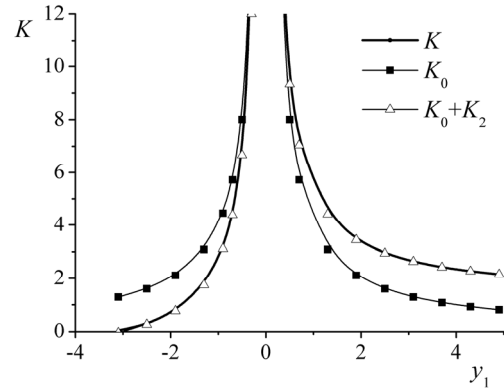


Figure 2: Comparison of the exact (K) and approximate values (K_0 and K_0+K_2) of the amplification

In zero approximation these expressions do not contain the second order terms. Second approximation for J in this case is the same as the exact solution; the amplification is

defined by (23), and $K_2 = \frac{1}{8\gamma(1-\gamma)}$.

Fuller consideration of this and other examples have shown convincingly that the second order corrections in the solutions of the lens equation allow us to extend appreciably the domain of validity of the approximation formulae with a preassigned accuracy. Note also that in this approximation we take into account the terms in the amplification coefficient which do not depend upon the vicinity parameter.

References

- Александров О.М., Жданов В.И., Федорова О.В.: 2003, *Вісник Київ. Ун-ту. Астрономія*, № 39–40, 52.
- Alexandrov A. N., Koval S.M., Zhdanov V.I.: 2012, *Advances in Astronomy and Space Phys.*, **2**, 184.
- Alexandrov A.N., Zhdanov V.I.: 2011, *Mon. Not. Roy. Astron. Soc.*, **417**, 541.
- Alexandrov A.N., Zhdanov V.I., Fedorova E.V.: 2010, *Astron. Lett.*, **36**, 329.
- Congdon A.B., Keeton C.R., Nordgren C.E.: 2008, *Mon. Not. Roy. Astron. Soc.*, **389**, 398.
- Keeton C.R., Gaudi B.S., Petters A.O.: 2005, *Astrophys. J.* **635**, 35.
- Schneider P., Ehlers J., Falco E. E.: 1992, *Gravitational Lenses*. – Berlin: Springer.
- Schneider P., Weiss A.: 1992, *Astron. Astrophys.*, **260**, 1.
- Zhdanov V.I., Alexandrov A.N., Fedorova E.V., Sliusar V.M.: 2012, *ISRN Astron. Astrophys.*, vol. 2012, ID 906951.

THE KINEMATICS OF REGULAR STRUCTURES

G.B. Anisimova

Southern Federal University, Rostov-on-Don, Russia
galina@iubip.ru

ABSTRACT. Three kinds of movements, providing stability of Universal Sky Net (USN), are listed. The series of peculiar kinematical parameters, connected with the USN structure are also given.

Key words: Galaxy, structure, kinematics.

There are many regular structures in all Universe scales.

The order in the Universe is supported by the regular motions and the chaotic motions play not the main role.

The regularities can be described, using Universal Sky Net (USN). This USN one can build by the method of fractal branching in the triedr vertex of 0-order ξ , η , ζ or by its rotation around the vertexes (poles) for angles multiple $\pi/4$ and $\pi/6$ (Shatsova, Anisimova).

$$tgb = ctg\Omega_p \sec b_p \sin(l-l_p) + tgb_p \cos(l-l_p),$$

here $P(l_p, b_p)$ – the Pole coordinates, Ω_p – its meridians positional angles.

l_p, b_p, Ω_p : $k\pi/n$, here k and n – integer small numbers: 2, 4, 6...

The USN is the system of ladder's rail, passing through the whole Universe.

This ladder is hierarchical and contains of stairs:

- Solar system
- The Galaxy
- Clusters of galaxies
- Supergalaxies
- Metagalaxy

The chaotic motions are not compatible to the USN stability. This stability puts the limits on the kinematics.

Here are the valid motions:

- the expansion of Universe saves the shape and orientation of main structures, that is its similarity to itself and non-dimensionality
- the rotation of structures in USN planes will preserve these planes (the rotation in MW plane of our Galaxy or in Λ plane of Supergalaxy Virgo)
- the cosmic objects' streams along the USN axis and in its meridian planes. The streams may be really progressive (moving stellar clusters), or vortical, having small deviations from progressive or rotating ones in limits of sky belts where meridians pass.

To make sure on compatibility of known stellar streams and USN we used both the data obtained by different authors and our own.

The members of known stellar streams are scattered all over the sky, but the coordinates of its radiants are measured and have precision of several degrees. Δ – the angle distance of radiants from the nearest USN meridian.

$$\sin \Delta = \sin B \times \cos b^* - \cos B \times \sin b^* \times \sin(L - l^*)$$

here l^* & b^* - the parameters of meridian in the equation

$$tgb = tgb^* \times \sin(l - l^*)$$

Table 1. The coordinates of USN meridians

№	l^*	b^*	meridian
II	203	-12	Γ
III	230	-20	Z
IV	199	-2	MW
V	219	-25	\perp VD
VI	204	-22	GB
VII	11	-34	VD
VIII	209	-9	Γ
IX	242	6	$\perp\Gamma$

We investigated:

- 20 Eggen groups,
- About 10 groups, selected by Agekyan and Orlov and processed by Ninckovich and Popovich

The radiants fit into the meridian belts (width $<3^\circ$, Table 2). More often they are the meridians of Z and η poles.

The totality of Z-meridians was selected by Dolidze in 1980. This part of USN may be named "Dolidze net".

The projection of velocity ellipsoid to the celestial sphere determined for the stars $V < 9^m$ over SAO catalogue is given in Fig. 1. The vectors of deviation from velocity ellipsoid are shown in the areas. They form the stream parallel to E and Loop I.

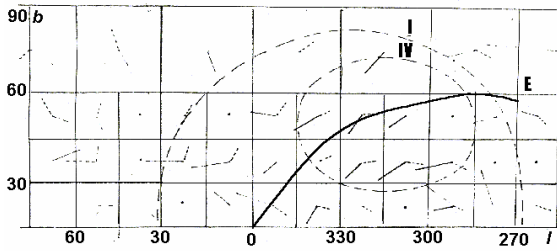


Figure 1. The vectors of deviation from velocity ellipsoid in projection to the celestial for the stars $V < 9^m$

Table 2. The radiants of moving clusters and Eggen groups and its distances from the nearest USN meridian

	Group	L	B	V(k m/s)	Belt	Δ
t=1	Uma	4	-32	15	\perp MW, VD	1.4
	Sirius	8	-32	15	\perp MW, VD	1.0
	α Per	215	17	16	\perp F	1.5
	Sun I	180	57	19	MC, S	-2.6
t=2	Sco-Cen	227	-14	26	\perp Γ Z'	3.0
	Sun II	0	-90	27	Π '	0
	Pleiad	254	-30	30	Γ	-1.9
t=3	Hyades	203	-4	44	MW, Γ	4.5
	Wolf630	305	-24	44	Γ	2.9
t=4	HR1614	267	16	60	\perp VD	0.2
t=5	ξ Her	224	-14	69	VD	1.3
	γ Leo	357	-6	76	Γ	0.4
	ϵ Ind	208	-1	84	MW, VD	-1.0, -4.1
t=7	η Cep	251	-4	103	MW, \perp VD	-4, -1.9
	δ Cyg	210	-3	106	MW, VD	-3, 0.2
	σ Pup	232	-3	111	MW, \perp Γ	-3, 2.5
t=8	Arctur	250	-3	124	\perp VD, MC, MW	-0.5, -1.8 3
t=9	Gr1830	320	0	303	S, MW	-1.0, 0
	Kapteyn	270	2	289	MW, Λ	2, 6.7
	Untilted	297	1	357	GB, MW	1, 1.1

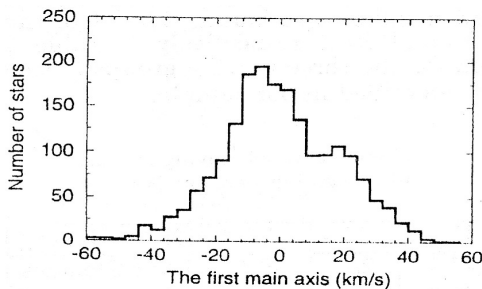


Figure 2. The histogram for the main axis of velocity ellipsoid (Chen, Torra, Figueras, Asiain).

Table 3. The velocities of stars in the layer η (-5° - -16°) in interval $|v|$ (107 - 117 km/s)

N ₀	v_ξ	v_η	v_ζ	v
HIC	km s ⁻¹			
70536	1	-107	-27	110
95223	-24	105	-11	108
95575	10	101	-32	107
948	-31	95	-44	109
78241	-44	96	-36	111
74537	-34	84	-73	116
70865	-40	80	-69	113
109461	65	-94	-26	117
110035	26	107	-32	115
3170	26	103	-10	107
95447	8	108	-14	109
67487	-15	97	-55	112
103458	-92	-21	-56	110
98792	-53	-90	-24	107
91605	22	-105	-18	109
109601	19	-115	-12	117
mean	-18	28	-20	111
abs. mean	32	94	34	
dispersion	36	94	34	3.5

Several groups, having vortical movements, were selected from catalogues Gliese - Jahreiss и Hipparcos: almost the same large velocity components η and recurrently changing smaller ξ and ζ (in ecliptical system) $\xi_{n+1} = \zeta_n$.

There is also the movement of galaxies, having dispersion $\sigma = 61 \pm 8$ km/s. The equality of $|v_r|$ for opposite objects means approximate equality of residual velocities v_r of different signs for pairs or even for triplets of objects. It is similar to streams, having large distances between the members, up to $\Delta r \approx 1-2$ Mpc:

LMC and Dragon galaxy $v_r = 271$ and -281 , peculiar $(v_r)_{pec} = 47$ km/s, $\Delta r \approx 130$ kpc

Group of galaxies Andromeda ($v_r \approx 300 \pm 70$ km/s) and Antlia (300 - 360); $\Delta r \approx 2$ Mpc

If this is a stream, then it consists of large part of Local group' galaxies.

The large semi-axis of velocity ellipsoid is directed to the vertex. It was shown long ago, that the vertex must coincide with the centre of Galaxy in axis-symmetrical rotating galaxy. But the observations give the vertex deviation to the side of positive longitudes differently for various stellar groups up to 20° .

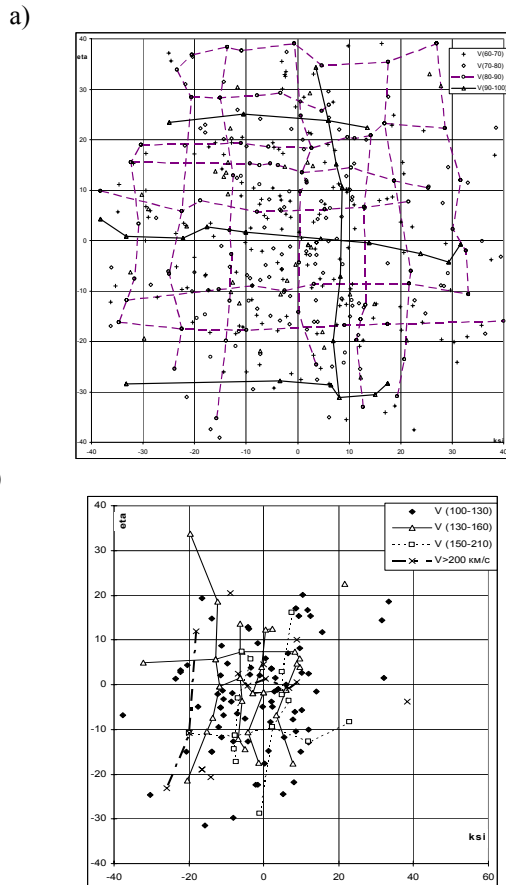


Figure 3. The stars from catalogues Gliese, Jahreys and Hipparcos in groups on velocity v (ξ , η) projection.

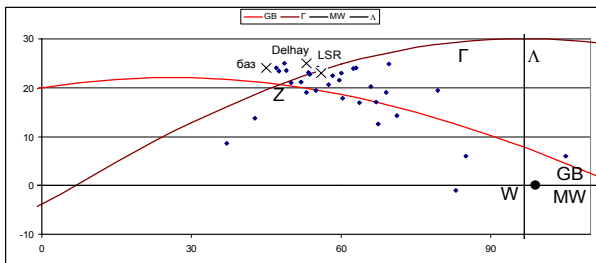


Figure 4. The \odot apexes of 32 groups of stars (over Bobylev; Delhay)

Table 4. The vertex longitudes (over Bobylev)

8±1	12±2	6±2	11±2	13±0	19	15	10
14	15	8	8	15	12	7	7

So, the vertex deviation is $7 \div 15^\circ$, that is beginning from η' and further.

Beginning with Kempbell, the positive K-member or K-effect was found in the OB-stars radial velocity distribution. Usually it is explained by the expansion of the group of OB-stars from some centre $v_r \approx 4 \text{ km/s}$, for example, from the Local system centre. But this centre is not observed. Comerón thinks, that the expansion is not from the centre point, but from the line $l=135-315^\circ$. Let's note, that $l=137-317^\circ$ is the node line of spurs belt S. On our opinion S is the equator of Local system, perpendicular to Z axis. And its spurs I-IV are the expanding shell structures, having the velocities 3-13 km/s. Probably, the nature of expansion is the same for spurs and stars.

Conclusion

- The USN stability is compatible to the next kinds of motions:
 - o the expansion of Universe
 - o the rotation of structures in USN planes
 - o the streams of cosmic objects along the USN axis and in its meridian planes.
- The peculiarities of the kinematic parameters show their connection with USN. So, the USN factor must be taken into account in stellar kinematics.
- The radiant of moving clusters and Eggen groups are in the belts of USN meridians.
- The vectors of deviations from the velocity ellipsoid form the stream along E
- The nearby stars form series parallel to the USN axis, having small dispersion $\sigma(v) - \Delta v$ multiple $v=11 \pm 2 \text{ km/s}$.
- The \odot apexes are along USN axis
- The vertex deviation is $7 - 15^\circ$ (η' pole)

References

Shatsova R.B., Anisimova G.B.: 2010, *Natural Science*, **2**, №.10, 1049.
 Bobylev V.V., Baikova A.T.: 2007, *AJ*, **84**, 418.
 Gliese W., Jahreiss H.: 1991, *Astron. Rechen-Institut, Heidelberg*
 Comerón F.: 1997, *Structure and evolution of stellar systems*, St. Peterburg, 161.
 Popovic G.M., Nincovic S., Pavlovic R.: 1997, *Structure and evolution of stellar systems*, St. Peterburg, 108.

COMPARISON OF OPTICAL AND X-RAY MASS ESTIMATES OF THE CHANDRA GALAXY CLUSTERS AT $Z < 0.1$

Iu.V. Babyk^{1,2,3}, I.B. Vavilova¹

¹ Main Astronomical Observatory of NAS of Ukraine, Kyiv, Ukraine

² Dublin Institute for Advanced Studies, Dublin, Ireland

³ Dublin City University, Dublin, Ireland,

babikyura@gmail.com, irivav@mao.kiev.ua

ABSTRACT. We used the optical data taken from SDSS DR7 galaxy and group catalog to determine the optical mass of 37 nearer Chandra galaxy clusters for comparison with the X-ray mass estimates. Using the assumption that mass follows the galaxy distribution, we computed the mass of each cluster by applying the virial theorem to the member galaxies. We have found a good agreement between optical and X-ray mass estimates and confirm that about 70 % of nearby galaxy clusters are not far from dynamical equilibrium.

Key words: Galaxy clusters: optical mass of galaxy clusters.

1. Introduction

The knowledge of the main characteristics of galaxy clusters plays a significant role in the study of the large-scale structure of the Universe. Among these characteristics the correct mass estimates are important for understanding both the intrinsic visible/dark matter distribution in clusters and evolution processes at the cosmological scales. The classical method of cluster mass calculation is the virial theorem to positions and velocities of cluster member galaxies. Another recent methods are based on the dynamical analysis of X-ray gas in clusters, and on the gravitational lensing of background galaxies etc.

Mass estimates obtained from the dynamical analysis of gas or cluster member galaxies based on the virial theorem assume that clusters are the systems in dynamical equilibrium. This assumption is not strictly valid; in fact, although clusters are the gravitationally bound galaxy systems, they collapsed recently in the cosmological sense or are being collapsed, which is confirmed by the observed frequent presence of substructures. Nevertheless, the estimate of optical virial mass still remains robust even with the presence of small substructures in galaxy clusters.

In this paper we use the SDSS DR7 group catalogs by Yang et al. (2007), which are constructed from the SDSS spectroscopic data. These catalogs provide us

with galaxy clusters that have reliable galaxy memberships, which are important in probing the halo occupation distribution statistics and galaxy formation models. The SDSS DR7 group catalogs also span a large halo mass range, from rich clusters to the isolated faint galaxies, allowing us to investigate the X-ray luminosity and hot gas distribution not only in massive clusters but also in relatively small halos.

The aim of this work is to obtain the optical mass estimates of 37 nearer Chandra galaxy clusters for comparison with the X-ray mass estimates obtained in our previous works (Babyk et al. 2012a,b,c,d). The paper is organized as follows. We describe briefly the data sample and selection procedure for cluster membership assignment in Section 2. We explain the methods to compute the masses of clusters using member galaxies in Section 3 and discuss our results in Section 4. We used the cosmological parameters $H_0 = 73$ km/s/Mpc, $\Omega_M = 0.27$, and $\Omega_\Lambda = 0.73$.

2. The optical data collection

We collected the optical data for 37 nearer Chandra galaxy clusters at $0.01 < z < 0.1$ using literature and databases. We considered the clusters for which Yang et al. (2007) gave an estimate for the velocity dispersion using the optical data from SDSS galaxy group catalogs. It was compiled with the adaptive halo-based group finder by Yang et al. (2005) and then updated to SDSS DR7. They select all galaxies in the Main Galaxy Sample with an extinction-corrected apparent magnitude brighter than 17.72, with redshifts in the range $0.01 < z < 0.20$ and with a redshift completeness $C_z > 0.7$. The resulting SDSS galaxy catalog contains a total of 639359 galaxies, with a sky coverage of 7748 square degrees. It is important to note that a very small fraction of galaxies in this catalog have redshifts taken from the Korea Institute for Advanced Study (KIAS) Value Added Galaxy Catalog (VAGC) (e.g. Choi et al. 2010).

3. Determination of the mass of clusters from the Virial theorem

3.1. Theoretical approach

One of the best way to estimate the mass of clusters from member galaxies requires that galaxies should be in the equilibrium with a cluster potential. As result, the cluster mass can be found from positions and velocities of the same population of galaxies. We describe below the main steps which were applied to compute the masses of galaxy clusters from the virial theorem.

The virial mass of clusters, M_{vir} , depends from the spatial distribution of the galaxy population and the global velocity dispersion, σ , as

$$M_{vir} = \frac{\langle v^2 \rangle}{G \langle r^{-1} F \rangle} \quad (1)$$

where r is the distance from center of cluster, v is the galaxy velocity, and F is the mass fraction within r . Then, if equation $\rho_{mass} \propto \rho$ is correct (i.e. that mass is distributed as in the observed galaxies) we can rewrite Eq. (1), as

$$M_{vir} = \frac{2 \langle v^2 \rangle}{G \langle r_{ij}^{-1} \rangle} = \frac{\sigma^2 R_{vir}}{G}, \quad (2)$$

where R_{vir} is the virial radius, which depends on the distance between any pair of galaxies r_{ij} . Because of the velocity dispersion and consequently the total mass is independent on any possible anisotropy of galaxy velocities, we can rewrite the Eq. (2) in the case of spherical galaxy systems for the projected quantities σ_P and R_{PV} as

$$M_{vir} = \frac{3\pi}{2} \frac{2 \langle V^2 \rangle}{G \langle R_{ij}^{-1} \rangle} = \frac{3\pi}{2} \frac{\sigma_P^2 R_{PV}}{G}, \quad (3)$$

In our work, the projected virial radius, R_{PV} , and velocity dispersion, σ_P , are derived as

$$\sigma_P = \sqrt{\frac{\sum_i V_i^2}{N-1}}, \quad (4)$$

$$R_{PV} = \frac{N(N-1)}{\sum_{i>j} R_{ij}^{-1}}. \quad (5)$$

3.2. Measurements

Using assumption that the number galaxies distribution traces the mass distribution we can calculate the masses of cluster by the virial theorem. We can determine the observational dispersion profile $\sigma_P(R)$ combining the data from many clusters because of such profile requires a huge amount of members (galaxies). To estimate the values of projected velocity dispersions, σ_P , we used the procedure suggested by Fadda et al. (1996). It is significant to note again that the virial

theorem is reliable if the galaxy system is in the dynamical equilibrium within the considered region. As result, we are able to determine the masses of clusters within the some radius of virialization, R_{virial} . To determine this radius we applied the methods suggested by Girardi et al. (1995, 1998). In this way, the virial mass ($M_{vir} = 4\pi R_{virial}^3 \rho_{virial} / 3$) can be found as $(3\pi/2)(\sigma_P^2 R_{PV} / G)$ (see Eq. (3)). As result,

$$R_{virial}^3 = \frac{\sigma_P R_{PV}}{6\pi H_0^2}, \quad (6)$$

where R_{PV} is the projected virial radius. Girardi et al. (1995) showed that R_{PV} is related to the radius of the sampled region, i.e. the aperture A (here equal to R_{virial}) as

$$R_{PV} = 1.193A \frac{1 + 0.032(A/R_c)}{1 + 0.107(A/R_c)}, \quad (7)$$

here R_c is the core radius, which is equal to $0.17 h^{-1}$ Mpc. Using Eq. (6) and (7) we can find relation between R_{virial} and σ_P , as

$$R_{virial} \sim 0.002 \sigma_P (h^{-1} \text{Mpc}), \quad (8)$$

here σ_P is given in km s^{-1} .

We extract the galaxy distribution of 37 studied clusters with at least ten galaxies up to R_{virial} . The galaxy distribution inside these clusters was analyzed by the method suggested by Girardi et al. (1995), where the galaxy surface density was approximated by King profile with a variable exponent

$$\sum(R) = \frac{\sum_0}{[1 + (R/R_c)^2]^\alpha}, \quad (9)$$

where α is the value which describes the galaxy distribution (usually equal 1). Using Eq. (9), we can calculate the surface density in the following way $\rho = \frac{\rho_0}{[1 + (r/R_c)^2]^{3\beta_{fit,gal}/2}}$, where $\beta_{fit,gal} = (2\alpha + 1)/3$, as result, $\rho(r) \propto r^{-3\beta_{fit,gal}}$ when $r \gg R_c$. We have used likelihood technique to perform our fit. We varied α and R_c from 0.5 to 1.5 and 0.01 to 1, respectively, and verifying fitted profiles using χ^2 -test. We found that $\alpha = 0.70_{-0.04}^{+0.08}$ for 2σ confidence level, as result, $\beta_{fit,gal} = 0.8$, i.e. $\rho \propto r^{-2.4}$. Fixing α , we re-fit the distribution of galaxy of clusters, extracting median values of $R_c = 0.05_{-0.01}^{+0.02}$ and $R_c/R_{virial} = 0.05$. Using all the aforementioned measurements and applying Eq. (7), we can calculate the virial masses of galaxy clusters using Eq. (3).

4. Results and discussions

In Tab. 1 we list the cluster parameters computed above: the name of sampled clusters (col. 1), the number of member galaxies N_m (col. 2) contained within the radius R (col. 5) and redshift (col. 3) with richness

Table 1: The optical masses and other parameters as compare with X-ray masses for 37 nearer Chandra galaxy clusters.

Name	N_m	z	rich	R_{max} , Mpc	σ_P , km s ⁻¹	N	R_{vir} , Mpc	α^a	R_G^a , Mpc	R_{PV} , Mpc	M_{vir} , 10 ¹⁴ M_\odot	M_X , 10 ¹⁴ M_\odot
A2589	28	0.042	0	0.59	470±100	28	0.94	1.50	0.10	0.33±0.15	10.79±0.54	10.05±1.29
MKW4	51	0.019	1	3.58	525±75	42	1.05	1.10	0.07	0.47±0.06	1.42±0.43	2.22±2.10
AWM4	23	0.032	1	3.50	119±89	23	0.24	0.70	0.01	0.18±0.09	3.03±0.03	6.55±0.85
A2063	92	0.035	1	3.87	667±55	70	1.33	1.18	0.13	0.66±0.07	3.24±0.62	10.30±1.94
A576	199	0.038	1	1.74	914±55	199	1.83	1.03	0.25	1.22±0.15	17.15±1.84	21.11±2.16
A3376	75	0.046	1	2.29	688±68	65	1.38	0.62	0.01	0.89±0.07	24.63±0.99	26.61±3.72
A2717	55	0.049	1	1.16	541±65	54	1.08	0.76	0.08	0.80±0.09	12.57±0.68	12.94±2.11
A3391	50	0.051	1	0.87	663±195	50	1.33	0.73	0.06	0.92±0.15	14.45±2.72	18.91±1.28
A2124	61	0.065	1	1.22	878±90	61	1.76	1.50	0.30	0.88±0.15	7.40±1.98	13.12±1.37
A400	58	0.024	2	1.22	599±80	57	1.20	0.83	0.04	0.70±0.08	2.76±0.81	3.44±1.02
A262	82	0.017	2	3.95	525±47	40	1.05	0.59	0.01	0.87±0.13	2.64±0.60	2.93±0.73
A539	160	0.028	2	2.47	629±70	70	1.26	0.78	0.02	0.68±0.09	4.96±0.76	8.38±1.77
A2634	69	0.031	2	0.86	700±97	69	1.40	0.62	0.02	1.03±0.15	5.51±1.73	11.88±2.15
A3571	69	0.039	2	0.98	1045±109	69	2.09	1.23	0.14	0.73±0.15	18.69±2.55	30.41±3.84
A119	62	0.044	2	1.27	679±107	62	1.36	0.66	0.01	0.86±0.15	14.32±1.55	24.06±4.16
A1644	84	0.046	2	1.94	759±61	76	1.52	1.01	0.34	1.28±0.10	8.09±1.44	14.60±1.47
A3562	100	0.047	2	2.15	736±49	89	1.47	0.66	0.15	1.22±0.05	7.62±1.01	14.05±1.56
A754	77	0.054	2	2.60	662±77	62	1.32	1.50	0.31	0.98±0.08	34.71±1.16	40.30±3.71
A2256	86	0.058	2	1.19	1348±86	86	2.70	0.92	0.12	1.32±0.15	36.26±4.49	47.78±5.37
A3158	123	0.059	2	1.67	976±70	123	1.95	0.77	0.04	1.06±0.15	21.08±2.23	25.80±3.17
A1795	81	0.063	2	1.81	834±85	80	1.67	0.77	0.03	0.91±0.09	16.92±1.57	19.34±2.18
A399	79	0.071	2	1.56	1116±89	79	2.23	1.50	0.42	1.19±0.15	26.26±3.31	37.90±4.11
A401	106	0.074	2	2.00	1152±86	106	2.30	1.50	0.42	1.19±0.15	25.99±3.22	37.97±4.16
A2029	73	0.077	2	1.57	1164±98	73	2.33	1.10	0.05	0.48±0.15	17.19±2.54	33.43±4.12
A2142	86	0.091	2	1.63	1132±110	86	2.26	1.50	0.51	1.36±0.15	19.12±4.27	29.87±3.17
A3921	29	0.094	2	1.33	490±140	24	0.98	0.78	0.19	0.93±0.15	22.45±1.30	29.61±2.15
A1060	82	0.012	3	2.06	610±52	79	1.22	0.80	0.03	0.69±0.07	5.80±0.56	9.81±1.32
A2199	50	0.030	3	3.29	801±92	42	1.60	0.79	0.05	0.96±0.14	6.76±1.85	12.38±2.18
A496	55	0.033	3	1.10	687±89	55	1.37	1.50	0.27	0.76±0.15	5.91±1.27	9.10±1.27
MKW3s	30	0.045	3	3.47	610±69	27	1.22	0.75	0.01	0.59±0.15	12.40±0.81	12.02±3.19
A3395	99	0.050	3	1.14	852±84	99	1.70	1.50	0.25	0.76±0.15	26.05±1.68	33.67±4.27
A85	125	0.055	3	1.75	969±95	124	1.94	1.50	0.53	1.31±0.15	15.49±3.10	25.68±4.89
A3667	154	0.056	3	2.22	971±65	152	1.94	0.52	0.02	1.55±0.07	15.98±2.18	26.84±2.48
A3266	128	0.059	3	1.34	1107±82	128	2.21	0.64	0.19	1.91±0.15	25.67±4.31	33.25±4.16
A2670	197	0.076	4	2.22	852±50	186	1.70	0.93	0.12	0.99±0.06	7.89±1.02	16.62±1.62
Coma	283	0.023	5	3.90	821±50	171	1.64	0.79	0.09	1.08±0.07	37.98±1.09	41.94±4.72
A3558	341	0.048	5	1.99	977±40	338	1.95	0.85	0.18	1.25±0.05	13.10±1.16	21.27±3.27

(col. 4) and the global projected velocity dispersion σ_P with the respective errors (col. 6); the number of galaxies N (col. 7) within R_{virial} (col. 8); the values of α and R_c resulting from the fit to the galaxy distribution (cols. 9 and 10, respectively); the projected virial radius, R_{PV} , computed at P_{virial} (col. 11); the virial mass (col. 12) and the cluster's X-ray mass from Babyk et al. 2013a (col. 13). By applying σ_P and R_{PV} , we compute the virial mass M_{vir} within R_{virial} through the Eq. (3). We used the X-ray mass estimates for these clusters, which were obtained in our previous works (Babyk et al., 2012c; Babyk et al. 2013a).

We found correlations between X-ray and optical mass. The masses of individual clusters do not extremely agree in several cases. Our estimates of virial masses is based on the assumption that mass follows the galaxy distribution, whereas X-ray masses do not require any assumption about the cluster mass distribution. This correlation between optical and X-ray masses shows a large scatter that cannot be explained by the observational errors (X-ray masses are systematically larger). The absence of trend in dependence of redshift is also in favor of a good quality observational data. The main discrepancies are related to the clusters of richness class 3 and suggest the presence of an intrinsic scatter, possibly due to some deviation from the ‘‘mass follows galaxies’’ law or from pure dynamical equilibrium (we did not analyze cluster substructures in detail).

Although our work is not devoted to the analysis of galaxy distribution, we have had to address this issue in the computation of cluster masses. In our previous works, the X-ray mass estimates (Babyk et al., 2013a) allowed to estimate a tight correlation between c_{200} and M_{200} , $c \propto M_{vir}/(1+z)^b$ with $a = -0.56 \pm 0.15$ and $b = 0.80 \pm 0.25$ (95% confidence level). In addition, it was found that the inner slope of the density profile α correlates with the baryonic mass content M_b , namely: α is decreasing with increasing the baryonic mass content. Our previous calculations of physical parameters of intracluster gas in the wide redshift range was used then to obtain constraints on the ‘‘luminosity - temperature - mass of gas’’ relationship for the Chandra galaxy clusters at $0.4 < z < 1.4$ (Babyk et al., 2013b).

In this work using a King-like profile, we obtain good alternative estimates of individual virial radii (see Fig. 1), which we need in order to obtain reliable cluster mass estimates for the nearer clusters. Moreover, when one or two parameters (α , R_c) are fixed, the estimates of virial radii results are less good, supporting the existence of an intrinsic spread of cluster parameters. As for the comparison with previous King-like fits, we find good agreement with the value of the exponent α obtained by Girardi et al. (1995) ($\alpha = 0.8^{+0.3}_{-0.1}$). So, the agreement between optical and X-ray masses is well explained in the context of two common assumptions: that mass follows the galaxy distribution, and

that about 70 % of studied nearer clusters are not far from dynamical equilibrium.

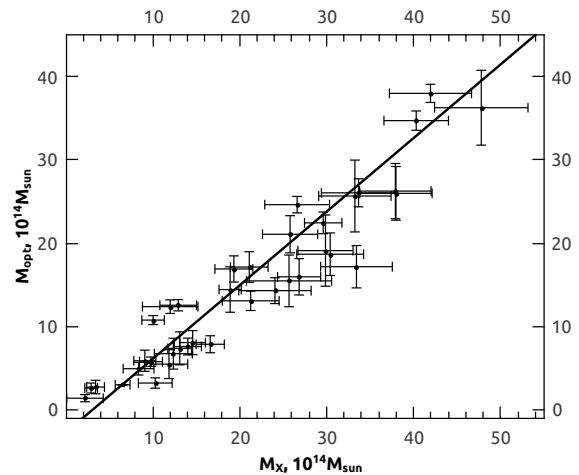


Figure 1: The correlation between optical and X-ray masses of clusters determined by different methods. The solid line corresponds the linear fit of sample.

Acknowledgements. This work was partially supported in frame of the Target Program of Space Scientific Research of the NAS of Ukraine (2012-2016).

References

- Babyk Iu., Melnyk O., Elyiv A. et al.: 2012a, *Kinematics and Physics of Celestial Bodies*, **28**, p.69.
 Babyk Iu.: 2012b, *Journal of physical studies*, **16**, p.7.
 Babyk Iu., Vavilova I., Del Popolo A.: 2013a, *submitted to Astronomy Reports*, **arXiv:1208.2424**.
 Babyk Iu., Vavilova I.: 2013b *Astrophys. and Space Sci.*, DOI **10.1007/s10509-013-1630-z**.
 Babyk Iu., Vavilova I.: 2012c, *Odessa Astronomical Publications*, **25**, p. 119.
 Babyk Iu.: 2012d, *Izvestiya Krymskoi Astrofizicheskoi Observatorii*, **108**, p.127.
 Choi Y., Han D., Kim S.: 2010, *JKAS*, **43**, p.191.
 Fadda D., Girardi M., Giuricin G. et al.: 1996, *ApJ*, **473**, p.670.
 Girardi M., Biviano A., Giuricin G. et al.: 1995, *ApJ*, **438**, p.527.
 Girardi M., Borgani S., Giuricin G. et al.: 1998, *ApJ*, **506**, p.45.
 Yang X., Mo H., van den Bosch F., Jing Y.: 2005, *MNRAS*, **356**, p.1293.
 Yang X., Mo H., van den Bosch F. et al.: 2007, *ApJ*, **671**, p.153.

SCHWARZSCHILD-DE SITTER AND MECHANICAL APPROACHES COMPARISON WITH RESPECT TO DARK MATTER HALOS

R. Brilenkov¹, M. Eingorn² and A. Zhuk³

Odessa National University named after I.I.Mechnikov

Odessa, Ukraine

¹ ruslan.brilenkov@gmail.com, ² maxim.eingorn@gmail.com, ³ ai_zhuk2@rambler.ru

ABSTRACT. We compare the Schwarzschild-de Sitter approach to deriving mass and potential distributions and corresponding parameters associated with dark matter halos for clusters of galaxies with the mechanical one, taking into account cosmological effects, in particular, dark energy influence.

Potential of pseudo-isothermal profile of the halo in two different metrics:

1. Schwarzschild –de Sitter

$$\begin{aligned}\Phi(R) = & -\frac{8\pi G_N}{3} \rho_\Lambda \left(\frac{R^2}{2} - R_\Lambda^2 + \frac{R_\Lambda^3}{R} \right) + \\ & + 8\pi G_N \rho_c \frac{R_c^3}{R} \left(\arctan \frac{R}{R_c} - \arctan \frac{R_\Lambda}{R_c} \right) - \\ & - 8\pi G_N \rho_c R_c^2 \left(1 - \frac{R_\Lambda}{R} \right) + \\ & + 4\pi G_N \rho_c R_c^2 \ln \frac{R^2 + R_c^2}{R_\Lambda^2 + R_c^2} - \frac{G_N m}{R_\Lambda}\end{aligned}$$

2. Friedman

$$\begin{aligned}\Phi(R) = & -\frac{\ddot{a}}{a} \left(\frac{R^2}{2} - R_H^2 + \frac{R_H^3}{R} \right) + \\ & + 8\pi G_N \rho_c \frac{R_c^3}{R} \left(\arctan \frac{R}{R_c} - \arctan \frac{R_H}{R_c} \right) - \\ & - 8\pi G_N \rho_c R_c^2 \left(1 - \frac{R_H}{R} \right) + \\ & + 4\pi G_N \rho_c R_c^2 \ln \frac{R^2 + R_c^2}{R_H^2 + R_c^2} - \frac{G_N m}{R_H}\end{aligned}$$

We found potentials, which give us an opportunity to consider motion of test massive bodies and light taking into account gravitational attraction to inhomogeneities and cosmological expansion of the Universe.

References

Eingorn M., Zhuk A.: 2012, *Hubble flows and gravitational potentials in observable Universe*. JCAP 09 (2012) 026, arXiv:1205.2384.

DARK SIDE OF QUARK BAG MODEL

Maxim Brilenkov ¹, Maxim Eingorn ², Laszlo Jenkovszky ³, Alexander Zhuk ⁴

¹ Department of Theoretical Physics, Odessa National University, Dvoryanskaya st. 2, Odessa 65082, Ukraine; *maxim.brilenkov@gmail.com*

² Physics Department, North Carolina Central University, Fayetteville st. 1801, Durham, North Carolina 27707, U.S.A; *maxim.eingorn@gmail.com*

³ Bogolyubov Institute for Theoretical Physics, Kiev 03680, Ukraine; *jenk@bitp.kiev.ua*

⁴ Astronomical Observatory, Odessa National University, Dvoryanskaya st. 2, Odessa 65082, Ukraine; *ai.zhuk2@gmail.com*

ABSTRACT. We calculate the present expansion of our Universe endowed with relict colored objects – quarks and gluons – that survived hadronization either as isolated islands of quark-gluon nuggets or spread uniformly in the Universe. The QNs can play the role of dark matter.

Key words: dark matter theory

1. Introduction

We consider the possibility that a small fraction of colored objects – quarks and gluons – escaped hadronization. They may survive as islands of colored particles, called quark-gluon nuggets (for brevity sometimes also quark nuggets (QNs)). This possibility was first considered by E. Witten [1] and scrutinized further in [2-4]. In his paper [1], E. Witten discusses the possibility that QNs can survive even at zero temperature and pressure. If so, the “hot” quark-gluon phase in the form of QNs may affect the present expansion of the Universe. Indeed, our investigation shows that nuggets can contribute to dark matter provided that their interaction with ordinary matter is weak.

2. Equations of state in the quark-gluon bag model

We first briefly remind the quark bag equation of state, a simple model of quark confinement. For vanishing chemical potential, $\mu = 0$, it is a system of two equations:

$$p_q(T) = A_q T^4 - B, \quad (2.1)$$

$$p_h(T) = A_h T^4. \quad (2.2)$$

The first line corresponds to the “hot” phase of deconfined quarks and gluons, and the second one relates to confined particles, i.e. hadrons. A system of strongly interacting particles, made of free quarks and gluons, is cooling down and meets the “cold” phase transforming into colorless hadrons. The coefficients are defined by the

degrees of freedom and are equal to: $A_q \approx 1.75$, $A_h \approx 0.33$, $B = (A_q - A_h)T_c^4$ and $T_c \approx 200 \text{ MeV}$. Knowing the pressure, $P(T)$, for $\mu = 0$, one can easily calculate the remaining thermodynamical quantities, e.g., for the energy density we have

$$\varepsilon(T) = T \frac{dp}{dT} - p. \quad (2.3)$$

The above equations of state (EoS) is not unique. Here we will use one, which was considered by C. Källman [5], who introduced a temperature-dependent bag “constant”, namely, by replacing in the first line of the EoS, eq. (2.1), $B \rightarrow B(T) = \bar{B}T$, where $\bar{B} = (A_q - A_h)T_c^3$. This modification has immediate consequences, namely, by producing a minimum in the “hot” line of the EoS, corresponding to metastable deeply supercooled states of the deconfined strongly interacting matter. Also, it drives inflation of the Universe, as shown in [6, 7].

Since our idea is that a small fraction of deconfined quarks and gluons survives to present days, we are interested in the “hot” branch of the bag EoS. As we mentioned above, there is a number of different modifications of eq. (2.1). For our present purposes, however, two simple representatives will be sufficient. They are the Källman modified model (which we call Model I):

$$p_q(T) = A_q T^4 - \bar{B}T \equiv \bar{A}_1 T + \bar{A}_4 T^4, \quad (2.4)$$

and the original model (Model II) described by eq. (2.1):

$$p_q(T) = A_q T^4 - B \equiv \bar{A}_0 + \bar{A}_4 T^4. \quad (2.5)$$

3. Quark nuggets

Now, we want to investigate cosmological consequences of this assumption. Obviously, for considered models, a cosmological scenario strongly depends on thermodynamical properties of quark-gluon

plasma (QGP). We focus on two possible eqs. (2.4) and (2.5). With the help of standard thermodynamical eq. (2.3) we get the expressions for the energy density:

$$\varepsilon = 3\bar{A}_4 T^4 \quad (3.1)$$

and

$$\varepsilon = -\bar{A}_0 + 3\bar{A}_4 T^4 \quad (3.2)$$

for Model I and Model II, respectively. Eqs. (2.4), (2.5), (3.1) and (3.2) describe the pressure and energy density inside of the nuggets. The total pressure and energy density of all nuggets in the Universe can be calculated as follows. Let us take, e.g., Model I with eq. (2.4). Then, for total pressure of nuggets we get

$$P = \frac{\sum_i p_{qi} v_i}{V} = \frac{A_1 T + A_4 T^4}{a^3}, \quad (3.3)$$

where p_{qi} is the pressure of the i -th nugget with the volume v_i and $V \propto a^3$ is the total volume of the Universe (a is the scale factor of the Friedmann-Robertson-Walker metric). We consider the case where all nuggets have the same pressure (2.4) and their volumes are either constant or only slightly varying with time. The total volume of nuggets $\sum_i v_i$ is included in the coefficients A_1 and A_4 (i.e. $A_{1,4}$ have dimension $\bar{A}_{1,4} \times cm^3$). Therefore,

$$\frac{A_1}{A_4} = \frac{\bar{A}_1}{\bar{A}_4} = -0.8114 T_c^3. \quad (3.4)$$

Similarly, from eq. (3.1), for the energy density of all nuggets we get

$$E = \frac{3A_4 T^4}{a^3}. \quad (3.5)$$

The same procedure holds for the Model II. Let us consider two models separately.

Model I

Here, the pressure and energy density of all nuggets are given by the above formulae (3.3) and (3.5), respectively. In these formulae, temperature is a function of the scale factor a : $T = T(a)$. Let us specify this dependence. From the energy conservation equation

$$d(Ea^3) + Pd(a^3) = 0 \quad (3.6)$$

we can easily get

$$T = \left(\frac{(C/a)^{3/4} - A_1}{A_4} \right)^{1/3}. \quad (3.7)$$

We consider the model where the coefficients $A_1 < 0$ and $A_4 > 0$. In eq. (3.7), $C \geq 0$ is the constant of integration which is defined by the temperature T_0 and scale factor a_0 at the present time:

$$C = (A_1 + A_4 T_0^3)^{3/4} a_0 = A_4^{4/3} (-0.8114 T_c^3 + T_0^3)^{4/3} a_0. \quad (3.8)$$

The temperature T tends to the constant value when the scale factor approaches infinity:

$$T \rightarrow T_\infty = \left(\frac{-A_1}{A_4} \right)^{1/3} = 0.9327 T_c \text{ for } a \rightarrow \infty, \quad (3.9)$$

and the pressure goes asymptotically to zero: $P \rightarrow 0$. On the other hand, for $C \equiv 0$, the temperature is constant all the time $T \equiv T_\infty$, and nuggets behave as a matter with zero pressure $P = 0$. It is worth noting that in this model the temperature of the QNs at present time is not arbitrary low, rather it is close to the critical temperature T_c of the phase transition.

We consider our Universe starting from the moment when we can drop the radiation. It is well known that the radiation dominated (RD) stage is much shorter than the matter dominated (MD) stage. Hence, the neglect of the RD stage does not affect much the estimate of the lifetime of the Universe. Starting from the MD stage, the first Friedmann equation for our model reads

$$3 \frac{H^2 + K}{a^2} = \kappa E + \kappa \varepsilon_0^{mat} \left(\frac{a_0}{a} \right)^3 + \Lambda. \quad (3.10)$$

where we take into account the cosmological constant Λ and the (usual + dark) matter with the present value of the energy density ε_0^{mat} . In (3.10), $H = a'/a = (da/d\eta)/a$, $\kappa = 8\pi G_N/c^4$, G_N is the gravitational constant and $K = \pm 1, 0$ is the spatial curvature. The conformal time η is connected with the synchronous time t : $ad\eta = cdt$. Taking into account eqs. (3.5) and (3.7), we get for the Hubble parameter $H = (1/a)da/dt = (c/a^2)da/d\eta$ the following expression:

$$H^2 = H_0^2 \left\{ \beta \left(\frac{a_0}{a} \right)^3 + \gamma \left(\frac{a_0}{a} \right)^{9/4} \right\}^{4/3} + \Omega_M \left(\frac{a_0}{a} \right)^3 + \Omega_\Lambda + \Omega_K \left(\frac{a_0}{a} \right)^2, \quad (3.11)$$

where the cosmological parameters are

$$\Omega_M = \frac{c^2}{3H_0^2} \kappa \varepsilon_0^{mat}, \quad \Omega_\Lambda = \frac{c^2}{3H_0^2} \Lambda, \quad \Omega_K = -K \left(\frac{c}{a_0 H_0} \right)^2 \quad (3.12)$$

and we introduce the dimensionless parameters

$$\beta = \left(\frac{C}{a_0} \right)^{3/4} \frac{1}{A_4^{1/4}} \left(\frac{\kappa c^2}{a_0^3 H_0^2} \right)^{3/4}, \quad \gamma = -\frac{A_1}{A_4^{1/4}} \left(\frac{\kappa c^2}{a_0^3 H_0^2} \right)^{3/4}. \quad (3.13)$$

From the second Friedmann equation

$$\frac{2H' + H^2 + K}{a^2} = -\kappa P + \Lambda \quad (3.14)$$

after some obvious algebra we obtain the deceleration parameter

$$-q = \left(\frac{H_0}{H} \right)^2 \left\{ \frac{\gamma}{2} \left[\beta \left(\frac{a_0}{a} \right)^{39/4} + \gamma \left(\frac{a_0}{a} \right)^9 \right]^{1/3} - \left[\beta \left(\frac{a_0}{a} \right)^3 + \gamma \left(\frac{a_0}{a} \right)^{9/4} \right]^{4/3} - \frac{\Omega_M}{2} \left(\frac{a_0}{a} \right)^3 + \Omega_\Lambda \right\}. \quad (3.15)$$

At the present time t_0 , eqs. (3.11) and (3.15) read

$$1 = (\beta + \gamma)^{4/3} + \Omega_M + \Omega_\Lambda + \Omega_K, \quad (3.16)$$

$$-q_0 = \frac{\gamma}{2}(\beta + \gamma)^{1/3} - (\beta + \gamma)^{4/3} - \frac{\Omega_M}{2} + \Omega_\Lambda. \quad (3.17)$$

Additionally, we obtain from (3.11) the differential equation

$$d\tilde{t} = \frac{\tilde{a}d\tilde{a}}{\sqrt{(\beta + \gamma\tilde{a}^{3/4})^{4/3} + \Omega_M\tilde{a} + \Omega_\Lambda\tilde{a}^4 + \Omega_K\tilde{a}^2}}, \quad (3.18)$$

where we introduce the dimensionless quantities

$$\tilde{a} = \frac{a}{a_0}, \quad \tilde{t} = H_0 t. \quad (3.19)$$

Therefore, the age of the Universe \tilde{t}_0 is defined by the equality

$$-\tilde{t}_0 = \int_1^0 \frac{\tilde{a}d\tilde{a}}{\sqrt{(\beta + \gamma\tilde{a}^{3/4})^{4/3} + \Omega_M\tilde{a} + \Omega_\Lambda\tilde{a}^4 + \Omega_K\tilde{a}^2}} \quad (3.20)$$

Now, we consider the case of the flat space $K = 0 \rightarrow \Omega_K = 0$. Then, eq. (3.16) reads

$$1 = (\beta + \gamma)^{4/3} + \Omega_M + \Omega_\Lambda. \quad (3.21)$$

Eq. (3.17) demonstrates that accelerated expansion of the Universe at the present time (i.e. $-q_0 > 0$) can be ensured by the first and the last terms on the right side of this equation. It is tempting to explain the acceleration only at the expense of the first term, i.e. due to the presence of QNs when the cosmological constant is absent. However, simple analysis of eqs. (3.17) and (3.21) in the case $\Omega_\Lambda = 0$ shows that the acceleration $-q_0 > 0$ is achieved only for $\beta < 0$ that contradicts our model. The inclusion of the negative curvature $\Omega_K > 0$ does not affect this conclusion due to the smallness of Ω_K .

As we have mentioned above, nuggets behave as matter either asymptotically when $a \rightarrow \infty$ or for all time in the case $C = 0 \rightarrow \beta = 0$. In the latter case we can exactly restore the Λ CDM model so long as eqs. (3.17) and (3.21) take the usual form for this model:

$$1 = \Omega_{M,total} + \Omega_\Lambda \quad (3.22)$$

and

$$-q_0 = -\frac{1}{2}\Omega_{M,total} + \Omega_\Lambda \Rightarrow \Omega_\Lambda = \frac{1}{3} - \frac{2}{3}q_0, \quad (3.23)$$

where $\Omega_{M,total} \equiv \gamma^{4/3} + \Omega_M$. Let Ω_M correspond to just the visible matter. According to observations, $\Omega_M \approx 0.04$. Then, we can easily restore the parameters of the Λ CDM model. For example, taking the deceleration parameter $q_0 \approx -0.595$, as in the Λ CDM model, we get $\Omega_\Lambda \approx 0.73$ and $\gamma \approx 0.33 \rightarrow \gamma^{4/3} \approx 0.23$. Therefore, $\Omega_{M,total} \approx 0.27$.

For the Universe age we get from (3.18) (where we should put $\beta = 0$, $\Omega_K = 0$) $\tilde{t}_0 \approx 1 \Rightarrow t_0 \approx H_0^{-1} \sim 13.7 \times 10^9 \text{ yr}$. Hence, weekly interacting QNs may be candidates for dark matter.

A similar analysis of Model 2 leads to the same physical results

4. Conclusion

We introduced the expansion of the present Universe, using the ‘‘hot’’, i.e. the quark-gluon branch of the bag EoS. Although we made reference to the role of this type of the EoS during the early universe, namely its inflation phase, here we postponed possible speculations about the continuous evolution of the universe, within the present formalism, from its early, quark-gluon stage to the present days, admitting only the possible continuity in the existence in the present Universe of a small fraction of colored objects – quarks and gluons – which escaped hadronization. Our scenario showed that the colored objects survived in the form of isolated islands, called quark-gluon nuggets. This cosmological scenario is defined by EoS of QGP. We focus on two possible eqs. (2.4) and (2.5) dubbed Model I and Model II, respectively. We have shown that there are no fundamental differences in the obtained conclusions for these models, and that weekly interacting (with visible matter) QNs can play the role of dark matter for both of the models. Therefore, the considered scenario provide new possible ways of solving the problems of dark matter.

References

- [1] E. Witten, Cosmic Separation of Phases, Phys. Rev. D 30 (1984) 272.
- [2] J. Applegate and C. Hogan, *Relics of Cosmic Quark Condensation*, Phys. Rev. D 31 (1985) 3037.
- [3] E. Farhi and R. Jaffe, *Strange Matter*, Phys. Rev. D 30 (1984) 2379.
- [4] D. Chandra and A. Goyal, *Dynamical evolution of the universe in the quark hadron phase transition and possible nugget formation*, Phys. Rev. D 62 (2000) 063505 [hep-ph/9903466].
- [5] C. Källman, *Mean field qcd model for hot dense matter*, Phys. Lett. B 134 (1984) 363.
- [6] L.L. Jenkovszky, B. Kampfer and V. Sysoev, *On the expansion of the universe during the confinement transition*, Z. Phys. C 48 (1990) 147.
- [7] V.G. Boyko, L.L. Jenkovszky, B. Kämpfer and V.M. Sysoev, *Mini-ination of the Universe under the confinement phase transition*, J. Nucl. Phys. 51 (1990) 1134.

TWO-BODY PROBLEM IN KALUZA-KLEIN MODELS WITH RICCI-FLAT INTERNAL SPACES

Alexey Chopovsky

Astronomical Observatory of I.I.Mechnikov Odessa National University
Odessa, Ukraine

ABSTRACT. We consider the dynamics of a two-body system in the model with additional spatial dimensions compactified on a Ricci-flat manifold. To define the gravitational field of a system and to construct its Lagrange function we use the weak-field approach. It is shown, that to avoid the contradiction with the experimental restrictions on the value of PPN-parameter γ , the massive sources must have nonzero pressure/tension into the extra dimensions and also must be uniformly smeared there. This fact leads directly to the absence of the Kaluza-Klein modes, which looks unnatural from the point of quantum mechanics.

Key words: Kaluza-Klein models, two-body problem.

1. Introduction

Many modern theories of unification of fundamental interactions, such as superstring theory and its generalizations, are based on the Kaluza-Klein (KK) approach, where the product manifolds with the topology $\mathcal{M}_{\mathcal{D}} = \mathcal{M}_4 \times \mathcal{M}_d$ correspond to the physical space-time. Here \mathcal{M}_4 is the (external) 4-dimensional space-time and \mathcal{M}_d is a compact (internal) d -dimensional space. The compactification of extra spatial dimensions enables to unify gravity and the Standard Model gauge fields.

The models, based on the KK approach, predict the existence of so-called KK-particles, which correspond to the excited states of the Standard Model particles into the extra dimensions. It is experimentally established, that the lower limit of masses of the KK-particles (and, accordingly, the scale of the internal space) is of the TeV order. Thus, if the scale of extra dimensions exceeds 14 TeV, then it is impossible to find KK-particles and to check the existence of additional dimensions on LHC experiment.

In the light of this fact, it is of interest to investigate the astrophysical consequences of the Kaluza-Klein models, which allows to verify or falsify the KK models with the help of highly accurate gravitational experiments.

Hereinafter, we accept the following notation:

Greek indices μ, ν run from 0 to 3, $\tilde{\mu}, \tilde{\nu}$ – from 1 to 3 accordingly, while Latin ones M, N run from 0 to D , $m, n = 4, \dots, D$ and $\tilde{M}, \tilde{N} = 1, \dots, D$, where D is the total dimensionality of the space. The total number of additional spatial dimensions is $d = D - 3$ and $\mathcal{D} = D + 1$. Also X^M is for coordinates on $\mathcal{M}_{\mathcal{D}}$, $x^\mu = X^\mu$ is for coordinates on \mathcal{M}_4 and $y^m = X^m$ is for coordinates on \mathcal{M}_d .

2. The model

Let

$$[\hat{g}_{MN}^{(\mathcal{D})}(y)] = [\eta_{\mu\nu}^{(4)}] \oplus [\hat{g}_{mn}^{(d)}(y)] \quad (1)$$

be a background metric tensor field on a \mathcal{D} -fold $\mathcal{M}_{\mathcal{D}}$. Here $\eta_{00} = 1$, $\eta_{\tilde{\mu}\tilde{\nu}} = -\delta_{\tilde{\mu}\tilde{\nu}}$ and $\hat{g}_{mn}^{(d)}(y)$ is a certain metric tensor on \mathcal{M}_d . We perturb this geometric background introducing the matter in the form of two compact gravitating bodies with rest masses m_1 and m_2 . We also suppose, that these bodies are pressureless into the external space (this is a natural assumption for such bodies as stars) and generally may have certain pressure p into the compact subspace, which is the invariant property of multidimensional particles. Then the corresponding energy-momentum tensor (EMT) has the following contravariant components

$$\begin{aligned} T^{M\nu} &= \rho c^2 \frac{ds}{dx^0} u^M u^\nu, \quad u^M = \frac{dX^M}{ds}, \\ T^{mn} &= -p g^{mn} + \rho c^2 \frac{ds}{dx^0} u^m u^n. \end{aligned} \quad (2)$$

Here g_{MN} is a *perturbed* metric tensor on $\mathcal{M}_{\mathcal{D}}$, which corresponds to the considering matter distribution, and $ds^2 = g_{MN} dX^M dX^N$. Also ρ is the rest mass D -density of the system. The equation of state into the internal space $p = \omega \rho c^2 (u^0)^{-1}$ contains the parameter of state ω . As we shall see below, ω must be nonzero to provide an accordance with the gravitational experiments.

The dynamics of a system is investigated within the framework of a weak-field approach. To construct the Lagrange function up to $1/c^2$ terms it is necessary to define the perturbed metric components g_{00} , $g_{0\tilde{M}}$ and $g_{\tilde{M}\tilde{N}}$ up to $1/c^4$, $1/c^3$ and $1/c^2$ terms respectfully.

The perturbed metric tensor up to $1/c^2$ terms reads:

$$g_{MN} \approx \hat{g}_{MN} + h_{MN}, \quad g^{MN} \approx \hat{g}^{MN} - h^{MN}, \quad (3)$$

where $h_{MN} \sim O(1/c^2)$ and by definition $h_M^N \equiv \hat{g}^{NT} h_{MT}$. To get these terms we should solve (in corresponding order) the multidimensional Einstein equation:

$$R_{MN} = \frac{2S_D \tilde{G}_D}{c^4} \left[T_{MN} - \frac{1}{D-1} T_L^L g_{MN} \right]. \quad (4)$$

S_D is a total D -dimensional solid angle and \tilde{G}_D is a gravitational constant in \mathcal{D} -spacetime.

It's easy to calculate the approximate components and the trace of (1):

$$T_L^L = T_\lambda^\lambda + T_l^l \approx \rho c^2 (1 - \omega d), \quad (5)$$

$$T_{00} \approx \rho c^2, \quad T_{\bar{\mu}\bar{\nu}} \approx 0, \quad T_{mn} \approx -\omega \rho c^2 \hat{g}_{mn}. \quad (6)$$

Hence, for the nonzero (up to $O(1/c^2)$) right-hand sides of (4) we get:

$$R_{00} \approx \frac{2S_D \tilde{G}_D}{c^2} \left(\frac{D-2+\omega d}{D-1} \right) \rho, \quad (7)$$

$$R_{\bar{\mu}\bar{\nu}} \approx \frac{2S_D \tilde{G}_D}{c^2} \left(\frac{1-\omega d}{D-1} \right) \rho \delta_{\bar{\mu}\bar{\nu}}, \quad (8)$$

$$R_{mn} \approx -\frac{2S_D \tilde{G}_D}{c^2} \left(\frac{1+2\omega}{D-1} \right) \rho \hat{g}_{mn}, \quad (9)$$

The approximate (up to $1/c^2$ terms) Ricci-tensor components in general case have the following form:

$$R_{MN} \approx \hat{R}_{MN} + \frac{1}{2} \left[-\hat{\nabla}_L \hat{\nabla}^L h_{MN} + Q_{MN} \right], \quad (10)$$

$$\begin{aligned} Q_{MN} \equiv & \left[\hat{\nabla}_M \left(\hat{\nabla}_L h_N^L - \frac{1}{2} \partial_N h_L^L \right) \right. \\ & \left. + \hat{\nabla}_N \left(\hat{\nabla}_L h_M^L - \frac{1}{2} \partial_M h_L^L \right) \right] \\ & - \left(\hat{R}_{NPM}^L + \hat{R}_{MPN}^L \right) h_L^P \\ & + \hat{R}_{PM} h_N^P + \hat{R}_{PN} h_M^P; \partial_M \equiv \frac{\partial}{\partial X^M}. \end{aligned} \quad (11)$$

Hereinafter all symbols marked with "hats" correspond to the background metric \hat{g}_{MN} . In particular \hat{R}_{NPM}^L is an unperturbed Riemann tensor and $\hat{\nabla}_M$ is a covariant derivative on the background.

A rather bulky equality (11) may be simplified. Firstly, we use the freedom of coordinate system choice and impose the gauge conditions:

$$\hat{\nabla}_L h_N^L - \frac{1}{2} \partial_N h_L^L = 0. \quad (12)$$

Then a pair of terms in square brackets in (11) is equal to zero. Secondly, if we take into account the

isotropic character of the considering EMT (1) with respect to the internal space, we may conclude, that the topology of the internal space remains unchanged after the matter introduction and $[h_{MN}^{(D)}] = [h_{\mu\nu}^{(4)}] \oplus [h_{mn}^{(d)}]$, where $h_{mn}^{(d)} = \xi \hat{g}_{mn}^{(d)}$. The prefactor ξ is a certain scalar field. Taking it into account one can easily find that the rest of terms in (11) vanishes. Consequently, for the considering matter distribution (1) and under the accepted gauge conditions (12), the relation $R_{MN} \approx \hat{R}_{MN} - (1/2) \hat{\nabla}_L \hat{\nabla}^L h_{MN}$ is valid. In the general case of Ricci-flat internal spaces ($\hat{R}_{mn} = 0$) we obtain up to $1/c^2$ -terms:

$$R_{MN} \approx -\frac{1}{2} \hat{\nabla}_L \hat{\nabla}^L h_{MN} \approx -\frac{1}{2} \hat{\nabla}_{\bar{L}} \hat{\nabla}^{\bar{L}} h_{MN}. \quad (13)$$

Then the approximate 00-component of the Einstein equations reads:

$$(7), (13) \Rightarrow -\frac{1}{2} \hat{\nabla}_{\bar{L}} \hat{\nabla}^{\bar{L}} h_{00} = \frac{2S_D \tilde{G}_D}{c^2} \frac{D-2+\omega d}{D-1} \rho. \quad (14)$$

Let's suppose that the physically reasonable solution $h_{00}(X^{\bar{M}})$ of the equation (14) exists. Then it describes the nonrelativistic multidimensional gravitational potential φ of the given matter distribution: $h_{00} \equiv 2\varphi/c^2$. Therefore, using (8), we obtain

$$-\frac{1}{2} \hat{\nabla}_{\bar{L}} \hat{\nabla}^{\bar{L}} h_{\bar{\mu}\bar{\nu}} = -\frac{1}{2} \hat{\nabla}_{\bar{L}} \hat{\nabla}^{\bar{L}} \left(\frac{1-\omega d}{D-2+\omega d} h_{00} \delta_{\bar{\mu}\bar{\nu}} \right). \quad (15)$$

Hence

$$h_{\bar{\mu}\bar{\nu}} = \frac{1-\omega d}{D-2+\omega d} h_{00} \delta_{\bar{\mu}\bar{\nu}}, \quad (16)$$

and, analogically

$$h_{mn} = -\frac{1+2\omega}{D-2+\omega d} h_{00} \hat{g}_{mn}. \quad (17)$$

These solutions must satisfy the conditions (12). It's not difficult to check, that for the ν -th component of (12) the equality $\hat{\nabla}_L h_\nu^L - (1/2) \partial_\nu h = 0 + O(c^{-3})$ fulfills, while for the n -th component we have the equation:

$$\hat{\nabla}_L h_n^L - \frac{1}{2} \partial_n h = -\frac{\omega(D-1)}{D-2+\omega d} \partial_n h_{00} = 0. \quad (18)$$

We consider a general case $\omega \neq 0$, hence, to satisfy (18) we must demand $\partial_n \varphi = 0$. Obviously, as φ depends only on the external coordinates so does ρ . In other words, the massive sources must be uniformly smeared over the internal space: $\rho = \varrho_3/V_d$, where ϱ_3 is a rest mass density into the external space and $V_d \{g_{mn}^{(d)}\} = \int_{\mathcal{M}_d} d^d y \sqrt{|\det(g_{mn}^{(d)})|}$ is the volume of the internal space.

For two point-like masses, particularly

$$\varrho_3(\mathbf{r}) = [-\det(g_{\mu\nu}^{(4)})]^{-1/2} \sum_{i=1,2} m_i \delta(\mathbf{r} - \mathbf{r}_i), \quad (19)$$

where $\mathbf{r} = (x^1, x^2, x^3)$, and \mathbf{r}_i is a position vector of the i -th particle.

Then the equation (14) is reduced to a 3-dimensional Poisson equation:

$$\Delta_3 \varphi(\mathbf{r}) = 4\pi G_N \sum_{i=1,2} m_i \delta(\mathbf{r} - \mathbf{r}_i), \quad \Delta_3 \equiv \sum_{\tilde{\mu}} \partial_{\tilde{\mu}}^2. \quad (20)$$

The Newtonian gravitational constant is connected with the multidimensional one as follows:

$$G_N = \frac{S_D(D-2+\omega d)}{2\pi \hat{V}_d(D-1)} \tilde{G}_D, \quad \hat{V}_d \equiv V_d \{\hat{g}_{mn}^{(d)}\}. \quad (21)$$

The solution of (20) is a Newtonian potential:

$$\varphi(\mathbf{r}) = -G_N \sum_{i=1,2} \frac{m_i}{|\mathbf{r} - \mathbf{r}_i|}. \quad (22)$$

As we pointed out above, to construct the Lagrange function of the considering system up to $1/c^2$ terms, we must also define the correction terms $f_{00} \sim O(1/c^4)$ and $f_{0\tilde{\mu}} \sim O(1/c^3)$ in the expansions $g_{00} \approx \hat{g}_{00} + h_{00} + f_{00}$ and $g_{0\tilde{\mu}} \approx f_{0\tilde{\mu}}$. The obtained tensor h_{MN} enable us to construct the corresponding approximate Einstein equations. Within the required accuracy, we have for 00 and $0\tilde{\mu}$ approximate covariant components of the EMT (1) and its trace:

$$T_{00} \approx \frac{\varrho_3 c^2}{\hat{V}_d} \left[1 + \frac{3D-4+\omega d}{D-2+\omega d} \frac{\varphi}{c^2} + \frac{v^2}{2c^2} \right], \quad (23)$$

$$T_{0\tilde{\mu}} \approx -\frac{\varrho_3 c}{\hat{V}_d} v^{\tilde{\mu}}, \quad (24)$$

$$T \approx \frac{\varrho_3}{\hat{V}_d} (1-\omega d) \left[c^2 + \varphi \frac{D-\omega d}{D-2+\omega d} - \frac{v^2}{2} \right]. \quad (25)$$

Here $v^{\tilde{\mu}} \equiv cd x^{\tilde{\mu}}/dx^0$, $v^2 \equiv \delta_{\tilde{\mu}\tilde{\nu}} v^{\tilde{\mu}} v^{\tilde{\nu}}$. Obviously, for the particle uniformly smeared over the internal space $v^m = 0$. Hence, the right-hand sides of the approximate 00 and $0\tilde{\mu}$ components of (4) are

$$R_{00} \approx \frac{2S_D \tilde{G}_D}{c^2} \frac{\varrho_3}{\hat{V}_d} \left[\frac{D-2+\omega d}{D-1} + \frac{v^2}{c^2} \frac{D-\omega d}{2(D-1)} + \frac{\varphi}{c^2} \frac{3D-4+\omega d}{D-1} \right], \quad (26)$$

$$R_{0\tilde{\mu}} \approx -\frac{2S_D \tilde{G}_D}{c^3} \frac{\varrho_3}{\hat{V}_d} v^{\tilde{\mu}}. \quad (27)$$

The corresponding left-hand sides are

$$R_{00} \approx \frac{1}{c^2} \Delta_3 \varphi + \frac{1}{2} \Delta_3 \left(f_{00} - \frac{2}{c^4} \varphi^2 \right) + \frac{2}{c^4} \frac{D-1}{D-2+\omega d} \varphi \Delta_3 \varphi, \quad (28)$$

$$R_{0\tilde{\mu}} \approx \frac{1}{2} \Delta_3 f_{0\tilde{\mu}} + \frac{1}{2c^2} \partial_0 \partial_{\tilde{\mu}} \varphi. \quad (29)$$

The solutions of the equations (26)-(28) and (27)-(29) are (for more details see ref.):

$$f_{00} = \frac{2\varphi^2}{c^4} + \frac{2G_N^2}{c^4} \sum_p \frac{m_p}{|\mathbf{r} - \mathbf{r}_p|} \sum_{q \neq p} \frac{m_q}{|\mathbf{r}_p - \mathbf{r}_q|} - \frac{D-\Sigma}{D-2+\Sigma} \frac{G_N}{c^4} \sum_p \frac{m_p v_p^2}{|\mathbf{r} - \mathbf{r}_p|}, \quad (30)$$

$$f_{0\tilde{\mu}} = \frac{G_N}{2c^3} \sum_p \frac{m_p}{|\mathbf{r} - \mathbf{r}_p|} \left[\frac{3D-2-\Sigma}{D-2+\Sigma} v_p^{\tilde{\mu}} + n_p^{\tilde{\mu}} (\mathbf{n}_p \mathbf{v}_p) \right], \quad (31)$$

where $n_p^{\tilde{\mu}} \equiv (x^{\tilde{\mu}} - x_p^{\tilde{\mu}})/|\mathbf{r} - \mathbf{r}_p|$ and $(\mathbf{n}_p \mathbf{v}_p) \equiv \sum_{\tilde{\mu}} n_p^{\tilde{\mu}} v_p^{\tilde{\mu}}$.

Thus, now we may construct the Lagrange function of the system. For the i -th body the Lagrange function is defined as follows: $L_i = -m_i c(ds_i/dt) = -m_i c^2 \sqrt{g_{00} + 2g_{0\tilde{\mu}} v_i^{\tilde{\mu}}/c + g_{\tilde{\mu}\tilde{\nu}} v_i^{\tilde{\mu}} v_i^{\tilde{\nu}}/c^2}$. With the help of the approximate expressions for g_{00} , $g_{0\tilde{\mu}}$ and $g_{\tilde{\mu}\tilde{\nu}}$, we may calculate L_i . Further, to get the Lagrange function \mathcal{L} of a hole system, we use the relation $\partial \mathcal{L}/\partial \mathbf{r}_i = (\partial L_i/\partial \mathbf{r})|_{\mathbf{r}=\mathbf{r}_i}$. After a number of calculations we finally obtain the sought-for approximate Lagrange function \mathcal{L} of the two-body system:

$$\mathcal{L} \approx \sum_{i=1}^2 \frac{m_i v_i^2}{2} + \sum_{i=1}^2 \frac{m_i v_i^4}{8c^2} + \frac{G_N m_1 m_2}{|\mathbf{r}_1 - \mathbf{r}_2|} - \frac{G_N^2 m_1 m_2 (m_1 + m_2)}{2c^2 |\mathbf{r}_1 - \mathbf{r}_2|^2} + \frac{G_N m_1 m_2}{2c^2 |\mathbf{r}_1 - \mathbf{r}_2|} \left[\frac{D-\omega d}{D-2+\omega d} (v_1^2 + v_2^2) - \frac{3D-2-\omega d}{D-2+\omega d} (\mathbf{v}_1 \mathbf{v}_2) - (\mathbf{n}\mathbf{v}_2)(\mathbf{n}\mathbf{v}_2) \right], \quad (32)$$

where $\mathbf{n} \equiv (\mathbf{r}_1 - \mathbf{r}_2)/|\mathbf{r}_1 - \mathbf{r}_2|$.

3. Experimental restrictions. Conclusions

It's not difficult to check, that in case $\omega = -1/2$ the expression (32) exactly coincides with the relativistic analog. It is of interest to find the empirical restrictions on the value of the parameter ω , which defines the immanent pressure/tension of the matter into the internal space. Let's assume for this purpose, that there may be a certain deviation $\delta\omega$: $\omega = -1/2 + \delta\omega$.

From the formula (16), rewritten for a solitary particle, we conclude that the parameterized post-Newtonian parameter γ is

$$\gamma = \frac{1-\omega d}{1+(1+\omega)d}. \quad (33)$$

The Shapiro time-delay experiment using the Cassini spacecraft gives: $\gamma = 1 + (2.1 \pm 2.3) \times 10^{-5}$. Hence, for $\delta\omega$ the following limitation is valid

$$|\delta\omega| \leq \frac{d+2}{2d} \times 10^{-5}. \quad (34)$$

From the perihelion shift of Mercury experiments it follows the less strong condition (for details see ref.):

$$|\delta\omega| \leq \frac{3(d+2)}{8d} \times 10^{-3}. \quad (35)$$

Anyway, to achieve the accordance with gravitational tests, we must introduce the internal pressure/tension with the parameter of state $\omega = -1/2 \pm (1/2 + 1/d) \times 10^{-5}$ for usual astrophysical bodies. The interpretation of such strange immanent non-kinetic pressure/tension of the matter is not the only problem of the model. As we have shown in sec. 2, the appearance of such pressure leads directly to the uniform smearing of the masses over the internal space, and, as a consequence, to the absence of the excited KK-states.

This fact looks very unnatural from the point of quantum physics. Such situation emerges in all KK-models with Ricci-flat internal manifolds, e.g. in models with Calabi-Yau manifolds, which are widely used in the superstring theory.

Acknowledgements. The author is deeply grateful to his scientific supervisors Alexander I. Zhuk and Maxim V. Eingorn.

References

- Chopovsky A., Eingorn M., Zhuk A.: 2013, *Many-body problem in Kaluza-Klein models with toroidal compactification*, (arXiv:gr-qc/1302.0501).

THE NEW GALAXY SAMPLE FROM SDSS DR9 AT $0.003 \leq Z \leq 0.1$

D.V. Dobrycheva

Main Astronomical Observatory of the National Academy of Sciences of Ukraine,
Kyiv, Ukraine, *dariadobrycheva@gmail.com*

ABSTRACT. To test the relationships between morphological types of galaxies in pairs/groups and their physical properties (luminosity, mass, color index, the radial velocity, the inverse concentration index, the absolute magnitude, the radius of the de Vaucouleurs or scale radius, etc.) on a larger sample of the local Universe, we need the more representative data. With this aim we processed and prepared a sample of galaxies with $0.003 \leq z \leq 0.1$ based on the latest SDSS DR9. The initial sample was about 724,000 objects and, consequently, 407,000 galaxy images after the preliminary processing. Because of the large number of duplicate and faulty images, we checked its carefully and obtained finally about 260,000 galaxies in the studied sample at $z < 0.1$. We discuss this procedure and properties of the studied galaxy sample.

Key words: Galaxies, SDSS DR9.

1. Introduction

The study of galaxy groups and clusters is an important clue to the conditions of galaxy evolution as well as to the role of intragalaxy/intracluster gas dynamics and hierarchical clustering in the process of galaxy formation. The major physical characteristics are “mass-to-luminosity” ratio as well as dependencies of morphological type on such parameters as the color index, diameters, absolute magnitude etc., i.e. in context of the dense environmental influence. For example, the rich clusters contain mainly the elliptical and SO galaxies while the poor groups account them for only 10-20% of the population. This well-known problem is still discussed as concerns with the processes that effect on the morphological changes of galaxies during encounters or intrinsic processes connected with a stellar density, star formation rate or ram-pressure stripping. To evaluate a better model for the relation between the baryonic component of a galaxy and its massive dark halo as well as a common halo of galaxy group/cluster, which should be supported by the reliable observational data is still also under development.

In the previous works of our team by Dobrycheva

et. al. (2012), Melnyk et. al. (2012), Pulatova et al. (2013), Vavilova et al. (2009), Melnik et al. (2009), Melnyk et al. (2008) we have studied physical properties of galaxies in poor groups (from isolated galaxies till 10 group members) selected from SDSS DR5 and other databases as well as for the galaxy systems in the Local Supercluster (Melnyk et al. (2006), Vavilova et al. (2005), Karachentseva et al. (2005, 1994a, 1994b)) and X-ray clusters (Babyk et al. (2012, 2013)) as concerns also with the visible and dark matter distribution. See, also, the recent papers in context of our research by Tempel et al. (2012, 2011), Carollo et al. (2013), Luparello et al. (2013), Blanton et al. (2012), Szabo et al. (2013), Sheldon et al. (2011), and Vollmer (2007). So, for continuation of our research we need the more representative galaxy sample to construct a distribution of galaxies in pairs/groups in a way proposed by Elyiv et al. (2009), namely to apply the modified Voronoi tessellation for identifying the galaxy groups of different population with the better defined morphological types, spectra and other galaxy data.

2. The Sample

The main aim of this work was to create a good quality sample of nearby galaxies with $z < 0.1$ for analyzing its properties in context of the tasks aforementioned in Introduction. We worked with a sample of the latest SDSS DR9. “The SDSS observes galaxies in five photometric bands (u, g, r, i and z) centered at (3551, 4686, 6165, 7481 and 8931 Å). The photometric and spectroscopic observations were conducted with the 2.5-m SDSS telescope at the Apache Point Observatory in New Mexico, USA” (www.sdss3.org). We downloaded the file, which contains the list of all spectra for a given data release with associated parameters from the 2D and 1D pipelines. This sample was conformed to FITS standard, therefore the fv program for work with the sample was used, because of fv is appropriated with graphical program for viewing and editing any FITS format image or table.

The preliminary preparation of the sample had several steps: limitation by z; checking for non-galaxy

objects; checking for faulty and duplicate objects. In order to avoid congestion on the server, the list was currently limited to 1000 objects and submitted our list in 10 bins by z (Table 1, Col. 1). So, after limiting the sample by redshifts $0.003 < z < 0.1$, it contained 724,000 objects and required the significant cleaning. First of all, the quasars and star-like objects were removed and, consequently, 407,000 galaxy objects were left after this rejecting (Col. 2). It is known that SDSS gives several duplicate images for the same galaxies in many cases. We used SDSS DR9 Image List Tool and own IT-code to find duplicate objects as well as we inspected visually each final galaxy image in our sample. As result, the sample has contained more 360,000 galaxies after this reduction (Col. 3).

Table 1: Quantitative distribution of galaxies in the studied SDSS DR9 sample before and after processing/rejecting faulty objects

redshifts	with duplicates	without duplicates
$0.003 \leq z < 0.01$	5240	3782
$0.01 \leq z < 0.02$	10900	8687
$0.02 \leq z < 0.03$	29825	25492
$0.03 \leq z < 0.04$	35723	31579
$0.04 \leq z < 0.05$	39593	34803
$0.05 \leq z < 0.06$	43459	39116
$0.06 \leq z < 0.07$	56101	50429
$0.07 \leq z < 0.08$	67787	61445
$0.08 \leq z < 0.09$	66229	59345
$0.09 \leq z < 0.1$	52289	47900
total	407146	362588

Because of this sample is being used for identifying galaxy groups by the method of Voronoi tessellation, which is sensitive to the boundary effects, we taken it into account and obtained the sample consisting of 290,000 galaxies (Fig. 1). We note that the ‘‘Legacy targets are those taken as part of the SDSS Legacy survey, which is the wide-field survey of galaxies brighter than $r=17.77$ (Main Sample), Luminous Red Galaxies, and QSOs’’ (www.sdss3.org/dr9/algorithms/photo_z.php). This recommendation required the new reduction. Namely, we limited our sample by magnitude $modelMag_r < 17.7$.

3. Astronomical corrections

To take into account completeness of the sample, it should be limited according to the dependencies on the luminosity from redshift, as well as the evolution to the k -corrections, and the luminosity depending on the distance, as well as galactic extinction.

K -correction is a correction to an astronomical object’s magnitude (or equivalently, its flux) that al-

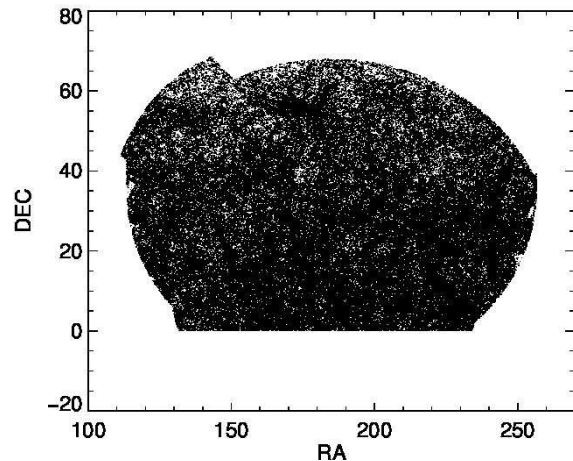


Figure 1: Angular-redshift completeness of the SDSS DR9 sample of nearby galaxies

lows a measurement of a quantity of light from an object at a redshift z to be converted to an equivalent measurement in the rest frame of the object. The K -corrections for galaxies of different morphological types are necessary to interpret the magnitude-redshift relation, the luminosity function of galaxies and for most of the spectrophotometric studies of distant objects (see Poggianti (1997)). For the calculation of k -correction we used code by the M.R. Blanton (2002). The version of the K -correction code ($v1.11$) implementing the calculations described here, along with electroplates and filter curves, is publicly available (physics.nyu.edu/~mb144/kcorrect). The whole of the code was used through the Research Systems, Incorporated, IDL language; everything except for the template-fitting also exists in stand-alone C programs (which call the same routines, guaranteeing consistency).

‘‘The spectra released in DR9 have not been corrected for Galactic extinction, because the SDSS includes a substantial number of spectra of Milky Way stars whose extinction would differ from that given in the Galactic dust maps, as they don’t lie beyond the full dust column. The extinction is a relatively small effect over most of the survey area, since the median $E(B-V)$ over the survey is around 0.04; however, for some SEGUE pointings the reddening can be substantially larger’’. Following this SDSS recommendation, we took into account the extinction coefficients by Yuan et al. (2013) for our SDSS DR9 sample (Fig. 2).

As result of all the aforementioned reject procedures and astronomical corrections, we created the new galaxy sample about of nearby 260,000 galaxies till $z < 0.1$ based on SDSS DR9 (Fig. 3). Now this sample is being used to analyze the physical properties (luminosity, morphological type, color index, the

radial velocity, the inverse concentration index, the absolute magnitude, the radius of the de Vaucouleurs, mass-to-luminosity ratio etc.) of galaxies in groups.

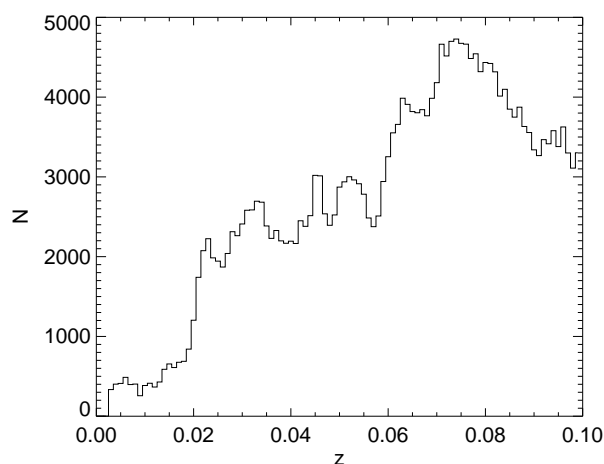


Figure 2: The distribution of nearby galaxies from SDSS DR9 within $0.003 \leq z \leq 0.1$

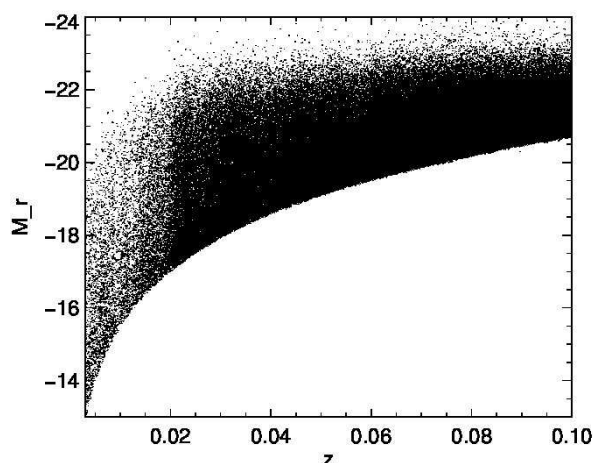


Figure 3: Luminosity versus redshift relation for nearer galaxies from SDSS DR9

Acknowledgements. The author thanks I.B. Vavilova, O.V. Melnyk, A.A. Elyiv, I.A. Zinchenko, and Yu.V. Babyk for valuable comments that have improved preparation of the studied sample. Our especial gratitude is to the SDSS team, where the funding for the SDSS and SDSS-II has been provided by the Alfred P. Sloan Foundation, the Participating Institutions, the National Science Foundation, the U.S. Department of Energy, the National Aeronautics and Space Administration, the Japanese Monbukagakusho, the Max Planck Society, and the Higher Education Funding Council for England.

was supported by SFFR project F50.2-2013. This work was partially supported in frame of F53.2/015 project of the State Fund of Fundamental Researches of Ukraine.

References

- Babyk I., Vavilova I.: 2013, *Astrophys. Space Sci.*, DOI 10.1007/s10509-013-1630-z
- Babyk I., Vavilova I., Del Popolo A.: 2012, *arXiv* 1208.2424
- Blanton M.R., Brinkmann J. et al.: 2002, *The Astrophysical Journal* **125**, 2348.
- Carollo C.M., Cibinell A., Lilly S.J. et al.: 2013, *Astrophys. J.* **776**, 71.
- Dobrycheva D. and Melnyk O.: 2012, *Advances in Astronomy and Space Physics* **2**, 42.
- Elyiv A., Melnyk O., Vavilova I.: 2009, *Mon. Not. R. Astron. Soc.* **394**, 1409.
- Karachentseva V.E., Melnyk O.V., Vavilova I.B., Makarov D.I.: 2005, *Kinematika i Fizika Nebesnykh Tel* **21**, 217.
- Karachentseva V.E., Vavilova I.B.: 1994a, *ESO Conference and Workshop Proceedings* **49**, 91.
- Karachentseva V.E., Vavilova I.B.: 1994b, *Bulletin of the Special Astrophysics Observatory* **37**, 98.
- Karachentseva V.E., Vavilova I.B.: 1995, *Kinematics and Physics of Celestial Bodies* **11**, 38.
- Luparello H.E., Lares M., Yaryura C.Y. et al.: 2013, *arXiv:1304.0456*
- Melnik O.V., Elyiv A.A., Vavilova I.B.: 2009, *Kinematics and Physics of Celestial Bodies* **25**, 43.
- Melnyk O.V., Dobrycheva D.V., Vavilova I.B.: 2012, *Astrophysics* **5**, 293.
- Melnyk O.V., Vavilova I.B.: 2008, *Advances in Space Research* **42**, 591.
- Melnyk O.V., Elyiv A.A., Vavilova I.B.: 2006, *Kinematika i Fizika Nebesnykh Tel* **22**, 283.
- Poggianti B.M.: 1997, *Astron Astrophys.* **122**, 399.
- Pulatova N., Vavilova I., Berczik P.: 2013, *IAU Symposium* **290**, 297.
- Szabo T., Pierpaoli E.: 2013, *AAS Meeting Abstracts* **221**
- Sheldon E.S., Cunha C.E., Mandelbaum R. et al.: 2012, *Astrophys. J. Suppl.* **201**, 32.
- Tempel E., Tago E., Liivamgi L.J.: 2012, *Astron. Astrophys.* **540**, DOI dx.doi.org/10.1051/0004-6361/201118687
- Tempel E., Saar E., Liivamgi L.J. et al.: 2011, *arXiv:1012.1470*
- Vavilova I.B., Karachentseva V.E., Makarov D.I., Melnyk O.V.: 2005, *Kinematika i Fizika Nebesnykh Tel* **21**, 1.
- Vavilova I. B., Melnyk O. V., and Elyiv A. A.: 2009, *Astron. Nachr.* **330**, 1004.
- Vollmer B.: 2007, *Planets, Stars and Stellar Systems*, 207.
- Yuan H. B., Liu X. W. and Xiang M. S.: 2013, *Mon. Not. R. Astron. Soc.* **430**, 2188.

SCALAR PERTURBATIONS IN f(R)-COSMOLOGIES

M. Eingorn¹, J. Novak²

¹ North Carolina Central University,
Durham, NC, U.S.A., *maxim.eingorn@gmail.com*

² Charles University in Prague,
Faculty of mathematics and physics, Czech republic, *jnovak@math.cas.cz*

ABSTRACT. We take first steps to generalizing the recently developed mechanical (non-hydrodynamical), or discrete (discontinuous), approach to cosmological problems on intermediate, semiastronomical semic cosmological, scales to the case of nonlinear gravity. In the framework of the f(R) theory we study the scalar perturbations in the flat space and derive the corresponding gravitational potentials.

Key words: alternative theories of gravity: f(R) nonlinear theories; cosmological perturbation theory: scalar perturbations; scalaron; Yukawa potential

1. Introduction

Observations of the Ia supernovae and cosmic microwave background have revealed that the Universe is undergoing an accelerating phase in its expansion. The explanation of this acceleration in the context of general relativity has stimulated a lot of ideas, the most notable of which is the introduction of mysterious cosmic fluid, the so called dark energy. In more recent times, modified theories of gravity, constructed by adding correction terms to the usual Einstein-Hilbert action, have opened a new window to study accelerated expansion of the universe where it has been shown that such correction terms could give rise to accelerating solutions of the field equations without having to invoke concepts such as dark energy.

2. Scalar cosmological perturbations

In our work we do a scalar cosmological perturbation. The background metric is the flat FLRW metric. We divide our analysis of perturbed equations to two cases: the scalaron's mass is large enough and then we reproduce the standard General Relativity; or we don't neglect the scalaron's contribution (but we neglect the influence of cosmological background) and then we find that scalar perturbations - we have two variables Ψ and Φ in conformal Newtonian gauge - represent the mix

of the standard potential and the additional Yukawa term:

$$\Psi = \frac{F'}{2F} \left[\frac{\kappa^2 m}{12\pi a F'} \frac{\exp\left(-\sqrt{\frac{a^2 F}{3F'}} r\right)}{r} - \frac{\kappa^2}{F a^3} \bar{\rho}_c \right] + \frac{\varphi}{a},$$

$$\Phi = -\frac{F'}{2F} \left[\frac{\kappa^2 m}{12\pi a F'} \frac{\exp\left(-\sqrt{\frac{a^2 F}{3F'}} r\right)}{r} - \frac{\kappa^2}{F a^3} \bar{\rho}_c \right] + \frac{\varphi}{a},$$

where $F = \frac{df}{dR}$, $\varphi = -\frac{G_N m_0}{r} - \frac{G_N m_0}{2r_0^3} r^2 + \frac{3G_N m_0}{2r_0}$, a is a scale factor and ρ_c is the rest mass density in comoving coordinates ($\delta\rho_c = \rho_c - \bar{\rho}_c$).

3. Next future work

We will try to reproduce our results in computations in NP-formalism.

References

De Felice A., Tsujikawa S.: 2010, *Living Reviews Relativity* 13, **arXiv:1002.4928**, f(R)-theories.

MOTION TYPES OF NEUTRAL TEST PARTICLES IN THE FIELD OF CHARGED OBJECT IN GENERAL RELATIVITY AND THEIR CLASSIFICATION

V.D. Gladush¹, D.A. Kulikov²

Theoretical Physics Department, Dnipropetrovsk National University
72 Gagarin av., Dnipropetrovsk 49010, Ukraine,
¹vgladush@gmail.com, ²kulikov_d_a@yahoo.com,

ABSTRACT. In the previous work of one of the authors the radial motions of charged test particles in the field of a spherically symmetric charged object in general relativity were considered and their classification was built. The present paper generalizes this approach to study the motion of particles with non-zero orbital momentum. We limit the consideration to neutral particles and stress on the peculiarities that emerge in the case of the Reissner-Nordström field with super-extremal charge.

Key words: effective potential, scale invariance, classification of motions, Reissner-Nordström metric.

1. Introduction

The analysis of test particles motion is a classical method for studying the space-time structure near a gravitating massive object. The electric charge of the gravitational field source, if present, affects substantially the space-time geometry. Search for particles motion peculiarities that emerge in this case receives considerable attention (see, for example, Chandrasekhar S. (1983) and other authors in the references) as it constitutes an important part of the investigation of relativistic configurations. In the present work we study the radial component of motion for neutral test particles with mass m and orbital moment L in the field of a central source with mass M and charge Q . This field is described by the Reissner-Nordström metric

$$ds^2 = Fc^2 dt^2 - F^{-1} dR^2 - R^2 d\sigma^2, \quad (1)$$

where

$$F = 1 - \frac{2\kappa M}{c^2 R} + \frac{\kappa Q^2}{c^4 R^2}, \quad d\sigma^2 = d\theta^2 + \sin^2 \theta d\varphi^2. \quad (2)$$

Note that we consider all the possible types of spherically symmetric charged objects, namely: $Q^2 < \kappa M^2$ - black hole (BH), two horizons, $Q^2 = \kappa M^2$ - extreme BH, twofold horizon, $Q^2 > \kappa M^2$ - super-extremal (abnormally) charged object or naked singularity (NS).

In the case of static and spherically symmetric field we have the conservation of particle energy

$$E = c\sqrt{F} \sqrt{m^2 c^2 + F p_R^2 + \frac{1}{R^2} \left(p_\theta^2 + \frac{p_\varphi^2}{\sin^2 \theta} \right)}, \quad (3)$$

and the square of the total orbital angular momentum

$$L^2 = p_\theta^2 + \frac{p_\varphi^2}{\sin^2 \theta} = const, \quad (4)$$

where $P^\mu = mcdx^\mu/ds$ is the particle four-momentum. These formulae yield the expression for the radial component of velocity

$$\left(mc^2 \frac{dR}{ds} \right)^2 = E^2 - F \left(m^2 c^4 + \frac{c^2 L^2}{R^2} \right). \quad (5)$$

2. Scale invariance, new parameters and effective potential

The problem of how to investigate the motion can be simplified by using the potential method and scale invariance of the system. The dynamical system under consideration has five parameters: $\{M, Q, m, E, L\}$. However, the number of essential ones is less than five because the system admits the two-parametric group G^2 of scaling transformations:

$$\begin{aligned} \tilde{E} &= E/\alpha, \quad \tilde{m} = m/\alpha, \quad \tilde{L} = L/\gamma, \quad |\tilde{Q}| = \alpha|Q|/\gamma, \\ \tilde{M} &= \alpha M/\gamma, \quad \tilde{R} = \alpha R/\gamma, \quad \tilde{s} = \alpha s/\gamma. \end{aligned} \quad (6)$$

As a new set of parameters and variables we choose the independent invariants of the G^2 transformations:

$$\begin{aligned} \epsilon &= \frac{E}{mc^2}, \quad \eta = \frac{|Q|m\sqrt{\kappa}}{c|L|}, \quad \mu = \frac{Mm\kappa}{c|L|}, \\ z &= \frac{Rmc}{|L|}, \quad \tau = s \frac{mc}{|L|}, \quad \varpi = \omega \frac{|L|}{mc^2}, \end{aligned} \quad (7)$$

where $\{\epsilon, \eta, \mu, z, \tau\}$ are the reduced energy, charge, mass, radius and proper time, respectively.

In their terms equation (5) becomes

$$\left(\frac{dz}{d\tau}\right)^2 = \epsilon^2 - 1 + \frac{2\mu}{z} - \frac{1 + \eta^2}{z^2} + \frac{2\mu}{z^3} - \frac{\eta^2}{z^4} = -W_V \quad (8)$$

where W_V is the velocity potential. Allowed regions and turning points can be found from the conditions $W_V \leq 0$ and $W_V = 0$, whereas the circular orbits result from $W_V = 0$, $\partial W_V / \partial z = 0$.

Introduction of a suitable potential will further simplify the situation. In our case the energy potential (see Gladush V., Galadgyi M. (2011)) is the most convenient one, which is hereinafter called the effective potential (Pugliese B., Quevedo H., Ruffini R. (2011))

$$W_\epsilon^2 = 1 - 2\mu z^{-1} + (1 + \eta^2)z^{-2} - 2\mu z^{-3} + \eta^2 z^{-4}. \quad (9)$$

Then the equation of motion becomes

$$(dz/d\tau)^2 + W_\epsilon^2 = \epsilon^2. \quad (10)$$

Now the allowed and forbidden regions and turning points are determined by the conditions $W_\epsilon^2 \leq \epsilon^2$ and $W_\epsilon^2 = \epsilon^2$. As a consequence, the classification of motions relies on distinguishing different types of the potential W_ϵ^2 . Because of the scale invariance, it involves solely the reduced mass μ and charge η of the central body.

The circular orbits are determined by conditions $W_\epsilon^2 = \epsilon^2$, $\partial W_\epsilon^2 / \partial z = 0$ that lead to algebraic equations

$$(1 - \epsilon^2)z^4 - 2\mu z^3 + (1 + \eta^2)z^2 - 2\mu z + \eta^2 = 0, \quad (11)$$

$$\mu z^3 - (1 + \eta^2)z^2 + 3\mu z - 2\eta^2 = 0. \quad (12)$$

For a stable circular orbit, it is necessary to fulfill the condition of minimum $\partial^2 W_\epsilon^2 / \partial z^2 > 0$. If there is an inflection point, then we have $\partial^2 W_\epsilon^2 / \partial z^2 = 0$ that corresponds to the last circular orbit.

3. Circular orbit radii and their classification

Let us bring the cubic equation for circular orbits (12) to the standard form

$$z^3 + az^2 + bz + c = 0, \quad (13)$$

$$a = -(1 + \eta^2)/\mu, \quad b = 3, \quad c = -2\eta^2/\mu. \quad (14)$$

Then the types of its solutions can be established from the sign of the discriminant

$$D = (-a^2/3 + b)^3/27 + (2a^3/27 - ab/3 + c)^2/4. \quad (15)$$

Equation (13) may have (i) one real root and a pair of complex conjugate roots ($D > 0$); (ii) three real roots from which at least two are equal ($D = 0$); (iii) three different real roots ($D < 0$). For identifying these cases, we rewrite the discriminant as

$$D = (1 - \mu_+^2 \mu^{-2})(1 - \mu_-^2 \mu^{-2}), \quad (16)$$

$$\begin{aligned} 72\mu_\pm^2 &= 3(1 + 14\eta^2 + \eta^4) \pm \\ &\pm \sqrt{3}(1 - 5\eta^2) \sqrt{(3 + \eta^2)(1 - 5\eta^2)} \end{aligned} \quad (17)$$

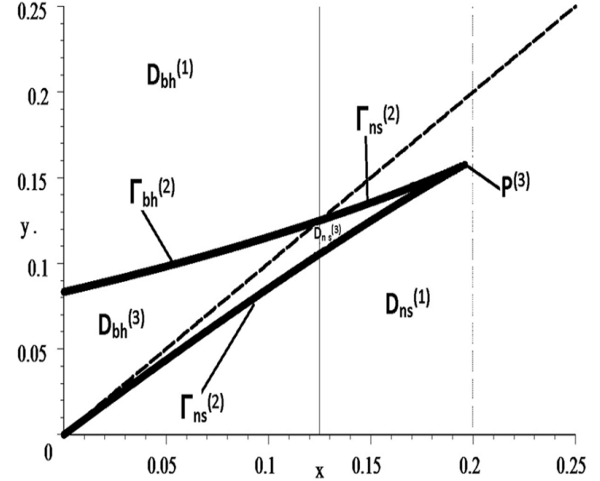


Figure 1: The curve $D = 0$ in the plane of parameters ($x = \eta^2, y = \mu^2$) and the different regions of the roots.

In the (μ, η) plane the equality $D = 0$ is the boundary of the curvilinear angle $\Gamma^{(2)} = \Gamma_{bh}^{(2)} \cup \Sigma_{ns}^{(2)}$, which is depicted in Fig.1 by a heavy line and corresponds to the case of multiple roots ($z_1 = z_2, z_3$ or $z_1, z_2 = z_3$). The point $p^{(3)} \in \Gamma^{(2)}$, is associated with the triple root ($z_1 = z_2 = z_3$). The region $D^{(3)} = D_{bh}^{(3)} \cup D_{ns}^{(3)}$ that lies inside the angle $\Gamma^{(2)}$ refers to the case of $D < 0$, i.e., to three different real roots z_1, z_2, z_3 . For points that lie outside the angle $\Gamma^{(2)}$, in the region $D^{(1)} = D_{bh}^{(1)} \cup D_{ns}^{(1)}$, we have $D > 0$. Here one root is real z_3 (a circular orbit) whereas two others are complex $z_1 = m_1 + im_2, z_2 = m_1 - im_2$.

Note that the dotted line $\eta^2 = \mu^2$ corresponds to the extreme BH. The regions above and below the line $\eta^2 = \mu^2$ relate to BH ($\eta^2 > \mu^2$) and NS ($\eta^2 < \mu^2$) respectively.

4. Parameterization in terms of circular orbits radii and classification of effective potentials

The roots of equation (13) and its coefficients (14) are interrelated as follows

$$\begin{aligned} z_1 + z_2 + z_3 &= (1 + \eta^2)/\mu, \quad z_1 z_2 z_3 = 2\eta^2/\mu, \\ z_1 z_2 + z_1 z_3 + z_2 z_3 &= 3. \end{aligned} \quad (18)$$

Taking into account these formulae, we obtain the parametrization for the effective potential (9) in terms of the roots of equation (13), i.e. in terms of the circular orbits radii,

$$W_\epsilon^2 = 1 - \frac{\mu}{z} \left(2 - \frac{z_1 + z_2 + z_3}{z} + \frac{2}{z^2} - \frac{z_1 z_2 z_3}{2z^3} \right), \quad (19)$$

$$\mu = (z_3 + z_2 + z_1 - z_1 z_2 z_3 / 2)^{-1}, \quad \eta^2 = \mu z_1 z_2 z_3 / 2. \quad (20)$$

This representation permits us to reduce the problem of classifying the trajectories to the task of identifying the type of the potential.

In the case of multiple roots, when $z_2 = z_3$, we get

$$W_\epsilon^2 = 1 - \frac{\mu}{z} \left(2 - \frac{z_1 + 2z_2}{z} + \frac{2}{z^2} - \frac{z_1 z_2^2}{2z^3} \right). \quad (21)$$

while $\mu = 2(2z_1 + 4z_2 - z_1 z_2^2)^{-1}$, $(2z_1 + z_2) z_2 = 3$. At the point $z = z_1$ the potential has an inflection. In the case of the triple root $z_1 = z_2 = z_3$ we have

$$W_\epsilon^2 = 1 - 0.4z^{-1}(2 - 3z^{-1} + 2z^{-2} - 0.5z^{-3}), \quad (22)$$

and $\mu = 0.4$, $\eta = 1/\sqrt{5}$, $z_1 = 1$.

In Fig. 1 the regions of parameters $\{\mu, \eta\}$ for the different types of the potential are shown. Choosing an arbitrary point inside each of these regions and calculating the roots of equation (13), we compose the potential according to (19). Some plots of $W(z)$ are given in Figs. 2 and 3. Here the allowed regions for particles with given energy ϵ are the horizontal line segments $W_\epsilon^2 = \epsilon^2 = const$ bounded by the intersection points with the curve $W^2 = W^2(z)$ (turning points).

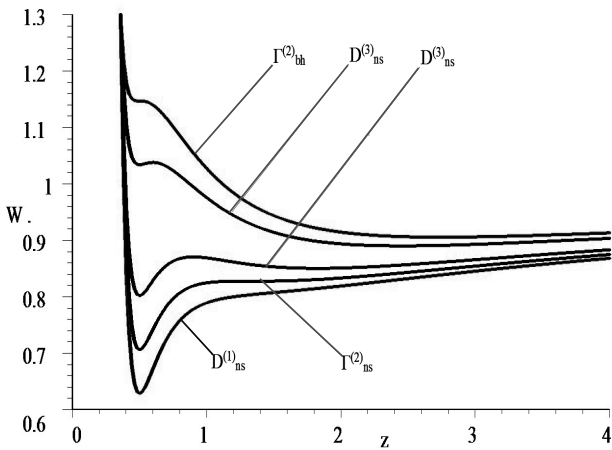


Figure 2: Effective potential versus radius z for different regions in the plane of parameters (η^2, μ^2) .

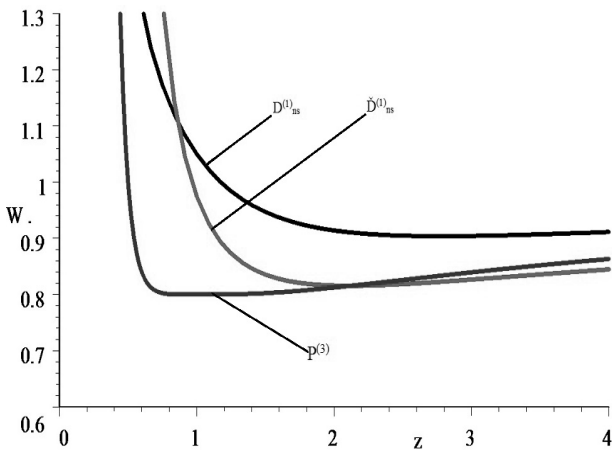


Figure 3: The same as Fig. 2 for other regions.

In Tables 1-3 we list the values of circular orbit radii z and particle energies ϵ calculated for parameters (η^2, μ^2) selected from the regions that correspond to different signs of D , assuming the super-extremely charged object ($\eta^2 > \mu^2$).

Table 1: Circular orbit radii and energies of particles for selected values of parameters, $D > 0$.

	$D_{ns}^{(3)}$			$D_{ns}^{(3)}$		
μ	0.314			0.356		
η	0.334			0.382		
z	0.5	0.6	2.455	0.5	0.9	1.821
ϵ	1.017	1.019	0.944	0.896	0.933	0.538

Table 2: The same as Table 1, $D = 0$.

	$\Gamma_{ns}^{(2)}$		$\Gamma_{bh}^{(2)}$	$P^{(3)}$	
μ	0.373		0.294	0.40	
η	0.398		0.318	0.447	
z	$z_1 = 0.5$	$z_{2,3} = 1.3$	$z_{1,2} = 0.5$	$z_3 = 2.75$	$z_{1,2,3} = 1$
ϵ	0.84	0.91	1.071	0.954	0.894

Table 3: The same as Table 1, $D < 0$.

	$D_{ns}^{(1)}$	$D_{ns}^{(1)}$	$D_{ns}^{(1)}$
μ	0.447	0.387	0.3
η	0.632	0.410	0.354
z	2.111	0.5	2.778
ϵ	0.903	0.793	0.951

A more detailed analysis of all the types of particles motion will be presented elsewhere.

5. Conclusion

Thus we have derived the characteristics of neutral particles motion in the field of the super-extremely charged object. The main peculiarity of this motion is that there may exist bound states with energy greater than the rest value ($\epsilon > 1$). For example, this occurs for the effective potential from $D_{ns}^{(3)}$ (see Fig. 2) where the finite motions for the object with $\mu = 0.314, \eta = 0.334$ are allowed, so that the particles with energy $\epsilon = 1.017$ move along the circular orbit with radius $z = 0.5$. As seen from Fig. 2, the curve $\Gamma_{bh}^{(2)}$ for the object with $\mu = 0.294, \eta = 0.318$ has an inflection point at the radius $z = 0.5$ that corresponds to the last stable circular object with energy $\epsilon = 1.071$.

References

Chandrasekhar S. The mathematical theory of black holes. Oxford, 1983.
 Dymnikova I.G.: 1986, *Uspekhi Fiz. Nauk*, **148**, 393.
 Gladush V., Galadgyi M.: 2011, *General Relativity and Gravitation* **43**, 1347.
 Pugliese B., Quevedo H., Ruffini R.: 2011, *Phys. Rev. D* **83**, 024021.
 Pyragas A.K., Akeksandrov A.N., et al. Qualitative and analytic methods in relativistic dynamics. Minsk, 1995.

QUANTUM SPECTRUM ON THE NAKED REISSNER-NORDSTRÖM BACKGROUND

V.D. Gladush¹, D.A. Kulikov²

Theoretical Physics Department, Dniepropetrovsk National University
72 Gagarin av., Dniepropetrovsk 49010, Ukraine,
¹vgladush@gmail.com, ²kulikov_d_a@yahoo.com,

ABSTRACT. The eigen frequencies of a massless scalar field in the space-time of the Reissner-Nordström singularity are studied by using the WKB approximation and by numerical integration of the wave equation. Both these approaches indicate the existence of long living states for the singularity charge-to-mass ratios being close enough to the extremal value $Q/M = 1$.

Key words: naked singularity, scalar field, bound state, Reissner-Nordström metric.

1. Introduction

The Reissner-Nordström (RN) solution describes electrovacuum in general relativity. If the electric charge exceeds the central mass, $Q > M$, this solution corresponds to a naked singularity. Quantum excitations on the naked RN geometry have recently attracted considerable attention; in particular, quasinormal modes (QNMs) of the massless scalar field were calculated [Chirenti]. On the other hand, it was shown [Gladush] that metastable bound states (MBSs) with the longer live-times may also exist in the same case.

The purpose of this work is to compare the frequencies (energies) of the different scalar field excitations that emerge on the naked RN background among themselves and with the frequency extracted from numerical evaluation of probe signal propagation.

2. Wave equation and effective potential

Consider the massless Klein-Gordon equation $\square\psi = 0$ in the external RN geometry

$$ds^2 = F dt^2 - F^{-1} dr^2 - r^2 d\sigma^2, \\ F = 1 - \frac{2M}{r} + \frac{Q^2}{r^2}, \quad d\sigma^2 = d\theta^2 + \sin^2\theta d\varphi^2. \quad (1)$$

Introducing the tortoise coordinate x by $dx = F^{-1}dr$ and seeking for the solution with angular variables separated, $\psi = \exp(-i\omega t)Y_{lm}(\theta, \varphi)\phi(x)/r$, one obtains

$$\frac{d^2\phi}{dx^2} + [\omega^2 - \mathcal{V}(r(x))]\phi = 0, \\ \mathcal{V}(r(x)) = \left[\frac{l(l+1)}{r^2(x)} + \frac{2M}{r^3(x)} - \frac{2Q^2}{r^4(x)} \right] \cdot F(r(x)). \quad (2)$$

To establish possible types of the solutions, one inspects the shape of the effective potential $\mathcal{V}(r)$. It is shown [Chirenti] that there are essentially two different cases: (i) for $Q/M < (Q/M)_{cr}$, $\mathcal{V}(r)$ has one maximum, (ii) for $Q/M > (Q/M)_{cr}$, $\mathcal{V}(r)$ has 3 extrema, one smaller "outer" maximum, one "inner" maximum and minimum in the potential valley between them. Here the critical value $(Q/M)_{cr} = 1.048, 1.056, 1.059, \dots$ for $l=0,1,2,\dots$. It tends to $(Q/M)_{cr} = \sqrt{9/8} \approx 1.061$ when $l \rightarrow \infty$ [Chirenti]. In Fig. 1 $\mathcal{V}(r)$ is plotted to illustrate those two cases. Since the dependence $r(x)$ is monotonous the plot of \mathcal{V} versus x has similar shape.

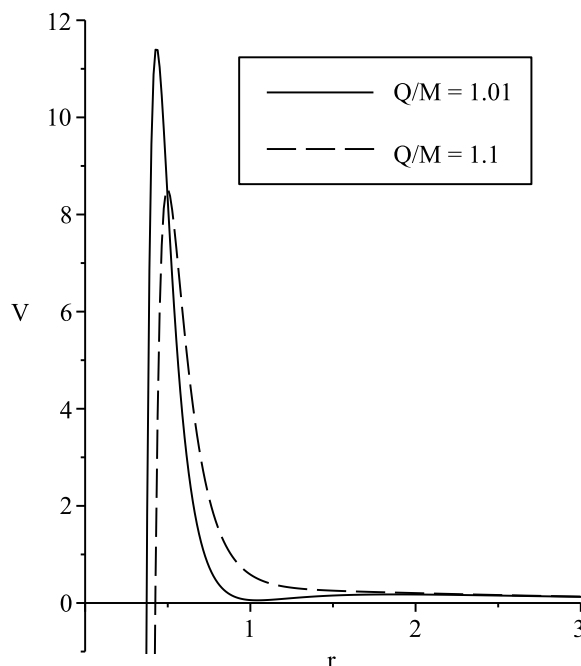


Figure 1: Effective potential $\mathcal{V}(r)$ for $l = 1$ and $M = 1$, $Q = 1.01$ (solid line) and $M = 1$, $Q = 1.1$ (dashed line).

3. Spectrum via WKB approximation

The above suggests that apart from the scattering states there may be two different types of the quasis-

tationary states, namely, QNMs near the top of one of the effective potential peaks and MBSs in the potential valley between peaks.

The QNM spectrum of the problem in the WKB approximation reads as [Chirenti]

$$\omega = \sqrt{\mathcal{V}(r_{max})} - i(n+1/2)F(r_{max})\sqrt{-\frac{\mathcal{V}''(r_{max})}{2\mathcal{V}(r_{max})}} \quad (3)$$

with r_{max} being the position of the "outer" maximum, n being the excitation number and the prime denoting the derivative with respect to r .

The WKB approximation for the eigen frequencies of the MBSs has been developed in [Gladush] by applying the conventional approach [Landau] to the wave equation rewritten in terms of the areal coordinate r

$$y'' + \frac{1}{F^2}(\omega^2 - V(r))y = 0 \quad (4)$$

where $y = \sqrt{F}\phi(r)$ and $V(r) = \mathcal{V}(r) - (2M/r^3 - 2Q^2/r^4)F + (Q^2 - M^2)/r^4$. The new effective potential $V(r)$ goes very closely to $\mathcal{V}(r)$ except for a small region near the origin. Also $V(r)$ has a potential valley behind a low peak provided that $1 < Q/M < \sqrt{(8 + 9l(l+1))/(8 + 8l(l+1))}$.

Defining quasiclassical momenta $k(r)$ and $\kappa(r)$ for the classically allowed and forbidden regions respectively by

$$k(r) = \frac{1}{F}\sqrt{\omega^2 - V(r)}, \quad \kappa(r) = \frac{1}{F}\sqrt{V(r) - \omega^2}, \quad (5)$$

one can write down the Bohr-Sommerfeld formula

$$\int_{r_1}^{r_2} \frac{1}{F}\sqrt{\omega_R^2 - \mathcal{V}(r)}dr = \pi(n + 1/2) \quad (6)$$

that determines the real part ω_R of the frequency ω of the MBS. Here $r_{1,2}$ are the turning points at the ends of the $V(r)$ potential valley.

For the imaginary part of ω , the Gamow-type formula has been derived [Gladush]

$$\omega_I = \left[4\omega_R \int_{r_1}^{r_2} \frac{dr}{F^2 k(r)} \right]^{-1} e^{-2 \int_{r_2}^{r_3} \kappa(r) dx}, \quad (7)$$

which is valid if the forbidden region (r_2, r_3) (potential barrier represented by the peak of $V(r)$) is nearly impenetrable. It means that the calculated value of ω_I has to obey the condition $|\omega_I| \ll \omega_R$.

For the sake of comparison, another approximation can be made. Since the main contribution to ω_R comes from the region in vicinity of the minimum r_{min} of the potential, one can expand $\mathcal{V}(r)$ in powers of $(r - r_{min})$. On substituting this into wave equation (2) and retaining only the quadratic term, the problem reduces to the harmonic oscillator one with the spectrum

$$\omega_R^2 = \mathcal{V}(r_{min}) + (n + 1/2)F(r_{min})\sqrt{2\mathcal{V}''(r_{min})}. \quad (8)$$

The exponentially small decay width ω_I vanishes in this approximation.

Equation (8) is to be compared with the QNM spectrum (3). One makes sure that the MBS frequencies are indeed concentrated near the bottom of the potential valley whereas the QNMs frequencies near the potential peak.

4. Probe signal propagation

Since the spectrum of the system contains the states of different types and with different frequencies, it is tempting to explore what is the frequency that dominates in the propagation of an "arbitrary" probe signal.

To this end, the numerical method [Gundlach] will be employed that is based on treating the Klein-Gordon equation in terms of the light-cone coordinates $u = t - x$ and $v = t + x$. For the field $\psi = Y_{lm}(\theta, \varphi)\Phi(u, v)/r$, one gets

$$\left(4\frac{\partial^2}{\partial u \partial v} + \mathcal{V}(u, v) \right) \Phi(u, v) = 0. \quad (9)$$

This is simply discretized on a (u, v) grid as

$$\begin{aligned} \Phi(N) &= \Phi(W) + \Phi(E) - \Phi(S) - \\ &- \frac{h^2}{8}\mathcal{V}(S)(\Phi(W) + \Phi(E)) + \mathcal{O}(h^4) \end{aligned} \quad (10)$$

where the points N, S, E and W form a rectangle with relative positions indicated by the points of the compass (see Fig. 2), and h is the integration step, so that

$$\Delta u = u_N - u_E = h, \quad \Delta v = v_N - v_W = h. \quad (11)$$

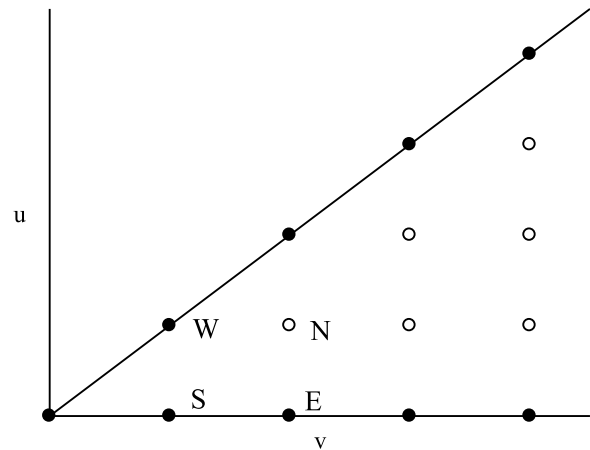


Figure 2: Numerical grid used for integration.

The boundary conditions are chosen as follows

$$\begin{aligned} \Phi(r = 0, t) &= \Phi(u, v = u + 2x(r = 0)) = 0, \\ \Phi(u = 0, v) &= e^{-\frac{(v-v_c)^2}{2\sigma^2}}. \end{aligned} \quad (12)$$

This amounts to the Dirichlet condition in the origin and the data on the $u = 0$ line modelling an "arbitrary" initial signal to be propagated.

Starting from these null data depicted by filled circles in Fig. 2, integration proceeds to the "north" and the field in the points depicted by empty circles is calculated according to algorithm (10).

5. Numerical results

Calculations were made for the case of $Q/M < (Q/M)_{cr}$ because for $Q/M > (Q/M)_{cr}$ it is argued [Chirenti] that there are no low-damped QNMs at least in the $l \gg 1$ limit and the MBSs are absent too [Gladush].

The QNM spectrum was computed according to formula (3) whereas the MBS spectrum was evaluated by means of formulae (6) and (7). It should be noticed that since the depth and the width of the potential valley are finite, the number of the MBSs is limited.

In Table 2 the first QNM frequencies calculated using the values $Q = 1.01$, $M = 1$ are presented.

Table 1: QNM frequencies on the naked RN background with $Q = 1.01$, $M = 1$.

$l = 0$	
$n = 0$	$0.224344 - i0.092955$
$l = 1$	
$n = 0$	$0.420128 - i0.088186$
$l = 2$	
$n = 0$	$0.656772 - i0.087090$

For comparison, the frequencies of all the existing MBSs with $l = 1, 2$ (there are no $l = 0$ states) calculated with the same parameters are listed in Table 2.

Table 2: Frequencies of the MBSs on the naked RN background with $Q = 1.01$, $M = 1$.

$l = 1$	
$n = 0$	$0.294636 - i0.263 \times 10^{-3}$
$l = 2$	
$n = 0$	$0.423194 - i0.164 \times 10^{-5}$
$n = 1$	$0.537046 - i0.227 \times 10^{-3}$

The striking difference between Tables 1 and 2 is that the MBSs have much smaller decay widths and thus are much more long living than the QNMs. This is because the MBSs are concentrated near the bottom of the potential valley and have to penetrate the potential barrier in order to decay.

Using the same parameters, the propagation of the probe signal (12) with $v_c = 1$ and $\sigma = 1$ was computed via scheme (10). In Figs. 3 and 4 the time evolution of the field $\Phi_{l=0}(x, t)$ and $\Phi_{l=1}(x, t)$ at given $x = 10$ is shown. The plotted data were further approximated by the least-squares method to the single mode $\Phi_{app}(t) = Ae^{-\alpha t} \sin(\Omega t + \beta)$ in order to extract the dominant frequency. The results are $\Omega - i\alpha = 0.2015 - i0.552 \times 10^{-2}$

for $l = 0$ and $\Omega - i\alpha = 0.3013 - i0.223 \times 10^{-3}$ for $l = 1$. The last value is remarkably close to the MBS frequency with $l = 1$ and $n = 0$ in Table 2.

Thus the results of both the numerical integration and the WKB approximation indicate that the scalar field on the naked RN background possesses long living excitations. These are associated with the states lying near the bottom of the effective potential valley.

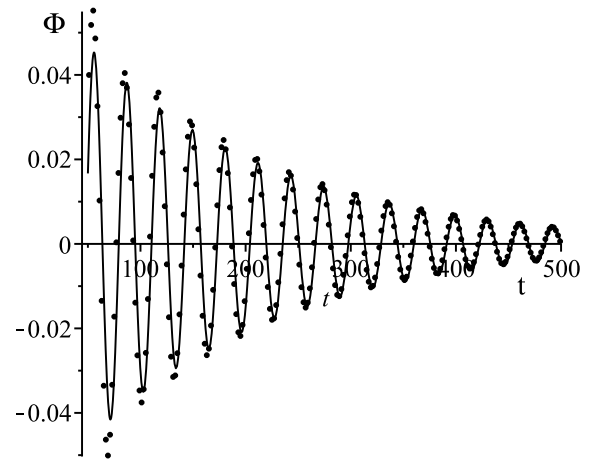


Figure 3: $\Phi(x = 10, t)$ vs. t for $Q = 1.01$, $M = 1$ and $l = 0$. The circles depict the result of integration, the curve is the least-squares single-mode approximation.

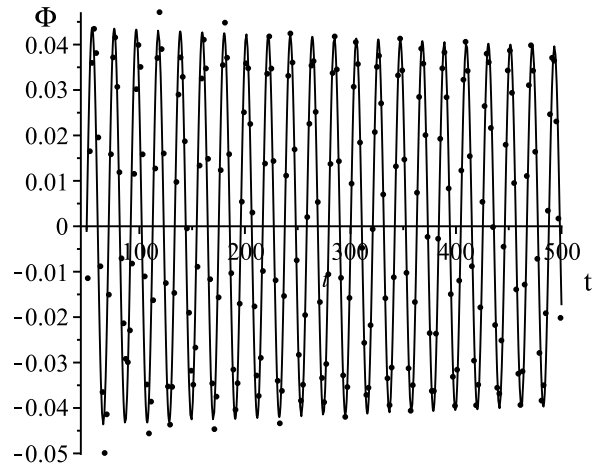


Figure 4: The same as Fig. 3 for $l = 1$.

References

- Chirenti C., Saa A., Skákala J.: 2012, *Phys. Rev. D* **86**, 124008.
 Gladush V.D., Kulikov D.A.: 2013, *Int. J. Mod. Phys. D* **22**, 1350033.
 Landau L.D., Lifshitz E.M. *Quantum Mechanics: Non-relativistic Theory*. Oxford, 1965.
 Gundlach C., Price R.H., Pullin J.: 1994, *Phys. Rev. D* **49**, 883.

DYNAMICAL FRICTION IN THE LOCAL GROUP

A.V. Kudinova

Odessa National I.I.Mechnikov University, Department of Theoretical Physics
Odessa, Ukraine, *aleksandra.kudinova@gmail.com*

ABSTRACT. In this paper we consider dynamical behavior of the astrophysical objects in the Local Group. The motion of Andromed and The Milky Way is studied. We distinguish two different models: for the first one we do not take into account the influence of the Intra-Group Matter (IGrM), for the second one we take into account the dynamical friction due to the IGrM. We obtained some characteristic IGrM parametres such as particle masses for principle cases of the collision between the giant galaxies and the situation when the merger becomes problematic. We also define the region in the vicinity of our Local Group where the formation of the Hubble Flows starts.

Key words: Local group; Hubble flows; Galaxies: Milky Way, Andromeda.

1. Introduction

Modern observational cosmology provides enough data to confirm that there is no clear evidence of spatial homogeneity up to sizes ~ 150 Mpc [1]. Deep inside of such scales Universe now consists of a set of discrete inhomogeneities (galaxies, groups and clusters of galaxies), which disturb the background Friedmann Universe. Hence, classical mechanics of discrete objects provides more adequate approach than hydrodynamics with its continuous flows. In [2] this approach has been elaborated for an arbitrary number of randomly distributed inhomogeneities on the cosmological background.

In this paper we continue this investigation. First we consider the Andromeda and the Milky Way relative motion in the free-fall approximation and reveal the conditions for the possible collision and recession. We show that in the absence of IGrM for the currently known parameters of this system the collision is hardly plausible in future because of the angular momentum. For the second model we take into account the dynamical friction due to the IGrM. Here, we find a characteristic value of the IGrM particle velocity dispersion. For the values less than the characteristic one the merger will take place but for bigger values the merger can be problematic.

Then we define a region where the formation of the Hubble flows starts. There is no zero-acceleration surface in the vicinity of the Local Group, but there is a nearly closed area around the MW and M31 where the absolute value of the acceleration is approximately equal to zero. The Hubble flows are formed outside of this area.

2. Free-fall approximation

We consider our Local Group of galaxies which consists of two giant galaxies (our Milky Way and Andromeda) and approximately 40 dwarf galaxies. At the present time the giant galaxies are located at the distance 0.78 Mpc and move towards each other with the speed 120 km/sec. For these two galaxies we can apply our method up to the separation distance of the order of 100 Kpc, where the process of the merger starts.

In the centre of mass system the Lagrange function is

$$\tilde{\mathcal{L}}_{AB} = G_N \frac{m_A m_B}{L} + \frac{1}{2} \frac{m_A m_B}{m_A + m_B} \left(\frac{\dot{a}^2}{a^2} L^2 - 2 \frac{\dot{a}}{a} \dot{L} L + \dot{L}^2 + L^2 \dot{\psi}^2 \right), \quad (1)$$

where without loss of generality we put $\theta = \pi/2$. Therefore, the Lagrange equation for the separation distance is

$$\ddot{L} = -G_N \frac{2\bar{m}}{L^2} + \frac{M^2}{\mu^2 L^3} + \frac{\ddot{a}}{a} L, \quad (2)$$

where we introduced the reduced mass, the average mass and the angular momentum:

$$\frac{m_A m_B}{m_A + m_B} \equiv \mu, \quad \bar{m} = \frac{m_A + m_B}{2}, \quad \mu L^2 \dot{\psi} \equiv M = \text{const}. \quad (3)$$

The first term in the right hand side of (2) is due to the gravitational attraction, the second term is the centrifugal force and the third term originates from the cosmological expansion of the Universe.

The observations indicate the proper motion of Andromeda perpendicular to our line of sight. This transverse velocity $V_{\perp 0} \sim 100$ km/sec [3]. The collision of

the galaxies is possible if the smallest separation distance between them (which corresponds to the turning point) is less than the merger distance 100 – 150 Kpc. For the given transverse velocity the smallest separation distance is $L \approx 290$ Kpc at time $t \approx 4.44$ Gyr from present. This distance is much bigger than the merger distance. Therefore, for the chosen initial conditions, the collision between the Milky Way and Andromeda is absent. The collision may take place for a smaller transverse velocity.

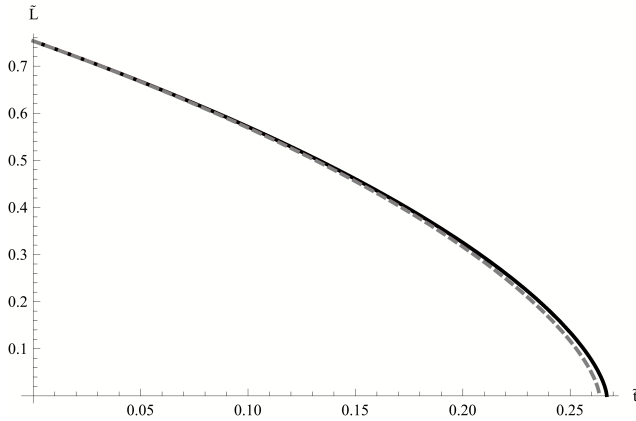


Figure 1: Evolution of the separation distance between the MW and M31 in the case of the zero angular momentum.

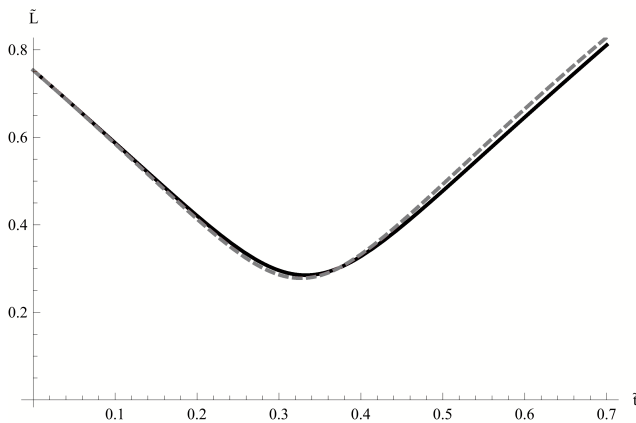


Figure 2: Evolution of the separation distance between the MW and M31 in the case of the non-zero angular momentum.

Figures 1, 2 show the change with time of the separation distance between the Milky Way and Andromeda starting from the present ($\tilde{t} = 0$) in the case of the absence of the dynamical friction. The solid black lines take into account both gravitational attraction and cosmological expansion, while the grey dashed lines disregard the cosmological expansion. The transverse velocity is absent on the Fig. 1. On the Fig. 2, the transverse velocity is equal to 100 km/sec.

3. Dynamical Friction

It is well known that a massive body with a mass M moving through surrounding matter, which consists of discrete particles of the mass m , will lose its momentum and kinetic energy due to the gravitational interaction with these particles. Such effect is called dynamical friction. The force of the dynamical friction is given by the Chandrasekhar formula [4]:

$$\frac{d\mathbf{V}_M}{dt} = -\frac{4\pi Q G_N^2 M \rho_{ph,m}}{V_M^3} \times \left[\text{erf}(\chi) - \frac{2\chi}{\sqrt{\pi}} \exp(-\chi^2) \right] \mathbf{V}_M, \quad (4)$$

where \mathbf{V}_M is the physical velocity of the mass M , $\rho_{ph,m}$ is the physical rest mass density of IGrM, $\chi \equiv V_M/(\sqrt{2}\sigma)$ and erf is the error function. Here, $Q \equiv (1/2) \ln(1 + \lambda^2)$ is the so called Coulomb logarithm defined by the largest impact parameter b_{max} , the initial relative velocity V_0 and the masses M and m : $\lambda = b_{max} V_0^2 / [G_N(M + m)] \approx b_{max} V_0^2 / (G_N M)$. The formula (4) is defined with respect to a frame where the IGrM particles have the Maxwell's speed distribution with the dispersion $\sigma = \sqrt{kT/m}$. The typical value of the IGrM temperature in the Local Group is $T \sim 10^5 \text{K} \rightarrow kT \sim 8.6 \text{ eV}$ [3].

Therefore, the Milky Way and Andromeda should slow down moving through the IGrM because of the dynamical friction (4).

Comparatively little is known about truly intergalactic medium. Most probably this is a mixture of the baryonic matter (mainly in the form of ionized hydrogen) and dark matter. There is a great variety of candidates for dark matter with masses ranging from $\mu\text{eV} \div \text{eV}$ (e.g., axions) to TeV (e.g., WIMPs). Therefore, in the formula for the dispersion σ , the parameters T and m are some effective values. It makes sense not to specify them separately, but to consider their ratio, i.e. σ^2 . As we mentioned above, our approach works up to the first touch of the galaxies which occurs approximately at the separation distance 100 Kpc between their centers. On the figures 3, 5, this event is marked by the grey points on the bottom black solid lines. In this case, the merger of the galaxies will take place. Our approach does not describe this process. The continuations of the lines (the separation distance) after the first touch is very schematic. On the figures 4, 6, this event corresponds to the touch of two thin grey circles. The distance between their centers is equal to 100 Kpc. We do not continue the trajectories after this first touch.

We found two characteristic values for the dimensionless parameter $\tilde{\sigma}$. The first one is $\tilde{\sigma}_1 = 1.17$ and

corresponds to the situation when the first close passage occurs at the separation distance $L = 100$ Kpc (see the grey point on the Fig. 3 and two grey touched circles on the Fig. 4) which corresponds to the touch of the galaxies. Obviously, for all $\tilde{\sigma} < \tilde{\sigma}_1$, this distance will be less than 100 Kpc and the first touch of the galaxies will take place during the first passage. For the bigger values of $\tilde{\sigma}$, the first passage occurs at the separation distance larger than 100 Kpc. The second characteristic value is $\tilde{\sigma}_2 = 2.306$ and describes the situation when the galaxies, after the first close passage, grow apart to the turning point at the separation distance 1 Mpc from each other (see the black point on the upper black line on the Fig. 5). At these and greater distances, the rest mass density of IGrM decreases and the dragging effect of the dynamical friction can be too small to force the galaxies to converge again. Therefore, for $\tilde{\sigma} > \tilde{\sigma}_2$, the merger of the galaxies becomes problematic. For $\tilde{\sigma}_1 < \tilde{\sigma} < \tilde{\sigma}_2$, the touch will take place during the second passage. It is of interest to estimate masses of the IGrM particles which correspond to these characteristic values of $\tilde{\sigma}$. The masses m can be expressed via the temperature T and dimensionless dispersion $\tilde{\sigma}$ as follows: $m(\text{MeV}) \approx \{ [kT(\text{erg})/8.464 \times 10^{13}(\text{cm}^2/\text{sec}^2)] \times 0.5604 \times 10^{27}(\text{MeV/g}) \} / \tilde{\sigma}^2$. The temperature of IGrM in the Local Group is usually estimated as $T \sim 10^5$ K [3]. Then, for this value of T , we get $m_1 \sim 67$ MeV and $m_2 \sim 17$ MeV for $\tilde{\sigma}_1$ and $\tilde{\sigma}_2$, respectively. Therefore, for the chosen initial conditions and the value of T , the touch of the galaxies will take place during the first passage for the IGrM particle masses $m \geq 67$ MeV and the merger can be problematic for masses lighter than 17 MeV.

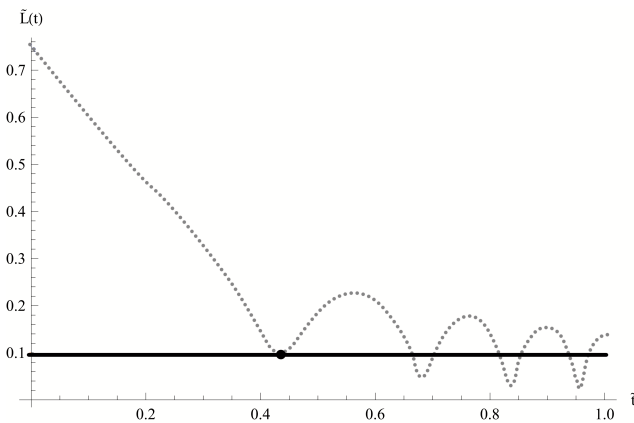


Figure 3: Evolution of the distance between the MW and M31 in the case of the dynamical friction. $\tilde{\sigma} = \tilde{\sigma}_1 = 1.17$.

These figures show the change with time of the separation distance between the Milky Way and Andromeda (Fig. 3) and the corresponding trajectories for the MW (the solid line) and M31 (the dashed line)

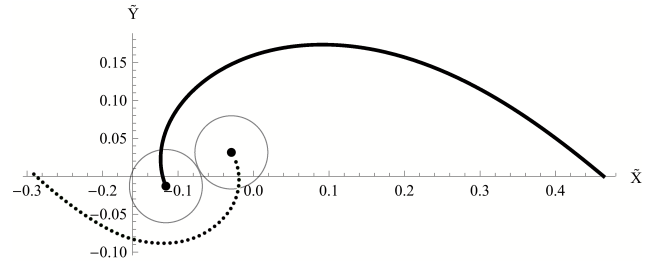


Figure 4: Trajectories of the MW and M31 in the case of the dynamical friction. $\tilde{\sigma} = \tilde{\sigma}_1 = 1.17$.

on the Fig. 4 in the case of dynamical friction. The initial conditions are chosen as on the Fig. 2. The dynamical friction is calculated for the dispersion parameter $\tilde{\sigma} = \tilde{\sigma}_1 = 1.17$.

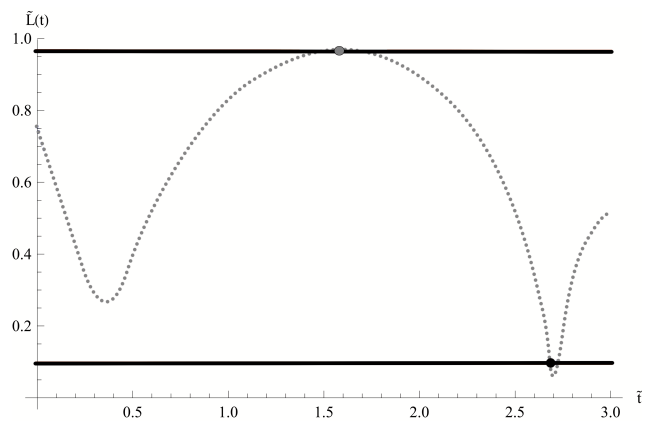


Figure 5: Evolution of the distance between the MW and M31 in the case of the dynamical friction. $\tilde{\sigma} = \tilde{\sigma}_2 = 2.306$.

These figures are drawn in the case of the dynamical friction with the dispersion parameter $\tilde{\sigma} = \tilde{\sigma}_2 = 2.306$. For this value of $\tilde{\sigma}$, there is no touch of the galaxies during the first passage because the closest separation distance here is larger than 100 Kpc (the bottom black line on the Fig. 5). After that, the galaxies grow apart to the turning point at the separation distance 1 Mpc from each other (see the black point on the upper black line in the left panel). At these and greater distances, the rest mass density of IGrM decreases and the dragging effect of the dynamical friction can be too small to force the galaxies to converge again. Therefore, for $\tilde{\sigma} > \tilde{\sigma}_2$, the merger of the galaxies becomes problematic.

4. Formation of Hubble flows in the vicinity of the Local Group

To study the formation of the Hubble flows in the vicinity of our group of galaxies, we need to determine the spatial distribution of vectors of acceleration of as-

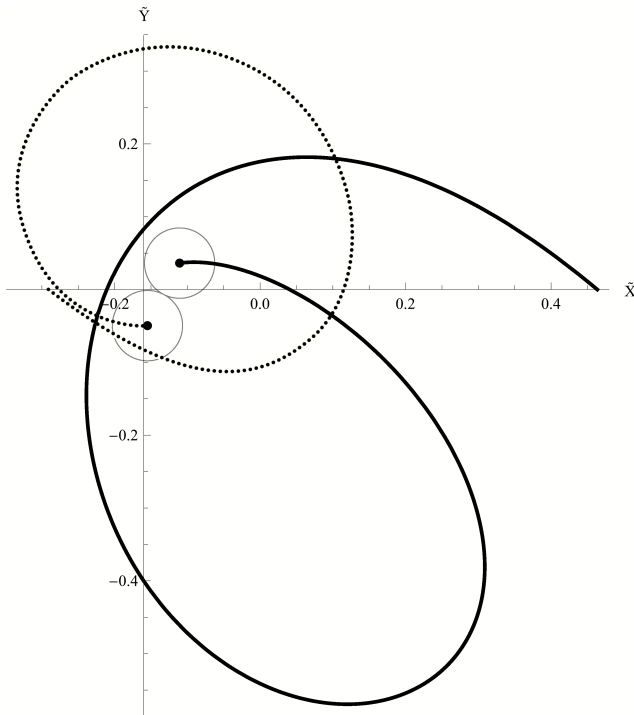


Figure 6: Trajectories of the MW and M31 in the case of the dynamical friction. $\tilde{\sigma} = \tilde{\sigma}_2 = 2.306$.

trophysical objects (e.g. dwarf galaxies) in the gravitational field of two giant galaxies taking into account the cosmological expansion of the Universe. Obviously, near the galaxies, the vector must be oriented in the direction of galaxies due to the gravitational attraction, and with the distance from galaxies he has to turn in the opposite direction due to the cosmological accelerated recession.

On the Fig. 8 vectors are directed towards the MW and M31 (the black points) in the vicinity of the galaxies and turn out with the distance from the galaxies. The solid and dashed lines correspond to the conditions $\tilde{W}_x = 0$ and $\tilde{W}_y = 0$, respectively.

References

- Labini F.S.: 2011, *Class. Quant. Grav.*, **28**, 164003. [arXiv:1103.5974]
 Eingorn M., Zhuk A.: 2012, *JCAP*, **09**, 26. [arXiv:1205.2384]
 Cox T, Loeb A.: 2008, *Mon. Not. Roy. Astron. Soc.*, **386**, 461. [arXiv: 0705.1170]
 Binney J., Tremaine S.: 1987, *Princeton University Press*, 741.

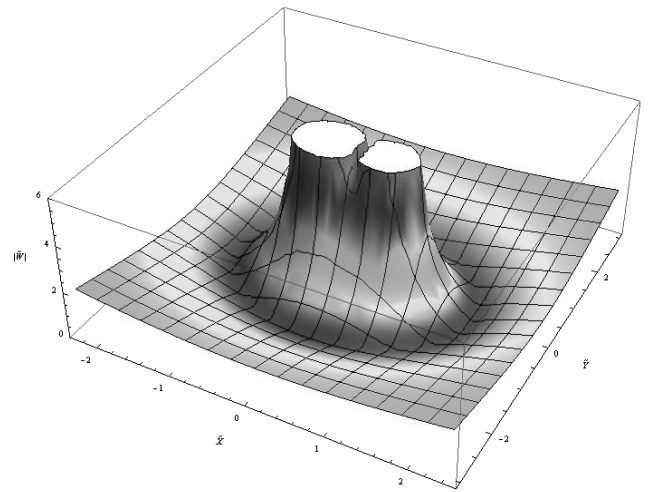


Figure 7: This plot shows the absolute value of the acceleration of dwarf galaxies in the Local Group. The dark area around the peaks corresponds approximately to the zero acceleration region.

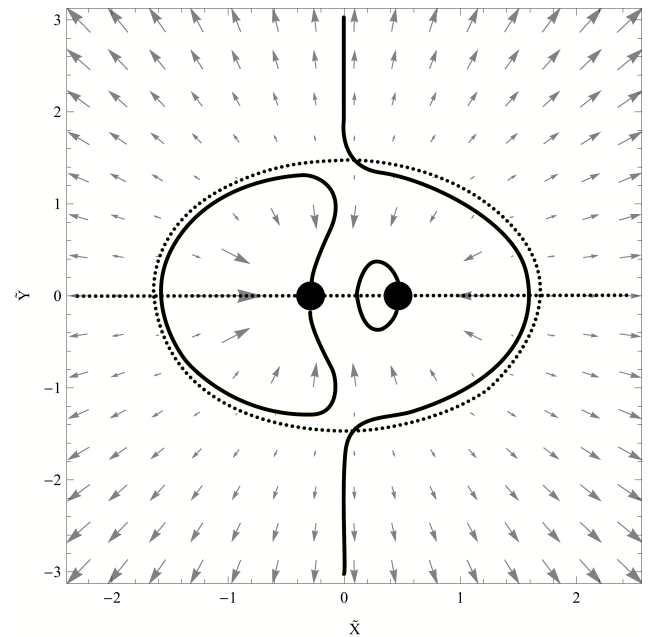


Figure 8: This figure shows the vector field of the dwarf galaxy acceleration.

ONE-DIMENSIONAL SIMULATIONS OF INHOMOGENEITY GROWTH IN PRESSURELESS GRAVITATING MATTER

V.I. Zhdanov¹, V.M. Sliusar²

^{1,2} Taras Shevchenko National University of Kyiv, Kiev, Ukraine

¹ *ValeryZhdanov@gmail.com*, ² *vitaliy.slyusar@gmail.com*

ABSTRACT. We study a model of the inhomogeneity growth in the Universe filled with a pressureless matter. The standard hydrodynamical equations for the cosmological perturbations in the comoving frame are treated taking into account all nonlinear terms. We consider perturbations of the uniform isotropic cosmological background but with plane periodic initial conditions for the perturbations. The problem is reduced to ordinary differential equations for an infinite chain of Fourier coefficients for hydrodynamical variables. We perform a numerical integration of these equations (with proper truncation) for an ensemble of random initial conditions. The power spectrum of the density contrast is obtained by means of an averaging procedure.

Key words: large scale structure, cosmology, hydrodynamics.

1. Introduction

It is now well known that the (non-baryonic) dark matter (DM) constitutes a considerable fraction of the cosmological density. However, little is known about the DM structure. This presents the serious challenge to computational astrophysics because different DM models can manifest themselves in different scenarios of structure formation on the galactic and extragalactic level. The related problems involve numerical simulations of the galaxy formation process, working out predictions concerning the galactic environment (number of dwarf satellite galaxies) and structure of their central regions (the cusp-core problem) either with cold dark matter (DM) or within warm DM models (Navarro *et al.* 1996, Navarro *et al.* 1997, Avila *et al.* 2001, Bode *et al.* 2001, Moore *et al.* 2006, Schneider *et al.* 2012). Interesting possibility to obtain bounds on masses of DM particles stems from observations of Ly- α forest (see, e.g., Boyarsky *et al.* 2009) and references therein; comparison of theory with observations requires accurate calculations of the power spectrum of cosmological inhomogeneity on kiloparsec scales. In this field the computational methods are well

known that use the N-body simulations combined with the smoothed particle hydrodynamics (Springel 2005, Brandbyge *et al.* 2008, Schneider *et al.* 2012). However, it is important to have independent numerical schemes.

On the other hand, some analytical and semi-analytical methods to study a weak cosmological inhomogeneity were proposed (Bernard *et al.* 2002, Taruya *et al.* 2002, Wong 2008), which work with the Fourier-transformed hydrodynamical variables. These schemes either use some low order perturbative schemes or deal with the correlation functions under some additional *a priori* assumptions in order to close the infinite chain of unknown functions (Pietroni 2008, Lesgourgues *et al.* 2009). A comparison of different approaches can be found in (Carlson *et al.* 2009).

In this paper we use an alternative method with a direct integration of hydrodynamical equations in the Fourier space. The hydrodynamical variables are considered within the spatial "cell of periodicity", so we can reduce the problem to an infinite chain of interacting equations for the Fourier coefficients. Therefore, we also must use some truncation for these coefficients, which, however, can be controlled by usual numerical means. Here our aim is to demonstrate a workability of the numerical method.

In our previous work (Sliusar & Zhdanov 2012) we treated analogous fully one-dimensional problem using the same method. The problem treated in the present paper is in fact a special case of *three-dimensional* problem though with the plane initial conditions that depend upon only one spatial variable x . The main distinctive feature of this paper is due to different relations for the uniform background. In (Sliusar & Zhdanov 2012) we succeeded to find an analytical (though implicit) solution that made it possible a comparison with the numerical solution; in the present paper we do not have such a possibility.

In section 2 we write down the equations for the Fourier coefficients and present some results for the solutions with a special initial conditions in order to see how initial perturbation proliferates from low

wavenumbers to larger ones. Then we consider a set of solutions with randomly distributed initial conditions to obtain a power spectrum after a statistical averaging.

2. Numerical simulations

Further we deal with the homogenous cosmological background; R stands for the cosmological scale factor and τ is the "conformal time", x is the comoving spatial coordinate. For the epoch after the recombination one can neglect the contribution of the cosmological constant up to the redshifts $z \sim 2 \div 3$ so it is quite reasonable to assume $R \sim \tau^2$ typical for purely cold dark matter model. Hereafter $\delta(x, \tau)$ is the density contrast, $\theta(x, \tau) = \partial v / \partial x$, v is the peculiar velocity. We assume L to be a spatial periodicity scale so we can deal with the (one-dimensional) Fourier coefficients ($n = 0, \pm 1, \pm 2, \dots$)

$$\theta(x, \tau) = \sum_n a_n(\tau) \exp(ik_n x),$$

$$\delta(x, \tau) = \sum_n b_n(\tau) \exp(ik_n x),$$

where $k_n = 2\pi n/L$ and choice of L depends on a concrete problem, its scale accuracy etc. For simplicity we confine ourselves to a symmetric case: $\theta(x, \tau) = \theta(-x, \tau)$ and $\delta(x, \tau) = \delta(-x, \tau)$ are even functions yielding

$$a_n(\tau) = a_{-n}(\tau), \quad b_n(\tau) = b_{-n}(\tau). \quad (1)$$

Also, we shall exclude terms $a_0 \equiv 0$, $b_0 \equiv 0$. One can show that this assumption (as well as the previous one about symmetry) can be obtained as a consequence of appropriate initial conditions. These simplifications are not essential in principle, and in a concrete situation they can be compensated by some choice of L . Therefore, below we deal only with natural values of n .

Standard considerations (see, e.g., (Wong 2008, Pietroni 2008, Lesgourgues *et al.* 2009, Sliusar & Zhdanov 2012) of hydrodynamical equations, which also take into account Poisson equation for the gravitational potential, lead to the equations for the Fourier coefficients. We rewrite these equations taking into account symmetry relations (1):

$$\frac{da_n}{d\tau} = -\frac{2a_n}{\tau} - \frac{6b_n}{\tau^2} - n \sum_{p=1}^{\infty} \frac{a_p}{p} (a_{|n-p|} - a_{n+p}), \quad (2)$$

$$\frac{db_n}{d\tau} = -a_n - n \sum_{p=1}^{\infty} \frac{a_p}{p} (b_{|n-p|} - b_{n+p}) = 0, \quad (3)$$

$n = 1, 2, \dots$

The numerical solution of the equations (2), (3) was performed using the 4-th order Runge-Kutta method

after a truncation of the infinite chain of coefficients a_n, b_n . Calculations were carried out by the specially written GPGPU code using OpenCL SDK by AMD. The time, required to calculate a_n and b_n , in case of 256 values of n (values of wavenumbers k) is 10 seconds for single realization of initial conditions. It is important to note that it is easy to extend the corresponding algorithms to the 3-D case.

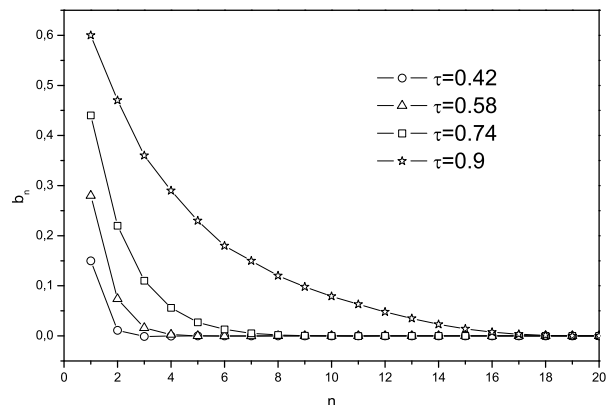


Figure 1: Symmetric problem: Fourier coefficients for the density contrast at conformal times $\tau = 0.42, 0.58, 0.74, 0.9$. Initial conditions at $\tau = 0.1$: all $a_n = 0$, $b_n = 0$ except $b_1 = 0.01$

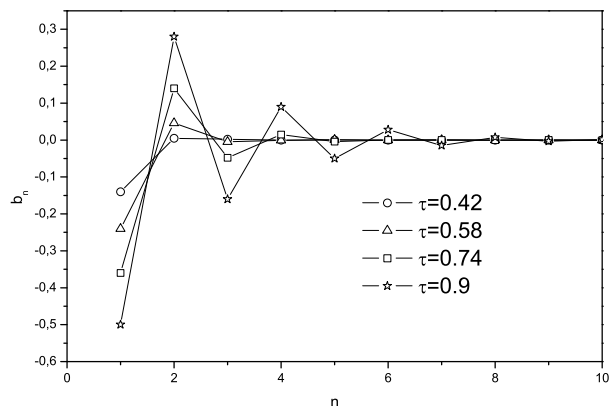


Figure 2: The same as on Fig.1 with initial conditions at $\tau = 0.1$: $b_1 = -0.01$, the other coefficients = 0

We calculated coefficients a_n, b_n for several values of τ with the same initial conditions given at $\tau = 0.1$. All coefficients a_n, b_n at $\tau = 0.1$ were assumed zero except b_1 which has been chosen in different ways (see figure captions). This means that at the initial time only a mode with the largest scale was present and the fluid

velocity is exactly that of the homogeneous expansion. On Figs.1,2 we present the coefficients b_n of the density contrast for several values of τ . We observe a successive growth of $|b_n|$. For example, on Fig. 1 we see almost monotonous growth of b_n with time which shows a proliferation of perturbation from smaller to larger values of n (in fact there is also a very small precursor wave of negative amplitude which is indistinguishable on this figure). An analogous proliferation from larger to smaller wavenumbers is well known in the hydrodynamical turbulence theory. The solution of Eqs.(2,3) cannot be extended for all τ that is typical for ordinary differential equations with a right-hand side containing a nonlinear (here quadratic) terms. In our case the solution described on Fig. 1 diverges after $\tau \sim 0.9$. This infinite growth corresponds to collapse due to the absence of peculiar velocity at the initial moment and absence of pressure that might resist the gravitational attraction.

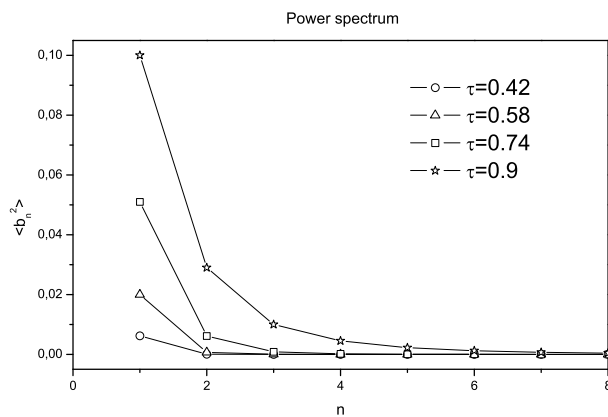


Figure 3: Averages $\langle b_n^2(\tau) \rangle$ over 100 realizations for $\tau = 0.42, 0.58, 0.74, 0.9$ with random initial data $b_1(0.1)$ that have been distributed uniformly on $[-0.01, 0.01]$

Then we calculated a set of solutions with random initial data for b_1 with subsequent averaging to obtain $\langle b_n^2(\tau) \rangle$, which is essentially a power spectrum of the inhomogeneity (here $\langle \dots \rangle$ stands for the statistical average). The result is shown on Fig. 3.

Acknowledgements. This work has been supported in part by Swiss National Science Foundation (SCOPES grant 128040) and by Cosmomicrophysics program of National Academy of Sciences of Ukraine.

References

- Navarro J.F., Frenk C.S., White S.D.M.: 1996, *ApJ*, **462**, 563.
 Navarro J.F., Frenk C.S., White S.D.M.: 1997, *ApJ*, **490**, 493.
 Avila-Reese V., Colín P., Valenzuela O., et al.: 2001, *ApJ*, **559**, **Is.2**, 516.
 Bode P., Ostriker J.P., Turok N.: 2001, *ApJ*, **556**, **Is.1**, 93.
 Goerdt T., Moore B., Read B., et al.: 2006, *MNRAS*, **368**, **Is.3**, 1073.
 Schneider A., Smith R.E., Macciò A.V., et al.: 2012, *MNRAS*, **424**, **Is.1**, 684.
 Boyarsky A., Lesgourgues J., Ruchayskiy O., et al.: 2009, *JCAP*, **05**, id. 012.
 Springel V.: 2005, *MNRAS*, **364**, 1105.
 Brandbyge J., Hannestad S., Hangbølle T., et al.: 2008, *JCAP*, **08**, id. 020.
 Brandbyge J., et al.: 2009, *JCAP*, **05**, id.002.
 Bernardeau F., Colombi S., Gaztañaga E., et al.: 2002, *Phys. Rep.* **367**, **Is.1-3**, 1.
 Taruya A., Hiramatsu T.: 2002, *Astrophys. J.*, **674**, **Issue 2**, 617.
 Wong Y.Y.Y.: 2008, *JCAP*, **10**, id. 035.
 Pietroni M.: 2008, *JCAP*, **10**, id.19.
 Lesgourgues J., Matarrese S., Pietroni M., et al.: 2009, *JCAP*, **06**, id.017.
 Carlson J., White M., Padmanabhan N.: 2009, *Phys.Rev.*, **D80**, 043531.
 Sliusar V.M., Zhdanov V.I.: 2013, In: *Proceedings of the Workshop "Astrophysical and cosmological problems of invisible mass and dark energy in the Universe". November 21-22, 2012 Institute for Nuclear Research*, 51.

ASTROPHYSICS

COMPARATIVE ANALYSIS OF NUMERICAL METHODS
OF DETERMINATION OF PARAMETERS OF BINARY STARS.
CASE OF SPHERICAL COMPONENTS

I.L.Andronov¹, M.G.Tkachenko²

Department “High and Applied Mathematics”, Odessa National Maritime University
Odessa, Ukraine

¹*il-a@mail.ru*, ²*masha.vodn@yandex.ua*

ABSTRACT. We discuss methods for modeling eclipsing binary stars. There are few realizations of the Wilson-Devinney (1971) code and its improvements, e.g. “Binary Maker”, “Phoebe”. A parameter search using the Monte-Carlo method was realized by Zola et al. (2010), which is efficient in expense of too many evaluations of the test function. We compare existing algorithms of minimization of multi-parametric functions. To study methods, we adopt a simplified model of an eclipsing binary at a circular orbit assuming spherical components with an uniform brightness distribution. This model resembles more advanced models in a sense of correlated parameter estimates due to a similar topology of the test function. Such a model may be applied to detached Algol-type systems, where the tidal distortion of components is negligible.

Key words: variable stars, eclipsing binaries, algols, data analysis, time series analysis, parameter determination.

Introduction

Determination of the model parameters of various astrophysical objects, comparison with observations and, if needed, further improvement of the model, is one of the main directions of science, particularly, of the study of variable stars.

There is some software which allows to compute theoretical light curves of binary stars taking into account physical processes taking place there. Methods of modeling light curves of binary stars have been described by many authors (Kopal 1959, Tsessevich 1971, Shul’berg 1971, Rucinski 2010, Kallrath and Milone 2009).

Since the paper of Wilson and Devinney (1971) and its further improvements (Wilson 1979, 1994), there are some realizations of the corresponding method. The well known programs are “Binary Maker” (Bradstreet, 2005, <http://www.binarymaker.com/>), PHOEBE (Prsa et al. 2011, <http://sourceforge.net/projects/phoebe/>).

To determine the statistically best sets of the parameters, there are some methods for optimization of the test function which is dependent on these parameters (cf. Cherepashchuk 1992).

As for the majority of binary stars the observations are not sufficient to determine all parameters, for smoothing the light curves may be used “phenomenological fits”. Often were used trigonometric polynomials (=“restricted Fourier series”), following a pioneer work of Pickering (1881) and other authors, see Parenago and Kukarkin (1936) for a detailed historical review. Andronov (2012) proposed a method of phenomenological modeling of eclipsing variables (most effective for algols, but also applicable for EB and EW – type stars).

Model

The simplest model is based on the following main assumptions: the stars are spherically symmetric (this is physically reliable for detached stars with components being deeply inside their Roche lobes); the surface brightness distribution is uniform. This challenges the limb darkening law, but is often used for teaching students because of simplicity of the mathematical expressions, cf. Andronov (1991). Similar simplified model of an eclipsing binary star is presented by Dan Bruton (<http://www.physics.sfasu.edu/astro/ebstar/ebstar.html>).

The scheme is shown in Fig.1. The parameters are L_1 , L_2 (proportional to luminosities), radii R_1 , R_2 , distance R between the projections of centers to the celestial sphere.

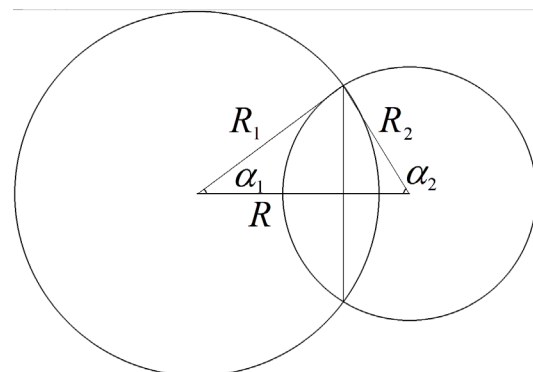


Fig. 1. Scheme of eclipsing binary system with spherical components.

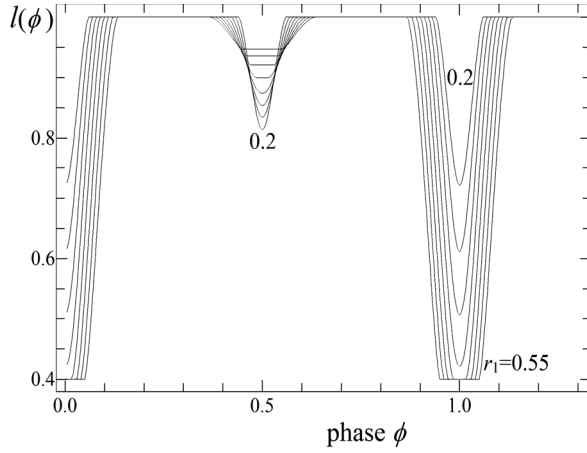


Fig. 2. A set of light curves generated for R_1 in a range from 0.2 to 0.55 with a step of 0.05 for fixed values of other parameters listed in the text.

$$\begin{aligned} \text{The square of the eclipsed segment is } S &= S_1 + S_2, \\ S_1 &= R_1^2 (\alpha_1 - \sin \alpha_1 \cos \alpha_1) \\ S_2 &= R_2^2 (\alpha_2 - \sin \alpha_2 \cos \alpha_2) \end{aligned} \quad (1)$$

where the angles α_1 , α_2 may be determined from the cosine theorem:

$$\begin{aligned} \cos \alpha_1 &= \frac{R^2 + R_1^2 - R_2^2}{2R_1R} = \frac{R^2 + \eta}{2R_1R}, \\ \cos \alpha_2 &= \frac{R^2 + R_2^2 - R_1^2}{2R_2R} = \frac{R^2 - \eta}{2R_2R}, \end{aligned} \quad (2)$$

where obviously $\eta = R_1^2 - R_2^2$. The total flux is $L = L_1 + L_2$, if $R \geq R_1 + R_2$ (i.e. both stars are visible, $S=0$). For $R \leq R_1 + R_2$, $S = \pi R_2^2$ (assuming that $R_2 \leq R_1$). Generally, $L = L_1 + L_2 - S/\pi R_j^2$, where j is the number of star which is behind another, i.e. $j=1$, if $\cos 2\pi\phi \leq 0$, and $j=2$, if $\cos 2\pi\phi \geq 0$. Here ϕ is phase ($\phi=0$ corresponds to a full eclipse, independently on which star has larger brightness). For scaling purposes, a dimensionless variable $l(\phi) = L(\phi)/(L_1 + L_2)$ is usually introduced.

For tests, we used a light curve generated for the following parameters: $R_1=0.3$, $R_2=0.2$, $L_1=0.4$, $L_2=0.6$ and $i=80^\circ$. The phases were computed with a step of 0.02. This light curve as well as other generated for a set of values of R_1 is shown in Fig.2.

As a test function we have used:

$$F = \sum_{i=1}^n \frac{(x_i - \alpha x_c(\phi_i))^2}{\sigma_i^2} \quad (3)$$

where x_i (or l_i) are values of the signal at phases ϕ_i with a corresponding accuracy estimate σ_i , and x_c are theoretical values computed for a given trial set of m parameters.

For normally distributed errors and absence of systematic differences between the observations and theoretical values, the parameter F is a random variable with a

χ_{n-m}^2 statistical distribution (Anderson, 1958, Cherepashchuk 1992). For the analysis carried out in this work, we used a simplified model with $\sigma_i = 1$. This assumption doesn't challenge the basic properties of the test function.

The scaling parameter is sometimes determined as $x(0.75)/x_c(0.75)$, i.e. at a phase where both components are visible, and the flux (intensity) has its theoretical maximum (in the "no spots" model). To improve statistical accuracy, it may be recommended to use a scaling parameter computed for all real observations:

$$\alpha = \frac{\sum_{i=1}^n \frac{x_i}{\sigma_i^2}}{\sum_{i=1}^n \frac{x_c(\phi_i)}{\sigma_i^2}} \quad (4)$$

Even in our simplified model, the number of parameters is still large (4). At Figure 3, the lines of equal levels of F are shown. One may see that the zones of small values are elongated and inclined showing a high correlation between estimates of 2 parameters. In fact this correlation is present for other pairs of parameters. This means that there may be relatively large regions in the multi-parameter space which produce theoretical light curves of nearly equal coincidence with observations.

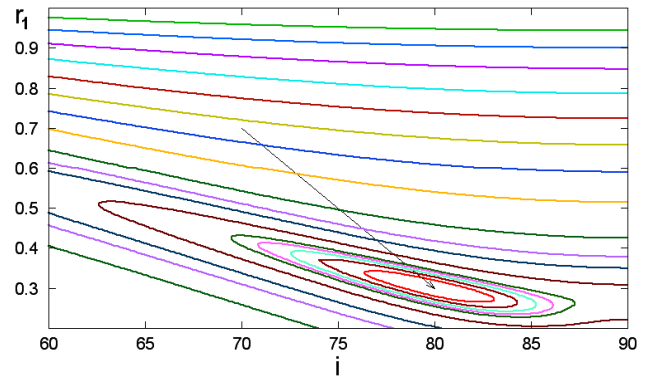


Fig. 3. Lines of equal values of the test function F for fixed values of other parameters. The arrow shows position of the "true" parameters used to generate the signal.

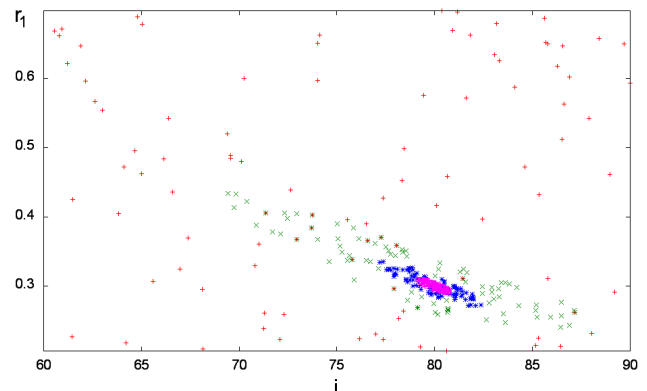


Fig. 4. Best 100 points after 10^2 , 10^3 , 10^4 , 10^5 trial computations, respectively.

In the software by Zola et al. (2010), the Monte-Carlo method is used, and at each trial computation of the light curve, the random parameters are used in a corresponding range:

$$C_k = C_{k,min} + (C_{k,min} - C_{k,min}) \cdot \text{rand}, \quad (5)$$

where **rand** is an uniformly distributed random value.

Then one may plot “parameter – parameter” diagrams for “best” points after a number of N trial computations. The “best” means sorting of sets of the parameters according to the values of the test function F .

Initially, the points are distributed uniformly. With an increasing N , “better” (with smaller F) point concentrate to a minimum. There may be some local minima, if the number of parameters will be larger (e.g. spot(s) present in the atmosphere(s) of component(s)).

Andronov and Tkachenko (2013) had made computations for an artificial function of m ($=1,2,3$) variables. The minimal value δ (as a true value was set to zero), which was obtained using N trial computations in the Monte-Carlo method is statistically proportional to

$$\delta \sim N^{-2/m}, \quad (6)$$

i.e. the number of computations $N \sim \delta^{-m/2}$ drastically increases with both an increasing accuracy and number of parameters.

For our simplified model, the numerical experiments statistically support this relation. Also, the distance between the “successful computations” (when the test function becomes smaller than all previous ones) $\Delta N \sim N$. Obviously, it is not realistic to make computations of the test function for billions times to get a set of statistically optimal parameters.

In the “brute force” method, the test functions are computed using a grid in the m – dimensional space, so the interval of each parameter is divided by n_i points. The number of computations is $N=n_1n_2\dots n_m$ should be still large. Either the Monte–Carlo method, or the “brute force” one allow to determine positions of the possible local extrema in an addition to the global one.

However, if the preliminary position is determined, one should use faster methods to reach the minimum. Classically, there may be used the method of the “steepest descent”, where the new set of parameters may be determined as

$$C_{k+1,i} = C_{k,i} - \lambda h_{k,i}, \quad (7)$$

where $C_{k,i}$ is the estimated value of the coefficient C_i at k -th iteration, $h_{k,i}$ – proposed vector of direction for the coefficient C_i , and λ is a parameter. Typically one may use one of the methods for one–dimensional minimization (cf. Press et al. 2007, Korn and Korn, 1968), determine a next set of the parameters $C_{k,i}$, recompute a new vector $h_{k,i}$ and again minimize λ . In the method of the steepest descent, one may use a gradient $h_{k,i} = \partial F / \partial C_i$ as a simplest approximation to this vector. Another approach (Newton-Raphson) is to redefine a function $F(\lambda) = F(C_i, i=1..m)$, compute the root of equation $\partial F / \partial \lambda = 0$, and then to use a parabolic approximation to this function. Thus

$$\lambda = (\partial F / \partial \lambda) / (\partial^2 F / \partial \lambda^2). \quad (8)$$

There may be some modifications of the method based on a decrease of λ , which may be recommended, if the shape of the function significantly differs from a parabola.

In the method of “conjugated gradients”, the function is approximated by a second-order polynomial. Finally it is usually recommended to use the Marquardt (1963) algorithm. We tested this algorithm with a combination of the “steepest descent” (when the determinant of the Hessian matrix is negative) and “conjugated gradients” (if positive), which both are efficient for a complex behavior of the test function.

We developed the software realizing various methods for study of variable stars. The results of this study will be used in the frame of the projects “Ukrainian Virtual Observatory” (UkrVO) (Vavilova et al., 2012) and “Inter-Longitude Astronomy” (Andronov et al., 2010).

References

- Anderson T.W.: 1958, *An introduction to multivariate statistical analysis*, New York. John Wiley & Sons,
 Andronov I.L.: 1991, *Structure and Evolution of Stars*, v.1, (in Russ.), Odessa Inst. of Adv. Teachers, 84pp.
 Andronov I.L. et al.: 2010, *Odessa Astron. Publ.*, **23**, 8.
 Andronov I.L.: 2012, *Astrophys.*, **55**, 536.
 Andronov I.L., Tkachenko M.G.: 2013, *Arxiv.org*, 2013arXiv1310.1967A
 Bradstreet D.H.: 2005, *SASS*, **24**, 23.
 Cherepashchuk A.M.: 1992, *Astron. Zh.*, **70**, 1157.
 Kallrath J., Milone E.F.: 2009, *Eclipsing Binary Stars: Modeling and Analysis*, Springer, 428pp.
 Kopal Z.: 1959, *Close Binary Systems*, J. Wiley and Sons, New York.
 Korn G.A., Korn Th.M.: 1968, *Mathematical Handbook for Scientists and Engineers*. - McGraw-Hill Book Company, N.Y. et al.
 Marquardt D.: 1963, *SIAM J. Appl. Math.* **11**, 2.
 Parenago P.P., Kukarkin B.V.: 1936, *Z. f. Astrophysik*, **11**, 337.
 Pickering E.: 1881, *Proc. Amer. Acad. Arts and Sciences* **16**, 257.
 Press W.H., Teukolsky S.A., Vetterling W.T., Flannery B.P.: 2007, *Numerical Recipes: The Art of Scientific Computing*, Cambridge University Press.
 Prsa A., Matijevic G., Latkovic O., Vilardell F., Wils P.: 2011, *Astrophysics Source Code Library*, record ascl:1106.002, 2011ascl.soft06002P
 Rucinski S.: 2010, *AIP Conference Proceedings*, **1314**, 29.
 Shul'berg A. M.: 1971, *Close Binary Systems with Spherical Components*, Moskva: Nauka, 246 pp., 1971cbsw.book.....S
 Tsessevich V.P.: 1971, *Eclipsing Variable Stars*, Moscow, Nauka
 Vavilova I.B.: 2012, *Kinem. Phys. Celest. Bodies*, **28**, 85, 2012KPCB...28..85V
 Wilson R.E.: 1979, *ApJ*, **234**, 1054.
 Wilson R.E.: 1994, *PASP*, **106**, 921.
 Wilson R.E., Devinney E.J.: 1971, *ApJ*, **166**, 605.
 Zola S., Gazeas K., Kreiner J.M. et al.: 2010, *MNRAS*, **408**, 464.

BVRI – OBSERVATION OF AGN NGC 4151 IN 2009-2011

B. Artamonov ¹, V. Oknyanskij ², O. Ezhkova ³, N. Metlova ⁴

.Sternberg Astronomical Institute (SAI), Moscow Lomonosov State University, Moscow, Russia

¹ artamon@mail.ru, ² oknyan@mail.ru, ³ eozh@sai.msu.ru, ⁴ metlova@sai.msu.ru

ABSTRACT. The observation of AGN NGC 4151 was completed in BVRI filters on 1.5 meter telescope of Maidanak observatory and Zeiss-600 telescope of Crimean laboratory SAI in 2009-2012. We made photometric processing of obtained CCD frames and presented the result in pictures.

Key words: AGN, CCD photometry

SyG NGC 4151 is observing as typical AGN and very variable object during 100 years (Oknyanskij 2012). We are presenting our observational data obtained on Maidanak observatory and Crimean laboratory SAI in 2009-2011. Multicolor BVRI observations of NGC 4151 was realized by 1.5 meter telescope AZT-22 of Maidanak observatory with CCD camera SNUCAM 4096*4096 cooling Crio Tiger system (-109°C) and Zeiss-600 of Crimean laboratory SAI with CCD camera VersArray 1300B 1024*1024. CCD cameras have set from Bessel filters.

First standard processing of CCD frames was made in MIDAS: creation of superflat, superdark, superbias; cleaning for cosmic rays.

Integral photometry of central region galaxy was received in circle 27.5 angular sec. We made calibration of obtained photometric data with using the coefficients of instrumental photometric system from Lim (2009), Artamonov (2010) for Maidanak observatory, D.Yu.Tsvetkov (2006) for Crimean laboratory SAI and standard stars from Doroshenko (2005). Photometric average error composes about 0.01-0.02 mag.

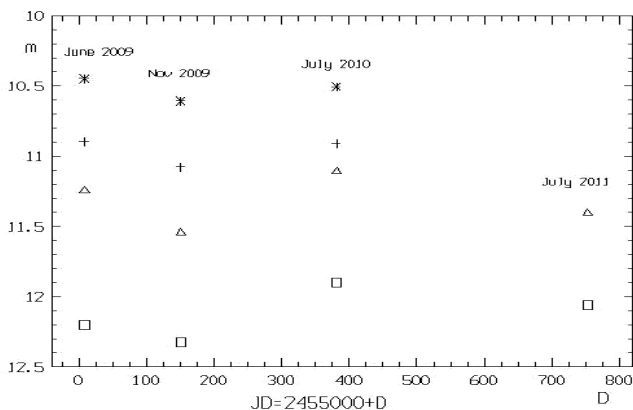


Figure 1. Average photometric data in B (square), V (triangle), R (cross), I (star) filters for NGC 4151 in 2009-2011

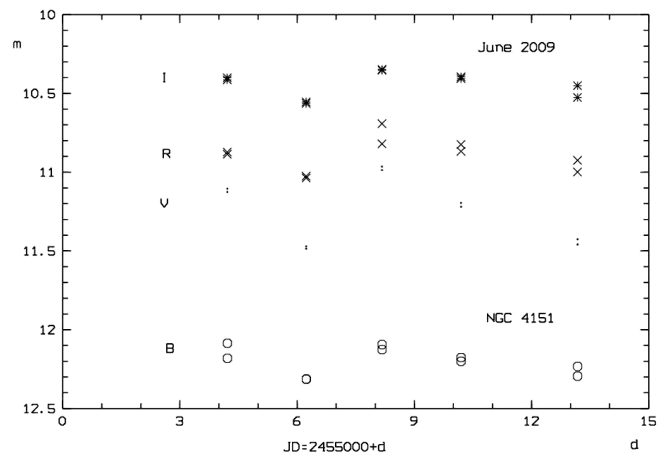


Figure 2. Average during one night photometric data for NGC 4151 in June 2009

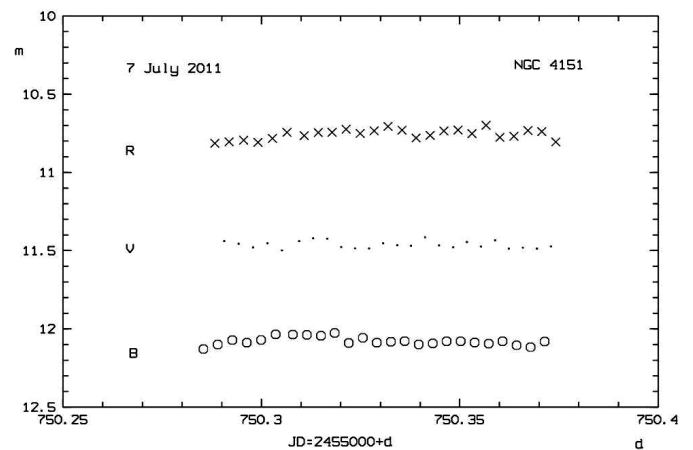


Figure 3. Variability during one night 7 July 2011 for NGC 4151

Our photometric data 2009-2011 in filter B was presented on historical light curve for NGC 4151 (see Oknyanskij, 2012). In present work we add new data in VRI filters. Observation in BVRI filters was made at 23, 25, 27, 30 June 2009: 15 November 2009: 1,4,6 July 2010, 7,11 July 2011.

Average (during one month) data in 2009-2011 shown on fig. 1. We present the light curve for June 2009 on fig. 2 and the light curve for one night 7 July 2011. We can agree

the variability on different times and with historical light curve (Oknyanskij, 2012). We see maximum in July 2010 on fig. 1. The agreement of this maximum with minimum on historical light curve shown the difference about 0.9 mag in B filters. Variability during one month June 2009 is about 0.1-0.2 mag. On fig.2. Variability during one night 7 July 2011 is in limit 0.1 mag. The behavior of light curve is similar in different filters on all figures.

References

- Artamonov B.P., Bruevich V.V., Gusev A.S. et al.: 2010, *ARep*, **54**, 1019.
Doroshenko V.T. et al.: 2005, *Astrophysics*, **48/3**, 304.
Lim B., Sung H., Bessel M. et al.: 2009, *Korean Astron. Soc.*, **42**, 161.
Oknyanskij V. et al, *OAP*, **25/2**, 179.
Tsvetkov D.Yu. et al, 2006, *A&A*, **460**, 769.

NUMERICAL MODELLING OF GAS DYNAMIC STRUCTURES IN SPIRAL GALAXIES

A.Lugovskiy¹, E.Filistov²

Keldysh Institute of Applied Mathematics, Moscow, Russia

¹*alex_lugovsky@mail.ru*, ²*filistov.ru@mail.ru*

ABSTRACT. Observations show that in the global morphology of spiral galaxies appear and form multi-scale features that are embedded in a complex complete picture of the galaxy. The origin and nature of the observed heterogeneity of the global spiral pattern of galaxies are not firmly established at this time. Based on the numerical simulation a possible new mechanism of appearance and formation in the two-armed global spiral galaxies' morphology of a number of gas-dynamic elements similar to each other in shape and independent in brightness is analyzed. Numerical simulation of unsteady gas-dynamic processes occurring under the influence of an external gravitational field is done. It is shown that as a result of the nonlinear supersonic interaction of occurring spiral formations with the flow of the matter features with hydrodynamic nature are appeared, with modeling results well matching with the observations.

Key words: numerical modeling, spiral galaxies, gas-dynamic structures, shock waves, contact discontinuities

Introduction

Based on the numerical simulation study a new possible mechanism (the idea and the theoretical justification are offered in the Chernin, 2002) of appearance and formation in the two-armed global spiral galaxies' morphology of a number of gas-dynamic elements similar to each other in shape and independent in brightness is analyzed in this paper. The arms are taken as two related distributions, each of which contains the shock fronts bordering the arm, contact discontinuities between them and also the emerging system of small-scale shock waves. The physical conditions that give rise to this kind of non-linear quasi-stationary gas configuration can be implemented in a global two-armed spiral gravitational field and can be connected, either to the nature of the spiral density wave, or with the specific behavior of a large-scale shock compression of the gas flowing through the gravitational potential profile of the density wave. The presence of this kind of dynamic structure of the matter flow in the disks of spiral galaxies is shown by observations (eg: Zwicky, 1957; Sandage, 1961; Vorontsov-Vel'yaminov, 1978; Elmegreen et al., 1984;

Sandage et al., 1994; also refer to: Block et al., 1994; Block et al., 1999; Block et al., 2001; Zhang et al., 2012).

At the gas-dynamic framework for the interpretation of this phenomenon also points morphological difference of images of the galaxy NGC 309 seen nearly flat when viewed in the light of different ranges of wavelengths (see Fig. 1) obtained in the paper Block et al. (1991).

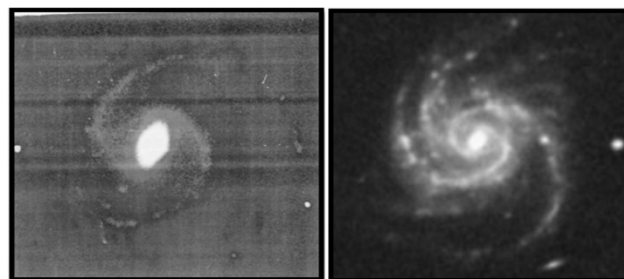


Figure 1: Various images of the spiral galaxy NGC 309. On the left – image received using near-infrared light: two short, wide and plain major arms, originating from the ends of the central bar.

On the right – image received using blue light: well distinguishable multi-armed expanding from the disk center geometrical structure.

The origin and nature of the observed heterogeneity of the global spiral pattern of galaxies are not firmly established at this time. Mesoscale features such as spurs, feathers, etc. are found in the major geometric structures - representatives of the spiral Grand Design galaxies of Hubble type. They appear as feeble intermediate links that are embedded in a complex complete picture of the galaxy. Even in very small (located around the nucleus) volumes special methods of processing of images clearly enough indicate the presence of regular substructures in the spiral arms.

Our calculations allow to monitor the complex shockwave configuration with contact discontinuities. The structure of the resulting flow pattern has been studied and it was found that the emerging series of interacting wave disturbances can create a new quasi-stationary configurations developing in an essentially nonlinear transient mode.

Mathematical model and numerical method

Without going into detail to the description of the model (for details see: Landau, 1979; Lugovskii, 2012; Abakumov, 1996) let us say that we consider the dynamics of an axisymmetric gas disk is immersed in a gravitational field created by a rotating stellar disk.

The gravitational influence at the gas environment is determined by gravitational potentials formed mainly by external sources located both inside and outside the area of modeling. The total gravitational potential is represented by the algebraic sum of the axisymmetric and non-axisymmetric parts. The axisymmetric part of the gravitational potential is the algebraic sum of the potential of self-gravitating stellar disk, bulge potential and potential of the dark halo (the explicit form of the axially symmetric gravitational potentials is represented, for example, in: Morozov, 2005). Additional non-axisymmetric gravitational spiral potential is the potential associated with a density wave in the disk, and providing two-armed spiral pattern of the galaxy (Toomre, 1964). This potential is a small perturbation introduced at the initial time to the equilibrium state eventually leading to the formation of large spiral-shaped structures that cover the entire volume of the disk.

The flow of gas in an external gravitational field is described by the Euler equations of classical gas dynamics. For the solution of gas dynamic equations the monotonic 1st order approximation TVD scheme by Roy with the limiters of antidiffusion flows in the form of Osher which increase the order of scheme approximation (up to the third order in space) with minimal numerical dissipation and preserving the property of monotony was used. Moreover initial scheme was modified by the method of Einfeldt to improve stability. General description of the method can be found in (Velikhov, 2007). TVD-method is effective for describing significantly unsteady, for example, turbulent flow (Velikhov, 2007; Lugovskii, 2008; Lugovskii, 2012) as well as flow wherein small-scale system of shock waves is formed (see, eg, Filistov, 2012; Khoperskov, 2003).

For the borders of the area free boundary conditions were set. To eliminate the effect of boundary conditions at the behavior of internal regions of the disk its configuration was selected so that the radial dimension of the computational domain significantly exceeds the characteristic size i.e. bulk concentration region of the disk and the density at the outer border is significantly lower than in the central zone. Note that without making any perturbation gas disk retains its equilibrium state for sufficiently long time period; during the calculations the outer layers of the disk evolved while at the same time the bulk of the disk remained stable, density changed slightly and the radial velocities developed insignificantly.

Results

The results of the numerical simulation allow to distinguish several stages in the evolution of the gas disk in which the phenomenon of formation of transient non-stationary configuration of a global two-armed spiral pattern is observed including a series of hydrodynamic

discontinuities such as shock waves and contact discontinuities between them.

The general structure of the solution for an ideal gas flow evolving over 6 characteristic times (one unit of time in our model calculations correspond to the physical time in 68 million years) is shown in Fig. 2. This figure shows the gas pressure distributions in the equatorial plane of the system illustrating the flow dynamics and its state at different equally spaced time points. Shock waves formed in the disk are seen in the figures as a condensation of pressure contours.

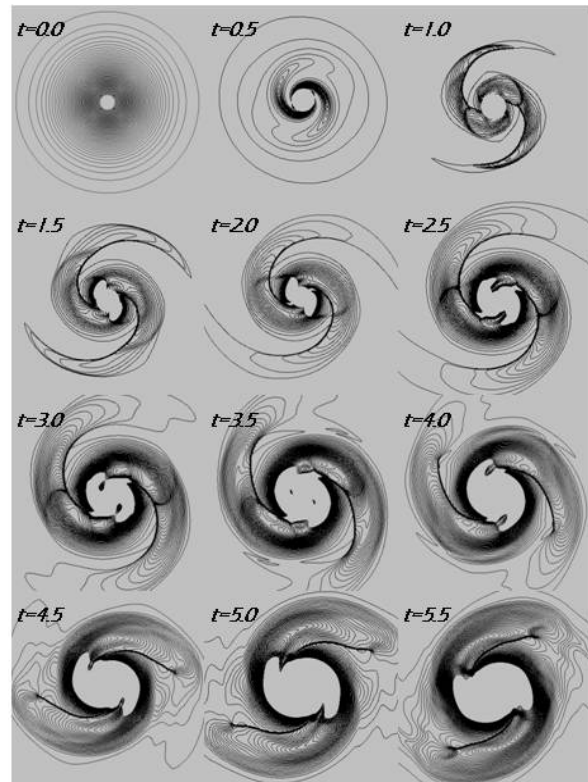


Figure 2:

- $t=0$ – equilibrium configuration
- $t=0.5$ – appearance of smooth spiral shock waves
- $t=1.0$ – small-scale secondary shock waves
- $t=1.5$ – increasing the size of spiral structures
- $t=2.0$ – blurred main shock waves
- $t=2.5$ – spurs inside the arms
- $t=3.0$ – 3.5 – transient nature of the spurs, beginning of the polygonalization (straightening segments of the shock wave front)
- $t=4.0$ – arc-shaped spiral shock waves
- $t=4.5$ – straight line segments of shock waves (length is proportional to the distance from the center)
- $t=5.0$ – development of the structural instability of the shock wave, interaction with the contact discontinuity
- $t=5.5$ – the formation of the spur in the spiral design, the development of polygonal pattern of the spiral arm

Numerical simulation shows the formation of some spiral elements in the global two-armed spiral galaxy morphology similar to each other in shape and independent in brightness. These series of strong shockwave disturbances interacting with each other create

new small-scale irregular secondary shock waves which develop over time in different kinds of heterogeneity in small and medium spatial scales that contribute to the generation of polygonal structures in the gas disk. This paper is not aimed at exploring and embracing of the entire spectrum of phenomena arising in a rotating gas disk with formation of transient global morphology of the spiral structures in the two-arm gravitational potential. The general course of the evolution of spirals for ~ 6 characteristic times is studied. However, it is natural to assume that at this stage of the appearance of two straight segments the gasdynamic process of general polygonalization is not finished. This circumstance is also indicated by the fact that the presence of straight-line segments (rows) in the spiral arms of galaxies is not an exception (Chernin, 1999; Chernin, 2000) at least for late-type ordering spirals (Grand Design Sbc-Sc).

Analysis of the distribution of the geometric parameters of the individual structural elements obtained in the course of numerical simulation of the gas disk in the potential of spiral density wave of stellar component and analysis of fragments of the spiral pattern of the galaxy M51 shows a good agreement (Fig. 3).

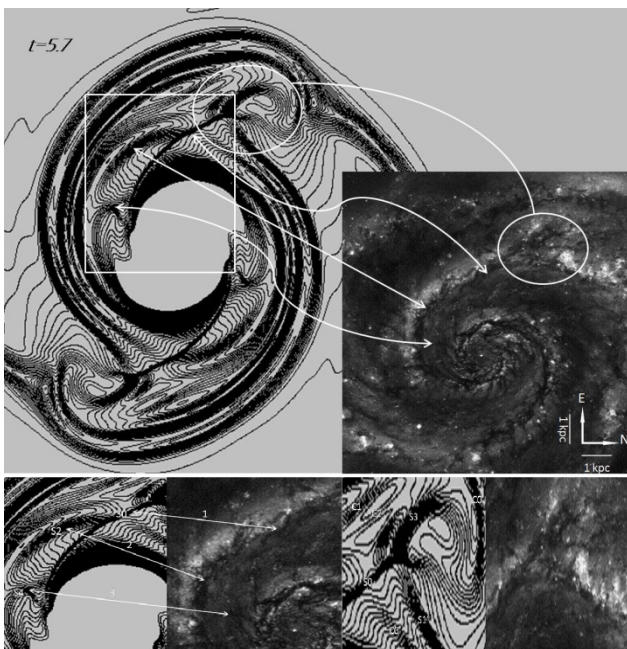


Figure 3:

Top: the nonlinear stage of the formation of the spiral pattern, gas density contours are shown at the time $t = 5.7$. The inset – the image of the spiral galaxy NGC 5194 (M 51).

Bottom left: at the left – an enlarged image of the part of the spiral arm bordered by the rectangle in the top figure; at the right - a fragment of the picture of the galaxy M 51.

Bottom right: at the left – an enlarged image of the part of the spiral arm bordered by the ellipse in the top figure; at the right – photo: Northwestern fragment of the galaxy M 51 bordered by the ellipse in the top figure.

Thus it is found that the behavior and geometrical properties of the resulting transient structures in the numerical simulation in the constructed model agree well with the behavior and basic properties of the global picture of the observed spiral patterns.

Conclusions

Based on numerical simulations the possibility of the formation of non-stationary transient gas configuration in the global two-armed spiral gravitational potential was investigated and the analysis of emerging complex wave pattern of the flow was made in this paper.

The results of numerical simulation and flow features identified during the gas dynamic calculations lead to the following conclusion confirming the theoretical basis for this phenomenon provided in the article [Chernin 2002]: configurations of this kind can be formed as a result of a non-linear supersonic interaction of the spiral formations with the flow of the disk matter and the appearance of the hydrodynamic discontinuities including the fronts of varying intensity shock waves and contact discontinuities separating these fronts.

Acknowledgements. This work has been supported by the Russian Foundation for Basic Research (project code 12-01-31348) and Grant of the President of the Russian Federation for the State Support of Young Russian PhD Scientists (grant MK-946.2012.2).

References

- Chernin A.D.: 2002, *AAPTr*, **21**, 1.
 Zwicky F.: 1957, *Morphological Astronomy*, Springer, Berlin.
 Sandage A.: 1961, *The Hubble Atlas of Galaxies*, Carnegie Inst., Washington, DC.
 Vorontsov-Vel'yaminov B.A.: 1978, *Extragalactic Astronomy*, Moscow: Nauka.
 Elmegreen B.G., Elmegreen D.M.: 1984, *Astrophys. J. Suppl.*, **54**, 127.
 Sandage A., Bedke J.: 1994, *The Carnegie Atlas of Galaxies*, Carnegie Inst., Washington, DC.
 Block D.L., Bertin G., Stockman A. et al.: 1994, *Astron. Astrophys.*, **288**, 365.
 Block D.L., Puerari I.: 1999, *Astron. Astrophys.*, **342**, 627.
 Block D.L., Puerari I., Takamiya M. et al.: 2001, *Astron. Astrophys.*, **371**, 393.
 Zhang X., Buta R. J.: 2012, *arXiv:1012.0277v2* [astro-ph.GA].
 Block D.L., Wainscoat R.J.: 1991, *Nature*, **353**, 48.
 Landau L.D., Lifshitz E.M.: 1979, *Fluid Mechanics*, Oxford: Pergamon Press.
 Lugovskii A.Yu., Chechetkin V.M.: 2012, *Astron. Rep.*, **56**, 96.
 Abakumov M.V., Mukhin S.I., Popov Yu.P., Chechetkin V.M.: 1996, *Astron. Rep.*, **40**, 366.
 Морозов А.Г., Хоперсков А.В.: 2005, *Физика дисков*, Волгоград: Изд-во ВолГУ.
 Toomre A.: 1964, *Astrophys. J.*, **139**, 1217.
 Velikhov E.P., Lugovskii A.Yu., Mukhin S.I. et al.: 2007, *Astron. Rep.*, **51**, 154.
 Lugovskii A.Yu., Mukhin S.I., Popov Yu.P., Chechetkin V.M.: 2008, *Astron. Rep.*, **52**, 811.
 Filistov E.A.: 2012, *Astron. Rep.*, **56**, 9.
 Khoperskov A.V., Khrapov S.S., Nedugova E.A.: 2003, *Astron. Lett.*, **29**, 246.
 Chernin A.D.: 1999, *Mont. Not. Roy. Astron. Soc.*, **308**, 321.
 Chernin A.D.: 2000, *MNLet*, **318**, 201.

VARIABILITY OF NGC4151 DURING 2008-2013

V. L.Oknyanskij, N.V.Metlova, B.P.Artamonov, A.V.Lyuty, V.M.Lyuty

Sternberg Astronomical Institute, Moscow M.V. Lomonosov State University,
Moscow, Russian Federation, oknyan@sai.msu.ru

ABSTRACT. We present the historical light curve of NGC 4151 for 1906 – 2013 and the detailed light curve for 2008 - 2013 the light curve of NGC 4151 for 2008 – 2013 (our photoelectrical and CCD data obtained at 2 observatories during last 6 years). See details in our paper Oknyanskij et al. (2012). NGC 4151 has been in high state during 2009-2012 and relatively at low in 2008 and 2013. So one circle of slow component about 6 years was observed during 2008-2013. Also we see one fast flash in 2013 with duration time about 150 days. Applying Fourier (CLEAN) algorithm to the data from 1906 till 2013 (smoothed with step 100 days), we find a periodic component $P \sim 16$ years in the 107-year light curve. 30 years ago, nearly the same "period" was first revealed just from Odessa photometric data. There are also found another significant components about 1.5P, 2P. These circles probably correspond to some accretion dynamic time.

Key words: AGN, optical variability, historical light curve

NGC4151 is one of the most popular and well studied AGNs, it is most bright and high variable object, which is very often used as an example object: typical Sy1, typical Sy1.5, typical object changing classification type between Sy1 and Sy1.9.

NGC 4151 – is one of the several Seyfert galaxies which were firstly discovered at 1967 as variable in optical region (Fitch et al., 1967). Shortly after that (at 1968) the photoelectric UBV monitoring of NGC 4151 object was started at Crimean Laboratory of Sternberg Astronomical Institute (Lyuty, 1977). See more references and details about photometrical history for the object at our pervious publication Oknyanskij et al. (2012)

At the present work we continue the optical monitoring of NGC 4151. Our new data include the photoelectric UBV measurements (with the same telescope and equipment) for 2013.

The historical light curve for 1906-2013 years is presented at Fig. 1. It is clear seen that after minimum at 1984 the type of variability is not the same as it was before: the amplitude of the fast variations become smaller relative to the slow ones. The light curve with our new data for 2008-2013 years is shown at Fig. 2. At the light curves (Fig. 1 and 2) we can see different variable

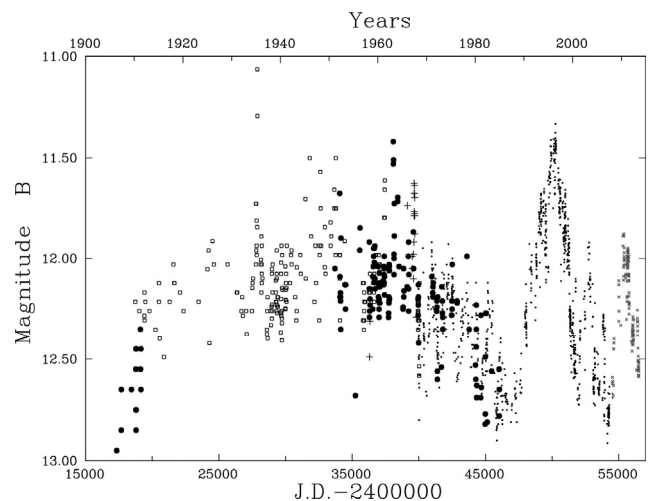


Figure 1: The historical light curve of NGC 4151. Filled circles – our photographic data, open circles – Pacholszyk et al. (1983), pluses - photoelectric data obtained before 1968, dots – Crimean photoelectric monitoring, x – our photoelectric and CCD data for 2008-2013. The errors are of the order of 0.2 mag for Pachalszyk's data, 0.1 mag or better for our photographic points, and $\sim 0,02$ mag for our photoelectric and CCD data.

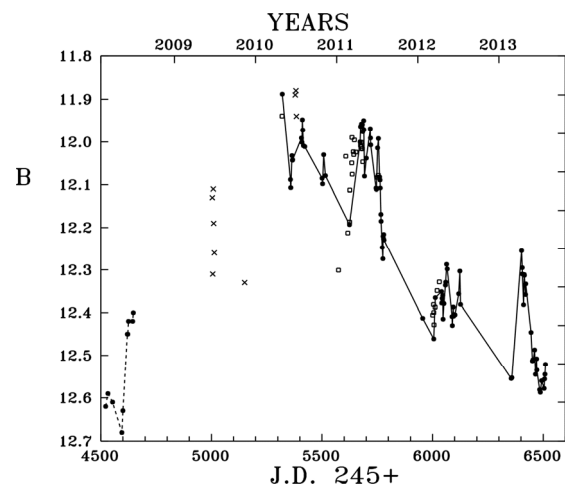


Figure 2: The light curve of NGC 4151 at 2008-2013, including new, unpublished before data for 2013: filled circles – photoelectric data, x – Maidanak CCD observations, boxes – Crimean CCD data.

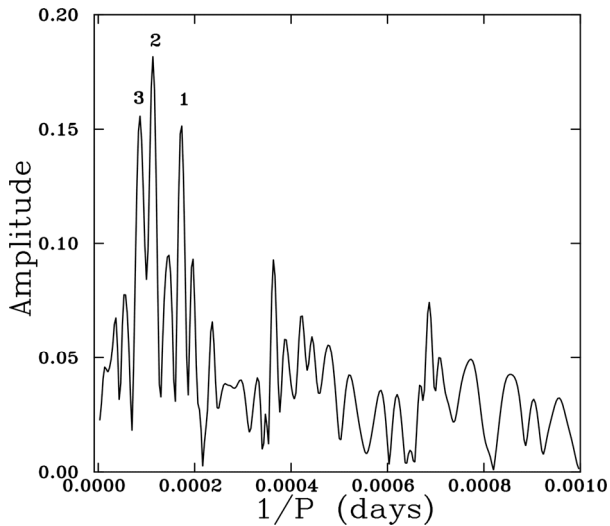


Figure 3: Power spectra obtained by the CLEAN method. There are several significant maxima: **1** $P \sim 16$ years, **2** $\sim 1.5P$, **3** $\sim 2P$

components: **1** – fast variations with a characteristic timescale of tens of days, **2** – slow variations with a characteristic timescale of several years, **3** – very slow component with a characteristic timescale of tens of years.

NGC 4151 has been in high state during 2009-2012 and relatively at low in 2008 and 2013. So one circle of slow component about 6 years was observed during 2008-2013. Also we see one fast flash in 2013 with duration time about 150 days.

Applying Fourier (CLEAN) algorithm (Roberts et al., 1987) to the data from 1906 till 2013 (smoothed by a step equal to 100 days), we find a periodic component $P \sim 16$ years in the 107-year light curve. 30 years ago, nearly the same "period" was first revealed just from Odessa photometric data. There are also seen (Fig. 3) another significant components about $1.5P$, $2P$. These circles probably correspond to some accretion dynamic times.

References

- Fitch W.S., Pacholczyk A.G., Weymann R.J.: 1967, *Astrophys. J.*, **150**, L67.
 Lyutyi V.M.: 1977, *Soviet. Astron.*, **21**, 655.
 Oknyansky V., Metlova N., Artamonov B., et al.: 2012, *Odessa Astron. Publ.*, **25/2**, 111.
 Pacholczyk A.G., Penning W.R., Ferguson D.H. et al.: 1983, *Astrophys. Lett.*, **23**, 225.
 Roberts D.H., Lehar J., Dreher J.W.: 1987, *Astron. J.*, **93**, 968.

PHOTOMETRICAL STUDY OF CLOSE BINARY SYSTEM V841 Cyg

O.G. Sergienko¹, D.V. Bodryagin¹, E.A. Panko^{1,2}

¹ V.O. Suckomlinsky Mykolaiv National University, Mykolaiv, Ukraine

² Visiting Astronomer, Department of Astronomy,
Saint Mary's University, Halifax, Nova Scotia, Canada
panko.elena@gmail.com

ABSTRACT. We present the results of research of scantily explored close binary system V841 Cyg with possible period variations. It was attributed as β Lyr and as near contact binary star. We obtained light curve of the star in July 2013 in V-band. Both eclipses are partial, the depths of primary and secondary minima are $0^m.53$ and $0^m.20$. Light curve has feature near primary minimum: practically horizontal parts in phases $\pm(0.1 - 0.16)$. We found new time minima: $HJD_I = 2456504.48122$, $HJD_{II} = 2456493.44562$.

We obtained new parameters of binary system using Binary Maker 3 package. The system contains from A6 V+G5 V stars with mass ratio about 0.49. The components have temperatures $T_{effI} = 8550^\circ$, $T_{effII} = 5500^\circ$ and estimated masses $M_I = 1.85$, $M_{II} = 0.90$; they fill own Roshe lobes on 95% and 92% correspondingly and both components are deformed. The distance between components is about $5R_\odot$, the distance between component surfaces is about $1.4R_\odot$. We confirm the V841 Cyg classification as is NCB system, with not significant mass transfer.

Key words: Stars: eclipsing: close binary stars: individual: V841 Cyg.

1. Introduction

Close binary systems with period variations are test for evolution scenarios of these objects. Period variations in binary systems are explained either due to change of large axis in the system, either due to change of mass of system or due to both these factors. Unfortunately the number of well-studied eclipsing binaries is a small fraction of the total number listed in the last edition of the General Catalogue of Variable Stars (Samus et al., 2012).

In 2000 Kreiner et al. collected 1140 eclipsing binaries with period variations according to the next criteria: 1) at least 10 minima had been timed; 2) these minima spanned at least 2,500 cycles; 3) the 2,500 cycles represented no fewer than 40 years. The list of

these eclipsing binaries was published as “An Atlas of $O - C$ Diagrams Of Eclipsing Binary Stars”, Atlas hereinafter (Kreiner et al., 2000). We selected in the Atlas about 150 binary systems with the two-bit of the known time minima for the “Programm of Observations of Insufficiently Explored Eclipsing Binaries with Period Variations”, which was initiated in Kalinikov Astronomical Observatory (AOK) of Nikolaev National University in 2004. The results of investigation of Programm binaries such as CU Peg, V609 Aql and BM UMa were published (Panko et al., 2006, Turner et al., 2008, Virnina et al., 2010).

We present the study results of the next Programm star. The binary system V841 Cyg ($RA_{2000} = 19^h 22^m 18^s.4$, $DEC_{2000} = +28^\circ 41' 08''$, $V = 11^m.1$) according to GCVS database (Samus et al., 2012) was described as variable by Wachmann (1963). The times minima according Kreiner et al. (2000), were determined in two sets of observations: 26 photographic time minima were found by Wachmann from 1948 to 1960 and 2 photoelectric ones by Agerer in 1993 and 1997. The depths of primary and secondary minima in V-band were noted as $0^m.2$ and $0^m.1$. Positions of time minima on the $O - C$ diagram of the star in the Atlas are random.

Brancewicz & Dworak (1980) included V841 Cyg into their “A catalogue of parameters for eclipsing binaries” and determined the parameters of the system, including the type of variability as β Lyr and specter as A5. In 1994 V841 Cyg was included in a List of Near Contact Binaries (NCB), a new subclass of close binary systems defined by Shaw (1994). NCB systems have periods of less than a day, exhibit the effects of tidal interaction, and have facing surfaces less than 0.1 orbital radius apart, but are not in contact. Such systems may be the evolutionary precursors to the A-type W UMa systems, and are probably in the early stages of mass transfer.

We initiated a new study of V841 Cyg system in order to obtain and to analyze light curve, as well as to find additional times of light minima for the in-

Table 1: The reference stars for V841 Cyg frame.

N	RA_{J2000}	Dec_{J2000}	TASS 4	V	SD
1	$19^h 22^m 17^s .70$	$+28^\circ 42' 13'' .8$	1788884	$12^m .658$	$0^m .154$
2	19 22 12.06	+28 41 20.0	3488546	12.973	0.091
3	19 22 06.97	+28 40 06.0	1788858	10.268	0.163
4	19 22 11.78	+28 39 13.4	1788868	13.021	0.202
5	19 21 51.40	+28 40 03.8	1788805	11.434	0.095

tent being to clarify the nature of its period variability.

2. Observations

The observational data were obtained using the 70-cm telescope ZTS-702 of AOK, equipped with a SBIG ST-7 camera in an instrumental photometric system closely approximating the standard V-band. The focal length of the telescope is 2.804 m and CCD-frame corresponds to $5' \times 8'$ sky area. V841 Cyg was observed on 8 nights in July 2013. Frames were taken with 30 sec exposure time, S/N ratio for variable was in limits 17 – 20. The standard reduction included dark signal and flat field correction was executed for all 719 frames. Barycentric Julian Dates (HJD) were calculated using Eastman et al. (2010) code.

We used TASS Mark IV photometric catalog, version 2 (Droege et al., 2007) for reference stars search. The positions of variable and reference stars are shown in Fig. 1; information from TASS Mark IV is placed in the Table 1. Note the 3rd star in V 841 frame (TASS Mark IV 1788858) was not reference one. It is semi-regular pulsating star V840 Cyg according GCVS (Samus et al., 2012). Its brightness diminished by $0^m .16$ from JD 2456493.46 to JD 2456513.38.

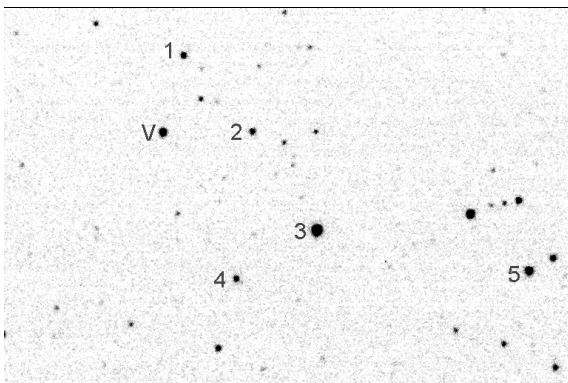


Figure 1: The reference stars in V 841 Cyg frame.

The reduction of the CCD frames was carried out using the MUNIPACK software (Motl, 2003-2012). The method of aperture photometry was used. The MU-

NIPACK software allows to determine the difference in magnitudes between comparison, control and variable stars. We assumed equal air mass for all stars in our small frames. The background has been estimated from neighboring pixels. The SD for individual relative magnitudes was not worse $0^m .040$.

The season light curve of V841 Cyg for 2 periods is shown in Fig. 2a by open circles. The magnitudes as $m_{var} - m_c$ were phased using an existing ephemeris (Kreiner et al., 2000), namely:

$$HJD_I = 2434629.425 + 0.76113618 \cdot E \quad (1)$$

where E is the number of elapsed cycles.

The light curve allows as to determine the depths of primary and secondary minima, the new minima times and to reconstruction of the system.

3. Light curve analyze

The depths of minima on our phase curve are different from Kreiner et al.(2000) data - it is clearly seen in the Fig. 2a. We supposed the difference is connected with the some feature near the primary minimum of V841 Cyg. The part of light curve near the primary minimum is detailed in lower panel of Fig. 2. Our light curve with error bars is placed in Fig. 2b, the individual light curve in absolute magnitudes, obtained by Ogmen (2009), is shown in Fig. 2c. Our light curve has practically horizontal parts in phases $\pm(0.1-0.16)$. Ogmen data are in agreement with our results. It is possible, the understated value of depths connected with comparison of this part of light curve, not with maximal value of flux. The difference is about $0^m .12$.

From analyze of V841 Cyg light curve we obtained $\Delta m_I = 0^m .53$, $\Delta m_{II} = 0^m .20$ and new time minima $HJD_I = 2456504.48122$, $HJD_{II} = 2456493.44562$.

We modelled the light curve for V841 Cyg using Binary Maker 3 along with reasonable estimates for the properties of the two components. The spectral class A5 and mass ratio 0.74 according to paper Brancewicz & Dworak (1980) was used as first approach. An initial effective temperature for the primary was established according its spectral class as 8700K. The spectral type and temperature of the fainter star in V841 Cyg

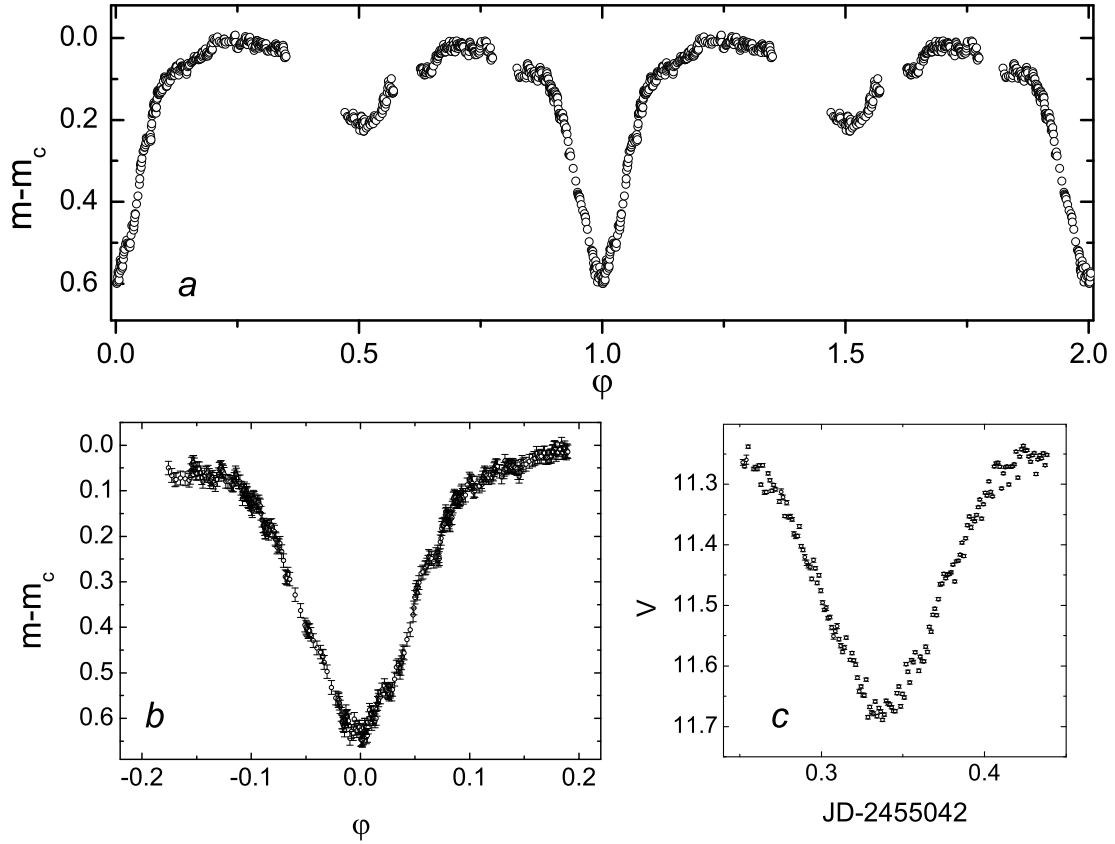


Figure 2: The light curve of V841 Cyg (a) and features of magnitudes variations in primary eclipse according our measurements (b) and Ogmen (2009) observations (c). Error bars for magnitudes are shown on lower panel.

system can be established through analysis of the light curve.

The final solution was chosen in model grids calculated with steps: 0.01 in mass ratio and Ω -potentials, 50K in temperature and 0.25° in inclination. The best solution implies $T_{effI} = 8550K$ and $T_{effII} = 5500K$, the temperatures corresponding to A6 and G5 spectral classes. The linear limb darkening coefficients were assumed according to van Hamme (1993) as 0.598 for primary and 0.851 for secondary taking into consideration the final temperatures. A mass of $M_I = 1.85M_\odot$ was adopted for the primary from its main-sequence spectral type, and the eclipse solution yielded a reasonably well-defined mass ratio of $M_{II}/M_I = 0.49$. The resulting implied secondary mass of $M_{II} = 0.90M_\odot$ is, in fact, the value expected for a G4 – G6 dwarf, apparently confirming the eclipse solution. The mass ratio for eclipsing systems is difficult to establish without radial velocity information, so, our solution we can

assume as estimated.

The Ω -potentials estimated as 3.02 and 3.12 determine the fillout parameter f . Binary Maker 3 used the parameter f defined following Lucy & Wilson (1979):

$$f = \frac{\Omega_{inner}}{\Omega} - 1 \quad (2)$$

where Ω_{inner} is inner critical surface potential and Ω is surface potential of the component.

The fillout parameter represents the percentage that the surface potential of the binary component lies outside the inner critical surface. It is positive for component bigger its Roche lobe. In case V841 Cyg we found $f_I = -0.05$, $f_{II} = -0.08$. So, the system is NCB, however the mass transfer in the system is not significant.

Using the period and mass sum we calculated the major semiaxis of system: $0.023 a.u.$ or $5.0R_\odot$. Ω -

potentials determined by Binary Maker 3 correspond to component radii 0.43 and 0.28 of the major semiaxis. So, we obtained the acceptable radii of stars as $2.1R_{\odot}$ and $1.4R_{\odot}$. The radii note to Main Sequence stars.

The light curve solution for the system is illustrated in Fig. 3, the system reconstruction on phase 0.25 in Fig. 4. Both eclipses are partial and inclination of system is 77.5° . Both primary and secondary are deformed by mutual gravity.

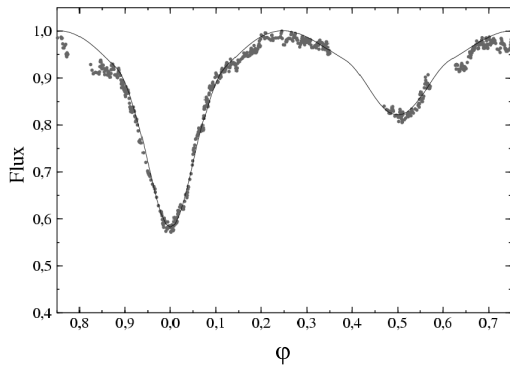


Figure 3: The light curve solution for V841 Cyg. Observational data are marked as gray dots, our final solution curve is black line.

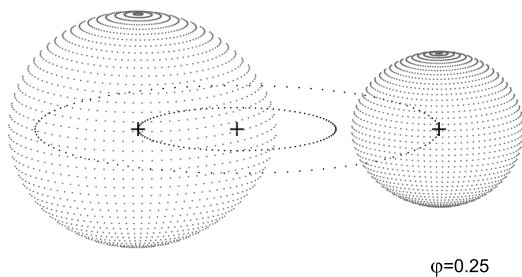


Figure 4: The view of reconstructed V841 Cyg system in phase 0.25.

According “All-sky spectrally matched Tycho 2” catalogue (Pickles & Depagne, 2010) V841 Cyg is F5 V star with weak metal lines, and its magnitude $V=11^m.534 \pm 0^m.098$. We did not find the satisfactory solution for light curve with beginning temperature of primary star corresponded to F5 V spectrum. Our light curve solution for parameters of V841 Cyg is different of Brancewicz & Dworak (1980) catalogue, mainly for secondary component. Binary Maker 3 for their parameters constructed synthetic light curve, which is noticeably different from observed one.

4. $O - C$ variations.

Project B.R.N.O. of Brno Observatory (Czech Astronomical Society) was crated in traditional for the Observatory field: observing eclipsing binaries. The part the project named “ $O - C$ Gateway” (administrator A. Paschke) collects the time minima for considerable quantity of eclipsing systems in the B.R.N.O. database, particularly it contains 45 records for V841 Cyg. The variable was attributed in the database as EB/KE (β -Lyrae contact system) with comment “deprecated”.

The B.R.N.O. database used modified ephemeris:

$$HJD_I = 2434629.43 + 0.76113617 \cdot E \quad (3)$$

where E is the number of elapsed cycles.

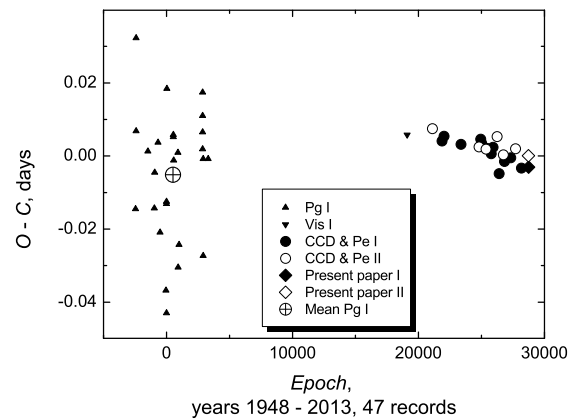


Figure 5: $O - C$ diagram for V841 Cyg. Mean value for photographic minima is noted additionally.

We calculated the $O - C$ values for out time minima using B.R.N.O. database modified ephemeris and compared the results with “ $O - C$ Gateway” data. Common $O - C$ diagram is shows in Fig. 5. On left part of Fig. 5 only photographic data present. The scattering of these $O - C$ variations too big in comparison with photoelectric and CCD observations, which were beginning in 1993 year. The possible trend of $O - C$ values for all time minima can’t be analyzed with sufficient accuracy. Mean value of photographic time minima excludes line trend and note to possible period decrease corresponding to mass transfer form primary to secondary. We assumed the absence of intensive mass transfer according our V841 Cyg system parameters. Possible trend in $O - C$ variations during two last decades are small and confirm our solution.

5. Conclusion.

From analyze of light curve, obtained in AOK (Nikolaev), we obtained the parameters of the eclipsing binary system V841 Cyg. It contains form A6 V+G5 V stars with mass ratio about 0.49. The components have estimated masses $M_I = 1.85$, $M_{II} = 0.90$ and temperatures $T_{effI} = 8550^\circ$, $T_{effII} = 5500^\circ$; they fill own Roshe lobes on 95% and 92% correspondingly and both components are deformed. The distance between components is about $5R_\odot$, the distance between component surfaces is about $1.4R_\odot$.

The depths of light minima in V-band are $0^m.53$ and $0^m.20$. We found new time minima: $HJD_I = 2456504.48122$, $HJD_{II} = 2456493.44562$. We confirm the V841 Cyg classification as is NCB system, with not significant mass transfer.

Acknowledgements. This research has made use of NASA's Astrophysics Data System. We used information from *O - C* Gateway in the research. This research has made use of the SIMBAD database, operated at CDS, Strasbourg, France. E. Panko is thankful to professor D. Turner and Saint Mary's University, Halifax, Canada for support of this research.

References

- Agerer F. & Huebscher J.: 1998, *IBVS*, **4606**, 1.
 Agerer F. & Huebscher J.: 2001, *IBVS*, **5016**, 1.
 Brancewicz H.K., Dworak T.Z.: 1980, *Acta Astr.*, **30**, 501.
 Eastman J., Siverd R., Gaudi B.S.: 2010, *Publ. Astron. Soc. Pac.*, **122**, 935.
 Droege T.F., Richmond M.W., Sallman M.P. et. al.: 2006, *Publ. Astron. Soc. Pac.*, **118**, 1666, on-line data: <http://spiff.rit.edu/tass/patches/>
 Kreiner J.M., Kim C.H., Nha L.S. et al.: 2000, "An Atlas of Diagrams of Eclipsing Binary Stars", Krakow, Poland, on-line data: <http://www.as.up.krakow.pl/o-c/index.php3>
 Motl D.: 2003-12, <http://c-munipack.sourceforge.net>
 Lucy L.B. & Wilson R.E.: 1979, *ApJ*, **231**, 502.
O-C gateway, on-line data: <http://var.astro.cz/ocgate/ocgate.php?star=V%20841%20Cyg>
 Ogmen Y.: 2009, http://www.aavso.org/apps/web_obs/results/?star=V841+CYG
 Panko E., Flin P., Pikhun A.: 2006, *ApSS*, **305**, 385.
 Pickles A., Depagne E.: 2010, *Publ. Astron. Soc. Pac.* **122**, 1437.
 Samus N.N., Durlevich O.V., Kazarovets E.V. et al.: 2012, *General Catalog of Variable Stars, GCVS (GCVS database)*, Version 2012 Feb., <http://www.sai.msu.su/groups/cluster/gcvs/gcvs/iii/html/>.
 Shaw J.S.: 1994, *Mem. Soc. Astr. It.*, **65**, 95.
 Turner D.G., Panko E.A., Sergienko O.G. et al.: 2008, *The Observatory*, **128**, 2.
 van Hamme W.: 1993, *AJ*, **106**, 2096.
 Variable Star and Exoplanet Section of Czech Astronomical Society: <http://var2.astro.cz/>
 Virnina N.A., Panko E.A., Sergienko O.G. et al.: 2010, *OAP*, **23**, 148.
 Wachmann A.A.: 1963, *Astron. Abh. Hamburg. Sternw.*, **6**, 97.

THE IONIZED GAS AROUND STARFORMING GALAXIES

E.O. Vasiliev¹, M.V. Ryabova², Yu.A. Shchekinov²

¹Institute of Physics, Southern Federal University, Stachki Ave. 194,
Rostov-on-Don, 344090 Russia, *eugstar@mail.ru*

²Department of Physics, Southern Federal University, Sorge 5,
Rostov-on-Don, 344090 Russia

ABSTRACT. We consider the evolution of metal-enriched gas exposed to a superposition of time-dependent radiation field of a nearby starburst galaxy and nearly invariant (on timescales 100 Myr) extragalactic ionization background. We study the evolution of ionic species (particularly those commonly observed in galactic circumference) depending on the galactic mass and star formation rate, and derive conditions for the highly ionized oxygen, OVI, to appear in extended galactic haloes in absorption or emission spectra. We have found that the maximum OVI fraction can reach $\sim 0.4 - 0.6$ under the action of both ionizing radiation field, which is typical in haloes of starforming galaxies, and the extragalactic background, the fraction remains high in a wide temperature range. We have shown that the OVI fraction is high enough that *even* for $\sim 0.1Z_{\odot}$ metallicity we can explain large OVI column densities ($\log[N(\text{OVI}), \text{cm}^{-2}] \sim 14.5 - 15.3$) observed in the haloes of starforming galaxies by Tumlinson et al. (2011). Thus, the requirements to the sources of oxygen supply into the extended haloes become reasonably conservative.

Key words: galaxies: evolution – haloes – starburst – theory – diffuse radiation – intergalactic medium – quasars: general – absorption lines – physical data and processes: atomic processes

1. Introduction

Huge (up to 150 kpc) halos of ionized gas in star-forming galaxies contain a substantial mass of metals and gas (Tumlinson et al., 2011). OVI is a fragile ionic state in the sense that under standard assumptions of thermal ionization its fraction never exceeds ~ 0.2 and such a high value is reached only in a narrow temperature range (Gnat & Sternberg 2007). Then, conservative estimates of a typical circumgalactic gaseous mass force to assume solar metallicity for gas extending up to 150 kpc in the halos of star-forming galaxies.

Here we study the evolution of ionic composition of a gas in the halos of star-forming galaxies taking into

account starformation history.

2. The model and initial conditions

Our model includes the following ingredients

- the ionization and thermal evolution of gas (in a lagrangian element): nonequilibrium (time-dependent) ionization kinetics for H, He, C, N, O, Ne, Mg, Si, Fe and self-consistent cooling and heating rates, in total 96 ordinary differential equations (see details in Vasiliev, 2011);
- the extragalactic spectrum: Haardt & Madau (2001) spectra for 49 redshifts;
- the UV galactic spectrum was calculated using the PEGASE code (Fioc & Rocca-Volmerange 1997);
- the X-ray galactic spectrum calculated using the “ $L_X - SFR$ ” relation (Gilfanov et al., 2004);
- a power-law starformation rate (SFR): $SFR(t) = M_g^{p_1}/p_2$, where M_g is the galactic gaseous mass and $p_1 = 2$;
- the galactic halo gas exposed to the cumulative galactic and extragalactic ionizing radiation, the galactic part of the spectrum being attenuated by the underlying neutral gas: $\tau_{\nu} = \sigma_{\nu}^{\text{HI}}N_{\text{HI}} + \sigma_{\nu}^{\text{HeI}}N_{\text{HeI}}$, where $N_{\text{HI}} = 10^{20} \text{ cm}^{-2}$, $N_{\text{HeI}} = 10^{19} \text{ cm}^{-2}$ are assumed.

3. The initial conditions

We consider a gas in outer halo of massive starforming galaxies with stellar mass several $\times 10^{10} M_{\odot}$. So that these galaxies are similar to the Milky Way. According to the recent simulations of the Milky Way galactic halo the number density of a gas in the the Galactic halo is found to range within $\sim (0.5 - 2) \times 10^{-4} \text{ cm}^{-3}$ at distances $\sim 50 - 300 \text{ kpc}$ (Feldmann et al., 2013). The observational estimates of the circumgalactic gas density give $\sim (1 - 3) \times 10^{-4} \text{ cm}^{-3}$ at $r \sim 40 - 150 \text{ kpc}$ (e.g. Anderson & Bregman 2010). So that in our calculations we adopt $n = 10^{-4} \text{ cm}^{-3}$ for the number density of the circumgalactic gas.

We start our calculation at $z = 2$ (the lookback time is ~ 10 Gyrs). At first, this timescale is about cooling time for hot gas with $T \sim 10^6$ K and $\sim (0.5 - 2) \times 10^{-4}$ cm $^{-3}$ (Feldmann et al., 2013). At second, the last major merging for the Milky Way type galaxies is thought to be earlier than $z \sim 2$ (Hammer et al., 2007).

The initial ionic composition and temperature are set to the ones corresponding to photoequilibrium in a gas exposed to the extragalactic Haardt & Madau spectrum at $z = 2$. This radiation background is sufficiently high to force such low density gas into photoequilibrium (Vasiliev 2011). But one should note that the time of calculation is long enough compared to the relaxation scale of the ionization and thermal evolution of a gas exposed to the time-dependent spectrum adopted here.

We study the evolution of a gas with metallicity ranged from 10^{-2} to $0.1 Z_{\odot}$. Higher metallicity is expected to be overestimation, the lower limit is corresponded to the upper limit of the IGM metallicity at $z \sim 2 - 3$ (e.g., D’Odorico et al., 2010).

4. Results

From the chemical evolution models calculated using the PEGASE code we obtain the time-dependent SFR, stellar mass, metallicity of a gas and spectral luminosity. We assume the initial gaseous mass is $M_g^i = 10^{11} M_{\odot}$. Here we consider two models with different parameter p_2 : 3×10^4 Myr M_{\odot}^{-1} – model A, and 5×10^3 Myr M_{\odot}^{-1} – model C. Gas in model C is almost converted into stars up to ~ 10 Gyr, whereas the galaxy in model A still remains gas-rich one: only ~ 10 % of gaseous mass goes into stars. In model A the SFR (absolute) is nearly constant at $\sim 6 M_{\odot}/\text{yr}$ during first 200 Myr afterwards decreases down to $\sim 0.6 M_{\odot}/\text{yr}$ at 10 Gyr. The corresponding values of SFR in model C are about 7 times higher, but the timescale, where the rate is constant, is shorter, ~ 50 Myr. Thus, the rates in both models remain still high at $\sim 5 - 10$ Gyr (redshifts $z \sim 0.5 - 0$) to consider such galaxies as star-forming ones (Schiminovich et al., 2007).

Figure 1 presents the galactic spectral luminosity at $t = 7.5$ Gyr (that corresponds the time elapsed from $z = 2$ to 0.2) is shown by dash-dotted line (the right axis). One can note a significant break at 91 \AA , this value corresponds to the minimum wavelength in the spectrum obtained in the PEGASE code. This value is reasonable because of the exponential decrease of number of such hard photons emitted by stellar population (see e.g. Rauch 2003). Figure 1 demonstrates an example of the total spectral distribution: the cumulative ionizing background flux (thick grey line) at $z = 0.2$ and distance $d = 100$ kpc from the galaxy. The total spectrum consists of the galactic (dash line) and extragalactic (dotted line) ionizing backgrounds. The

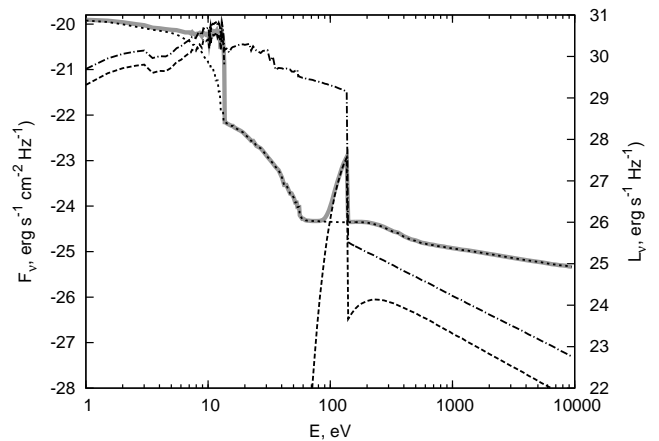


Figure 1: The cumulative ionizing background flux (thick grey line) at $z = 0.2$ and a distance from the galaxy $d = 100$ kpc, which consists of the UV and X-ray galactic spectrum, attenuated by galactic neutral gas (dash line), the extragalactic ionizing background (dotted line). The galactic spectral luminosity is shown by dash-dotted line (the right axis).

strong absorption of the galactic photons within energy range, $E \sim 13.6 - 90$ eV, in the galactic disk leads to the control of ionic composition by the extragalactic background. To estimate a significance of the absorption one can see the galactic spectral luminosity (see the right axis). Note that there is a bump around $E \sim 90 - 136$ eV, because not all photons emitted by galactic stellar population are absorbed in the disk. Certainly, this is due to our choice of the neutral column densities N_{HI} and N_{HeI} in the disk. In case of the higher column densities the amplitude of the bump decreases. Also the decrease is taken place at large distances from the galaxy, where the extragalactic radiation is dominant. Note that in the range $E \sim 90 - 136$ eV there is the OV ionization potential, $I_{\text{OV}} = 113.9$ eV. So that the excess of such photons is expected to change the ionization kinetics of oxygen and may lead to higher OVI fraction.

Figure 2 shows the evolution of OVI fraction in a gas located at different distances from the galactic center. Because of high flux of ionizing radiation at $z \sim 2$ oxygen is mainly locked in the OVII state. The decrease of the ionizing flux with redshift or/and due to decrease of SFR leads to the OVII recombination and growth of the OVI fraction. Actually, after $\sim 1 - 2$ Gyr because the SFR goes down in $\sim 3 - 4$ times compared to the initial value, galactic luminosity decreases, so that the transition from OVII to OVI becomes faster. Under the standard conditions the OVI state is fragile and further recombination leads to lower ionic states. However, the excess of photons with $E > I_{\text{OV}} = 113.9$ eV emitted by starforming galaxies does not allow to develop recom-

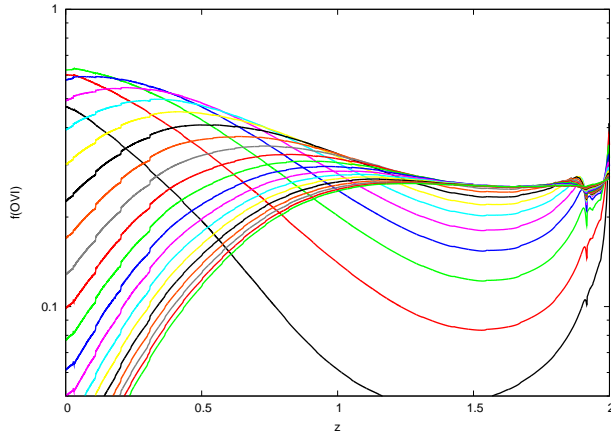


Figure 2: OVI fraction evolution of gas at different distances from the galactic center (the distances vary from 50 to 250 kpc with step 10 kpc from bottom line)

bination so efficiently: it is almost frozen out at OVI. In our models the OVI fraction reaches $\sim 0.4 - 0.6$ in a gas with metallicity $0.1 Z_{\odot}$. This results in a factor of 2-3 more conservative estimate of the oxygen mass in haloes compared to $M_O = 1.2 \times 10^7 (0.2/f_{OVI}) M_{\odot}$ (Tumlinson et al., 2011). Thus, the OVI fraction is higher than that in the standard (photo-)equilibrium case, where the maximum OVI fraction is $\sim 0.1 - 0.2$ (e.g., Gnat & Sternberg 2007).

Figure 3 presents the dependence of the OVI column density on the impact parameter assuming 1/10 of solar metallicity gas exposed to the ionizing background evolved as in models A and C (small symbols near right axis, types of symbols correspond to different redshifts). For $0.1 Z_{\odot}$ the OVI column density ranges in $\log[N(\text{OVI}), \text{cm}^{-2}] \sim 14.3 - 15.3$ at impact parameter $b < 150$ kpc, that exhibits a good coincidence with the observational data obtained by Tumlinson et al. (2011). Higher OVI fraction obtained in our model leads to more conservative estimate of the oxygen mass in haloes, and consequently weaker constrains on the sources of oxygen.

5. Conclusions

With minimum assumptions we have found physical conditions (density, metallicity of gas, the spectrum shape) under which the OVI fraction can reach ~ 0.6 .

Using the PEGASE code we have calculated chemical and spectro-photometric evolution of galaxies, and have chosen two of the models whose sSFR and stellar masses are close to the star-forming galaxies with large OVI column densities (Tumlinson et al., 2011).

We have found that OVI column densities range in $\log[N(\text{OVI}), \text{cm}^{-2}] \sim 14.5 - 15.3$ for $0.1 Z_{\odot}$ gas, and $\sim 12.9 - 14.2$ for $0.01 Z_{\odot}$ gas at impact parameters

up to < 150 kpc. This results in a factor of 2-3 more conservative estimate of the oxygen mass in haloes compared to $M_O = 1.2 \times 10^7 (0.2/f_{OVI}) M_{\odot}$ (Tumlinson et al., 2011).

Acknowledgements. This work is supported by the RFBR through the grants 12-02-00365, 12-02-00917, 12-02-92704, and by the Ministry of education and science of Russian Federation (state contracts 14.A18.21.1304, 2.5641.2011, 14.18.21.1179). EV is grateful for support from the "Dynasty" foundation.

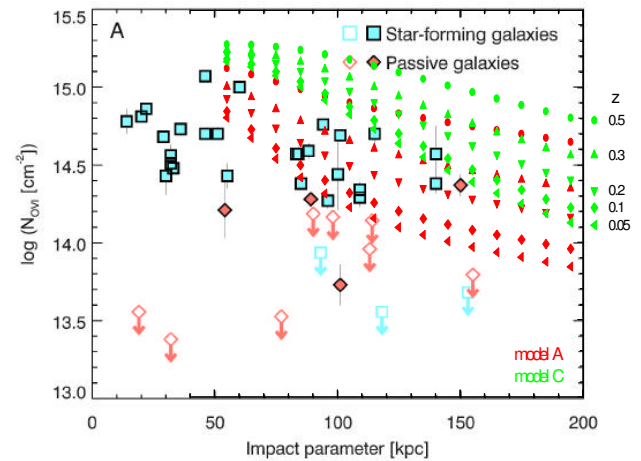


Figure 3: The dependence of the OVI column density on the impact parameter. The filled red and green symbols correspond to models A and C. Different type of symbols show the column densities for several redshift z (depicted near the right axis). The metallicity of gas is $0.1 Z_{\odot}$. The underlying picture is taken from the paper by Tumlinson et al. (2011).

References

- Anderson M.E., Bregman J.N.: 2010, *ApJ*, **714**, 320.
 D'Odorico V., Calura F., Cristiani S., Viel M.: 2010, *MNRAS*, **401**, 2715.
 Fioc M., Rocca-Volmerange B.: 1997, *A&A*, **326**, 950.
 Gilfanov M., Grimm H.-J., Sunyaev R., 2004, *MNRAS*, **347**, L57.
 Gnat O., Sternberg A.: 2007, *ApJS*, **168**, 213.
 Haardt F., Madau P.: 2001, in *Clusters of Galaxies and the High Redshift Universe Observed in X-rays*, ed. D.M.Neumann & J.T.V.Tran
 Hammer F., Puech M., Chemin L. et al.: 2007, *ApJ*, **662**, 322.
 Rauch T.: 2003, *A&A*, **403**, 709.
 Schiminovich D. et al.: 2007, *ApJSS*, **173**, 315.
 Tumlinson J. et al.: 2011, *Science*, **334**, 948.
 Vasiliev E.O.: 2011, *MNRAS*, **414**, 3145.

Subsection Virtual observatories are practice of application

FLATBED SCANNERS IN GOLOSIIV PLATE ARCHIVE DIGITIZATION

V.Andruk, L.Pakuliak

Main Astronomical Observatory NAS of Ukraine, Kyiv, Ukraine

pakuliak@mao.kiev.ua

ABSTRACT. The problems associated with the application of budget flatbed scanners to digitize astronegatives are discussed.

Key words: digital archive, scanner, image processing

The key moment of Ukrainian Virtual Observatory project currently running in Ukraine is the digitizing of glass photographic archives with a total number of plates above 300 thousand. Vast collections of stored astronomical images require the development of tools for their fast, robust calibration, vetting, search and retrieval. Recent years many observatories in the world have used flatbed scanners as the digitizers for their glass collections. But until this moment, the quality of digitizing with commercial scanners causes many questions. Nevertheless, flatbed scanners remain the most available appliances for relatively rapid archive digitizing and application of the proper scan procedure and proper algorithms of a digitized image processing provide the best accuracy, which could be achieved for given appliance and given observational material (Pakuliak et al., 2012; Vavilova et al., 2012a, 2012b, 2011, 2010).

Since 2008, the process of MAO NASU archive plates digitizing and inclusion of plate preview images into GPA database has been under way, using two models of flatbed scanners. It started with Microtek ScanMaker 9800XL TMA and now has been continued with Epson Expression 10000XL. Digitizing is carried out in two modes: a) with high resolution of 1200 dpi, dynamic range of 16 bits and two scans for every plate for current cataloging and b) with lower resolution or lower dynamic range and only one scan with the aim of fast online visualization.

The database with metadata of plates is allocated on the computational resources of MAO. The results of digitizing are immediately registered into the database with plate metadata and after the uploading to its server storage place become available for search and browsing on the pages of DBGPA (<http://gua.db.ukr-vo.org>). To date we digitized a set of about 1 thousand plates with Microtek ScanMaker and more than 5 thousand plates with Epson Expression (of GPA 26 thousands plates in total). The result of their comparison shows a somewhat better accuracy for Epson Expression 10000XL vs Microtek ScanMaker 9800XL TMA (Table 1).

R.m.s. errors before the correction for scanner instrumental errors are $\pm 0.173''$ and $\pm 0.303''$ for RA, $\pm 1.141''$ and $\pm 1.941''$ for DEC for Epson and Microtek correspondingly. The ultimate accuracy is of $\pm 0.106''$ and $\pm 0.156''$ for RA, of $\pm 0.110''$ and $\pm 0.153''$ for DEC (Epson and Microtek correspondingly). It follows that internal instrumental errors for Epson Expression 10000XL can be excluded from pixel coordinates more accurately than those of Microtek without application of any specific appliances but using only the digital data of the plate itself. So this model of a flatbed scanner is used for both types of images as it allows accounting the systematic errors more accurately, and Microtek SkanMaker 9800XL is used for the preview images only.

Table 1. Comparison of accuracies, achieved for two models of scanners, used for digitizing of astronegatives

Resolution	900 dpi	1200 dpi	1600dpi
Epson Expression 10000XL			
N of stars	6056	8235	6134
$\sigma_{RA,arcsec}$	± 0.62	± 0.49	± 0.41
$\sigma_{DE,arcsec}$	± 0.63	± 0.54	± 0.46
$\sigma_{m,mag}$	± 0.24	± 0.22	± 0.22
Microtek ScanMaker 9800 TMA			
N of stars	10421	9717	6473
$\sigma_{RA,arcsec}$	± 0.90	± 0.78	± 0.63
$\sigma_{DE,arcsec}$	± 1.18	± 1.07	± 0.98
$\sigma_{m,mag}$	± 0.40	± 0.35	± 0.36

References

- Pakuliak, L., Kazantseva, L., Virun, N., Andruk, V.: 2012, *IAUS*, 285, 389.
- Vavilova, I. B.; Pakuliak, L. K.; Protsyuk, Yu. I. et al: 2012, *Baltic Astronomy*, 21, 356-365.
- Vavilova, I. B., Pakuliak, L. K., Shlyapnikov, A. A. et al.: 2012, *Kinematics and Physics of Celestial Bodies*, 28, 85-102.
- Vavilova, I. B., Pakuliak, L. K., Protsyuk, Yu. I. et al.: 2011, *Kosmichna Nauka i Tekhnologiya*, 17, 74-91.
- Vavilova, I. B., Pakuliak, L. K., Protsyuk, Yu. I.: 2010, *Kosmichna Nauka i Tekhnologiya*, 16, 62-70.

INTERACTIVE POSSIBILITY OF WORKING WITH A DIGITAL VERSION OF THE JOURNAL "IZVESTIA OF THE CRAO"

N. Bondar¹, M. Gorbunov², A. Shlyapnikov³

SRI "Crimean Astrophysical Observatory" of T. Shevchenko KNU
Nauchny, Crimea, Ukraine

¹ bondar@crao.crimea.ua, ² mag@crao.crimea.ua, ³ aas@crao.crimea.ua

ABSTRACT. The main problem that arises when working with a scanned version of any published scientific journal related to the presentation of digital information displayed. In this paper, we consider the statistics, which represents the journal "Izvestia of the Crimean Astrophysical Observatory" in the SAO/NASA ADS. As the example of articles from the print version of the journal we consider the possibility to access the world's astronomical databases for obtaining additional information about the investigated objects. We describe briefly on-line virtual applications for the graphical information display.

Key words: database, virtual observatory, e-library

1. Introduction

Since the establishment of the "Izvestiya of the Crimean Astrophysical Observatory" journal (CrAO) in 1947, the 108 volumes have been printed, including original articles and 13 volumes of conferences materials which were held at the CrAO. Starting with the volume 99, the archive of "Izvestiya CrAO" in PDF format is available on the website of the National Library of Ukraine (<http://archive.nbuv.gov.ua/portal/natural/IKAO>). Access to the content of all volumes, including the conference proceedings, is provided in PDF format on the website of the CrAO (<http://crao.crimea.ua>).

For ensure remote work with the information published in "Izvestiya CrAO", it is needed online access to the original articles. The most representative astronomical publication's database is a portal of digital library of the Smithsonian Astrophysical Observatory, supported by grants from NASA (SAO/NASA Astrophysics Data System - ADS) (<http://adsabs.harvard.edu/index.html>). Till mid-2013 the ADS search system provided a gateway to the information on 1,283 articles published in the "Izvestiya CrAO". Here we look at the completeness of presentation of this journal in ADS, taking into account that 99 volumes are available on-line.

The histograms shown in Figure 1, illustrate the number of publications per the number of volumes presented in ADS. Note that during the last six years (Shlyapnikov, 2007), the number of links to the "Izvestiya CrAO" has enlarged by 406 publications; however, it is only 57% of the entire list of publications. The main suppliers of information for ADS are as follows: a program of scientific and technical information NASA (<http://www.sti.nasa.gov/>) (609 publications); Astronomical Center of the University of Heidelberg (Germany) (<http://ari.uni-heidel>

berg.de/) (491 publications), and the Astronomical Data Center in Strasbourg (France) (<http://simbad.u-strasbg.fr/Simbad>) (136 publications). The interest of various organizations to this journal is due to the information contained in the articles, including the observational results. However, the main problem is still unavailability to access original publications and, in some cases, their abstracts. So, to improve this situation, we have undertaken a work on the digitization of articles in the "Izvestia CrAO".

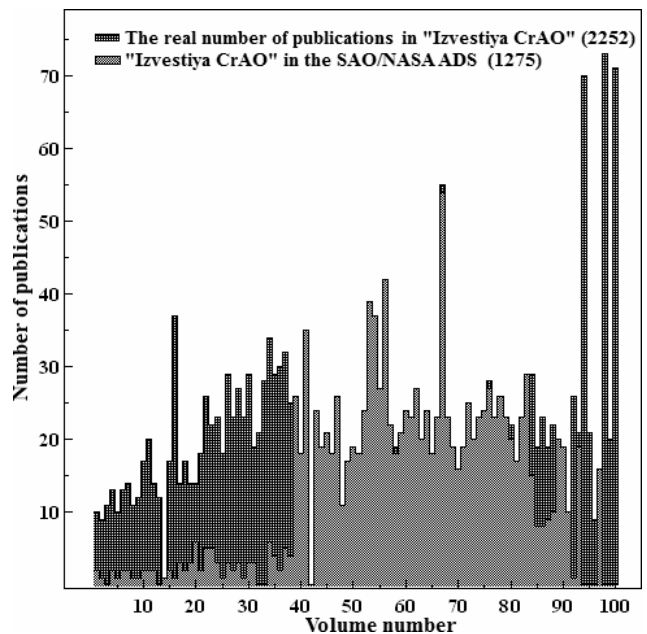


Figure 1: Number of publications in the original edition of "Izvestiya CrAO" and as they are represented in ADS

2. "Izvestiya CrAO": digital version

2.1. Scan and presenting of journals

Working on a digitized version of "Izvestiya CrAO" we understood that it should be in the formats similar to the representation of articles in the ADS. Figure 2 illustrates a simplified HTML version of the paper by Bondar (2001) containing thumbnails of pages in JPG format (size ~ 4 kB) as the example for general viewing and navigating in our article, and a full-scale GIF image (size ~ 100 kB), designed for reading and printing. The page is scanned and saved in GIF format in 8-color palette for the smooth transfer of polygraphic text and print quality.

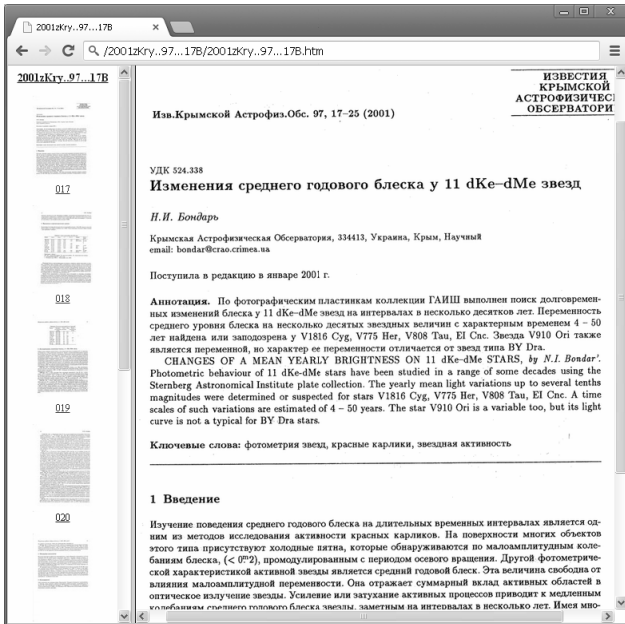


Figure 2: The version of the submission article of "Izvestiya CrAO" in a format similar to ADS

The main disadvantage of this submitting articles is impossibility to transfer it to another data sources and to use tools for work with the published information without further modification of HTML code.

When we convert the scanned article in PDF format we have a more opportunities for its interactive use. In figure 3 a fragment of Table 1 from paper by Bondar (2001) is shown, where hyperlinks to the object to the database SIMBAD in the second information layer in the main text of the printed version were added. This provides access to bibliographies in ADS and other resources of the Astronomical Data Center in Strasbourg.

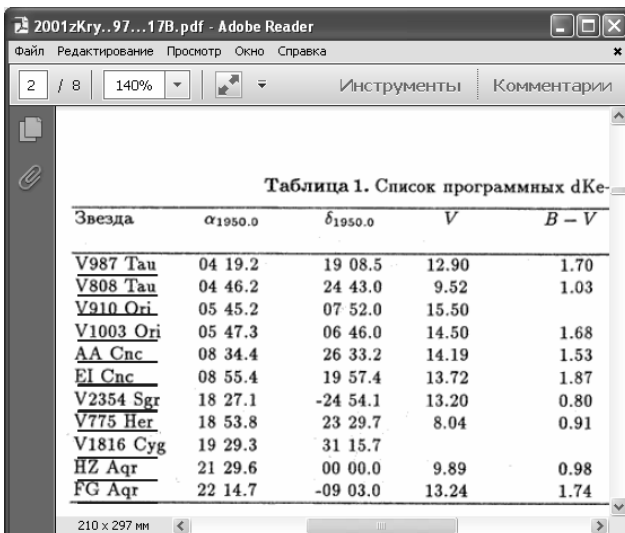


Figure 3: Fragment of articles from "Izvestiya CrAO" in PDF format with links to the SIMBAD database

Obviously, the best option for providing information published in the "Izvestiya CrAO" would be a digital version. However, the procedure for recognition of text and

further edition is a quite time-consuming and not always justified process.

2.2. Abstracts and tables

The first priority in creating a digital version of "Izvestiya CrAO" is the addition of ADS titles of missing articles in order to eliminate discrepancies between the actual numbers of publications and those that are presented in the ADS (see Figure 1). The next step is to add abstracts. For many journals published in the last century, as we see, the ADS provides the scanned abstracts, which simplify the process of adding abstracts of "Izvestiya CrAO". However, the most important information that enables communication with ADS and SIMBAD, must be submitted in digital format. First of all, we say about the list of celestial objects, which were described or presented in articles. We should take into account that astronomical articles contain references to stars with letters of the Greek alphabet as well as specific catalogue identifiers for stars and extragalactic sources. So, we need to put the names of the objects from their basic designations in SIMBAD. The HTML page with a list of objects that are discussed in this article, make it easier for access to relevant digital version of "Izvestiya CrAO".

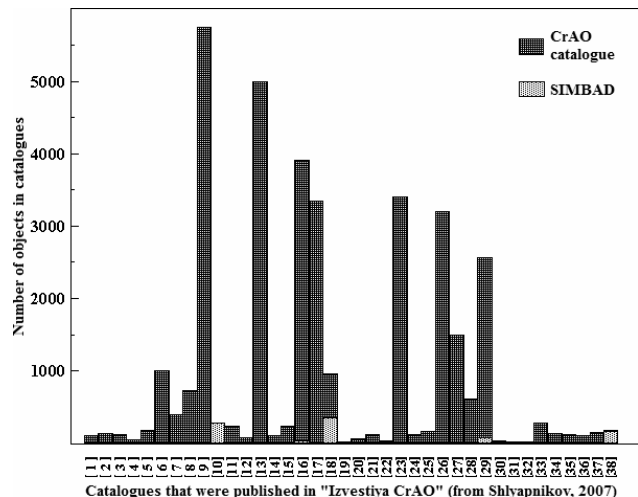


Figure 4: (see comments in text)

Figure 4 gives the example of 38 catalogues published in the "Izvestiya CrAO". It is shown how are by the number of objects in a real publications represented and how it is displayed in SIMBAD. Analysis of the histogram shows that the most of the observational data for celestial objects, obtained at the CrAO and published in catalogues in the "Izvestiya CrAO", are unknown for the world astronomical community.

The same situation with a representation of the tables in articles published in the "Izvestiya CrAO". It requires also the form of HTML pages, or IVOA formats with links to data files placed on HTML pages. The first step is the reation of digital versions of the tables or observation journals of objects, described in the articles. It will allow cross-matching the list of objects with the list published in the "Izvestiya CrAO", and searching time correlation of observations. We note also that the existence of such a list

in a format supported by the Aladin application (Bonnarel, 2000) provides access to search maps, SIMBAD, ADS, and other resources and databases.

The second and more urgent as well as time-consuming step is to represent the observed and/or modeled parameters of the objects from tables in a digital format. There may be the light curves, the data analysis of the color indices, the distribution of flux density or radial velocity in the spectra, periodic characteristics, etc. When transferring these data to digital format, they should be satisfied also to requirements of the aforementioned databases.

2.3. Figures and graphics

The illustrations in the printed version of "Izvestiya CrAO" can be a good quality after scanning process and contain clear information for their further use. The first category can be referred to the conventional illustrations without of interest for interactive use.

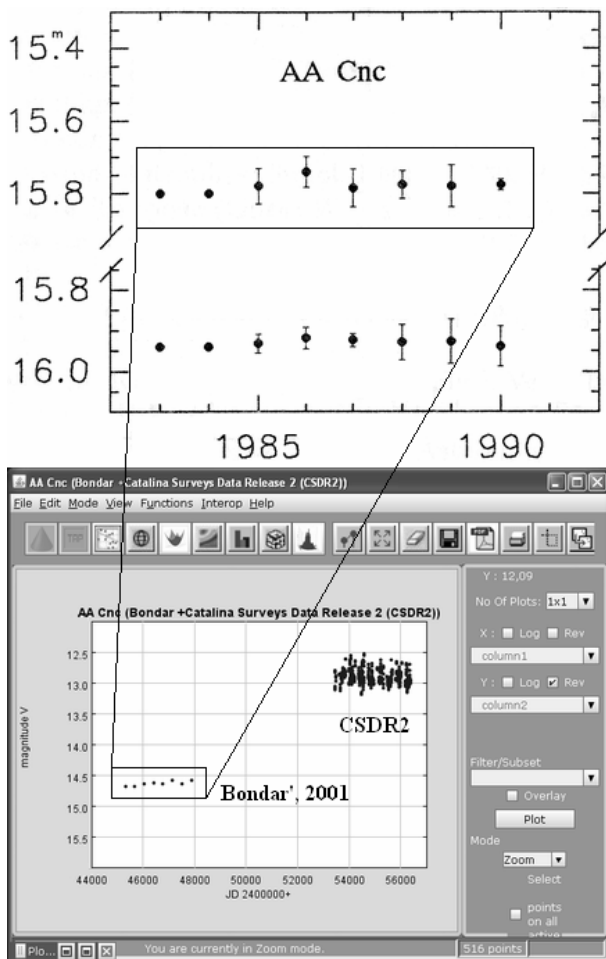


Figure 5: Observations AA Cnc according to the paper by Bondar (2001) and a review of CSDR (Drake, 2009) presented in VOPlot.

The second category may contain a finder chart for the identification of the described objects and graphics, which characterize their parameter. The finding charts are particularly relevant for the catalogues of objects that are not present in VizieR (Ochsenbein, 2000) or do not meet basic names in SIMBAD.

When such illustrations are preparing in the IVOA formats, they can be used in Aladin for identification simplicity.

Graphics, which accompany tabular information in printed articles, being converted into a digital format, allow to apply for their visualization and analysis by interactive applications tools. Figure 5 shows the light curve of AA Cnc. Top panel is the image from the original article (Figure 2, (Бондарь, 2001)); down panel is its representation in an interactive application of IVOA – Virtual Observations Plot (<http://vo.iucaa.ernet.in/~voi/voplot.htm>) with the additional data from Catalina Real-time Transient Survey (Drake, 2009).

3. Conclusion

We considered the possibility of interactive use and process of creation of the digital version of "Izvestiya CrAO", which we conduct to add the missing articles to the ADS as well as the data on observational celestial objects to the SIMBAD and other databases. They do not limit to the examples given in the article. First of all, it is needed to add the missing titles and abstracts of articles in the ADS in order to eliminate discrepancies between their actual number and available on-line. Creation of a digital version of such printed volumes of the "Izvestiya CrAO" must be accompanied by the data storage in formats that are supported by IVOA.

This work is a part of the UkrVO project (Vavilova et al., 2012a, 2012b) aimed on the support of e-libraries and heritage of the observational data, which were presented only in the printed format and are still unknown for the astronomical community.

Authors are grateful to I.B. Vavilova for her helpful comments and remarks on this article.

References

- Bondar N.I.: 2001, *Izvestiya CrAO*, **97**, 17.
- Bonnarel F. et al.: 2000, *Astron. Astrophys. Suppl.*, **143**, 33.
- Drake A.J. et al.: 2009, *Astrophys. J.*, **696**, 870.
- Ochsenbein F., Bauer P., Marcout J.: 2000, *Astron. Astrophys. Suppl.*, **143**, 23.
- Shlyapnikov A.A.: 2007, *Izvestiya CrAO*, **103/1**, 142.
- Vavilova I.B., Pakuliak L.K., Shlyapnikov A.A. et al.: 2012a, *Kinematics and Physics of Celestial Bodies*, **28**, 85-102.
- Vavilova I.B., Pakuliak L.K., Protsyuk Yu.I. et al: 2012b, *Baltic Astronomy*, **21**, 356-365.

DIGITAL ARCHIVE OF UKRVO: THE POSITIONAL ACCURACY OF MINOR PLANETS DETERMINATIONS

V. Golovnya, V. Andruk

Main Astronomical Observatory NAS of Ukraine, Kyiv, Ukraine
golov@mao.kiev.ua, andruk@mao.kiev.ua

ABSTRACT. Scanning and astrometric processing of two 30x30 cm photographic plates with images of minor planets were conducted. The plates were obtained at the double wide-angle astrograph (DWAA, 400/2000) on the program of photographic sky survey and the program of small planets' observations. The plates were digitized using a flatbed scanner Epson Expression 10000XL. Images were obtained in the gray range of 16 -bits with a resolution of 1200dpi ($> 11,000$ pix along the one of the axes) and included into the UkrVO Joint Digital Archive (JDA). The plates are related to GUA040C observational archive. Image processing has been carried out in software package LINUS/MIDAS/ROMAFOT. Topocentric equatorial coordinates for the second exposition minor planet images were obtained with a single measurement error $\pm 0.1''$ and $\pm 0.3''$ for coordinate and $\pm 0.2^m$ for magnitudes in the Tycho-2 catalog as reference.

Key words: UkrVO, DBGPA V2.0, 4179 Toutatis.

The methods of minor planets search (Sergeev, 2005; Breanne, N.M., 2006; Sergeeva, 2006) and the processing of digitized images of photographic plates has been discussed previously (Andruk, 2005, 2010, 2012; Muminov, M.M., 2013; Vavilova et al., 2010, 2011, 2012a, 2012b). The calculation of the exact topocentric coordinates of the asteroid in the digital images of plates with dimensions of $8^\circ \times 8^\circ$ was made for the first time (Golovnya et al., 2010).

First we used the 4179 Toutatis asteroids ephemerides which were taken from the Minor Planet Center (<http://cfa-www.harvard.edu/iau/mpc.html>) for time scale 1976-1996. The ephemerides of Toutatis were selected for the moments of the closest approaches when their V-magnitudes were brighter than 15.5^m .

The next step of our work was the searching for asteroids on the plates of JDA using ephemerides which stated below in Table 1 and Database of Golosiyiv plate archive (DBGPA V2.0, <http://www.mao.kiev.ua/ardb/index.php>, <http://194.44.35.19/vo-mao/DB/>). For many approaches there were no periods of astronomical observation. We found the plate number 2088 with possible image of Potentially Hazardous Asteroids

Toutatis and also possible images eight asteroids from Main Asteroid Belt. Fig.1 shows the digital image of GUA040C002088 plate with the marks of potential objects of interest. The plate parameters – center of the plate: $08^h15^m50^s+16^\circ09'45''$; Data 1993 Jan 14; Second $UT_{start}=22^h44^m23^s$, duration of exposure $22^m.5$.

Table 1. Ephemerides 4179 Toutatis in the moments of the closest approaches with the Earth's orbit.

Date Y M D	R.A.(J2000)DEC h m s deg ' "	M AU	V Mag
19850101	002220 +011237	0.29	15.5
19850119	030005 +162140	0.32	15.2
19881222	001014 -014443	0.12	13.7
19890104	032906 +170837	0.14	13.0
19921208	133250 -250913	0.02	13.1
19921214	095556 +050046	0.04	11.0
19930114	080413 +195414	0.26	13.2

Here: Date – year, month, date; R.A.(J2000)DEC – right ascension and declination of asteroids in 0^h UT; M – orbital intersection distances; V – visible magnitude.

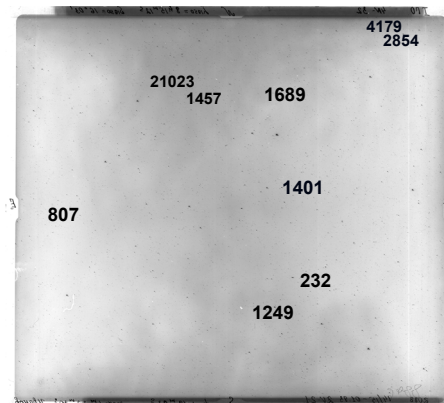


Figure 1: Image of the plate 2088.

Table 2 gives the list of minor planets, potentially appeared on the digital image of the plate. It is added to the list of the number, visible magnitude, right ascension

and declination of asteroids. Coordinates are taken from HORIZONS JPL-ephemerides for the moments of middle of second exposure.

Table 2: List of the asteroids on the plate 2088.

N	V	R.A.(J2000)DEC _{JPL}
2854	15.55	08 ^h 02 ^m 18.739 ^s +19°40'22.168"
4179	13.21	080315.448 +195930.590
1401	15.31	080827.771 +154536.553
232	13.31	081044.601 +141210.399
1689	14.66	081224.308 +185610.082
1249	13.66	081317.978 +135038.643
1457	14.40	081612.243 +191847.036
21023	15.45	081950.967 +191703.600
807	14.55	083033.604 +154212.304

On Figure 2 among the stars there is image of 4179 Toutatis with visible magnitude V=13.43.

The next step of our work was the derivation of minor planet topocentric coordinates.

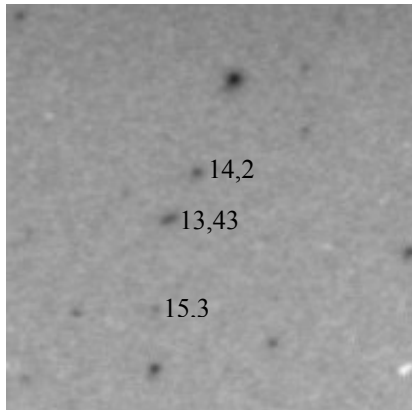


Figure 2: Image of 4179 Toutatis.

Image processing has been carried out in software package LINUS / MIDAS / ROMAFOT. Figure 3 (on the left) shows the trend of systematic differences between measured and catalog coordinates for right ascensions and declinations the correction for the instrumental errors of the scanner (left) and the trend of random differences between the measured values and catalog coordinates of stars after the correction for instrumental errors of the scanner (right). Differences in arcsec on 1a), 1b), 1d) and 1e) panels are given vs pixel coordinate axes of images X,Y and on 1c) and 1f) panels vs B-magnitudes of TYCHO-2. The rms unit errors $\Delta\alpha$, $\Delta\delta$ decrease from $\sigma = 0,306''$ to $\sigma = 0,104''$ and from $\sigma = 1,928''$ to $\sigma = 0,113''$ correspondingly after the scanner errors removing. N on 1a) - reference stars of TYCHO-2. The top ticks on 1a), 1e) panels fix the positions of minor planets on the plate; numbers are given according the MP column in Table 3.

We compare the calculated topocentric coordinates of minor planets with the coordinates, given by the theory DE-0431LE-0431 (Giorgini J., HORIZONS Web-Interface <http://ssd.jpl.nasa.gov/horizons.cgi>), to receive the appropriate residuals $(O-C)_\alpha$ and $(O-C)_\delta$.

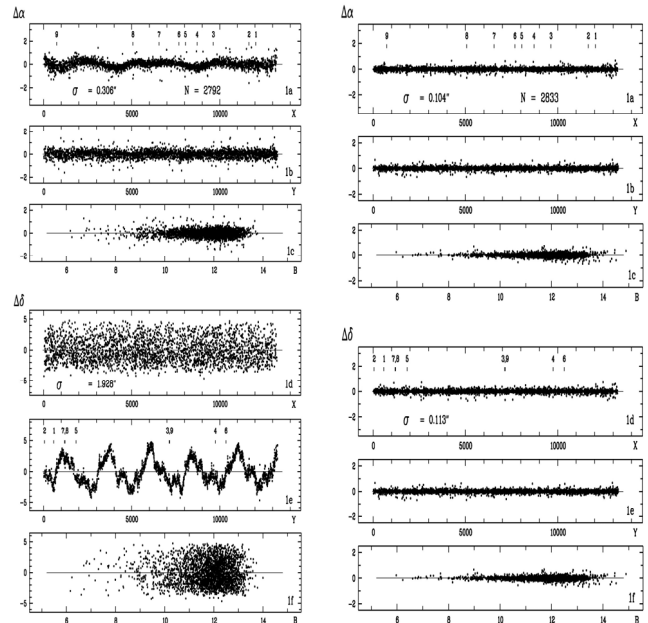


Figure 3: The trend of systematic differences between the measured values and catalog coordinates of stars before the correction for the instrumental errors of the scanner (left) and the trend of random differences between the measured values and catalog coordinates of stars after the correction for instrumental errors of the scanner (right).

Table 3 gives the calculated photographic magnitudes in TYCHO-2 photometric system with the above said residuals $(O-C)_\alpha$ and $(O-C)_\delta$. Minor planets 2854 and 21023 were not fixed on the plates images.

Table 3: Calculated B-magnitudes and residuals $(O-C)_\alpha$ and $(O-C)_\delta$.

Name	MP	Mph	$(O-C)_\alpha$, $(O-C)_\delta$.
2854 Rawson	1	-	-
4179 Toutatis	2	13.58	+0.050 ^s +1.150"
1401 Lavonne	3	16.46	+0.064 +0.144
232 Russia	4	13.60	-0.030 +0.374
1689 Floris-Jan	5	14.86	-0.042 +0.629
1249 Rutherfordia	6	13.83	-0.079 +1.306
1457 Ankara	7	14.61	-0.032 +0.868
21023 1989 DK	8	-	-
807 Ceraskia	9	14.95	+0.127 -0.510

The residuals are very different to each other, possibly due to inaccurate ephemerides. To verify this, we have calculated the residuals of some reference stars, given in Table 4. Additionally, the same method was applied to the calculation of coordinates for 2 Pallas – selected minor planet, fixed on the 2471 plate of the same observational archive. The plate parameters - center of the plate: 18h28m13s +19°05'; Data 1986 08 02; First exposure "S"; Second UT_{start}=215605, duration of exposure 5^m.0 (<http://www.mao.kiev.ua/ardb/index.php>).

Table 4: $(O-C)_\alpha$, $(O-C)_\delta$ for reference and control stars and selected minor planet 2 Pallas.

Stars/minor planet	Mph	$(O-C)_\alpha, (O-C)_\delta$
Tyc 1377-940-1	12.39	$-0.001^s +0.024^m$
USNOA2 0975-05756822	15.17	$+0.040 +0.60$
USNOA21050-55623614	14.49	$+0.015 +0.27$
2 Pallas	10.68	$-0.015 -0.092$

The calculated coordinates of potentially hazardous asteroid 4179 Toutatis and selected minor planet 2 Pallas coincide with their ephemeris values. Residuals $(O-C)_\alpha$, $(O-C)_\delta$ can be improved only by elimination of those reference stars, which coordinates have significant errors, especially stars with magnitudes $B \geq 14^m$.

The software package LINUS / MIDAS / ROMAFOT permits to build aberration masks of telescope optics on the data of the digital image itself. These masks can give the indirect signs of the correction of plate reduction and scanner errors elimination. Figure 4 shows the example of the above said mask on the data of processed plate.

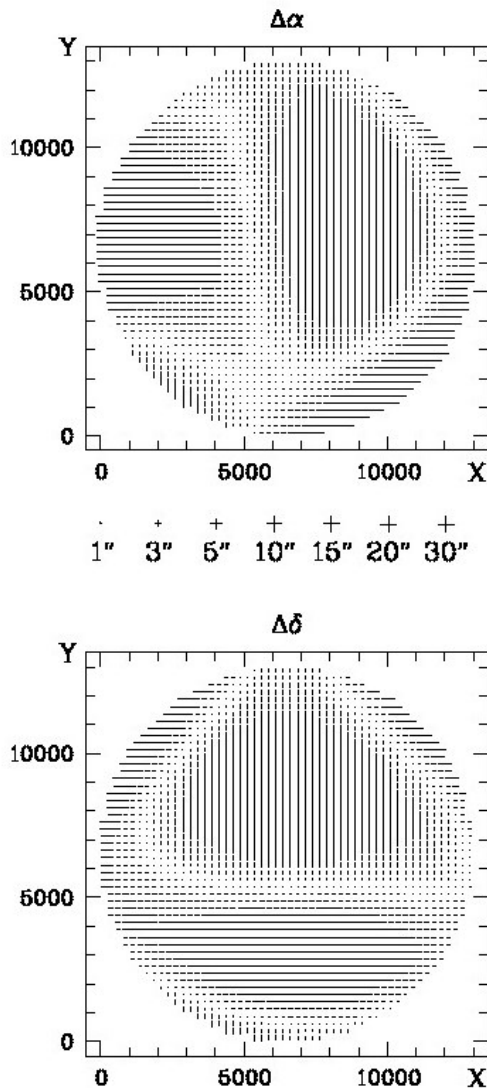


Figure 4: The aberration mask for DWAA optics on the data of 2088 plate processing.

References

- Andruk V., Ivanov G., Pogoreltsev M., Yatsenko A.: 2005, *Kinematics and Physics of Celestial Bodies*, 21, N5, 396.
- Andruk V.M., Butenko G.Z., Yatsenko A.I.: 2010, *Kinematics and Physics of Celestial Bodies*, 26, N3, 75-81.
- Andruk V.M., Ivanov G.O., Yatsenko A.I. et al.: 2012, *Visnyk "Astronomia" T.Shebchenko National University of Kyiv*, 48, 11-13.
- Breanne N. Morelli *Using Astronomical Databases in the Search for Minor Planets*, City High School, April 5, 2006.
- Golovnya V., Andruk V., Yatsenko A.: 2010, *Journal of Physical Studies*, 14, N2, 2902
- Muminov M.M. et al.: 2013, *Izvestia GAO Pulkovo*, 220, 517-52.
- Sergeev A.V., Sergeeva T.P., Golovnya V.V.: 2005, *Kinematics and Physics of Celestial Bodies Supplement*, N 5, 577.
- Sergeeva T.P., Golovnya V.V., Yizhakevych E.M., et al.: VO: Plate Content Digitization, Archive Mining and Image Sequence Processing, Eds. M.Tsvetkov, V.Golev and others, Sofia, 2006, p.161-166
- Vavilova I.B., Pakuliak L.K., Shlyapnikov A.A. et al.: 2012, *Kinematics and Physics of Celestial Bodies*, 28, 85-102.
- Vavilova I.B., Pakuliak L.K., Protsyuk Yu.I. et al: 2012, *Baltic Astronomy*, 21, 356-365.
- Vavilova I.B., Pakuliak L.K., Protsyuk Yu.I. et al.: 2011, *Kosmichna Nauka i Tekhnologiya*, 17, 74-91.
- Vavilova I.B., Pakuliak L.K., Protsyuk Yu.I.: 2010, *Kosmichna Nauka i Tekhnologiya*, 16, 62-70.

EXAMPLES OF DIGITAL VERSIONS OF THE CRAO SPECTRAL PHOTOGRAPHIC ARCHIVES

M.Gorbunov¹, A.Shlyapnikov²

SRI “Crimean Astrophysical Observatory”, Taras Shevchenko National University of Kyiv
Nauchny, Crimea, Ukraine

¹mag@crao.crimea.ua, ²aas@crao.crimea.ua

ABSTRACT. The glass library of Crimean Astrophysical Observatory (CrAO) comprises of about 15,000 photoplates and films with the spectra of planets, stellar, nebula and extragalactic objects. All spectra were obtained in period from 1929 to 1990 years and separated on different collections. Some results of the digitizing photoplates from these collections are presented in this paper.

Key words: database, virtual observatory, spectroscopy

1. Introduction

The CrAO has a long history of spectral observations. The first observations of astronomical objects in the Crimea (solar prominences with a spectroscope) were started in the southern branch of the Pulkovo Astronomical Observatory near Simeiz on the mount Koshka (“The Cat”) in the first quarter of the XX century (Polosukhina et al., 2008). Later on the photographic spectral observations with the objective prism at the astrograph with the 117-mm objective “Unar” (Kurbasova, 2007) and since 1926 on a quartz spectrograph for the Newtonian focus and large prism spectrograph with a thermostat and two different cameras at the 40-inch reflector “Goward Grabb” firm (Kryuchkov et al., 2009) were followed. For example, a large program of observations to determine the radial velocities of stars (Shajn, Albitzky, 1932) was conducted with this telescope. Since 1950th the spectroscopic observations with 400-mm astrograph, 1200-mm and 2600-mm reflectors were carried out in the new Crimean Astrophysical Observatory, which was built near Bakhchisarai in the Crimean Mountains.

This article gives the examples of digital versions of the CrAO non-solar spectral photographic archives. Conventionally, all spectral observations have been divided into several collections obtained on the astrographs with objective prism and on the reflector telescopes. All old negatives were digitized on the EPSON Expression 10000XL scanner with a resolution 2400 dpi, the output files were saved in FITS formats. When creating a digital version of archives of spectral observations, a special attention can be paid to the data preparation in formats that are used in interactive applications recommended by IVOA: Aladin (Bonnarel et al., 2000), VOSpec (savo1.esac.esa.int/vospec), Specview (www.stsci.edu/institute/software_hardware) etc.

Our work is carried out within the project of LADAN – Crimean Astronomical Virtual Observatory (Shlyapnikov, 2007) as a part of the Ukrainian Virtual Observatory – UkrVO (Vavilova et al., 2010, 2011).

2. Brief description of spectra collections

2.1. Objective prism spectroscopy

Collection of spectral observations conducted with an objective prism consists of three parts determined by three types of astrographs (table 1), on which the spectra were obtained.

Table 1: Basic parameters of astrographs and dispersion for digitized spectra.

Astrograph	Diameter of objective (mm)	Focal length (mm)	Dispersion at H _γ (Å/pix)
Unar	117	600	1.5
Dogmar	167	750	1.4
400-mm	400	1600	1.5

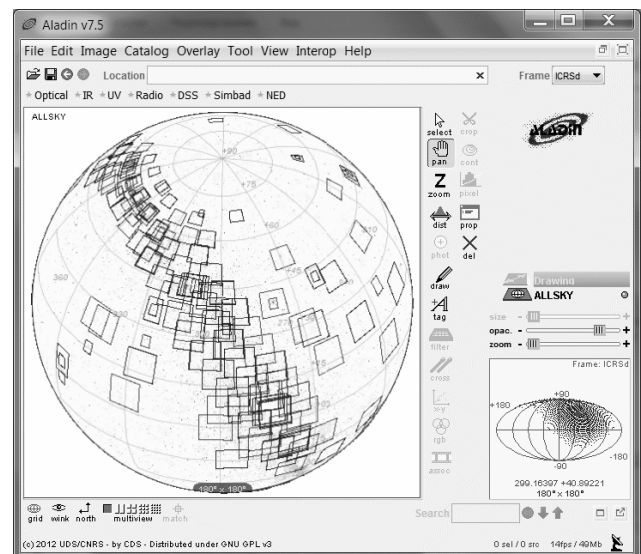


Figure 1: The SwOP collection presented in the interactive sky atlas Aladin

“Spectroscopy with Objective Prism” (SwOP) collection contains about 1000 spectral plates obtained with Unar, Dogmar, and 400-mm astrographs in 1929 – 1965 years. The largest number of negatives was obtained for studying the stellar and dust components of the Galaxy and for revealing the stars, which excite intergalactic medium. The Shajn’s areas collection contains more 500 spectral plates obtained on 400-mm astrograph in 1950–1965 years with a goal to investigate a structure of the Milky Way. Figure 1 illustrates the sky coverage of the plates from SwOP collection.

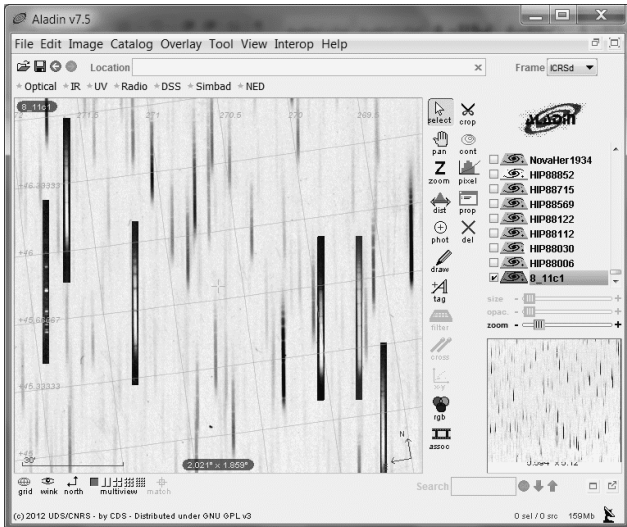


Figure 2: Fragment of full image photographic plate (negative) with the spectra of the extracting objects (positive)

The examples of spectra extracted from the photographic plate obtained on the Unar astrograph are shown in Figures 2 and 3.

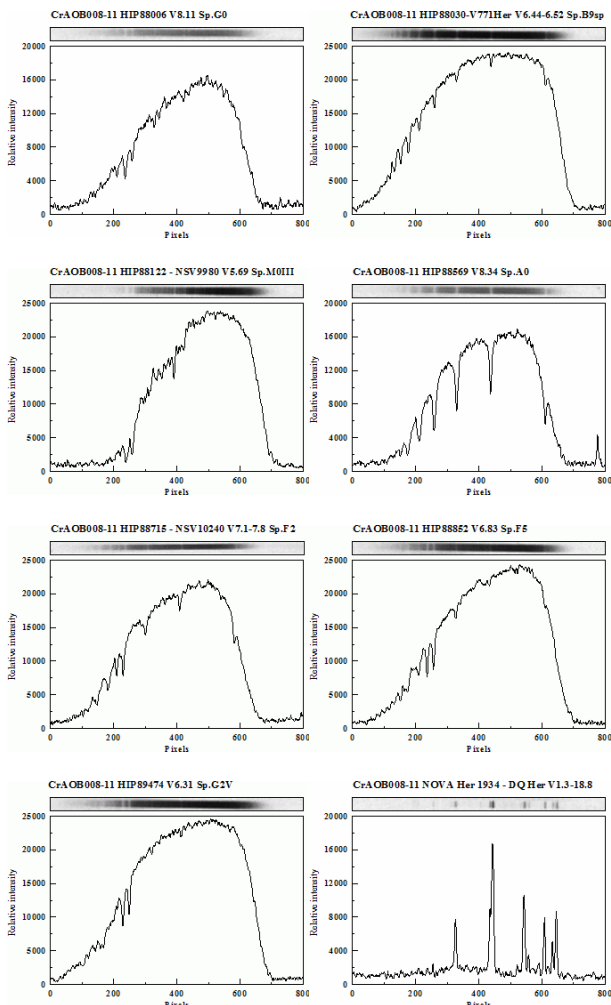


Figure 3: Examples of spectra extracted from the plate obtained with an objective prism on the Unar astrograph.

We conducted measurements for different A-stars to convert pixels scale in wavelength scale. Figure 4 illustrates the dispersion curves for Unar, Dogmar, and 400-mm astrographs.

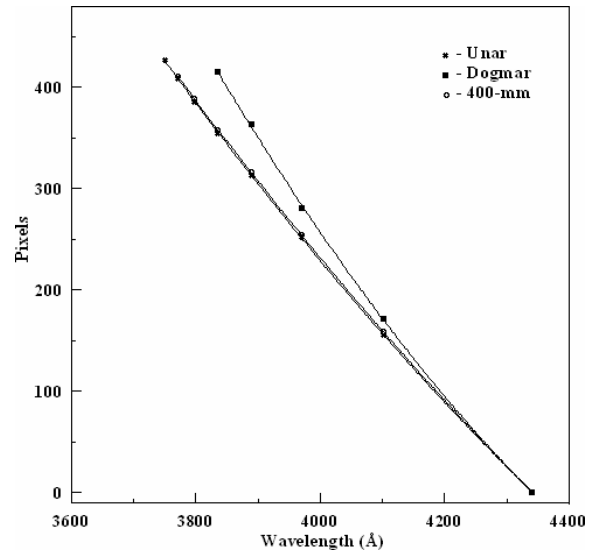


Figure 4: Dispersion curves for digitized plates obtained with different astrographs.

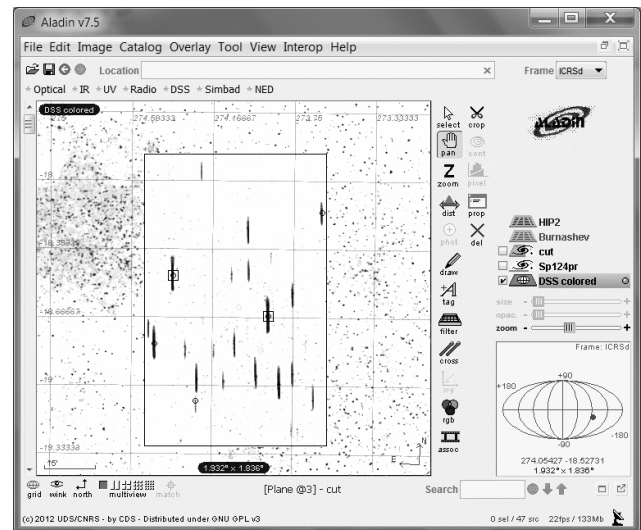


Figure 5: Fragment of a full-format image with spectro-photometric standards.

The figure 5 illustrates a fragment of a full-format image obtained with an objective prism on the 400-mm astrograph (circles – stars from the HIPPARCOS catalog, squares – spectrophotometric standards from the catalog by Burnashev (1985)).

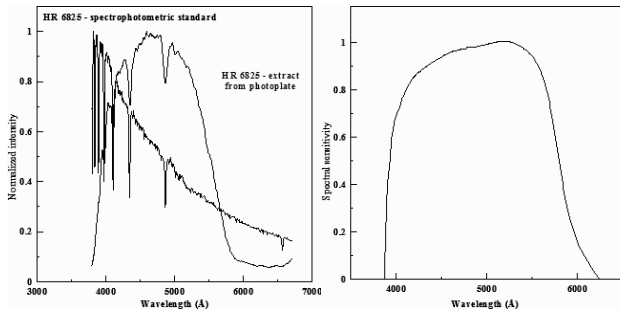


Figure 6: (see comments in the text)

We used SEDs to determine the spectral sensitivity of the negative in the SwOP collection. It is given in Fig. 6: left panel – a comparison of the normalized data of spectrophotometric standard with the data extracted from the digitized negative; right panel – a certain spectral sensitivity of the negative (from the data presented on the left panel) for the further reduction of the extracted spectra. More information about spectroscopy with objective prism and these astrographs see papers by Brodskaya (1953) and Pronik (1958).

2.2. 40-inch reflector "Goward Grabb" collection

About 3,200 spectra were obtained with 40-inch telescope (Shain, 1926) at the Simeiz observatory in 1929-1941 (distribution of the observed objects on the sky is given in Fig. 7).

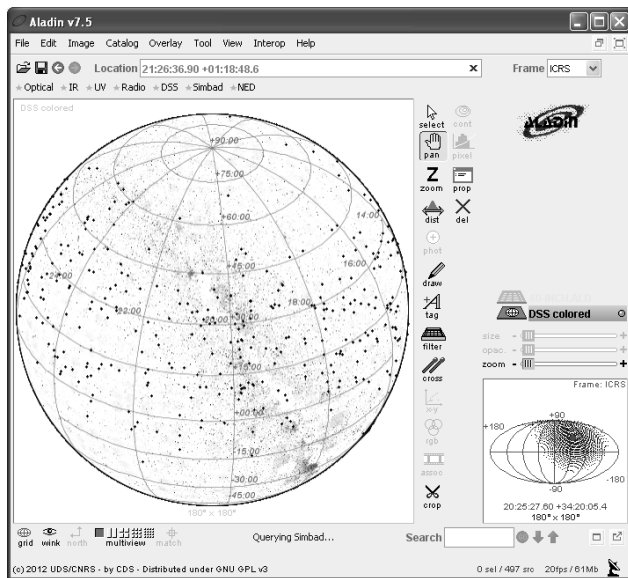


Figure 7: The sky of 40-inch reflector

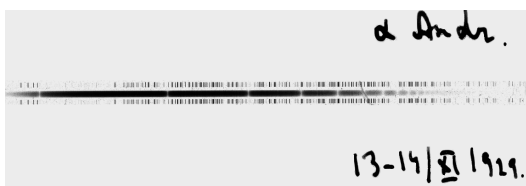


Figure 8: The alfa And spectrogram obtained with 40-inch reflector on November, 13-14, 1929.

The spectrogram number 1, which is preserved in the collection of the CrAO spectral observations with 40-inch reflector, is presented in Figure 8.

All the data from this collection were extracted from the negatives and converted to formats supported by the IVOA applications. Figure 9 illustrates an example of the spectra of alfa And by Specview program.

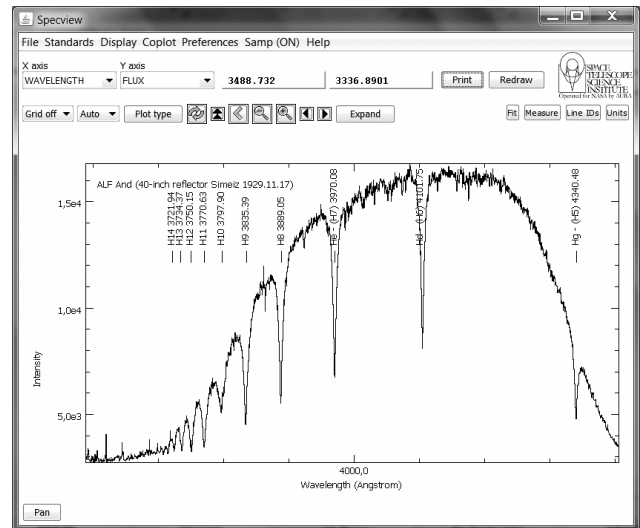


Figure 9: The alfa And spectrum in Specview

2.3. The 1200-mm reflector of collection spectra

More than 5,500 direct spectra and 1,000 spectra with FKT-1A image convertor were obtained using 1200-mm telescope (Kopylov, 1954) in 1953-1990 (distribution of the observed objects on the sky is given in Fig. 10).

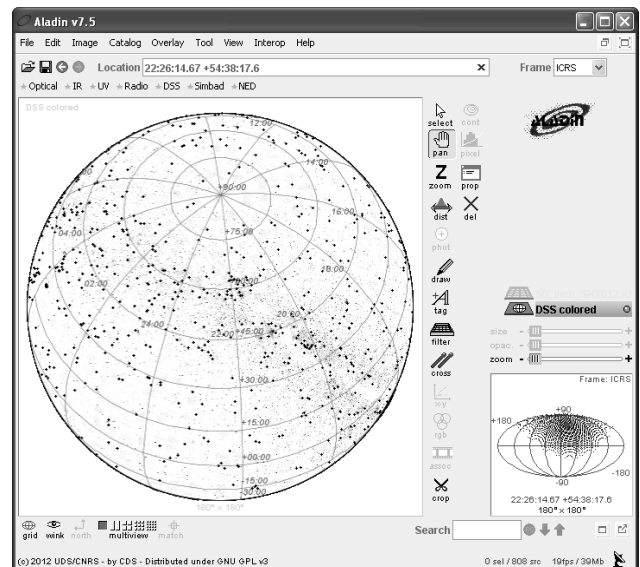


Figure 10: The sky of 1200-mm reflector

Full version of the database of observations conducted on the 1200-mm telescope with the image convertor FKT-1A, presented in the form of HTML-pages is illustrated in Fig. 11. Example of the VOSpec presentation of infrared spectroscopic observations eps Aur, obtained with these instruments as compared with the data for the object taken from the IVOA database, is illustrated in Fig. 12.

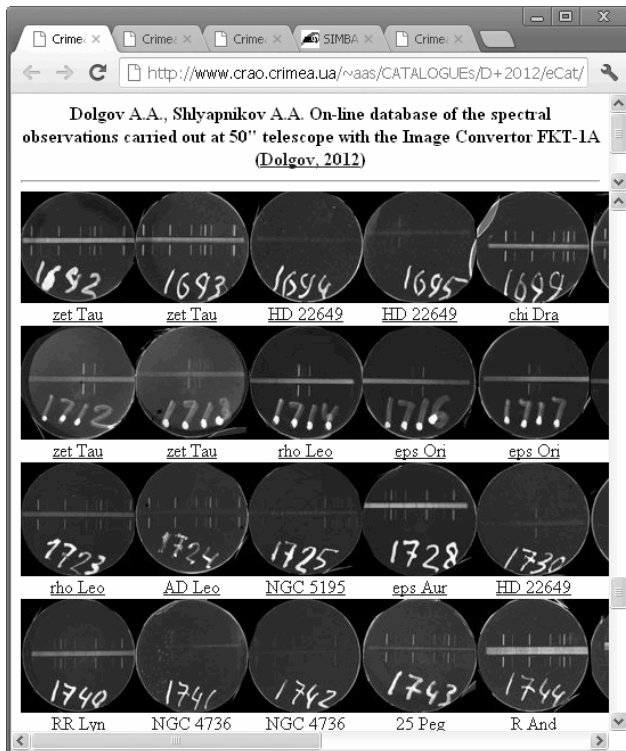


Figure 11: (see comments in the text)

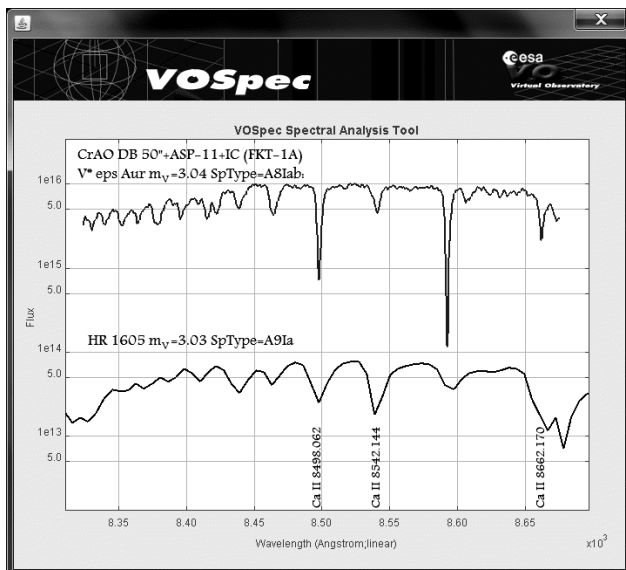


Figure 12: The alf And infrared spectrum in VOSpec

2.4. Collection of the ZTSh

More than 3,000 spectra of different objects and 3,000 spectra with image convertor for active galactic nuclei and the comparison stars were obtained using the 2600-mm telescope ZTSh (Ionnisiani et al., 1976) in 1964-1990. The examples of digitized spectra of extragalactic objects obtained by Chuvaev (1985) is illustrated in Figure 13.

3. Conclusion

This worked out technology of the conversion of photographic spectral observations of various astronomical

objects in a digital format is the first step in creating a database of the CrAO collection for on-line use. It is also a part of the UkrVO Joint Digitized Archive of astronomical observations conducted at the observatories of Ukraine since 1880th (Vavilova et al., 2012a, 2012b).

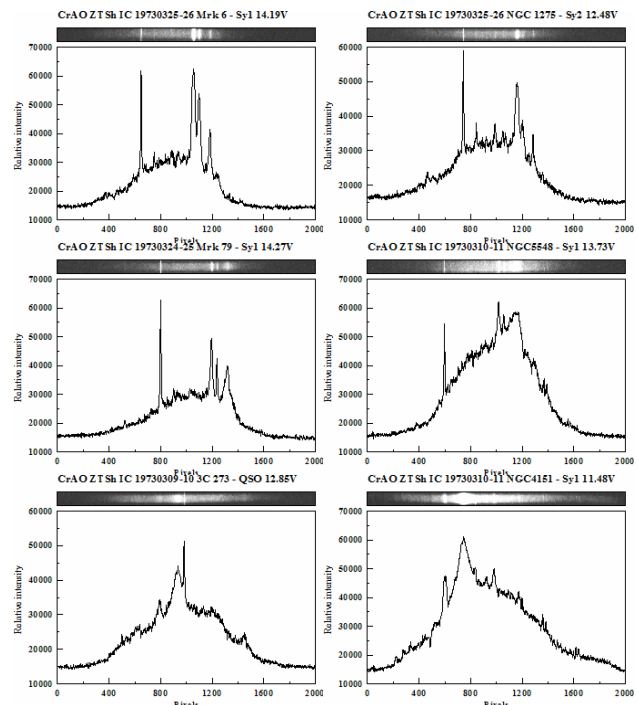


Figure 13: The examples of digitized spectra of extragalactic objects

Acknowledgements. Authors are grateful to Prof. R.E.Gershberg and Dr. I.B. Vavilova for the comments and remarks on this research. We thank the authors of VOSpec and Specview software, which was used in this work.

References

- Ionnisiani B.K. et al.: 1976, *IzKry*, **55**, 208.
 Bonnarel F. et al.: 2000, *A&A Suppl.*, **143**, 33.
 Brodskaya E.: 1953, *IzKry*, **10**, 104.
 Burnashev V.I.: 1985, *Bull. of the Crimean Astrophys. Obs.*, **67**, p. 10-24.
 Chuvaev K.K.: 1985, *Pis'ma AZh*, **11**, 803.
 Kopylov I.M.: 1954, *IzKry*, **11**, 44.
 Kryuchkov S.V. et al.: 2009, *IzKry*, **104/6**, 188.
 Kurbasova G.S.: 2007, *IzKry*, **103/2**, 90.
 Polusukhina et al.: 2008, *IzKry*, **104/5**, 27.
 Pronik I.: 1958, *IzKry*, **20**, 208.
 Shajn G.: 1926, *MiPul*, **10**, 450.
 Shajn G., Albitzky V.: 1932, *MNRAS*, **92**, 771.
 Shlyapnikov, A.: 2007, *IzKry*, **103/1**, 142.
 Vavilova I.B., Pakuliak L.K., Protsyuk Yu. I. et al: 2012a, *Baltic Astronomy*, **21**, 356-365.
 Vavilova I.B., Pakuliak L.K., Shlyapnikov A.A. et al.: 2012b, *Kinematics and Physics of Celestial Bodies*, **28**, 85.
 Vavilova I.B., Pakuliak L.K., Protsyuk Yu. I. et al.: 2011, *Kosmichna Nauka i Tekhnologiya*, **17**, 74.
 Vavilova I. B., Pakuliak L. K., Protsyuk Yu. I.: 2010, *Kosmichna Nauka i Tekhnologiya*, **16**, 62.

DEVELOPMENT OF MYKOLAIV VIRTUAL OBSERVATORY

A. Mazhaev¹, Yu. Protsyuk²

Research Institute – Nikolaev Astronomical Observatory
Mykolaiv, Ukraine

¹ mazhaev@mao.nikolaev.ua, ² yuri@mao.nikolaev.ua

ABSTRACT. Results obtained in 2010-2013 on the development of astronomical databases and web services are presented. Mykolaiv Virtual Observatory (MVO) is a part of the Ukrainian Virtual Observatory (UkrVO). At present, MVO consists of three major databases containing data on: astrometric catalogues, photographic plates, CCD observations. The databases facilitate the process of data mining and provide easy access to the textual and graphic information on the results of observations and their reduction obtained during the whole history of Nikolaev Astronomical Observatory (NAO).

Key words: database, web service, virtual observatory

Astrometric catalogues of stars were compiled in the form of XML files in accordance with the VOTable standard. Access to the databases of photographic and CCD observations is implemented via a graphical web interface on the MVO site (<http://nao.db.ukr-vo.org/vo3.php>), as well as via the web interface of the stand alone application - Aladin (<http://nao.db.ukr-vo.org/vo1.html>), which has been developed at Strasbourg Astronomical Data Center (CDS) since 1999. Despite the difference between the web interfaces, in both cases we use the same databases, which are managed by using the MySQL database management system. Using the Aladin web interface, the server of MVO is integrated with other leading astronomical servers located in different parts of the world.

The first version of MVO containing astronomical data resources of NAO was created in 2008 (Protsyuk et al., 2005; Protsyuk et al., 2008). The further development of MVO has been carried out since 2010 (Mazhaev, Protsyuk, 2010) by integrating data of photographic observations and astronomical catalogues, which were obtained in other observatories of Ukraine.

In 2012, the first astronomical web services (AWS) were created in Ukraine. The AWS provide data mining for three astrometric catalogues. The operation of these AWS is fully compliant with the Simple Cone Search standard, which was adopted and has been developed by the International Virtual Observatory Alliance (IVOA). All three AWS were successfully tested on the web site of the Virtual Astronomical Observatory (VAO, USA) by means of

special test programs. The AWS were also inscribed in the astronomical registry, which operates in accordance with the IVOA standard. The registry includes all available astronomical resources for carrying out further investigations. The AWS were developed in the form of search scripts in a programming language – PHP. Application of the AWS for data mining can be implemented by using a browser as well as by any other application that supports the standards adopted by the IVOA.

Databases of the MVO

Stellar astrometric catalogues, obtained in 1832-2012 years, are available on the corresponding web page (<http://nao.db.ukr-vo.org/vo2.html>). The database contains 33 short descriptions and relevant files compiled in accordance with the VOTable standard, which was adopted and has been developed by the IVOA for storing and sharing any astronomical tabular data. In 2010-2012, we compiled and added to the database six astrometric catalogues obtained at three observatories: NAO (AMC2009 catalogue); the Main Astronomical Observatory (MAO) of Ukraine (MEGA-G, MEGA-H, ASSC-2.5, FONAC-2.0 catalogues); Institute of Astronomy of Kharkiv National University (XPM catalogue).

The XPM is the largest astronomical catalogue in Ukraine, which contains about 280 million stars. To facilitate access to astronomical data from this catalogue for selected region of interest within the celestial sphere, we created a search engine for 360 archive files of XPM catalogue in two formats: xml.gz and txt.gz (Fig. 1).

Figure 1. The search interface for the XPM catalogue.

The user may easily choose the necessary format of the catalogue data (Fig. 1). The XML files were compiled in accordance with the IVOA standard - Votable1.2. The search results are available for download (Fig. 2). The search system is available on the corresponding web page of the UkrVO site (<http://xpm.db.ukr-vo.org/xpm.php>).

32° to 32.5° -> [244.xml.gz](#) | 32.5° to 33° -> [245.xml.gz](#)
 34° to 34.5° -> [248.xml.gz](#) | 34.5° to 35° -> [249.xml.gz](#)
 36° to 36.5° -> [252.xml.gz](#) | 36.5° to 37° -> [253.xml.gz](#)

Figure 2. Search results for the XPM catalogue.

The databases of photographic and CCD observations operate on the basis of the MySQL relational database management system. The databases allow users to conduct automatic search of astronomical images in accordance with the IVOA standards and the IAU Resolution – Public access to astronomical archives, adopted in 2003. The database of photographic observations contains more than 34 thousand plates (Fig. 3), which have been obtained and stored at two institutions: NAO and MAO. It contains textual information for all plates as well as preview images in JPG format for more than 8000 plates.

<input checked="" type="checkbox"/> Stars around Radio Source: 485 plates	<input checked="" type="checkbox"/> Stellar Cluster: 2350 plates
<input checked="" type="checkbox"/> Variable Star: 1842 plates	<input checked="" type="checkbox"/> Nebula: 48 plates
<input checked="" type="checkbox"/> Fundamental Star: 2105 plates	<input checked="" type="checkbox"/> Association of Stars: 4 plates
<input checked="" type="checkbox"/> Zodiac Stars: 1127 plates	<input checked="" type="checkbox"/> Equatorial stars: 489 plates
<input checked="" type="checkbox"/> Moon: 854 plates	<input checked="" type="checkbox"/> Asteroid: 4527 plates
<input checked="" type="checkbox"/> Artificial Satellite: 4156 plates	<input checked="" type="checkbox"/> Field: 5925 plates
<input checked="" type="checkbox"/> Undefined object: 52 plates	<input checked="" type="checkbox"/> Galaxy: 1320 plates
<input checked="" type="checkbox"/> Group of Galaxies: 139 plates	<input checked="" type="checkbox"/> Cluster of Galaxies: 5 plates
<input type="button" value="Check all 34198 plates"/>	<input type="button" value="Uncheck all plates"/>

Figure 3. Observational campaigns with photo plates.

The preview images of plates are available in two resolutions of 300DPI and 600DPI, obtained by reducing the original scanning resolution of 1200DPI. Original images are available by request. The database of CCD observations contains more than 72 thousand frames. All preview images of plates and CCD frames are available without user registration. The user may get access to CCD images in FITS format only after online registration. The access is automatically granted after receiving email confirmation from the user.

The web interface of the database allows the users to make flexible requests taking into account the following parameters: equatorial coordinates, search sizes, time period, object types, plate parameters, CCD parameters, telescope names (Fig. 4).

<input checked="" type="checkbox"/> Triple Astrograph 11/120 cm, GUA011: 72 plates	<input checked="" type="checkbox"/> Triple Astrograph 15/170 cm, GUA015: 159 plates
<input checked="" type="checkbox"/> Double Astrograph 40/550 cm, GUA040A, GUA040B: 9135 plates	<input checked="" type="checkbox"/> Double Astrograph 40/200 cm, GUA040C, GUA040D, GUA040E: 9720 pl.
<input checked="" type="checkbox"/> Double Astrograph 40/300 cm, TAS040A, TAS040B: 169 plates	<input checked="" type="checkbox"/> Schmidt 53/183 cm, BYU053: 52 plates
<input checked="" type="checkbox"/> Reflector 70/1050 cm, GUA070B: 443 plates	<input checked="" type="checkbox"/> Reflector 70/311 cm, GUA070C: 66 plates
<input checked="" type="checkbox"/> Zeiss Double Astrograph 40/200 cm, EA0040B: 146 plates	<input checked="" type="checkbox"/> Zonal Astrograph 12/200 cm, MYK012, PUL012: 8402 plates
<input type="button" value="Check all telescopes"/>	<input type="button" value="Uncheck all telescopes"/>

Figure 4. Telescope names for selection of photo plates.

We have developed the search scripts written in PHP programming language. The user may easily make requests from one database or both of them, and obtain one or two result tables, correspondingly (Fig. 5).

Plate	RA, h:m:s	Dec, d:m	300dpi	600dpi
MYK012 000488B	00:52:42	+03:53	preview	preview
MYK012 000489A	00:52:42	+03:53	preview	preview
MYK012 000489B	00:52:42	+03:53	preview	preview
GUA040A 007229	00:53:17	+00:35	–	–
GUA040A 000421B	00:53:22	+03:57	–	–

Figure 5. Search results for photo plates.

The user may also get access to the databases of observations via the web interface of such stand alone application as Aladin (Fig. 6), which has been developed since 1999 in Strasbourg astronomical Data Center (CDS). Aladin allows the user to retrieve and process astronomical images and catalogues from many servers around the world. The user may get access to the UkrVO databases by taking several simple steps described on the corresponding web page (<http://nao.db.ukr-vo.org/vol1.html>).

The databases were used to compile the astrometric catalogues. In 2012, a catalogue of positions, proper motions and magnitudes for about 200 thousand stars up to 16^m was compiled. The stars in the frames within a declination range of $\pm 15^\circ$ near the galactic plane were processed by using the databases of photo plates, modern CCD observations as well as cross identification of stars taken from other catalogues. A catalogue of about 2000 stars with proper motions exceeding 150 mas/year was also compiled by using the results of modern CCD observations and the cross identification of stars taken from many other astrometric catalogues.

We continue to expand and populate the databases.

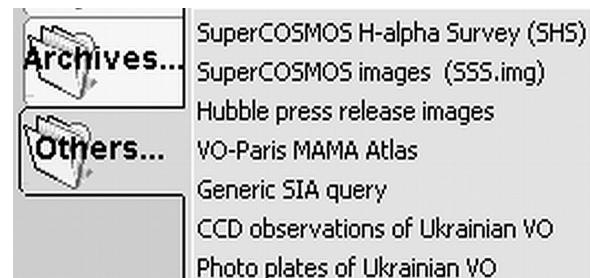


Figure 6. Selection of image servers via Aladin.

Web Services of the UkrVO

In 2012, we created the astronomical web services (AWS) for three astrometric catalogues: the All Sky Compiled Catalogue (ASCC-2.5, 3rd version) (Kharchenko et al., 2009), the FON Astrographic Catalogue (FONAC 2.0) (Kislyuk et al., 2005), the Catalogue of Absolute Proper Motions (XPM) (Fedorov et al., 2009). The web services operate in accordance with the IVOA standard – Simple Cone Search (SCS). The user may get access to the web services via a browser and web address (http://nao.db.ukr-vo.org/ws_SCS.html) or through any other program that supports the IVOA standards, for example Aladin (Fig. 7). The AWS permit the user to carry out the search of scientific information by using: a network server, a browser, special scripts, data directories.

The search scripts were written in the programming language PHP. The ASCC contains more than 2.5 million stars (J2000, epoch 1988.19). The FONAC contains more than 2.0 million stars (J2000, epoch 1991.25). The XPM catalogue contains absolute proper motions for more than 280 million stars (J2000, epoch 2000.0). Each entry of any catalogue contains the textual data of a star, and consists of 10 to 30 values of astronomical parameters. The user may select any combination of equatorial coordinates and radius of search on the celestial sphere, using the appropriate Uniform Resource Locator (URL). The search results are displayed in the browser window in accordance with the IVOA standard – SCS.

In essence, the AWS allow the user to carry out data selection from the large astronomical catalogues for a relatively small region of interest in the sky. The radius of search is limited by the maximum value, which varies from 0.49° to 2.5° depending on the data volume of a given catalogue. The SCS protocol contains the following three parameters as a part of the URL:

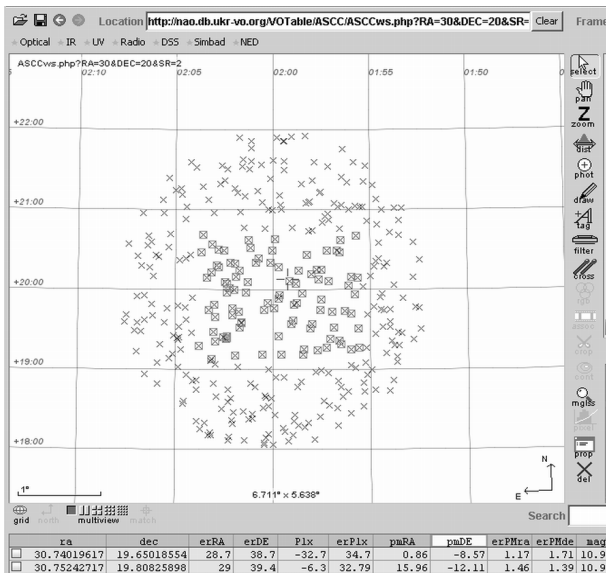


Figure 7. Search results via Aladin for the AWS.

RA - a right-ascension in the ICRS for the position of the center of the cone to search, given in decimal degrees;
 DEC - a declination in the ICRS for the position of the center of the cone to search, given in decimal degrees;
 SR - the radius of search, given in decimal degrees.

The AWS also provide users the possibility of further data processing of these astronomical catalogues by using additional software developed in accordance with the IVOA standards.

Information about the AWS was included into the registry developed by VAO. The AWS were successfully tested (Fig. 8) by using special programs at the web site of VAO (USA) (<http://heasarc.gsfc.nasa.gov/vo/validation/vresults.pl?querystring=nao.ua>).

The AWS were created and established for the first time in Ukraine. General information on the web services and examples of their usage, including technical details omitted in this paper, are available on the relevant page of the UkrVO site (http://nao.db.ukr-vo.org/ws_SCS.html).

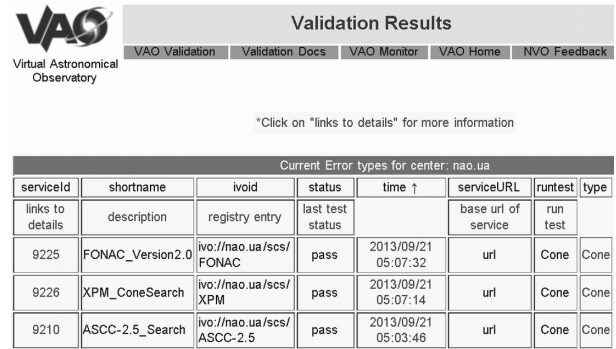


Figure 8. Test results at the web site of the VAO (USA).

Other Astronomical Databases

Astronomers of the RI NAO carry out joint projects to apply technologies of virtual observatory for data storing and processing, which are currently not included in the UkrVO. In particular, they take part in three international projects to populate the following online catalogues and databases:

- potentially hazardous asteroids (PHA) (<http://newton.dm.unipi.it/neodys/index.php?pc=0>);
- optical meteors - Virtual Meteor Observatory (<http://vmo.imo.net/>);
- Radio Meteor Observing Bulletin (<http://www.rmob.org/index.php?lng=en>).

The focus of the work is directed towards the electronic data processing such as: reduction of CCD observations of stars, the PHA, artificial Earth satellites, meteors. Obtain-ed results should be automatically submitted to the corresponding data center.

The RI NAO and other members of the Ukrainian network of optical stations carry out regular observations of the artificial Earth satellites. They all conduct the joint project to determine the orbital elements and to create online catalogue of the near-Earth objects.

The results of this work conducted in the RI NAO will be integrated with the UkrVO. The integration will empower the UkrVO to provide users access to both historical and modern observations as well as the results of their reduction in a wide range of astronomical topics (Vavilova et al., 2010; Vavilova et al., 2011; Vavilova et al., 2012a; Vavilova et al., 2012b).

References

Mazhaev A.E., Protsyuk Yu.I.: 2010, *Izvestia GAO Pulkovo*, **219**, Issue 4, 185-188.
 Fedorov P.N., Myznikov A.A., Akhmetov V.S.: 2009, *MNRAS*, **393**, Issue 1, 133-138.
 Kharchenko N.V., Roeser S.: 2009, *VizieR Online Data Catalog: I/280B*.
 Kislyuk V.S., Yatsenko A.I.: 2005, *Kinematika i Fizika Nebesnykh Tel*, **5**, 33-39.
 Protsyuk Yu., Mazhaev A.: 2008, *IAUS*, **248**, 548-551.
 Protsyuk Y., Pinigin G., Shulga A.: 2006, *Kinematika i Fizika Nebesnykh Tel*, **5**, 580-584.
 Vavilova I.B., Pakuliak L.K., Protsyuk Yu.I. et al.: 2012a, *Baltic Astronomy*, **21**, 356-365.
 Vavilova I.B., Pakulyak L.K., Shlyapnikov A.A. et al.: 2012b, *Kinematics and Physics of Celestial Bodies*, **28**, 85-102.
 Vavilova I.B., Pakuliak L.K., Protsyuk Yu.I. et al.: 2011, *Kosmichna Nauka i Tekhnologiya*, **17**, 74-91.
 Vavilova I.B., Pakuliak L.K., Protsyuk Yu.I.: 2010, *Kosmichna Nauka i Tekhnologiya*, **16**, 62-70.

UKRVO JOINT DIGITAL ARCHIVE: CURRENT STATUS AND PERSPECTIVES

L.Pakuliak¹, V.Golovnya¹, N.Virun², L.Kazantseva³, S.Kashuba⁴

¹Main Astronomical Observatory NAS of Ukraine, Kyiv, Ukraine,
pakuliak@mao.kiev.ua

²I.Franko Lviv National University, Lviv, Ukraine

³T.Shevchenko Kyiv National University, Kyiv, Ukraine

⁴I.Mechnikov Odessa National University, Odessa, Ukraine

ABSTRACT. We discuss the current state of the UkrVO joint digital archive of photographic astronomical observations and the basic problems of its creation.

Key words: virtual observatory, UkrVO, database, digital archive

UkrVO project was originally conceived as a method of combining all the archives of astronomical observations of Ukrainian observatories. The project was supposed to include the data obtained in all wavelength ranges, not only optical or photometric. Such an association should provide data search and filtration in old archives, allow its regular replenishment with data of modern observational projects in any technological solutions, provide software tools for sharing early and recent observational data, thus carrying out the process of data mining (Vavilova et al., 2012a, 2012b, 2011, 2010; Pakuliak et al., 2012).

At the initial stage, this task involves the creation and development of joint digital archive (JDA) of photographic observations. The total number of photographic plates in the collections of Ukrainian observatories exceeds 300 thousand, including not only the positional but also the spectral and photometric observations. The pilot version of JDA includes only positional observations (<http://ukrvo.org/science/index.php?b1&2>).

By the current moment, JDA database contains more than 38 thousand records and more than 6 thousand digitized images from glass collections of Main astronomical observatory NAS of Ukraine (MAO NASU), Scientific-Research Institute “Mykolaiv Astronomical Observatory” (SRI MAO), astronomical observatories of T. Shevchenko Kyiv national university (AO KNU), I. Franko Lviv national university (AO LNU) and I. Mechnikov Odessa national university (AO ONU). Among them are:

- 26 thousand records of astronegatives' metadata and more than 6000 digital images of MAO NASU glass collection (GPA);
- 4 000 records of plates' metadata and more than 1 000 digital images (from 4 000 digitized ones) of AO

LNU glass collection;

- 8500 records of plates' metadata of SRI MAO glass collection (without images, which are available on the VO page of the official website of SRI MAO, the database obtained by the mutual exchange of information between MAO NASU and SRI MAO);
- metadata of 24 partially filled observational archives of AO KNU glass collection with digitized images of more than 1 000 individual plates selected for the solution of current scientific problems;
- 300 records and 300 digitized images of selected plates of AO ONU glass collection (out of 120 thousand plates).

MAO NASU digital archive (GPA)

GPA comprises data of about 26 thousand of direct photographic plates, obtained with 14 instruments in 9 observational sites, having plate scales varying from 20 to 412 arcsec per mm, exposition duration from 10 second up to 1.5 hour with a number of expositions from 1 to 10 and the different structure of star images depending on observational method.

GPA operates under the control of server software DBGPA V2.0 and is accessible via web browsers on the search pages of UkrVO JDA (<http://gua.db.ukr-vo.org/>).

The screenshot shows a web form titled "SEARCH PARAMETERS" with the instruction "To select data fill at least one of search parameters, please". The form includes several sections:

- SEARCH IN ARCHIVE:** A dropdown menu set to "anywhere".
- OR for INSTRUMENT:** A dropdown menu.
- Center, geometry and dimensions of the field:** Fields for RA (h, m, s) and DEC (d, m, s). A "Geometry of the field" dropdown is set to "round". A "radius/half-diagonal/width" field and "units" dropdown (set to "deg of arc") are also present.
- Date or period:** Fields for start and finish year, month, and day.
- Exposition and color:** Fields for "maximum exposure low limit" (min. of time) and "color system" (set to "any").
- A checkbox for "select only available plates".
- A "SELECT..." button.

Figure 1: The search interface of JDA.

Digitizing of the archive started in 2008 on the Microtek ScanMaker 9800XL TMA flatbed scanner, continued in 2010 on the Epson Expression 10000XL and runs in two modes. In the first one we obtain images with a high level of resolution in two positions for plates of satisfactory quality (visually estimated) used in the current research. Images are obtained in 16-bit grey range with the resolution 1200 dpi. Original files are stored in TIFF format. Linear dimensions of images are 13 thousand pixels (30x30 cm) on both sides. The file size is about 380 Mb.

Currently, about 3 thousand plates of FON program and more than 2 thousand plates of other observational programs are scanned in two positions. The second scan mode - preview image in 8-bit gray range with the resolution 1200 dpi, stored in JPG format. Linear dimensions of images are up to 1500 pixels on the larger side. At the moment, in this mode more than 1 thousand plates are scanned.

In addition to positional observations, GPA archive comprises about 50 thousand spectral plates. This collection has not yet systematized and cataloged and is waiting for its researchers. To make a decision, if it is possible to use these plates for research purposes, the scanning of the spectral collection with the observations of variables such as R Corona Borealis began and the first attempts of digitized images' processing have been made (<http://ukr-vo.org/spectral/>, Fig.2).

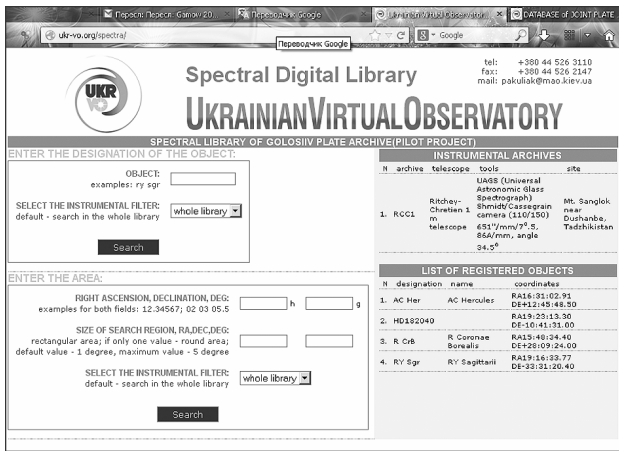


Figure 2: The interface of Spectral Digital Library, currently created on the UkrVO site.

AO LNU series of plates

Digital archive of AO LNU consists of direct images taken in a period 1939-1976 (a few plates are attributed since 1936). This archive contains about 8 thousand photographic plates, among them there are more than six thousands of direct northern sky area plates (mostly of wide-field). Observational programs concerned the search and study of variable stars by means of multicolor photometry, photographic photometry of circumpolar stars, novae stars, selected areas, occultations of stars by the Moon, Solar System bodies, and lunar eclipses. This almost 40 year coverage is a unique resource for studying of given objects. Instruments used: the camera with Zeiss lens triplet (D /F= 100/500 mm), Mertz refractor, astronomic camera (D/F=140/700 mm) and the Zeiss

refractor (D/F = 130/2400 mm). Part of the collection had never been processed at all or processed only partially. The complexity of data digitizing results from the fact that the most of the observational record books are in Polish and require decoding. Plates with emulsions of 15 sorts were used.

For now metadata of 4100 plates of AO LNU collection have been included into JDA (<http://gua.db.ukr-vo.org/createlist.php?aid=LAO010>) and more than 300 are ready to being added. At the moment, 3120 plates are digitized: among them there are 497 plates of historic interest as they were obtained in the first half of 20th century.

Historic plates are presented not only on the general search web pages of the JDA. It was decided to organize them into the historical online exposure on the UkrVO site (<http://ukr-vo.org/history/index.php?b2&4>). Also, these expositions are interesting from the point of view of educational historical and astronomical purposes (Fig.3).

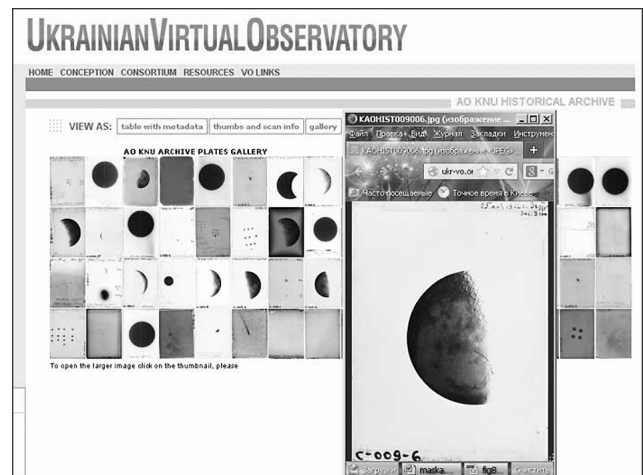


Figure 3: The example of historical exposition of photographic plates on web pages of UkrVO.

Glass collection of AO ONU

The archive contains about 100 thousand plates. The so called "old collection" contains 20 thousand plates, obtained since 1909, including the collection of Simeiz (Crimea) observatory. The other part of the archive is taken since 1957 and includes more than 80 thousand plates obtained in Odessa on the Mayaki observation station. Greater part of the collection consists of direct photos in photographic light. The instruments of the "old collection" were the long focus photographic camera – "large astrograph" – on the Cooke refractor with the aperture 165 mm; it was replaced with "small astrograph" equipped with 2 cameras and then three short-focus camera astrograph.

Observations were conducted using plates with "Ilford", "Agfa Astro", "Izoorto" emulsions with yellow, red filters or without filter. The registered stellar magnitude was 13.5. The exposure time was from 0.5 to 3 hours.

Digitizing of the collection is selective, based on the computer facilities of MAO NASU since the observatory has no its own capabilities for the organization of this

process. To date, JDA includes metadata and digitized images of 300 plates. Scans were obtained by the Epson Expression 10000XL scanner. Pre-processing of digital images in the software MIDAS / ROMAFOT, made in the MAO NASU, showed that the evaluation of object centers and photometric characteristics of objects provides a standard positional and photometric accuracy of photographic observations and plates can be used for further research.

These plates form two observational archives - JDA components: CRI012A and CRI012B. Access to data and digitized images of plates is through search interface UkrVO JDA (<http://gua.db.ukr-vo.org/createlist.php?aid=CRI012A>). Fig.4 shows the results of joint query to JDA sent from search interface, which display data from all archives, included into JDA.

Glass archives of AO KNU

According to preliminary estimates the collection of astronegatives has about 20 thousand plates, obtained in 1898-1996. To date, about a quarter of plates is cataloged and classified. 65% of the collection are glass plates, and the rest includes large-format films. The observations are divided into approximately 200 series, which corresponds to 200 JDA components. To date, 24 metadata files are organized and replenished.

Most of the plates have dimensions of 13 x 18, 13 x 13 and 16 x 16 cm, the maximum size of plates - 30 x 30 cm, the minimum one 6 x 9 cm. The collection includes some amount of images obtained as the contact imprints, which requires further analysis of digitized images for the maximum possible precision they can provide. Pre-processing of digital images from the collections of AO KNU showed positional accuracy of 0.1 sec in both coordinates and photometric accuracy of 0.07^m.

Images	map	Archive ID	RA Meaning	DEC Meaning	Date	Expos. in	Dimensions	Instrum.	Object	Place of Storage
		MYK012 002591	7 39 48	+24 17 0	751154	5	20x20	ZZA	Interamnia	Available in Mykola
		KAO070A165002	7 38 0	9 11 0	750206	0.5	13x13	AZT8	433 Eros	upon request
		MYK012 009566	7 36 18	+13 2 0	660212	5	20x20	ZZA	Laetia	Available in Mykola
		KAO070A165003	7 37 0	3 30 0	750211	0.5	13x13	AZT8	433 Eros	upon request
		GUA040B093367	7 37 47	+11 6 35	750203	3	24x24	DLA	433 Eros	sh.342 box110
		GUA040B093368	7 37 47	+11 6 35	750203	4	24x24	DLA	433 Eros	sh.342 box110
		MYK012 003307	7 37 48	+21 52 0	753226	2	20x20	ZZA	Vesta	Available in Mykola
		GUA040C001654	7 37 51	+25 44 37	530329	6.4	24x24	DLA	192 Nausikaa	sh.341 box75
		GUA040C001578	7 37 6	+0 34 16	791226	3	30x30	DWA	(3) Juno	sh.10 box71
		GUA040C001588	7 37 6	+0 34 16	791226	3	30x30	DWA	(3) Juno	sh.10 box72
		KAO070A165004	7 38 0	0 13 0	750215	0.5	13x13	AZT8	433 Eros	upon request
		MYK012 006362	18 7 6	-3 48 0	830519	5	24x24	ZZA	Hebe	Available in Mykola
		CR012A010825	18 8 0	-7 0 0	520620	45	13x18	ZDAO		upon request
		CR012B010826	18 8 0	-7 0 0	520620	45	13x18	ZDAO		upon request
		MYK012 006398	18 8 12	-18 8 0	830706	5	24x24	ZZA	Herodina	Available in Mykola
		MYK012 006153	18 9 24	-4 49 0	820654	5	24x24	ZZA	Juno	Available in Mykola
		LA0610 033482	19 0 0	-15 0 0	560705	30	13x18	Zeiss50/10	45 Eugenia	Available in the AO
		LA0610 033388	19 0 0	-5 30 0	560707	30	13x18	Zeiss50/10	3 Juno	Available in the AO
		LA0610 033491	19 0 0	-5 0 0	560705	30	13x18	Zeiss50/10	3 Juno	Available in the AO
		MYK012 008770	19 0 0	+20 0 0	970709	5	9x24	ZZA	Pallas	Available in Mykola
		LA0610 033387	19 0 0	-15 0 0						in the AO
		LA0610 033428	19 0 0	-15 0 0						in the AO
		LA0610 033477	19 0 0	-15 0 0						in the AO
		LA0610 033369	19 0 0	-14 0 0						in the AO
		GUA040C001587B	7 37 6							in the AO
		GUA040D001588	7 37 6							in the AO
		KAO070A165004	7 38 0							in the AO
		MYK012 006362	18 7 6							in the AO
		CR012A010825	18 8 0							in the AO
		CR012B010826	18 8 0							in the AO
		MYK012 006398	18 8 12							in the AO
		MYK012 006153	18 9 24							in the AO
		LA0610 033482	19 0 0							in the AO

Figure 4: Results of joint data search in JDA.

Currently database recorded metadata of about 1 thousand plates. Access to data is organized via the UkrVO JDA search interface (Fig.1,4).

Until recently, digitizing of the collection was conducted sporadically, mostly the plates with the bodies of the Solar System (Saturn, Jupiter, Pluto and their satellites), as well as plates of historical significance. The latter is similar to AO LNU historical part of the collection and is presented also as separate historical online exposition on the UkrVO site (Fig.3) (<http://ukr-vo.org/history/index.php?b1&4>).

Currently under contract with UAA the systematic digitizing of AO KNU plates and their linking to a database began. Digitizing is made on the Microtek ScanMaker 9800XL TMA scanner of MAO NASU.

Common problems of archival work

Large volumes of work require more resources, both technical, financial and human. The digitizing of early photographic observational archives is facing serious difficulties.

On the one side, we experience the lack of scanning and computer facilities in most of the small observatories as well as a staff enough to handle the vast collections. Another problem is the improper storage places of glass collections that create the risk of fatal collection damage before the collection is being totally digitized. As a result, we face the necessity of essential financial input without explicit and quick response.

On the other side, there is a low rate of digitizing with flatbed scanners: the process is stretching in time for years and gives way to organize poorly. In addition, there is the lack of distinctive scientific tasks with immediate scientific output, and, as a result, we have the decline of interest (that means – funds) in projects of such types.

References

- Pakuliak, L., Kazantseva, L., Virun, N., Andruk, V.: 2012, *IAUS*, **285**, 389.
- Vavilova, I. B.; Pakuliak, L. K.; Protsyuk, Yu. I. et al: 2012a, *Baltic Astronomy*, **21**, 356-365.
- Vavilova, I. B., Pakuliak, L. K., Shlyapnikov, A. A. et al.: 2012b, *Kinematics and Physics of Celestial Bodies*, **28**, 85-102.
- Vavilova, I. B., Pakuliak, L. K., Protsyuk, Yu. I. et al.: 2011, *Kosmichna Nauka i Tekhnologiya*, **17**, 74-91.
- Vavilova, I. B., Pakuliak, L. K., Protsyuk, Yu. I.: 2010, *Kosmichna Nauka i Tekhnologiya*, **16**, 62-70.

THE KYIV MERIDIAN AXIAL CIRCLE' OBSERVATIONAL ARCHIVE AS THE UKRVO SCIENTIFIC RESOURCE

A. Zolotukhina

Main Astronomical Observatory NAS of Ukraine, Kyiv, Ukraine

nastya@mao.kiev.ua

ABSTRACT. We describe the database of CCD-observations conducted with Meridian Axial Circle in 2001-2003. In that time it was equipped with a ISD017AP CCD having 1040x1160 pxs, 16 mkm pixel size and 1.394" per pixel scale which is the component of UkrVO astro-information resource. We developed the software for management and accumulation of these and new data, which will be used to create a catalogue for clarification of coordinates of faint stars. We note that the MAC is a refractor (D=180 mm, F=2.3 m) which is used now in a CCD astrometric survey of the equatorial zone.

Key words: virtual observatory, Meridian Axial Circle, CCD-archive

In 2000, the Kyiv Meridian Axial Circle (MAC) was equipped with a new modern micrometer based on a CCD image sensor (manufactured at the Mykolaiv Astronomical Observatory). Since 2001, after necessary tests of electronics and the matrix quality, the telescope is in operation for observational programs. The photometric system of the MAC reproduces standard V photometric system; the limiting magnitude is about $V=17$. Star pixel coordinates are measured with an accuracy of 0.02 pxs and star fluxes to 0.02 mag. The telescope is used for observations of equatorial stars with the aim of measuring their positions, proper motions, and magnitudes. These observations are performed by a group of astronomers from the Astronomical Observatory of the T. Shevchenko National University of Kyiv and from the Main Astronomical Observatory of the National Academy of Sciences of Ukraine (Babenko et al, 2005).

In 2001-2003 years, a pilot program of observations of stars in 192 fields with extragalactic ICRF sources in the declination zone from 0° up to $+30^\circ$ were performed (Telnyuk-Adamchuk et al., 2002). These observations have formed the basis for compilation of the catalogue KMAC1 of positions, photometric data, and proper motions of 115000 stars (Lazorenko et al., 2005). We created the database of these observations as well as developed the software for information management and accumulation of new data.

In 2009 the Kyiv Meridian Axial Circle was equipped with CCD-camera Apogee Alta U47 with the CCD-matrix e2v CCD47-10. It has the format 1024x1024 pxl with size

of pixels $13 \times 13 \mu\text{m}$, dark signal 0.66e/px/s, and noise of reading of 10 e for $T=-20^\circ\text{C}$. In CCD-camera the 16-digit analog-digital converter (ADC) is used. In comparison with previous camera with 12-digit ADC the new CCD camera allows us to register the more bright stars (mainly, reference Tycho2 stars) without repletion ADC image of star along all the length of CCD-matrix. Thus, the range of stellar magnitude in equatorial zone was succeeded and extended from $11.5^m - 17^m$ up to $8.5^m - 17^m$. Now the conduction of observations with new camera is the main aim of a the long-time observational program of stars in equatorial zone.

Currently the CCD-archive of the MAO NAS of Ukraine contains of about 16,000 CCD scans obtained in 2001-2003 in equatorial zone of the sky. These scans are saved on CD-ROMs, namely the CCD-frames with ICRF radiosources from 192 fields of KMAC1. The total size of archive is about 5.5 Gbyte and contains almost 800,000 images of stars.

Since 2009 this archive is a supplement by new observations. We are working on the creation of the database of the CCD-observations and tools for its administration under the UkrVO program (Vavilova et al., 2012a, 2012b, 2011, 2010).). The Web-interface for data search is realized in the form of package of the scripts in PHP script language, which has the wide library of functions for interaction with MySQL. It represents the HTML-form called from a browser.

References

- Babenko Yu., Lazorenko P., Karbovsky V. et al.: 2005, *Kinematics and physics of celestial bodies Suppl.*, **5**, 316.
 Telnyuk-Adamchuk V., Babenko Yu., Lazorenko P. et al.: 2002, *Astron. & Astrophys.*, **386**, №3, 1153.
 Lazorenko P., Babenko Yu., Karbovsky V. et al.: 2005, *Astron. & Astrophys.*, **438**, 377.
 Vavilova I.B., Pakuliak L.K., Protsyuk Yu. I. et al: 2012a, *Baltic Astronomy*, **21**, 356.
 Vavilova I.B., Pakuliak L.K., Shlyapnikov A.A. et al.: 2012b, *Kinematics and Physics of Celestial Bodies*, **28**, 85.
 Vavilova I.B., Pakuliak L.K., Protsyuk Yu.I. et al.: 2011, *Kosmichna Nauka i Tekhnologiya*, **17**, 74.
 Vavilova I.B., Pakuliak L.K., Protsyuk Yu.I.: 2010, *Kosmichna Nauka i Tekhnologiya*, **16**, 62.

RADIO-ASTRONOMY

ANALYSIS OF THE VARIABILITY AND THE SPECTRUM OF PERIODS OF EXTRAGALACTIC SOURCE OJ 287 IN THE RADIO WAVES

A. Donskykh¹, M. Ryabov², A. Suharev², M. Aller³

¹ I.I.Mechnikov Odessa National University

² Odessa observatory "URAN-4" of the Radio-astronomical institute NAS Ukraine

³ Radio observatory of Michigan University, Ann Arbor, USA

ABSTRACT. We analyzed long-term monitoring of data flux of extragalactic source OJ 287 obtained at frequencies of 14.5 GHz (1974-2011), 8 GHz (1971-2011), 4.8GHz and (1979-2010), on the RT-26, University of Michigan, USA. Variability of the flux of the radio source was investigated by applying wavelet analysis. There were identified long-period (in the range of 3.6 to 13.6 years) and short (in the range from 1.2 to 1.8 years) components at all studied frequencies and it was determined the time of their existence. The "spectra periods" for each year of observation were built to assess the contribution of individual periods in the formation of the most powerful phase of activity of the radio source. The dynamics of the manifestations of active periods at different frequencies was observed. The obtained data was compared with the results of MOJAVE VLBI monitoring for the period of 1995-2012 years at a frequency of 15.4 GHz. It allowed to investigate the structure of emissions during periods of manifestation activity maxima.

Introduction

According to current views, in the center of active galactic nuclei are supermassive black holes weighing 10^6 - $10^{10}M_{\odot}$. The material falling into a black hole, has got an angular momentum and forms the accretion disc. Part of the disk material falls into the black hole, and the other part of the disk material is accelerated by strong magnetic fields and forms a jet that is ejected perpendicular to the plane of the accretion disc.

Extragalactic source OJ 287 refers to blazars, that is, his jet is directed toward the observer. Blazars exhibit variability across the electromagnetic spectrum. In the article [1], the authors suggest that blazar OJ287 contains a system that consists of two black holes. The secondary black hole rotates around the primary the more massive black hole with a period of ~ 12 years.

The main characteristics of OJ 287: $z\sim 0.306$, the distance to the object ~ 1576 Mpc. We used data from observations at frequencies of 14.5 GHz (1974-2011), 8 GHz (1971-2011) and 4.8 GHz (1979-2010). Earlier, we published an article on the four sources, including the OJ

287 [2]. In comparison with the previous one, in this article there was expanded an application of wavelet analysis.

Observations

We investigated the monitoring data on the frequencies 14.5 GHz, 8 GHz and 4.8 GHz flux blazar OJ 287, received a 26-meter radio telescope of the Observatory of Michigan (USA). Details of the calibration and analysis techniques are described in [3].

We used the average values of the fluxes of sources at regular intervals samples every 7 days.

With the use of a polynomial moving average (half width of the interval 5 points), there was a decrease of noise and remove the casual bursts [4]. Total flux densities of a radio source OJ 287 are shown in Fig. 1. Sixth-degree polynomial was subtracted for each frequency.

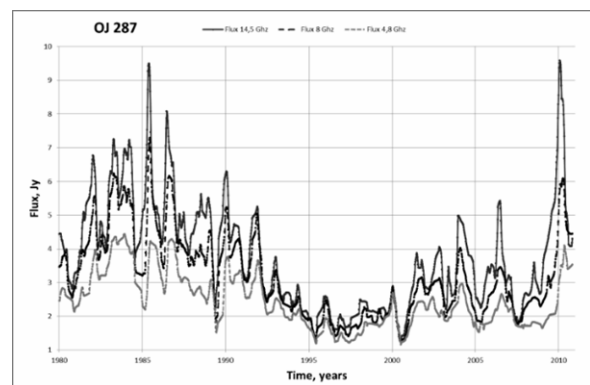


Figure 1: Graph of the fluxes at frequencies of 14.5, 8, 4.8 GHz, for the blazar OJ287.

FOURIER-analysis

In order to determine the periods Lomb-Scargle periodogram for data with an uneven readings on the time axis was built [5]. The spectral densities were calculated using the spectral Bartlet window. Example of Fourier spectra is shown in Fig.2.

WAVELET-analysis

Two-parameter analyzes function of one-dimensional wavelet transform is well localized in time and frequency. This distinguishes it from the ordinary Fourier analyzing function covers the entire time axis. Thus, it is possible to see the detailed structure of the process and the evolution of the harmonic components of the signal in time. We used a continuous wavelet transform based on Morlet function. The example of the wavelet spectrum is shown in Fig. 3 and Fig. 4. On the wavelet spectra of the harmonic components of the signal are visible as bright spots, pulling in a strip along the time axis. The calculation of the integral wavelet spectra in the frequency range allows us to study the spectral variation of the signal power over time.

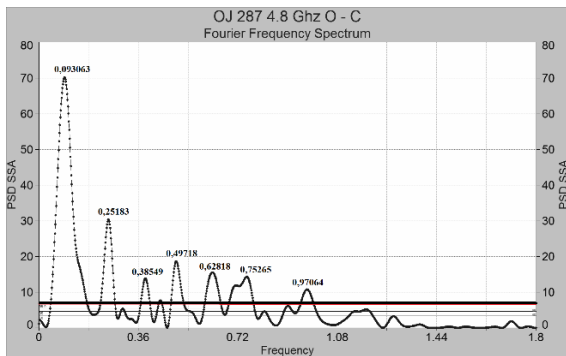


Figure 2: Periodogram for the source OJ287 at a frequency of 4.8 GHz. In the figure the frequency of 0.093063 corresponds to the period 10.7 years, the frequency of 0.25183 4-year period, the frequency of 0.38549 – 2.6 years, the frequency of 0.49718 – the period of 2 years, the frequency of 0.62818 – the period of 1.6 years, the frequency of 0.75265 – 1.3 years, the frequency of 0.97064 – 1 year.

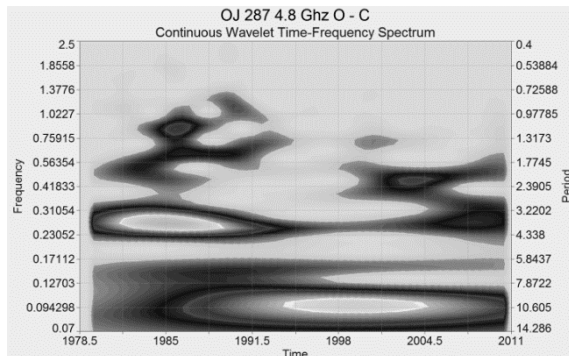


Figure 3: Continuous wavelet spectrum for the source OJ287 at a frequency of 4.8 GHz.

The main periods

Monitoring data of the source OJ287 at three frequencies were processed using wavelet analysis. Among the periods are allocated long-period and short-period.

The trend component. The source OJ 287 at frequencies of 14.5 and 8 GHz has got periods of 7-8.7 years and 13.6 years. At a frequency of 4.8 GHz is detected the period 10.9 years.

Short-period component. Of short-period component at the source there noted the existence of the period of 3.6-4.4 years at frequencies 4.8 and 8GHz. There Fig. 4, in the

time interval since 1976 till 1990, shows a spot in the form of a "jellyfish", which is formed by two periods – 1.2 and 1.6 years. Such a "jellyfish" is visible on the wavelet spectra at all three frequencies, but the highest spectral power is observed at a frequency of 14.5 GHz. In the period since 2004 till 2011 at all three frequencies there appeared period of 1.8 years.

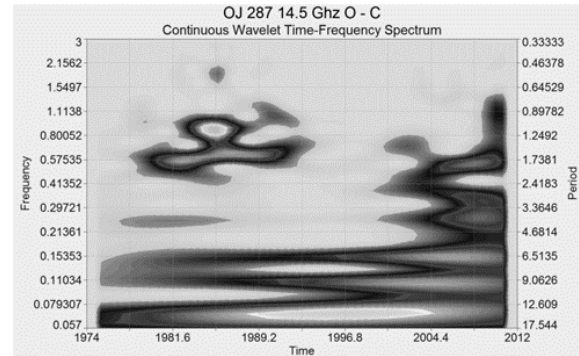


Figure 4: Continuous wavelet spectrum for the source OJ287 at a frequency of 14.5 GHz.

Phases of the activity

The distribution of the total energy of the signal on the scale can be traced through the global wavelet spectrum, which corresponds to the power spectrum, smoothed on every scale Fourier spectrum of the analyzing wavelet. Thus, the global spectrum reflects the relative contribution of the different scales in the total energy and detects the energy distribution of process scales. With the global wavelet spectrum are identified the main periods of activity of the flux of the radio source at the studied time interval (Fig. 5).

Phases of activity for the source observed at a frequency of 14.5 GHz – 1985, 1989 and 2010, at a frequency of 8 GHz – 1985 and 1989 and at a frequency of 4.8 GHz – 1985 and 1989.

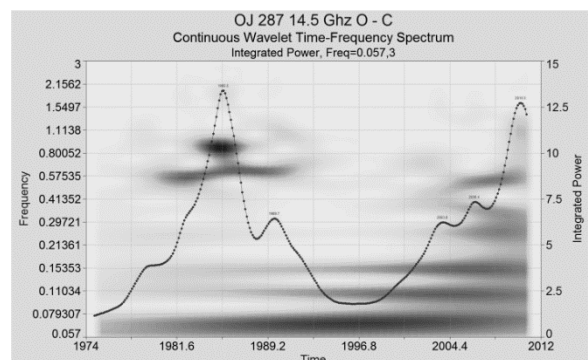


Figure 5: Graph of the integral wavelet spectrum (time – the spectral power) for OJ287.

"The spectra periods"

For each year of observations graphics "spectraperiods" were built to assess the contribution of individual periods in the activity of the radio source. In Fig. 6 shows an example of such a graph. The use of a "spectrum of periods" allows comparisons with VLBI observations to determine the nature and dynamics of the processes in the jets.

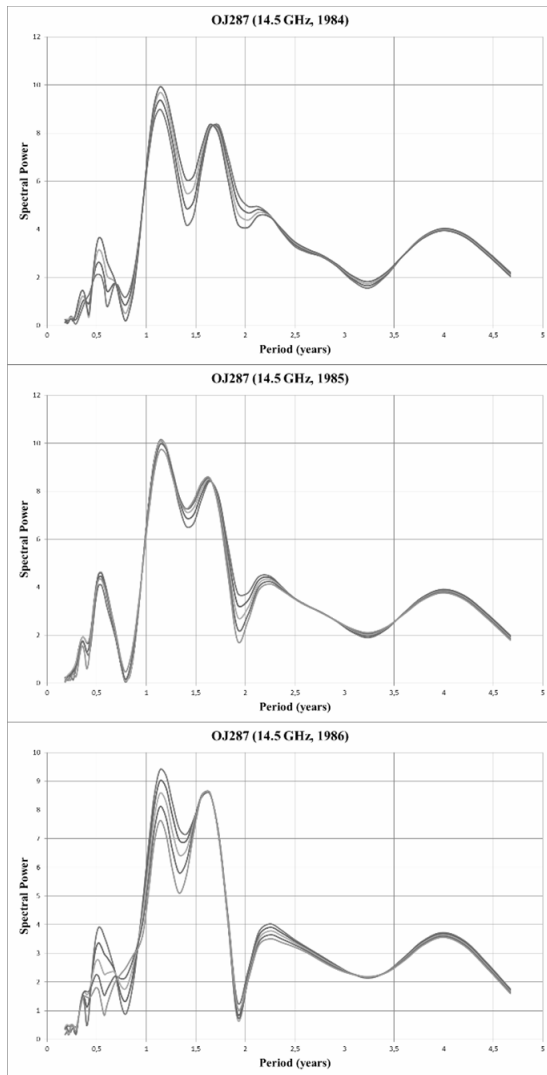


Figure 6: The graph shows the contributions of the individual periods in the activity of the source OJ287 at a frequency of 14.5 GHz for 1984-1986 years.

Stationary components in the jet

In the study of the bright components in the jet on VLBI data at a frequency of 15.4 GHz (Fig. 8) [6] there has been observed that there are gradually receding components and the component which episodically occur on the same distance from the core. In the articles of some authors [7],[8],[9] one discussed the existence of a stationary components in the jets which are in the fixed position. These knots brightness were explained as standing shock wave caused by the interaction of the jet with the environment.

Conclusions

Data processing based on wavelet analysis indicates the presence of radio source OJ287 short-and long-period component, the time of their existence, the main phases of activity. "The trend" component of the activity of radio fluxes formed by the longterm oscillations with a period in the range of 7 – 13.6 years. At coincidence of peaks of the trend component with maximum flux density of short-period changes with periods ranging from 1.2 to 4.4 years,

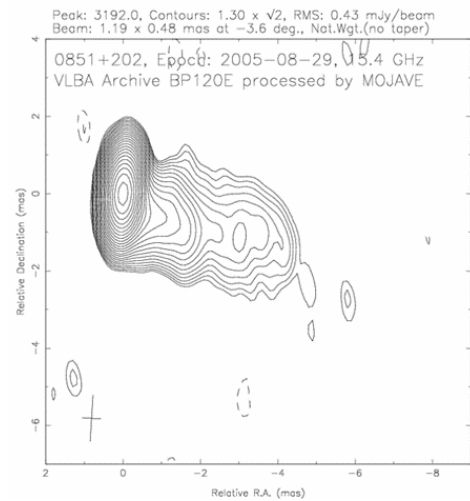


Figure 7: Radio card for Blazar OJ287 at a frequency of 15.4 GHz for the epoch 2005-08-29. This image is obtained from the MOJAVE database.

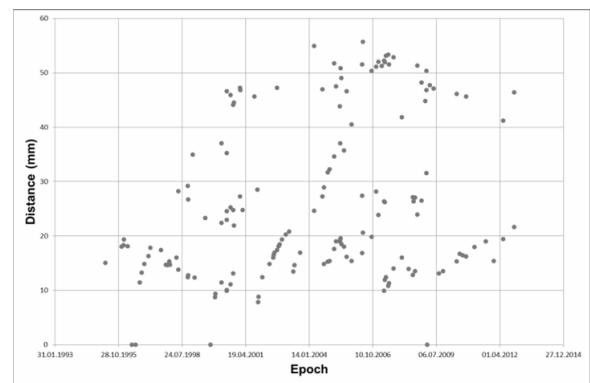


Figure 8: The motion of the jet components relative to the core.

there are marked phases of increased activity. The obtained data were compared with the results of MOJAVE VLBI monitoring for the period 1995 -2012 years at a frequency of 15.4 GHz, allowing to investigate the structure of emissions during periods of manifestation activity maxima. In the jet there marked the existence of certain structures that move with the times and of the bright knots, occurring at the same distances from the core.

References

1. Lehto H.J., Valtonen M.J.: 1996, *ApJ*, **460**, 207.
2. Ryabov M., Donskyh A., Suharev A., Aller M.: 2012, *Odessa Astron. Publ.*, **25/2**, 200.
3. Aller H.D., Aller M.F., Latimer G.E., Hodge P.E.: 1985, *ApJS*, **59**, 51.
4. Gaydyshev I.: 2001, Analysis and data processing (thespecial directory), St.Petersburg Publishing house.
5. Smolentsev N.: 2010, *Wavelet-analysis in MATLAB*, DMKPress.
6. The MOJAVE database (Lister et al., 2009, *AJ*, 137, 3718).
7. Jorstad et al.: 2001, *ApJS*, **134**, 181.
8. Britzen et al.: 2008, *A&A*, **484**, 119.
9. Alberdi et al.: 2000, *A&A*, **361**, 529.

OBSERVATION ON THE RADIO TELESCOPE URAN-4 OF RADIO SOURCES, CONNECTED WITH THE CORONAL MASS EJECTION ON THE SUN

Galanin V.V.¹, Derevjagin V.G.², Kravetz R.O.³

Institute of Radio Astronomy of National Academy of Science of Ukraine,
Odessa, Ukraine

¹ *gvv@breezeine.net*, ² *dvg@gmail.com*, ³ *krro@ukr.net*

ABSTRACT. In 2012 and 2013 the observations of radio sources covering by the solar corona was conducted on the radio telescope URAN-4. In obtained data there was fixed the records of the strong radio sources, which had flow level comparable with the 3c461 source. As a result of information analysis from miscellaneous observatories about the solar activity conditions there is done the conclusion that they are connected with the coronal mass ejections which was took place that time.

Key words: radio source, solar corona.

Radio telescope URAN-4 (RT) is the part of long base radio interferometer system (LBRS), which is located on the Ukraine territory from west to east [1]. Working frequency band of this instrument is 10-30 MHz. Radio telescope consist of antenna array with the phased system, system of precision time synchronization and information registration system.

Antenna of the radio telescope is represents the electrically controlled phased array that consist of 128 tourniquet vibrators with the linear size of 232.5 on 22.5 m. It can select two polarized components of the signal. Direction diagram width of this antenna, measured on the half power level on the frequency 25 MHz has value 2.7×22 degrees. In the long base radio interferometer regime there is 2 seconds resolution provided.

In the year 2010 in Odessa radio astronomy observatory URAN-4 of RI NAN of Ukraine there was made the modernization of the equipment resulting in the creation of digital radiometer and software for processing of obtained information.

In 2011 was begun the observations of outer regions of solar corona by the radio sources radiation using the “translucence” method, which is widely used for study of near sun plasma. First experiments used this method was made in 60-th of past age by V.V.Vitkevitch and A.Hjuish. Next years until today many works of researchers from various countries was dedicated to this subject.

In our institute in 1970 in Astronomy journal there was published an article “Crab nebula decameter radiation scattering in solar corona” by S.Y.Braude, A.V.Megn, L.L.Baseljan dedicated to “translucence” observations through the solar corona. Same year and in same publishing

was published theoretical work by P.V.Blyoch, V.G.Sinitsyn, and N.M.Phuks in which considering problems of flat wave spreading in solar corona with account of it scattering and refraction on the large-scale irregularities.

In 2012 the experiments on the RT URAN-4 were continued. In the period from 06.06 to 21.06 the flow of Crab nebulae (3c144) was measured on two frequencies 20 and 25 MHz. During the eclipse the sharp increasing of the source flow was observed on the small elongation angles from Sun, which is comparable with the flow of supported source 3c461. Analyzing the processes which took place that time on the Sun and on the base of information from radio spectrographs of Nancey and San-Vito observatories and also from satellites SOHO and STEREO we intended that these phenomena are connected with the solar flashes.

For the validation of our conclusions, in 2013 we make an experiment, sense of which is showed on the fig.1. For this purpose in the period from 26.05 to 20.06 there were measured flows of Sun and 3c123 and 3c144 sources on two frequencies.

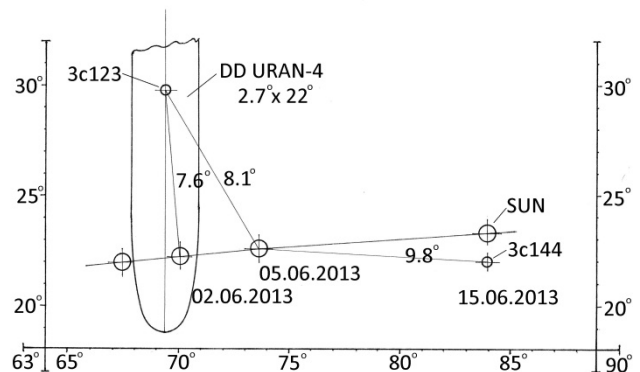


Figure 1: Scheme of experiment.

During the observations 05.06 some source was recorded (fig.2) which flow was similar to those ones that we observed previous year.

That day Sun was placed between two sources with elongation angle 8.1 degree to 3c123 and 9.8 degree to 3c461. Power level of this source three times exceeds level of supported source 3c461.

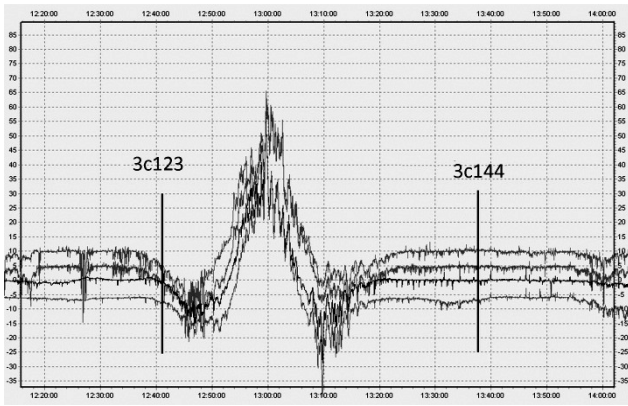


Figure 2: The observed source.

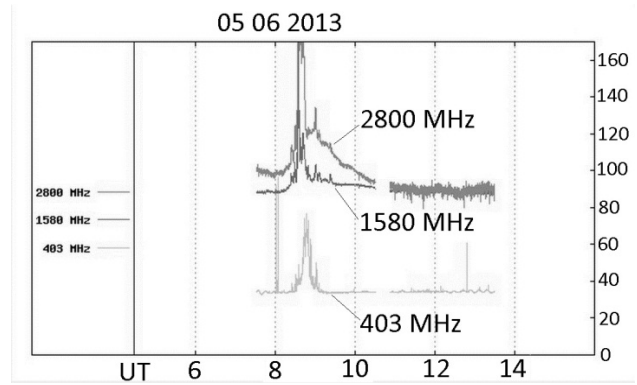


Figure 3: Sun flash on three frequencies.

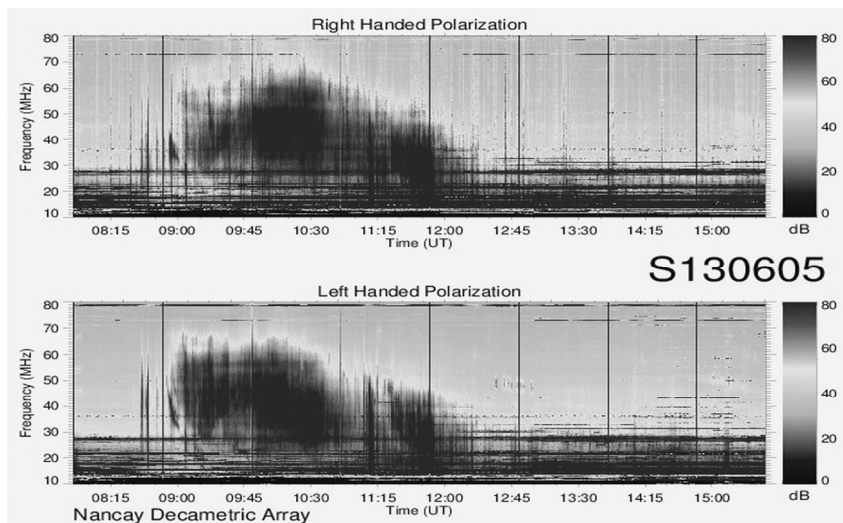


Figure 4: Spectrograph data from Nancay observatory.

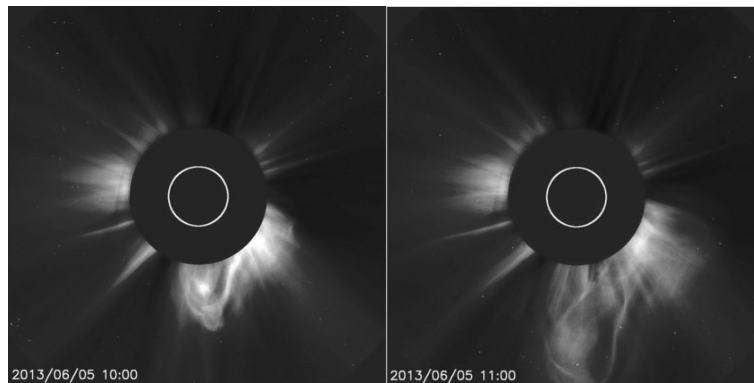


Figure 5: Active processes on the Sun

Analysis of the observations obtained by miscellaneous observatories which we made for this day showed, that according to polish astronomers (fig. 3) who measured on 403, 1500 and 2800 MHz frequencies from 11 hours to 14 hours the solar flashes were took place.

According to spectrograph data of Nancay observatory (fig. 4) which works in the band 20-70MHz, the active processes on the Sun begun in 11.15. In 15.45 the process finished, but some separate flashes were continued until 18.40 and they are visible on the spectra from 20 to 60 MHz frequencies.

According to SOHO observatory data showed on fig. 5, the active processes on the Sun that is connected with the coronal

mass ejections begun in 12.12 (LASCO-2). An expected finish of this process is 15.00, but diffused remainders of the ejected matter were visible until the end of the day.

So, analysis of data from miscellaneous observatories and our observations that we made from 06.06 to 21.06.2012 along with our observations 05.06.2013 showed that we was observe the sources, that was created as a result of solar coronal mass ejections.

References

Galanin V.V. et al.: 1989, Kinematics and Physics of celestial bodies, 5, 5, 87.

PECULIARITIES OF SPORADIC E_s LAYER IN THE PERIOD OF SOLAR CYCLE ACTIVITY MAXIMUM

Kravetz R.O.¹, Galanin V.V.²

Institute of Radio Astronomy of National Academy of Science of Ukraine,
Odessa, Ukraine

¹ *krro@ukr.net*, ² *gvv@mail.ru*

ABSTRACT. We consider the year and a half row of observed ionosphere data from European ionosonde network DIAS in the period of 24 solar cycle activity maximum. The season changes of the mean critical frequency of sporadic E_s layer are determined. We show that the frequency of appearing of this layer in summer months is essentially exceeding it frequency of appearing in the winter ones. We compare critical frequency of E_s layer with the critical frequency of F2 layer.

Key words: ionosphere, ionogram.

The Earth ionosphere is point of issue during the many years. It caused by the fact, that ionosphere play significant role in the spreading of radio waves with various wavelengths. Particularly, due to ionosphere ability to reflect the radio waves, the decameter waves can spread for a very long distances, reaches thousands of kilometers. Herewith the firm radio communication is only possible when the reflected layer of ionosphere is stable. If this reflected layer is changes it characteristics than radio communication can grow worse and even disappear. Therefore the special services are watch for ionosphere condition, they control it current parameters and forecast the radio wave passing on the various routes.

Ionosphere play significant role also in radio astronomy, because signals of cosmic radio sources is passed through it and distorted to some degree for the expense of this. For example, this radio signals can be absorbed in ionosphere or partially reflected by it various layers, that to it turn induce the distortion of information which radio telescope received. During ionosphere disturbances, when it parameter is changes, this distortions may significantly intensify. So, further study if ionosphere is very important task.

As known, ionosphere have layer structure [3], it main layers are D, E and F. These layers are regular, because they are present in ionosphere almost always. However, in ionosphere exists also non regular layer E_s, called sporadic, because it arrival has spontaneous character. Herein, reflection ability of this layer can be very high and particularly exceed the reflect ability of all other layers. The reflect ability of every ionosphere layer is expressed by the value of it critical frequency, that represents maximum frequency of the signal which this ionosphere layer can reflect at vertical sounding.

In other words, critical frequency of sporadic E_s layer can exceed critical frequencies of all other ionosphere layers and particularly, critical frequency of the F layer. In this case the conditions of radio waves spreading in ionosphere are significantly changes, because there is arrived the additional reflected screen, which reflect signals of same and even more frequencies that the regular F layer. This can lead to an additional multibeaming in radio communication channel or to an additional refraction at the radio astronomy observations.

In some cases sporadic E_s layer can caused the blanketing effect, when it hide higher ionosphere layers. In this case, for example, the signals of cosmic radio sources may not reach the earth surface. Therefore, study of sporadic F_s layer and his peculiarities is a very important task.

Study of ionosphere and it peculiarities are in particular interest during the maximum of solar activity cycle. Nowadays the maximum of 24-th solar activity cycle is present, so the subject of further consideration is the ionosphere conditions and its peculiarities in past year and a half.

The main instrument to study the ionosphere is ionosphere station called ionosond. It represents the special radar which radiates vertically up with the frequency change from 1 to 30 MHz. The result of ionosond sounding is the ionogram, which represents the plot of reflected layer height dependence from radiated frequency. The ionograms are the initial material to get all main ionosphere parameters.

In Europe the ionosondes are united to the common system called DIAS (European Digital Upper Atmosphere Server) [1,2]. Provided by this system data allow to qualitative estimate the ionosphere state and particularly to decide the question about presence or not the ionosphere disturbances. In present work we mainly used Chilton ionosond data obtained from international data center WDC-C2.

Fig.1 show several consequent ionograms. On this ionograms we can see sporadic E_s layer arrival that looks as a straight horizontal track unlike other layers which reflecting height is changes with frequency. Time of existing of sporadic E_s layer is not big and can be from several minutes to several hours. Therefore, when considering some sequential ionograms the sporadic E_s

layer is looks as one-two ionograms that differs significantly from neighboring ones because they have straight horizontal track at 100 km height.

For study the peculiarities of sporadic E_s layer we has consider the ionograms recorded by ionosond for the last year and a half, namely for all 2012 and first half of 2013 years. Preliminary processing of ionograms consist of determine critical frequencies of all ionosphere layers and

its heights. It can be made either manually or automatically by means of special software. Modern ionosondes as a rule have such software, so they provide data in text format as a time rows of critical frequencies and heights of all ionosphere layers and at the same time the initial ionograms are also accessible. Below we consider data obtained by automatic processing – autoscaling.

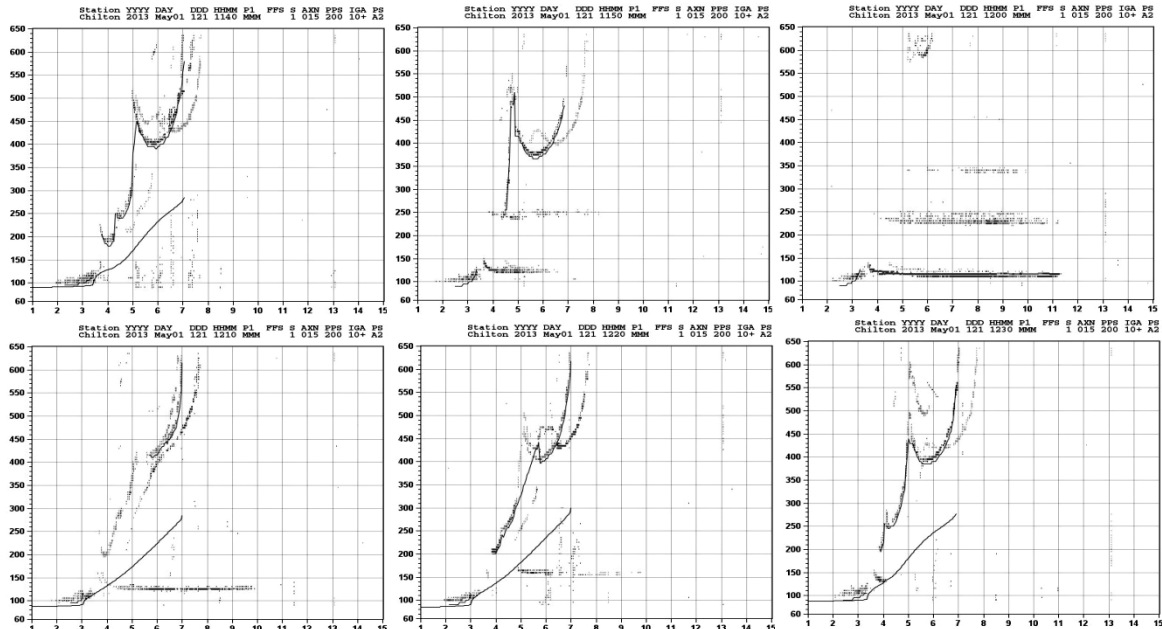


Figure 1. Arrival of the sporadic E_s layer.

Preliminary evaluation of ionosphere layers critical frequencies rows showed that generally speaking, sporadic E_s layer is regular, because it present almost every day, however it critical frequency as a rule not big. Only some separate days it critical frequency exceeds 5-7 MHz and sometimes exceeds critical frequency of the F layer. In these cases we can speak about sporadic layer itself. Fig.2 shows an example of E_s critical frequency changes for three days and F2 critical frequency for the compare. This plot shows that on the background of sporadic E_s layer critical frequency regular changing there is exist some separate peaks exceeding 5-7 MHz value. Same situation is take place in other days during almost all the year.

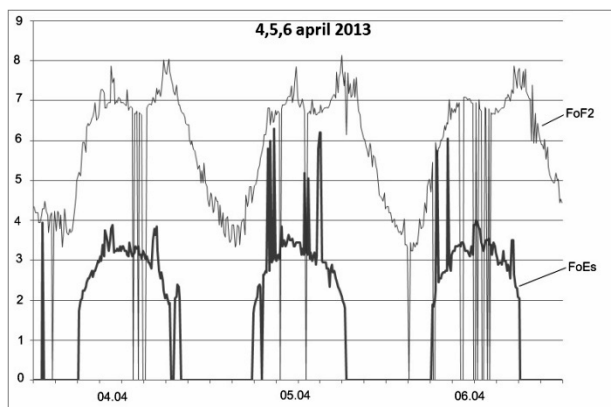


Figure 2. Critical frequencies of E_s and F2 layers.

So, time dependence of sporadic E_s layer critical frequency we can conditionally separate to some regular part which maximum value not exceed 2-3 MHz and sporadic part which maximum value can be significantly higher and even can exceed critical frequency of F2 layer.

To find the time characteristics of regular and sporadic parts we smoothed out critical frequency values of sporadic layer for one day boundaries and determine the maximum of the smoothed value for this day. This was made by the sliding mean value method for two hours time. For the same day we also had determine the maximum of non smoothed value to distinguish the sporadic part. Same manner we determined maximums of smoothed and non smoothed values of F2 layer critical frequency. These calculations was made for every day of the studied period resulting in data rows that characterizes regular and sporadic parts of E_s and F2 layers critical frequencies for a long period. These data is shows on the fig.3, where time dependencies of mentioned values for 2012 year are given, and fig.4 shows same values for the first half of 2013 year.

As it seen from this plots, regular part of sporadic E_s layer critical frequency have an expressed season dependence which consist of three periods: from January to May it grow, in summer from June to August it value practically not change and from September to December it decreased. Herein for critical frequency of F2 layer such dependence is not seen. Sporadic part of sporadic E_s layer critical frequency also has an expressed season dependence that consists in next: frequency of arrive of this layer in summer months is significantly higher than in winter ones. Here frequency of arrive was calculate as a number of times when critical frequency value exceeding F2 critical frequency.

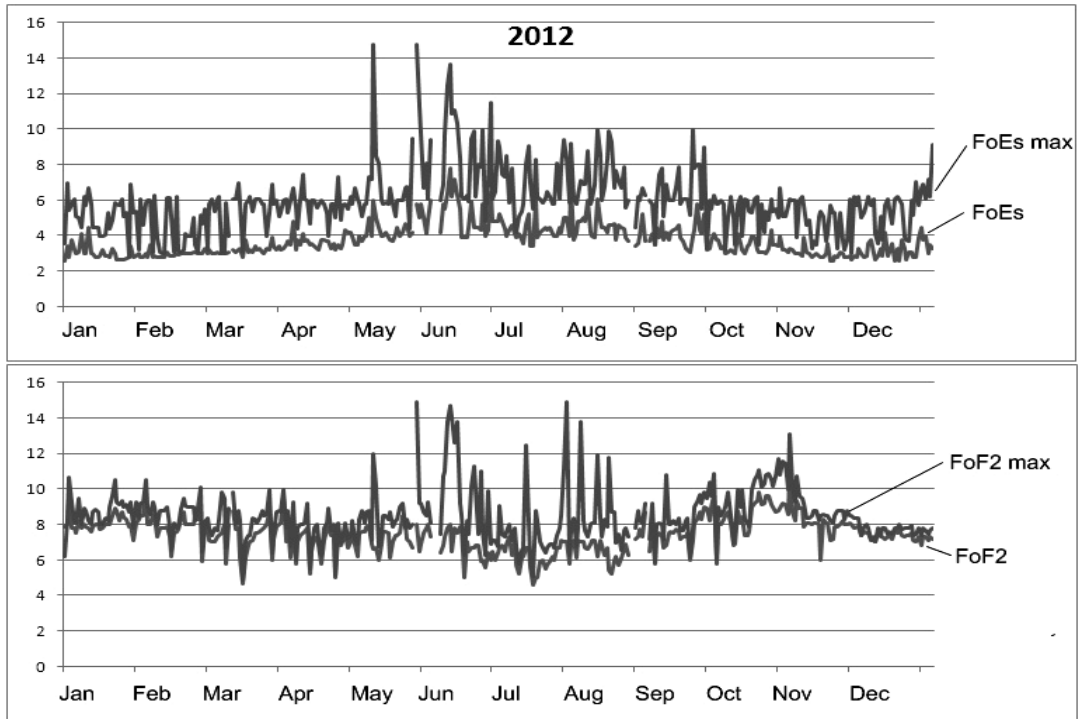


Figure 3. Maximum and smoothed values of critical frequencies in 2012 year.

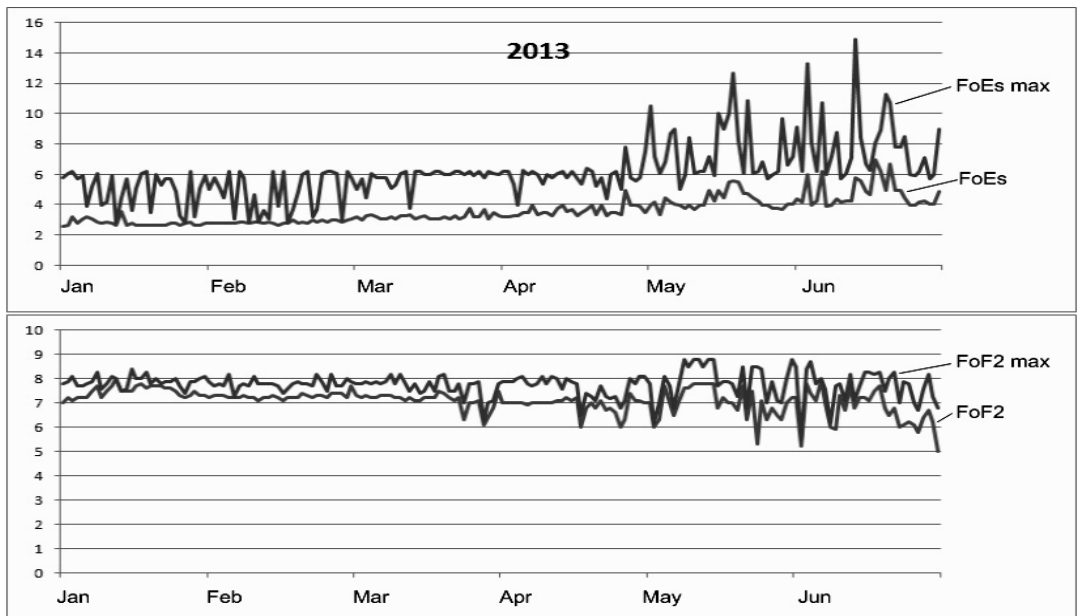


Figure 4. Maximum and smoothed values of critical frequencies in 2013 year.

These plots also show that increase of E_s layer critical frequency is accompanied by some decreasing of F2 critical frequency. This peculiarity is take place as in 2012 and in 2013 years and also on the shorter periods that can be seen on every day records of these critical frequencies.

References

1. DIAS: European Digital Upper Atmosphere Server. <http://www.iono.noa.gr/dias>.

2. Belehaki A., Cander Lj.R., Zolesi B., Bremer J., Jurén C., Stanislawski I., Dialektis D., Hatzopoulos M. DIAS Project: The establishment of a European digital upper atmosphere server, 2005, *J. Atmos. Sol-Terr. Phys.*, **67(12)**, 1092.
 3. Brunelli B.E., Namgaladse A.A. *Physics of ionosphere*. M.: Nauka, 1988.

THE TIMING SCALE OF THE STEEP-SPECTRUM SOURCES

A.P. Miroschnichenko

Institute of Radio Astronomy of the NAS of Ukraine
Kharkov, Ukraine
mir@rian.kharkov.ua

ABSTRACT. We continue to study the properties of the steep-spectrum sources from the Grakovo catalogue received with the radio telescope UTR-2. At this paper the lifetimes of steep-spectrum sources have been estimated. We have used two methods to determine the characteristic ages of the steep-spectrum galaxies and quasars: 1) at independent estimate of the source's magnetic field strength; 2) at well-known condition of the equipartition of the magnetic field energy and the energy of the relativistic particles in objects. The derived alternative estimates of the characteristic age of steep-spectrum sources have been compared. The relations of ages and some physical parameters of the examined objects have been considered. The values of the source's lifetime and the characteristic age indicate on the possibility of the activity recurrence of galaxies and quasars with steep radio spectrum.

Key words: radio spectrum, characteristic age, galaxy, quasar, lifetime

Introduction

The most probable reason of origin of steep-spectrum sources (the spectral index $\alpha \gg 1$) at the decametre band is their long evolution. The great extent of radio structure (\sim Mpc) of galaxies and quasars with steep spectra testifies in favour of this statement. So, it is important to estimate the characteristic age of objects with steep radio spectra.

The particular interest present sources with great rising of the radio spectrum after a break at low frequencies (it is the spectral type C+). We have selected objects with spectrum C+ at the domain of declinations $\delta = -13^\circ \dots +20^\circ$ and $\delta = 30^\circ \dots 40^\circ$ detected at the catalogue of extragalactic sources UTR-2 (Grakovo catalogue) [1-6] with flux density more than 10 Jy at the frequency 25 MHz. It was found that 148 radio sources correspond to the selection criteria, including 52 galaxies, 36 quasars and 60 optically non-identified sources. As we have analysed, 10 objects from the galaxy sample have X-ray emission, and the quasar sample reveals 15 X-ray sources.

The necessary optical and high-frequency data for the sample objects have been get from the NED database (<http://nedwww.ipac.caltech.edu>) and the connected with NED sites.

The characteristic age and lifetime of sources with radio spectrum C+

We estimate the characteristic ages of examined sources with radio spectrum C+ in the UTR-2 catalogue by two methods: 1) at the independent estimate of the source's magnetic field strength; 2) at the well-known condition of the equipartition of the magnetic field energy and the energy of relativistic particles in sources. The independent estimation of the magnetic field strength B_{IC} of the sample sources has been derived at the assumption on origin of X-ray emission of objects by the inverse Compton scattering (IC) of microwave background photons by relativistic electrons.

Like at the recent paper [7], we use in the calculations the relation by Harris & Grindley [8] with our transforming to estimate the value B_{IC} at the frequency of

X-ray emission $\nu_x = 2.42 \cdot 10^{17} \text{ Hz}$ (at the energy of X-ray photons 1 keV) and the radio frequency $\nu_r = 2.5 \cdot 10^7 \text{ Hz}$ (the decameter band). So, we have determined the mean values of the magnetic field strength:

for galaxies in the sample with spectrum C+:
 $\langle B_{IC} \rangle = 0.88(\pm 0.21) \cdot 10^{-6} \text{ Gauss}$;

for quasars in the sample with spectrum C+:
 $\langle B_{IC} \rangle = 1.69(\pm 0.29) \cdot 10^{-6} \text{ Gauss}$.

2) Also we have derived the estimates of the magnetic field strength B_{equip} of examined sources by the ordinary method – at the condition of equipartition of the magnetic field energy and the energy of relativistic particles in the sources. In that case, the mean values of the magnetic field strength B_{equip} are the next:

$\langle B_{equip} \rangle = 8.14(\pm 0.58) \cdot 10^{-6} \text{ Gauss}$ – for galaxies in the sample with spectrum C+;

$\langle B_{equip} \rangle = 6.15(\pm 0.30) \cdot 10^{-6} \text{ Gauss}$ – for quasars in the sample with spectrum C+.

Thus, the values of the magnetic field strength B_{IC} have noticeable smaller quantities comparatively with values B_{equip} (within the limits of one order).

It is known, that the characteristic age of source is determined as the time of synchrotron decay of relativistic electrons in the magnetic field of a source [9]:

$$t_{syn} = 50.3 \frac{B^{0.5}}{B^2 + B_{CMB}^2} [\nu_b (1+z)]^{-0.5},$$

where t_{syn} is the characteristic age of objects, 10^6 years; B is the magnetic field strength of source, 10^{-5} Gauss, the value $B_{CMB} = 0.32(1+z)^2$ is the strength of the equivalent magnetic field which corresponds to the intensity of the microwave background, 10^{-5} Gauss, ν_b is the critical frequency of the synchrotron spectrum of the source, GHz. In this paper the calculations of t_{syn} have been carried out at the value of the critical frequency $\nu_b = 10$ MHz.

1) So, we have get the estimates of the characteristic ages of the considered objects with radio spectrum C+ at the independent estimate of their magnetic field strengths B_{IC} : the characteristic age t_{syn} for the sample galaxies (the mean value) is; $\langle t_{syn} \rangle = 7.44(\pm 1.25) \cdot 10^8$ years

the characteristic age t_{syn} for the sample quasars (the mean value) is $\langle t_{syn} \rangle = 1.76(\pm 0.27) \cdot 10^8$ years.

2) We have estimated the characteristic age of considered sources with spectrum C+ t_{equip} at the energy equipartition condition:

the characteristic age t_{equip} for the sample galaxies (the mean value) is $\langle t_{equip} \rangle = 4.66(\pm 0.42) \cdot 10^8$ years;

the characteristic age t_{equip} for the sample quasars (the mean value) is $\langle t_{equip} \rangle = 2.02(\pm 0.25) \cdot 10^8$ years.

Thus, the values of estimated characteristic age of sources with steepness spectrum C+ are enough great and cover the time interval from 10^8 to 10^9 years.

At the same time as it is interesting to estimate the lifetime t_W for examined radio sources. One can derive this value as the relation of energy of relativistic electrons W_e and low-frequency radio luminosity of source L :

$$t_W = W_e / L$$

We have used the corresponding relationships from [10]. It turned out that the mean lifetime $\langle t_W \rangle$ for the sample galaxies is

$$\langle t_W \rangle = 2.13(\pm 0.85) \cdot 10^{10} \text{ years};$$

and the mean lifetime $\langle t_W \rangle$ for the sample quasars is

$$\langle t_W \rangle = 5.18(\pm 1.21) \cdot 10^9 \text{ years}.$$

Since the values of the lifetime of radio sources with spectrum C+ exceed the values of the characteristic age of these objects it is possible to assume the activity recurrence for galaxies and quasars with spectrum C+.

It is important to consider the relationships of the characteristic ages and other parameters of examined objects. As one can see from Figure 1 the relation of the age t_{syn} versus the linear size of objects may point out on two branches in this relation.

We have found that the ratio of infrared and X-ray luminosities, and one of decameter (at 25 MHz) and X-ray luminosities of considered sources correlates with their characteristic ages (see Figure 2,3,4). Hence, the contribution of the relatively low-frequency emission increases at the increase of the characteristic age of the steep-spectrum galaxies and quasars. Also, note that the ratio of the energy of relativistic particles and the magnetic field energy decreases at the increase of the characteristic age of the steep-spectrum sources (Figure 5).

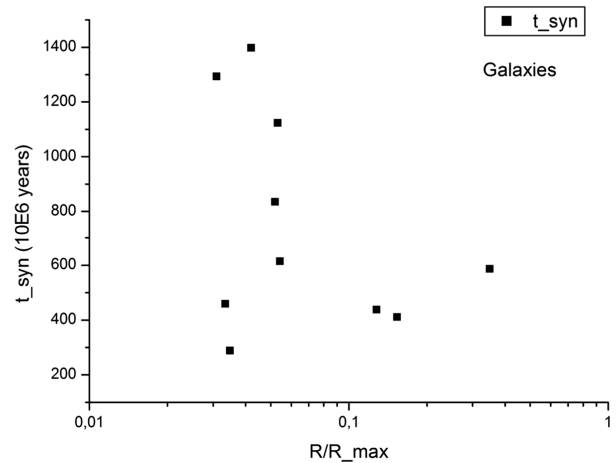


Figure 1: The relation of the characteristic age and the linear size of steep-spectrum sources

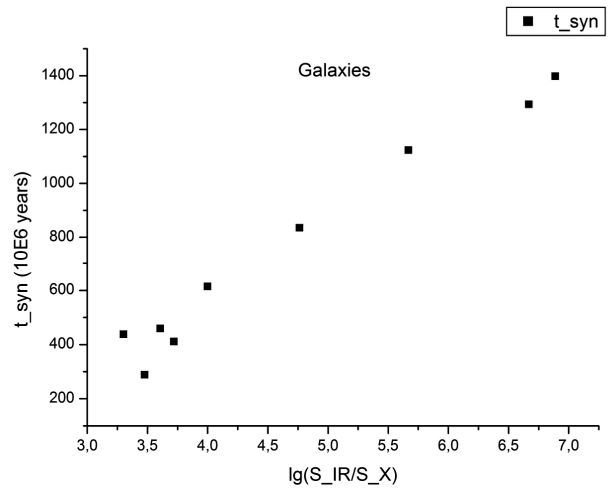


Figure 2: The characteristic age versus the ratio of galaxy's monochromatic luminosities at the infrared and X-ray bands

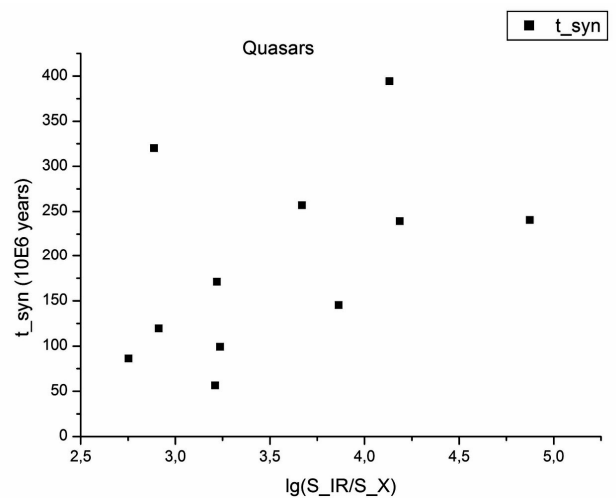


Figure 3: The characteristic age versus the ratio of quasar's monochromatic luminosities at the infrared and X-ray bands

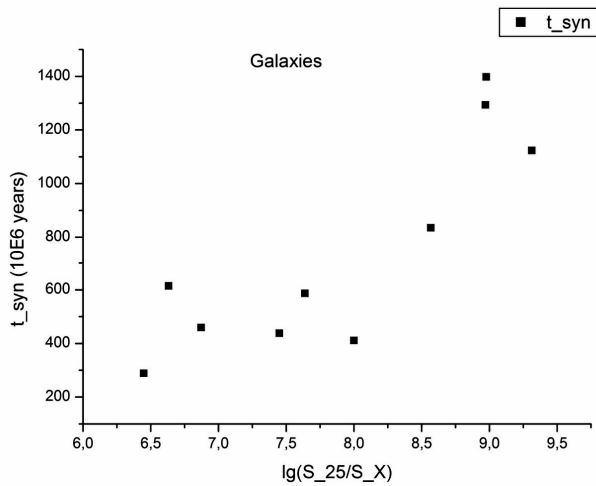


Figure 4: The characteristic age versus the ratio of monochromatic luminosities at the decimeter and X-ray bands

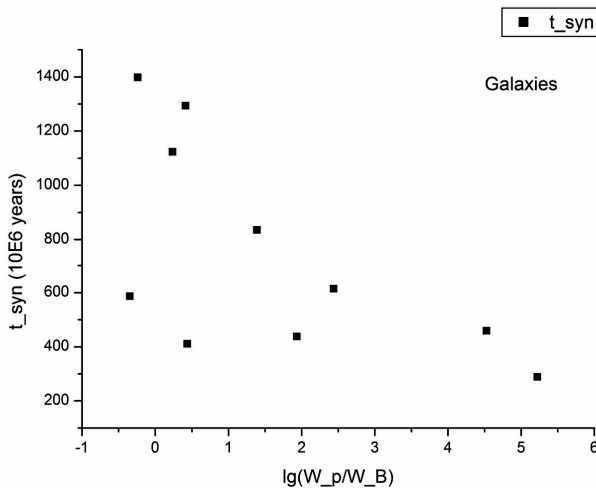


Figure 5: The characteristic age versus the ratio of the source's energy of relativistic particles and energy of magnetic field

Conclusions

The steep-spectrum galaxies and quasars possess the great characteristic age ($\sim 10^8 - 10^9$ years).

The estimate of the lifetime of the steep-spectrum sources has value $\sim 10^{10}$ years. So, it is possible to assume the activity recurrence for the examined sources.

The contribution of the low-frequency emission increases at the greater characteristic age of steep-spectrum objects.

The ratio of the energy of relativistic particles and the energy of the magnetic field decreases at the greater characteristic age of a source with steep spectrum.

References

1. S.Ya.Braude, A.V.Megn, S.L.Rashkovski, B.P.Ryabov, N.K.Sharykin et al.: 1978, *Astrophys. Space Sci.*, **54**, 37.
2. S.Ya.Braude, A.V.Megn, K.P.Sokolov, A.P.Tkachenko, N.K.Sharykin: 1979, *Astrophys. Space Sci.*, **64**, 73.
3. S.Ya.Braude, A.P.Miroshnichenko, K.P.Sokolov, N.K.Sharykin: 1981, *Astrophys. Space Sci.*, **74**, 409.
4. S.Ya.Braude, A.P.Miroshnichenko, K.P.Sokolov, N.K.Sharykin: 1981, *Astrophys. Space Sci.*, **76**, 279.
5. S.Ya.Braude, S.L.Rashkovski, K.M.Sidorchuk, M.A.Sidorchuk et al.: 2002, *Astrophys. Space Sci.*, **280**, 235.
6. S.Ya.Braude, A.P.Miroshnichenko, S.L.Rashkovski, K.M.Sidorchuk, M.A.Sidorchuk, N.K.Sharykin: 2003, *Kinematics and Physics of Celestial Bodies*, **19**, 291.
7. A.P.Miroshnichenko: 2012, *Odessa Astron. Publ.*, **25**, 129.
8. D.Harris, J.Grindley: 1979, *MNRAS*, **188**, 25.
9. M.Jamrozy, J.Machalsky, K.-N.Mack, U.Klein: 2005, *Astron. Astrophys.*, **433**, 467.
10. K.Lang: 1974, *Astrophysical Formulae*, Berlin: Springer – Verlag.

STUDY OF SATURN ELECTROSTATIC DISCHARGES IN A WIDE RANGE OF TIME SCALES

K.Mylostna^{1,a}, V.Zakharenko^{1,b}, A.Konovalenko¹, V.Kolyadin¹, P.Zarka², J.-M.Grießmeier³,
G.Litvinenko¹, M.Sidorchuk¹, H.Rucker⁴, G.Fischer⁴, B.Cecconi², A.Coffre⁵, L.Denis⁵,
V.Nikolaenko¹, V.Shevchenko¹

¹ Institute of Radio Astronomy, Kharkiv, Ukraine

² LESIA, Observatoire de Paris, CNRS, UPMC, Université Paris Diderot

³ ASTRON, Netherlands Institute for Radio Astronomy, Postbus 2, 7990 AA, Dwingeloo

⁴ Space Research Institute, Graz, Austria

⁵ Station de Radioastronomie de Nancy, Observatoire de Paris, 18 Nancy, France

^a *milostnaya@rian.kharkov.ua*, ^b *zakhar@rian.kharkov.ua*

ABSTRACT. Saturn Electrostatic discharges (SED) are sporadic broadband impulsive radio bursts associated with lightning in Saturnian atmosphere. After 25 years of space investigations in 2006 the first successful observations of SED on the UTR-2 radio telescope were carried out [1]. Since 2007 a long-term program of ED search and study in the Solar system has started. As a part of this program the unique observations with high time resolution were taken in 2010.

New possibilities of UTR-2 radio telescope allowed to provide a long-period observations and study with high temporal resolution. This article presents the results of SED study in a wide range of time scales: from seconds to microseconds. For the first time there were obtained a low frequency spectrum of SED. We calculated flux densities of individual bursts at the maximum achievable time resolution. Flux densities of most intensive bursts reach 4200 Jy.

Key words: electrostatic discharges, microstructure, flux density, dispersion delay

Introduction

The study of thunderstorm activity in planet atmospheres in the solar system is the new direction in the planetary astrophysics. For the last seven years both of ground-based and space observations made a great progress in ED study. Cassini space craft (SC) monitoring and new UTR-2 results provided gives new findings storm activity seasonality, episode variations of frequency characteristics, microsecond time structure.

Due to the modernization of the receiving equipment on the UTR-2 radio telescope it became possible to study the SED with high temporal resolution, as well as long-time observations give the opportunity to study hourly variations of lightning activity.

The interest to high time resolution SED study is caused by several reasons. The main one is that it can pro-

vide more deep investigation of SED nature. Only in 2009 there were finally established that SED is a radio emission from lightning. There were first detected optical flashes simultaneously with SEDs in Saturn atmosphere in the time of spring equinox [2]. But we still don't know what kind of lightning they are. The most common suggestion is intra-cloud lightning. Moreover, SED study with high time resolution gives us opportunity to investigate energy characteristics of SEDs.

This paper present the results of observation of Saturnian storm called J conducted in 2010. The storm J was a fascinating and incredible phenomenon [3], the largest and one of the longest storms in SED investigations history. CS Cassini registered the peak number of bursts and the most powerful bursts. The last one is very important for ground-based high time resolution studies.

Observations and data processing

Search of wide-band cosmic signals in presents of earth lightning and different nature interference, is a very difficult task. Therefore, we use a number of methods [4,5] to confirm the origin of cosmic signals.

UTR-2 can provide simultaneous observations with 5 spatially separated beams. To select the signal from direction toward the source (i. e. Saturn) we use ON-OFF mode of observation when the third (central) beam of UTR-2 telescope is pointed at the source, and the fifth-

We used correlation recording mode for observation with time resolution of 20 milliseconds. We use such time resolution for data volume compressing and increasing of sensitivity of the radio telescope in comparison to waveform mode. The ability of back-end facility of UTR-2 to record large amounts of data allows carrying out several hours lasting observations. The average length of a single recording was 6-6.5 hours (except waveform mode). That

gives us the possibility to keep track of the full period from the rising and setting of the planet without any a priori information about phase of storm (longitude of storm source on the Saturn's surface).

We used 3 receivers for observations in December 2010 session. Two receivers were in correlation mode to provide ON-OFF regime respectively. This data were used for SED identification and search of extremely high intensity bursts. Such regions were found in the record for 23 December [7]. The third digital receiver was in the waveform mode with data time resolution of 15 ns. The third receiver was used to record only signals from the third beam.

Automatic search was provided by the multichannel algorithm described in details in [4]: signal is detected only in case of its presence in 2 or more sub-bands (bandwidth of sub-band is equal 1 MHz) with limit 4σ . According to the Voyager and Cassini data the maximum duration of the signal was determined as 500 ms. In our algorithm the duration of detectable signals should not exceed this value.

After identification of SED signals with time resolution 20 ms there were conducted high time resolution study. Below there are some estimations of expected flux densities of registered signals.

As a minimum detectable flux density value we use the 4σ - level:

$$4\sigma = \frac{4 \cdot 2kT}{A_e \sqrt{\Delta f \Delta t}}, \quad (1)$$

where k – is the Boltzmann constant, T is the galactic background temperature (30000K at 20 MHz considering the Saturn position for 23 December 2010), A_e is the effective area of the UTR-2 in Saturn direction on 23 December 2010 (declination $-4^\circ 11' 09''$) (90000 m²), Δf and Δt , are bandwidth and time resolution, respectively. For frequency band 1 MHz and time resolution 20 ms (in correlation mode) we have 4σ flux density level equal to 26 Jy. For waveform mode: in case of accumulation by a factor of 16 (time resolution 484 ns) and for 14 MHz frequency band the 4σ - level equals to 2000 Jy. From this calculation, it follows that parts of records (selected according to results of detection in low time resolution data), where the signal-to-noise ratio (S/N) varies from a few dozen to hundreds are perspective for studying with microsecond time resolution.

To resolve SED fine structure we had to modernize multichannel algorithm. We used only the strongest SEDs choosing by criterion discussed above. For data analysis we used different time scales: subsecond, submillisecond and microsecond time resolution.

Results and discussion

Figure 1 shows the spectrograms of lightning at different time scales. The top panel shows the sequence of several bursts with a typical duration of tens of milliseconds. This coincides with a time measured for SED according to Cassini and ground-based measurements [4,8,9].

In the paper [10] there are considered two possible variants of Saturnian lightning nature: a superbolt variant when the fine time structure of SED consists of several tens of microseconds peaks with the energy 1013 J of one burst. And second one - if those tiniest peaks have one-microsecond duration, when the total energy decrease to

107 J. In figure 1 on the middle and lower panels it shown the internal structure of lightning with millisecond and microsecond time resolution. An important result is that the SED consists of short (about one hundred microseconds) discharges of varying intensity. When passing to microsecond resolution (lower panel), a fine structure is almost indistinguishable or absent.

On the spectrograms in figures 1, 2 it can be clearly seen a time delay between high (f_{\max}) and low (f_{\min}) frequencies. It is a propagation delay t (due to dispersion phenomenon) in ionized medium (ionospheres of the Saturn and Earth, and interplanetary medium), that is equal [11]

$$t = 10^{16} \cdot \frac{DM}{2.410331} (f_{\min}^{-2} - f_{\max}^{-2}), \quad (2)$$

where DM is "dispersion measure" in pc cm⁻³. For $DM = 4 \cdot 10^{-5}$ pc cm⁻³, $f_{\max} = 33.0$ MHz and $f_{\min} = 16.5$ MHz the value of this propagation delay is several hundred microseconds.

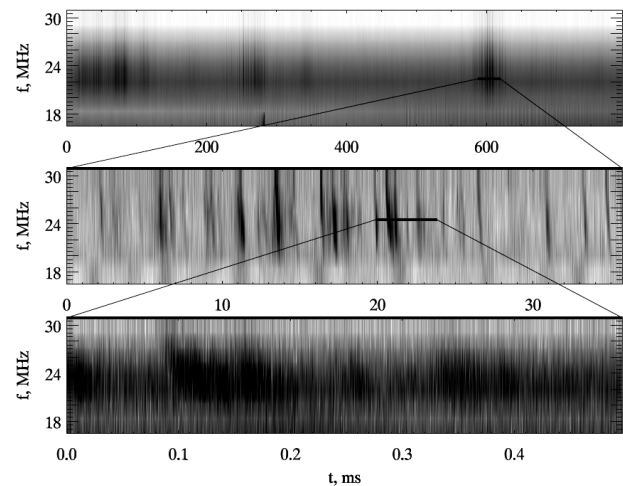


Figure 1. Different time scales of SEDs

The dispersion observed in fine time structures is both the SED criteria and the confusing factor for SED characteristics investigations.

At higher frequencies earth lightning signals are reflected from higher layers of earth ionosphere and pass longer trace than at lower ones. Terrestrial lightnings fully light up and are not detectible for ground-based equipment at frequencies where the Earth's ionosphere becomes transparent. As a result they have cut-off at some frequency and also the delay at high frequency in contrast of dispersive delay (2) of SED spectra [12].

Time delay of the signals at different frequencies leads to "smearing" of the lightning fine structure. Therefore, we applied a coherent method of removing the dispersion delay [12]. After this step, we can improve the S/N ratio with the aid of the signal accumulation by time or frequency.

For the first time, we obtain the lightning low-frequency spectrum. In figure 2 the time sequence (the bottom panel) and the result of its FFT (the top panel) are shown. This result is valid if SED spectrum is plain and has no peculiarities in radio band and we can estimate some features of that spectrum.

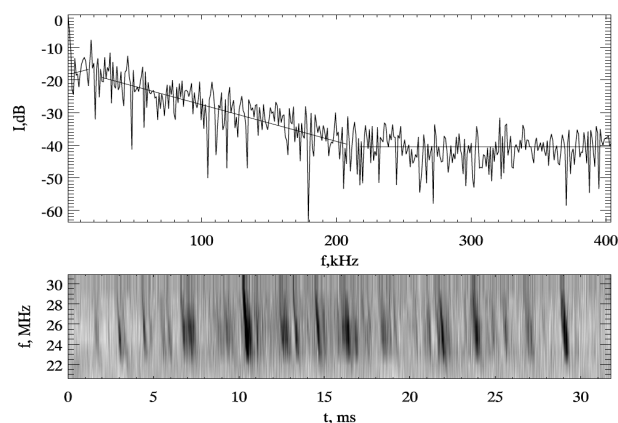


Figure 2. Low frequency spectrum of 32 milliseconds record

As we can see Saturnian lightning have similar frequency characteristics as earth ones [13]. Terrestrial lightning have the maximum power at frequencies near 7 kHz. Above that frequency the spectrum drops as f^{-1} up to 40 kHz, and f^{-2} above 100 kHz [13].

Characteristics of the SED, defined from Fig. 2 are next. Spectral index defined in the frequency range 20 ... 200 kHz is approximately equal to -2 . The maximum intensity is close to 17 kHz. Above 200 kHz the power of SEDs is masked by external noise. To increase the sensitivity the accumulation of a large number of lightning in a high-frequency part (200 kHz and above) is required. The obtained results also show that the elements of the temporal structure of lightning (with typical durations of the order of a microsecond) are a small contributor to the total power. The main part of power has the components of a typical duration of hundreds of microseconds. It also speaks in favor of the fact that the total energy of lightning is about 10^{12} ... 10^{13} J [10].

Signal accumulation by frequency results in a higher sensitivity (1). It is necessary to find a compromise between increasing the time resolution and maintaining sensitivity. To search for a microsecond elements in the time structure, we have chosen $\Delta t = 484$ ns. Only SC Voyager-1 could record data with $\Delta t = 0.1$ ms. Although the microstructure was not identified, but it has been concluded that it probably exist.

Figure 3 shows the structure of the individual bursts. The burst consists of a great number of short peaks. Attempts to find unresolved counts (intensity of the nearest points falling down in ϵ times) in the most intense lightning did not lead to positive results. Thus, we can assume that, for time resolution of 484 ns, the fine structure of SED was resolved.

As mentioned in [4], increasing of the time resolution will reveal the most intensive bursts. In our data their intensity reaches approximately to 4200 Jy.

Conclusion

The ground-based observations of storm J in 2010 extended our knowledge of the possibility of ground-based studies of extraterrestrial planetary lightning. The results accumulated to date have several points. For the first time there were resolved SED signals with submicrosecond time resolution. There have been found a multilevel structure of SED signals. The submillisecond structure (signals with a typical duration of the order of 0.1 ms) first was identified together with the well-known millisecond structure. The presence of the microsecond structure, which

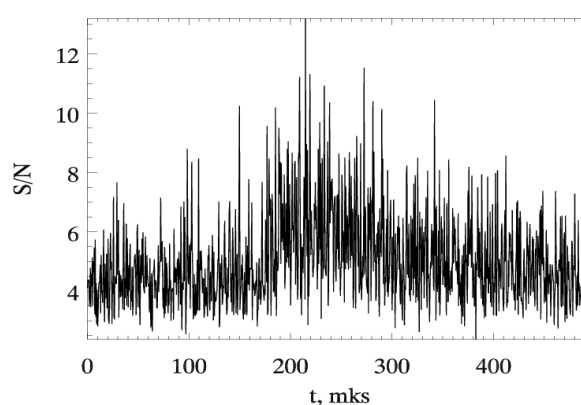


Figure 3. The example of fine time structure of SED. Burst profile in frequency band 14-28 MHz.

gives a significant contribution to the total radiation power of the lightning, is questionable. The achieved signal-to-noise ratio shows that the number of unresolved microsecond bursts in the records is very low or even zero.

For the first time there were obtained a low frequency spectrum, and its character is in good agreement with the existing theory (for terrestrial lightning) and observations.

Thus, the ground-based observations with the UTR-2 radio telescope give us the unique opportunity to explore the lightning on Saturn over a wide range of time scales: from long-term SED variations investigations to fine time structure study.

References

1. Konovalenko A.A., Kalinichenko N.N., Rucker H.O., et al.: 2013, *Icarus*, **224**, 14.
2. Dyudina U.A., Ingersoll A.P., Ewald S.P., Porco C.C., Fischer G., Kurth W.S., West R.A.: 2010, *Geophys. Res. Lett.*, **37**, №9, L09205.
3. Fischer G., Kurth W.S., Gurnett D.A., Zarka P., Dyudina U.A., Ingersoll A.P., Ewald S.P., Porco C.C., Wesley A., Go C., Delcroix M.: 2011, *Nature*, **475**, №7354, 75.
4. Zakharenko V., Mylostna K., Konovalenko et. al.: 2012, *Planetary and Space Science*, **61**, №1, 53.
5. Mylostna K., Zakharenko V., Konovalenko A.A., Litvinenko G.V.: 2013, *Proc. MSMW'13 Symposium*, Kharkiv (Ukraine), 474.
6. Konovalenko A., Falkovich I., Rucker H. et al.: 2011, *Proc. of PRE VII*, Graz (Austria), 521.
7. Mylostna K.Y., Zakharenko V.V.: 2013, *Radiofizika i Radioastronomia*, **18**, №1, 12.
8. Fischer G., Kurth W.S., Dyudina U.A., Kaiser M.L. et. al.: 2007, *Icarus*, **190**, №2, 528.
9. Zarka P., Pedersen B.: 1983, *J. of Geophys. Res.*, **88**, Issue A11, 9007.
10. Farrell W.M., Kaiser M.L., Fischer G., Zarka P., Kurth W.S., Gurnett D.A.: 2007, *Geophys. Res. Lett.*, **34**, №6, L06202.
11. Backer D.C., Hama S., Hook S.V., Foster R.S.: 1993, *ApJ*, **404**, 636.
12. Hankins T.H.: 1971., *ApJ*, **169**, 487.
13. Farrell W.M., Desch M.D.: 1992, **19**, Issue 7, 665.

DATA PROCESSING CENTER FOR RADIOASTRON PROJECT HARDWARE OPTIMIZATION

M.Shatskaya¹, A.Abramov¹, I.Guirin¹, E.Isaev^{2,3}, V.Kostenko¹, S.Likhachev¹, A.Pimakov¹,
S.Seliverstov¹, N.Fedorov¹

¹ Astrospace Center P.N.Lebedev Physical Institute RAS Moscow, Russia, mshatsk@asc.rssi.ru

² Pushchino Radio Astronomy Observatory ASC LPI, Pushchino, Russia

³ National research university Higher school of economics, Moscow, Russia

ABSTRACT. The RadioAstron is an international space VLBI project led by the Astro Space Center of Lebedev Physical Institute in Moscow, Russia. The payload - Space Radio Telescope, is based on spacecraft Spektr-R, that have been designed by the Lavochkin Association. The Spektr-R space craft was successfully launched 18 th July 2011.

In this article we want to summarize Radioastron data processing center work during 2 last years. Tasks facing of the scientific data processing center are organization of service information exchange, collection of scientific observations, storage of scientific observations, processing of scientific observation data Radioastron project.

Key words: Radioastron, data processing center, VLBI.

Data Processing Center (DPC) actively participated in service data exchange between tracking station, ballistic center, ground telescopes, tracking headquarters, center of experiment planning.

For this aim we organized ftp-server and received different kind of information:

from Institute of applied mathematics predicted and reconstructed orbit; scientific and telemetric data from ground telescopes; from tracking station scientific and telemetric and other data. We also receive telemetric information from tracking headquarter.

There is intensive exchange between center of experiment planning and ground headquarter and ground telescope about plans of observation also over our ftp-server.

We can say that this structure corresponds to our requirements. All this information is various, but it has small size. We collect about 0.5 TB during 2 years.

Our next task is collection of scientific data from space and ground telescopes. Especially for transferring data of space telescope observations we organized a direct channel of 1 Gbit /s between the monitoring station and Astro Space Center. 1:00 hour observation takes about 50 GB of memory. The data comes to DPC in Moscow and stored there.

For transferring data from ground telescopes in the most cases we use Internet. The hour of observations at ground radio telescope takes about 100 GB of memory.

Today we have two channels Internet with 200 Mbit/s and 70 Mbit/s for this data transferring.

More than 20 ground-based telescopes participate in the observations with Radioastron. This telescopes from Europe, Asia, Australia, Africa, America. Many different countries take part in Radioastron project. They are Spain, Japan, Germany, Italy and others. The Torun telescope is actively involved in the work only in January 2013.

We connected with these telescopes and tested communication between us. Transfer rates with almost all quite good, allowing us to collect the data. For transmission, we use multi-threading. This increases the speed of transmission of information and makes life easier for us. The biggest speed of transferring with Medicina and Noto is up to 70 Mbit/s.

In general, the rate of transmission over the Internet depends on many factors: time of day, day of the week, the number of threads, the state of the Internet in general, and we do not know what else.

The human factor plays an important role in this process. The number of sessions is increases. It results to delay in the transmission of data. People sometimes forget, sometimes make a mistakes. For this reason, delay growth, especially in the winter because of the large number of sessions, New Year's Eve.

Sometimes, in the case of large amounts of data, we use the data transferring on hard disks. From the places where there are no high-speed communication channels, the information is also delivered on disks.

All information is delivered to a processing center of scientific information Radioastron project. This is a special room equipped with air conditioning and fire suppression, video surveillance, uninterruptible power supplies for electricity stabilization.

The initial scheme of DPC was simple. We bought a cluster of 11 servers, storage of 200 TB. We connected their by 10Gbit/c network and SAS interface. And we thought that everything will work as we want. We thought that would be enough.

But a lot of reasons have led us to optimization and reorganization of the storage structure and the work com-

puter system as a whole. We have organized the work center in a new way.

This reasons are:

Increasing the number of observations,

Increasing the number of ground-based telescopes,

As a result of overflow storage.

Hardware failures, after which we were forced to save observations.

Processing features (large amount of output).

Store all the data.

Bottlenecks.

– disks (reference to the same disks in the collection, processing and archiving of data)

– Problems of network interaction between storage and computing cluster in processing.

For optimization DPC work we divided the collection, archiving and processing of information, to divided the flow of information in the correlation and postcorrelation processing.

Any rewriting of information is accompanied by verifying checksums md5.

We also have a 400 TB tape. We rewrite the data on magnetic tape. This will be the second copy of the data. Today we have collected about 400 TB information.

Everything I said above is about the work of the early scientific program. The structure and functions of ASC Data Processing Center correspond the necessary requirements.

In July 2013 began a key scientific program. We have received proposals for observation for the next year.

Over the next year observations, we have to accept about 2,000 TB.

For this volume we are expanding our storage and channels, and we organizing new server room.

STUDY ON THE VARIABILITY OF BLAZAR 3C345 IN RADIO FREQUENCY RANGE

Sukharev A.L.

Odessa observatory «URAN-4» Radio-astronomical institute NAS of Ukraine

ABSTRACT. 3C345 – intensively studied for many years in a wide range of the electromagnetic spectrum. Since 1965, the RT-26 radio telescope of the University of Michigan at frequencies of 14.5, 8 and 4.8 GHz conducted long-term monitoring of the radio source. Applied method of wavelet- analysis, allowed investigating changes in the harmonic signal components over time. For the main trend component period is 16 – 6 years, for the short-time component: 4.7 – 1.7 years. Based on global wavelet spectra in frequency range, calculated "spectra periods", characterizing the basic phases of the source activity and compared with VLBI.

Introduction

3C345 blazar ($z = 0.595$) shows variability in a wide range of wavelengths, from radio to X-rays. 3C345 has extended jet in which moves bright components with speed 2 – 20 c. The trajectories of these components curved on parsec scales. Their curvature decreases with distance from the core. The study of the variability of the radio flux makes a significant contribution to the understanding of the mechanisms of formation and kinematics of a relativistic jet.

Data processing

Initial data at three frequencies (14.5, 8, 4.8 GHz) were obtained at 26-m radio telescope of the University of Michigan (original data provided by M.F. Aller). The method of obtaining and processing data on the PT-26 is described in [1]. Observation interval 1965 – 2011 years (Figure 1).

The average interval between counting is 7 days. In preparing the data for analysis was conducted smoothing with polynomial moving average, subtraction trends and trigonometric interpolation. [2] The variability of the radio emission is divided into long-term (trend) and fast (O-C) components. FFT filtering is used for extract O-C components from signal [3].

WAVELET-analysis

If the frequency spectrum of the analyzed signal varies greatly in the time interval, then Fourier transform shows

only average frequency values with a constant resolution. The use of continuous wavelet-transform possible to study the change of harmonic components of the signal over time. Details of the methodology written in works [4, 5, 6, 7].

Wavelet-spectrum of an one-dimensional signal – a surface in three-dimensional space. Often used its projection to the frequency-time plane with the isolevels showing change of intensity of amplitudes at different scales and in time (figure 2, 3). Visualization of ranges is executed in logarithmic coordinates. Existence harmonic component in a signal is shown by horizontal strips. Inclinations and bends of strips show change of the periods in a signal.

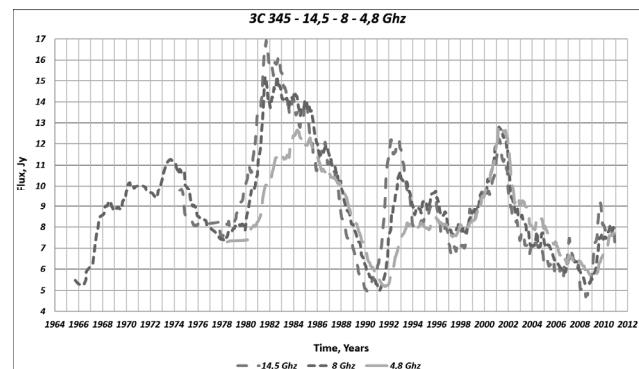


Figure 1: Plots of change in radio flux at frequencies of 14.5, 8, 4.8 GHz for source 3C345.

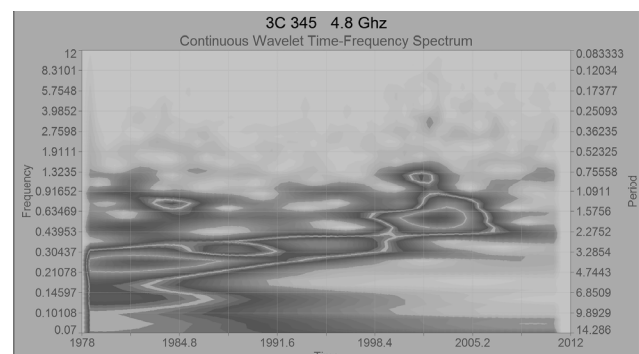


Figure 2: Wavelet-spectrum of O-C signal component at a frequency of 4.8 GHz. The period of fluctuations decreases over time.

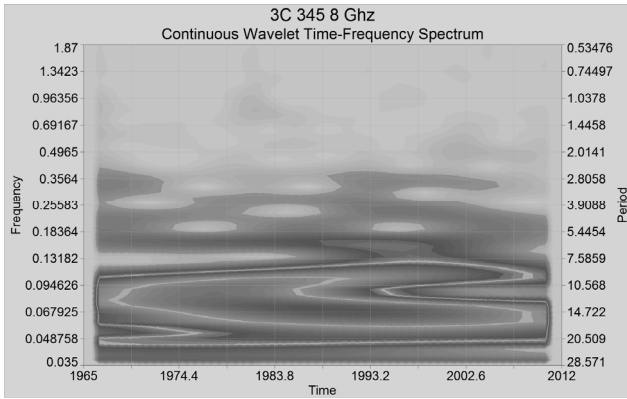


Figure 3: Wavelet-spectrum of trend component of signal at frequency of 8 GHz.

As a result of spectra analysis were received values of the periods which are shown in tables 1 (trend component) and 2 (O-C component).

Table 1: Main periods for a trend components of signals.

F, GHz	P	PSD	T max
14.5	15.8	3544	1985
	9.6	3041	1989
8	14.1	4050	1988
	10.2	2721	1984
	6.3	705	1993
4.8	16.0	3185	1994
	9.0	900	1991
	6.0	415	1997

Table 2: Main periods for O-C components of signals. Designations: F – frequency of data set, P – period in years, PSD – spectral density of power, Tmax – a timepoint when the spectral density of power for harmonica with the period P was maximum.

F, GHz	P	PSD	T max
14.5	4.7	672	1991
	3.4	385	1992
	1.7	46	2008
8	4.3	188	1995
	2.7	123	1992
	1.8	32	2001
4.8	4.0	30	1982
	2.8	15	1995
	1.7	32	2002

«SPECTRA PERIODS» and activity phases

Observed activity of source in radio frequency range consists from sum of fluxes of core and jet. In this work make attempt to connect quasiperiodic changes of a flux a radio emission with transiting brighting spots in jet. Phases of activity determined with using global wavelet-spectra with averaging on frequency. This type of a spectrum shows the moments of best coincidence analyzing wavelet and a signal at different scales and on one interval of time. To each date for a maximum spectral

density of power there match with set of periods forming a phase activity of a radio source [8].

Spectral maxima for a trend components: 14.5 GHz – 1992; 8 GHz – 1993; 4.8 GHz – 2000 years. Spectral maxima for O-C a components: 14.5 GHz – 1981.6, 1985.0, 1992.2, 2009.6; 8 GHz – 1974.5, 1981.6, 1993.0, 2002.0; 4.8 GHz – 1982.0, 2002.1 years. For the specified timepoints "spectra periods" are constructed. It is variant visualization of wavelet-spectra in a series of plots "period-spectral density of power" for every year separately.

Such method allows to define what periods make the greatest contribution to formation of a phase of activity in radiation source. When comparing of "spectra periods" with VLBI maps (MOJAVE Program [9]) on dates activity of radio source, it is visible that transiting each new bright spot on jet significantly changes a range of a short-time component of a signal. Therefore it is the most probable that fast variability of a radio emission is formed by jet activity and long-term – core of source. Possible, when a spot in jet is bright, in a spectrum O-C the short periods prevail, with distance from a core brightness of a spot weakens and the periods O-C component increase. The corresponding examples are given in figures 4 and 5. Certain regularities can be extended to an interval of observation, when sessions of VLBI of measurements weren't.

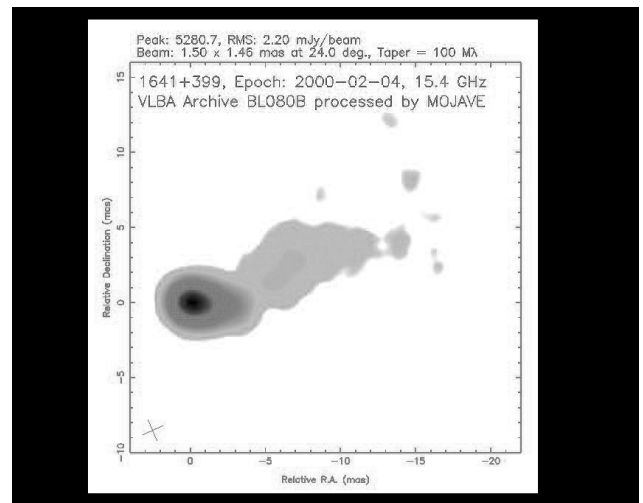
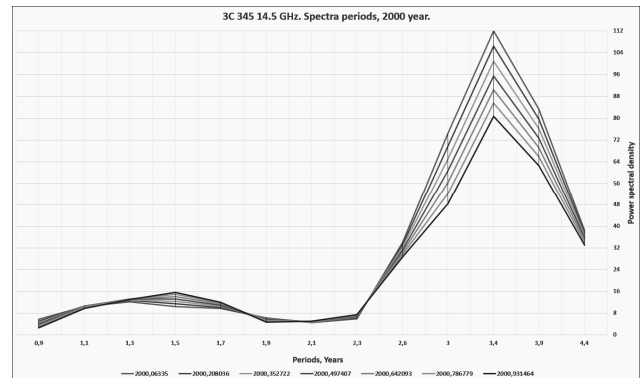


Figure 4: On VLBI image (2000.02.04) component in jet has low brightness. The prevailing period for 2000 – 3.4 years.

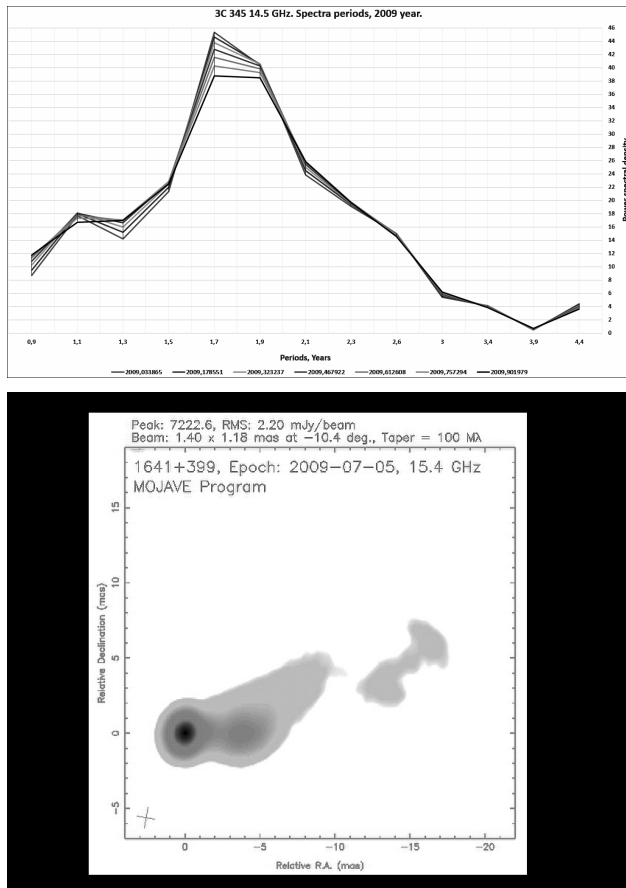


Figure 5: On VLBI the image (2009.07.05) visible bright component separated from a core. The prevailing period for 2009 – 1.7 years.

The jet structure

Frequent VLBI observation of radio source 3C345 allow get detailed information on movement bright spots in jet. If numbered position of spots with distance from a core, get the plot of quasiperiodic jet structure (fig. 6). At some spots brightness changes but the distance from a core remains approximately constants. This effect can be described by model of a standing wave in jet [10].

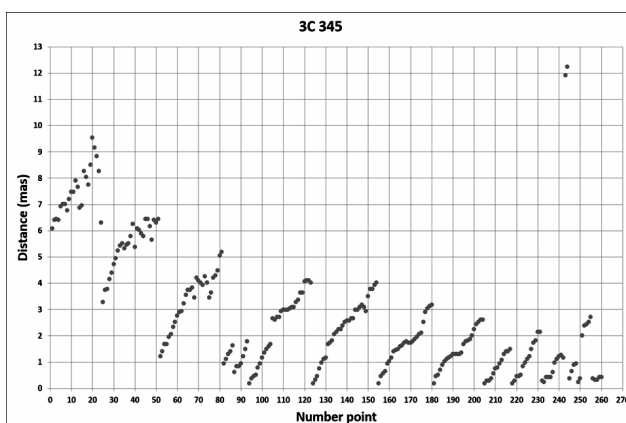


Figure 6: Quasiperiodic jet structure of radio source 3C345. Chains of points show movement a separate components in jet.

Results

Data processing basis on wavelet-analysis shows existence at radio source long-periods (6 – 16 years) and short-periods (1.7 – 4.7) a components. At a frequency of 4.8 GHz in O-C data fluctuations given the period decreases over time. At a frequency of 14.5 GHz in O-C data since 2000 there is a sharp reduction of the period. On 8 GHz in O-C data there is a reduction of the period of fluctuations since 1980 and increase since 1994. At a trend component change of the main periods at frequencies of 14.5, 8 GHz were ~ 1.4 years, at a frequency of 4.8 GHz change of the periods less than 0.5 years.

For verify the correctness of results were used trigonometric polynoms with the periods received from wavelet-spectra. Error of definition periods ~ 0.1 years. The main phases of activity of a radio source and forming them "spectra periods" are defined.

The use of "spectra periods" allows to select individual harmonic components, which provide the main contribution to the phase activity, and compare them with the VLBI images at this time. Moved in jet, bright components form a quasi-periodic rapid changes in the radio flux. The slow long-term flux changes are probably related to the core activity of the radio source. It should be noted that the VLBI "core" is not a jet base.

"Long waves" of variability reflect macroscopic processes, change rate of accretion a gas shell on a core [11], instability and radial pulsations of an accretion disk [12].

Fast variability of a radio emission can be explained with the shock waves extending in jet. Interaction of a superlight component with the jet is shown view form many shock waves behind it. At a source 3C345 components near a core show small shift that can be a consequence interaction direct and the return shock waves in jet. The last researches show that VLBI core also can be manifestation of constant wave in a point of the greatest jet turbulence [13, 14].

On the variability of radio emission is also affected by processes in the accretion disc. Distributed model of jet precession through the misalignment between the axes of rotation of the black hole and the accretion disc. But for 3C345 limited applicability of this model [15]. Precession of jet can appear if in a radio source there is the second black hole – the satellite. In this event besides a jet precession the satellite can create tidal indignations in accretion disk influence on long-term variability. Spiral movement of components in jet 3C345 indicates probable applicability of model a double black hole. However the spiral trajectory not necessarily demands satellite existence. The similar effect can be observed at rotation of internal parts of jet [16].

Research of a historical light curve of 3C345 in the optical range showed existence of the main period with value of 10.1 years [17]. By our results the nearest period with value of 10.2 years is observed at a frequency of 8 GHz. At frequencies of 14.5, 4.8 GHz the closest to optical the periods have values of 9.6 and 9.0 years. Probably, close values of the periods in optical and radio range indicate existence of global physical process providing long-term variability of 3C345.

References

1. Aller M. F., Aller H.D., Hughes P.A.: 2001, *Bull. of the American Astron. Soc.*, **33**, 1516.
2. Gajdyšev I. *Analysis and processing of data (a special handbook)*. Publishing house "Piter", 2001.
3. Davydov A. Digital signal processing: thematic lectures / "MINERAL PROCESSING" of Ekaterinburg, IGiG, Departament of geoinformatics, 2007.
4. Vityazev V.V. Analysis of irregular time series. Publishing House of the St. Petersburg University, 2001.
5. Smolentsev N. *Wavelet analysis in MATLAB*. DMK press, 2010.
6. Ryabov M.I., Sukharev A.L., Sych R.A.: 2012, *Odessa Astron. Publ.*, **25/2**, 135.
7. Astafyeva N.M.: 1996, *Successes of physical sciences*, **166**, No. 11.
8. Ryabov M., Donskyh A., Sukharev A., Aller M.: 2012, *Odessa Astron. Publ.*, **25/2**, 132.
9. Database by the MOJAVE team (Lister et al.: 2009, *AJ*, **137**, 3718).
10. Agudo I., Gomez J.-L., Marscher A.P., Alberdi A.: 2001, *Astrophys. J.*, **549**, 183.
11. Dibaj E.A.: 1987, *Active nuclei and stellar cosmogony*, Moscow Univ. Publ. House, P. 6-19.
12. Dibaj E.A., Lyuty V.M.: 1984, *Astron. J.*, **61**, 10.
13. Nagakura H., Yamada Sh.: 2008, *Astrophys. J.*, **689**, 391.
14. Alan P.Marscher: 2008, *ASP Conf. Ser.*, **386**.
15. Anderson Caproni, Herman J.Mosquera Cuesta, Zulema Abroham: 2004, *Astrophys. J.*, **616**, 99.
16. Frank M.Rieger: <http://arXiv.org/abs/astro-ph/0506720v1>
17. Zhang X., Xie G.Z., Bai J.M.: 1998, *Astron. Astrophys.* **330**, 469.

THE EVOLUTION OF THE ACCELERATION MECHANISMS OF COSMIC RAYS AND RELATIVISTIC ELECTRONS IN RADIO GALAXIES

N. Tsvyk

Radio Astronomy Institute of NASU, Kharkiv, Ukraine
tsvyk@rian.kharkov.ua

ABSTRACT. There are estimated an efficacy for different acceleration mechanisms of e- and p-cosmic rays (CRs) in radio galaxies, using an evolution model for jet gaps and shock fronts with a turbulence. It is shown that diffusion shock acceleration of the CRs is the most efficient mechanism in the FR II radio galaxies (RGs). At the same time, there are a break-pinch mechanism (for a short-term at a jet gap moment), and a stochastic turbulent mechanism (for an all time when RG exist), that to play a grate part in acceleration of the CRs (give to 10-50 % of the all acceleration efficiency). It is predicted what properties of radio emission spectra give us to recognize a type of acceleration mechanisms of e-CR in the RG.

Key words: radio galaxies, acceleration mechanisms, cosmic rays, radio emission spectra

It is usually assumed that the acceleration of p- and e-CRs in the radio galaxies (RG) is associated with regular mechanism of diffusive shock acceleration (DSA) at the shock fronts. However, in the jet and cocoon of RGs can work the other mechanisms too: (PnA) – an acceleration on break-pinch and (StA) – a stochastic acceleration that occurs when CRs scatter on MHD turbulence waves. The PnA-acceleration is widely discussed in connection with the energy spectra of p-CR, which recorded by counters in extensive air showers. The spectra of these CRs have index $s_{1Pn}=4.7$ ($N \propto p^{-s_{1Pn}}$), which is consistent with the PnA-mechanism. The observed radio emission spectra of e-CR in the RG also give the average index of 0.8, which is consistent with the index PnA-spectrum s_{1Pn} . StA-mechanism is widely used to explain the radio and X-ray emission in galaxy clusters such as Coma. Also, it is closely connected with the shock fronts, as the shock is evolving always with the MHD and vortex turbulence.

There are in this paper analyzed the characteristics and conditions in RGs to work of these CR-acceleration mechanisms. We write the equations describing the acceleration of CRs in the whole volume of the RG, in a *unified* form that is easy to compare several concurrent mecha-

nisms. The effectiveness of different acceleration mechanisms for p- and e-CR are estimated, considering the model of the spatial and temporal evolution of the turbulence with the jet and shock fronts in the RG. It is shown when you can "share" arrangements, and how to restore the correct properties of these mediums according to the spectra of radio galactic radiation.

The principles of the CR-acceleration mechanisms

To compare the efficiency of the PnA, regular DSA and stochastic acceleration mechanisms, we present a *unified* view of the equation by integrating the basic equations for the acceleration (injection) of the CRs in volume of $V(t)$, that filled at time moment (t):

$$\frac{\partial^2}{\partial p^2} (D(t, p)N) - (A(t, p) - \beta(t, p)) \frac{\partial}{\partial p} N + Q_0(t) \delta(p - p_0) = \left(\frac{N}{\tau^*(t)} \right) + \frac{\partial}{\partial t} N$$

The total number N of CRs in the volume $V(t)$ is determined by the source of injected particles $Q_0(t)$, and the terms $A(t, p)$ and $D(t, p)$ of acceleration efficiency. It should separate the areas in which different (or several together) acceleration mechanisms is working, and to consider the time-evolution of RG shape. We have interesting in quasi-stationary decision of this *uniform* equation.

PnA: the break-pinch acceleration mechanism. It works when a thin skinning jet of magnetized relativistic plasma is rapidly destructed. The initial PnA-equations are the Euler equations for a flow in a narrow channel approximation (Vlasov, et al., 1989). The particles are injected from the gap site and released into the environment during the time $t \ll a/c$ (a jet thin a divide to light velocity), filling the volume $V \sim ct \sim 10^2 \text{ pc}^3$. We find the total number of CRs injected into the volume V at time t , which are free expanding into this area in vicinity of the jet break point, and the e-CRs loss its energy through synchrotron radiation.

Pn-acceleration gives a transient (pulse) emission of CRs, near the gaps (knots) of jet, which works in two phases: 1 – phase of pinch break, 2 – phase of induction.

Phase of jet break lasts of $t \sim T_{\text{esc}} \sim a/c \sim 1-100$ years. At the moment of gapping, the magnetic field in the current thread is much greater than the energy of plasma, $B > 2J/ca$, which leads to injection of e- and p- plasma form jet into the CRs (an initial spectrum index is $s_{1\text{Pn}} = 4.7$). The e-CRs cool due to synchrotron losses in a magnetic field, disperse moving from a break point, and it changes they spectrum index to more steep, $s_{1\text{syn}} \geq s_{1\text{Pn}} + 1$, so the "jet breaks" moment become invisible in the radio emission.

When $t > a/c$, the phase turns to next (2), an induction acceleration of CRs at the jet gap, giving the p-CR spectra with $s_{2\text{Pn}} = 3$, and e-CR ones with $s_{2\text{syn}} \sim 4$. At this stage a local shock front forms in the vicinity of the jet knot, and the PnA-mechanism is transformed into DSA-mechanism, with no change of spectrum for e-CRs ($s \sim 4$).

The PnA-mechanism may provide CR-injection effectively in the pc-jets (in vicinity of a RG-core), that fills of ep-relativistic plasma. It is also possible to cascade injection of secondary e-CR in pc-jet knots due to the interaction of p-CRs with jet-shock fronts, and this process fills a jet of relativistic e-plasma at kpc-distances. This e-plasma has a larger magnetic viscosity then ep-ones, so the kpc-jet becomes more resistant to the "instantaneous" pinch breaks than the pc-jet.

DSA-mechanism: the regular acceleration at the shock.

At fist, it described by equations of CR-particles transport through the shock front surface (Krymskiy 1977, Bykov, Petrosian 2008). DSA works in a bow- and jet-shocks within the radio galaxies. To integrate it over the area of volume $V(t)$ and filling of the CRs, which move inside the shock front at time t , we obtain the *unified equation* in which the effectiveness of regular acceleration is given by:

$$A_{\text{sh}} \frac{\partial N}{\partial p_1} \rightarrow \int_{r_{\text{br}}(p)}^{u_1 t} \frac{p_1}{3} \Delta u \delta(r - u_{\text{sh}} t) \frac{\partial f}{\partial p_1} \cdot 4\pi r^2 dr \rightarrow \frac{p_1}{s_{\text{sh}} T_{\text{sh}}(t)} \frac{\partial N}{\partial p_1}$$

Here $T_{\text{sh}}(t)$ is an effective time of the CR-acceleration; $T_{\text{sh}}(t) < t$. The total number N of CRs changes follow with their injection at the shock, $Q(t) \equiv Q_0 \xi(t) \propto V(t)$, and for e-CRs it have to add the energy loss due to the synchrotron radiation (β -term). If $\xi(t) = t \cdot \exp(-t/\tau)$, we find a steady-state solution of the equation (1) for the total number of the CRs as: $N(p_1, t) \propto p_1^{-s_{\text{sh}}(t)} \xi(t)$. In it: $s_{\text{sh}}(t)$ is increasing with the t when the shock slope is steeping, and an index s will add +1 for a large CR-momentum (p_1) due to synchrotron losses of e-CR energy. So, e-CRs cool as they distance to the shock growing; and we got a smooth increase in the spectrum index of N -function at the some momentum energy range. The most part of overall CR-number accelerates at the bow shock of RG, which is gaining a particle of intergalactic plasma into the cocoon as the form of e- and p-CRs. The DSA-mechanism works during the bow shock exist, $\tau \sim 10^6-10^7$ yr for typical RGs.

StA: stochastic acceleration mechanism. It works in entire volume of RG-cocoon where the accelerated CRs is diffusion mixing by turbulence, and it is working continuously overall time when RG exists (longer then bow-shock exists). The volume of the RG-cocoon is order of 10^{14} pc^3 ; and StA can work more then 10^7 yr.

The terms of StA-mechanism are: $D(p_1, t) \rightarrow D_0(t) p_1^{-\alpha}$, $A_{\text{st}}(t) = (\alpha - 2) D_0(t) \cdot p_1^{-\alpha-2}$ (Brunetti., Setti, 2001; Cho, Lassarain, 2005). Those are related to the spectrum of turbulent MHD-waves, $W(k) = W_0 k^{-q}$ (occupying from $k \sim L_0^{-1}$ to $k \sim R_0^{-1}$; L_0 is a correlation scale of wave turbulence, R_0 is a Larmor radius for thermal-CRs), and they can be expressed in terms of the coefficients of the spatial diffusion of CRs: $D_{\text{st}} = \frac{1}{2} p_1^2 \kappa(p_1) L_0^{-2} \propto p_1^{4-q}$, where $\alpha \sim 4 - q$. We believe that the spatial diffusion κ is described the function by (Toptygin, 1983), as the CRs scatter on MHD-waves in resonance: $p_1 \sim 1/(kR_0)$.

Quasi-stationary solution of the CR-acceleration: the total number N of St-accelerated CRs takes the form of a power function by p_1^{-s} with $s \sim \alpha + 1$, and for the e-CR, the index (s) increases and N "exp-collapses" due to synchrotron and inverse-Compton radiations of e-CR at the large p_1 -momenta.

The collaboration of DSA and StA-mechanisms of CRs inside the radio galaxy cocoon by shock bounded

We trace the evolution of the turbulence near the bow shock front of RG, and estimate how the effectiveness of the StA- and DSA-mechanisms change when the RG was a young, a developing and an old jet-ejection. We consider the RG of FR II type, with the following parameters at the stage of "developing" jet: a jet age is $t \sim \tau = 10^6$ yr, a pc-jet radius is 0.1 pc, a jet length is 30 kpc, and it equals of 0.5 of cocoon radius; the plasma density in jet is some less then ones in the cocoon that is 10^{-3} cm^{-3} ($r/40 \text{ kpc}$)^{-0.7} (decrease at r-distance). The parameters of bow shock and turbulence run with time as we show in fig.1 (the model).

Stage 1, $t_1 \sim 10^4$ years: it is "young-ejection" and a powerful shock front with turbulence. The power spectrum of MHD-turbulence $W(k)$ has an index $q=1.9$, and it is strongly developed in the range of $k \sim k_{\text{min}} \sim 1/L_0 \sim 10^{-13} \text{ cm}^{-1}$ to $k \sim k_{\text{max}} \sim 1/R_0 \sim 10^{-10} \text{ cm}^{-1}$, where it is pumped by the vortex-turbulence. During the time, a spectrum $W(k)$ expands slowly by k , mainly to low k -range. In this *Stage 1*, St-acceleration works in concert with the regular DSA-mechanism (so as $\alpha = 4 - q \sim 2$). And if we have $D_0 > A_0$, it forms a hard CR-spectrum ($s=3$), because of StA is the most effectively. For e-CR, StA compensate its synchrotron losses at large p_1 , up to $p_{\text{max}} \sim L_0/R_0$.

Stage 2, $t_2 \sim 10^6$ years: *developing ejection* of jet, a quasi-stationary shock front with the turbulence in the cocoon. It is DSA dominated and supplemented by StA (see fig.2). Turbulence spectrum: $q = 1.5..1.66$, $\alpha = 2.5..2.33$, so $\kappa(p) \propto p^{2-q} \sim p^{0.5..0.33}$. StA affects on the spectrum of e-CR at large p_1 , partially offset by synchrotron losses.

Stage 3, $t_3 \sim 10^7$ years: it is *the old jet* and a weak bow-shock with turbulence. Turbulence is dissipated from all k , and its spectrum becomes: $q \sim 1$, $\alpha \sim 3$. The shock dissipate too, and it give us $D > A$ in the main p_1 -band of CR energy momentum. So, we have StA dominated again, at some range of large p_1 , and this StA is described by Bohm transport diffusion of CRs, $\kappa \propto p_1$. This mechanism smooths the spectrum of e-CRs to the $s(t) = \alpha + 1 \sim 4$ and corrects they energy losses (by synchrotron or inverse-Compton radiation cases). Alternative, at range of small p_1 , the DSA-mechanism is working for both e- and p-CRs.

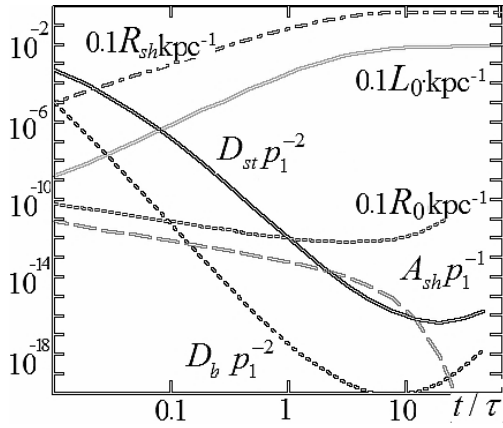


Figure 1: Dependence for turbulence characteristics (L_0 corr.-length, R_{sh} shock and R_0 Larmor radii) and A_{sh} , D_{st} , D_b acceleration terms (at $p_1=1$) from age-time of RG

D -term goes to zero at $p_1 \rightarrow 0$ and at the range of the most large $p_1 > L_0(t)R_0^{-1}$, because the correlation scale L_0 came to infinity and the turbulence spectrum $W \rightarrow 0$.

The collaboration of DSA and PnA in the RG

A particle number in the Pn-acceleration is obtained from the jet particles flow through the gap, which exists 1-100 yr. This number N_{Pn} are very small compared to a number N_{DSA} (CRs accelerated by bow shock in RG). So, PnA have a very low efficiency compared to the other mechanisms; but it is essentially CR-acceleration on some time-moments when jet is braking, and when we see the vicinity of this jet-brake point volume.

Conclusions

1. Pinch (PnA) mechanism contributes to the rapid destruction of the jet, and the short-term release of its e-plasma in the form of the CR in the hot spots and knots, where it formed local jet's shock fronts. It is predicted that the pinch point of jet's gap can be detected only at low radio frequencies, due to the fact that it gives the radio emission with a very steep spectrum. PnA is the most effective within the pc-jets and in the young RGs; and its relative effectiveness runs to less 1% (as a number of particles accelerated by PnA have divided to all CRs in the RG at fixed time).

2. Regular DSA-mechanism runs close to the shock front surface and fills the tiled-shock areas in RG by cosmic rays accelerated. It is the most effective mechanism in RG at the time when the bow shock is strong; and DSA relative effectiveness runs to 50-90% at that fixed time. DSA creates the spectra of CRs that the power index increases by the time, as the power of the shock have reduced; and it creates the emission spectra of e-CR with the index growing with distance from a shock because of Syn/IC losses. DSA is in competition with StA at all when RG exist.

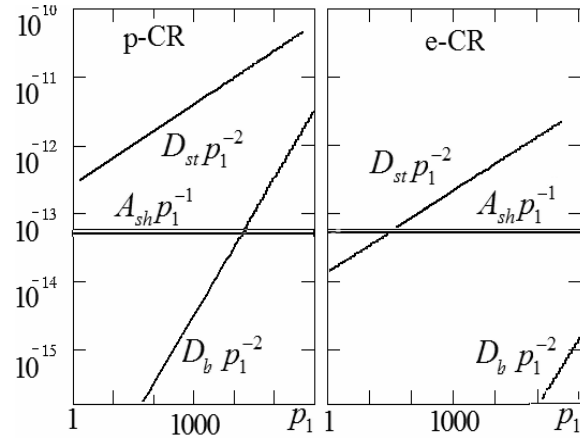


Figure 2: Dependence for $A_{sh}(p_1)$, $D_{st}(p_1)$, $D_b(p_1)$ acceleration terms from (p_1) -moments of energy for p- and e-CRs at the RG-age $t=\tau$

3. The stochastic (StA) mechanism works continuously and almost the entire volume of the RG, and it creates a flat spectra in the radio emission observations. The p- and e-CRs are re-accelerated effectively by this mechanism in ahead of the shock front and inside the jet, as well as in the cocoon-periphery and in the halo of FR II-RGs. In this way, the synchrotron radiation losses on e-CRs compensate partially by this mechanism, and it "restrained" obstruction of their spectrum at high frequencies. The index of the CR-spectrum that accelerated by stochastic mechanism depends on the spectrum of a turbulence, and it increases towards the edges of the RG (going far from the jet and from the hot spot of the RG). StA relative effectiveness runs to 10-50% usually at fixed times, and it is the most effective in the last evolution stage of the RG.

At first, the type of acceleration mechanism can be found from the spectral index of the e-CR radiation. Then in reality, the indexes of the acceleration mechanisms overlapped in a wide range, and to determine the mechanism needs to involve the physical considerations about the evolution of turbulence with shocks in the RG.

References

- Власов В.П., Жданов С.К., Трубников Б.А.: 1989, *Письма ЖЭТФ*, **49**, 581.
 Крымский Г.Ф.: 1977, *Доклады Акад. наук*, **234**, 1306.
 Выков V., Petrosian B.: 2008, *Space Sci. Rev.*, **134**, 207.
 Petrosian B., East W.: 2008, *Astrophys. J.*, **682**, 175.
 Brunetti G., Setti G, et al.: 2001, *Mon.Not.Roy.Astron.Soc.* **320**, 365.
 Cho J., Lasarian A.: 2006, *Astrophys. J.*, **638**, 811.
 Топтыгин И.Н. *Космические лучи в межпланетных магнитных полях*. Москва: Наука, 1983.

SUN AND SOLAR SYSTEM

DAILY AND SHORT-PERIOD CHANGES DYNAMICS OF THE EARTH'S MAGNETIC FIELD IN THE 24-TH CYCLE OF SOLAR ACTIVITY ACCORDING TO MAGNETIC OBSERVATORY "ODESSA"

L.I.Guglya¹, M.I.Orlyuk², M.I.Ryabov¹, A.L.Suharev¹, I.M.Orliuk²

¹ Radioastronomical Institute of National Academy of Sciences of Ukraine

² Geophysics institute of S.I.Subbotin NAS of Ukraine

ABSTRACT. The Registration of B_x , B_y , B_z – vector components of the Earth's magnetic field, with a time resolution in 1 second is carried out on magnetic observatory "Odessa". Results of calculated module of a full vector of magnetic field variations for 2008-2010 are analyzed. "The quasi-daily period" of solar dynamics is determined by wavelet analysis. The daily period and the spectra of shorter duration periods are subtracted by digital filtering method. In consequence of the received data magnetic storm time specifications are shown.

Introduction

"Odessa" Magnetic Observatory was founded by Imperial Novorossiysk University in the Botanical Garden at the beginning of the twentieth century. Odessa State University moved the observatory to Stepanovka village near Odessa in 1936. The station was transferred to the Institute of Geophysics NASU in the postwar period. The registration of B_x , B_y , B_z – components of the Earth's magnetic field with a time resolution of 1 second was started at the beginning of the 2008. [1]The radio telescope "URAN- 4 " RI NASU is working near Odessa since 1987. It is one of the VLBI elements of the "URAN" decametric range. Monitoring on RT "URAN- 4" "translucence" of the ionosphere by powerful cosmic radio source program is running since 1987 [2]. Combined analysis of radio-astronomical observations and magnetic field changes allow us to find out basic laws of displaying the condition of space weather[3-4].

Observational data

Spatiotemporal structure of Earth's magnetic field \mathbf{B} is the sum of fields from different sources [8]:

$$\mathbf{B} = \mathbf{B}_n + \mathbf{B}_a + \mathbf{B}_e$$

where \mathbf{B}_n – normal (main) field of the Earth, which is generated by processes in the liquid kernel and mantle boundary and defines a global spatial and temporal structure of the field of the planet; \mathbf{B}_a – anomalous magnetic field (the lithosphere) caused chiefly mainly magnetization of rocks; \mathbf{B}_e – the external field due to the influence of solar

and cosmic radiation, magnetic fields of the Sun and near-Earth space. External field that makes the short-period variations in the mid-latitudes, can be represented as:

$$\mathbf{B}_e = \mathbf{DR} + \mathbf{DT} + \mathbf{DCF} + \mathbf{DP} + \mathbf{Sq}$$

where \mathbf{DR} – a variation of the magnetospheric ring current (includes partial ring current); \mathbf{DT} – variation of currents in the magnetotail; \mathbf{DCF} – a variation of the currents at the magnetopause; \mathbf{DP} – variation of ionospheric currents in the auroral zone and reverse currents spreading in the Middle latitude; \mathbf{Sq} – quiet solar-diurnal variation.

Long-period changes (over a year) of the geomagnetic field caused by internal sources. In this paper we study the short-period variations of these changes (characterizing the dynamics of the external field) for 2008-2010 years by the analysis module full magnetic field vector with a one-minute resolution. For computing module used in its B_x , B_y , B_z – components measured with 1s interval and accuracy of 0.1 nTl magnetic observatory "Odessa" (Geophysics institute of S.I.Subbotin NAS of Ukraine).

Figure 1 shows the initial series data characterizing the vector magnetic field of the Earth in July 2008. To smooth short-term fluctuations and highlight the main trends were calculated moving average value and applied a trigonometric polynomial (Figure 1).

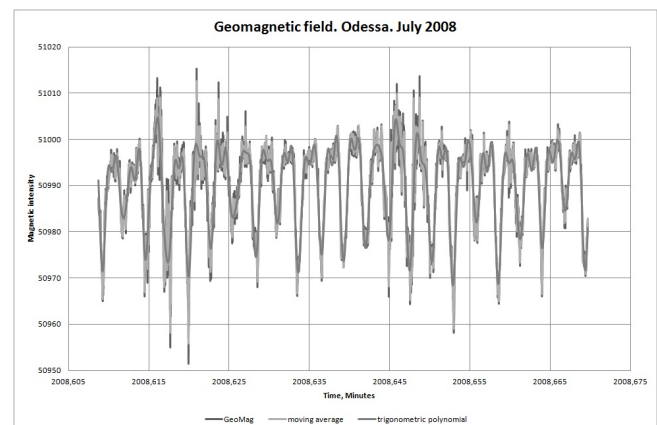


Figure 1: Variations of the Earth's geomagnetic field (Odessa, July 2008).

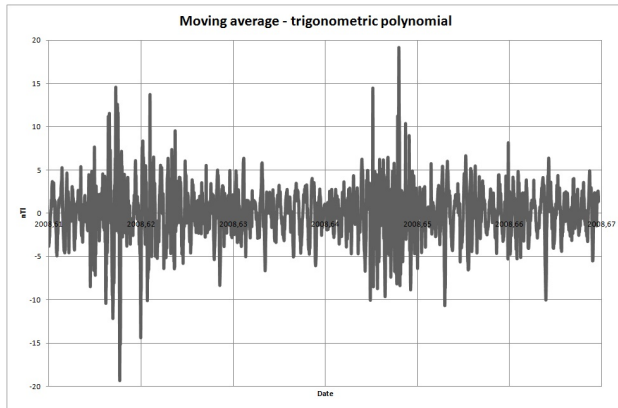


Figure 2: Variations of geomagnetic field (O-C) in July 2008. (Odessa magnetic station)

To calculate the amplitude of the oscillations of short processes was carried out the procedure for calculating the values of O-C (moving average of the values of the trigonometric polynomial subtracted). Results of computations O-C shown in Figure 2.

Solar activity in 2008 (July-December)

In July 2008 solar activity was significantly lower – just one small group of spots was detected at the end of the second decade. Maximum relative number of spots observed in June 19 $W = 9$. On June 28 there were no spot detected on the Sun. Flare activity was very low during the whole month, no active important phenomena was noticed. Geomagnetic situation was determined by the passage of the Earth's high-speed solar wind streams from coronal holes this month. July 12 a small magnetic storm was detected.

Sunspot activity of the Sun in August 2008 has shortly decreased. Maximum relative number of spots observed on August 22 with a value of $W = 8$ and visible solar disk was without spots for 29 days. Flare activity was very low during the whole month. At the same time ground-based observatories have detected geomagnetic disturbances such as two low magnetic storms on the 9 and 18 of August. Totally it was three days detected in August when geomagnetic conditions were disturbed.

Solar activity was much lower till September 22, 2008 only one small group of spots at the end of the second decade was detected. Flare activity was at a very low level the whole month. Significant active phenomena were not observed. Coronagraph on SOHO registered 18 coronal emission substances in August. This month the passage of three coronal holes on the visible sun's disk were detected, two in August and a new one. At the 4th and 14th of September two low recurrent magnetic storms were executed. Disturbed geomagnetic situation was registered within 3 days.

In October sunspot activity of the Sun in comparison with September little increased. Maximum relative number of spots observed on October 16 with a value of $W = 14$, visible solar disk was without spots for 20 days. Medium magnetic storm was detected on the 14th of October. Totally 6 days with disturbed geomagnetic state were noticed in October. A high level of high-energy electrons flow on geostationary orbit was registered for 16 days.

Low solar flares have executed on the 3 and 4th of November. Maximum relative number of spots observed on the 12th of November with a value of $W = 13$, and for 16 days there were no spots on the sun. Coronagraph space observatory SOHO has registered 18 small coronal mass blowouts in August. A high level of high-energy electrons flow was recorded in geostationary orbit during 17 days.

Maximum relative number of spots observed on the 10th and 12th of December with a value of $W = 9$, and visible solar disk was without spots for 28 days. Flare activity was very low during the whole month. It was three coronal holes passage registered across the visible sun's disk which did not cause any significant disturbances in the near-Earth space. Totally 6 days with disturbed geomagnetic situation were noticed in December. A high level of high-energy electrons flow was recorded on the geostationary orbit for 4 days.

For the July – December period outbreaks of sudden onset were not reported otherwise there were 11 outbreaks with a gradual onset, which are listed in Table 1.

Table 1.

Date from	Date to	Dur.,hh	Intens.	Amp.D	Amp.H	Amp.Z
2008/07/11 23:00	2008/07/12 22:00	24	1	65	97	4
2008/07/22 11:00	2008/07/24 01:00	39	1	70	86	6
2008/08/09 00:00	2008/08/10 10:00	35	1	99	117	5
2008/08/18 10:00	2008/08/19 06:00	21	1	99	118	5
2008/09/03 23:00	2008/09/05 00:00	26	1	162	101	8
2008/09/14 19:00	2008/09/15 22:00	27	1	116	74	5
2008/10/02 09:00	2008/10/03 02:00	18	1	86	91	5
2008/10/03 09:00	2008/10/04 12:00	28	1	60	91	5
2008/10/11 08:00	2008/10/12 22:00	39	2	284	161	10
2008/11/07 20:00	2008/11/09 01:00	30	1	91	86	6
2008/12/05 10:00	2008/12/07 01:00	40	1	178	81	4

Wavelet analysis of the Earth's magnetic field

To obtain data on the spectral and spatial characteristics of the Earth's magnetic field index for 2008 (June – December) wavelet analysis was used. Wavelet analysis provides information about the existence of main periods and time of their existence. The method of application of the wavelet analysis is presented in [5].

As a result of this analysis a wavelet time-frequency spectrum of the density distribution of energy was built (Fig. 3).

On this spectrum Solar the most intense circadian period is clearly displayed. Wavelet analysis allows calculating of duration and the intensity of detected periods.

Variations circadian periods are shown in Figure 4. Figure 5 shows the fluctuation of leading period that reached 31.9 hours during 2008. On the 13th, 28th of June and the 12th of August this period is demonstrated most actively.

To identify short-period processes (less than day) time-frequency wavelet spectrum for data filtered trend component was calculated. The calculation results are displayed in Figure 6.

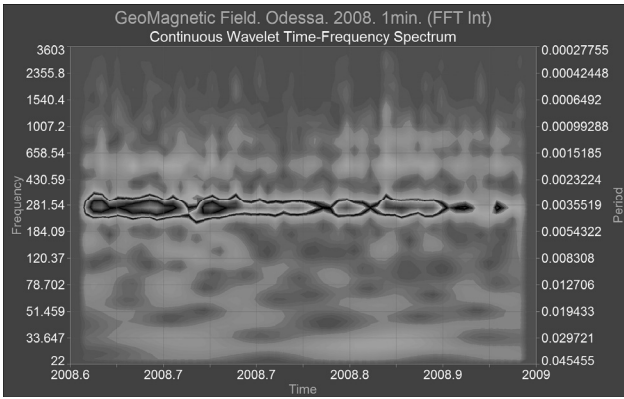


Figure 3: Wavelet time-frequency spectrum of density spreading for geomagnetic activity energy (2008)

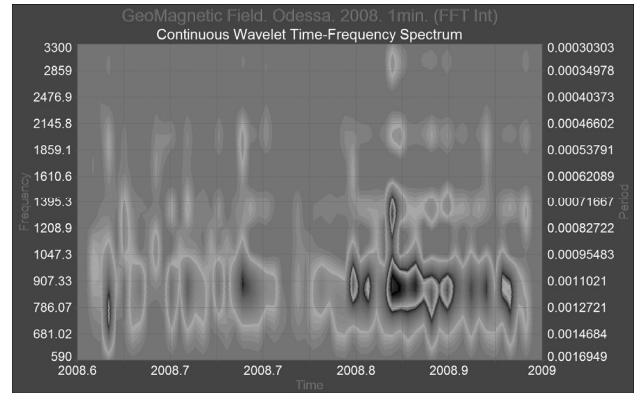


Figure 6: Time-frequency wavelet spectrum of density spreading for geomagnetic activity energy (2008). A day period is subtracted.

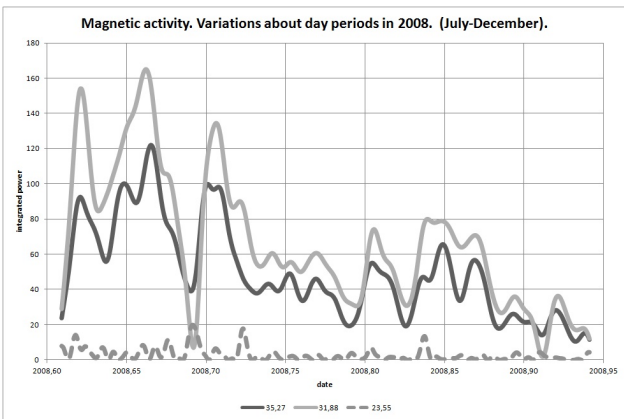


Figure 4: Circadian period variations in 2008 (July-December).

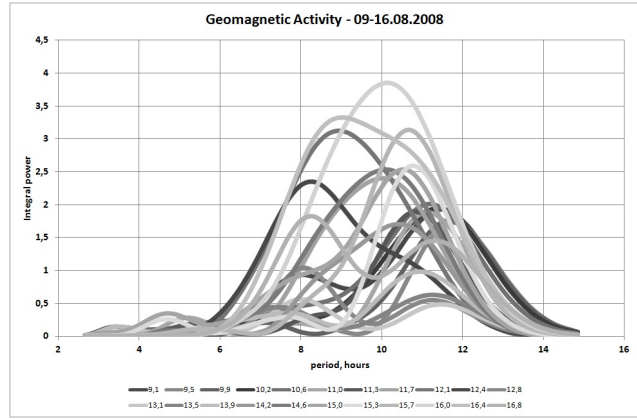


Figure 7: Duration and intensity of Earth's magnetic field periods

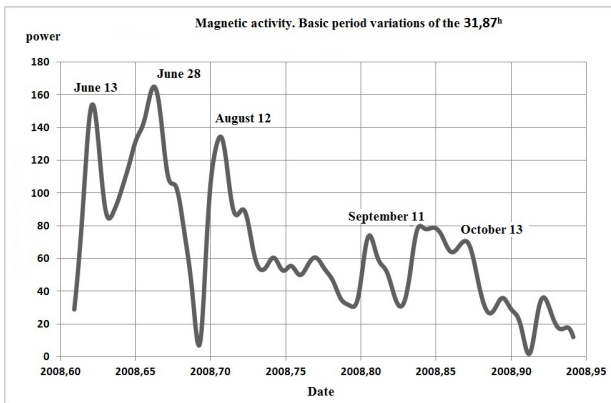


Figure 5: The leading period variations (31.9 hours) in 2008 (July-December).

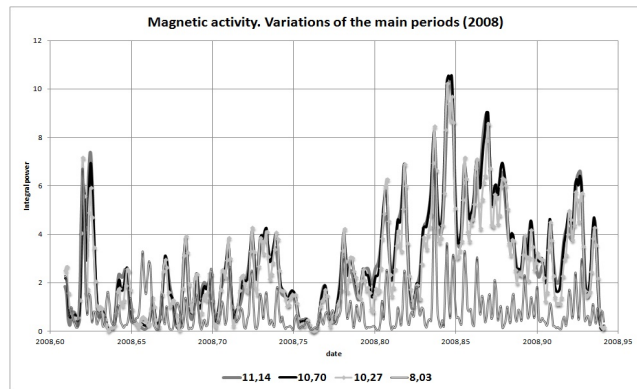


Figure 8: The most intense periods of 2008

Characteristics of less than day periods during 2008 were calculated. Appeared on 9-16 July 2008 periods are shown as an example (Figure 7). The leading periods that characterize the whole 2008 year were discovered as a result of this analysis (Table 2).

Table 2: Leading periods that characterize the July-December (2008)

date	Period (Hours)	intensity	Period (Hours)	intensity	Period (Hours)	intensity
09-16.07.2008	9,1	9,13	11,61	7,03	4,3	1,77
17-23.07.2008	11,14	2,56	7,1	1,91	4,3	0,56
24-31.07.2008	7,1	4,04	8,01	3,29	10,3	2,48
01-08.08.2008	10,3	3,92	8,01	1,09	5,5	1,28
09-16.08.2008	10,3	3,84	9,1	3,2	4,9	0,33
17-24.08.2008	10,3	4,28	8,01	1,98	4,9	1,7
25-31.08.2008	10,3	4,06	10,69	3,79	6,03	0,83
01-08.09.2008	10,69	1,89	11,14	1,65	8,01	0,84
09-16.09.2008	10,3	4,22	10,69	3,48	8,01	0,92
17-23.09.2008	10,3	6,26	10,69	5,31	6,54	2,33
24-30.09.2008	10,69	7,39	11,14	5,84	8,01	1,82
01-08.10.2008	10,69	10,55	7,1	6,39	3,25	2,59
09-16.10.2008	10,69	9,03	11,14	8,97	6,03	0,79
17-23.10.2008	10,69	6,66	11,14	4,09	4,3	0,73
24-31.10.2008	10,69	4,62	11,14	4,29	4,9	1,37
01-08.11.2008	11,61	6,61	11,14	5,82	6,81	1,73

A general picture of the most intense periods of year 2008 is got: 8 hour, 10.67 hour and 11.14 hour (Figure 8). These periods most actively identified themselves on the 14th of July 4th and 12th of October, 24th September and the 3rd of November.

The daily periodicity Evolution in 2009, 2010.

For receiving data about the progress in daily periodicity in 2009 – 2010 years wavelet analysis was used. The index of the Earth's magnetic field was used as the test material.

Wavelet time-frequency spectrum of energy density distribution for 2009 and 2010 was built as a result of this analysis (Figure 9, 10).

Solar circadian period, which is the most an intense and continuous is greatly allocated on spectrums.

Based on calculations of wavelet analysis numerical values of these periods were allocated (Figure 11, 12).

On figures 11 and 12 it is visible that the leading period in 2009 and in 2010 is equal 23,9 and 24,4 hours, respectively.

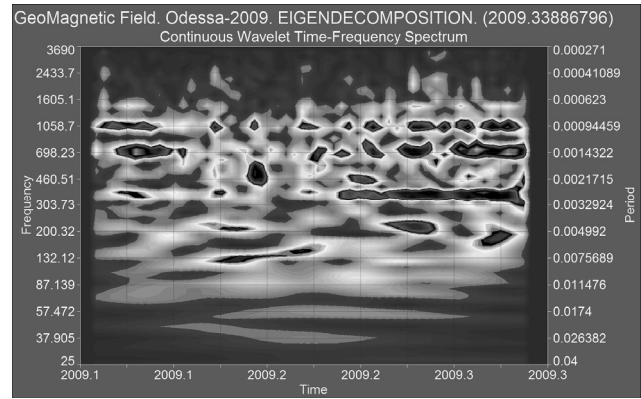


Figure 9: Wavelet time-frequency spectrum of density spreading of geomagnetic activity energy (2009)

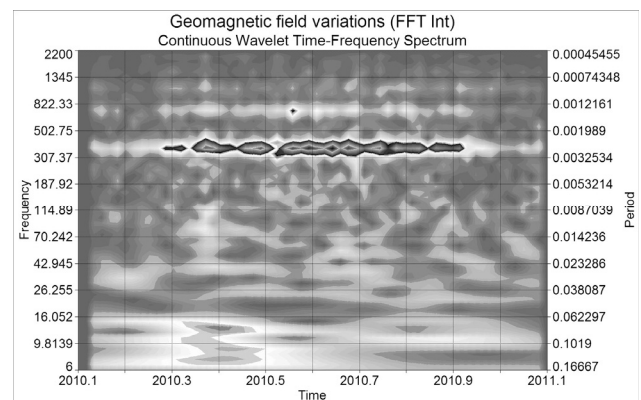


Figure 10: Wavelet time-frequency spectrum of the density spreading of geomagnetic activity energy (2010)

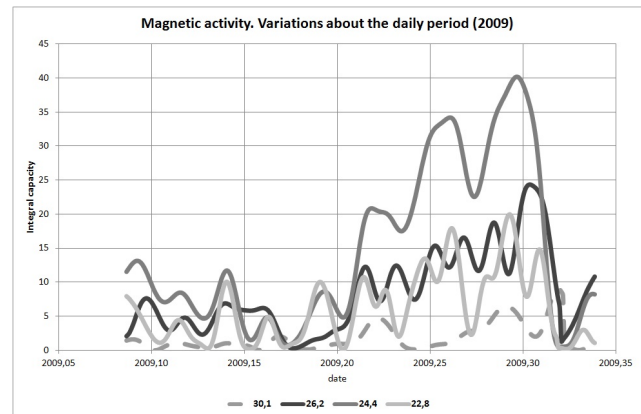


Figure 11: Circadian variations period in 2009 (January-March)

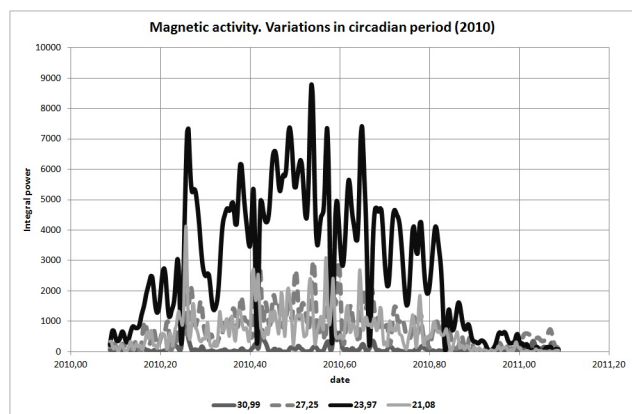


Figure 12: Circadian variations period in 2010.

Conclusion

- The dynamics of short time variations full vector magnetic field module in 2008-2010 years of the magnetic observatory Odessa data was investigated by wavelet analysis.
- Leading periods that characterize the state of geomagnetic activity were identified as a result of researches. The intensity and duration of their existence is calculated.
- The most intensive solar circadian period stands out clearly for researched period. It turned out that during

the minimum solar activity leading period is – 31.9 hours (2008). During the increase of solar activity leading period is near by 24 hours (2009, 2010)

- Leading periods of less than one day duration, the calculation results of wavelet analysis are: 11.14, 10.67, 8:00 hours. These periods most actively are shown on the July 14, October 4, 12 and November 3 (2008). The magnetic storms with gradual start, caused by streams of energetic solar pieces from the solar coronal holes were observed on these days. During magnetic storms the circadian period was disturbed and shorter periods were increased.

References

1. Orliuk M.I., Romenets A.A., Sumaruk T.P., Sumaruk Yu.P.: 2012, *Odessa Astron. Publ.*, **25/2**, 102.
2. Guglya L.I., Ryabov M.I., Panishko S.K.: 2011, in *11-th Gamow's astronomical conference-school*, 159.
3. Druzhinin I.P., Sazonov B.I., Jagodinsky V.N. *Space-earth Forecasts*, Moscow, 1974.
4. Ivanov-Holodni G.S., Nikolsky G.M. *The Sun and ionosphere*, Moskow: Nauka, 1969.
5. Smolentsev N.K. *Introduction in the wavelet theory*, Moscow-Izhevsk, 2005, 401 p.

STATISTICAL ANALYSIS OF THE MAGNETIC FIELD MEASUREMENTS

L.Kozak¹, A.Lui², S.Savin³

¹ Kyiv National Taras Shevchenko University, Kyiv, Ukraine, kozak@univ.kiev.ua

² Johns Hopkins University Applied Physics Laboratory, Laurel, Maryland, USA

³ Space Research Institute, Russian Academy of Sciences, Moscow, Russian

ABSTRACT. Investigation of statistical features of the magnetic field fluctuations in bound regions of Earth's magnetosphere, on different time scales, is carried out in this work. Measurements of Cluster-II with frequency 22.5 Hz for 2004-2008 years have been used for the analysis. During these investigations we have studied the changes of shape and parameters of probability density function for magnetic field fluctuations for periods of presence of the satellite in magnetosheath, solar plasma wind and in region of magnetopause. We have considered the evolution of change of maximum of probability density function and investigated structure functions of different orders as characteristics of turbulent processes for different time scales. Investigation of structure functions of high orders helped us to determine the character of turbulent processes and study diffusion in the considered regions. We have found, that the highest intermittence is observed in the postshock region; for the middle magnetosheath the results of experimental data correspond to log-Poisson turbulent cascade model, and for the description of processes in SW plasma one can use the Iroshnikov-Kraichnan's model.

Key words: turbulent model, intermittency, statistical properties of boundary layers, Earth's magnetosphere

1. Introduction

Investigation of the processes in the magnetosheath is significantly complicated by presence of the turbulence. Since the processes in boundary layers of space plasma is characterized by a great number of degrees of freedom, nonlinearly interacting modes, multi-scale structure and random fluctuations of velocities so that the methods of statistical physics and theory of probability are most suitable for its description. In order to describe an random process one have to determine the probability density function for plasma parameters and the moments of this probability function. The most often the probability distribution of fluctuation amplitudes corresponds to Gauss (normal) law with quickly decreasing correlations. There are other known distribution laws in the theory of probability which can describe processes with far correlations. The distribution probability functions for such processes are not always described by known mathematical functions and series, and for many types of random processes one knows only a method for fitting of their distribution functions. Investigation of statistical symmetries of turbulence allows us to obtain information about a character of

dependence of structure functions (statistical moments of probability function) of different orders on time and space, without to resort to detailed consideration of individual conditions of its exciting.

Random pulsations in the medium under structure heterogeneity of the turbulent process (intermittency) have the distribution function different from the Gaussian distribution [Kozak et al., 2011, Kozak et al., 2012].

The research of the statistical properties of boundary layers allows to determine the role of turbulent processes in the interaction of plasma flows with the magnetic obstacles, whether these are fields of planets, stars, or laboratory traps, and to reveal the actual mechanisms of the energy transformation in collisionless plasma. In this study based on the satellite Cluster-II measurements the characteristic turbulent regions in the boundary layers of Earth's magnetosphere.

2. Used observational data

In order to analyze the features of turbulent processes in the transition regions of the Earth's magnetosphere twenty-five events of the magnetic field measurements obtained by Cluster-II mission for 2004-2008 years with frequency resolution 22.5 Hz were considered. The satellite moving from SW passed through the foreshock (FSH) the bow shock (BSH), the magnetosheath (MSH), crossed the magnetopause (MP), and came into the magnetosphere.

During the transition from SW to MP the rate of fluctuations of the field changed dramatically the dispersion of plasma variations normalized to a current mean value accounts for: SW – 0.02 – 0.05; FSH 0.2 – 0.3; PSH – 0.5; deep in the MSH region the rate of fluctuations drops to 0.1– 0.2.

3. Results of analysis

3.1. Features of the probability density functions of fluctuations

In order for investigations of features of the probability density functions of magnetic field fluctuations we analyzed the statistical properties of the absolute value of magnetic field variations $dB = B(t + \tau) - B(t)$ in the different regions of near earth space and for different time scales.

The dependence of a maximum of the probability density distribution of the fluctuations P_0 on the shift in time τ can be approximated by the power-law dependence $P_0(\tau) \sim \tau^{-S}$. For the case of Gaussian distribution parameter $S = 0.5$; in the general case (the Levi distribution) $S > 0.5$. For the turbulence with intermittency the presence of considerable fluctuations on distribution's wings appears due to abundance of energy of large-scale disturbances, which are generated by external source or boundaries of flows. The investigation of changes of a maximum of the probability density function of magnetic field fluctuations on various time scales was applied, for example, for studying the magnetic turbulence in the magnetospheric tail during the period of transverse current disruption [Consolini et al., 2005, Kozak et al., 2008].

The dependence of maximal value of probability density function of magnetic field fluctuations $P_0(\tau)$ on time shift τ being divisible to 0.0445 s (time step of initial data) for the event May 15, 2005 is shown in the Fig. 1. For short time scales from 0.00445 s to 1 s The values of the power s are presented in the Tab. 1.

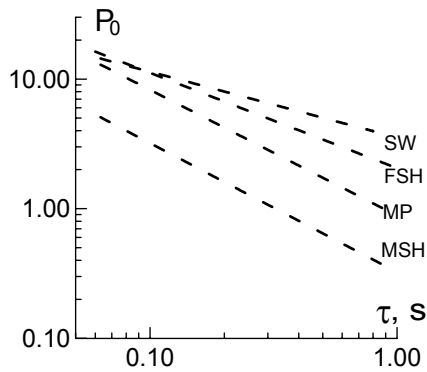


Figure 1: Logarithmic dependence of the probability density distribution function maximum of magnetic field fluctuations $P(0)$ on the time step in the SW, FSH, MP, MSH. The experimental points are approximated by a straight line

Table 1: The values of the power s in the transition regions of the Earth's magnetosphere

	04/03 2004	15/05 2005	10/03 2006	05/04 2007	08/08 2008
SW	0.52	0.52	0.48	0.45	0.55
FSH	0.7	0.75	0.68	0.6	0.76
PSH	0.98	0.9	0.95	0.92	0.97
MSH	0.95	0.87	0.94	0.87	0.91
MP	0.65	0.8	0.8	0.67	0.73

Thus, during the time of satellite location in SW, the found value of S in the entire interval of studied scales is close to the Gaussian distribution ($S = 0.5$). For FSH, MSH, MP, TBL and cusp the distribution corresponds to Levi distribution (intermittency).

3.2. Kurtosis values comparison

For quantitative characterization of possible deviations of fluctuation statistics from the normal distribution, the

kurtosis (excess) $K(\tau)$ is used, which is defined through moments of the second and fourth orders:

$$K(\tau) = S_4(\tau) / (S_2(\tau))^2,$$

where $S_q(\tau) = \langle |X(t+\tau) - X(t)|^q \rangle$ is the moment (structural function) of the q -th order [Benzi et al., 1993], angular brackets ($\langle \rangle$) designate time averaging of studied parameter $X(t)$, τ is the time shift. For the normal distribution one must have $K(\tau) = 3$ [Zaks, 1976].

The value of kurtosis is one of parameters displaying the character of intermittency of the process. However, this parameter does not allow one to make a quantitative comparison of the degree and mechanism of intermittency. If remains constant on various time scales τ , this indicates to the absence of intermittency.

The values of kurtosis of magnetic field fluctuations on scaling parameter τ were constructed (fig.2). It is clearly seen in the plots, that for SW the $K(\tau)$ function value varies around 3. This feature indicates to the Gaussian distribution function, which confirms the results obtained above in analyzing function $P_0(\tau)$. For FSH and MSH regions the value of function $K(\tau)$ on small scales sharply grows (up to 23), and on large time scales (> 2 s) this value approaches 3.

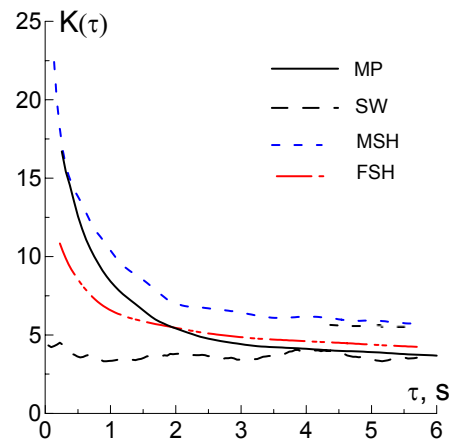


Figure 2: Dependence of the kurtosis value on the scale parameter τ for different magnetospheric regions and SW

3.3. ESS analysis results

In order to specify the type of turbulent processes the analysis of structure function features (moments of PDF) of different orders according to time interval for dataset $X(t)$ was performed in the study – Extended Self-Similarity analysis. Structure functions of high orders allow characterizing the properties of heterogeneity at the small scales of process. The dependence of structure function on the time shift τ assumes to be power law $S(\tau) \sim \tau^{\zeta(q)}$.

In a case of fully homogeneous isotropic Kolmogorov 3D (K41) turbulence the values of exponent are defined by a relationship $\zeta(q) = q/3$ [Frisch et al., 1978], and for the

Iroshnikov-Kraichnan model (IK), which describes plasma turbulence in the strong magnetic field, $\zeta(q) = q/4$ [Kraichnan, 1965].

To describe the intermittent turbulence it is very often to use log-Poisson model which considers the stochastic multiplicative cascade [Dubrulle, 1994]:

$$\zeta(q) = (1-\Delta)q/3 + \Delta/(1-\beta)[1-\beta^{q/3}].$$

Index β characterizes the degree of intermittency ($\beta=1$ for the non-intermittent homogeneous fully developed turbulence, for instance, in K41 model), Δ – the parameter related to the geometry of dissipative structures and edge effects. For the model of Pulitano-Pukke (PP):

$$\zeta(q) = q/8 + 1 - (1/2)^{q/4}.$$

ESS analysis consists in the determining of a relative value of power index for the different structure function orders. In the general case, for q -th and p -th orders the following relationship is assumed:

$$S_q(\tau) \sim S_p(\tau) \tau^{\zeta(q)/\zeta(p)}.$$

The following regions were examined with ESS analysis: FSH, MSH, MP (fig. 3).

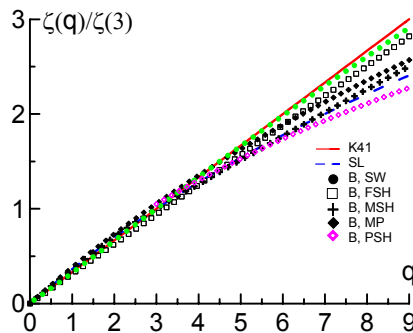


Figure 3a: Ratio of the power of the q -th order structural function to the third order function power on May 15, 2005. The experimental data for the magnetic field are marked with symbol; the dotted line corresponds to the value calculated using the formula in the log-Poisson cascade model for $\beta = \Delta = 2/3$ (SL), and the solid line corresponds to the $q/3$ (K41)

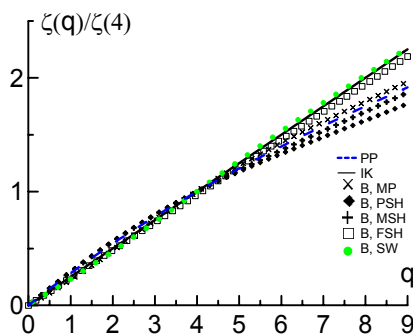


Figure 3b: Ratio of the power of the q -th order structural function to the fourth-order function power on May 15, 2005. The experimental data for the magnetic field are marked with symbol; the dotted line corresponds to the value calculated using the Pulitano-Pukke model (PP), and the solid line corresponds to the $q/4$ (IK)

ESS analysis demonstrates the intermittency of turbulent processes in MSH well described with log-Poisson SL cascade model, the values in the SW and FSH region are close to Iroshnikov-Kraichnan model of inhomogeneous anisotropic turbulence which describes plasma turbulence in the strong magnetic field.

4. Discussion and conclusions

The used set of techniques for determining the statistical properties of fluctuations has shown various properties of oscillations in FSH, PSH, MSH and MP.

Amplitude of fluctuations in MSH just after crossing BSH exceeds in a few time amplitude of fluctuations for non-perturbed SW or FSH.

The character of turbulent plasma flux in MSH is not associated directly with turbulence in SW but represents, to a considerable degree, the manifestation of intrinsic processes in MSH.

The use of the technique of probability density function for magnetic fluctuations has shown the following characteristic features of turbulence in the process of transition from SW through FSH deep into MSH. In SW the amplitude of fluctuations is minimal, the dependence of maximum of probability density function $P_0(\tau)$ corresponds to Gaussian distribution. In FSH, PSH, MSH and MP for small time scales the observed features are better described by the Levi distribution (intermittency).

ESS analysis demonstrates the intermittency of turbulent processes in MSH, PSH, FSH and MP also.

Moreover the turbulent processes in the SW can be described by Iroshnikov-Kraichnan model of turbulence, and the processes in MSH correspond to the log-Poisson cascade SL-model.

Acknowledgments. The authors express their gratitude to L.M. Zelenyi, V.N. Ivchenko for useful discussions.

The work is done in the frame of complex program of NAS of Ukraine on space researches for 2012-1016, and under a partial support of the grant No. F 53.2/039.

References

- Benzi R., Ciliberto S., Tripicciono R. et al.: 1993, *Phys. Rev. E.*, **48**, 29.
- Consolini, G., Kretzschmar M., Lui A.T.Y. et al.: 2005, *J. Geophys. Res.*, **110**, A07202.
- Dubrulle B.: 1994, *Phys. Rev. Lett.*, **73**, 959.
- Frisch U., Sulem P., Nelkin M.: 1978, *Fluid Mech.*, **87**, 719.
- Kozak L.V., Lui A.T.: 2008, *Kinem. i Fiz. Nebesnykh Tel*, **24**, 72.
- Kozak L.V., Pilipenko V.A., Chugunova O.M. et al.: 2011, *Kosm. Issled.*, **49**, 202.
- Kozak L.V., Savin S.P., Budaev V.P. et al.: 2012, *Geomagnetism and Aeronomy*, **52**, 445.
- Kraichnan R.H.: 1965, **8**, 575.
- She Z., Leveque E.: 1994, *Phys. Rev. Lett.*, **72**, 336.
- Zaks L.: 1976, Moscow: Statistics, 598 p.

DIFFERENT MODES OF TURBULENCE IN THE ACTIVE REGIONS OF THE SOLAR PHOTOSPHERE

L.V. Kozak¹, R.I. Kostik², O.K. Cheremnykh³

¹ Kyiv National Taras Shevchenko University, Kyiv, Ukraine, kozak@univ.kiev.ua

² Main Astronomical Observatory of the National Academy of Sciences of Ukraine, Kyiv, Ukraine

³ Space Research Institute of the National Academy of Sciences of Ukraine and State Space Agency of Ukraine, Kyiv, Ukraine.

ABSTRACT. In work the range of different methods for the analysis of characteristics of turbulent processes in the active regions of the solar photosphere has been used. The changes of fluctuations distribution function and its moments were analyzed, spectral analysis was carried out.

It was found out from the observations of active region carried out with the 70-cm vacuum tower telescope VTT in Isanie (Tenerife Island, Spain) that the turbulent processes in the sun photosphere are characterized by two different spectra of turbulence. The first one of them is well known Kolmogorov spectrum, which describes the plasma with zero mean magnetic field. The second one is the Kraichnan spectrum with a different from zero mean magnetic field. Transition from one spectrum type to another one occurs at scale of 3 Mm.

We have to note that the scale 3 Mm corresponds to one of mesogranulation and testifies about non-zero mean magnetic fields for the consideration of regions exceeding the granulation in active regions of the photosphere. Besides, this clears the possibility of appearance of self-organizing magnetic plasma structures such as spots, active regions and complexes of activity.

Key words: solar photosphere, turbulent processes in the sun photosphere, turbulent model, self-organizing magnetic plasma structures, mesogranulation.

1. Introduction

Studying the statistical and spectral properties of velocity fields makes it possible to determine the role of turbulent processes in the interaction between plasma flows and reveal the real mechanisms of the energy and magnetic field transformation

In this work, we consider the features of turbulent processes and their relation to the average magnetic fields in the solar photosphere. This is important for understanding the many processes studied in solar physics, magnetosphere of the stars and planets.

A classical approach to studying the statistical properties of a turbulent flow consists in calculating structural functions with local scale l (distribution function statistical

moments) of different orders. Kolmogorov's theory [Kolmogorov, 1941] (K41) predicts the Gaussian statistics of homogeneous isotropic turbulence and the power law dependence for structural function

$$S_q(l) = \langle |v(x+l) - v(x)|^q \rangle \sim l^{\zeta(q)},$$

in the inertial range when the Reynolds numbers are large, where $\langle \dots \rangle$ is averaging over an ensemble. When Kolmogorov (1941) postulated that structural functions only depend on the energy dissipation scale and rate, he deduced that the energy flux spectrum depends on wave number k as $E_K \sim k^{-5/3}$. This law relatively adequately describes the spectrum with developed isotropic hydrodynamic turbulence; however, more precise measurements of turbulent flows indicated that the exponent differs from 5/3. This discrepancy was related to the presence of structural inhomogeneity of a turbulent process (intermittency) [Novikov and Stewart, 1964]. Random pulsations in an intermittent medium have a distribution function different from the Gaussian distribution.

We should note that plasma in a strong magnetic field is described by an approach, which allows for a consideration of the dynamics in the plane across the magnetic field in the scope of a two dimensional model. This model is illustrated by the Iroshnikov–Kraichnan two dimensional model (IK) of MHD turbulence [Kraichnan, 1965], which is very often used to interpret properties of turbulent boundary plasma. The energy spectrum in the Iroshnikov–Kraichnan model is defined by the relation $E_{IK}(k) \propto k^{-3/2}$. In comparison with the Kolmogorov spectrum, this spectrum exhibits a significantly reduced level of energy transfer on small scales, perturbations of MHD variables propagate at a speed of the order of the Alfvén speed.

In spite of the fact that analytical methods have been developed in the theory of turbulence, they are not as detailed and accurate as semiempirical models that are based on statistical methods. This is of special importance in cases when turbulence with intermittency is described, because not only intermittency results from inhomogeneous turbulence, but inhomogeneity itself is also distributed chaotically.

2. Used observational data

For the statistical and spectral analysis, we used solar active region observations obtained on November 13, 2007, at the German vacuum tower telescope (VTT) [Schroter et al., 1985] at Izaña (Tenerife, Spain) in three wavelength ranges: Fe I $\lambda\lambda$ 1564.3–1565.8 nm, Ba II λ 455.4 nm, and Ca II λ 396.8 nm an active region (facula) near the solar disk center. The spatial resolution was 0.185".

Following the standard procedure, all the images were corrected for the dark current, variations in the transparency of Earth's atmosphere, and different sensitivities of CCD camera pixels. The subsequent processing of the observational data included the finding of the velocity at the center (height in the solar atmosphere of $h = 650$ km) and in the farout wings ($h = 0$) of the Ba II line. For this purpose, we used the lambda meter procedure [Stebbins and Goode, 1987].

The parameter fluctuations of the velocity field are due largely to convective and wave motions. To distinguish between the granulation and wave components of the velocity field, we built a diagnostic diagram $k - \omega$, i.e., the dependence of the power of the δV variations on the temporal (ω) and spatial (k) frequencies [Kostyk and Khomenko, 2002]. In this work we used only the convective velocity field component (Fig. 1).

3. Determination of the type of turbulent processes

For the identification of the turbulence we used the function of the probability density of fluctuation amplitudes of the velocity $P(dv, l)$. It should be noted that, the random noncorrelated fluctuations of the difference of measured velocities between the observations, shifted in space, will be described by the Gaussian distribution. For the turbulence with intermittency the probability of considerable fluctuations on distribution's wings will be rather high due to excess energy of large scale disturbances.

The distribution functions of $P(dv, l)$ are shown in Fig. 2. Narrow wings of the distribution function indicate on the homogeneity of turbulent processes, which pertains both to the Kolmogorov type and Iroshnikov–Kraichnan type processes [Kozak et al., 2008, Budaev et al., 2011, Kozak et al., 2012].

To determine the type of turbulent processes, we analyzed the moments of the probability density function for different orders. In the turbulence theory, this commonly used analysis is referred to as extended self-similarity (ESS) analysis [Benzi et al., 1993]. It allows researchers to considerably narrow down the possible types of turbulent processes.

In a case of fully homogeneous isotropic Kolmogorov 3D (K41) turbulence the values of exponent are defined by a relationship $\zeta(q) = q/3$ [Frisch et al., 1978], and for the Iroshnikov-Kraichnan model (IK), which describes plasma turbulence in the strong magnetic field, $\zeta(q) = q/4$ [Kraichnan, 1965].

The main idea of this approach is to find dependences of a relative value of power index for the different structure function orders. In the general case, for q -th and p -th orders the following relationship is assumed:

$$S_q(\tau) \sim S_p(\tau) \tau^{\zeta(q)/\zeta(p)}.$$

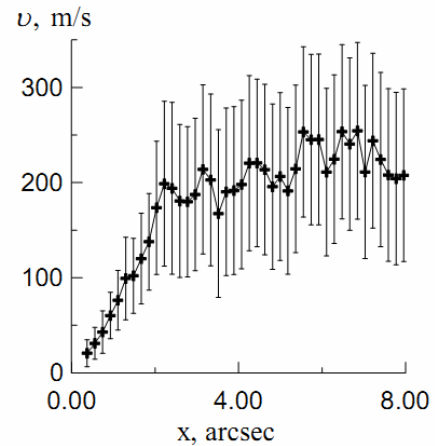


Figure 1: Observed velocity fluctuations in active regions ($h = 650$ km).

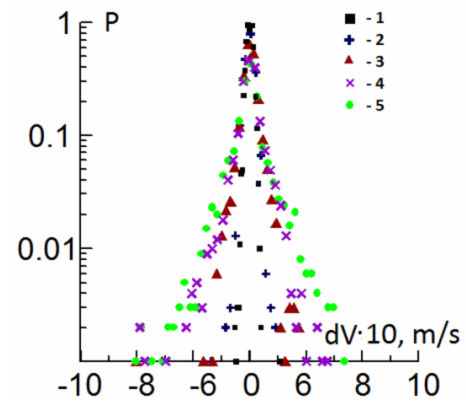


Figure 2: Distribution functions P of probability density of velocity fluctuations for various spatial shifts l (1 – 0.185 arcsec, 2 – 0.37 arcsec, 3 – 0.74 arcsec, 4 – 1.11 arcsec, 5 – 1.85 arcsec).

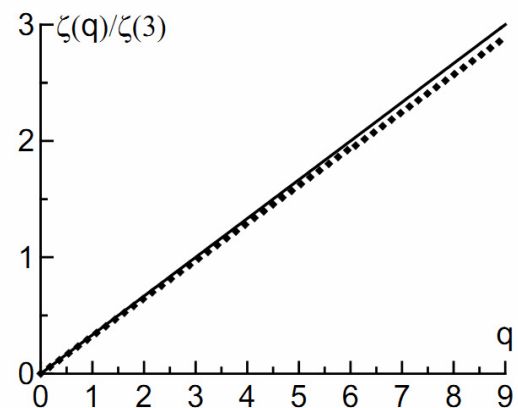


Figure 3: The ratio of the structural function of the q th order to the structural function of the third order: dots are the observations; the continuous line shows the model values calculated by the Kolmogorov model.

Once such dependence is found, it is compared with the analogous dependences for different turbulence models.

For comparison with the Kolmogorov model, we investigated the ratio between the power of the moment of the q th order probability density function and the power of the third order $p = 3$ (Fig. 3). The ESS analysis shows a good consistency of the turbulent processes with the Kolmogorov turbulence model for $q < 6$.

To compare the observations with the Iroshnikov–Kraichnan model, we also analyzed the ratio between the power of the moment of the q th order probability density function and the power of the fourth order $p = 4$ (Fig. 4). We see that, at $q > 6$, the dependence is closer to the Iroshnikov–Kraichnan model. This approach does not allow us to determine the scale of transition from one process to another, but we can infer that there are two distinct types of turbulence.

In order to refine the scale of the turbulent processes, we investigated the spectral dependences of the changes in velocity for active regions (Fig. 5). It is evident that the spectral density has a break on a scale of approximately 3000 km. The linear approximation ($\sim k^{-p}$), which was calculated separately for large and small scales, shows that the spectral indices vary significantly when moving from one region to another. This behavior suggests that turbulences are qualitatively different at different scales. The values of the exponent tend to $-5/3$ on scales up to 3000 km and to $-3/2$ on larger scales. Thus, the turbulent processes that can be described within the Kolmogorov model dominate on small scales, but there is anisotropy of turbulent processes on large scales owing to the nonzero mean magnetic field, and the turbulent processes resemble the Iroshnikov–Kraichnan pattern. Note that this result is consistent with the above results of the statistical analysis.

Conclusions and discussion

The statistical and spectral analysis of the convective velocity field component found that:

- solar active regions exhibit two fundamentally different spectra of turbulence;
- the Kolmogorov type turbulent processes dominate on small scales, and the Iroshnikov–Kraichnan type turbulent processes are observed on large scales;
- the transition from the Kolmogorov spectrum to the Iroshnikov–Kraichnan spectrum takes place on a scale of approximately 3 Mm.

This scale corresponds to that of mesogranulation and is evidence of nonzero mean magnetic fields.

Moreover, it indicates the possibility of development of self-organized magnetic plasma structures (spots, bipolar groups, active regions, activity complexes, etc.).

It should be noted that this result is the first step towards finding the relationship between the mean magnetic field and the observed large scale solar magnetic structures. We emphasize that the modern concept of the solar mean turbulent magnetic field, which is commonly used in the dynamo theory, says nothing of structures, such as faculae and spots. Therefore, the discovery of the second turbulence spectrum with a nonzero mean magnetic field is essential to the further development of the theory and finding the relationship between the observed structures and the turbulent medium parameters.

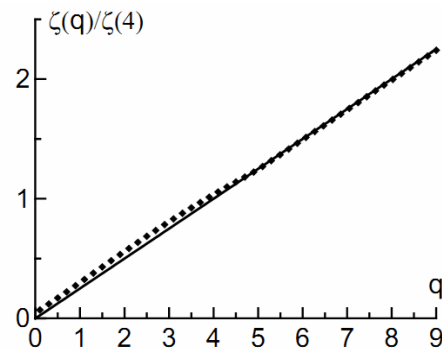


Figure 4: The ratio of the structural function of the q th order to the structural function of the fourth order: dots are the observations; the continuous line shows the model values calculated by the Iroshnikov–Kraichnan model.

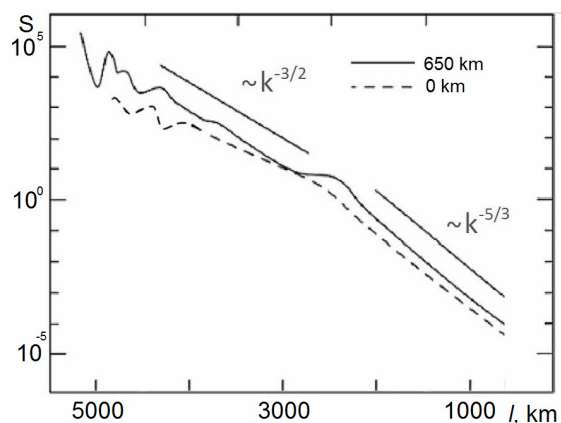


Figure 5: Spectral density S of the convective velocity field component for the active region of the photosphere.

Acknowledgments. The authors express their gratitude to A.A. Solov'ev, V.G. Lozitskii, and A.S. Parnovskii for useful discussions. The work is done in the frame of complex program of NAS of Ukraine on space researches for 2012-1016, and under a partial support of the grant No. F 53.2/039.

References

- Benzi R., Ciliberto S., Tripicciono R. et al.: 1993, *Phys. Rev. E.*, **48**, 29.
- Budaev V.P., Savin S.P., Zelenyi L.M.: 2011, *Usp. Fiz. Nauk*, **181**, 905.
- Kolmogorov A.: 1941, *Dokl. Akad. Nauk SSSR*, **30**, 299.
- Kostyk R.I., Khomenko E.V.: 2002, *Astron. Rep.*, **46**, 925.
- Kozak L.V., Lui A.T.: 2008, *Kinematika Fiz. Nebesnykh Tel*, **24**, 72.
- Kozak L.V., Savin S.P., Budaev V.P. et al.: 2012, *Geomagnetism and Aeronomy*, **52**, 445.
- Kraichnan R.H.: 1965, *Phys. Fluids*, **8**, 575.
- Novikov E.A. Stewart R.W.: 1964, *Izv. Akad. Nauk SSSR. Ser. Geofiz.*, **3**, 408.
- Schroter E.H., Soltau D., Wiehr E.: 1985, *Vistas Astron.*, **28**, 519.
- Stebbins R.T., Goode P.R.: 1987, *Solar. Phys.*, **110**, 237.

ABOUT EXPANSION OF TERRESTRIAL RADIOPHYSICAL METHODS FOR DETECTION OF ULTRA-HIGH-ENERGY COSMIC RAY

V.B.Kozhukhar, I.O.Lytvynenko, O.A.Lytvynenko

Observatory URAN-4 of Institute of radioastronomy of NASU
Odessa, Ukraine, *uran4@te.net.ua*

ABSTRACT. Low arrival density of the ultra-high-energy cosmic rays is one of the main obstacles of their experimental research.

Overcoming this problem was based on the increase in the sensitive area of terrestrial facilities. Currently, the area of such installations reached a practical limit. The further development of researches is connected with remote registration of accompanying electromagnetic radiation. The projects of remote sensor installation on space vehicles are known. In this work the opportunity of use of ground-based radio telescopes and Moon, as return reflector, for global remote detection of electromagnetic bursts caused by space ultra-high-energy cosmic rays in an atmosphere of the Earth is considered.

Key words: cosmic rays, extensive air showers, HF signal, Moon reflection, radio telescopes.

Result of interaction of cosmic ray (CR) with substance is the cascade shower of secondary particles. The cascade shower in an atmosphere have the name of extensive air showers (EAS). The observation of EAS is the main method of CR study in case of kinetic energy $W > 10^{15}$ eV. The ground observatories with ionization and scintillation detectors have ensured study of CR with energy up to 10^{17} eV. The intensity of cosmic ray sharply decreases with increase of energy of particles. There are 10^7 events with $W > 10^{15}$ eV and only one event with $W > 10^{19}$ eV on the area 1 km^2 per one year. Therefore increase of the detector area is necessary for study of ultra-high-energy cosmic ray. Therefore for study of ultra-high-energy cosmic ray increase of the detector area is necessary. The modern ground installations have the area up to thousand square kilometers (for example Pierre Auger Observatory – 3000 km^2) That allows to register events with energy of particles up to 10^{20} eV. The following stage is connected to use of remote sensor placed on space vehicles. One of the projects is EM-EUSO. This is a new type of observatory that uses the transient luminous phenomena taking place in the earth's atmosphere caused by particles coming from space. The sensor will detect extreme energy particles with energy above 3×10^{19} eV. The EM-EUSO observation area exceed exceeding 10^5 km^2 .

One of remote methods of superhigh-energy cosmic ray study is the detection of shower radioemission (Filonenko, 2002). Radio signal generates by the secondary electrons and positrons of the shower.

In this paper we consider an opportunity of use of the Moon as reflector EAS radioemission from all terrestrial

hemisphere. As remote sensors can be used decameter wavelength radiotelescopes of URAN VLBI.

Space diversity on hundred kilometers radiotelescopes are triangulation network for definition of EAS coordinates and angle of cosmic ray arrival. In a fig. 1 presents the plan of EAS observation with lunar radio reflections.

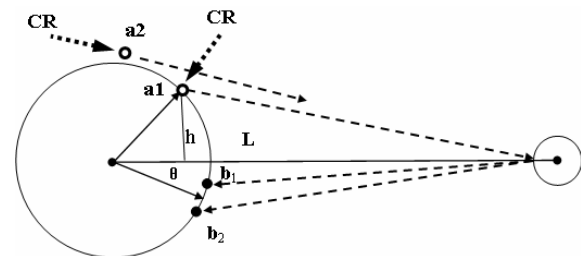


Figure 1: The plan of EAS observation with lunar radio reflections. **CR** and **dashed line** – transit and non transit cosmic ray way, **dashed line** – radio propagation paths, **a₁** and **a₂** – places of EAS radioemission, **b₁** and **b₂** – radiotelescopes, **L** – line connecting Earth with Moon, **θ** – the angle between **L** and direction to triangulation base of radiotelescopes.

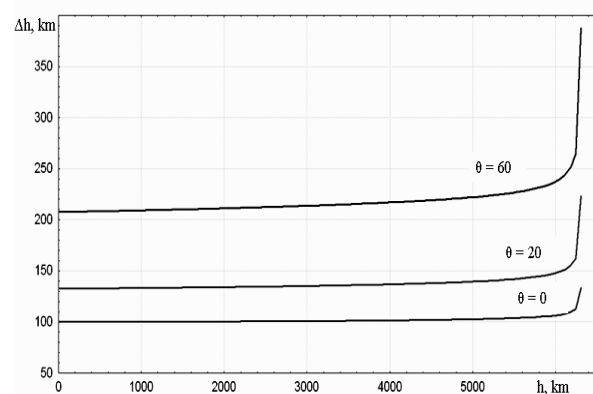


Figure 2: Absolute errors of EAS coordinates definition (triangulation base is 500 km , time resolution is 10^{-6} s)

After synchronic measurement of EAS radio signal lag on three telescopes we can calculate coordinates of EAS. Now afford calculate angle of cosmic ray arrival, if relative position Moon end Earth is known. In a fig. 2 presents absolute errors of EAS coordinates (Δh) definition as function of argument h (look fig.1). Three curves correspond to three sizes of a angle θ , degree.

The realization of this plan is possible if: radiowave power flux density will be sufficient; intensity of CR events will be sufficient. We shell estimate this conditions below.

The moving clot of EAS particles takes the form of a disk. Its thickness is about 2 meters and diameter from tens up to hundreds meters and more. Power of coherent radioemission of disk dominates among other type of EAS emission in high frequency range. Therefore directivity diagram of EAS radioemission define by directivity diagram of disk aperture.

Approximation of the directivity diagram in the field of the main lobe:

$$F(\alpha) = \exp\left[-1,38(\alpha/2\alpha_0)^2\right],$$

where α – angle between beam axis end emission direction, $2\alpha_0$ – beam width ($2\alpha_0 \approx 60\lambda/d$).

Me assume that the area of the disk is proportional W . Experimental result is $d = 100$ m, when $W = 10^{17}$. It is possible to write: $d = 2,16 \cdot 10^{-6} \sqrt{W}$. In a fig. 3 presents directivity diagram of EAS radioemission.

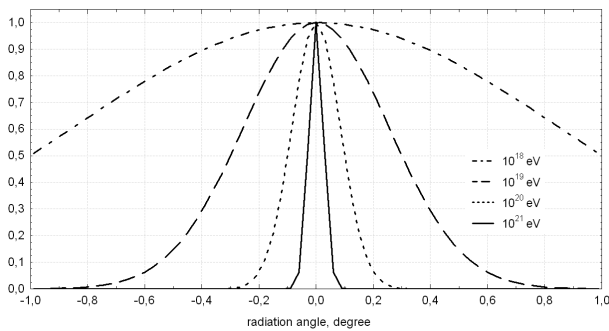


Figure 3: Power pattern of EAS radioemission. Frequency 30 MHz, X-axis radiation angle α , degree.

For estimation of radiowave power flux density me are used next formulas $|\bar{\Pi}_0(\alpha, \beta)| = (P'G_1/4\pi R_L^2)F(\alpha)^2$, where $G_1 = 1,98 \cdot 10^{-12} W/\lambda^2$, P' – EAS radioemission power, R_L – distance between the Earth and the Moon. For estimation of P' me are used theoretical and experimental data from Filonenko (2002). It was assumed, that $P' = b \cdot W$. For $W = 10^{21}$ and frequency band 1 MHz estimation is $P' = 80$ Watt. Appropriate power flux density near the radiotelescope is $5 \cdot 10^6$ Jn. It considerably is exceed power flux density of cosmic sources and solar bursts in decameter wavelength.

The estimation of intensity of EAS-events which can be registered by ground-base radiotelescopes is carried out. The results presents in Table 1.

Table 1: Intensity events in EAS-Moon reflection method

particle energy, lgW eV	angle of aspect, steradian	number of events	
		per annum	per diem
19	$3 \cdot 10^{-4}$	71154	195
20	$3 \cdot 10^{-5}$	7906	21.66
21	$3 \cdot 10^{-6}$	1	

References

Filonenko A.: 2002, *Uspehi fizicheskikh nauk*, **172**, 439.

DEVELOPMENT OF 23 CYCLES ACTIVITY IN NORTHERN AND SOUTHERN HEMISPHERES OF THE SUN

M.I.Ryabov, A.L.Sukharev, S.A.Lukashuk

Odessa observatory of Radioastronomical Institute NANU

ryabov-uran@ukr.net

ABSTRACT. On an example of the 23rd cycle of solar activity the basic properties of its development in northern and southern hemispheres were researched (daily values of Wolf Sunspot Number – W, the daily values of Sun spots areas – Sp and daily values of flare index – FI.) Effects of application of full-scale Wavelet analysis for studying the temporary structure of formation of a solar cycle show the difference in northern and southern hemispheres. The "leading" periods (in northern hemisphere – 340 days, and in southern hemisphere – 709 days) differ. Thus, the activity period in two years is predominate in southern hemisphere. The "leading" period for the flare index for northern hemisphere is 555 days, and for southern hemisphere is 709 days. In general the basic periods W in northern hemisphere are in the range of 37-555 days, and in southern – 78-906 days, SpN (61-906 days), SpS (61-1477 days), FIN (37-555 days), FIS (23–709 days), FIS – (14-709 days) depending on the phase of solar cycle.

Introduction

Analysis of the data on the Wolf sunspot number – W, the total area of all groups of sunspots – Sp and Flare index – FI for each hemisphere of the Sun alone shows the distinction of forms of their activity. There is the characteristic "asymmetry of activity". It is defined as the value of relations index values of the earth hemispheres or the magnitude of their difference. The results of earlier studies of North-South asymmetry are reflected in [1]. For its research monthly averages of various solar indices were used. The smoothed monthly values of the total area of groups of sunspots showed a significant difference in the development of the activity in the northern and southern hemispheres [2]. However, research into the nature of the North-South asymmetry most effectively on the basis of the daily values of solar indices. Examines the Wolf number of WN – northern and WS – the southern hemisphere, the total area of groups of spots-SpN and SpS, the Flare index – FIN and FIS. Data on WN and WS are only from 1992 onwards and cover only the 23rd cycle. At the same time, the SpS are presented with SpN and 1874. This paper discusses the dynamics of daily values of

WN, WS, SpN, SpS, FIN, FIS with the full-scale application of wavelet analysis for 23 first-cycle activity. It is getting clear that the study of the North-South asymmetry is up-to-date and it is possible to obtain new interesting results.

1. Wavelet-analysis

Since explored observational data in astronomy are complex, non-stationary processes, the use of wavelet analysis allows to get more information about the variability of the data at different periods (or frequencies) than using Fourier analysis. Used in the continuous Wavelet transform based on the Morlet function. This allows you to select individual harmonic components on different time scales, track changes over time and determine the duration of their existence [3].

2. Time – frequency wavelet spectra

The wavelet analysis as a result of the calculations is the matrix of coefficients of the continuous Wavelet transform of surfaces in three-dimensional space. The most informative outcome of these calculations in time-frequency structure of the signal is a representation of the frequency-time. The isolines enable you to trace the changes in the intensity of wavelet transform on different scales and in time. The spectra are built in a logarithmic coordinates. The results of calculations for the WN, WS, SpN, SpS, FIN, FIS is shown in Fig. 1.

Data from table 1 mean that the "lead period" for the northern hemisphere for the WN and SpN is 340 days. In the phases maximum and slow cycle leading periods are 163 and 128 days. For Flare index FIN dominated the 555 days period. For the southern hemisphere predominate "lead period" is 709 days for indexes WS, SpS, FIS. On the slow phase the leading period is 906 days. For flare index in the northern hemisphere – FIN spacing leading periods in the interval 37-555 days and southern hemisphere of 23-709 days. The spectral power at all leading periods the southern hemisphere is systematically higher than in the northern hemisphere.

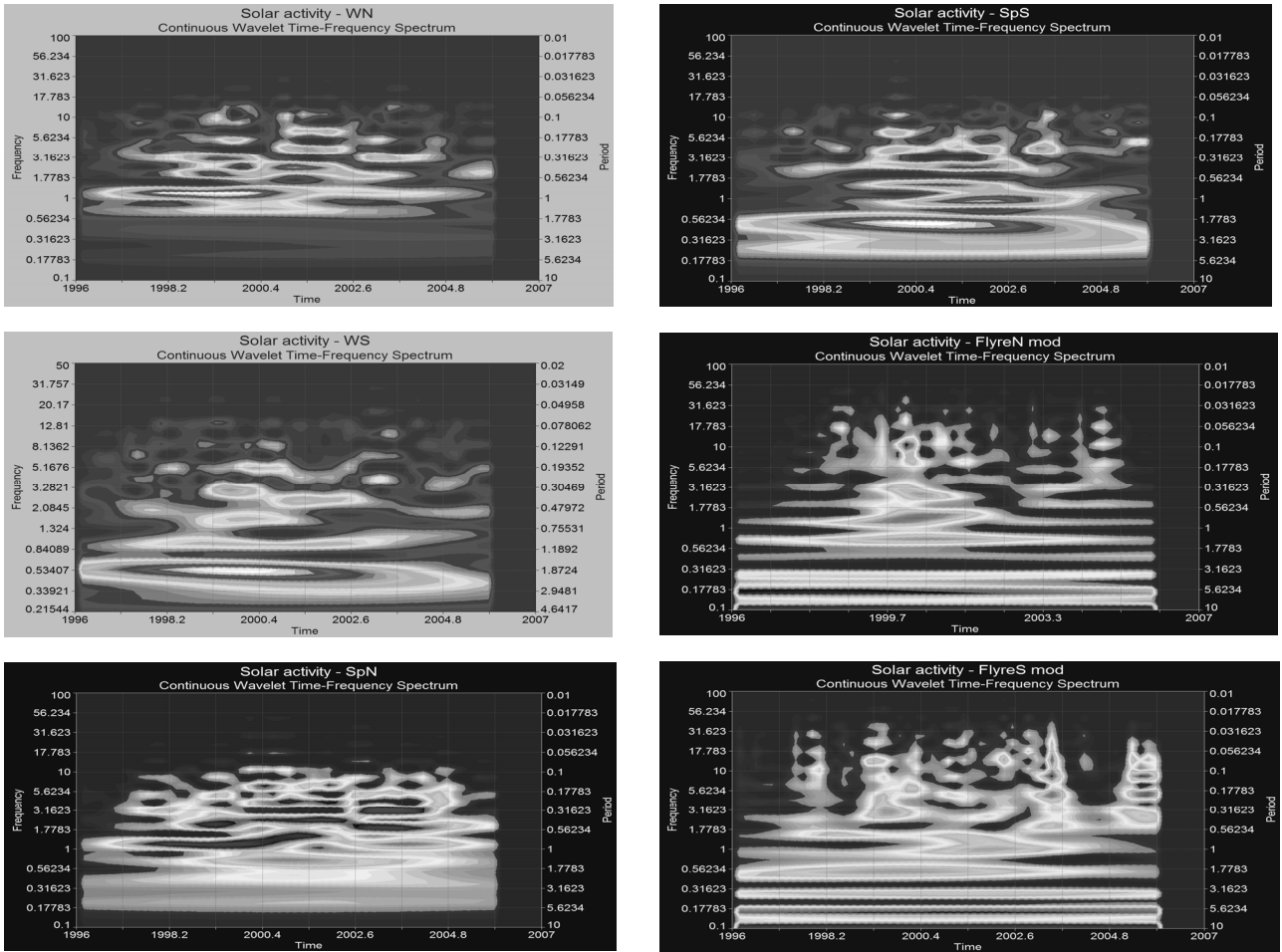


Figure 1: Wavelet spectra for WS WN indexes, SpN, SpS, FIN, FIS (on the horizontal axis, the vertical-years-period and frequency). The "leading periods" are determined on the basis of wavelet Spectra. They show the maximum spectral power. The results are shown in Table 1.

Table 1.

	WN		WS		SpN		SpS		FIN		FIS	
Год	Per	Power	Per	Power	Per	Power	Per	Power	Per	Power	Per	Power
1996	340	1,8E+04	709	4,3E+04	340	3,9E+06	709	1,9E+07	555	4,8E+02	709	5,8E+02
1997	340	5,4E+04	709	6,9E+04	340	1,2E+07	709	3,3E+07	555	7,9E+02	709	8,2E+02
1998	340	8,4E+04	709	9,0E+04	340	2,0E+07	709	4,8E+07	555	1,1E+03	709	9,8E+02
1999	340	8,5E+04	709	9,9E+04	340	2,0E+07	709	5,8E+07	266	2,4E+03	128	1,0E+03
2000	340	7,2E+04	709	9,8E+04	266	1,8E+07	709	6,0E+07	37	3,5E+03	709	1,0E+03
2001	163	5,4E+04	709	9,1E+04	163	2,0E+07	709	5,8E+07	266	2,3E+03	709	9,1E+02
2002	163	3,4E+04	709	7,0E+04	163	1,9E+07	709	4,8E+07	555	8,9E+02	23	8,6E+02
2003	128	1,6E+04	709	4,4E+04	128	2,4E+07	709	3,1E+07	555	5,9E+02	29	1,3E+03
2004	340	1,2E+04	906	2,5E+04	128	1,4E+07	906	2,3E+07	61	6,3E+02	128	4,1E+02
2005	163	9,5E+03	906	1,7E+04	163	4,6E+06	906	1,5E+07	555	2,6E+02	78	1,2E+03

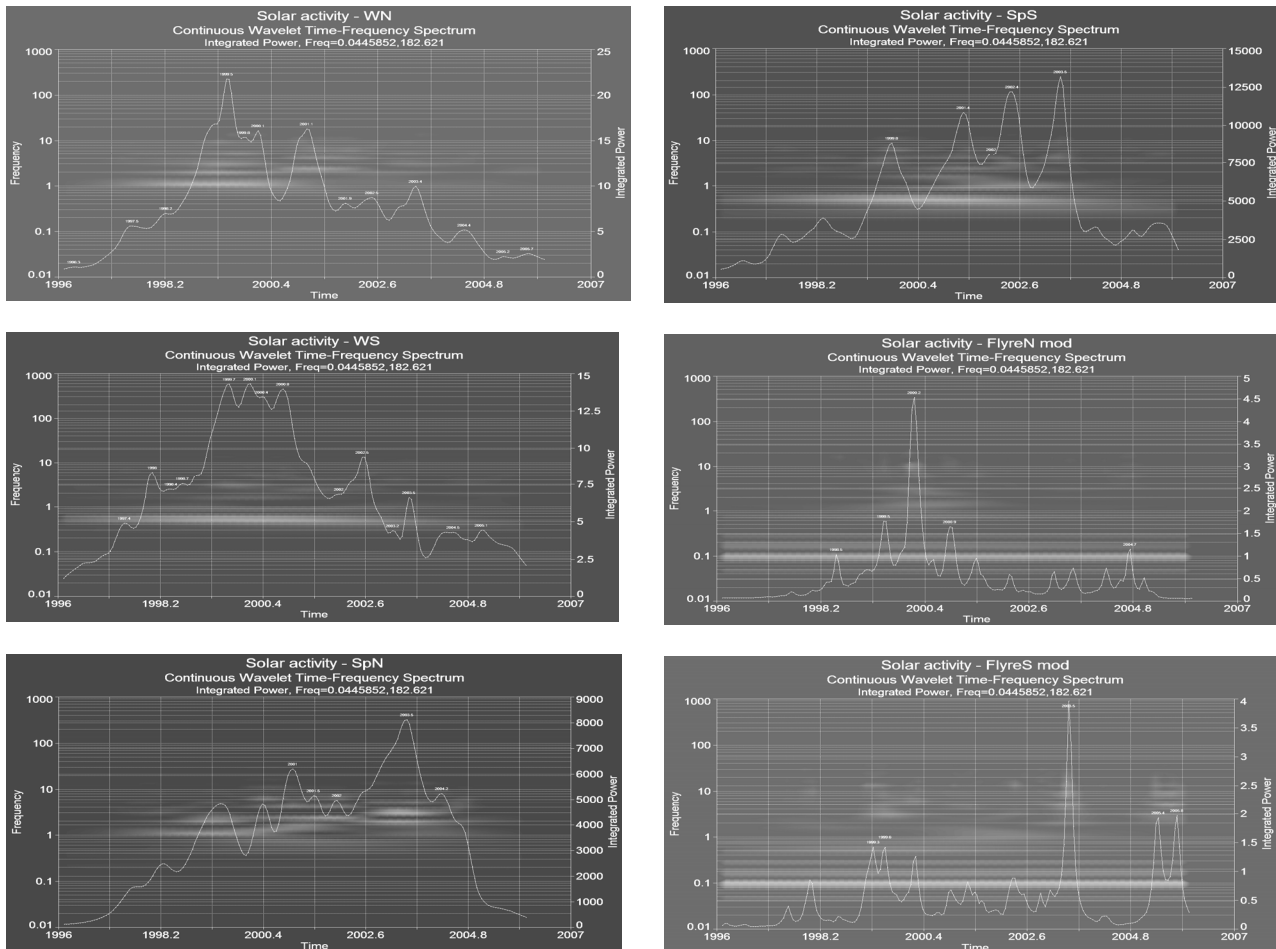


Figure 2. The global spectrum of wavelet for indexes WN, WS, SpN, SpS, FIN, FIS (on the horizontal axis is vertical, spectral power and frequency).

3. Global wavelet spectra

Distribution of the total energy of the signal can be tracked using global Wavelet spectrum [4]. The integrated averaging in frequency spectrum shows the distribution of energy process on time. This type of range is required to determine the moments of greatest activity of the analyzed process that is the result of the addition of periodic processes on different time-scales.

Wavelet Spectra demonstrates global received a noticeable difference in the nature and timing of periodic processes shaping the dynamics of changes of W, Sp and FI. For each of these indices is the difference in their dynamics in the northern and southern hemispheres.

4. «Spectra of periods»

Wavelet transform can be more effective if you build it as a series of separate graphs "spectral power-period" for each year. This approach allows users to compare changes in periodic components of solar activity in a certain time interval with complexes activity that existed at that time. "Spectra periods" which correspond the maximums on global Wavelet spectra indicate what periodic elements contribute to the phase of increasing solar activity.

Conclusion

The wavelet analysis of Wolf sunspots numbers, the total area of all the spots and flare index separately for the northern and southern hemisphere allows to present the development of 23rd solar cycle as a sum of quasi-periodic processes. These processes have different time scales in both hemispheres. Also the development of the solar cycle on generation number and total area of activity is different. The dynamics of their development has been posted in time. The result of these processes is the varying degrees of the impact of the activity of the northern and southern hemisphere, depending on the position of the Earth in orbit around the Sun and its provisions regarding the hemisphere of the current layer. A similar analysis for other solar cycles will be the subject of subsequent publications.

References

1. Vitinskij Ju.I., Kopecky M., Kuklin G.V. *Statistics of the sunspots generation*, M.: Nauka, 1986.
2. Ryabov M., Lukashuk S.A.: 2009, *Cycles of activity on the Sun and the stars*, S.-Pb., 121.
3. Yakovlev A.N. *Introduction to Wavelet transform. Stud. Allowance*, Publish. House of the NSTU, Novosibirsk, 2003.
4. Astafyeva N.M.: 1996, *Physics-Uspekhi (Adv. in Phys. Sci.)*, **166**, 1145.

WHETHER THERE IS AN ASTROPHYSICAL SOURCE IN THE OSCILLATIONS OF GEOPHYSICAL PARAMETERS WITH A PERIOD OF 160 MINUTES?

S.Samsonov¹, L.Miroshnichenko^{2,3}, V.Kotov⁴, N.Skryabin¹,
V.Timofeev¹, D.Baishev¹

¹ Yu.G.Shafer Institute of Cosmophysical Research and an Aeronomy, SB RAS, Yakutsk, Russia

² N.V.Pushkov Institute of Terrestrial Magnetism, Ionosphere and Radio Wave Propagation, RAS, Moscow, Russia

³ D.V.Skobeltsin Institute of Nuclear Physics, MSU, Moscow, Russia

⁴ Scientific Research Institute "Crimean Astrophysical Observatory", Nauchny, Ukraine

ABSTRACT. Oscillations with a period of 160 minutes in the ground pressure and Z-component of the geomagnetic field revealed by authors earlier are studied the regular ground measurements. For the analysis the data of five stations on the territory of Europe (Moscow, Apatity, Oulu) and Siberia (Yakutsk, Tixie) obtained in December, 2003 are used. It is shown that the specified oscillations revealed by authors earlier, are manifested in Europe and Siberia synchronously. For December, 2003 the mean amplitude of oscillations in the ground pressure accounts for 0.012 ± 0.002 mb; in a Z-component their value is equal to 0.323 ± 0.070 nT. Authors discuss the possible nature of pulsations.

Key words: ground pressure, geomagnetic field, oscillations with a period of 160 minutes, astrophysical source, gravitational wave.

1. Introduction and problem statement

For the first time pulsations with a period of 160-min were trusty revealed in the luminosity of the Sun as stars [Kotov et al., 1985]. Some evidences of their possible cosmological nature were obtained [Kotov, Lyuty, 1992; Kotov V. & Kotov C., 1996]. Revealing of pulsations of the Sun afterwards were confirmed by other investigators and registered as a discovery [Kotov et al., 1985]. In the scientific literature those pulsations were named as P_0 -pulsations.

In the published scientific literature the appearance of 160-min pulsations in the ground pressure [Novikov et al., 1985; Karpova et al., 2002] was already noted. Those authors ascertained only the fact of their presence but without determination of their amplitudes and phases. Earlier similar pulsations were revealed in connection with the passage of interior gravitational waves (IGW) in the atmosphere [Bobova et al., 1985]. In that work the

160-min pulsations of geomagnetic AE-index were noted. Besides that publication, in [Pochtarev et al., 1983; Bobova et al., 1990; Petrova, 1992; Petrova et al., 1999; Petrova, 2008] the connection of seismic and geomagnetic pulsations of hourly periods was noted.

Synchronous manifestations of 160-min pulsations in the ground pressure at widely separated four stations were studied by authors [Timofeev et al., 2005, 2009]. Some peculiarities of pulsations (behavior of phases and amplitudes) revealed in those works, indicated to their possible extraterrestrial (solar or galactic) origin. It has induced us to carry out the more detailed analysis of a procedure of isolation of 160-min pulsations by the ground data and also to propose one of the possible hypotheses of their origin.

2. Experimental data and their treatment

In this work the experimental data of atmospheric ground pressure and geomagnetic field have been used. The data on atmospheric pressure represents 5-min measurements obtained with digital barographs with a measurement accuracy $\pm 0,01$ mb (st. Moscow, Apatity and Oulu) and $\pm 0,1$ mb (st. Yakutsk, Tixie). The data on the geomagnetic field Z-component represents 1-min measurement obtained with digital magnetometers with the accuracy not more than 0,1 nT. Fig.1a shows the results of treatment of the 5-min values of ground pressure using a superposed epoch technique in December, 2003. The beginning of superposition on the period of 160-min (32 five-minute points) is realized from the time moment of 00:05 UT. The plots shown in Figure are for the following five stations: Tixie, Apatity, Oulu (Finland), Yakutsk and Moscow. Fig.1b presents the results of treatment of the 1-min values of the geomagnetic field Z-component for the same periods for

the stations of Oulu, Moscow, Novosibirsk, Irkutsk and Lvov from the time period of 00:01 UT. For clear evidence two 160-min periods are shown: for the ground pressure 64 five-min points in the two periods (Fig.1 a) and for the Z-component - 320 one-min points (Fig. 1b) are shown. The plots have been obtained from the extended set of data for the same periods as the pressure. Superpositions begin from the time period of 00:01 UT.

Beforehand the whole primary set of data has been treated as follows. First we carry out smoothing using the normal law, in which $\sigma = T/4$, where $T = 180$ minutes or 36 five-min points (T is a smoothing period). As a result we will obtain a trend in which all variations with a period $< T = 180$ min will be absent. The trend is subtracted from a primary series, i.e. we filter off all variations with a period of more than 180 minutes.

The obtained filtered off series is smoothed by the normal law with $\sigma = 10$ minutes or 2 five-minute points that corresponds to a period of smoothing $T = 40$ minutes. As a result, we will obtain a new series in which there will be all variations with periods of less than 40 minutes and more than 180 minutes, i.e. the band-pass filtering with a pass-band from 40 to 180 minutes is realized. In order to decrease the influence of the "penetration" variations, we will repeat the band-pass filtration with the same parameters. The necessity of double filtration is caused by very high amplitudes of "outsider pulsations" in the low-frequency range. In Fig.1a it is seen that in the ground pressure all phases obtained by the December data coincide by all stations on the whole territory of Europe and Siberia. The mean amplitude of Po-pulsations averaged by all stations, accounts for 0.012 ± 0.002 mb. In the geomagnetic field (Fig. 1b) synchronism of the change of phases by all considered stations of Europe and Siberia (Oulu, Moscow, Novosibirsk, Irkutsk, and Lvov) is also observed. The calculation errors have been determined using the techniques developed specially for estimation of results obtained using the superposed epoch technique [Jamison and Regal, 1979].

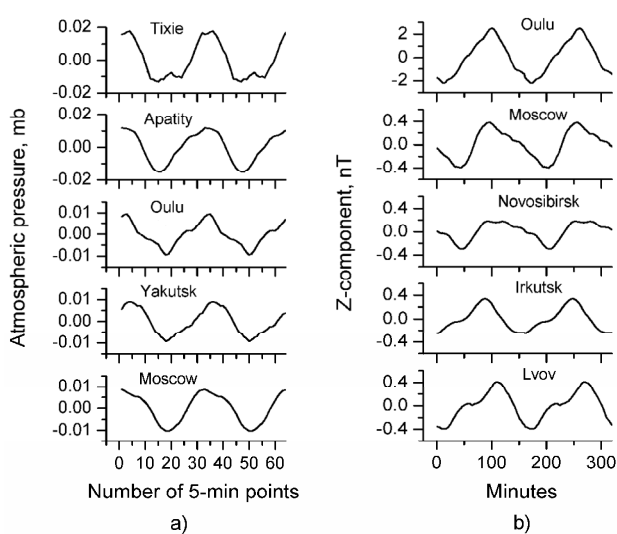


Fig.1. Phases of manifestation of 160-min pulsations in the ground pressure (a) and in the magnetic field Z-component (b). The mean temporal course of amplitudes in December 2003 in the ground pressure and in the Z-component on the territory of Europe and Siberia is shown.

3. The analysis of experimental data

The examination conducted by us testifies to the presence of synchronous oscillations in the ground atmospheric pressure and geomagnetic field. As it has been already noted in Introduction, the occurrence of pulsations of hourly periods in the ground pressure and geomagnetic field was also revealed earlier by various researchers. In this case various mechanisms capable to explain the observable synchronism of pulsations were offered. Let us consider some mechanisms in more details.

1. In [Karpova et al., 2002] the occurrence of 160-minute pulsations in the ground pressure manifested together with other periods was noted. It was noticed that they were manifested in connection with the passage of atmospheric internal gravitational waves (IGW) [Bobova et al., 1985]. The initial phases of IGW are distributed at the Earth's surface by various time zones not synchronously (i.e., their phases will not have coincidences). In our studies [Timofeev et al., 2005, 2009] at the considered stations of Europe and Siberia the synchronism of phases in the variations of both the ground pressure, and Z-components of geomagnetic field was observed. Thus, it is impossible to explain the observational facts marked by us at the expense of IGW.

2. In [Pochtarev et al., 1983; Bobova et al., 1990; Petrova, 1992; Petrova et al., 1999; Petrova, 2008] it was shown that seismic oscillations of the Earth can excite atmospheric waves which, in their turn, can affect auroral currents. In those works the fact of excitation in the atmosphere and AE-index of oscillations with the periods of seismic gravitational oscillations of the Earth was observationally established. However, it is necessary to note that in those works the synchronism of manifestation of seismic gravitational waves and pulsations of AE-index was obtained only by the coincidence of characteristics of power spectra but not phase pulsations. Besides, the presence of similar pulsations in the AE-index testifies to the presence of such pulsations in the high-latitude auroral field. In our case the effect of pulsations coinciding in phase was observed both at high and middle latitudes. Thus, this mechanism cannot describe the observational facts obtained by us completely.

3. Probably that it would be possible to explain the facts marked by us most completely by the presence of gravitational waves predicted by the Einstein's relativity theory. Recently the first observational instructions on a possibility of existence of such waves from remote astrophysical objects have been appeared (see, for example, [Hermes et al., 2012]). The presence of gravitational wave with the period P_0 would lead to synchronous squeezing and rarefaction of whole volume of the Earth and its atmosphere. In this case the pulsations of atmospheric pressure registered in any point on the globe, would coincide in phase, as was observed fact.

In the case of magnetic field we deal with the response to such actions in the current systems which are located at great depths in the Earth's core. Mechanisms of formation of such response are caused by periodic squeezings of the globe by the gravitational wave field. Under the influence of squeezing (pressure) a material resistance R (electrical resistance of iron-nickel core of the Earth) increases

[Zinoviev, 1952], hence, the currents in the core of the Earth decreases. It leads to some reduction of the Earth's magnetic field. Thus, pulsations of the Earth's geomagnetic field registered in any point on the globe would coincide in phase that also has been marked by us by data on GMF (Z-component).

4. Conclusions

1. By the data of observations at the stations of Europe and Siberia the existence of synchronous pulsations in phase with a period of 160-minutes in the ground atmospheric pressure and Z-component GMF is shown.

2. The nature of the revealed synchronous oscillations in the atmospheric pressure and GMF remains unclear. Apparently, the obtained facts can get the fullest explanation within the framework of a hypothesis on the existence of a gravitational wave with a period P_0 according to predictions of a general Einstein's relativity theory and recent astrophysical observations.

Acknowledgments. The work has been carried out under the partial financial support of the Russian Fund for Basic Research (grant №12-05-98522, the RFBR, grant № 12-02-98508, №13-05-00363).

References

- Bobova V.P. et al.: 1985, *Bull. Crimean Astrophys. Obs.*, **71**, 19.
- Bobova V.P. et al.: 1990, *Geomagnetism and Aeronomy*, **30**, 492.
- Hermes J.J. et al.: 2012, *Astrophys. J. Lett.*, **757**, L21.
- Jamison B. and Regal R.: 1979, *Reidel Publishing Co.*, Dordrecht, Holland, 175-179.
- Zinoviev V.A.: 1952, *The technical directory*, Part 1, Moscow, 632 p.
- Karpova N.V. et al.: 2002, *Ann. Geophysicae*, **20**, 823.
- Kotov V.A. et al.: 1985, *The certificate on opening №274*, Moscow: Goskomizobreteniy.
- Kotov V.A., Lyuty V.M.: 1992, *Izvestya Astrofizicheskoy Observatorii*, **86**, 108.
- Kotov V.A., Kotov S.V.: 1996, *Radiophysics and Quantum Electronics*, **39**, 1204.
- Novikov A.V. et al.: 1985, *Geomagnetism and Aeronomy*, **25**, 494.
- Petrova L.N.: 1992, *Biophysics*, **37**, 3.
- Petrova A.A. et al.: 1999, *Geomagnetism and Aeronomy*, **39**, 136.
- Petrova L.N.: 2008 S2, *Izvestiya, Physics of the Solid Earth*, 2008, **1**, 31.
- Pochtarev V.I. et al.: 1983, Moscow: IZMIRAN, 37.
- Timofeev V.E. et al.: 2005, *Proc. 29th ICRC*, Pune, India, **2**, 401.
- Timofeev V.Ye. et al.: 2009, *Proc. IAU Symposium No. 264*, Cambridge University Press, 449.

MONITORING OF THE INOPERATIVE ENVISAT SATELLITE'S BEHAVIOUR

L. Shakun, N. Koshkin, E. Korobeynikova, S. Melikyants, S. Strakhova, S. Terpan
Astronomical Observatory, Odessa National University, Odessa, Ukraine
nikkoshkin@yahoo.com

ABSTRACT. New positions data and light curves were received for the inoperative Envisat spacecraft still in orbit. The satellite pole and sidereal rotation period were determined on the base of the photometric data for the period from April to August 2013. The presence of a precession of the Envisat rotation axis was deduced.

Introduction

Optical tracking techniques based on the sunlight reflection by the space craft (SC) surface are used to provide remote sensing of the Earth-orbiting satellite's motion. In Odessa Astronomical Observatory we use a satellite tracking technique that enables to obtain characteristics of a satellite's orbital motion and rotation around its centre of mass. That technique is based on two principles: tracking of the apparent moving of a satellite by telescope and acquisition of its images against the background stars with maximum possible frame rate. The latter objective is ensued principally from the high-speed satellite photometry requirements. The indicated method enables to remotely determine parameters of the satellite self-rotation around its centre of mass. With the high-speed photometric techniques it is possible not only to record, for example, an occurred flash, but also to estimate the time profile of that flash, and hence, the indicatrix of light reflection from the corresponding surface of the satellite. That is a fundamental quality change of photometry, and sometimes it enables to distinguish specularly reflecting surfaces even when observing in a single spectral range. It should be noted that the accuracy of the time reference of all light curve features is critical for interpretation of the recorded satellite brightness variations.

A television camera WATEC-902H2 Supreme with the interlaced mode that works well in practice is used as the high-speed panoramic light receiver. The camera is installed in the focal plane of the 50-cm tube of the tracking telescope KT-50. The actual temporal resolution (Δt) is about 0.02 sec. To provide a reliable, stable and OS-independent time reference, the hardware introduction of the converted pps-pulses from the GPS receiver was applied (Dragomiretsky et al., 2013).

The EnviSat satellite monitoring

EnviSat is a satellite designed to capture high-resolution images of the Earth's surface. It was launched

in 2002 into the polar orbit altitude of 777 km with inclination $i = 98.4^\circ$. The main objective of EnviSat was to conduct altimetry of oceans and ice cover, as well as other monitoring of the Earth. On April 8, 2012, EnviSat unexpectedly shut down, and the contact with the satellite was lost rendering it inoperative. All efforts to re-establish contact with the satellite failed. As can be seen from the images received from Pleiades and Spot spacecrafts, EnviSat is fully intact, and its solar arrays are deployed.

In case of the EnviSat failure in-orbit, it is likely to collide with other operative satellites as it has a 26-meter cross section and weighs some 8000 kilograms. EnviSat is "a bomb", which poses an immense danger to the heavily crowded corridor in the polar orbit at altitude of 780 km. Its estimated lifetime is 100 years! The remaining fuel and energy reserves can only make it more hazardous.

Therefore, it is necessary to oversee the EnviSat orbital motion. However, the atmospheric drag at the given altitude is an important factor. To reliably predict the satellite's motion in the upper atmosphere of the Earth (below 1000 km), it is necessary to take into account the orientation of a complex-shaped body, i.e. rotation. At any moment it is essential to know not only cross-sectional areas of large satellite, but also its actual tilt and physical characteristics of surfaces, which interact with impinging atmospheric molecules.

The erroneous prediction of EnviSat's position in orbit in May 2013 is shown in Figure 1. The residuals between prediction (Kara I.V., 2009/2010) and actual position of the satellite reach 0.5° along its orbit (while 1" corresponds to ~ 5 m at a distance of 1000 km). As soon as the satellite monitoring by the International Laser Ranging Service (ILRS) and Ukrainian Network of Optical stations (UMOS) was resumed, the residual errors decreased to units of arcseconds.

The photometric observations (monitoring) started by Odessa Astronomical Observatory and the UMOS network in April 2013 enabled to gather plenty information to analyse. The results of simultaneous measurements of the EnviSat's brightness obtained on July 11, 2013 in Odessa and Yevpatoria are shown in Figure 2. The presence of bright flashes of the satellite allows of estimating the synodic period of its rotation in the given trajectory segment. The variation in the estimated synodic period values within 4 months of monitoring is presented in Figure 3.

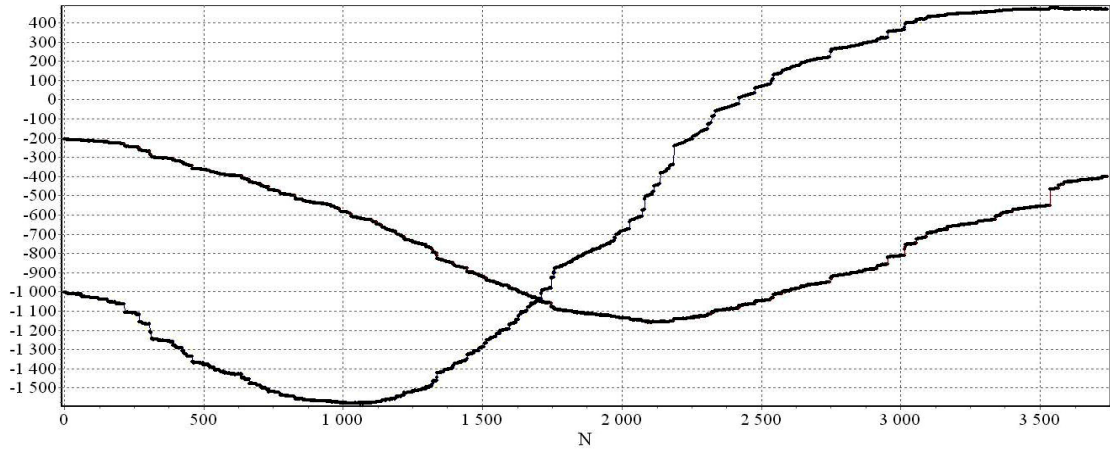


Figure 1: The EnviSat’s positions predicted as of the start of its monitoring: an example of residual errors in the predicted equatorial coordinates and astrometric observation data obtained on May 27, 2013 in Odessa using KT-50.

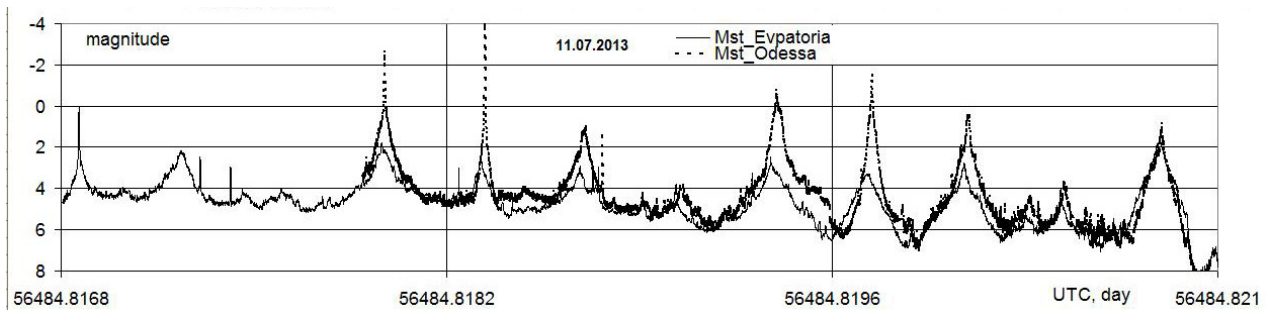


Figure 2: Simultaneous measurements of the satellite brightness from two UMOS observation points. The data received on July 11, 2013 in Odessa and Yevpatoria. Vertical lines correspond to the satellite’s rotation period.

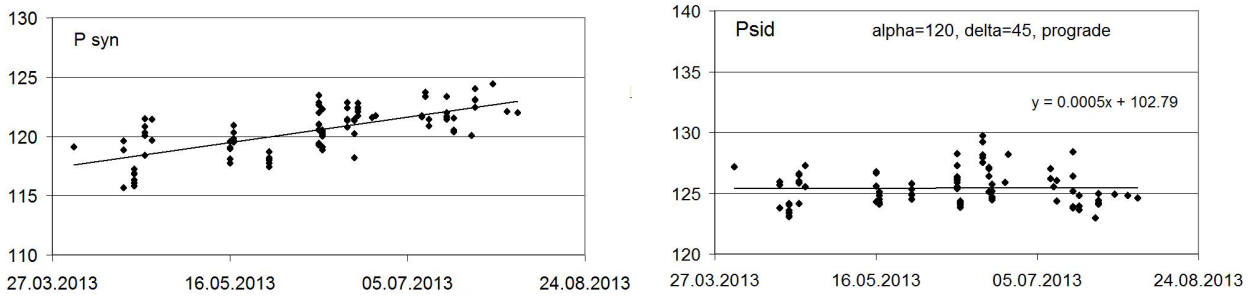


Figure 3: a) the measured values of the EnviSat space craft synodic rotation period; b) the optimal solution for the rotation pole ($\alpha_p = 120^\circ$, $\delta_p = 45^\circ$, the prograde rotation), deduced by the method accounting for parallactic shift of flashes on the light curve. At that, the average sidereal rotation period within 4 months is almost constant and equals to 125.6 sec.

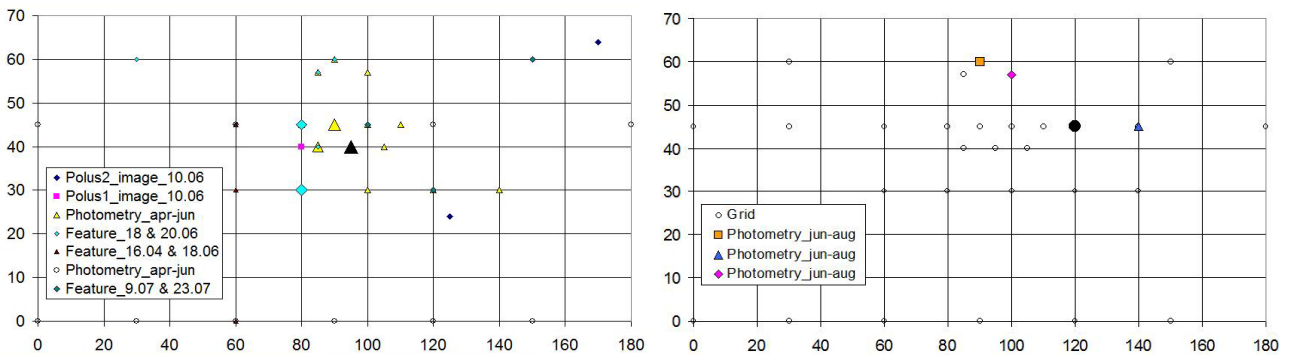


Figure 4: The optimal solution for the EnviSat satellite rotation pole obtained with various techniques for the period from: a) May to June 2013; b) June to August 2013.

There are two factors, which can have impact on the spread of synodic period values. First of all, that is the parallactic shift of the observer-spacecraft line, i.e. orbiting. When the body shape is too asymmetric as is the case with EnviSat, the satellite rotation is quite complicated (Zubov et al., 1968; Beletsky, 1975), and the rotation axis orientation changes during a single satellite's pass over the observer.

To refine the satellite rotation model, we used a classical method of simultaneous selection of the sidereal rotation period and pole position, which is called the method of photometric astrometry (MPA) when applied to asteroids.

Provided steady rotation, the sidereal period is constant only with the right position of the rotation pole. We computed the grid for the rotation axis spatial orientations; the optimal solution in this regard as such the minimum spread (minimum of the mean square error) and constant value of the sidereal period is shown in Figure 3b. However, the residual spread of the sidereal period values can not be explained by the errors of the synodic period measurements. That is definitely indicative of the presence of rapid variations of the instantaneous rotation axis.

Other methods also can be applied to determine the instantaneous rotation pole of the satellite. We analysed the method of similar features applied to the EnviSat light curves measured during different satellite's passes. In this case, the phase angle bisector at the moment of observation has the same latitude relative to the rotation pole, and that enables to select the pole. Our colleagues from the Space Agency of Ukraine estimated the orientation of rotation pole by the analysis of direct images of the satellite received using the long-focal-length telescope (private message). All estimations of EnviSat rotation pole positions are presented in Figure 4.

Apparently, there is no single agreed solution. It can be established that the rotation pole varies within middle latitudes $\delta_p \approx 30-60^\circ$. The estimated right ascension of the pole during the period from April to June 2013 was within $\alpha_p \approx 80-100^\circ$, and from June to August 2013 - $\alpha_p \approx 90-140^\circ$. That drift of the pole corresponds to the precession rate of the satellite's orbital plane.

Conclusions

To continue the in-depth study of the EnviSat satellite light curves, it is necessary to analyse its adequate optical-geometric model. That will allow of identifying all main specific features of the light curves and also accurate computing of instantaneous orientation of the space craft body. On having the model for the satellite's rotation around its centre of mass developed, the satellite body orientation relative to the orbital velocity direction (the flux of impinging atmospheric molecules) at any given moment will be computed. Accounting for the satellite interaction with molecules of the upper atmosphere will further the correct computation of the drag force (slowing down).

References

- Dragomiretsky V. et al.: 2013, *The Ukrainian Centre of Determination of the Earth Orientation Parameters report*, p. 37.
- Kara I.V.: 2009/2010, *Odessa Astron. Publ.*, **22**, 20.
- Zubov V.I., Ermolin V.S. et al. *Dynamics of free solid body and determination of its orientation in the space* / Ed. Chernetskii V.I. Publishing House of Leningrad University, 1968, 208 p.
- Beletsky V.V. *Motion of an artificial satellite about its center of mass*. Moscow: Nauka, 1975, 308 p.

GEOPHYSICAL EFFECTS OF THE EARTH'S MONTHLY MOTION

N. S. Sidorenkov¹, T. S. Zhigailo²

¹ Hydrometeorological Research Center of the Russia Federation, Moscow, Russia
Federation, *sidorenkov@mecom.ru*

² Odessa State Environmental University, Odessa, Ukraine

ABSTRACT. The generation of a lunar tidal force is a major geophysical effect of the Earth's monthly motion.

It is shown that synoptic processes vary simultaneously with tidal oscillations of the Earth's rotation rate and weather exhibits changes near their extremes, i.e., when the Earth is in certain positions on its monthly orbit.

It is found that the quasi-biennial oscillation of the wind direction in the equatorial stratosphere is a combined oscillation caused by three periodic processes experienced by the atmosphere: (a) lunisolar tides, (b) the precession of the orbit of the Earth's monthly rotation around the barycenter of the Earth–Moon system, and (c) the motion of the perigee of this orbit.

Interference of the 1.20-year Chandler wobble with sidereal, anomalistic, and synodic lunar oscillations gives rise to beats, i.e., to slow periodic variations in the wobble amplitude with periods of 32 to 51 years.

Key words: Earth's monthly motion, synchronization of synoptic processes, quasi-biennial oscillation, modulations of the Chandler wobble amplitude.

1. It is well known that the Earth and the Moon revolve around their center of mass (barycenter) with a sidereal period of 27.3 days. The orbit of the Earth's center of mass (geocenter) is geometrically similar to the Moon's orbit, but the orbit size is roughly 1/81 as large as that of the latter. The geocenter is, on average, 4671 km away from the barycenter. In the Earth's revolution around the barycenter, all its constituent particles trace the same nonconcentric orbits and undergo the same centrifugal accelerations as the orbit and acceleration of the geocenter. The Moon attracts different particles of the Earth with a different force. The difference between the attractive and centrifugal forces acting on a particle is called the tidal force [1, 2]. The generation of the lunar tidal force is a major geophysical effect of the Earth's monthly motion. The revolution of the Earth–Moon system around the Sun (Fig. 1) leads to solar tides. The total lunisolar tides vary with a period of 355 days (13 sidereal or 12 synodic months). This period is known as the lunar or tidal year.

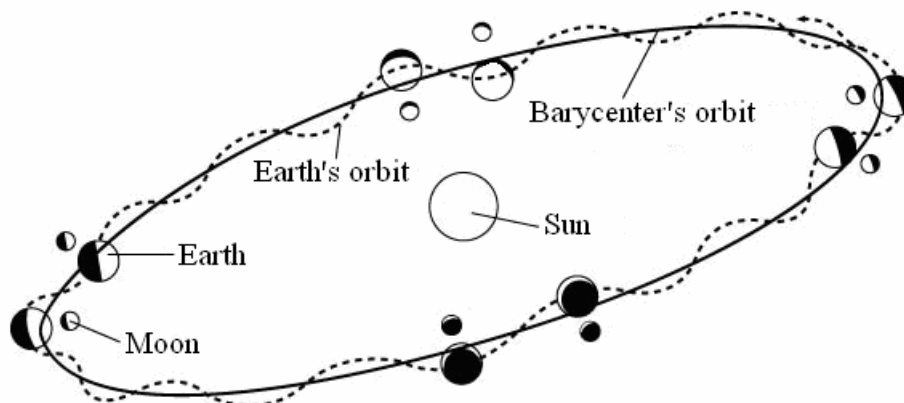


Figure 1: Revolution of the Earth–Moon system around the Sun.

2. The lunisolar tides are believed to be so small that they cannot affect meteorological processes. In recent years, however, components of lunisolar tides have been detected in the spectra (a) of the atmospheric angular momentum, (b) of quasi-biennial oscillation indices of the equatorial stratospheric wind, and (c) of anomalies in many hydrometeorological characteristics [2]. It was found that synoptic processes vary simultaneously with tidal oscillations of the Earth's rotation rate and weather exhibits changes near their extremes, i.e., when the Earth is in certain positions on its monthly orbit [3].

An analysis of the causes of the 2010 anomalously hot summer in European Russia has revealed that the sunshine duration, cloud amount, and, eventually, the incoming solar radiation are modulated by lunar tides [4]. The intensity of the modulation depends on the season of the year. The length of the terrestrial (lunar) months is not a multiple of the solar year. The lunar (tidal) year, which is equal to 13 sidereal or 12 synodic months, lasts 355 days. Therefore, the incoming solar radiation varies not only with a solar year period of 365.24 days but also with a lunar or tidal year period of 355 days. Interference of these two oscillations with slightly different frequencies generates 35-year beats of incoming solar radiation, of the components of the Earth's radiation and heat budgets, and of the forcing of geophysical processes, such as the decade nonuniformity of Earth's rotation, decade climate changes, the El Niño–Southern oscillation phenomenon, the intensity of the

Indian monsoon, the state of the Antarctic ice sheet, etc. [4].

3. It was shown in [1, 2] that the Earth, the ocean, and the atmosphere exhibit consistent oscillations, influencing each other, i.e., joint oscillations initiated by tides occur in the Earth–ocean–atmosphere system. Visual manifestations of these oscillations include the wobble of the Earth's poles, El Niño and La Niña in the ocean, and the Southern Oscillation and the quasi-biennial oscillation in the atmosphere. The quasi-biennial oscillation (QBO) in the equatorial stratospheric wind direction has stability comparable with that of the annual period of variations in meteorological elements generated by the Earth's rotation around the Sun. The QBO period averaged over the last 60 years is equal to 28 months, or 2.3 years [1, 2].

The mechanism of QBO excitation is associated with the absorption of lunisolar tidal waves in the equatorial stratosphere. The QBO period is equal to a linear combination of the frequencies corresponding to the doubled periods of the tidal year (0.97 year), of the node motion (18.6 years), and of the perigee (8.85 years) of the Earth's monthly orbit:

$$\frac{1}{2} \left(\frac{1}{0.97} - \frac{1}{8.85} - \frac{1}{18.61} \right) = \frac{1}{2.3}$$

In other words, the quasi-biennial oscillation of the wind direction in the equatorial stratosphere is a combined oscillation caused by three periodic processes experienced by the atmosphere: (a) lunisolar tides, (b) the precession of the orbit of the Earth's monthly rotation around the barycenter of the Earth–Moon system, and (c) the motion of the perigee of this orbit.

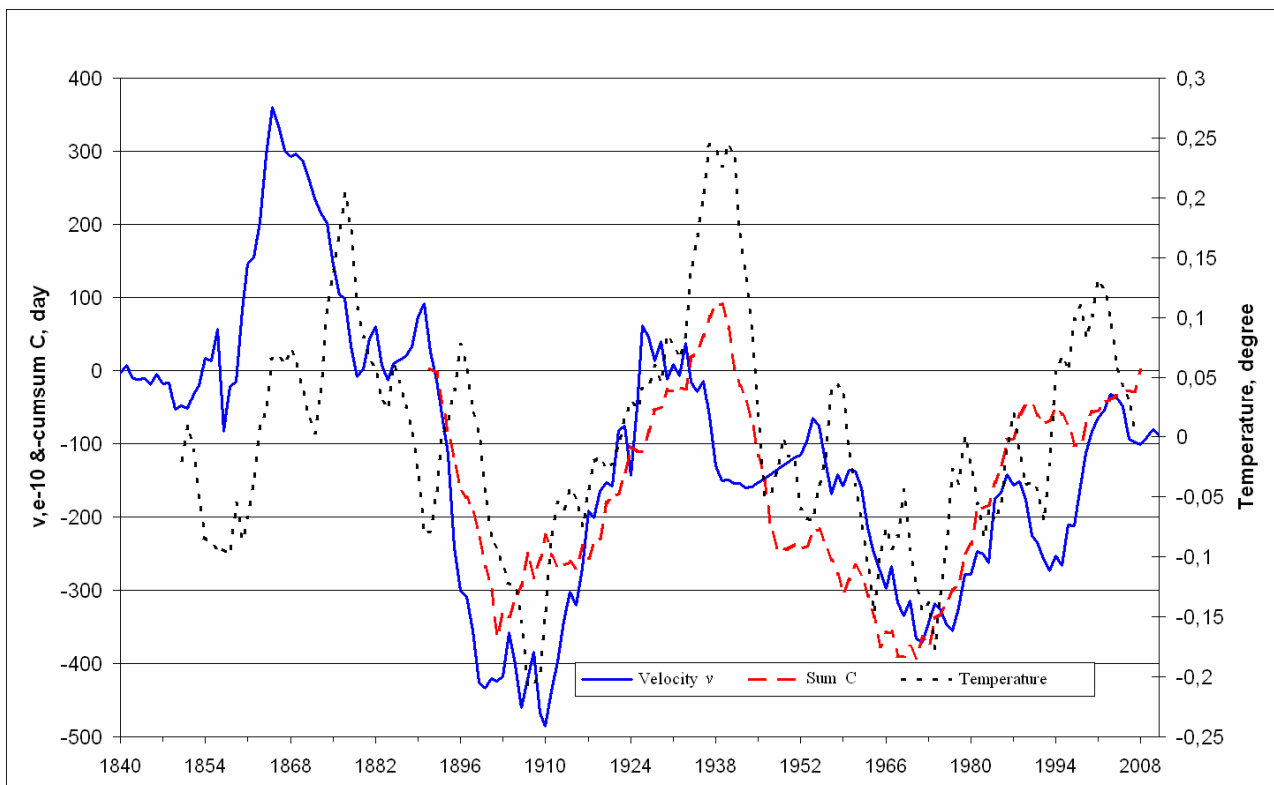


Figure 2: Earth's rotation rate v (solid), accumulated Vangengeim circulation pattern anomalies C taken with an opposite sign (dashed), and 5-year moving averages of anomalies in the global air temperature T HadCRUT3 (dotted).

The wobble of the Earth's poles and the QBO in the atmosphere have similar spectra (with the ratio of the periods being 1:2) [1, 2]. The period of the Chandler wobble of the poles (CWP) is believed to differ from the Euler period of 305 days because of the elastic properties of the Earth. However, it is physically unlikely that both QBO and CWP are caused by the features of the Earth's internal structure. A natural assumption is that QBO and CWP have a single cause, namely, the features of the Earth's monthly rotation in the Earth–Moon system and the rotation of this system around the Sun.

The wobble forcing with a solar year period of 365.24 days is modulated by the precession of the Earth's monthly orbit with a period of 18.61 years and by the motion of its perigee with a period of 8.85 years. Finally, the resulting solar annual forcing generates polar wobbles with a Chandler period of 1.20 year:

$$\frac{1}{1.0} - \left(\frac{1}{18.61} + \frac{1}{8.85} \right) = \frac{1}{1.20}$$

An analysis of observed pole coordinates suggests that the CWP amplitudes in 1890–1915 and 1947–1960 were three and five times larger than those in 1925–1943. The amplitude modulation of CWP is clearly exhibited. The period between the amplitude maxima – the period of beats – is equal to about 40 years. This suggests that the CWP is the sum of two oscillations with very close periods.

Since the 1980s, the hydrometeorological effects on the Earth's rotation have been continuously monitored at world's leading meteorological centers by computing the components of the effective atmospheric angular momentum (AAM) and oceanic angular momentum (OAM) functions [5]. It was found that the AAM and OAM functions are capable of accounting for up to 90% of the required CWP excitation (see <http://hpiers.obspm.fr/eop-pc>).

This excitation is believed to occur at the fundamental frequency of the climate system forcing with a period of 365.24 days. However, it was shown in the author's most recent works that, in addition to this basic forcing, the climate system experiences additional forcings caused by cloud amount variations with lunar-year periods. Climatic characteristics and the equatorial component of the atmospheric angular momentum h_2 were found to oscillate with a period of 355 days [2, 4].

The wobble forcing with a lunar sidereal year period of 355 days (13 sidereal months) is modulated by the precession of the Earth's monthly orbit with a period of 18.61 years and by the motion of its perigee with a period of 8.85 years. Finally, the resulting "lunar sidereal" forcing generates polar wobble with a period of 1.16 year:

$$\frac{1}{355.18 \text{days} / 365.24 \text{days} / \text{yr}} - \left(\frac{1}{18.61} + \frac{1}{8.85} \right) = \frac{1}{1.1606 \text{yr}}$$

Interference of the 1.20-year Chandler oscillation and the 1.16-year oscillation leads to beats, i.e., to periodic variations in the polar wobble amplitude with a period of 35.3 years:

$$\frac{1}{1.16} - \frac{1}{1.2} = \frac{1}{35.3}$$

Similarly, the lunar synodic year (12 synodic months) must excite polar wobble with a period of 1.1574 year:

$$\frac{1}{354.37 \text{days} / 365.24 \text{days} / \text{yr}} - \left(\frac{1}{18.61} + \frac{1}{8.85} \right) = \frac{1}{1.1574 \text{yr}}$$

Interference of this excitation and CWP generates beats with a period of 32.6 years.

The "lunar" annual (13 anomalistic months) excitation can generate polar wobble with a period of 1.172 year:

$$\frac{1}{358.21 \text{days} / 365.24 \text{days} / \text{yr}} - \left(\frac{1}{18.61} + \frac{1}{8.85} \right) = \frac{1}{1.172 \text{yr}}$$

Interference of this wobble with CWP can generate beats with a period of 50.9 years:

$$\frac{1}{1.172} - \frac{1}{1.2} = \frac{1}{50.9}$$

Thus, interference of CWP (1.20-year period) with these moon-caused oscillations gives rise to beats, i.e., to slow periodic variations in the CWP amplitude with periods of 32 to 51 years. They are observed in reality.

The QBO has been monitored since 1954. Accordingly, the amplitude modulation of the QBO is as yet difficult to reveal.

References

1. Sidorenkov N.S. *Physics of Instability in the Earth's Rotation*. Moscow: Nauka, 2002 (in Russian).
2. Sidorenkov N.S. The interaction between Earth's rotation and geophysical processes. Weinheim, WILEY-VCH Verlag GmbH & Co. KGaA, 2009.
3. <http://www.geoastro.ru>
4. Sidorenkov N.S., Sumerova K.A.: 2012, in *Proc. Hydrometeorological Center of Russia*, **348**, 195.
5. Barnes R.T.H., Hide R., White A.A., Wilson C.A.: 1983, in *Proc. Roy. Soc. London, Ser. A*, **387**, 31.

ON THE PROPAGATION OF RADIO EMISSION IN THE CROWN OF THE QUIET SUN WITH MAGNETIC FIELD

N. Tsvyk

Radio Astronomy Institute of NASU, Kharkiv, Ukraine
tsvyk@rian.kharkov.ua

ABSTRACT. There are searching for factors that influence on the brightness temperature distribution of the quiet Sun at decimeter radio waves which may explain the ellipsoidal shape and other features in the radio brightness profile.

Key words: quiet Sun, crown, radioemission, refraction

We estimate the influence of a magnetic field on the propagation of radio emission in the quiet solar crown, using a spherical model of the electron density distribution similar to Baumbach-Allen with constant temperature (10^6K). Models of the regular magnetic field of quiet Sun are: (1) the magnetic field with all turbulent magnetic field aligned along the pre-existing dipole lines that "enhanced" by turbulent currents to a level (Perebejnos et al., 2011) approximated as: $B \cong 5.29 G \cdot r^{-2.3+0.1 \ln(r/2)}$; (2), (3) dipole and quadruple magnetic fields, modified by currents at the solar equator on r - and θ - axis to the values with changing a sign at $r \sim 2.5$, see in details: (Sykora et al., 2003). The magnetic field strength was 0.1-0.2 G at the height of 2-4 R_0 ($R_0 = 6.96 \cdot 10^{10}$ cm; r measured in R_0 units).

The mechanism of radio emission from the quiet solar corona is the thermal radiation with the optical thickness less than (0.5). Due to the magnetic field, the radio waves of given frequency split into two modes, ordinary and fast extraordinary. There was carried out the refraction of rays in the solar corona, focusing rays and its absorption due to the free-free transitions and plasma damping (losses to the plasma currents). The emission flux is integrated over all layers along the ray path, that limited by a point of "tangle of parallel rays" (at the level where the beams have reflected by plasma resonance) and a position of the observer. Because of the ordinary mode is brighter and goes at lower heights (above the plasma resonance) than the extraordinary one (in a level higher than the first hybrid plasma frequency), we should observe a small circular polarization of the radio emission of the quiet Sun. The magnetic field shifts the radio rays on 0.1-0.3 R_0 in the

Sun disk plane from those positions in the model without the magnetic field. Thus, the ordinary rays decline in a direction perpendicular to the magnetic field lines, and fast extraordinary rays "dragged" along the lines. Due to such refraction, it is appeared the slight brightening spots near the center of the visible Sun ($<0.5 R_0$), as of which place can be predict the magnetic field structure.

The calculations give the top of Solar brightness temperature is nearly $3 \cdot 10^5$ K at 20 MHz in good agreement with observations (Brazhenko et al., 2012), and the apparent solar radius are approximately equal to the sizes of the corona at the level of a plasma resonance. The ratio of the polar and equatorial solar radii calculated of 0.97 ± 0.05 , so the magnetic field has a little influence on the radio rays in the solar corona, and it can not be a factor in explaining the ellipsoidal asymmetry observing in the solar corona size, equal of 0.7. The probable cause of the ellipsoidal shape of the observed Sun in decimeter wavebands may be non-spherical distribution of the plasma density in the corona, as show (Stanislavsky, Koval, 2013). With less likely, the effect of Sun's asymmetry can also give an asymmetrical profile of the plasma temperature.

References

- Stanislavsky A.A., Koval A.A.: 2013, *Radiofizika i radioastronomia*, **18** (in press.).
 Brazhenko A.I., Koval A.A. et al.: 2012, *Radiofizika i radioastronomia*, **17**, 3.
 Sykora J. et al.: 2003, *Solar Phys.*, **212**, 301.
 Perebejnos V.A. et al.: 2011, *Izv. CRAO*, **107**, 64.
 Thejappa G., Kundu M.R.: 1994, *Solar Physics*, **149**, 31.

SEA LEVEL AND GLOBAL EARTH TEMPERATURE CHANGES HAVE COMMON OSCILLATIONS

L.V. Zotov

Sternberg Astronomical Institute of Moscow State University, Russia, *tempus@sai.msu.ru*

ABSTRACT. Singular Spectrum Analysis (SSA) of Global Mean Sea Level (GMSL) and Global Average Earth Temperature (HadCRUT4) data revealed presence of quasiperiodic components with periods of 60, 20 and 10 years in both time series. 60-year component of sea level is anticorrelated with long-periodic changes in temperature, while 10 and 20-year components are correlated. The question what can be the nature of these common oscillations is discussed.

Key words: Climate Change, Sea Level, Earth Temperature.

1. Introduction

Recently approved IPCC Fifth Assessment Report (2013) presents comprehensive analysis of different aspects of Climate Change. Southends of scientist all over the world took part in this work. In recent decades the amount of data about the Earth from satellites and ground-based observational networks has drastically increased. New report contains useful indexes, time series and data grids and maps upon the climatic processes, affecting ocean, atmosphere, glaciers, ice sheets, etc. Manifestation of Global Warming is found in different components of Earth's system. The main goal of IPCC is to estimate their contribution into the warming trends and predict them into the future.

Using SSA – flexible and powerful time series analysis technique, we are investigating presence of different periodicities in such global indexes as Mean Sea Level and Average Earth Temperature. To our surprise, similar oscillations can be found in both indexes. Not very much studies are dedicated to this subject. But it is especially interesting to reveal the nature of this oscillations, because there are other processes, which demonstrate presence of similar periodicities.

For example, similarity of temperature changes and Earth rotation velocity was mentioned already in (Lambek, 1980) monograph. In (Zotov, 2012) we also compare recently reconstructed Chandler excitation with 20-year component of temperature changes and found correlations. Here, using new releases of climatological indexes, we are trying to put

all this similarities together in the line with the ideas of (Zotov, 2012; Lambek 1980; Sidorenkov 2009).

2. Data and method

Singular Spectrum Analysis (SSA) (Golyadina S.A. 2004) is a generalization of Principal Component Analysis (Jolliffe, 2001) and is widely used in time series processing for decomposition of time series into so-called Principal Components (PCs), which represent main patterns of signal variability (Zotov, 2011). Not going into details, SSA allows to decompose time series into PCs of different periods and filter out noises. The main parameter of the method is lag L , which should be chosen heuristically. The name of the method comes from Singular Numbers (SNs), which correspond to the signal components and sometimes should be grouped.

We used Global Average Earth Temperatures time series HadCRUT4 produced by the Met Office Hadley Centre and the Climatic Research Unit at the University of East Anglia (<http://www.metoffice.gov.uk/hadobs/hadcrut4/>). It is a combination of CRUTEM4 land-surface air temperature dataset and the HadSST3 sea-surface temperature (SST) dataset. In Fig. 1, top, HadCRUT4, its previous version HadCRUT3, and HadSST3 time series are represented. It is seen, that global Earth's temperature (HadCRUT4) is mostly defined by the sea-surface temperature (HadSST3). Parabolic trend shows temperature increase of $\sim 0.7^{\circ}$ in 150 yrs caused by the global warming and greenhouse effect. Trend for HadCRUT3 is lower. While most of IPCC studies are dedicated to these trends and their projections, we will pay attention to the remaining oscillations.

SSA was applied to the HadCRUT4 time series after parabolic trend was removed. Lag parameter $L = 20$ years was selected. Three main PCs were found to have quasi 60, 20 and 10 years periods. They are shown in Fig. 2. Earlier we already performed such an analysis for HadCRUT3 (Zotov, 2012). New results are quite similar (but with smaller amplitudes). They can also be compared to the obtained in (Qian, 2010).

GMSL time series were taken from CSIRO web site

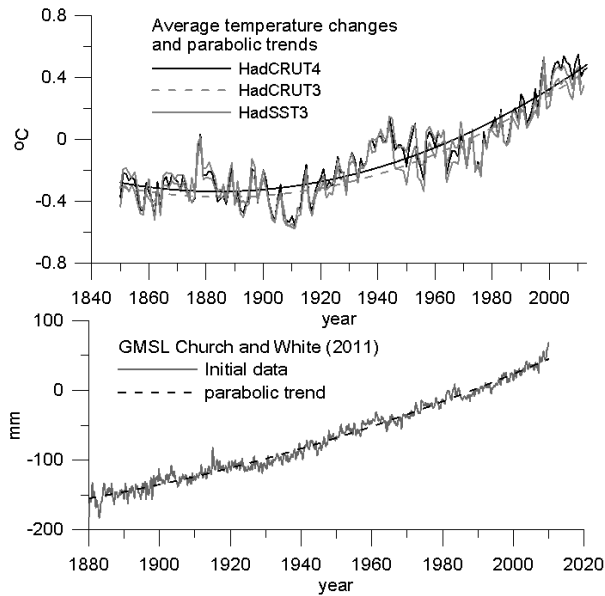


Figure 1: Initial time series of Earth Average Temperatures (top) and Sea Level (bottom) with parabolic fits.

http://www.cmar.csiro.au/sealevel/sl_data_cmar.html. They were derived from the Sea Level Gauges data using PCs of satellite altimetry (Church and White, 2011). The initial time series are represented in Fig. 1, bottom. Average Sea Level rise of ~ 1.8 mm/yr over the last century is caused by the temperature growth (Church et al., 2011). This trend is one of the main subject of IPCC research, but we will remove it before SSA. Main PCs obtained with SSA parameter $L = 240$ months (20 years) are compared to the temperature PCs in Fig 2. They also have the main periods close to 60, 20 and 10 years. Earlier SSA of Sea Level was performed by Shen et al. (2013), similar components were found.

3. Results and discussion

It is seen from Fig. 2 that temperature and Sea Level PCs have similar behaviour. PC 1 has ~ 60 -year period, it is obtained from SN 1; PC 2 has ~ 20 year period, it is obtained from SN 2 for temperature and SN 2+3 for GMSL; PC 3 has quasi-10-year variability, it is obtained as a sum of SN 3+4 for temperature and SN 4+5 for GMSL.

PC 1 (Fig 2, top) of temperature changes is anti-correlated with GMSL PC 1. Inversion of the y-scale of the latter makes the correspondence evident. PC 2 (middle) and PC 3 (bottom), on the contrary, are correlated. Maxima and minima of PC 2 repeat with ~ 20 -year period and more or less correspond to each other. For HadCRUT3 correlation was even better (Zo-

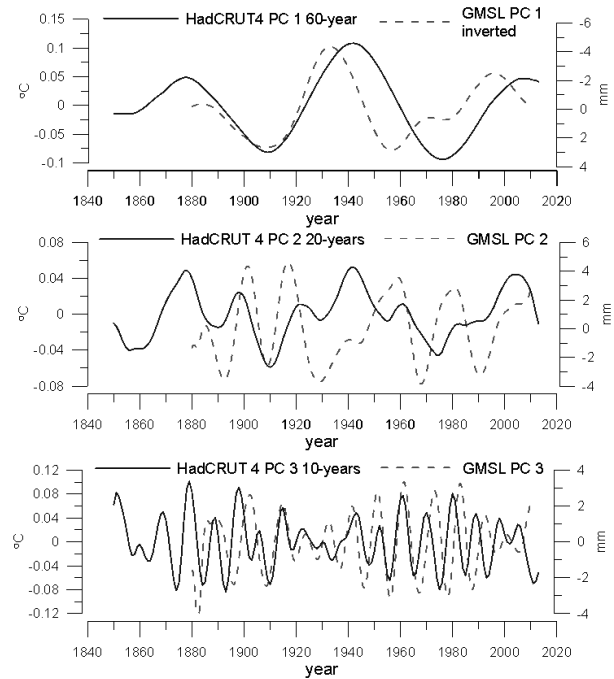


Figure 2: Comparison of three principal components of Average Temperature and Sea Level detrended changes.

tov, 2012).

Average Earth Temperatures are strongly dependent on the sea-surface temperatures, as seen from Fig. 1, top. It is quite reasonable to expect synchronous sea level changes, reflecting temperature changes. Increase of temperature could force expansion of the upper ocean layer and steric (without mass changes) sea level increase. Melting of land ice also could give a non-steric input, but it cools the ocean at the place of discharge and influence the salinity. The problem is that we see correlation for PC 2 and PC 3, but we observe anti-correlation on the time-scale of PC 1. With increase of temperature sea level rises for the 20-year PC 2 and 10-year PC 3, but drops on the 60-year scale of PC 1. It means that mechanisms of interconnections are different at these scales. Processes of different physical nature could be at the origin of these changes. Anyway, they should involve only upper ocean, because deeper ocean requires hundreds of years to be involved (private conversations with L. Polyak). It's interesting to note, that century-scale Length of Day (LOD) is anticorrelated with temperature PC 1 (Zotov, 2012). Increase of temperature on this scale is accompanied by the increase of Earth rotation velocity and Sea Level decrease. This is enigmatic. At this time-scale we know only Atlantic Multidecadal Oscillation, which could be responsible. For a joke, we can also mention that Jupiter (12-year) and Saturn (30-year) common multiple revolution period is 60 years.

Speaking about PC 2, it has some similarity with reconstructed Chandler excitation envelope (Zotov, 2012). Earlier we proposed, that Moon orbital regression cycle could be responsible for this variations. Regression influence the position of the moon orbit, its inclinations changes from 18.3° to 28.6° during this period. Fig. 3 represents 18.6-year lunar tidal wave, Chandler excitation envelope, PC 2 of temperature and sea level changes. LSM-fits with harmonics of 18.6-year period are also represented for every component. The phases of fitted harmonics found to be more or less consistent to each other and to the tidal wave. Sea Level fit precedes the temperature fit by $\sim 30^\circ$. Though all the tides should have been excluded from Tide Gauges data while calculating GMSL, there still could be some miss-modelling and tide-driven circulation changes and water flow, which influence the Sea Level on 18.6-year scale (from discussion with R. Ray).

Correspondence of maxima and minima on Fig. 2 is well seen. Periods of PCs 2 could be 21, 20 or 19 years. Its hard to estimate them precisely on a 150-year interval. Though 20-year harmonic fit gives for GMSL and temperature larger amplitudes, then 18.6-year fit, we still put forward the hypothesis, that Moon orbital nodes regression could modulate Chandler excitation, Sea Level, and even Earth's temperature changes. The picture could be distorted by influence of other processes, but we can distinguish repeatability.

There are works (IPCC report 2013; Foster, Rahmstorf, 2011) explaining variations in temperature by combined influence of Volcanoes and El Nino, but these factors can not be periodic.

Speaking about 10-year PC 3 (Fig. 2, bottom), correlation for it is even more evident, then for PC 2. The Sun 11-years variability, most likely, has no relation to this variability. Comparison of HadCRUT3 10-year PC with Wolf sunspot numbers made in (Zotov, 2012) has shown, that they are out of phase.

4. Conclusions

SSA of detrended Earth's Global Average Temperature and Sea Level revealed presence of similar components of quasi 60, 20 and 10 - year periods. 60-year components of temperature and sea level are anticorrelated while two others are correlated. The nature of connection between temperature and sea level changes with this periods should be investigated.

It is interesting, that 60-year components is also reflected in the Length of Day changes and ~ 20 -year component presents in the reconstructed Chandler excitation envelope. We think, that some external factor could modulate these global geophysical processes. For quasi-20-year scale changes of PC 2 we propose the influence of the Moon orbital nodes regression cycle with 18.6-year period as such a factor.

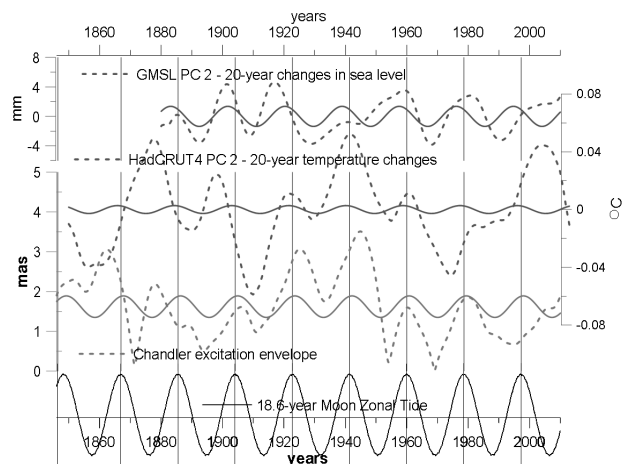


Figure 3: 18.6-year zonal tide from IERS model, Chandler excitation envelope, Earth Average Temperatures and Sea Level and their LSM fits by 18.6-year harmonic.

Acknowledgements. The author is thankful to Paris observatory and RFBR grant No 12-02-31184.

References

- Church J.A., White N.J.: 2011, *Surveys in Geophysics*, **32**, 585-602, doi:10.1007/s10712-011-9119-1.
- Church J.A. et al.: 2011, *GRL*, **38**, L18601, doi:10.1029/2011GL048794
- IPCC Fifth Assessment Report: 2013, Climate Change 2013: The Physical Science Basis, <http://www.climatechange2013.org/>.
- Foster G. and S. Rahmstorf: 2011, *Environ. Res. Lett.* **6** 044022 doi:10.1088/1748-9326/6/4/044022
- Golyadina S.A.: 2004, Method "Caterpillar-SSA": prediction of the time series, Snt-Petersburg.
- Jolliffe I.T.: 2001, *Principal Component Analysis*, Springer.
- Lambeck K.: 1980, *The Earth's Variable Rotation*, Cambridge University Press.
- Shen Yunzhong, Yi Chen & Yingchen Ao: 2013, Global Mean Sea Level Rise Analysis and Prediction by Using Singular Spectrum Analysis, APSSG-2013.
- Qian W.H., Lu Bo, Zhu C.W.: 2010, *Chinese Science Bull.*, **55**, 19. 1963-1967.
- Sidorenkov N.S.: 2009, *The Interaction Between Earth's Rotation and Geophysical Processes*, Wiley-VCH Verlag.
- Zotov L.V.: 2011, Theory of filtering and time series processing, course of lectures, MSU, Physics faculty.
- Zotov L.V.: 2012, *Odessa Astron. Publ.*, **2**, 225.

Subsection Astrobiology

FEATURES OF VASCULAR ENDOTHELIAL FUNCTIONING IN HEALTHY PERSONS IN DIFFERENT PERIODS OF SOLAR ACTIVITY

Parshina S.S.¹, Tokaeva L.K.², Dolgova E.M.³, Afanas'yeva T.N.⁴, Strelnikova O.A.⁵

Saratov state medical university n.a. V.I.Razumovsky, Saratov, Russia
¹ parshinasvetlana@rambler.ru, ² 624494@mail.ru, ³ emdolgova@list.ru,
⁴ protegemoi18@mail.ru, ⁵ strelnik222@mail.ru

ABSTRACT. Functional properties of vascular endothelium in healthy persons had been studied by probe with induced ischemia depending on a solar activity (SA) period during the 23rd solar cycle. The blood viscosity had been estimated before and after occlusion test. The nascency of angiospasm in a low SA is accompanied by adaptive increase of a blood flow property, and in a high SA this mechanism is been losing. So, in healthy persons the period of SA determines functional properties of vascular endothelium.

Key words: vascular endothelium, solar activity.

It is known that a solar activity (SA), determining by the number of sun spots and measured in Wolf numbers, changes after 11-years cycle. The Earth magnetic field strength caused by solar flares is one of the facts of adaptation failure and acute-on-chronic diseases. Geomagnetic activity causes feebleness of capillary circulation in healthy persons, increasing a blood viscosity (BV) and erythrocytes aggregation (Breus, 2003; Gurfinkel et al., 1995). There is no information in accessible medical literature about functional properties of vascular endothelium in the period of a SA.

The study aimed the research of functional properties of vascular endothelium in healthy persons by probe with induced ischemia depending on a solar activity (SA) period during the 11-years solar cycle.

During the last 23rd solar cycle (September, 1996 – September, 2007) 80 healthy people had been examined: 40 of them – in the period of a high SA, 40 – in the period of a low SA. The groups were matched in age and sex characteristics.

To characterize the SA in the Wolf numbers there had been used the data of the Institute of space exploration of RSA. An average value of the Wolf numbers in the period of a high SA was $112,0 \pm 2,9$, in the period of a low SA - $62,4 \pm 3,9$ ($p < 0,05$).

The functional ability of endothelial vessel wall had been estimated by the occlusion test based on a modeling of a short 3-minute local ischemia, stimulating by the fixing of a sphygmomanometer on a patient's shoulder, and the pressure 10 mm of mercury higher than a systolic

pressure (Baluda V.P. et al., 1992). The substances that decrease the blood clotting and thrombocytes aggregation, influence the blood viscosity and erythrocytes functional properties, are released into the blood flow from a vascular endothelium at the occlusion test. The occlusion test models an angiospasm and let estimate a reserve of vessel wall of the subject at the short ischemia condition.

The BV had been estimated under the three rate-of-shear (200 sec^{-1} , 100 sec^{-1} , 20 sec^{-1}) with the help of the rheometer AKP-2 before and after the occlusion test (OT). There had been also fibrinogen measured (FG), as its increase in a blood plasma causes an increase of a BV.

We had introduced an index "rheological index of a vessel wall" (RIVW, relative unit – r.u.), determining as a relation of "BV after OT" value to "BV before OT" value. The RIVW lets assay the vascular endothelial ability to release substances influencing the BV into blood at the ischemia condition. In releasing the substances, decreasing the BV, RIVW has a value less than 1. In the case of an increase of the BV after OT, RIVW has the value more than 1, which indicates a deterioration of endothelium-dependent regulation of a blood flow property at the angiospasm condition. RIVW, to a certain extent, reflexes the endothelium condition in the vessels of a small, medium and macro diameters, which is clear from the BV analyze under the corresponding rate-of-shear (20 sec^{-1} , 100 sec^{-1} , 200 sec^{-1}).

It had been established that the blood flow property in healthy persons depends on the period of a SA as at rest, as at the angiospasm conditions (modeling by the OT).

In the period of a low SA the BV at rest under all rate-of-shear was lower ($p < 0,05$) then in the period of a high SA (Table 1).

At the same time, in the period of a low SA the BV under all rate-of-shear after OT adaptively decreases ($p < 0,05$) (Table 1), which indicates the release of substances increasing the blood flow properties at the angiospasm condition. This reaction is directed on the prevention of a hypoxia developing in the decreasing of a blood flow through a stenosed vessel. RIVW has a value < 1 .

The given type of a functioning of endothelial vessel wall can be considered as a totally compensated.

In a high solar activity there are no statistically valid changes in the BV 200 sec⁻¹, 100 sec⁻¹, 20 sec⁻¹ at the OT ($p > 0,05$) (Table 1). So, an increase of a SA leads to changes in functional properties of vascular endothelium: after OT there is no compensatory decrease of a BV, it means that there is no releasing of the substances increasing a blood flow property at the angiospasm. The changes in functional properties of vascular endothelium in the period of a high SA can also be connected with a higher ($p < 0,05$) fibrinogen concentration comparing with the period of a low SA (Table 1). In the period of a low SA RIVW has a value ≈ 1 . This type of a functioning of endothelial vessel wall should be considered as a subcompensated, as the absence of an adaptively improvement of a blood flow property at the angiospasm condition pre-determines hypoxic changes in organs at strain.

Table 1: Dynamic of a blood viscosity and fibrinogen concentration at the induced ischemia in healthy persons in different periods of solar activity ($M \pm m$)

Indices	Period of a solar activity	
	High solar activity (n=40)	Low solar activity (n=40)
BV 200 c ⁻¹ , mPa·sec <u>before OT</u> after OT	<u>6,47±0,33</u> ** 6,56±0,52	<u>4,49±0,22</u> 3,81±0,15 *
BV 100 c ⁻¹ , mPa·sec <u>before OT</u> after OT	<u>7,06±0,40</u> ** 7,12±0,64	<u>4,54±0,21</u> 3,89±0,21 *
BV 20 c ⁻¹ , mPa·sec <u>before OT</u> after OT	<u>9,62±0,46</u> ** 9,69±1,00	<u>5,29±0,33</u> 3,98±0,24 *
FG, g/l	3,59±0,20 **	3,09±0,17

Note: OT – occlusive test;

* - the difference between index values before and after OT is statistically valid ($p < 0,05$);

** - the difference between indices of a high and a low SA is statistically valid, $p < 0,05$.

It should be noted that in the period of a low, as well as in the period of a high SA, the endothelium reaction on the OT was unidirectional in the vessels of different diameters. In the period of a low SA compensated type of endothelium functioning had been revealed in the vessels of small, medium and macro diameters under the rate-of-shear (20 sec⁻¹, 100 sec⁻¹, 200 sec⁻¹) correspondingly. In the period of a high SA subcompensated type of endothelium functioning had been revealed also in the vessels of all studied sizes (small, medium and macro diameters under the rate-of-shear 20 sec⁻¹, 100 sec⁻¹, 200 sec⁻¹ correspondingly).

A unidirectionality of endothelium reactions in the vessels of different diameters indicates the retention of basic mechanisms of regulation in healthy people independent from the period of a SA. So, compensatory-adaptive mechanisms of functional properties of vascular endothelium at a SA change, change first in the local level (vascular system) keeping more complicated central adaptive processes unchanged. This, probably, explains normal functioning of a healthy organism in the period of a low and high SA.

The results of the study show that change in a SA causes blood rheological properties and compensatory-adaptive mechanisms of functional properties of an endothelial vessel wall in healthy people on retention of central regulating mechanisms. At the same time a period of a SA determines features of functional properties of vascular endothelium at the angiospasm condition: an angiospasm at a low SA is accompanied by an adaptive increase of a blood flow property ($RIVW < 1$, compensated type of endothelium functioning), at a high SA this mechanism is lost ($RIVW \approx 1$, subcompensated type of endothelium functioning).

The given results let us erect a proposition of a main role of a vascular endothelium as a primary aim for effects in a healthy organism at a changed solar activity.

References

- Breus T.K. *Thesis of a Doctor of Physics and Mathematics*, Moscow, 2003, 45 p.
Gurfinkel U. I., Lubimov V.V., Orayevskiy V.N. et al.: 1995, *Biophysics*, **40**, no. 4, 793.

ENDOTHELIAL DYSFUNCTION AND BLOOD VISCOSITY INPATIENTS WITH UNSTABLE ANGINA IN DIFFERENT PERIODS OF A SOLAR ACTIVITY

Parshina S.S.¹, Tokaeva L.K.², Dolgova E.M.³, Afanas'yeva T.N.⁴, Strelnikova O.A.⁵

Saratov state medical university n.a. V.I.Razumovsky, Saratov, Russia
¹ parshinasvetlana@rambler.ru, ² 624494@mail.ru, ³ emdolgova@list.ru,
⁴ protegemoi18@mail.ru, ⁵ strelnik222@mail.ru

ABSTRACT. The origin of hemorheologic and endothelial defects in patients with unstable angina (comparing with healthy persons) is determined by a solar activity period: the blood viscosity increases in a period of high solar activity in the vessels of small, medium and macro diameters, a local decompensate dysfunction of small vessels endothelium had been fixed (microcirculation area). In the period of a low solar activity there is an increase of a blood viscosity in vessels of all diameters, generalized subcompensated endothelial dysfunction is developed (on the background of the III phase blood clotting activating). In the period of a high solar activity a higher blood viscosity had been fixed, comparing with the period of a low solar activity.

Key words: solar activity, unstable angina, blood viscosity, endothelial dysfunction.

Change of a solar activity is one of natural risk factors for a human health. Active solar phenomenon are accompanied by oscillations of the Earth electromagnetic field. Geomagnetic field of the Earth is one of the few environmental factors which influences an organism and its regulatory mechanisms at all levels, including molecular, endocellular, intercellular, etc. Heliogeophysical activity damages a chronological sequence of informational signals which are used in our organism for coordination of biological processes rhythmic with an environment rhythmic.

It is known that a cardiovascular system is a primary target for a heliogeophysical activity (Breus, 2003). In the most of the patients with an ischemic heart disease geomagnetic irradiation provokes hypertension, arrhythmia episodes, blood rheological properties; it causes feebleness of capillary circulation, blood viscosity increase and erythrocytes aggregation change (Breus, 2003).

As rheological defects are independent risk factors of an ischemic heart disease (Backer et al., 2002), it is important to study the blood viscosity (BV) and functional properties of vascular endothelium in vessels of different diameters in patients with unstable angina (UA) in the

periods of high and low solar activity (SA) during the 11-years solar cycle.

During the last 23rd solar cycle (September, 1996 – September, 2007) 310 patients with II class unstable angina by Braunwald had been examined: 129 of them – in the period of a high SA, 81 – in the period of a low SA. The groups were matched in age and sex characteristics, severity of a disease, amount of myocardial infarction episodes, arterial hypertension, etc.

There were 80 apparently healthy persons in the control group (C), they had been examined at the same period (September, 1996 – September, 2007): 40 of them – in the period of a high SA, 40 – in the period of a low SA.

To characterize the SA in the Wolf numbers there had been used the data of the Institute of space exploration of RSA. An average value of the Wolf numbers in the period of a high SA was $112,0 \pm 2,9$, in the period of a low SA – $62,4 \pm 3,9$ ($p < 0,05$).

The BV had been estimated under the three rate-of-shear (200 sec⁻¹, 100 sec⁻¹, 20 sec⁻¹) with the help of the rheometer AKP-2, which let us measure a blood flow property in the vessels of small, medium and macro diameters correspondingly.

The functional ability of endothelial vessel wall had been estimated by the occlusion test (OT) based on a modeling of a short 3-minute local ischemia, stimulating by the fixing of a sphygmomanometer on a patient's shoulder, and the pressure 10 mm of mercury higher than a systolic pressure (Baluda V.P. et al., 1992). The substances that decrease the blood clotting and thrombocytes aggregation, influence the blood viscosity and erythrocytes functional properties, are released into the blood flow from a vascular endothelium at the occlusion test. The occlusion test models an angiospasm and let estimate a reserve of vessel wall of the subject at the short ischemia condition.

An endothelial dysfunction had been estimated by BV measuring results before and after OT under the three rate-of-shear (200 sec⁻¹, 100 sec⁻¹, 20 sec⁻¹) which reflexes the endothelium condition in the vessels of a small, medium and macro diameters.

There had been also fibrinogen measured (FG), as its increase in a blood plasma causes an increase of a BV.

It had been denoted that the character of hemorheologic and endothelial defects in patients with unstable angina (comparing with healthy persons) is determined by a solar activity period.

At a high SA in the patients with unstable angina there had been fixed an increase of a BV (comparing with healthy persons) in vessels of medium and small diametres (under the rate-of-shear 100 sec⁻¹, 20 sec⁻¹, p<0,05) (Table 1). But in vessels of macro diametres (200 sec⁻¹) there had not been revealed a significant change in a BV (p>0,05). So, rheological defects are fixed only in vessels of medium and small diametres.

During the OT in vessels of medium and macro diametres (200 sec⁻¹, 100 sec⁻¹) an endothelium reaction corresponds with reactions in healthy persons in the period of a high SA: a BV does not change before and after OT (p>0,05) (Table. 1). In vessels of small diametres (20 sec⁻¹) there had been fixed a statistically valid increase of a BV after OT (p<0,05).

Thus, at a high SA in the patients with UA (comparing with healthy persons) there had been fixed neither a BV, nor functional properties of endothelium changes in macrovessels. In the vessels of a medium diameter a blood viscosity is high, but endothelium reaction on an induced ischemia is kept. In small vessels the BV is high and an endothelial dysfunction was revealed – paradoxical increase of a BV after OT which indicates a failure of compensatory-adaptive of an endothelial properties at a spasm condition and developing of decompensated endothelial dysfunction. The given failures are not connected with an increase of procoagulative blood potency, as fibrinogen concentration in the patients with UA in the period of a high SA does not differ from the indices of healthy persons (p>0,05) (Table 1).

Table 1: Blood viscosity indices in an induced ischemia and fibrinogen in the patients with unstable angina in the period of a high solar activity (M±m)

Indices	High SA	
	UA (n=129)	C (n=40)
BV 200 sec ⁻¹ mPa·sec <u>before OT</u>	<u>6,58± 0,13</u>	<u>6,47±0,33</u>
after OT	6,99± 0,13	6,56±0,52
BV 100 sec ⁻¹ mPa·sec <u>before OT</u>	<u>10,50± 0,44 #</u>	<u>7,06±0,40</u>
after OT	11,67± 0,56 #	7,12±0,64
BV 20 sec ⁻¹ mPa·sec <u>before OT</u>	<u>11,73±0,45#</u>	<u>9,62±0,46</u>
after OT	13,52± 0,47 *#	9,69±1,00
FG, g/l	3,69± 0,08	3,59±0,10

Note: # – the difference between indices of the patients with UA and the control group is statistically valid (p<0,05);

* – the difference between index values before and after OT is statistically valid (p<0,05).

At a low SA in the patients with UA there is an increase of a BV (p<0,05) in vessels of all diameters (200 sec⁻¹, 100 sec⁻¹, 20 sec⁻¹) comparing with indices of healthy persons at the same period (Table 2).

During the OT a homotypic reaction had been revealed in vessels of all diameters (200 sec⁻¹, 100 sec⁻¹, 20 sec⁻¹): BV does not change before and after OT (p>0,05) (Table 2). At the same time in healthy persons in the period of a low SA during OT there is a decrease of a BV (p<0,05) (Table 2). Thus, an endothelial dysfunction progresses in vessels of all diameters in the patients with UA, the function failure is of a generalized origin. At the same time the origin of an endothelial dysfunction differs from the same one in the period of a high SA: BV does not change at a spasm condition, but in a high SA after OT there is an increase of BV (decompensated endothelial dysfunction). We had revealed endothelium function failure in the period of a low SA and it can be denoted as a subcompensated type of endothelium dysfunction.

The revealed failures come out on the background of FG level increase in the patients with UA (comparing with healthy persons) in the period of a low SA (p<0,05) (Table 2).

The results of the study show that unidirectional endothelium reactions on an induced ischemia in the vessels of different diameters is fixed only in the period of a low SA (generalized subcompensated endothelium dysfunction). In the period of a high SA there is a misfit in endothelium reactions on an induced ischemia in the vessels of different diameters and developing of a local decompensated endothelial dysfunction. Thus, in the period of a low SA there is more intensive retention of basic mechanisms of regulation, than in the period of a high SA.

Table 2: Blood viscosity indices in an induced ischemia and fibrinogen in the patients with unstable angina in the period of a low solar activity (M±m)

Indices	Low SA	
	UA (n=81)	C (n=40)
BV 200 sec ⁻¹ mPa·sec <u>before OT</u>	<u>6,38± 0,13#</u>	<u>4,49±0,22</u>
after OT	6,48± 0,19#	3,81±0,15*
BV 100 sec ⁻¹ mPa·sec <u>before OT</u>	<u>7,19± 0,18#</u>	<u>4,54±0,21</u>
after OT	6,9± 0,22#	3,89±0,21*
BV 20 sec ⁻¹ mPa·sec <u>before OT</u>	<u>10,59±0,39#</u>	<u>5,29± 0,33</u>
after OT	10,18± 0,47#	3,98±0,24*
FG, g/l	3,97± 0,11 #	3,09± 0,17

Note: # – the difference between indices of the patients with UA and the control group is statistically valid (p<0,05);

* – the difference between index values before and after OT is statistically valid (p<0,05).

We can see that in the patients with UA defects in microvasculature (20 sec^{-1}) develop independent from a period of a SA, but endothelium dysfunction in small vessels in a high SA is local but more dangerous (decompensated). In the low SA there is generalized (in vessels of all diameters), but less dangerous – subcompensated – endothelium dysfunction. The same is for BV defects (comparing with healthy persons): in the period of a high SA – in vessels of medium and small diameters, in the period of a low SA – in all vessels.

In comparison of BV in the patients with UA in the periods of low and high SA there had been revealed the following: the higher BV in the period of a high SA in macro vessels is only at the spasm conditions (after OT), in vessels of medium diameter – both at rest and at the spasm conditions (before and after OT), in small vessels – only at the spasm conditions (after OT) ($p < 0,05$) (Table 3). Fibrinogen concentration in the patients with UA is higher in the period of a low SA ($p < 0,05$) (Table 3).

Table 3: Blood viscosity indices in an induced ischemia and fibrinogen in the patients with unstable angina in different periods of a solar activity ($M \pm m$)

Indices	High SA (n=129)	Low SA (n=81)
BV $200 \text{ sec}^{-1} \text{ mPa}\cdot\text{sec}$ before OT after OT	$6,58 \pm 0,13$ $6,99 \pm 0,13^{**}$	$6,38 \pm 0,13$ $6,48 \pm 0,19$
BV $100 \text{ sec}^{-1} \text{ mPa}\cdot\text{sec}$ before OT after OT	$10,50 \pm 0,44^{**}$ $11,67 \pm 0,56^{**}$	$7,19 \pm 0,18$ $6,9 \pm 0,22$
BV $20 \text{ sec}^{-1} \text{ mPa}\cdot\text{sec}$ before OT after OT	$11,73 \pm 0,45$ $13,52 \pm 0,47^*$ **	$10,59 \pm 0,39$ $10,18 \pm 0,47$
FG, g/l	$3,69 \pm 0,08^{**}$	$3,97 \pm 0,11$

Note: * – the difference between index values before and after OT is statistically valid ($p < 0,05$);

** – the difference between high and low SA is statistically valid ($p < 0,05$).

Thus, the origin of hemorheologic and endothelial defects in patients with unstable angina (comparing with healthy persons) is determined by a solar activity period: the blood viscosity increases in a period of high solar activity in the vessels of small, medium diameters, a local dysfunction of small vessels (microcirculation area) endothelium is decompensate (pathological increase of BV at the induced ischemia condition). In vessels of macro diameters BV and endothelial functions are saved. In the period of a low solar activity there is an increase of a blood viscosity in vessels of all diameters, generalized subcompensated endothelial dysfunction is developed (on the background of the III phase blood clotting activating). In the period of a low solar activity in vessels of all diameters (200 sec^{-1} , 100 sec^{-1} , 20 sec^{-1}) blood viscosity increases and generalized subcompensated endothelial dysfunction (the absence of physiological decrease of BV in OT).

In the period of a low solar activity on the background of the III phase blood clotting activating (FG increasing), in the period of a high solar activity – without this mechanism activation.

In the period of a high solar activity in the patients with UA there is a higher BV and a misfit in endothelium vessels of different diameters (comparing with the period of a low SA).

References

- Breus T.K. *Thesis of a Doctor of Physics and Mathematics*, Moscow, 2003, 45 p.
 Backer T.L., Buyezere M., Segers P. et al.: 2002, *Atherosclerosis*, **165** (2), 367.

SPACE WEATHER AND A STATE OF CARDIOVASCULAR SYSTEM OF HUMAN BEING WITH A WEAKENED ADAPTATION SYSTEM

Samsonov S.N.

Yu.G.Shafer Institute of Cosmophysical Research and Aeronomy, Siberian Branch of the Russian Academy of Sciences, Yakutsk, Russia, *s_samsonov@ikfia.ysn.ru*

ABSTRACT. As has been shown in [Samsonov et al., 2013] even at the considerable disturbances of space weather parameters a healthy human being did not undergo painful symptoms although measurements of objective physiological indices showed their changes. At the same time the state of health of people with the weakened adaptation system under the same conditions can considerably be deteriorated up to fatal outcome. The analysis of results of the project “Heliomed” and the number of calls for the emergency medical care (EMC) around Yakutsk as to cardiovascular diseases (CVD) has shown:

- the total number of calls for EMC concerning myocardial infarction (MI) per year near the geomagnetic disturbance maximum (1992) exceeds the number of calls per year near the geomagnetic activity minimum (1998) by a factor of 1,5 and concerning to strokes – by a factor of 1,8.

- maxima of MI are observed during spring and autumn periods coinciding with maxima of geophysical disturbance;

- the coincidence of 30-32 daily periods in a power spectrum of MI with the same periods in power spectra of space weather parameters (speeds and density of the solar wind, interplanetary magnetic field, geophysical disturbance);

- the existence of 3 maxima of the number of calls for EMC: a) at the moment of disturbance on the Sun; during a geophysical disturbance (in 2-4 days after a disturbance on the Sun); in 2-4 days after a geophysical disturbance;

- the availability of coincidence of insignificant disturbances of space weather parameters with changes of the functional state of cardiovascular system of a human being with the weakened adaptation system and the occurrence of MI and strokes at considerable values of such disturbances is explained by a quasi-logarithmic dependence of the response of human being organisms to the environment disturbance intensity.

Key words: space weather, the Sun, cardiovascular system of a human being, a myocardial infarction

1. Experimental data

To detect real space weather parameters influencing a cardiovascular system (CVS) of human being with a weakened adaptation system the data of the numbers of calls for the emergency medical care (EMC) around Yakutsk for years of high and low geophysical activity have been used. More than 144000 cards of calls for EMC around Yakutsk have been treated. In this work a special attention is paid to years near to the maximum (1992) and minimum (1998) of geophysical disturbance.

As was shown in [Samsonov et al., 2005; Samsonov, Manykina, 2013] a CVS of a human being responds to changes of space weather parameters, such as: the electromagnetic solar radiation, interplanetary magnetic field, solar wind. In the work both phase methods and spectral ones of experimental data treatment are used.

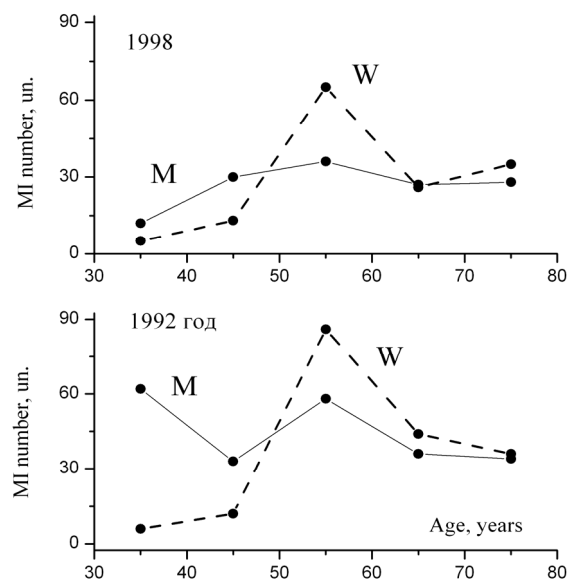


Figure 1: Distribution in sex and age of the number of myocardial infarctions diseases for women (W) and men (M) in 1992 and 1998

2. Analysis of experimental data

Fig. 1 presents a distribution in sex and age of the number of MI diseases for women (W) and men (M) in 1992 and 1998 by data of the Yakutsk EMC. As is seen from Figure the total number of calls concerning MI for EMC per year near to the geomagnetic disturbance maximum (1992) exceeds the number of calls per year near to the geomagnetic activity minimum (1998) by a factor of 1,5. And the total number of calls concerning strokes for EMC in 1992 exceeds the number of calls in 1998 by a factor of 1,8 (it is not shown in Figure). At the same time as has been shown in [Samsonov & Manykina, 2012] maxima of MI are observed in spring and autumn periods coinciding with maxima of geomagnetic disturbance. Thus, one can note that near the geomagnetic activity maximum there were more calls concerning CVD for EMC by a factor of 1,5-1,8 than near the geomagnetic activity minimum.

Besides, from Fig. 1 it follows that in 1992 the number of calls concerning MI for EMC to men at the age from 30 to 50 years old exceeded the number of calls to women of the same age by a factor of 5. And at the age from 50 to 60 years old the situation cardinally changes, the number of calls for EMC to women exceeds the number of calls to men by a factor of 1,5. At the age from 60 to 70 years old the number of calls for EMC to women exceeds number of calls to men, but only by a factor of 1,2. And at the age of 70-80 years old the number of calls to women and men is practically leveled off.

Hence it follows that men are magnetolabile and are exposed to the risk of development of ischemic heart disease (IHD) and its complications at the age of under 50. Men after 50 years old have a drop of magnetosensitivity, most likely it is caused by stabilization of adaptive processes of an organism, at the expense of formation of stability to factors of space weather. Women are more magnetosensitive after 50 years old and older (especially at the age of 50-60 years) during the period of peri- and post-menopause which is accompanied by a deficiency of estrogens, sexual globulin connecting steroids at the expense of natural fading of ovary function.

With applying of a phase method (superposed epoch technique) it was shown in [Samsonov et al., 2005] that the number of calls for EMC around Yakutsk as to: a hypertensive disease, a hypertensive crisis, CVD of the patients being registered on a dispensary, had two maxima. The first maximum took place at the moment of disturbance on the Sun, and second one in 2-4 days after a geomagnetic disturbance. At the same time, the number of calls for EMC concerning a MI and stroke, besides these two maxima, had also the third maximum at the moment of geomagnetic disturbance. In [Samsonov & Manykina, 2012] it has been shown that the first maximum of the number of calls for EMC concerning CVD coinciding with the disturbance on the Sun is connected with the increase of electromagnetic solar radiation. Thus it has been shown that the increase of electromagnetic solar radiation intensity immediately influences on CVD of a human being.

The power spectra calculated by the number of calls for EMC around Yakutsk concerning CVD [Samsonov et al., 2005] have shown the availability of maximum with a period of 30-32 days coinciding with the same maxima in the following space weather parameters: the interplanetary magnetic field (IMF), solar wind (SW), geomagnetic disturbance and auroral absorption. And in [Samsonov & Manykina, 2012] the coincidence of power spectra of the state of CVS of the volunteer group with the power spectra of space weather parameters (has been shown by the total intensity of IMF vector, speed, density and dynamic pressure of SW, geomagnetic disturbance) and the absence of such coincidence with power spectra of parameters of the usual ground weather. In the same place it has been shown that the disturbance of IMF and SW are transformed in the Earth's magnetosphere into the disturbance of the geomagnetic field which, finally, influences on CVD of a human being with the weakened adaptation system.

In [Garkavi et al., 1998] it has been shown that the response of living organism to the external action is described by the quasi-logarithmic law. In our case we have studied the dependence of response of the CVS of human being with the weakened adaptation system to geomagnetic field disturbances and have discovered that such response is quite well described by quasi-logarithmic dependence. Fig. 2 presents the plot describing the dependence of state of human being CVD on the level of geomagnetic disturbance. As an index of functional state of the CVS of human being such index of an electrocardiogram (ECG) as a T-wave symmetry coefficient (TSC) is used. One can acquaint oneself with applicability of TSC for the estimation of CVS state of a human being in more details in [Fainzilberg, 1998; Vishnevsky et al., 2003]. As is seen from Figure the dependence has three fields differing from each other designated by the numbers from 1 to 3. The first field is characterized by the increase of TSC with the growth of level of geomagnetic disturbance. The second field is characterized by a practical termination of the growth of TSC, and the third field leads to the sharp change of state of the CVS of human being, indicating to the approach of CVD.

Insignificant geomagnetic disturbances play a role of the "starting" adaptive factor transferring the work of CVS into the optimum mode corresponding to the level of geomagnetic disturbance. In this case the TSC starts to

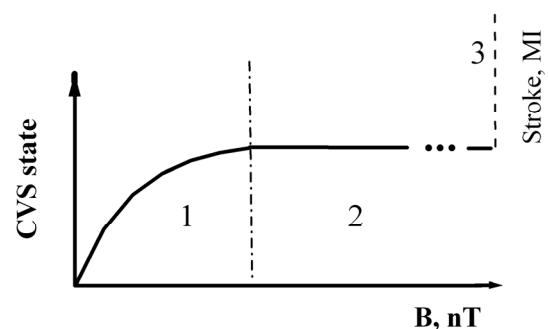


Figure 2: Dependence of the CVS state of a human being on the geomagnetic disturbance level

grow together with the growth of geomagnetic disturbance. When exceeding the level corresponding to the boundary of fields 1 and 2 by the geomagnetic disturbance, the functioning of CVS is stabilized in a state which is relatively refractory to the changes of external actions that can have the protection moment for patients with a cardiovascular pathology. In this case, TSC does not grow with the growth of geomagnetic disturbance. Definitely, a similar stability is reached by the effort of adaptation-compensating mechanisms of CVS.

The confirmation of given interpretation are observational results obtained in the course of the experiment "Heliomed". The volunteers are students (young and healthy) participating in the given experiment showed the coincidence of changes of geomagnetic disturbances with TSC all the time, i.e. they were in the field 1 all the time.

The volunteers of the middle (30-50 years) and older age (older than 50 years) participating in the experiment as relatively healthy people, usually were divided into two approximately identical groups by the response to geomagnetic disturbances. First half of group, also as well as students, showed the coincidence of changes of geomagnetic disturbance with TCS, i.e. they were in the field 1.

The second half of group showed only a partial coincidence of changes of geomagnetic disturbance with TSC, i.e. they were in the fields 1 and 2. Probably those examined "healthy" volunteers already had a certain state of latent "pre-disease" that was characterized by a tension of adaptation mechanisms of CVS and development of an adaptive stability to changes of geomagnetic disturbance.

By our assumption people with the weakened adaptation system the field 1 has a very narrow range of values, and the insignificant geomagnetic disturbance transforms the state of CVS to the field 2. Therefore such people don't show the coincidence of changes of geomagnetic disturbance with TSC.

3. Conclusions

The analysis of results of the project "Heliomed" and the number of calls of EMC around Yakutsk as to CVD has shown the following:

– the total number of calls concerning the MI for EMC per year near to the geomagnetic disturbance maximum (1992) exceeds the number of calls per year near to the

geomagnetic activity minimum (1998), and strokes- by a factor of 1,8;

– maxima of MI are observed during spring and autumn periods coinciding with maxima of geophysical disturbance;

– the coincidence of 30-32 daily periods in the power spectrum of MI with the same periods in the power spectra of space weather parameters (speeds and densities of the solar wind, interplanetary magnetic field, geophysical disturbance;

– the existence of 3 maxima of the number of calls of EMC: a) at the moment of disturbance on the Sun; b) during geophysical disturbance (in 2-4 days after a disturbance on the Sun); c) in 2-4 days after a geophysical disturbance;

– the availability of coincidence of insignificant disturbances of space weather parameters with changes of the functional state of cardiovascular system of a human being with the weakened adaptation system and approach of MI and strokes at insignificant values of such disturbances is explained by quasi-logarithmic dependence of the response of human being organisms to the intensity of environment disturbance.

Acknowledgments. The work has been carried out at a partial financial support of the Russian Fund for Basic Research grants (12-05-98522, 12-02-98508, №13-05-00363).

References

- Vishnevsky V.V. et al.: 2003, *Biomedical technologies and radioelectronics*, **3**, 3.
- Vishnevsky V.V. et al.: 2009, *Journal of New Medical Technologies*, **16**, 241.
- Garkavi L.Kh. et al.: 1998, Moscow: IMEDIS, 656.
- Samsonov S.N. et al.: 2005, *Zhurnal nevrologii i psikiatrii. Stroke*, **14**, 18.
- Samsonov S.N., Manykina V.I., 2012, *Proceed. of the Int. Conf. «Space Weather Effects on Human: in Space and on Earth»*, Moscow: SRI, **2**, 730.
- Samsonov S.N., Manykina V.I.: 2012, *Odessa Astron. Publ.*, **25/2**, 222.
- Samsonov et al.: 2013, *Odessa Astron. Publ.*, **26/2**, in press.
- Fainzilberg L.S.: 1998, *Operating systems and machines*, **4**, 40.

SPACE WEATHER AND THE STATE OF CARDIOVASCULAR SYSTEM OF A HEALTHY HUMAN BEING

Samsonov S.N.¹, Manykina V.I.¹, Krymsky G.F.¹, Petrova P.G.², Palshina A.M.², Vishnevsky V.V.³

¹ Yu.G.Shafer Institute of Cosmophysical Research and Aeronomy, Siberian Branch of the Russian Academy of Sciences, Yakutsk, Russia, *s_samsonov@ikfia.ysn.ru*

² Medical Institute of M.K.Ammosov North-Eastern Federal University, Yakutsk, Russia

³ Institute of Mathematical Machines and Systems Problems, National Academy of Sciences of Ukraine, Kiev, Ukraine

ABSTRACT. The term “space weather” characterizes a state of the near-Earth environmental space. An organism of human being represents an open system so the change of conditions in the environment including the near-Earth environmental space influences the health state of a human being.

In recent years many works devoted to the effect of space weather on the life on the Earth, and the degree of such effect has been represented from a zero-order up to apocalypse. To reveal a real effect of space weather on the health of human being the international Russian-Ukrainian experiment "Geliomed" is carried out since 2005 (<http://geliomed.immsp.kiev.ua>) [Vishnevsky et al., 2009]. The analysis of observational set of data has allowed to show a synchronism and globality of such effect (simultaneous manifestation of space weather parameters in a state of cardiovascular system of volunteer groups removed from each other at a distance over 6000 km). The response of volunteer' cardiovascular system to the changes of space weather parameters were observed even at insignificant values of the Earth's geomagnetic field. But even at very considerable disturbances of space weather parameters a human being healthy did not feel painful symptoms though measurements of objective physiological indices showed their changes.

Key words: space weather, the Sun, cardiovascular system of a human being.

1. Introduction

At the end of 20th century after the beginning of flights of space vehicles measuring parameters of fluxes of particles, electromagnetic fields and radiations, there appeared understanding of that fact what represents the near-Earth environmental space and how fields, particles and radiations can reach this or that area of the near-Earth environmental space and make a possible impact on the Earth's life. And at the beginning of our century there

appeared a term “space weather” characterizing a state of the near-Earth environmental space. The main effect on a state of the near-Earth environmental space exerts the Sun. So a detection of mechanisms of connection between the Sun's activity and functioning of various objects of the biosphere including a human being is one of fundamental problems of the up-to-date science.

The organism of a human being represents an open system so a change of environmental conditions has an effect on a state of a human being's health. A cardiovascular system (CVS) is one of the first one which joins in the process of adaptation to the varying external conditions. Besides the obviously influencing factors of environment, such as meteorological parameters, and also social factors it has been revealed that electrical and magnetic fields, electromagnetic radiations which are not registered by feelings of a human being can influence the state of health. So the purpose of this work is to study the effect of space weather parameters on a state of a human being's CVS.

2. Experimental data and registration methods

The experiment was carried out simultaneously at 3 points of observation: Yakutsk (Russia), Kiev (Ukraine) and Simferopol (Ukraine) on the same equipment (Fazagraf sensor) by a common protocol of examination on a group of volunteers invited at each point of observation in November-December, 2008. As an index of functional state of a human being's CVS a T-wave symmetry which is the index of electrocardiogram (ECG) has been used. In more detail about an applicability of T-wave symmetry for estimation of CVS state of a human being and about operation of Fazagraph complex, one can see in [Fainzilberg, 1998 or Vishnevsky et al., 2003]. Thus, for each patient the individual set of data has been obtained for the whole period of experiment. Then, to create a continuous number of data an indices of each volunteer has been interpolated because measurements

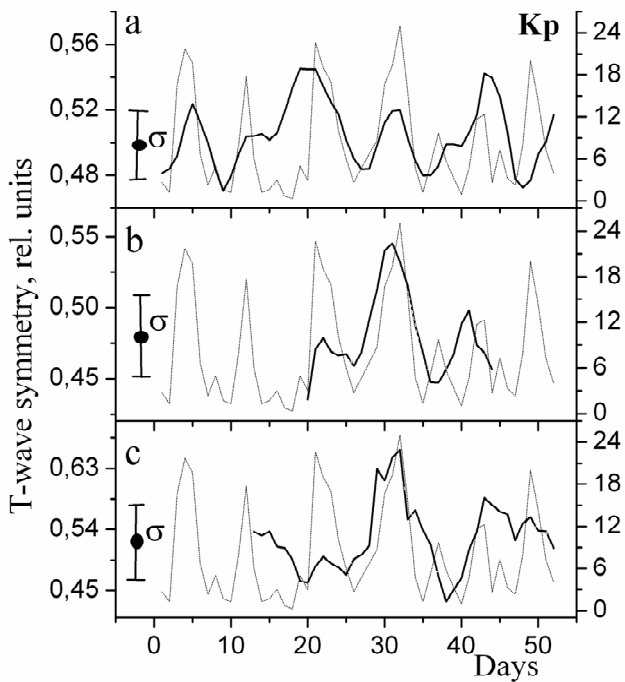


Figure 1: Temporal variations of the ECG T-wave symmetry coefficient (solid line) and geomagnetic disturbance Kp-index(dashed line) in : a) Yakutsk, b) Kiev, c) Simferopol.

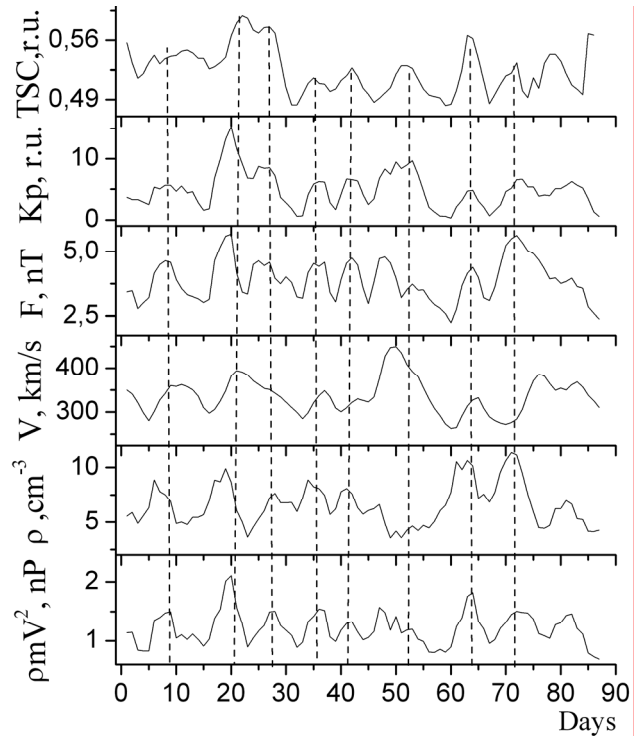


Figure 2: Changes of the CVS state of volunteer's group in Yakutsk and space weather parameters (October 5-December 30, 2009)

of the basic part of volunteer group were made only during the working days. For the purpose of smoothing of the T-wave symmetry coefficient (TSC) variations the data with a period less than 4 days have been filtered out.

The comparison of temporal TSC variations of each volunteer with temporal variations of the geomagnetic disturbance index has shown a coincidence of these indices of a part of volunteers. It is shown that 46,5 % of volunteers have had the temporary changes of TSC coinciding with changes of geomagnetic disturbance index. The mean age of volunteers with coinciding changes accounts for 46,9 years while the average age of volunteers with not completely coinciding changes accounts for 53,6 years. In the coinciding group it has been turned out to be 47,1 % of women and 46,2 % of men.

Contrastingly, in Kiev and Simferopol all volunteers have shown a coincidence of TSC variations with the changes of geomagnetic disturbance level both in the state of immobility and after emotional and physical loadings.

In Fig. 1 on the ordinate the averaged index of T-wave symmetry of volunteers' ECG in relative units (solid line) and the index of geomagnetic disturbance (dashed line) are shown, and on the abscissa the time in days (24 hours) from the beginning of experiment are given. The data of Yakutsk, Kiev and Simferopol are shown from top to down σ is a mean quadratic deviation. From Fig. 1 it is seen that virtually for each change of geomagnetic disturbance the organism of volunteers in all points of measurements responds by similar changes in TSC but with a various

relation of amplitudes. Such coincidence is observed even at low levels of geomagnetic disturbance (the geomagnetic field is considered to be disturbed if the daily value of Kp-index exceeds 18 rel. units). Thus, the global effect on CVS of a human being in the points of observation removed from each other at a distance of the order of 6000 km from each other is observed.

In Fig. 2 the changes of CVS state (TSC) of the volunteers' group in Yakutsk, and also space weather parameters are presented: the Kp-index of geomagnetic disturbance, the total intensity of the interplanetary magnetic field vector (total F), solar wind speed (V), density of solar wind particles (ρ), dynamic pressure of the solar wind ($\rho m V^2$, m is a proton weight).

As is seen from Fig. 2 virtually all maxima and minima of the given parameters coincide in time of occurrence with the same maxima and minima in the group response of volunteers' TSC. Such almost complete coincidence has been observed for half of volunteers' groups. Another half of volunteers has shown a partial coincidence of TSC with space weather parameters. The best coincidence is observed for TSC with the total F, solar wind dynamic pressure and Kp-index of geomagnetic disturbance. For example, the correlation coefficient between TSC in Yakutsk and Kp-index of geomagnetic disturbance has accounted for 0,6 and it is under condition of the fact that TSC represents not the index of one person but the averaged value (group parameter) of the half of volunteers participating in the experiment.

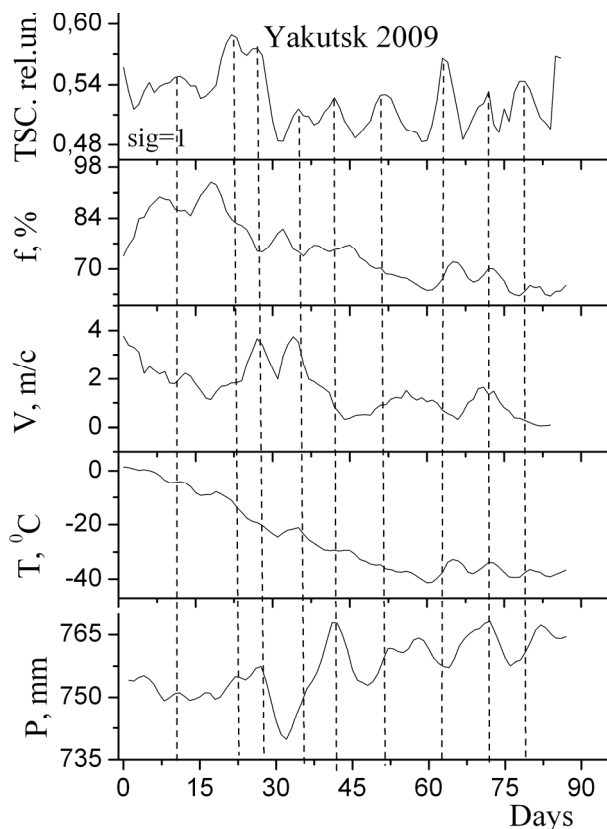


Figure 3: Change of CVS state of a half of volunteer group in Yakutsk with meteoroparameters (October 5-December 30, 2009).

It is known that a human being organism reacts to changes of usual Earth's weather. To be convinced whether in this study the usual Earth's weather has influenced or not the state of CVS volunteers we will compare changes of CVS state of volunteers with changes of parameters of usual Earth's weather. Fig. 3 presents changes of the state of CVS of the half of group of volunteers in Yakutsk with meteoroparameters (f % is the humidity, V is the solar wind speed, T is the temperature and P is the ground atmosphere pressure). As is seen from Fig. 3 the coincidence of separate changes of each of meteoroparameters with TSC is observed.

It means the availability, at best, of only the partial influence of absolute values of meteoroparameters on CVS of a human being for the considered period. Besides, in [Samsonov & Manykina, 2012] it was shown that power spectra of space weather parameters and a state of cardiovascular system have shown the complete similarity while power spectra of parameters of usual ground weather have not shown such similarity.

3. Conclusions

1. Studies of connection of space weather parameters with a state of cardiovascular system (CVS) of healthy people on the basis of such observational facts, as:

- the temporal coincidence of maxima and minima in the changes of space weather parameters (without conservation of a relation of amplitudes) with changes of TSC characterizing the state of CVS of a human being in Kiev-Simferopol-Yakutsk;

- the coincidence of only separate maxima and minima in the changes of meteoroparameters with changes of TSC in Yakutsk and Tixie

- the availability of set of coinciding period in the power spectra of space weather and TSC parameters ;

- the lack of set of coinciding periods in the power spectra of meteo- and TSC- parameters allows to make a conclusion that just space weather parameters such as the solar wind speed and density, total F transforming in the Earth's magnetosphere into a geomagnetic disturbance are manifested in a state of CVS of a human being at high latitudes.

2. The long evolutionary way of the development of mankind allows a healthy human being to compensate the effect of space weather without an obvious damage of his health at the expense of reserve possibilities of an organism of human being.

Acknowledgments. The work has been carried out at a partial financial support of the Russian Fund for Basic Research grants (12-05-98522, 12-02-98508, №13-05-00363).

References

- Vishnevsky V.V. et al.: 2003, *Biomedical technologies and radioelectronics*, **3**, 3.
- Vishnevsky V.V. et al.: 2009, *Journal of New Medical Technologies*, **16**, 241.
- Samsonov S.N., Manykina V.I.: 2012, *Proceed. of the Int. Conf. «Space Weather Effects on Human: in Space and on Earth»*, Moscow: SRI, **2**, 730.
- Fainzilberg L.S.: 1998, *Operating systems and machines*, **4**, 40.

STUDYING OF INFLUENCE OF THE LOW-FREQUENCY ELECTROMAGNETIC FIELD ON DNA MOLECULES IN WATER SOLUTIONS

E.E.Tekutskaya, M.G.Baryshev

Kuban State University
Krasnodar, Russia, Stavropolskaya St., 149, 350040
tekytska@mail.ru

ABSTRACT. Influence of a low-frequency magnetic field on the DNA water solutions was investigated. It became clear that the variation magnetic field with a frequency of 9 Hz has the greatest impact on the DNA water solutions. Methods pulse a nuclear magnetic resonance of spectroscopy change of time of backs – a spin relaxation of the conditioned water in comparison with control is revealed. In IK – a range of water were observed change of strips of absorption of the conditioned water in the field of deformation and valent fluctuations OH – communications.

Key words: electromagnetic fields of the low frequency, DNA,

Now rather large number of reliable experimental data about not thermal effects of electromagnetic fields of the low frequency (EMP LF), and also about extremely high sensitivity to electromagnetic fields of live organisms of the most various classes – from monocelled to the person [1-2] collected. The particular interest is attracted by biopolymers on the basis of nucleic acids. By numerous experiments it is established that in a molecule of DNA transfer of a charge on long distances is possible, and also emission of photons at excitement or after excitement of a molecule of DNA [3] is possible. Earlier in a series of works we showed possibility of regulation (activation and inhibition) functional metabolic properties of biosystems of various types by means of EMP LF [1]. The low-frequency electromagnetic field was used for change of speed of course of a number of important bioprocesses: reparations of separate sites of DNA with the revealed somatic mutations; generation of active forms of oxygen by neutrophils.

Relevance of work is connected with possibility of use of molecules of DNA as a carrier of information and creation of new types of molecular devices. Studying of action of superlow-frequency electromagnetic radiation on water solutions of nucleic acids was the purpose of this work.

According to a goal the following problems were solved: DNA allocation from a various biological material; carrying out the polimerazny chain reaction

(PCR) for the purpose of receiving short ампликонов; processing of water solutions of nucleic acids and them ампликонов EMP LF; removal of ranges of a hemilyuminestsention of model solutions of nucleic acids; definition of extent of influence of EMI LF on the DNA water model solutions.

Nucleic acids (DNA, RNA) integral blood of the person were object of research. Ампликона received from the control panel, length of ампликонов made about 410 couples of нуклеотидns. DNA from biological tests allocated by means of reactants of commercial sets of Амписенс – "DNK-sorb-V" (Moscow). For carrying out PTsR used an амплификатор of the rotor type "Rotor Gene" (Australia). The program of amplification included an unbraiding of double spirals of DNA, annealing of primers, cycling and chain elongation for accumulation of short pieces of DNA.

Radiation of solutions of nucleic acids and ампликонов by means of EMP LF carried out in a special glass vessel at the room temperature. Time of radiation made 10 minutes. Processing of water solutions of nucleic acids and them ампликонов was carried out by superlong electromagnetic radiation at frequencies from 5.5 - 8.5 Hz with a step of 0,1 Hz, from 9 – 15 Hz with a step of 1 Hz and from 15,5-16,5 with a step of 0,2 Hz. Thickness of the irradiated sample ~ 2 mm. The source of superlow-frequency signals which represents the generator of signals of G3 – 118 was applied to radiation. Intensity of a field in the location of a sample made 30 - 100мкТл. Instability of frequency in the range from 3 to 30 Hz reached 0,2%.

After each processing of a sample by means of EMP LF ranges of a hemilyuminestsention of the received solutions of ампликонов within 10 minutes for each allocated frequency were removed. Used Lum-5773 measures intensity of light arising in chemical and biological samples in work, values of intensity of a luminescence correspond to a light stream, i.e. quantity of photons in unit of time.

Nuclear magnetic resonances ranges of the received water solutions of ампликонов were removed on a pulse

nuclear magnetic resonance JEOL JNM-ECA 400MHz spectrometer. Shooting of ranges was carried out at the corresponding resonant frequency of kernels of a deuterium – 61.4 MHz. Shooting parameters: 6.7 with (acquisition time), 20 with (relaxation delay), 5.6 microsec (X-, 0.15 Hz (resolution).

During the made experiment dependence of intensity of a hemilyuminestention on radiation frequency set is received by DNA. It is established that the frequency of 9 Hz has the greatest impact on DNA solutions, in comparison with control intensity increased by 2-2,5 times.

Assuming that radiation of EMP LF leads to change of conformation of a molecule of DNA [4 - 5], for allocated DNA were removed a nuclear magnetic resonance ranges before EMP LF radiation.

The main restriction of the theoretical models describing possible mechanisms of action of EMP LF on biological objects, locality of initial parcels as a result of which all range of possible resonant mechanisms was reduced only to action on concentration of several ions was.

According to the point of view of V. V. Novikov by the constructive approach to the theoretical analysis of effects of effect of EMP LF can be had at the accounting of collective interactions of external electric and magnetic fields with ensemble of a large number of ions [2 - 3].

The system of interacting ions probably leads to formation of the loaded polyionic structures – clusters and to their interaction with EMP LF. These structures can possess property of the electrochemical accumulator transforming energy of external electric field, and also part of energy of the environment in energy of chemical reactions, at operating action on these processes of weak components of the field providing their coherence. It is obvious that low-frequency EMP can carry out only

operating function, making redistribution of total energy between solution components.

Thus initiation of chemical reactions of type of condensation of amino acids is a consequence of decrease in a barrier of energy of activation at the expense of the ionic organization of structure of solution, i.e. EMP LF can carry out function of the selective catalyst. According to this concept a number of restrictions on possibility of resonant selective action of such fields on biological systems is removed. The considerable number of new researches of fundamental properties of water solutions and their sensitivity to weak physical factors confirms a hypothesis of a defining role of the water environment as primary target of weak influences.

We believe that change of a gidratny cover of DNA under the influence of a low-frequency electromagnetic field, probably, also leads to restoration of N-communications, formation of stitchings and as a whole to DNA reparation that will be coordinated with opinion of authors [6 - 7].

References

1. Baryshev M.G. et al.: 2007, *News of higher education institutions Food technology*, **3**, 44.
2. Novikov V.V. et al.: 1999, *Biophysics*, **44**, №2, 224.
3. Novikov V.V.: 1998, *T biophysics*, **4**, 588.
4. Lakhno of EL: 2003, *Molecular biophysics*, **48**, No. 5, 797.
5. Ernst R. of a nuclear magnetic resonance in one and two measurements / Ruble Ernst, J. Bodenkhauzen, A. Vokaun. – M: World, 1990. – 709 p.
6. Deroum E. The nuclear magnetic resonances modern methods for chemical researches / E. Deroum. – M: World, 1992. – 401 p.
7. Steven R., Plantea L., Philip N. et al.: 2001, *Biophysical Chemistry*, **90**, 219.

Subsection Systems and methods of data processing

INFORMATION TELECOMMUNICATIONS OF PUSHCHINO RADIO ASTRONOMY OBSERVATORY, ASTRO SPACE CENTER OF LEBEDEV PHYSICAL INSTITUTE

D.V. Dumsky¹, E.A. Isaev^{1,2,3}, V.A. Samodurov^{1,2}, S.F. Likhachev⁴,
M.V. Shatskaya⁴, M.A. Kitaeva¹, A.Yu. Zaytcev³, I.L. Ovchinnikov¹, V.V. Kornilov^{2,3}

¹ Pushchino Radio Astronomy Observatory ASC LPI,
Pushchino, Russia, *dumsky@prao.ru*

² National research university Higher school of economics, Moscow, Russia, *is@itaec.ru*

³ Institute of Mathematical Problems of Biology, Russian Academy of Sciences,
Pushchino, Russia,

⁴ Astro Space Center LPI, Moscow, Russia

ABSTRACT. Buffer data center was created in the territory of the Pushchino Radio Astronomy Observatory three years ago. The necessity of its creation was caused by the high requirements to the speed and quality of the transmission large amounts of scientific and telemetry data received by tracking station RT-22 from the space radio telescope of the international project “Radioastron”. The transfer of this data is carried out over a long distance over 100 km from the Pushchino to Moscow center of processing and storage ASC FIAN. And now we use the data center as a center of local network of the Observatory.

Key words: Telecommunications: networks: virtualization.

1. Network

Buffer data center (BDC) was housed in the Pushchino Radio Astronomy Observatory (PRAO) polygon building in a server room isolated from external environment with cooling, raised floors, racks for network and computer equipment and has a sufficient number of UPS devices for uninterruptible power supply switches and servers in case of power failure. Observatory network communication center was moved from main building to the BDC this year (Fig. 1). And it is now used not only as the communication node for gigabit Ethernet channel to the Moscow data center and “Radioastron” buffer data storage. Along with the move of the central node of PRAO LAN some modernization of network equipment working on the second and third level network protocols took place. As the main gateway to the Internet and a network of Pushchino Research Center today we use the router

Mikrotik RB1100AHx2 which replaced the old Linux router. This device provides not only the routing, but also the function of a stateful firewall and DHCP server for local network of the observatory and has many other features such as traffic filtering and shaping, dynamic routing, network monitoring and so on.

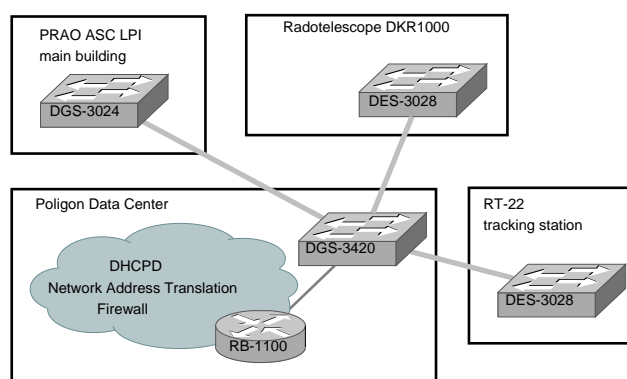


Figure 1: PRAO network diagram.

On distribution level we use managed Layer 2+ Gigabit switches D-link DGS-3420 with the ability to move in the future 10 gigabit Ethernet.

2. Local servers

Two servers mounted in the BDC we use as a virtualization platform based on GNU/Linux system. It helps us to isolate different network services such as DNS, NTP, WWW, email, sip and database from each other. One service - one virtual container. We did this to increase the safety and reliability of these services.

On one of the servers we use virtualization based

on an open platform OpenVz. And on another – system virtualization based on KVM (Kernel-based Virtual Machine) because it is more powerful (Intel Xeon 2.53-2.80 GHz and 24 GB of RAM, Adaptec RAID controller, 3.6 Tb disk space) and support hardware virtualization. KVM unlike Openvz allows one to run virtual servers running different operating systems, not only Linux. Last year we tried to use a virtualization system based on Linux container (LXC), but because it was unstable, we were forced to go to the KVM virtualization.

We have two file storage servers in the data center. One of which is used for backup storage project “Radioastron” (20 Tb disk space) and second storage data

of radio astronomy observations PRAO and of its processing (48 Tb). All servers are connected to a local network with two or more Ethernet cards to increase the speed of information exchange between servers and a local area network, and also for increase redundancy. This is possible thanks to the ability of our Gigabit switch D-link DGS-3420 to combine multiple twisted-pair or fiber Ethernet links into one fault-tolerant and load balanced logical link. In Linux systems this feature is called bonding, in switches its commonly referred to as a port channel or link aggregation. Either way, its using the LACP (802.1ad) protocol for that.

PROSPECTS OF CLOUDY TECHNOLOGIES IN THE SOLUTION OF THE TASK OF THE ANALYSIS OF LARGE VOLUMES OF THE DATA OBTAINED IN ASTRONOMICAL SUPERVISION

E.A. Isaev^{1,2}, V.V. Kornilov^{2,3}, V.A. Samodurov^{1,2}, A.A. Tarasova⁴

¹ Pushchino Radio Astronomy Observatory ASC LPI, Pushchino, Russia, *is@itaec.ru*

² National research university Higher school of economics, Moscow, Russia

³ Institute of Mathematical Problems of Biology RAS, Pushchino, Russia

⁴ FIAN, Moscow, Russia

ABSTRACT. In modern astronomy the problem of the big data obtained during scientific experiments is very actual. One of the perspective approaches to the solution of the problem of processing of superlarge volumes of experimental data in real time is the use of the technology of cloud computing which assumes ensuring remote dynamic access of users to services, computing resources and appendices on the Internet.

Key words: Big Data, Cloud Computing

The success in the development of modern computer technologies and electronics led to possibility of creation of scientific experimental installations of the new generation which characteristic is the large volumes of the data obtained during scientific experiments. Especially it is actual for astronomy and astrophysics. Devices for astronomical observing allow to obtain data with more and more high resolution, the observations of astronomical objects are conducted not only in visible light, and in all range of an electromagnetic range, thus the only observation which can last from several seconds to several minutes, gives from several megabytes to several gigabytes of information. Such astronomical projects as "Radioastron", "Millimetron", "Kvazar-KVO", "RATAN-600", PAN-STARRS, SDSS, LOFAR, ASKAP, SKA and others are

capable to generate tens and hundreds gigabytes of the supervision given for every second. So, for example, the data archive of the Telescope of Hubble for 15 years of its work is about 25 Tb [1]; the Large Survey Telescope (LSST) with a diameter of mirror of 8.4 meters and a 3 Gigapixels matrix will make 30 Tb of data only for one night, and the full volume of supervisory archive is estimated at 200 Petabyte [2].

The data obtained during experiments should be able to be stored, processed, transferred and analyzed to receive the new knowledge from these data. Enormous volumes of these data and high speed of their increasing do these tasks rather difficult for the effective decision.

The term Big data usually use for data sets with sizes beyond the ability of commonly used software tools to capture, curate, manage, and process the data within a tolerable elapsed time. In 2012, Gartner did the definition of Big data as follows: "Big data is high volume, high velocity, and/or high variety information assets that require new forms of processing to enable enhanced decision making, insight discovery and process optimization." [3]. Additionally, the new V: "Veracity" and "Visualization" now are often added to describe Big data [4].

The ability to extract knowledge from such huge data with the help of special analytical methods and modern computer technologies predetermines the success of modern science.

One of the perspective approaches to the solution of the problem of processing of superlarge volumes of experimental data in real time is the use of the technology of cloud computing which assumes ensuring remote dynamic access of users to services, computing resources and appendices on the Internet. Cloud computing is a type of computing that relies on sharing computing resources. To do this, cloud computing uses networks of large groups of servers typically running low-cost consumer PC technology with specialized connections to spread data-processing chores across them. This shared IT infrastructure contains large pools of systems that are linked together [5].

So, for processing of big data the huge computing capacities are required, and the cloudy computing is capable to present almost unlimited processor resources for processing of these volumes of data, and on very effective and flexible scheme – the necessary computing resources can be quickly provided with the minimum operational expenses. The Cloud Computing model is a perfect match for big data since cloud computing provides unlimited resources on demand. Thus, the role of cloudy technologies consists in the possibility of the effective analysis of large volumes of data, by their selection from various places of storage and use for their processing of necessary computing power.

The problem of big data in modern astronomy compels to look for non-standard ways for work with them. Transfer, storage and, the most important – the analysis of these data, in an ideal in real time, demands fantastic computer capacities. Alternative to creation of expensive supercomputer complexes of each experimental installation are the cloudy technologies which can successfully solve problems of processing of big data. Cloud computing provides the tools and technologies to build data/compute intensive parallel applications with much more affordable prices compared to traditional parallel computing techniques. But for successful implementation of this concept it is necessary to solve the number of problems, including the shortage of the qualified specialists for cloudy technologies and to the analysis of big data.

References

1. <http://hubblesite.org/>
2. <http://www.lsst.org/>
3. Laney D.: <http://www.gartner.com/resId=2057415>
4. Mayer-Schonberger V., Cukier K. "Big Data: A Revolution That Will Transform How We Live, Work, and Think". Eamon Dolan/Houghton Mifflin Harcourt, 2013.
5. Erl T., Puttini R., Mahmood Z. "Cloud Computing: Concepts, Technology & Architecture". Prentice Hall, 2013.

TRANSMISSION OF LARGE VOLUME OF ASTRONOMICAL DATA

Isaev E.A.^{1,2}, Kornilov V.V.², Samodurov V.A.^{1,2}, Tarasov P.A.³, Tarasova J.A.²

¹ Pushino Radio Astronomy Observatory ASC LPI, Russia, *is@itaec.ru*

² National research university Higher school of economics, Russia

³ OOO «NPK-INFORM», Moscow, Russia

ABSTRACT. This article shows an overview of the world's major astronomical research programs, for work requiring high-speed data, in particular, examples of major domestic (PRAM ASC LPI) and foreign projects (ALMA, VLA, SDSS, LSST, HESS, MWA, ACT). At the moment the local network to cope with data obtained from experiments load, but for future projects and the development and modernization of operating projects to the emergence of new technological solutions, due to the increased flow experimental data.

Keywords: radioastronomy, high-speed data transfer.

At the time in astronomy and astrophysics has been a rapid growth of information obtained in the course of scientific experiments. The resulting massive amounts of data must to be transmitted over local networks or to the place of storage to the point of filtering. For example, consider some of the largest domestic and foreign projects, estimate the volume of streaming data that is generated as a result of the observations and the presence of solutions that allow transfer large amounts of data obtained. One of the largest domestic astronomical projects is the Pushino Radio Astronomy Observatory. It's LAN has a bandwidth of 1 Gb/s to 10 Gb/s. This capacity is sufficient for the removal and processing of radio astronomy facilities PRAO. After that consider examples of major foreign research projects, which generate much more information, and for which the relevant high-speed data. In March 13, 2013, the official opening ceremony of the Observatory The Atacama Large Millimeter/submillimeter Array (ALMA). This project provides the following observations: detection of new galaxies and planetary systems, including at the stage of their formation; detailed study of the star formation process; study a wide range of phenomena on the Sun. The projected peak flow data from each antenna of the telescope in the future may be reach then 120 Gb/s. Another foreign project that can generate a large amount of data, it's Extended Very Large Array. This project made key contributions to the observations of black holes and protoplanetary disks around young stars. He is also used for atmospheric research, research weather, satellite tracking, and other scientific fields. After upgrading to the 2012 volume of the data obtained from the complex can be up to 350 Gb/s.

One of the most famous optical foreign project- Sloan Digital Sky Survey (SDSS) – large-scale research project of images and spectra of stars and galaxies. Researches with it began in 2000. Each night the telescope receive

200 GB of data. For work of this project is enough to have a network with a capacity of up to 1 Gb/s.

Most global optical astronomical project that is currently under development, is a project Large Synoptic Survey Telescope (LSST), which is scheduled to launch in 2020. LSST- a new kind of telescope that will use a digital camera with a resolution of 3,200 megapixels. It will take more than 800 panoramic images every night, and also this project will solve the problem of discovering new comets and asteroids. At the moment, it is planned that the flow of data from the telescope will be up to 10 Gb/s.

Next, consider the observatory HIGH Energy Stereoscopic System (HESS), which explores the cosmic gamma radiation. The project was officially launched on September, 28 2004. Stream of data from this telescope is 1.6 Gb/s. Another project that generates large amounts of data, is Murchison Widefield Array (MWA). This radio telescope designed to capture low-frequency radio waves from deep space, as well as for the study of solar radio emission. The generated data telescope data stream is more than 19 Gb/s.

Observatory Atacama Cosmology Telescope (ACT) serves mainly to study the cosmic microwave background radiation. After upgrading to the 2008 data stream is 230 gigabytes per day.

Despite the fact that not all networks can provide maximum transmission of the generated amount of data, research scientists can look with optimism to the future. For example, an international team of physicists, working under the guidance of experts from the California Institute of Technology, has forwarded the data at record speed – 339 gigabits per second. A huge amount of data has been sent to the channel connecting the Canadian Victoria and Salt Lake City, the researchers reported at the show Super Computing 2012. At the same time been set yet another record – the speed bi-directional communication over a single "core" has reached 187 Gb/s. Also recently, a group of scientists from the University of Southampton has created optical fiber with ultra-thin glass membrane, capable of transmitting a wide range of wavelengths with high speed. With this technology, large volumes of information can be transmitted at a rate of 99.7% of the velocity of light. British record – 73.7 terabits per second (distance was 310 meters). This is 15 000 times faster than with conventional hollow fiber.

Thus, new technologies and solutions in the near future will pass on the local network received large amounts of astronomical and astrophysical information projects that will significantly improve the efficiency of its processing.

MODULAR DATA CENTER FOR SCIENTIFIC DATA PROCESSING

E.A.Isaev^{1,2,3}, S.V.Lusakov², M.B.Amzarakov², R.R.Suhov², K.A.Isaev³

¹ Pushchino Radio Astronomy Observatory ASC LPI, Pushchino, Russia, *is@itaec.ru*

² National research university Higher school of economics, Moscow, Russia

³ Itaec, Pushchino, Russia

ABSTRACT. In mid-2000 there were the first mobile (containerized) data centers. The need to rapidly deliver IT infrastructure was partly satisfied by similar solutions. Stage by stage growth was implemented into a classical data centers even earlier. Modular data center brought together the benefits of mobility and maximum flexibility in the stage by stage of capacity growth. In this paper, shows the specificity of modular processing centers of scientific data and provides relevant examples of such data centers.

Key words: mobile data center.

Data centers are separate buildings with special equipment in the form of servers, networking devices and elements of uninterrupted and an independent power supply. The functional purpose of the data center is already clear from the title; they provide storage, transmission and processing of data for one or more elements and allow users to ensure the safety and integrity of data insertion. Data centers are very popular not only in the scientific community, and their services are in the same organization with extensive customer bases, as well as organizations that need to file storage with a high degree of security, in this case provides allocated space, maintenance of communication link, power supply, cooling and safety systems and the user creates a personal data center within that space. Despite a lot of positive aspects, the data center has one big disadvantage, which is short-lived. The development of information technology has a very high and ever-increasing speed, which leads to the rapid obsolescence of technical equipment data center. For example, a personal computer, purchased at a fixed price in a year significantly loses competitiveness in comparison with more modern, similar models. And if for a single PC, this loss seems insignificant, the scale data center performance decrease obviously. According to the most optimistic calculations fully formed center is able to be relevant on the market just for 3 years; this will not include the time it takes for building, equipping and setting up the equipment. Therefore, in the middle of the 2000s put into production, the so-called modular or mobile data center (MDC).

The main difference between the modular data center to data center is easiness and fast speed of installation and configuration of the necessary equipment. Average values for modular data centers show that the cost of the initial

installation is reduced by 13%, and deployment time by 60%. All of this is due to the fact that the MDC is the main frame that is not monolithic building that requires a great effort on the construction and design consisting of sandwich panels. To organize such a structure you do not need a lot of space, and the internal equipment is completely determined by the customer and can be scaled according to high requirements (with the same ease can be made and the reduction of production capacity). Modular data centers can be easily disassembled and transported, if necessary, to a new place and just as quickly starts to work.

Despite the fact that the various firms assemble their data centers in different configurations, the basic structural components remain unchanged. Container internal construction worker protection from the external environment is created from a wide range of materials and allows, within certain limits to vary the size of the container desired. The container can be installed on almost any surface topography due to adjustable racks. Such a solution cannot build a special area for placing mobile data center to install enough hard surfaces - asphalt or concrete. Placed inside the container stands for the installation of IT equipment. The number, height and overall size of racks completely by dimensions of the container. The power supply system includes all the wiring electricity network in the container - the main switchboard, power sources, uninterruptible power supply (UPS) and battery. If necessary, you can install an additional diesel generator to power the equipment in the event of failure of the primary network and the lack of power of the main unit. The complex also comprises a fuel system providing fuel generators, and a system to exhaust. The air conditioning system includes indoor and outdoor units of air conditioners with air heating systems, autonomous heating the condensate drain from air conditioners, excluding the possibility of freezing, and the protection of outdoor units from vandalism and accidental damage. Remote monitoring system enables real-time control of more than 100 environmental parameters and the state of MDC, such as temperature, humidity, state power and the status of the access control system. The cable system consisting of copper and fiber optic communications provides the versatility and flexibility when connecting and reconnecting equipment racks. All cables are routed in accessible troughs, making it easy to

diagnose and repair as necessary. It is also an integral part of the data center is the automatic fire extinguishing system, which provides safe extinguishing fires in case of emergency situations.

Step by step the mobile data centers are becoming increasingly popular. In 2011, their number in Russia was about 10. Over the years, the demand from the oil and gas industry, metallurgical and energy industries, industrial enterprises. Among the factors of growth in demand for mobile data center analyst firm J'son & Partners (J & P) refers to an increase in Internet traffic, the importance of continuous operation of Internet applications and integration with the global economy. Despite the small demand for the MDC in 2011, some of integrators in Russia continued to work on technological solutions in this area. It is companies such as Stack Group, offering a mobile solution Stack.Kub, "IT", "Radius VIP" and "Sitronics IT" and "Technoserv A/C". A number of projects in this direction was at such companies as "Cherus" and "Envision Group".

For example, a feature of the project was the ability to create Stack.Kub MDC both indoors and in the open space. Time of this data center indefinitely- some resources can be replaced on the fly, without stopping in the provision of services. Minimum set to create a data center includes a module size of $24 \times 6 \times 7$ cubic meters, which includes the server room, air locks and air cooling systems.

In the first quarter of 2013 a modular data center is the new generation was launched in Pushchino (Moscow region) to 150 racks with a load of 10 kW per rack. Capacities are commissioned as needed, allowing you to receive a return on investment almost immediately, and the modernization of the infrastructure for the new tasks carried out by a given deadline and without interruption in access to services already provided. The total power consumption of 2.5 MW, of which the equipment customers – 1.5 MW. Fault protection is provided in the power supply modular UPS with a total capacity of 1.5 MW, as well as backup power supply capacity of 3,000 kVA. Due to the specific technology Stack.KUB every 25 racks with 100 MDC comparable average data center racks or stationary container type.

In conclusion, I would say that the modular data centers occupy a special position among data centers, similar to that previously held the position of laptops desktops. Time has shown that often the mobility and ease of installation is more important than power.

Furthermore, the development of modern technology has led to the fact that a large number of current notebooks in its production capacity reached almost the same capabilities of modern personal computers, which means that over time, modular data centers will be comparable in strength to the stationary, while all the way is having its advantages in the form of constant mobility, easy upgrades and speed of installation.

NEW SKILLS OF RADIO ASTRONOMY DATA CENTER (RADC) AT PRAO ASC LPI

V.A.Samodurov^{1,2}, M.A.Kitaeva¹, E.A.Isaev^{1,2}, D.V.Dumsky¹, V.D.Pugachev¹,
S.V.Logvinenko¹, A.U.Zaitsev¹

¹ Pushchino Radio Astronomy Observatory ASC LPI, Pushchino, Russia

² National research university Higher school of economics, Moscow, Russia
sam@prao.ru

ABSTRACT. Now a day the task of comparative analysis of sample sources from different astronomical catalogs is becoming very topical for astronomers. It is useful both for the same spectral range data and for their cross-analysis for different spectral ranges. It is also important, that the real data from astronomical instruments is placed on-line. For the above purposes we are developing a website for the PRAO ASC LPI (www.prao.ru) and, based upon it, the Radio Astronomy Data Center (RADC). The RADC is a system for storage and processing of radio astronomical data. Here you can find a collection of tools for preparing radio astronomical observations, which includes a base set of main astronomical catalogues useful to radio astronomers, as well as a database of observation results from the Observatory.

Key words: radio survey, catalogues, database

The Radio Astronomy Data Center (RADC) at last three year was created and developed at PRAO of LPI. RADS consists of:

- a) a database of celestial sources on the basis of the most important astronomical catalogs;
- b) a base of observation data of Pushchino radio astronomy observatory.

The Astronomical Catalog Database <http://astro.prao.ru/db/> contains a most important astronomical catalogs which are necessary for planning of observations. Since 2011 a database of astronomical catalogs actively equipped with graphical tools for data visualization and cross-analysis of catalogues between one with other. The base of observation data of observatory <http://observations.prao.ru/> continuously gets results from the majority of observational devices and radio telescopes PRAO. This database provides access to observation instruments and telescopes descriptions, techniques of making data samples per instruments, information about types of observations, observers and dates of observations and so on. The database contains information about more than 270 thousands of files of the observational data of PRAO ASC LPI radio telescopes since 1981. The total amount of information is about one terabyte.

At present the database contains pulsar data (more than 131 thousand profiles for more than three hundred pulsars

for the last 7 years), spectral data for more than hundreds of space masers (for a number of them in the database are stored perennial series data since 1981) and the data of radio all-sky surveys on 102.5 and 111 MHz.

From the middle of 2013 the database gets the most volume observation data from the third 128-beam diagram of BSA (it is developed in 2011). The total size of the data is more than 680 Gb at the beginning of August, 2013.

The total flow of data, daily saved and described in the database of Observatory, has reached more than 2.2 Gb per day. All databases of observatory work under control of Postgresql and are written into special storage of data RAID-array with a general capacity of 24 Terabytes.

Database of astronomical catalogs

In order to support and preparation of the observations on the website PRAO the site "Working environment of the radio astronomer" <http://astro.prao.ru/> is created. The database of astronomical catalogs at PRAO ASC LPI site (<http://astro.prao.ru/db/>) is one of the part of this work space. This database contains the most important catalogs with common record count nearly 1,500,000 of sources.

Programs of filling of data base catalogs allow to expand the list of necessary catalogs easily at any time. Programs of data selection on any parameters of any catalog work for all catalogs. It allows to conduct statistics of data on the chosen parameters and to prepare selections of data for observations.

Thus for each catalog two versions of a request form are given: simple and complex. In a simple form the most important parameters of sources (for example, coordinates and fluxes) with already entered borders on them are automatically entered. Therefore it is enough to press the button «Select data» and all catalogs completely, with these basic parameters for each source, will be output. The complex form allows to select any source parameters (shown in the description of the catalog), and the necessary restrictions on them.

The database contains now several major astronomical catalogs, which are necessary for planning of observations of radio astronomers. The database is consisted from several summary tables of astronomical catalogs and the

some descriptions of the actual catalog tables. The adding of catalogs and dates in catalog tables and its maintenance is done by special programs written in Perl and PHP. Since 2011 a database of astronomical catalogs actively equipped with graphical tools for data visualization and cross-analysis of catalogues between one with other. This will allow us to produce statistical and cross-sectional analysis for various astronomical catalogs. So, catalogues of radio sources at different frequencies can be widely used in further theoretical and experimental research of the properties of extragalactic radio sources and objects of our Galaxy.

The statistical cross-analysis of these various catalogs is suitable for research of properties of separate objects, and for the statistical analysis of properties of various classes of objects, and for research of properties of catalog data (completeness, reliability, calibration of catalogs, etc.).

For the tasks we develop a facility to display the data by graphic tools (generally through the PHP language) both one and a few catalogues within a chosen area in the sky; to display of data and statistical analysis of main parameters of each catalogue as a whole; to show statistics of cross-identifications of the catalogs chosen by the user.

At present already works the system of automatic mapping for 50 thousand the brightest sources for each catalog. Fluxes of all sources are divided on a logarithmic scale of fluxes on 6 equal "stellar magnitude". Such general mapping of catalogs gives a simple, but very effective instrument of visual quality control of completeness of catalog data and possibility of rough comparison of populations of sources in different catalogs. On each of these catalogs it is possible to look at maps on our site of catalogs, under "map" links. It is interesting that on these maps difficulties in processing of each of catalogs are well shown also. For example, for the catalog on 1400 MHz [3] difficulties of processing of brighter (right) part of a area of the Milky Way become insuperable. As result we can see a gap in the catalog on this place.

Thus it is well traced weaker (and therefore easier for processing) the left part of the Milky Way, being traced by bright sources. As we can see, even a fluent comparative analysis of common graphical data for each catalog can provide food for thought and an evaluation of the quality of the catalog data.

Cross-identification and joint data visualization of several catalogs.

For more complex tasks we develop tools of the graphic cross-analysis of catalog data. By means of these tools will be displayed some catalogs within a chosen platform in the sky; will be generated the statistics of cross-identifications of the catalogs chosen by the user, etc.

In fig. 1 – an example of imposing of three catalogs within the chosen area: 4C [2] (178 MHz, green crosses) and catalogs on 1400 MHz [1] (pink circles) and 4850 MHz [3] (blue crosses). Avoiding of catalog data from high-frequency catalogs round a bright source from 4C of the catalog (3C144 – in the center) is noticeable.

It is obvious that such evident check of coincidence of sources of different catalogs gives a reliable and simple way of the analysis of catalog data. The most promising

part of work which is done while only out of a database of catalogs: flux identification of sources in various catalogs about mutual completeness of catalogs, the analysis of various selections of sources, the spectral indexes determined by various couples of the catalogs etc. Already fulfilled algorithms now are transferred under a database. That will allow to take a considerable step forward in development of the comparative statistical analysis of various radio-astronomical catalogs (and further - catalogs of astronomical objects in other spectral ranges), and in the on-line mode. Similar technologies is used in the world still slightly.

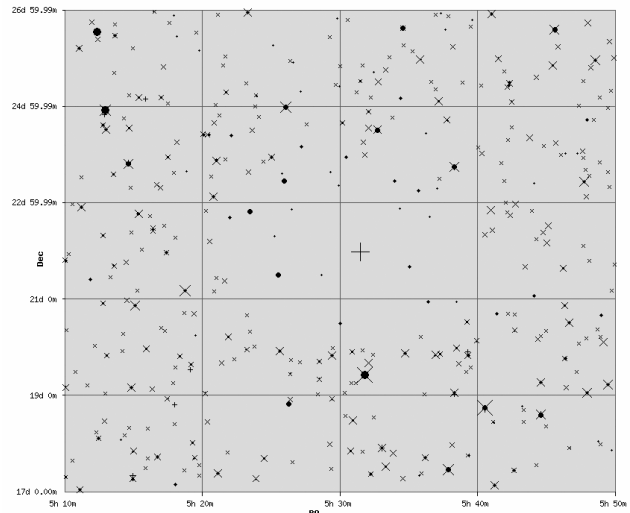


Figure 1: Example of the comparative analysis of the data field for 3 catalogs.

Database of observation results

After preparation of observations and forming observations schedule this observations are carried out at different PRAO ASC LPI radio telescopes. And we have quite differently data as results of this observation: pulsar, survey, observations of scintillate sources, spectral observation and other. The common database of radio sources observations at PRAO ASC LPI (meter and millimeter radio wavelength spectral diapason) was created for systematization and analysis of observation data. By this database of the site "Electronic database of observation results from radio telescopes of PRAO ASC LPI" was launched in 2006 year: <http://observations.prao.ru/>.

This database provides access to observation instruments and telescopes descriptions, techniques of making data samples per instruments, information about types of observations, observers, dates of observations and so on. For example, it is possible to view all data for the last few days or view changes of single chosen source. With the help of data analysis we can calibrate received signal from standard sources, monitoring states of antennas and noise level and levels of interference and so on. Below we propose to consider examples of the most common at the Observatory observations.

Pulsar observations

Currently, the database contains observational data for more than 300 pulsars, 131 thousand profiles of pulsars since the end 2006 on the end of March, 2013. Thus it is

possible to see both changes of profiles of a concrete pulsar day after day, and schedules of changes of brightness of a pulsar (measured in relation units signal/noise). It is noticeable that various pulsars possess a different behavior for all the time of observations: some practically don't change the brightness, in behavior of others seasonal (?) changes and even long-term trends are traced. All these changes are apparently partially connected with a condition of the effective area, partially reflect changes in the interstellar environment (long-period blinking, etc.). The part from them, probably, reflects a physical condition of the pulsar. These effects demand further studying and division into the specified components.

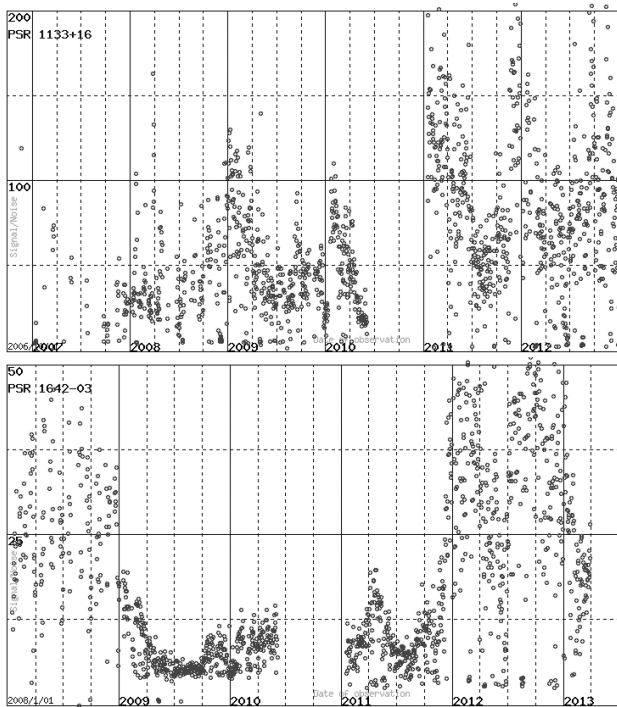


Figure 2 a,b: The signal/noise ratio for PSR 1133+16 (upper) and for PSR 1642-03 (bottom) in 2007-2013.

On the figure 2 a,b are graphs of the signal/noise ratio for PSR 1133+16 and for PSR 1642-03. For these pulsars systematization of changes is observed. Here are probable as the seasonal changes generated by change of characteristics of the antenna, as well as real changes in pulsars or in the environment of distribution of signals from them. There is evidence of the similarity of the changes some times, but identity isn't quite obvious. For PSR 1642-03 to appear there are considerable long-term changes of brightness between two levels.

The maser observations in water vapor line at 22 GHz

Similar long-term changes can be easily obtained from databases and for other types of sources. From 2009 observational database was supplemented by cosmic masers many years data (Fig. 5). The majority of the water maser sources (at 22 GHz) introduced its data for 1994-2010, but some sources - observations there are since 1981.

In 2010, the possibility of a database on data output and analysis of observations of the maser sources have been expanded (the new version of the database is located at <http://observations.prao.ru/cgi/new/index.pl> Now it is

possible to output summary information of a set of parameters depending on time on each of sources. Below we can see an example of such analysis for one of sources – W Hya. Because of the low situation in the sky ($\alpha_{1950} = 13\text{h } 46\text{m } 12\text{s}$ $\delta_{1950} = -28^\circ 7' 9''$) this source is very low and inconvenient for observation in middle latitudes. The height of the source of the close horizon, weather, and, of course, the condition of receiving equipment affect on measurements of the flux density of this source. All of this is clearly seen in figure 3 a,b where showed parameters of several observation sessions of this source in the April 2010.

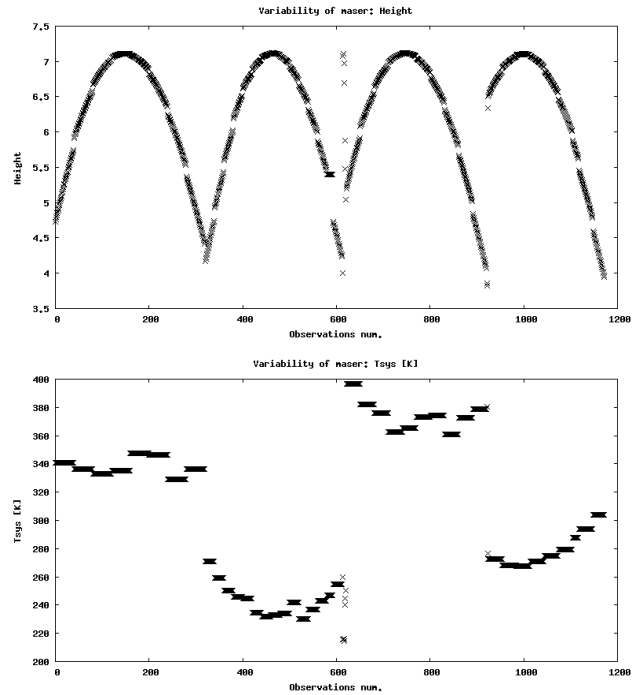


Figure 3 a,b: The statistic of 4 observational sessions of source W Hya:

- a) (upper) Dependence of the height of the source above the horizon from file number in April, 2010.
- b) (bottom) Dependence of T_{sys} from file number in April, 2010. It is well visible that in T_{sys} is lower, when source above.

The multi-beam survey observations of the northern hemisphere of the sky at 110 MHz with LPI's BSA.

PRAO ASC LPI has several world class radio telescopes. One of them is the Big Scanning Antenna (BSA). The BSA Radio Telescope is a phased array comprising 16384 dipoles and covering an area of 384x187 m (geometrical area is more than 70,000 m²; effective area of about 30,000 m²). The BSA's operating frequency is 109-112 MHz (since 1996 and 101-104 MHz pre-1996) and it is most sensitive telescope of this range in the world, as well as one of the most sensitive in the world in the meter wave band. The most important feature of the BSA is that it works in full-power receiving mode. It allows us to detect, besides discrete radio sources, the background radiation of our Galaxy and extended radio sources (with a typical size of up to 2-3 degrees). Another important feature of the BSA is that was originally designed with possibility to generate a multi-beam pattern. Until 2007 the

polar pattern of the BSA consisted of 16 beams, then a second, independent 16-beam chart was created. Finally, in 2010-11 a third beam former system was developed.

The new beam former system forms a 128-beam pattern with a field-of-view of 500 square degrees and requires a multi-channel registration system. Data channels from this multi-beam pattern are equipped by receivers in some stages. The first 48 beams were equipped with multi-beam receivers conducting 24/7 data recording since July 7 2012 (fig 4 a,b,c). Since April 1 2013 data is being recorded from 96 beams in the $-8^{\circ} < \delta < +43^{\circ}$ declination sector.

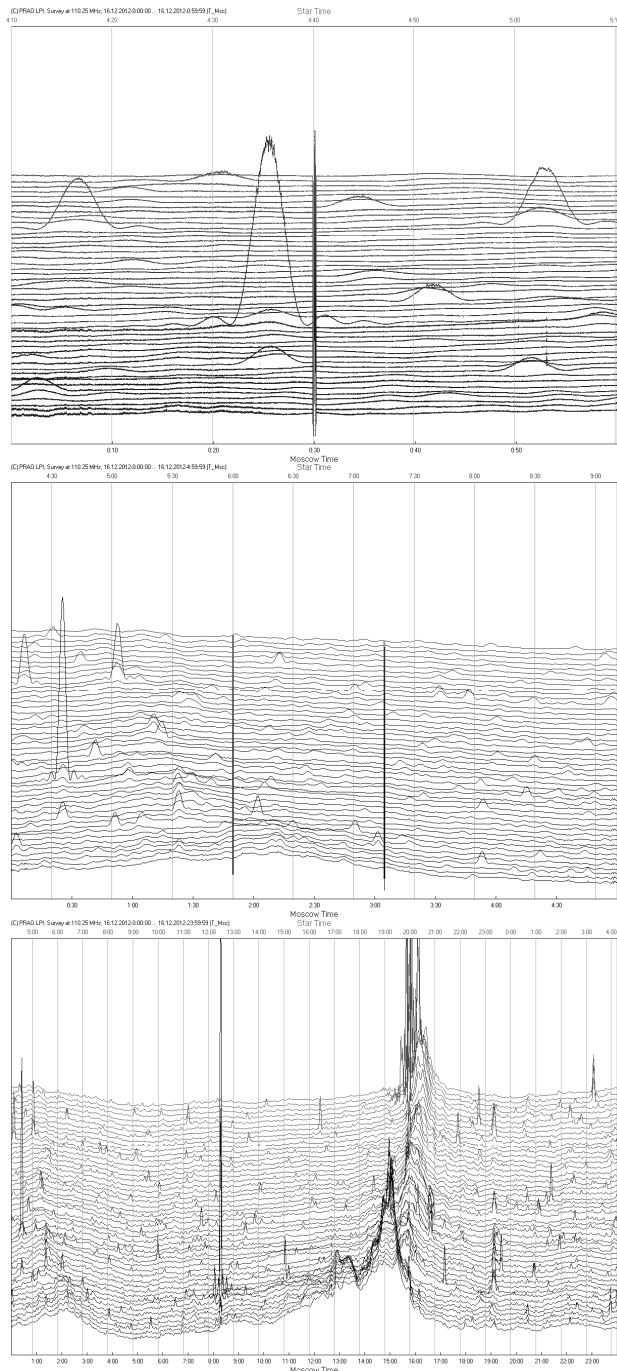


Figure 4 a,b,c: displayed observational dates for 1 hour observations (upper), 5 hour (middle) and day and night (bottom) observations.

Each of the 96 registered beams from BSA's third pattern captures data in 6 channels, 0.42 MHz wide, from 109 to 111 MHz with time resolution of 0.1 second. Each hour two 46 MB files are generated containing 48 channels from different beams. As a result 2.2 GB of data is generated every day. On fig. 4 a,b,c displayed examples 1 hour observations, 5 hour and day and night observations. We may look that dates have good and stable quality.

Additionally, test observations with time resolution of 0.02 s and 32 channel resolution (78 kHz per channel) have been conducted successfully. Daily volume of data generated by these observations was 55 GB. In 2014 all 128 channels will be operational. The 2nd radiation pattern is currently still active and is covering the $+49.1^{\circ} < \delta < +55.2^{\circ}$ declination sector.

As a result, scientific installations that are connected to all the diagrams of the BSA send enormous amounts of information. The volume of data from the 3rd multibeam diagram of the BSA from August 2013 has already reached 680 GB. This data presents huge resources for short and long term monitoring of various classes of radio sources (including transients), as well as observing space weather, Earth's ionosphere conditions, discovery of new radio sources etc. Currently a database is being developed for these type of observations. This database will feature an on-line graphical interface that will display current states of the BSA antenna, radio sky in the 109-111 MHz frequency band, currently monitored radio sources and more. Commissioning of functionality for full-time data output onto the PRAO ASC LPI website is planned for the end of 2013.

In view of the colossal volumes, the data requires new methods of processing. We are planning to integrate the use of supercomputers as well as distributed client network computing on the basis of BOINC technology.

Perspective applications of the database and new processing methods:

- Space weather – determining scintillation indexes of hundreds of radio sources on the scale of days and months
- Compilation of a catalogue of about 10,000 scintillation sources in our survey
- Monitoring of changes in flux of hundreds and thousands of sources
- Search for pulsars
- Search for radio transients
- And many others...

We also very hope on a possible co-operation and exchange of science dates with the Ukrainian radio astronomers working on the survey programs by radio decameter radio telescope UTR near Kharkov.

References

- White R.L., Becker R.H.: 1992, *Astrophys. J. Suppl. Ser.*, **79**, 331.
 Pilkington J.D.H., Scott, P.F.: 1965, *Mem. R. Astron. Soc.*, **69**, 183.
 Gregory P.C., Scott W.K., Douglas K., Condon J.J.: 1996, *Astrophys. J. Suppl. Ser.*, **103**, 4272.

EFFECT OF ROTATION ON CHANGES OF INTERFERENCE FRINGES IN THE MICHELSON INTERFEROMETER

Shahrukhanov O.S.

Astronomical Observatory, Odessa National University, Odessa, Ukraine

To perform the work was assembled interferometer with a rigid skeleton shoulders, made of pipes with the outside diameter of 22 mm and a wall thickness of 3 mm with platforms to mount the mirror. Tube covered with insulating layer porous plastic. The device builds on the basis of the optical bench with rubber tabs to eliminate the vibrations. A rotating disk drive attached to the ceiling of the laboratory suspensions, rubber-to eliminate the effect of mechanical vibrations on the interferometer. Scheme of the interferometer is depicted below (Fig. 1).

disk size: inside diameter of 11.5 cm, outer diameter 16 cm, weight 2.5 kg disk Speed 1370 U/ min. Used helium-neon laser with a wavelength of radiation 6328 Å. As a disk drive used engine manifold P = 30W speed 6300 U/min. To measure displacement of interference fringes used a stencil repeating the curvature of the interference lines.

Below is a table of displacement of interference fringes in two successive runs of a disk. During acceleration and braking measured. Photographing interferograms was conducted with an average interval of 10 seconds between shots. Measurements were carried out on photos using a stencil.

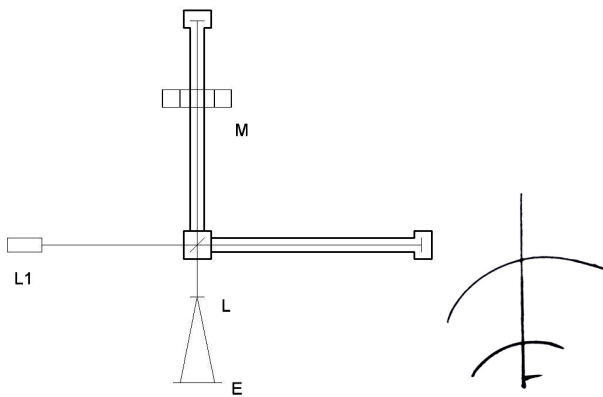


Figure 1.

Legend elements: L1- laser, E – screen, L – focusing lens, M – a rotating disk. The length of the shoulder is 87 cm. Hard

	First run		Second run	
0	1,7 mm	1,6 mm	2,3 mm	2,6 mm
0	2,0 mm	1,6 mm	2,7 mm	2,7 mm
0	2,0 mm	1,6 mm	2,7 mm	2,6 mm
	2,0 mm		2,7 mm	
			2,7 mm	

The graph (Fig. 2) shows the offset bands when turning the disk.

It is intended to further the development of devices and units to obtain more precise values for the clarification of the causes of the phenomenon. This development is preliminary and does not possess sufficiently broad capabilities for accurate measurements.

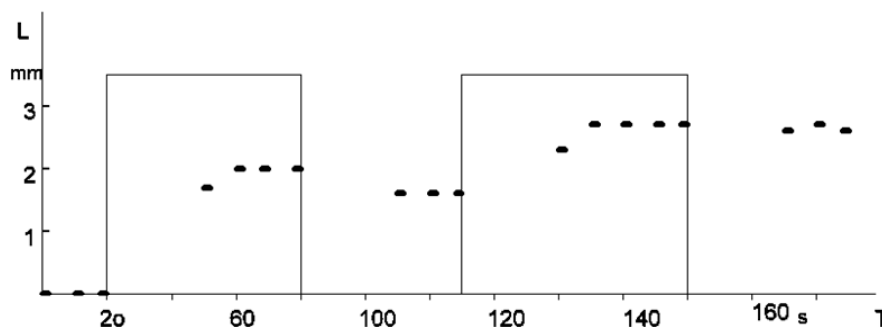


Figure 2.

Наукове видання

Одеські Астрономічні Публікації

том 26 випуск 2 (2013)

Англійською мовою

Зав. редакцією *Т. М. Забанова*
Технічний редактор *В. В. Ковтюх*
Комп'ютерна верстка *С. Л. Страхова*

Підписано до друку **04.11.12.**
Формат 60x84/8. Папір офсетний. Гарнітура «Times». Друк офсетний.
Ум. друк. арк. 20,9. Тираж 300 прим. Зам. № 772.

Видавництво і друкарня «Астропринт»
65091, м. Одеса, вул. Разумовська, 21.
Тел.: (0482) 37-07-95, 37-14-25, 33-07-17
www.astroprint.odessa.ua
Свідоцтво суб'єкта видавничої справи ДК №1373 від 28.05.2003 р.